Shashank Priya · Sahn Nahm *Editors*

Lead-Free Piezoelectrics

Springer

Lead-Free Piezoelectrics

Shashank Priya • Sahn Nahm
Editors

Lead-Free Piezoelectrics

Springer

Editors
Shashank Priya
Department of Mechanical Engineering
Virginia Tech
Blackburg, VA 24061, USA
spriya@vt.edu

Sahn Nahm
Korea University
Anam-dong 5-1
136-701 Seoul
Korea, Republic of (South Korea)
snahm@korea.ac.kr

ISBN 978-1-4419-9597-1 e-ISBN 978-1-4419-9598-8
DOI 10.1007/978-1-4419-9598-8
Springer New York Dordrecht Heidelberg London

Library of Congress Control Number: 2011940129

© Springer Science+Business Media, LLC 2012
All rights reserved. This work may not be translated or copied in whole or in part without the written permission of the publisher (Springer Science+Business Media, LLC, 233 Spring Street, New York, NY 10013, USA), except for brief excerpts in connection with reviews or scholarly analysis. Use in connection with any form of information storage and retrieval, electronic adaptation, computer software, or by similar or dissimilar methodology now known or hereafter developed is forbidden.
The use in this publication of trade names, trademarks, service marks, and similar terms, even if they are not identified as such, is not to be taken as an expression of opinion as to whether or not they are subject to proprietary rights.

Printed on acid-free paper

Springer is part of Springer Science+Business Media (www.springer.com)

Preface

Piezoelectric materials form the backbone of several components utilized in communication systems, defense systems, industrial automation, medical diagnostics, energy storage and harvesting, and information technology. In high performance piezoelectric applications the material of choice is based upon lead-based composition with $Pb(Zr,Ti)O_3$ (PZT) being the base. Recently worldwide environmental considerations are demanding the elimination of lead-based materials from all the consumer items. This has created urgency for finding alternative to PZT. Elimination of lead in applications such as actuators still remains a challenge but in some other applications such as high frequency electronic components it has been possible to utilize lead-free materials. At a recent Electronic Materials and Applications 2011 meeting, a group discussion was held on the topic of lead-free materials under the umbrella of National Science Foundation. Few important points agreed upon at this discussion were: (1) development of lead-free materials should be application specific, (2) emphasis should also be on design-based research in addition to discovery-based research, and (3) a compilation of all the results on important family of lead-free materials is needed. Further, the group identified the need for lead-free materials from Wikipedia. These recommendations were guiding factors in the arrangement of chapters in this book. All the important families of lead-free materials were addressed and each part/chapter provides relevant data for a given family.

The book is addressed to students, researchers, application engineers, educators, developers, and producers of piezoelectric materials and applications. The chapters mainly consist of technical reviews, discussions, and basic knowledge in the design, synthesis, and microstructure characterization of lead-free piezoelectric materials. The book brings the leading researchers from academia and industry in the world in the field of piezoelectric materials and applications on to one platform to provide a comprehensive overview of the fundamentals and developments. All the important classes of lead-free piezoelectric materials were addressed by the leading authors. Furthermore, the book covers the principles and design rules of the lead-free materials in depth. The chapters on applications of the lead-free materials will allow readers to conceptualize the promise of the field.

The first part in the book provides discussions on domain engineering and phase transformations covering the role of morphotropic phase boundary, electric-field induced phase transition, intermediate bridging phases, polarization rotation and adaptive phase theory, polymorphic phase boundary, and grain texturing. The second part covers the history, progress and current status of alkali niobate ceramics covering random polycrystalline ceramics, textured ceramics, and single crystals. The third part covers the progress made in synthesis and characterization of sodium bismuth titanate-based ceramics. The fourth part covers the fundamentals and properties of bismuth-layered structures. Thus, Parts II–IV provide in-depth coverage of the important lead-free materials. Last part provides an overview on the application of lead-free materials and their role in the emerging topic of magnetoelectrics.

The chapters published here are mostly the invited technical submissions from the authors. The editors did not make any judgment on the quality and organization of the text in the chapters and it was mostly left to the decision of the authors. In this regard, the editors do not accept the responsibility for any technical errors present in the chapters and those should be directly discussed with the authors of the relevant chapter.

It was an honor editing this book consisting of contributions from knowledgeable and generous colleagues. Thanks to all the authors for their timely assistance and cooperation during the course of this book. Without their continual support, this work would not have been possible. We hope that readers will find the book informative and instructive and provide suggestions and comments to further improve the text in eventual second edition.

Blackburg, VA, USA Shashank Priya

Contents

Part I Domain Engineering and Phase Transformations

1 Domain Engineering and Phase Transformations 3
Wenwei Ge, Jiefang Li, and D. Viehland

2 Ferroelectric Domains and Grain Engineering in $SrBi_2Ta_2O_9$ 53
H. Amorin, I. Coondoo, M.E.V. Costa, and A.L. Kholkin

Part II Alkali: Niobate-Based Ceramics

3 Development of KNN-Based Piezoelectric Materials 89
Shashaank Gupta, Deepam Maurya, Yongke Yan, and Shashank Priya

4 Low Temperature Sintering of the Alkali-Niobate Ceramics 121
Hwi-Yeol Park and Sahn Nahm

5 Lead-Free KNN-Based Piezoelectric Materials 139
Ahmad Safari and Mehdi Hejazi

6 Alkali Niobate Piezoelectric Ceramics 177
Akira Ando

7 Influence of the A/B Stoichiometry on Defect Structure, Sintering, and Microstructure in Undoped and Cu-Doped KNN 209
Michael J. Hoffmann, Hans Kungl, Jérôme Acker, Christian Elsässer, Sabine Körbel, Pavel Marton, Rüdiger-A. Eichel, Ebru Erünal, and Peter Jakes

Part III Sodium Bismuth Titanate-Based Ceramics

8 Sodium Bismuth Titanate-Based Ceramics 255
Tadashi Takenaka and Hajime Nagata

9 Perovskite Lead-Free Piezoelectric Ceramics 291
Hyeong Jae Lee and Shujun Zhang

10 Processing and Properties of Textured BNT-Based Piezoelectrics 311
Toshihiko Tani and Toshio Kimura

11 Crystal Growth and Electric Properties of $Na_{0.5}Bi_{0.5}TiO_3$-$BaTiO_3$ Single Crystals 337
Qinhui Zhang, Xiangyong Zhao, and Haosu Luo

12 Nonstoichiometry in $(Bi_{0.5}Na_{0.5})TiO_3$ Ceramics 353
Yeon Soo Sung and Myong Ho Kim

Part IV Bismuth Layer Structured Ferroelectric

13 Resonator Characteristics of Bismuth Layer Structured Ferroelectric Materials 373
Akira Ando and Masahiko Kimura

14 Defect Control and Properties in Bismuth Layer Structured Ferroelectric Single Crystals 405
Yuji Noguchi and Masaru Miyayama

15 Processing and Properties of Textured Bismuth Layer-Structured Ferroelectrics 461
Toshio Kimura and Toshihiko Tani

Part V Applications

16 Self-Biased Lead-Free Magnetoelectric Laminates 487
Su-Chul Yang and Shashank Priya

17 Applications of Lead-Free Piezoelectrics 511
Kenji Uchino

Part I
Domain Engineering and Phase Transformations

Chapter 1
Domain Engineering and Phase Transformations

Wenwei Ge, Jiefang Li, and D. Viehland

1.1 Introduction

1.1.1 Enhanced Piezoelectric Properties by an MPB

Since high piezoelectricity was found in $Pb(Zr_xTi_{1-x})O_3$ or PZT [1], PZT ceramics have become the most successful piezoelectric materials in practical applications over the past 50 years. Currently, PZT materials are widely used in commercial applications such as actuators, transducers, and sensors. This technical dominance results from high longitudinal electromechanical coupling (k_{33}) and piezoelectric d_{33} coefficients, in addition to a composition that is adjustable over a wide range of B-site stoichiometry and substituents. Such adaptability of composition offers capability in property control for a broad range of applications.

PZT ceramics are commonly used with compositions close to a nearly temperature independent morphotropic phase boundary (or MPB) separating tetragonal Ti-rich PZT from rhombohedral Zr-rich PZT, at $\sim x = 0.48PbTiO_3$ (see Fig. 1.1). MPB compositions show enhanced dielectric and piezoelectric properties [2], as shown in Fig. 1.2.

Innovations in actuators, sensors, and ultrasonic transducers have been the driving force for new developments in ultra high piezoelectric materials. The most important advancement in ferroelectric materials during the last decade was the discovery of $Pb(Zn_{1/3}Nb_2/3)O_3$-x%$PbTiO_3$ (PZN-x%PT) and $Pb(Mg_{1/3}Nb_{2/3})O_3$-x%$PbTiO_3$ (PMN-x%PT) single crystals [3]. Similar to PZT, rhombohedral and tetragonal MPB were also found for PZN-x%PT and PMN-x%PT at composition of $x = 9$–10.5 [4, 5] and 30–37 [6–8] or 35 [9, 10], as shown in Figs. 1.3 and 1.4.

When poled along a nonspontaneous <001> direction, an ultra-high piezoelectric coefficient d_{33} of 2,500 pC/N and electromechanical coupling coefficient k_{33} of

W. Ge (✉) • J. Li • D. Viehland (✉)
Department of Materials Science and Engineering, Virginia Tech, Blacksburg, VA 24061, USA
e-mail: wenweige@vt.edu; viehland@mse.vt.edu

S. Priya and S. Nahm (eds.), *Lead-Free Piezoelectrics*,
DOI 10.1007/978-1-4419-9598-8_1, © Springer Science+Business Media, LLC 2012

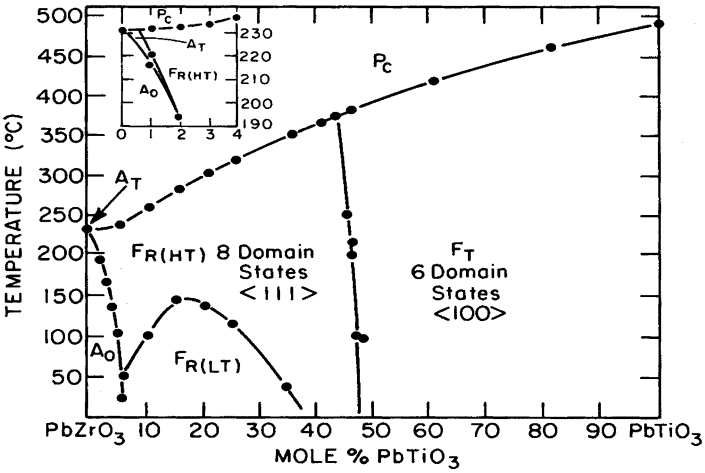

Lead zirconate titanate phase diagram.

Fig. 1.1 PZT phase diagram after Jaffe et al. Reprinted with permission from [1]. Copyright [1971], Elsevier

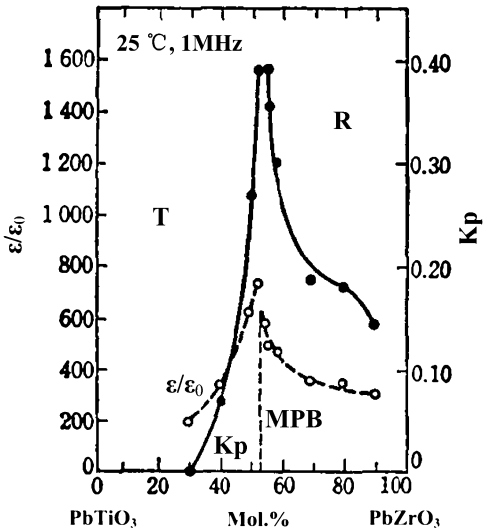

Fig. 1.2 Enhanced dielectric and piezoelectric properties in PZT after Berlincourt et al. Reprinted with permission from [2]. Copyright [1971], Springer

94% have been reported in PZN-PT or PMN-PT single crystals for compositions near the MPB, as shown in Figs. 1.5 and 1.6 [3, 10]. A domain-engineered state, due to an electric field (*E*-field) induced rhomobohedral-to-tetragonal phase transition, was originally proposed by Park and Shrout to explain the ultra-high electromechanical properties. Strain as high as 1.7% has been realized as a result of this

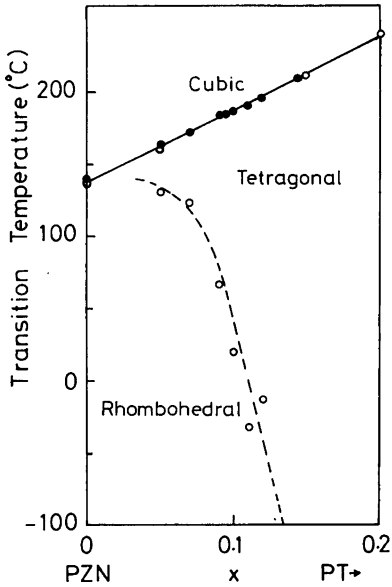

Fig. 1.3 Phase diagram of $Pb(Zn_{1/3}Nb_2/3)O_3$-$xPbTiO_3$ system near MPB. Reprinted with permission from [4]. Copyright [1981], Taylor & Francis

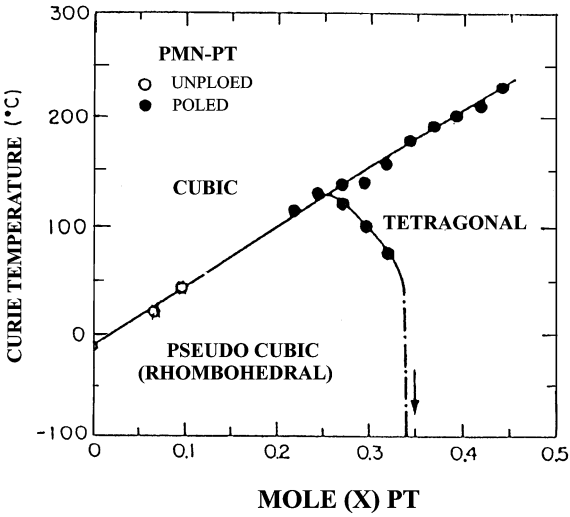

Fig. 1.4 Phase diagram of $Pb(Mg_{1/3}Nb_2/3)O_3$-$xPbTiO_3$ system near MPB. Reprinted with permission from [6]. Copyright [1989], Elsevier

E-field induced transition (Fig. 1.7) [3]. This property is considered to be an exciting breakthrough as improvements by a factor of 10 than PZT ceramics which are not easy to come by in a field that is 50 years old and considered mature [11].

It is generally accepted that the enhanced piezoelectric properties near MPB result from enhanced polarizability, arising from the coupling between two equivalent energy states of tetragonal and rhombohedral phases, allowing optimum domain reorientation during the poling process. Landau–Ginsburg–Devonshire

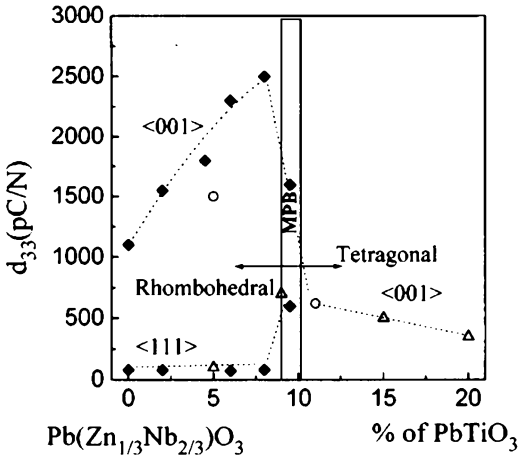

Fig. 1.5 The piezoelectric coefficient d_{33} dependence on PT concentration for PZN-PT. Reprinted with permission from [3]. Copyright [1997], American Institute of Physics

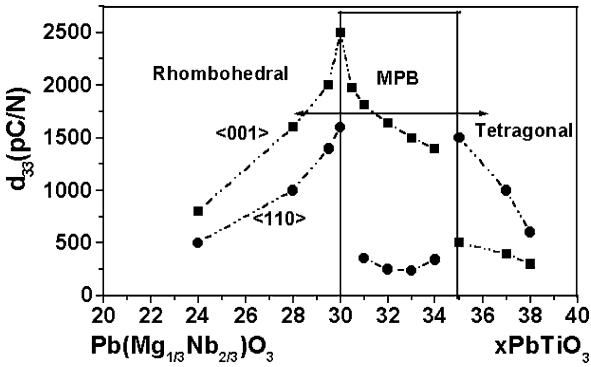

Fig. 1.6 The piezoelectric coefficient d_{33} dependence on PT concentration for PMN-PT. Reprinted with permission from [10]. Copyright [2003], Institute of Physics Publishing Ltd

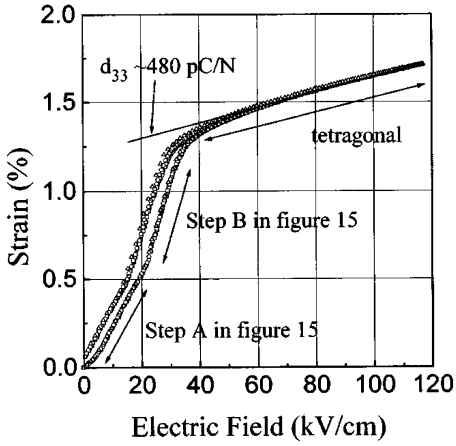

Fig. 1.7 Strain vs. *E*-field behavior for <001> oriented PZN-8%PT crystal. Reprinted with permission from [3]. Copyright [1997], American Institute of Physics

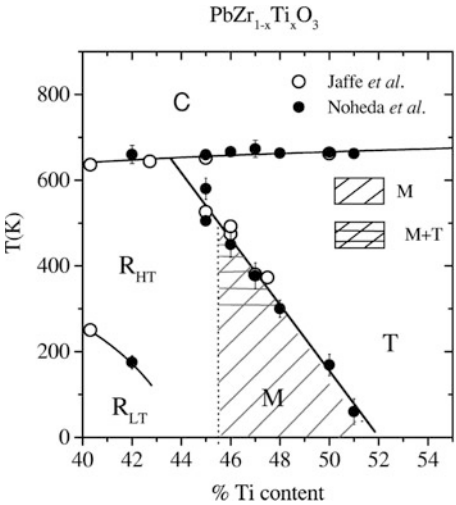

Fig. 1.8 Modified phase diagram of PZT around the MPB. Reprinted with permission from [15]. Copyright [2001] by the American Physical Society

phenomenological theory also suggests that the Gibbs free energy profile is flattened at the MPB [12]. However, since ultra high piezoelectric response was found in PZN-PT single crystals, many efforts have been focused on the physical and structural properties of piezoelectric ceramics and crystals near the MPB composition, and finding out the origin of the excellent electrical–mechanical properties: how the *R* phase transforms into *T* phase under *E*-field.

1.1.2 Discovery of Bridging Monoclinic Phase in PZT Ceramics

In 1999, Noheda first discovered a monoclinic phase, sandwiched between *R* and *T* phases near the MPB in PZT ceramics [13–15]. A revised PZT phase diagram around the MPB is shown in Fig. 1.8 [15]. This discovery completely changed the well-accepted picture of the MPB, since this new phase acts as a structural bridge between the *R* and *T* phases.

At the same time, using a Landau–Devonshire approach, Vanderbilt and Cohen expanded the free energy to the eighth power in the polar order parameter, providing the thermodynamic basis for a monoclinic phase [16, 17]. According to this theory, the direction of the polarization vector in a conventional ferroelectric tetragonal (or rhombohedral) phase is fixed to the [001] (or [111]) direction, while the monoclinic symmetry allows the polarization vector to continuously rotate in a plane and contributes to enhanced polarization and strain. Vanderbilt and Cohen further suggested three monoclinic phases: M_A, M_B, and M_C, according to their symmetry relations with the parent phase, as shown in Fig. 1.9 [16]. The M_A and M_B phases belong to the C_m space group, while M_C belongs to the P_m space group. The M_A unit cell has a unique b_m axis along the [110] direction, and is doubled and rotated 45° about the c-axis, with respect to the pseudocubic cell, whereas, the M_C

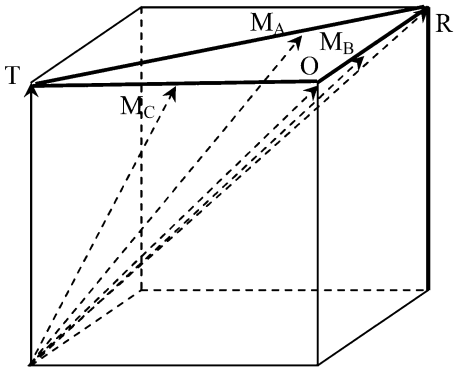

Fig. 1.9 Illustration of rotation of polarization vectors in perovskite unit cells. The *thick lines* represent the paths followed by the end of the polarization vector of rhombohedral (*R*) and tetragonal (*T*), orthorhombic (*O*), and monoclinic M_C, M_A, and M_B phases. The M_A, M_B, and M_C notation is adopted following Vanderbilt and Cohen [16]

unit cell is primitive having a unique b_m axis that is oriented along the pseudocubic [010]. Although both the M_A and M_B phases belong to the C_m space group, the difference lies in the magnitudes of the components of the polarization corresponding to the pseudocubic cell: for the M_A phase, $P_x = P_y < P_z$, whereas for the M_B phase, $P_x = P_y > P_z$.

1.1.3 Phase Stability Dependence of Thermal and Electrical History in PMN-PT Single Crystals

Single crystals provide the opportunity to conveniently investigate the phase transformation sequence under external *E*-field as a function of crystallographic orientations. Diffraction experiments of PZN-*x*%PT [18–23] and PMN-*x*%PT [7, 8, 24–38] single crystals have provided direct evidence of different monoclinic phases existed in both zero-field-cooled (ZFC) and field-cooled samples. A new revised MPB phase diagram for PMN-xPT ceramics in the ZFC condition was reported by Noheda et al. [8] based on high-resolution synchrotron X-ray-diffraction data. This revised phase diagram revealed the presence of an intermediate M_C phase ($0.31 < x < 0.37$), sandwiched between the *R* and *T* phases, as shown in Fig. 1.10 [8].

Systemic X-ray diffraction investigations on PMN-PT single crystals revealed that various intermediate monoclinic (*M*) phases that structurally "bridge" the rhombohedral (*R*) and tetragonal (*T*) ones across the MPB. The phase stability of these *M* phases can be altered by electrical history and by crystallographic direction along which that *E* is applied, as shown in Fig. 1.11. Figure 1.12 shows mesh scans taken around the (200) and (220) for PMN-30%PT when the sample was cooled under $E = 1$ kV/cm applied along [001] direction [29]. For $T = 375$ K, the lattice constant c_T is elongated, whereas a_T is contracted; this indicates phase with tetragonal symmetry. For $T = 350$ K, the (200) reflection was found to split into three peaks, consisting of two (200) peaks and a single (020) peak, whereas, the (220) reflection was found to be split into two peaks. These results indicate a phase

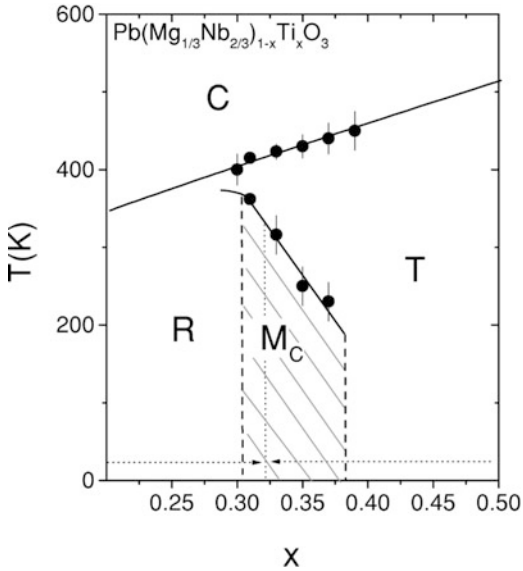

Fig. 1.10 Modified phase diagram of PMN-xPT around the MPB. The symbols separating the M_C and T phases represent the temperatures at which the M_C-T phase transition begins to take place. Reprinted with permission from [8]. Copyright [2002] by the American Physical Society

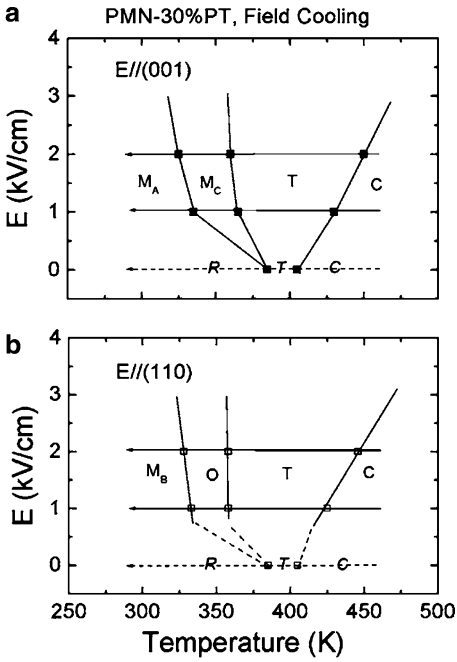

Fig. 1.11 *E-T* phase diagram for PMN-30%PT with *E*//[001] and [110]. *Dotted lines* indicate the ZFC condition, and *solid lines* indicate the FC condition. *Arrows* indicate the sequence of phase transition. Reprinted with permission from [29]. Copyright [2004], American Institute of Physics. Reprinted with permission from [31]. Copyright [2005] by the American Physical Society

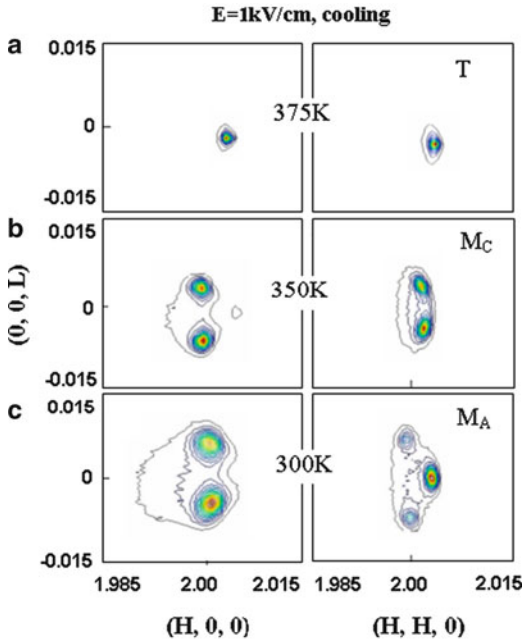

Fig. 1.12 Mesh scans taken around (200) and (220) reflections of PMN-30%PT with $E = 1$ kV/cm applied along [001] at (**a**) 375, (**b**) 350, and (**c**) 300 K in the FC condition. Reprinted with permission from [29]. Copyright [2004], American Institute of Physics

with monoclinic M_C symmetry. For $T = 300$ K, the (200) reflection was found to split only into two peaks, which can be attributed to the presence of two domains, whereas the (220) reflection was found to split into three peaks. This indicates a phase with monoclinic M_A symmetry. These results show a sequential phase transition from $C \rightarrow T \rightarrow M_C \rightarrow M_A$ in PMN-30%PT under FC condition with E applied along [001].

Figure 1.13 shows mesh scans taken around the (200) for PMN-30%PT with increasing E//[001] at 350 K beginning from the ZFC condition [29]. The corresponding lattice parameters are listed in Table 1.1. For $E = 0$ kV/cm, a rhombohedral phase was found. Under $E = 0.5$ kV/cm, the (200) reflection was found to be split into two peaks; this indicates an $R \rightarrow M_A$ transition with increasing E. Under $E = 3$ kV/cm, the (200) was found to be split into three peaks, revealing a monoclinic M_C phase. Also, under $E = 4$ kV/cm, the (200) was found to form one peak, revealing a tetragonal T phase. These changes in the mesh scans provide conclusive evidence of an $R \rightarrow M_A \rightarrow M_C \rightarrow T$ phase transition sequence with increasing E starting from the ZFC condition.

Relative to [001] FC PMN-30%PT [29], [110] field cooling results in a more complicated domain configuration. This complexity is because [001] field cooling fixes the prototype c-axis, whereas [110] field cooling only fixes the crystallographic [110] direction. Thus, more mesh scans along different zones are necessary for a more comprehensive understanding of the phase transitions in [110] field cooling condition. Figures 1.14–1.16 show mesh scans taken around

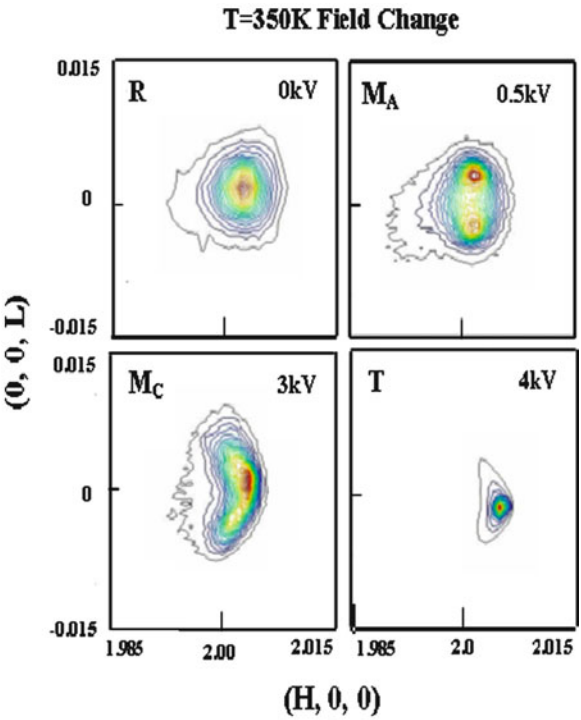

Fig. 1.13 (200) mesh scan at 350 K with increasing field// [001] for PMN-30%PT, which clearly shows a sequential phase transition from $R \rightarrow M_A \rightarrow M_C \rightarrow T$. Reprinted with permission from [29]. Copyright [2004], American Institute of Physics

Table 1.1 Lattice parameter for the PMN-30%PT at 350 K with increasing electric filed, measured by XRD

	a(Å)	b(Å)	$\alpha(=\gamma)(^\circ)$	$\beta(^\circ)$	Phase
ZFC from 550 K, $E = 0$	4.020				R
$E = 0.5$ kV/cm	4.023		90	90.08	M_A
$E = 2$ kV/cm	4.019	4.014	90	90.09	M_C
$E = 4$ kV/cm	4.015	4.015	90	90	T

Errors = ±0.002 Å

the (002), (200), (2$\bar{2}$0), and (220) for PMN-30%PT when the sample was cooled under E//[110] of 1 kV/cm [31].

Figures 1.14a–d show mesh scans at 375 K. The (002) reflection (see Fig. 1.14a) only has a single sharp peak. The lattice constant extracted from it was 4.0139 Å. However, the (200) reflection (see Fig. 1.14b) was split into two peaks along the longitudinal direction, with the lattice parameters of $a = 4.0142$ Å and $c = 4.0329$ Å. [110] field cooling constrains the polarization in the T phase to the (001) plane. The a_T lattice parameter is then derived from the (002), whereas c_T is obtained from the (200) reflection. Since [110] field cooling fixes the [110] crystallographic orientations, the (2$\bar{2}$0) mesh scan (see Fig. 1.14c) splits into two peaks along the transverse direction, but remains as a single peak for the (220) scan

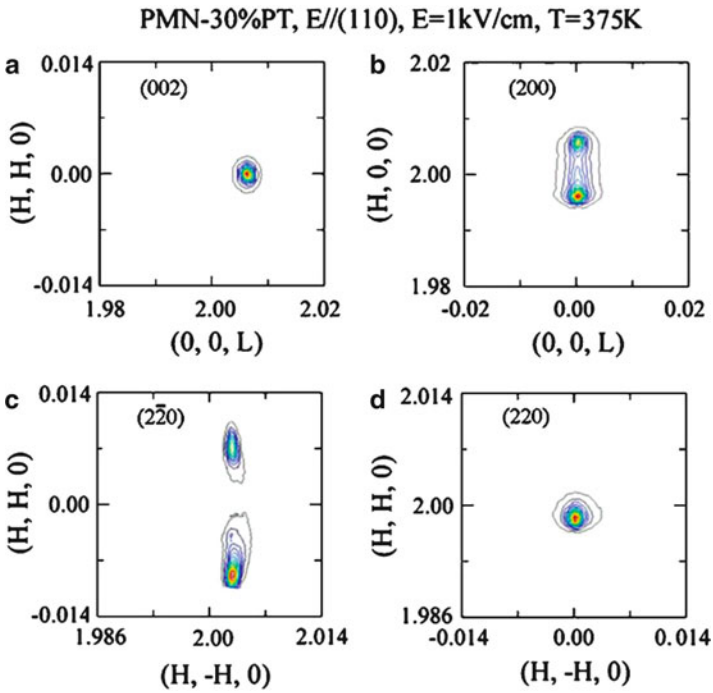

Fig. 1.14 Mesh scans of *T* phase of (**a**) (002), (**b**) (200), (**c**) (2$\bar{2}$0), and (**d**) (220) of PMN-30%PT with $E = 1$ kV/cm applied along [110] at 375 K in FC condition. Reprinted with permission from [31]. Copyright [2005] by the American Physical Society

(see Fig. 1.14d). Accordingly, for (2$\bar{2}$0) mesh scan, a-and b-twinning in the (001) plane is only seen along the transverse (220) direction. These results in Fig. 1.14 evidence a tetragonal lattice, with 90° domain formation only in the (001) plane, whose polarization is constrained along the [100] and [010] direction.

As the temperature was further decreased on [110] field cooling, the longitudinal splitting in the (200) mesh scan disappeared near 358 K, indicating another phase transformation. Figures 1.15a–d show mesh scans at 343 K within this phase field that were taken about the (002), (200), (2$\bar{2}$0), and (220) reflections, respectively. Only a single domain was observed in each of these scans, indicating the presence of a well-developed single domain state throughout the entire crystal. The structure of this phase was determined to be orthorhombic, where the polarization is fixed to the [110]. The lattice parameters of this orthorhombic phase were determined from these mesh scans to be $a_o = 5.6924$ Å, $b_o = 5.6812$ Å, and $c_o = 4.0070$ Å, where a_o was extracted from the (220) reflection, b_o from the (2$\bar{2}$0), and c_o from the (002).

At 298 K, the (002) mesh scan was found to split only along the transverse direction, revealing yet another phase transition. The (002) reflection (see Fig. 1.16a) can be seen to split into two peaks with the same wave vector length, whereas, the other three mesh scans remained as a single peak. This is a signature of

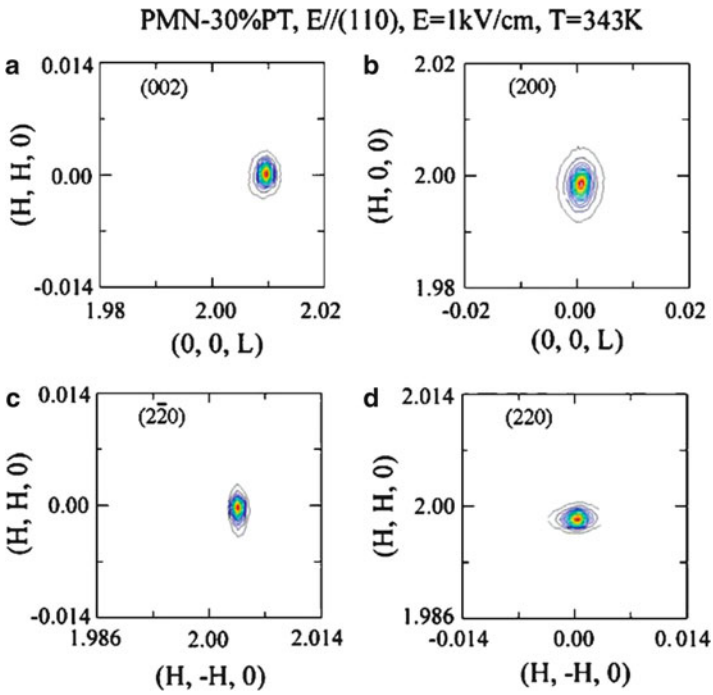

Fig. 1.15 Mesh scans of *O* phase of (**a**) (002), (**b**) (200), (**c**) (2$\bar{2}$0), and (**d**) (220) of PMN-30%PT with $E = 1$ kV/cm applied along [110] at 343 K in FC condition. Reprinted with permission from [31]. Copyright [2005] by the American Physical Society

the monoclinic M_A/M_B phase. The lattice parameters were then determined by extraction from these mesh scans to be $c_m = 4.0204$ Å, $a_m/\sqrt{2} = 4.0280$A, and $b_m/\sqrt{2} = 4.0181$A; where a_m and b_m were derived from the (220) and (2$\bar{2}$0) reflections, and c_m from the (002) one. Therefore on field-cooling below ~333 K, a single-domain *O* phase whose polarization is fixed to the [110], direction can no longer be saturated; rather, a transition to a polydomain monoclinic phase occurs. The unit cells of both the M_A/M_B phases are doubled with respect to the primitive pseudocubic one, where the polarization lies in the (1$\bar{1}$0) crystallographic plane. Although both the M_A and M_B phases belong to the C_m space group, there is a difference between their polarizations, for M_A, $P_x = P_y < P_z$; whereas for M_B, $P_x = P_y > P_z$. The fact $a_m/\sqrt{2} > c_m$ confirms that this monoclinic phase is the M_B one; this is consistent with Vanderbilt and Cohen's [16] thermodynamic theory that also allows for this transformation sequence. These results demonstrate a phase sequence of $C \rightarrow T \rightarrow O \rightarrow M_B$ for [110] FC PMN-30%PT, but different than the $C \rightarrow T \rightarrow M_C \rightarrow M_A$ for E//[001].

Figures 1.17a–d show the (002) scans for PMN-30%PT under the field sequence of $E = 0$, 2, 10, and 0 kV/cm (i.e., after removal of E) at 298 K, respectively. For $E = 0$ kV/cm, only a single broad peak was found in the (002) scan, although

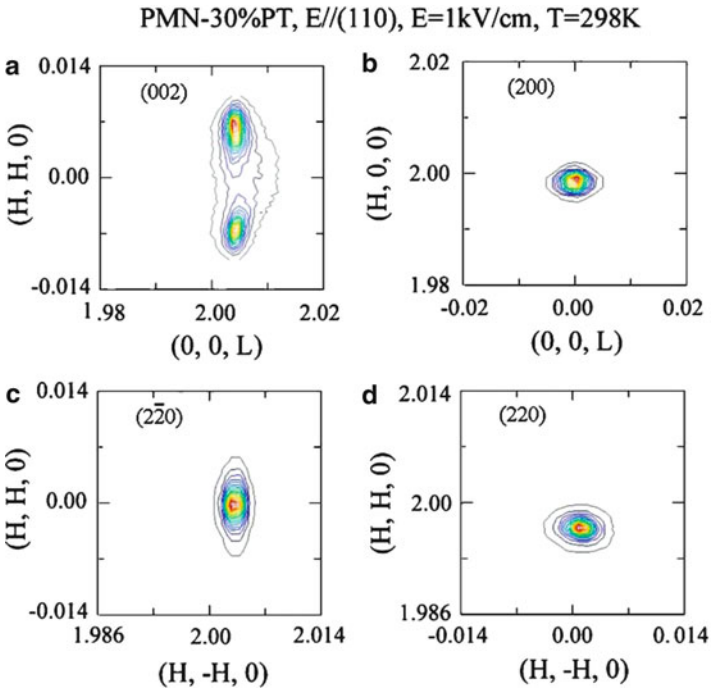

Fig. 1.16 Mesh scans of M_B phase of (**a**) (002), (**b**) (200), (**c**) (2$\bar{2}$0), and (**d**) (220) of PMN-30%PT with $E = 1$ kV/cm applied along [110] at 298 K in FC condition. Reprinted with permission from [31]. Copyright [2005] by the American Physical Society

a longitudinal splitting was observed in (220) scan (data not shown). The results show that the R phase is stable in the ZFC condition, with a lattice parameter of $a_r = 4.0220$ Å. Upon applying a field of 1 kV/cm, a peak splitting was found to develop along the transverse direction in the (002) reflection, whereas the (220) scan only possessed a single peak (data not shown). These features are signatures of the monoclinic M_B/M_A phase. The lattice parameters, c_m and a_m, extracted from (002) and (220) reflections show that $a_m/\sqrt{2}>c_m$. Thus, the phase transformational sequence beginning from ZFC condition is $R \rightarrow M_B \rightarrow O$ with increasing E. The monoclinic lattice parameters after removal of E were determined and found that$a_m/\sqrt{2}>c_m$. These results show that the M_B phase is the ground state condition for [110] poled crystals.

Based on the phase diagram reported by Noheda et al. [8], Cao et al. [35] reported two new phase diagrams for [001] and [110] electric field (E) cooled PMN-xPT crystals, as shown in Fig. 1.18. Comparisons of the [001] and [110] FC phase diagrams for PMN-xPT reveal that (1) the M_C phase in the [001] FC diagram is replaced by an O phase in the [110] FC diagram and (2) the R phase of the ZFC state is replaced by a M_A one in the [001] FC diagram, but with an M_B one in the [110] FC one. These differences in [001] and [110] FC diagram demonstrated that

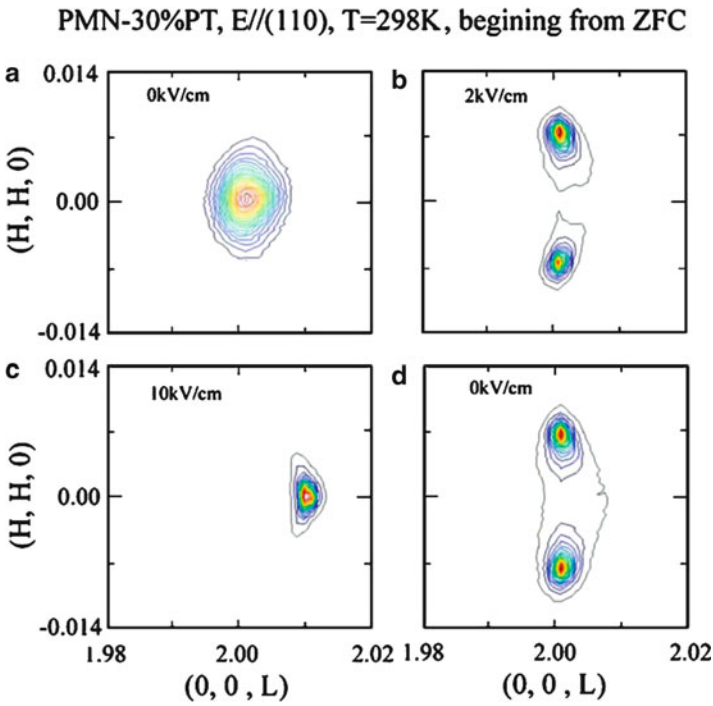

Fig. 1.17 (002) mesh scans with increasing *E*//[110] of (**a**) 0 kV/cm, (**b**) 2 kV/cm, (**c**) 10 kV/cm, and (**d**) after the removal of field in poled condition for PMN-30%PT. Reprinted with permission from [31]. Copyright [2005] by the American Physical Society

the phase stability of PMN-xPT crystals is quite fragile, depending not only on modest changes in E, but also on the direction along which E is applied. Structurally bridging monoclinic M_C or O phases were found to be associated with the T phase whereas the monoclinic M_A or M_B phases bridged the Cubic (C) and R ones.

1.1.4 Polarization Rotation Theory and Ferroelectric Adaptive Phase Theory

The monoclinic structure has the unique property that allows the polar direction to rotate within the basal plane; this freedom stands in sharp contrast to the uniaxial constraint imposed on the polar direction in both rhombohedral and tetragonal symmetries. This special feature may be responsible for the ultrahigh piezoelectric response near MPB since the existence of monoclinic phase was confirmed around the MPBs of PZT [13], PZN-*x*%PT [18], and PMN-*x*%PT [24] systems.

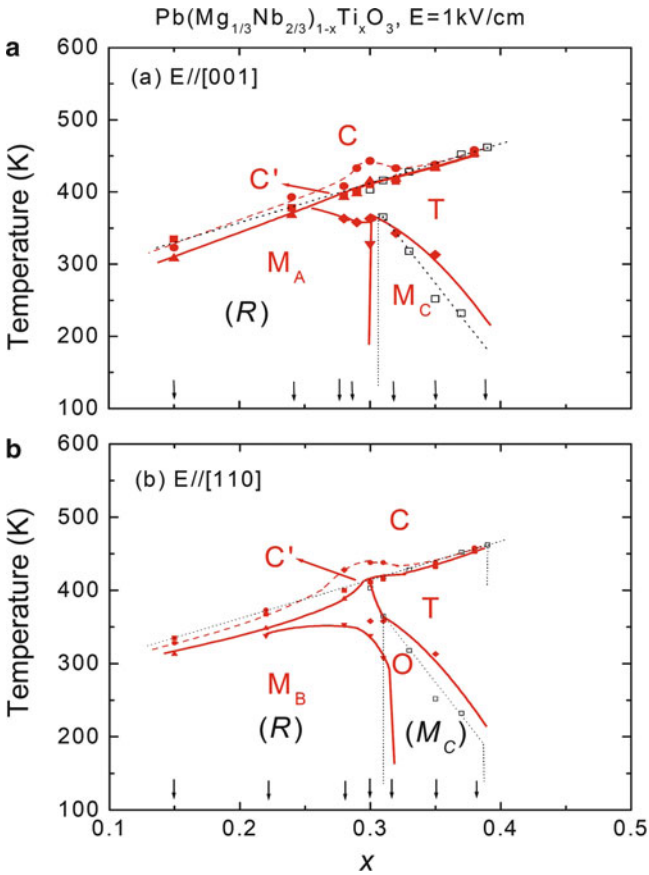

Fig. 1.18 Modified phase diagrams of (**a**) [001] and (**b**) [110] electric field cooled PMN-xPT crystals. The *dotted lines* and *open square* signs were based on studies by Noheda et al. [29]. The *bracketed italic R* and M_C represents the rhombohedral and monoclinic phases of the ZFC condition. The *solid square* signs represent the temperature of the dielectric maximum (T_m). The *solid circle* signs represent the temperature of phase transition in FC condition. The *C*' phase below the *upper dashed* curve was determined by a region of abnormal thermal expansion. *Solid curves* drawn through these data point are only for guide of eyes. Reprinted with permission from [35]. Copyright [2006] by the American Physical Society

$BaTiO_3$ has *R* and *T* ferroelectric phases in a perovskite cell, and can serve as a prototypical model for other perovskite system. Based on the first principle calculations of the *R* phase of $BaTiO_3$ single crystals as an *E* function applied along [001], Fu and Cohen [39] proposed a polarization rotation mechanism during an *E*-field-induced *R*-to-*T* phase transformation which takes a path with small energy change, and thus allows the existence of intermediate low symmetry phases. They predicted that polarization rotated along the lowest free energy path of $a \rightarrow f \rightarrow g \rightarrow e$ as shown in Fig. 1.19a will give high piezoelectric response (see Fig. 1.19b) as it had been observed in PZN-8%PT single crystal (see Fig. 1.7).

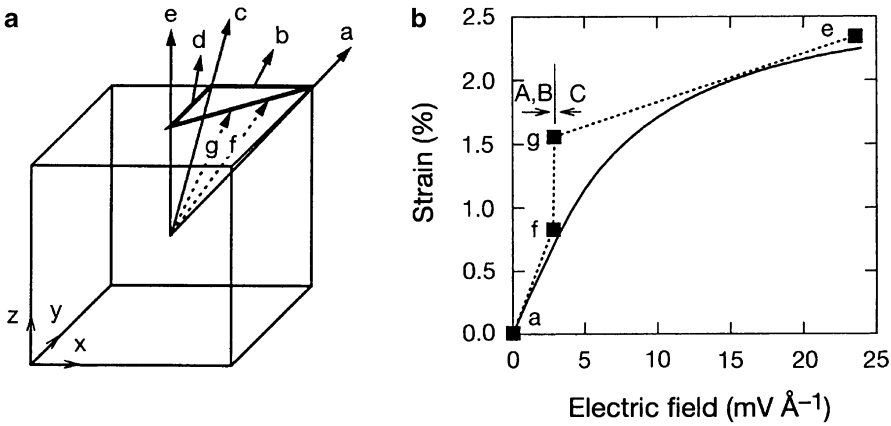

Fig. 1.19 (**a**) Schematic illustration of the polarization directions and (**b**) Theoretical results of strain responses under electric field for $BaTiO_3$ crystal along the lowest free energy path of $a \rightarrow f \rightarrow g \rightarrow e$. Reprinted with permission from [39]. Copyright [2000], Nature Publishing Group

Thus, they conjectured that the large piezoelectric response of the *M* phases of PMN-xPT and PZN-xPT crystals was due to changes in unit cell parameters due to a rotation of the polarization direction induced by electric field.

Although the polarization rotation mechanism was first based on ab initio calculations of the *R* phase of $BaTiO_3$, it is reasonable to conceptually extend its application to other more complex ferroelectric systems such as PZT, PMN-*x*%PT, or PZN-*x*%PT. Diffraction experiments have confirmed that different systems have different polarization rotation paths. For example, in PZN-4.5%PT [24], *E*//[001] would induce polarization rotation in the (110) plane following the $R \rightarrow M_A \rightarrow T$ path [19], similar to that predicted by ab initio calculations in the *R* phase of $BaTiO_3$. The same rotation path was also confirmed for PMN-*x*%PT under *E*//[001] for compositions at the left side of the MPB (i.e., $x < 0.30$) [35]. Experimentally, a $M_A \rightarrow M_C$ transition has been reported by XRD in PZN-8%PT [18] and in PMN-30%PT [29]. Accordingly, the polarization rotation would follow a $R \rightarrow M_A \rightarrow T$ path, but then abruptly jump to a $R \rightarrow M_A \rightarrow M_C \rightarrow T$ one. Polarization rotations could also occur in the *T* phase: for example, $T \rightarrow M_A \rightarrow R$ under *E*//[111] [40].

The polarization rotation theory can explain the origin of the extreme piezoelectric response observed in giant ferroelectric perovskite phases: the polarization rotation occurs in a homogeneous monoclinic phase. This theory provides an interpretation to the variously observed monoclinic phases. However, the theory cannot explain special observed relations between the crystal lattice parameters of the tetragonal (or rhombohedral) and monoclinic M_C (or M_A/M_B) phases with changes in electric field and applied stress [41–43]. Figure 1.20 shows the temperature dependence of the lattice parameters for PMN-xPT ceramics [42]. Two interesting crystallographic

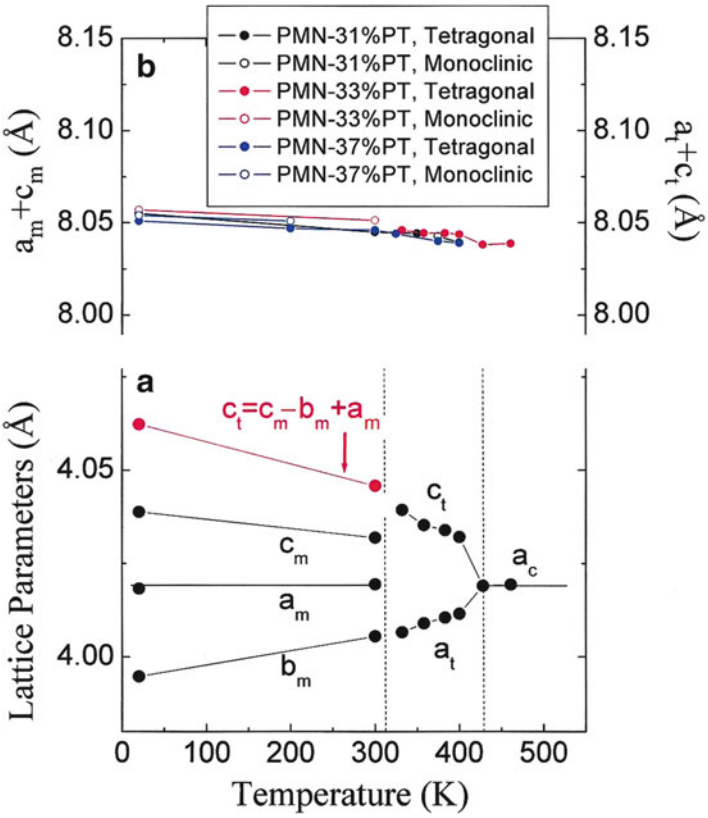

Fig. 1.20 (**a**) Temperature-dependent lattice parameters for PMN-33%PT ceramics. (**b**) Temperature dependence of the general invariance condition of $a_m + c_m = a_t + c_t$. Reprinted with permission from [42]. Copyright [2003] by the American Physical Society

relationships between lattice parameters can be observed in this figure at the $T \rightarrow M_C$ transition, which are

$$a_m + c_m = a_t + c_t \tag{1.1a}$$

$$b_m = a_t \tag{1.1b}$$

where (a_m, b_m, c_m) and (a_t, c_t) are the lattice parameters of the M_C and T phases.

Figure 1.20 also shows that the changes in the lattice parameters are entirely invariant with the general geometric conditions of (1.1). These general conditions are geometrically similar to those for twinning, following the classic Wechsler-Lieberman-Read (WZR) [44] theory of martensite; however, the conditions in (1.1) are reduced in length scale and applied to those of the lattice parameters, rather than twin boundaries.

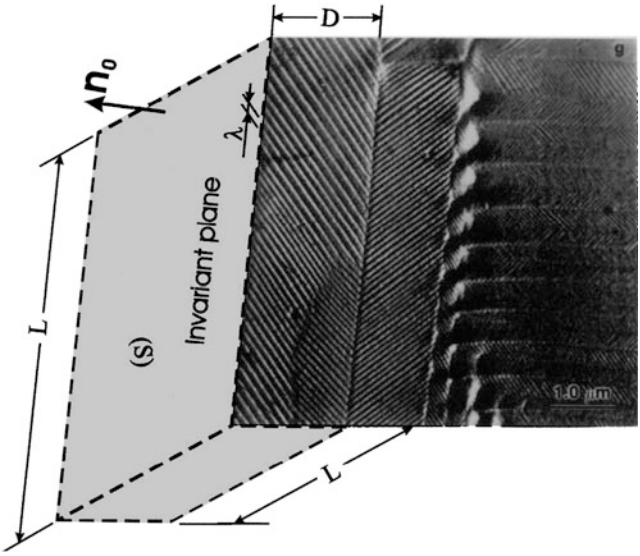

Fig. 1.21 Dark field TEM image of stress accommodating polydomain structure in CuAu alloy. Reprinted with permission from [45]. Copyright [1967], Wiley-VCHmVerlag GmbH & Co. KGaA

The underlying assumption is that the twinning of the *T* phase is conformally reduced to near atomic dimensions. The concept is illustrated in Fig. 1.21 [45]: the structure of the adaptive phase has the same morphology but is conformally miniaturized to reach nano- or subnanoscale. Then white and black stripes become microdomains that are "invisible" to the usual diffraction measurement and the macroplates become macrodomains that are perceived as domains of the "homogeneous" monoclinic phase (adaptive phase).

This is the alternate "ferroelectric adaptive phase" theory for monoclinic phases, originally proposed by Viehland [41] and subsequently expanded by Jin, and Wang [42, 43, 46, 47]. Following the adaptive phase model, the monoclinic phases consist of miniaturized *T* or *R* microdomains (nanotwins), whose apparent lattice parameters are determined by the accommodation of misfit stress and electric field. This adaptive phase is a structurally inhomogeneous on a microscale (~10 nm), but apparently homogeneous on a macroscale. Such an adaptive phase is formed by plates containing twin-related tetragonal microdomains, and observed as a homogeneous monoclinic phase by diffraction measurements: resolution of the *T* or *R* phases from the M_C or M_A ones is limited by the optics of diffractions. In order to accommodate the elastic stress and avoid misfits along the domain boundaries, particular relationships between lattice parameters of tetragonal and monoclinic M_C phase must be satisfied, given in (1.1) above. In this case, the monoclinic angle (β) has been shown by Wang [46, 47] to be

$$\beta = 90^{\circ} + 2A\omega(1-\omega)(\tan^{-1}\frac{c_t}{a_t} - 45^{\circ}) \tag{1.2}$$

where $\omega = \frac{c_m - b_m}{a_m + c_m - 2b_m}$ is the volume fraction of one of two variants and A is a fitting constant, that is close to 1. Furthermore, the O phase is a limiting case of M_C, where $\omega = 1/2$. A similar approach to conformal miniaturization of R domains would yield the monoclinic M_A/M_B phase, as discussed by these authors [46, 47].

This adaptive model can successfully explain the observed characteristic transformations in the lattice parameters with temperature. It also can explain changes in the lattice parameters with E or stress (σ). In this case, the extreme piezoelectricity of PMN-x%PT and PZN-x%PT can be attributed to changes in the distribution of microdomains. These changes with E and σ are restricted to occur along special geometrically invariant conditions that achieve elastic accommodation. Experimentally, changes in lattice parameters with E and σ have been shown to follow these restrictions. It is important to note that the adaptive phase model is based on an inherently structurally inhomogeneous state. This model is in sharp contrast to the inherently homogeneous one of the polarization rotation theory.

1.2 Domain Engineering and Phase Transformations in Lead-Free Piezoelectric Materials

1.2.1 Background

Lead-based materials pose environmental concerns due to the volatility and toxicity of PbO during material preparation. Thus, in recent years, the search for suitable Pb-free replacements for lead-based piezoelectric materials has been an important topic; in fact, ecological restrictions in numerous nations mandate the elimination of Pb from consumer items [48, 49]. Lead-free piezoelectric materials, including ferroelectrics of perovskite structure [50–63], tungsten bronze structure [53, 64–68], and bismuth layer-structure [69–79], have been reported. Among them, perovskite ferroelectrics display high piezoelectric properties, such as $Na_{0.5}Bi_{0.5}TiO_3$-based [58, 80–84], $K_{0.5}Na_{0.5}NbO_3$-based [85–90], and $BaTiO_3$-based materials [40, 91–96]. Longitudinal piezoelectric constants of $d_{33} \approx 500$ pC/N have been reported both under large amplitude drive in the $\varepsilon - E$ response and under weak-field drive using a Berlincourt-type meter in $Na_{0.5}Bi_{0.5}TiO_3$-x% $BaTiO_3$ single crystals near MPB [80, 84]. The comparable high piezoelectricity of $d_{33} \sim 416$ pC/N was reported for <001>-textured (Li, Sb, Ta)-modified K0.5Na0.5NbO3 (KNN) ceramics [85]. A piezoelectric d_{33} constant as high as ~500–1,000 pC/N measured using a resonance–anti-resonance method was reported in crystallographically engineered $BaTiO_3$ crystals and <110>-textured $BaTiO_3$ ceramics with fine domain size [91, 93]. The detailed piezoelectric properties of these lead-free materials were summarized in reviewer papers by Takenaka [97], Shrout [98], and Rödel [99] et al. However, the studies of understanding the origin that produce high piezoelectric response in lead-free piezoelectric materials are just beginning. In this section, the phase transition characteristics of $Na_{0.5}Bi_{0.5}TiO_3$-based, $K_{0.5}Na_{0.5}NbO_3$-based, and $BaTiO_3$-based materials will be discussed.

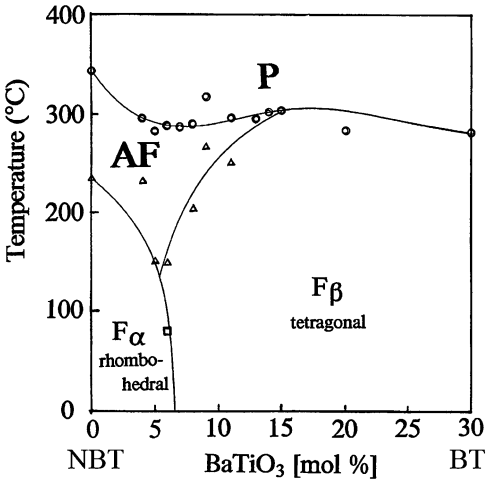

Fig. 1.22 Phase diagram of $Na_{0.5}Bi_{0.5}TiO_3$-x%$BaTiO_3$ [NBT-x%BT] system. (F_α: ferroelectric rhombohedral phase; F_β: ferroelectric tetragonal phase; *AF* antiferroelectric phase; *P* paraelectric phase). Reprinted with permission from [58]. Copyright [1991], Japan Society of Applied Physics

1.2.2 $Na_{0.5}Bi_{0.5}TiO_3$-Based Solid Solutions

Sodium bismuth titanate ($Na_{0.5}Bi_{0.5}TiO_3$ or NBT) is an A-site complex perovskite ferroelectric that has a high Curie temperature of $T_c = 320°C$, remnant polarization of $P_r = 38$ μC/cm^2, and coercive field of $E_c = 73$ kV/cm [53]. It is a potential lead-free piezoelectric, as solid solutions with other pervoskites such as $Na_{0.5}Bi_{0.5}TiO_3$-x%$BaTiO_3$ or $Na_{0.5}Bi_{0.5}TiO_3$-x%$K_{0.5}Bi_{0.5}TiO_3$ [58, 97] have enhanced piezoelectric properties due to an MPB between rhombohedral (*R*) and tetragonal (*T*) phases. Figure 1.22 shows the phase diagram of $Na_{0.5}Bi_{0.5}TiO_3$-x% $BaTiO_3$ (NBT-x%BT) system obtained from the dielectric and ferroelectric measurement [58]. An MPB exists near the composition of $x = 6$–7. Both the dielectric and piezoelectric properties are significantly enhanced, as evident in Fig. 1.23. Unlike that of the PZT system, the MPB is strongly curved in NBT-xBT%, and prior to the prototypic cubic transformation, a phase transformation to an antiferroelectric phase is believed to occurs, as shown in Fig. 1.22.

1.2.2.1 Domain Hierarchy in $Na_{0.5}Bi_{0.5}TiO_3$ Single Crystals

A complicated sequence of phase transitions for NBT has been reported by various experimental methods. Dielectric and pyroelectric studies have shown that NBT undergoes a ferroelectric ~ 200°C antiferroelectric phase transition with increasing temperature [55, 100–104]. X-ray and neutron diffraction studies complimented with dielectric measurements have revealed that it also undergoes structural phase

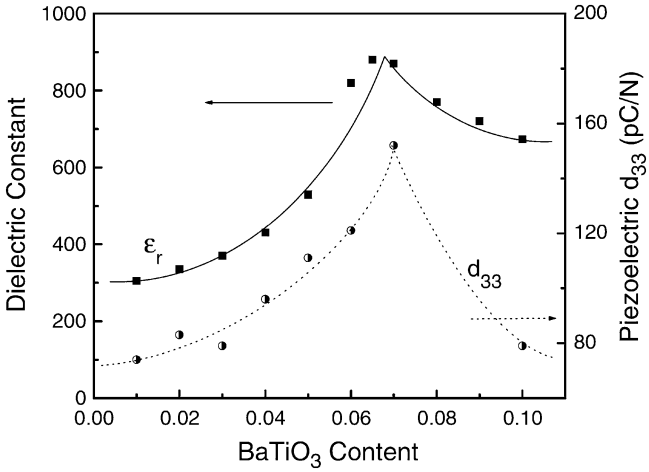

Fig. 1.23 Enhanced dielectric and piezoelectric properties in NBT-*x*%BT. Reprinted with permission from [98]. Copyright [2007], Springer

transitions of paraelectric Cubic (*C*) 540°C polar (presumably antiferroelectric) Tetragonal (*T*) 260°Cferroelectric Rhombohedral (*R*) with decreasing temperature [105–109].

Figure 1.24a shows ε_r as a function of temperature in the ZFC state for NBT crystals, taken at various frequencies [110]. These data show that the dielectric maximum occurs near 330°C, near and just below which the dielectric constant is frequency independent. On further cooling, an inflection was found near 250°C below which notably frequency dispersion was observed. This dispersion was similar to that of relaxors below T_{max}, indicating polar heterogeneities with low frequency fluctuations.

The temperature-dependent d spacing for (200) is shown in Fig. 1.24b. These data reveal a splitting of the c and a parameters in the temperature range between 300 and 530°C, demonstrating that both the polar (near and below T_{max}) and prototypic ($>T_{max}$) phases have tetragonal symmetry. Below 300°C, the structure transformed to rhombohedral (i.e., pseudo-cubic). No other structural changes were found at the Curie temperature, or at the inflection in the dielectric constant near 250°C. These XRD results do not preclude that a structural phase transition occurred on a local scale in some regions of the crystal near or above T_{max}. A diffuse phase transformation is apparent in the broad dielectric response with a maximum near T_{max}, consistent with this possibility.

Figure 1.25 shows PLM images taken at (a) room temperature in the *R* phase, (b) above the ferroelectric Curie temperature but below the $T \rightarrow C$ transition at 350°C, and (c) in the *C* phase at 580°C [111]. The angles (θ) provided in the images are that between the polarizer/analyzer (P/A) pair and the pseudocubic <110>. The images reveal the presence of tetragonal ferroelastic domains for temperatures below $T \rightarrow C$ transition, which have a width of about 10 ~ 100 μm

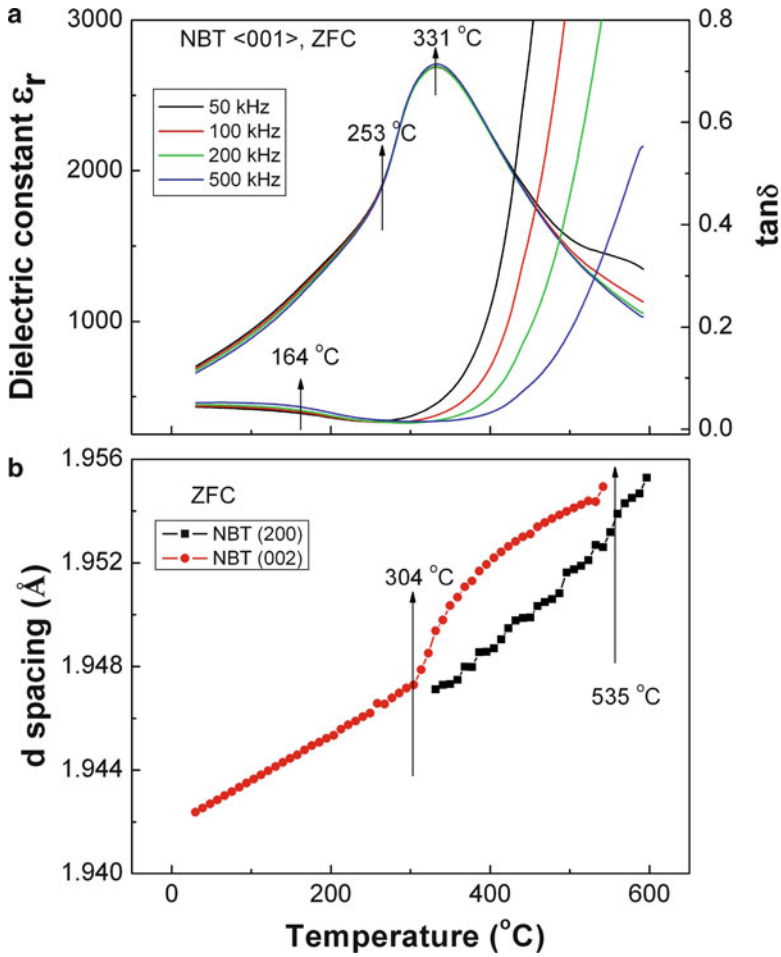

Fig. 1.24 Phase transformation characteristics of <001> oriented NBT single crystal in the ZFC condition, observed by (**a**) temperature-dependent dielectric constant measurements taken at various frequencies; and (**b**) temperature-dependent lattice parameter measurements. Reprinted with permission from [110]. Copyright [2010], American Institute of Physics

and a length on the order of hundreds of microns, and which are oriented along the <110>. These ferroelastic domains disappeared on heating at the $T \rightarrow C$ transition near 550°C. The contrast of these images could be changed by the P/A angle setting. As seen in Fig. 1.25d at 25°C, the contrast was darkest for $\theta = 28^{o}$: complete extinction could not be achieved, as one can clearly still see the ferroelastic domains. However, at 350°C, the domain structures became completely extinct for $\theta = 45^{o}$ (see Fig. 1.25e): i.e., when one of the P/A axes was oriented along the $<100>_{cub}$. This is the typical extinction position for a crystal structure with tetragonal symmetry, and is consistent with the XRD

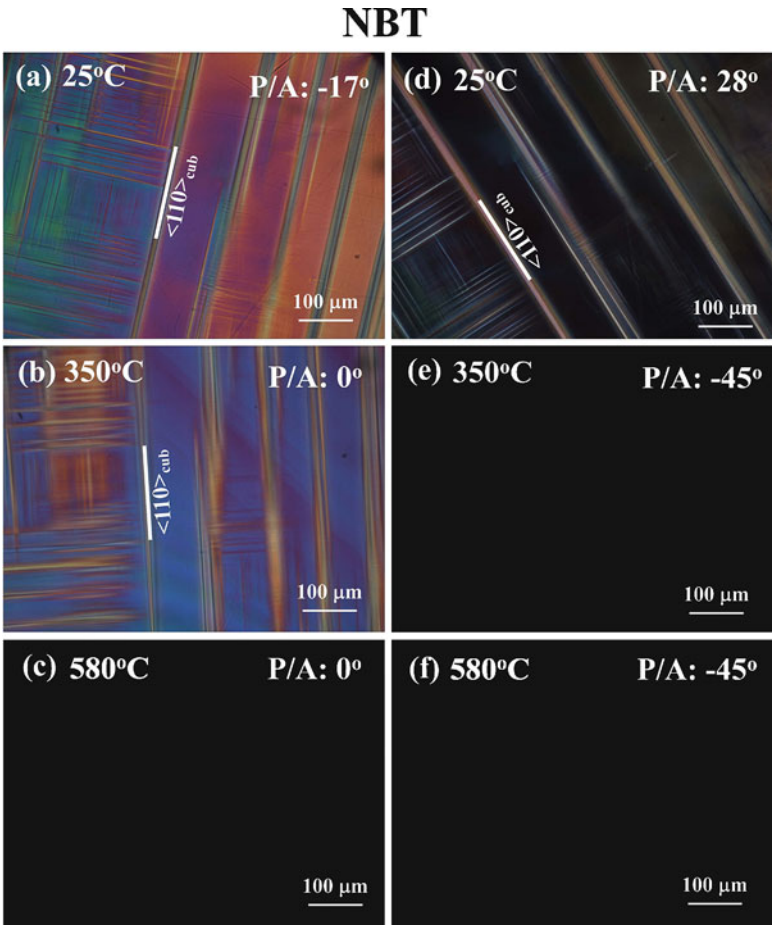

Fig. 1.25 Polarized light microscopy (PLM) images taken at various temperatures of (**a**, **d**) 25°C, (**b**, **e**) 350°C, and (**c**, **f**) 580°C. The angles (θ) provided in the images are that between the polarizer/analyzer (P/A) pair and the pseudocubic <110>. Reprinted with permission from [111]. Copyright [2010], John Wiley and Sons

results shown in Fig. 1.24b. Since the tetragonal ferroelastic domains persist into the *R* phase field, the ferroelectric *R* domains must then nucleate on cooling under the geometrical and elastic restrictions of the ferroelastic *T* domains. Thus, complete extinction could not be achieved in the *R* phase because the distribution of polar *R* microdomains within larger ferroelastic *T* macrodomians could not achieve a completely elastically relaxed condition. When the temperature was increased to *C* phase field, complete extinction was obtained with P/A angle changing in the range from 0 to 360° (see Fig. 1.25c, f). It is important to note that the size, shape, and position of these ferroelastic domains were somewhat unchanged with temperature on cooling between 550°C and room temperature, even though the sample went

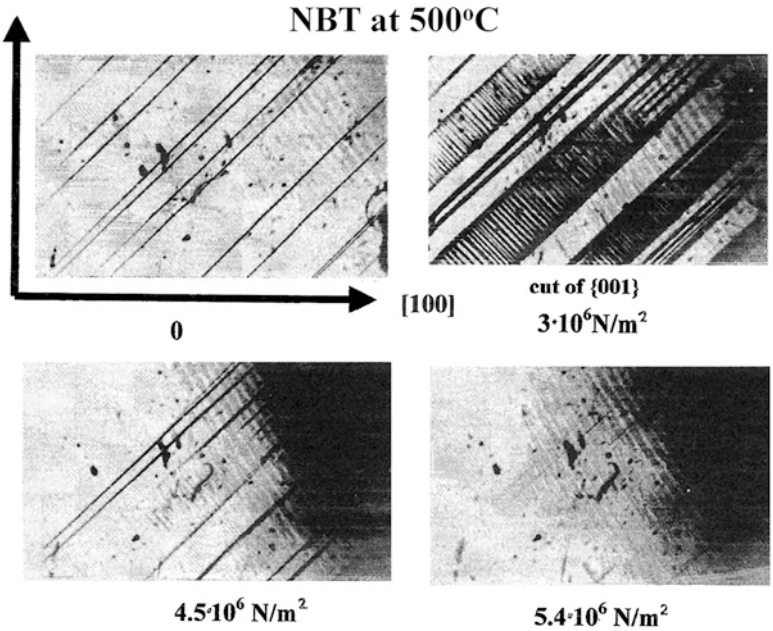

Fig. 1.26 Influence of uniaxial pressure applied along the [100] direction on the domain structure of NBT single crystal near 500°C. Reprinted with permission from [112]. Copyright [2001], Elsevier

through (1) two polar phase transformations on cooling, and (2) that the ferroelastic tetragonal strain (c/a) disappeared at 300°C on cooling into the *R* phase. These findings clearly demonstrate that the ferroelastic domain structure is inherited into the rhombohedral polar phase at room temperature.

The ferroelastic nature of $C \rightarrow T$ transition can be demonstrated by the change of domain structure under the influence of uniaxial stresses at *T* phase field, as shown in Fig. 1.26 [112]. It may be supposed that the cubic phase (above 540°C) is characterized by disordered arrangement of these ions in A-cation of the sublattice. At the high temperature phase transition, tetragonal distortions of TiO_6 octahedra take place and it may be the reason for definite ordering in the arrangement of Na^{1+} and Bi^{3+} ions. On cooling, partial "freezing" of this ion configuration is possible. At ~300°C, where another phase transition occurs, rhombohedral distortion of TiO_6 octahedra appears and new ordering configuration in the arrangement of Na^{1+} and Bi^{3+} ions should be profitable. However, a partially "frozen" A-sublattice still corresponds to the high temperature tetragonal phase. Thus, the orientation of domain walls in NBT single crystals does not practically change during cooling to room temperature. As a result, internal mechanical stresses appear in the crystal. On further cooling, rhombohedral distortions are increased which should lead to relaxation of Na^{1+} and Bi^{3+} ions to an ordered configuration in accordance with the rhombohedral phase. Investigations by Suchanicz [108] confirm the existence of

the relaxation processes for NBT in the temperature range ~220–360°C. It was observed that at fixed temperatures from this region, the value of the electric permittivity was achieved during ~40–50 min at 360°C and more than 200 min at 270°C. Taking into account that the relaxation time strongly increases with decreasing temperature, it is possible to expect that on insufficiently slow cooling, internal mechanical stresses may still remain at room temperature.

Scanning force microscopy (SFM), performed in the piezoresponse mode (PFM), provides a way to study the ferroelectric domain structures at various length scales with high spatial resolution [113]. This technique is based on the detection of local vibrations of a ferroelectric sample induced by a testing ac signal applied between the conductive tip of the SFM and the bottom electrode of the sample. The oscillations of the sample underneath the tip modulate the global deflection signal and are detected using a lock-in technique. Figure 1.27 shows the domain structure of NBT over various length scales investigated by using different types of microscopy at room temperature. These investigations have shown the presence of two different types of domain structures of different characteristic sizes. The presence of ferroelastic domains was confirmed by optical mode and Raman mode SPM as shown in Fig. 1.27a, b. In this case, <110> oriented domains were found. Figure 1.27c, d show typical PFM images, which reveal the presence of much smaller ferroelectric domains that exist within the ferroelastic domains of larger length scale. The size of these ferroelectric domains was on the order of 0.2–0.5 μm. Furthermore, the spatial distribution of these ferroelectric microdomains was not well organized.

Generally in a distortive phase transformation, changes in the domain variant distribution and population allow the achievement of the elastic compatibility conditions and minimization of the elastic free energy [114]. However, a unique sequence of phase transformations was found in NBT, where a ferroelastic *T* domain structure is inherited into a ferroelectric *R* phase. This is important because it means that the polar *R* phase is geometrically and elastically restricted by its high temperature ferroelastic *T* parent phase. On cooling into the *R* phase, ferroelectric microdomains then form within the ferroelastic *T* domains. The system can organize the ferroelectric microdomain distribution in an attempt to achieve the invariant plane strain conditions; however, a fully relaxed elastic state is clearly not achieved for NBT, i.e., spatial distribution of ferroelectric microdomains was not well organized, as shown in Fig. 1.27c, d. Because complete stress accommodation is not achieved, the polar microdomain ensemble may undergo low frequency dynamical fluctuations, typical of a relaxor ferroelectric state reflected by frequency-dependent dielectric constant.

1.2.2.2 Influence of Mn-Doping on the Structure and Properties of NBT Single Crystals

NBT single crystals are not easy to pole because of the combination of a low resistivity and a high E_c, thus making it difficult to study their piezoelectric properties. It was found that 0.24at% Mn-doping did not alter the phase

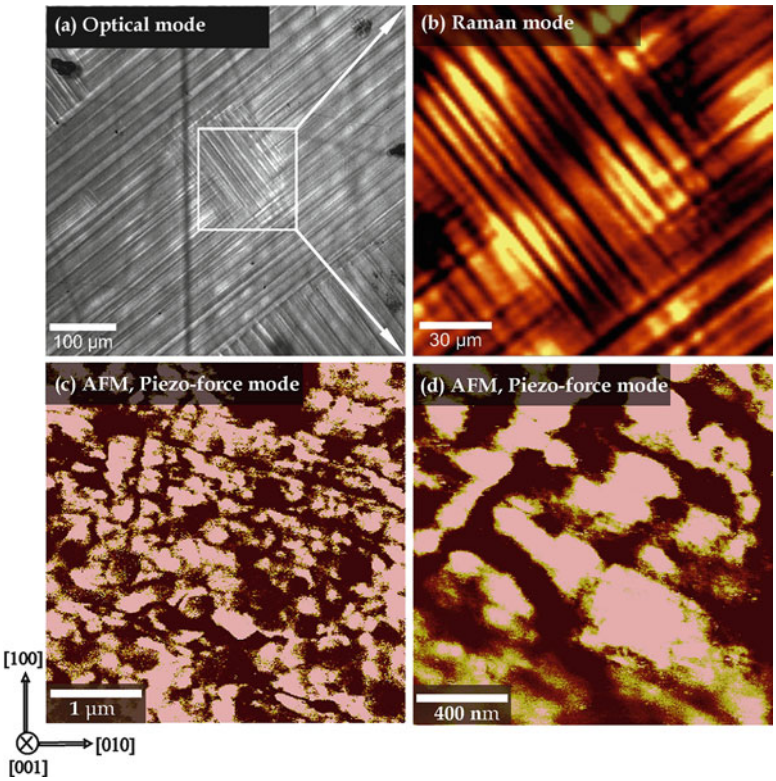

Fig. 1.27 Domain structure of NBT at different length scales taken by (**a**) atomic force microscopy using an optical mode; (**b**) atomic force microscopy using a Raman mode, which demonstrates ferroelastic domains of about 10 μm; (**c**) atomic force microscopy, which shows ferroelectric domains of about 0.2 ~ 0.5 μm in size; and (**d**) a higher resolution image of ferroelectric domains, which demonstrates much clear ferroelectric domains that exists within the feroelastic ones. Reprinted with permission from [110]. Copyright [2010], American Institute of Physics

transformational sequence for NBT, but rather resulted in a refinement of the domain size and an enhancement of the piezoelectric/dielectric properties.

Figure 1.28a shows a plot of l g (σ) vs. 1,000/T for both NBT and Mn:NBT in the temperature range of 30–210°C [111]. These data show that the dc electrical conductivity is notably decreased by over two orders of magnitude by Mn substitution. Above 130°C, the conductivity was near linearly dependent on 1/T for both crystals. Analysis by an Arrhenius type thermal activation for transport revealed that the activation energy E_a was nearly the same for NBT and Mn:NBT (1.094 and 1.061 eV, respectively). This value of E_a is close to the 1 eV previous reported for oxygen vacancy conductivity in perovskite ferroelectrics [115, 116].

Oxygen vacancies in NBT may result from Bi_2O_3 volatility during crystal growth: i.e., $2Bi^{3+} + 3O^{2-} \Leftrightarrow 2V_{Bi}''' + 3V_O^{\bullet\bullet} + Bi_2O_3 \uparrow$. Bismuth V_{Bi}''' and oxygen

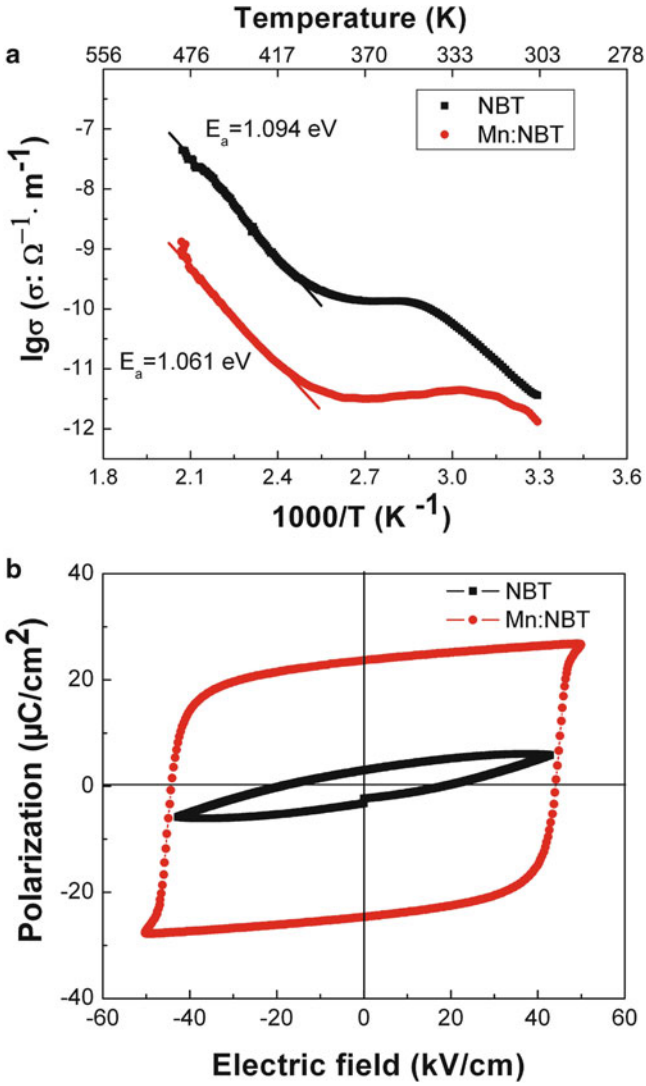

Fig. 1.28 (**a**) lg(σ) vs. 1,000/*T* curve and (**b**) polarization hysteresis loops for <001>-oriented NBT and Mn:NBT crystal. Reprinted with permission from [111]. Copyright [2010], John Wiley and Sons

$V_O^{\bullet\bullet}$ vacancies can lead to a space charge effect, enhancing the dielectric constant (see Fig. 1.29a) and electrical conductivity at low frequencies and high temperatures. According to energy dispersive X-ray (EDX) analysis reported by Takenaka et al., the ratio of Bi/Ti ions is 0.439 for 0.74at% Mn-doped NBT ceramics, which is much lower than that of Bi/Ti = 0.49 for NBT ceramics [117]. Thus, one can suppose that Mn substitutes on the A-site in NBT. When Mn is incorporated

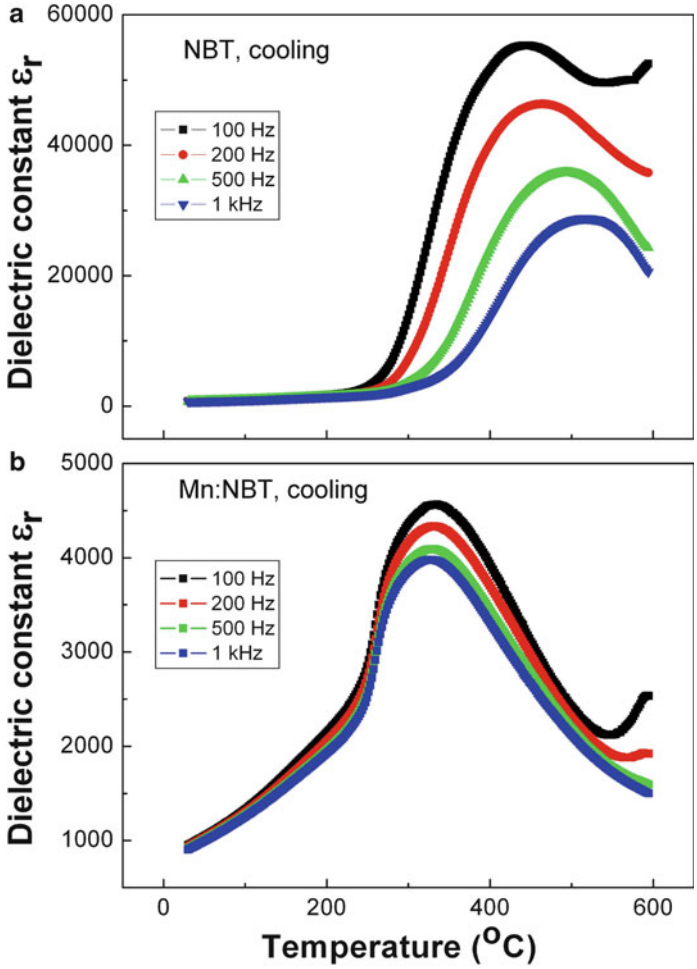

Fig. 1.29 Low frequency (100–1,000 Hz) dielectric constant as a function of temperature for NBT (**a**) and Mn:NBT (**b**). Reprinted with permission from [111]. Copyright [2010], John Wiley and Sons

onto the A-sites of NBT, the concentration of $V_O^{\bullet\bullet}$ will be decreased as $2Mn^{3+} + 2Bi^{3+} + 3O^{2-} \Leftrightarrow 2Mn_{Bi}^{\times} + Bi_2O_3 \uparrow$. Accordingly, space charge conduction may be suppressed by Mn, which should enhance the high temperature electrical resistivity. Interestingly, Mn might also substitute on the B-site of NBT, creating additional oxygen vacancies that could decrease the electrical resistivity when the Mn-doping concentration exceeds 0.36at% [117].

Figure 1.28b shows polarization (P-E) hysteresis loops for both NBT and Mn:NBT at room temperature [111]. For Mn:NBT, near complete polarization switching was achievable under $E \leq 50$ kV/cm, with a remnant polarization of

$P_r = 23.9$ μC/cm^2 and a coercive field of $E_c = 43.85$ kV/cm. However, the P-E loops are far from saturated for NBT. P-E hysteresis loops revealed a 6.8× increase in P_r between NBT and Mn:NBT under $E \leq 50$ kV/cm. The piezoelectric constant d_{33} was determined to be only 20–30 pC/N for NBT crystals, while for Mn:NBT the value of d_{33} could reach 120 pC/N. This increase by a factor of 5× in d_{33} by Mn can be explained by a conventional Landau-Devonshire relation: $d_{33} = 2 \bullet Q_{33} \bullet \varepsilon_{33}^{T} \bullet P_r$, where P_r is the remnant polarization and Q_{33} is the electrostriction coefficient.

Figure 1.29a, b show the low frequency (100–1,000 Hz) dielectric constant as a function of temperature [111]. For NBT, a dramatically enhanced ε_r was found in the temperature range of 300~600°C, yielding values of $\varepsilon_r > 5.5 \times 10^4$, which were extremely frequency dispersive. These data evidence the presence of a space charge conduction mechanism at elevated temperatures, as previously reported [118]. For Mn:NBT, no evidence of enhanced permittivity was observed in this elevated temperature range, rather the maximum dielectric constant was only 4,500: ~12× lower than that of unmodified NBT. Clearly, Mn substitution is extremely effective in suppressing low frequency conduction contributions to ε_r.

Figure 1.30a shows the temperature-dependent dielectric constant for <001> oriented NBT and Mn:NBT at frequencies of 50 kHz $< f <$ 500 kHz. The higher phase transition temperature T_m corresponded to the maximum in the dielectric constant or Curie temperature. The value of T_m was only slightly shifted to lower temperatures by ~12°C with Mn; however, the maximum value of ε_r was notably increased by Mn from about 2,700 to 3,840. In addition, the temperature dependence of ε_r was notably broadened by Mn: typical of a diffuse phase transition resulting from random-site occupancy of different ions. However, below a secondary phase transition, which was shifted to lower temperatures (~30°C) by Mn and which is designated $T_{F\text{-}AF}$ for ferroelectric → antiferroelectric, frequency dispersion became clearly evident in ε_r on further cooling for both crystals. It can be seen in the temperature range below $T_{F\text{-}AF}$ that the value of ε_r and the relaxation strength were notably increased by Mn. Figure 1.30b shows the temperature-dependent lattice parameter data for NBT and Mn:NBT. With decreasing temperature, both crystals were found to undergo a phase transformational sequence of cubic (C) → tetragonal (T) → rhombohedral (R). However, after Mn substitution, these transition temperatures were decreased by 20 and 40°C respectively.

Figure 1.31 shows PLM images taken at (a) room temperature in the R phase, (b) above the ferroelectric Curie temperature but below the $T \rightarrow C$ transition at 350°C, and (c) in the C phase at 580°C. The angles (θ) provided in the images are between the polarizer/analyzer (P/A) pair and the pseudocubic <110>.

Comparison of the PLM images for Mn:NBT to those for NBT (see Fig. 1.25) reveals that the tetragonal ferroelastic domains in Mn:NBT became notably smaller having widths of 15~25 μm. Interestingly, stripe-like color bands were observed as shown in Fig. 1.29a (25°C, P/A = 0°), which had a preferred orientation along $<100>_{cub}$. It must be noted that the ferroelectric domain boundaries were aligned along the $<100>_{cub}$ in the R phase, which is what would be expected by optical

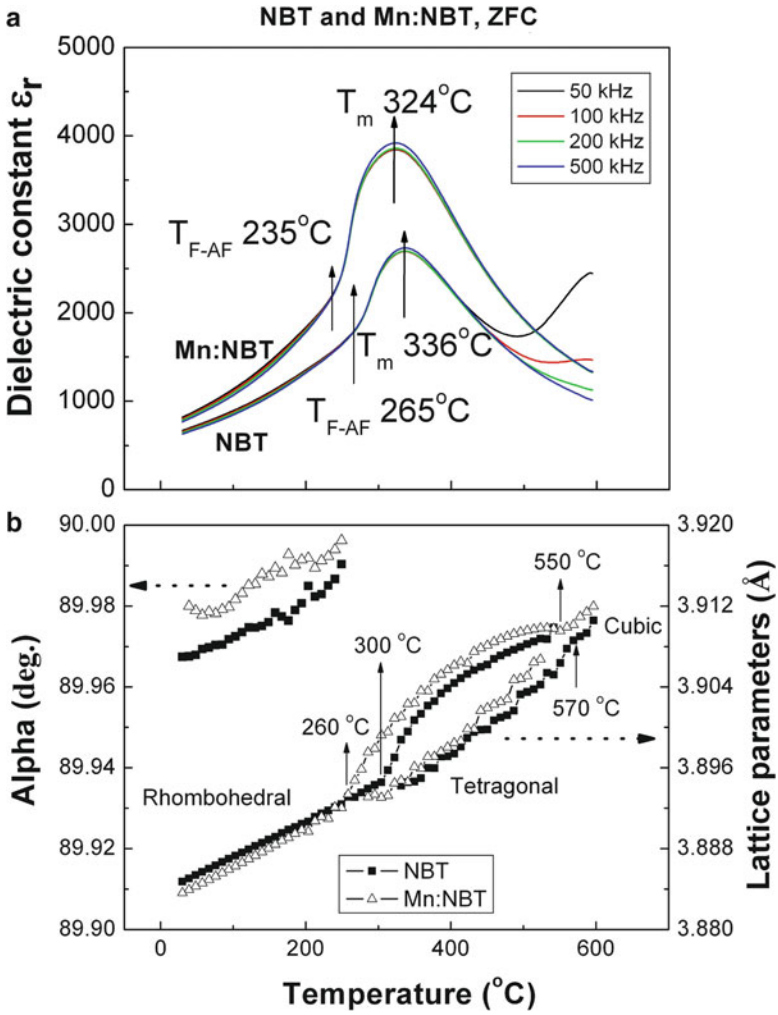

Fig. 1.30 (**a**) Dielectric constant and (**b**) crystal lattice parameters as a function of temperature for NBT and Mn:NBT in the ZFC condition. Reprinted with permission from [111]. Copyright [2010], John Wiley and Sons

crystallography principles for an *R* phase. Thus, the stripe-like color bands might be a manifestation of finer-scale ferroelectric *R* domains separated by micron-sized ferroelastic *T* domains. At 25°C, the contrast in the image for $\theta = 0^o$ (Fig. 1.31a) was darker than that for $\theta = 45^o$ (Fig. 1.31d), which may be because the *R* ferroelectric domain structures went extinct at $\theta = 0^o$.

Mn:NBT crystal was polished to a thickness of about 100 μm, and two interdigital Au electrodes were deposited on the top surface of the sample for *E*-dependent domain investigations. The experimental configuration is illustrated in Fig. 1.32.

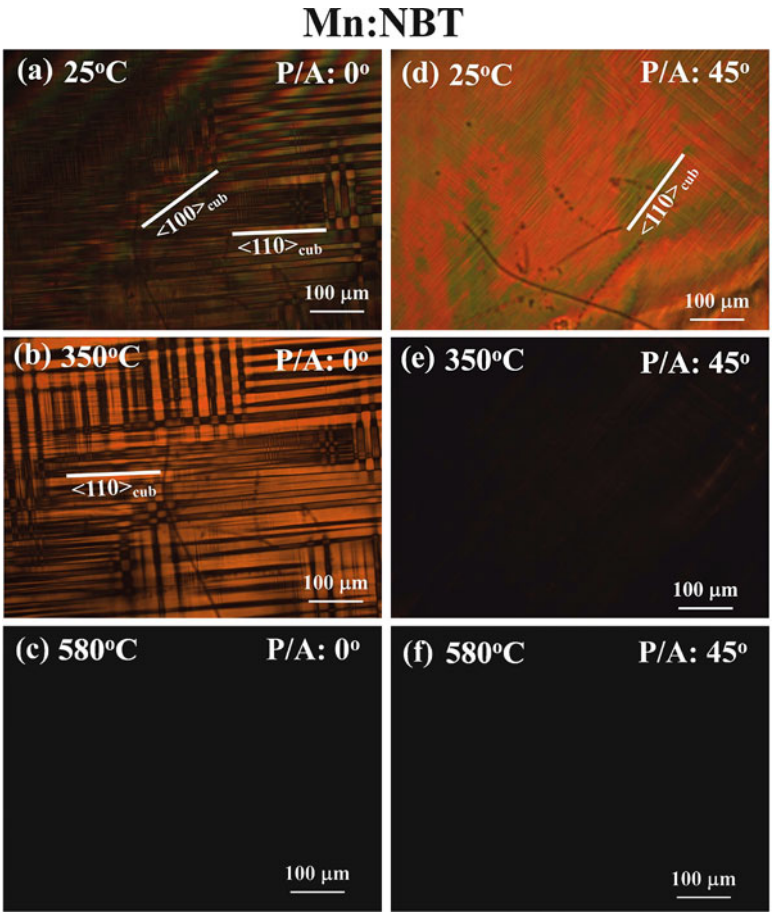

Fig. 1.31 Polarized light microscopy (PLM) images taken at various temperatures of (**a**, **d**) 25°C, (**b**, **e**) 350°C, and (**c**, **f**) 580°C. Reprinted with permission from [111]. Copyright [2010], John Wiley and Sons

Figure 1.33 shows the temperature evolution of the domain structure for Mn: NBT under zero field heating conditions [119]. At room temperature, ferroelastic *T* domains persist within the *R* phase field, where stripe-like color bands are present, as can be seen in Fig. 1.33a. These stripe-like color bands had a preferred orientation along $<110>_{cub}$. With increasing temperature, ferroelastic *T* domains and stripe-like color bands gradually became indistinct (see Fig. 1.33b), becoming optically isotropic at 300°C (see Fig. 1.33c), where no domain features could be found. The exact ferroelastic *T* domain structures then reappeared rather quickly with further increase of temperature in the range of 305–320°C ($T_{F\text{-}AF}$), as can be seen in Fig. 1.33d, e. This domain structure was then retained on further heating

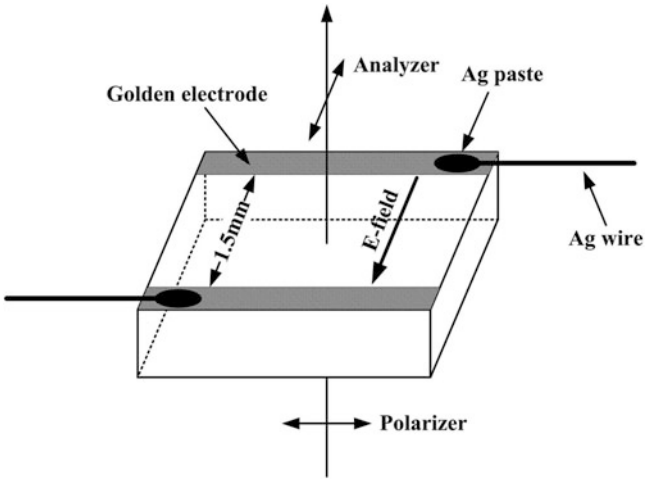

Fig. 1.32 The experimental configuration for domain observation under a polarizing microscope. A dc bias field was applied along <100> during the field-cooled process

above $T_{\text{F-AF}}$ (see Fig. 1.33f) up to 550°C (data not shown) where the $T \rightarrow C$ phase transition occurred. On subsequent recooling, the ferroelastic domain structure reappeared near 550°C (data not shown) and was retained (see Fig. 1.34a) with decreasing temperature to 280°C (see Fig. 1.34b), becoming optically isotropic at 265°C (see Fig. 1.34c). The ferroelastic *T* domains and stripe-like color bands then reappeared again on continued cooling below 200°C (see Fig. 1.34d, e), both remaining present on cooling to room temperature [119].

Comparison of Figs. 1.33 and 1.34 indicates that the stripe-like color bands within the PLM images are a manifestation of fine-scale ferroelectric *R* domains which exist within the ferroelastic *T* ones. This can be inferred because the stripe-like domains only appeared in the ferroelectric *R* phase field, then disappeared on heating above 300°C, and did not reappear on further heating. Fine-scale ferroelectric domains with sizes of 0.1~0.3 μm were directly observed by SFM performed in the piezo-response mode at room temperature, as shown in Fig. 1.34f. These results clearly demonstrate that small ferroelectric microdomain regions nucleate within the geometrical and elastic restrictions of the ferroelastic *T* macrodomain platlets. One can then infer that the nucleation of these microdomains is delayed in temperature on cooling relative to heating. Thus, the thermal hysteresis in the isotropization for Mn:NBT between heating (300°C) and cooling (265°C) was observed.

Figures 1.35 and 1.36 show the temperature evolution of the domain structure for Mn:NBT under $E = 1.1$ kV/cm and 2.7 kV/cm field cooling conditions [119]. Comparison of Fig. 1.35 ($E = 1.1$ kV/cm) to Fig. 1.36 ($E = 2.7$ kV/cm) will reveal that the dominant domain patterns were not changed by *E*: this can be explained by

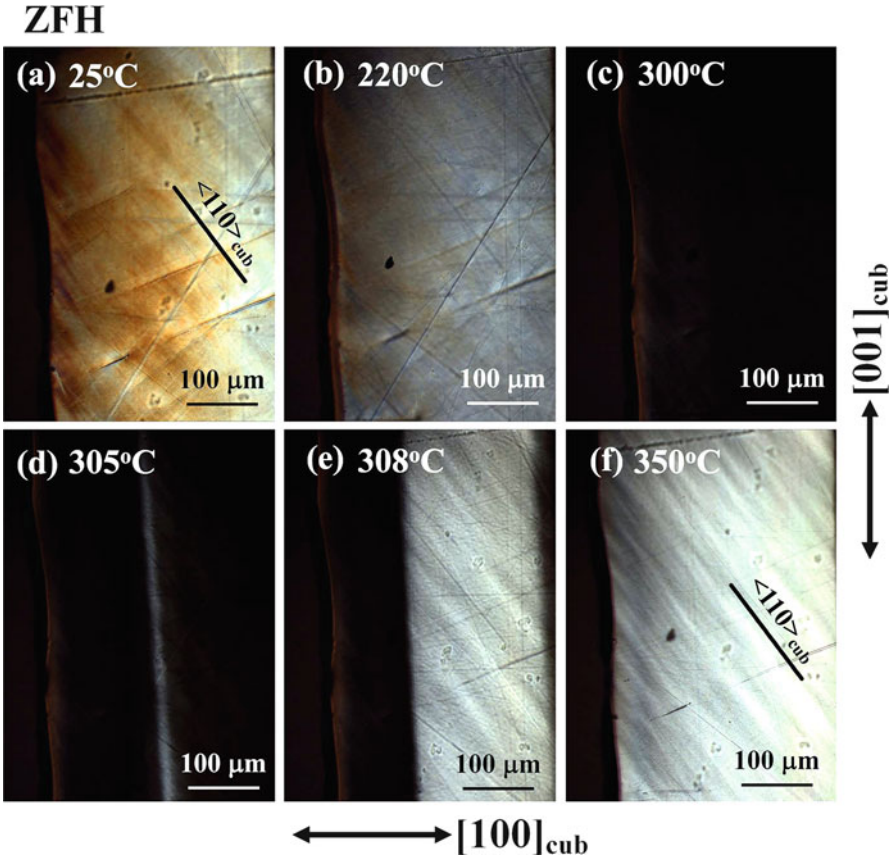

Fig. 1.33 Temperature-dependent domain structures for <001> oriented Mn:NBT crystal under ZFH condition: (**a**) 25°C, (**b**) 220°C, (**c**) 300°C, (**d**) 305°C, (**e**) 308°C and (**f**) 350°C. Reprinted with permission from [118]. Copyright [2011], John Wiley and Sons

the fact that the tetragonal ferroelastic domains from the high temperature (paraelectric) ferroelastic *T* phase remained present in the low temperature ferroelectric *R* phase, i.e., they are not ferroelectric. However, the stripe-like color bands became more evident on cooling under an applied electric field: the temperature at which the stripe-like color bands formed on cooling was increased from 200° to 220°C and 240°C with an increasing field from 0 to 1.1 kV/cm and 2.7 kV/cm, respectively. These results show that an electric field can notably influence the formation of the stripe-like color bands. This proves that the stripe-like color bands result from the ferroelectric domains, and that its nucleation temperature within the ferroeleastic domains can be increased by electric field.

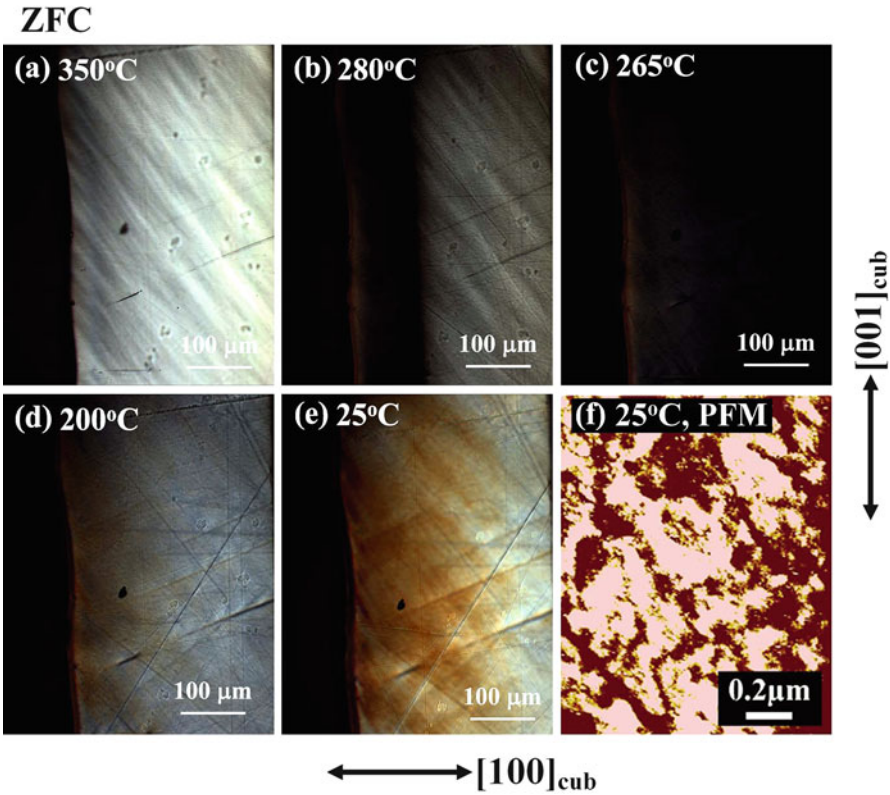

Fig. 1.34 Temperature dependent domain structures for <001> oriented Mn:NBT crystal under ZFC condition: (**a**) 350°C, (**b**) 280°C, (**c**) 265°C, (**d**) 200°C, (**e**) 25°C and (**f**) PFM image at 25°C. Reprinted with permission from [118]. Copyright [2011], John Wiley and Sons

1.2.2.3 Influence of dc-Bias on Phase Stability in Mn-Doped $Na_{0.5}Bi_{0.5}TiO_3$-5.6at%$BaTiO_3$ Single Crystals

High piezoelectric and ferroelectric properties have been found in Mn-doped $Na_{0.5}Bi_{0.5}TiO_3$–$BaTiO_3$ single crystals. The piezoelectric constant d_{33} and electromechanical coupling coefficients k_t and k_{31} in 0.14at% Mn-doped NBT-5.6%BT were found to be as high as 483 pC/N, 0.56, and 0.40, which demonstrate the real possibility of developing Pb-free NBT-BT crystals as alternatives to conventional PZT piezoelectrics [84].

Figure 1.37 shows the temperature dependent dielectric constant ε_r and loss factor tanδ for <100> oriented 0.14at% Mn:NBT-5.6at%BT crystals taken on heating under $E = 0$, 8 and 12 kV/cm [120]. Investigations focused on a secondary ferroelectric transition in the range of 100–200°C, which was below the dielectric

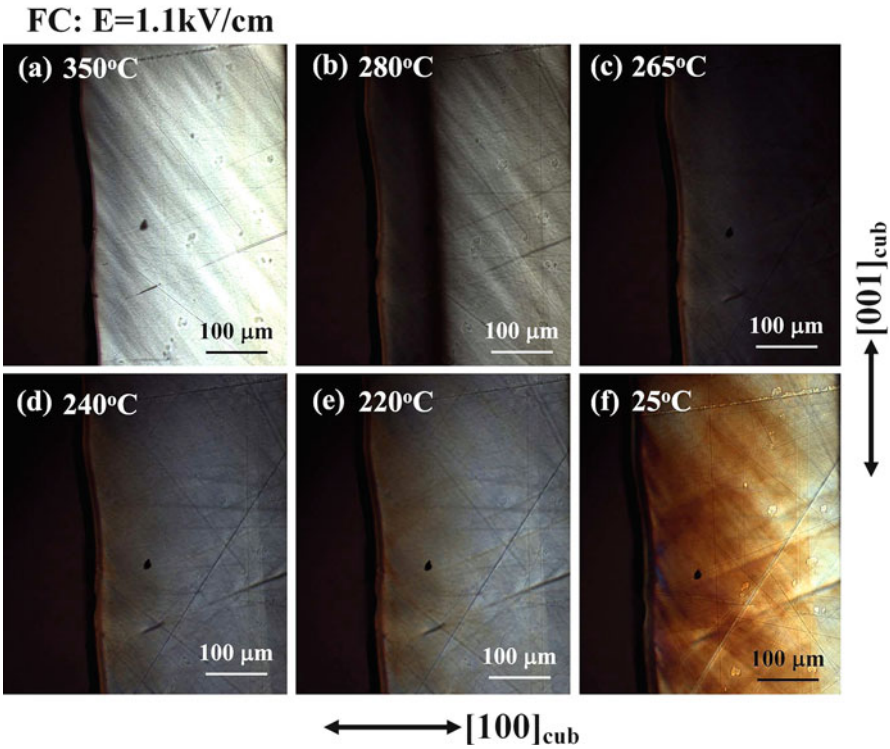

Fig. 1.35 Temperature dependent domain structures for <001> oriented Mn:NBT crystal under FC condition of $E = 1.1$ kV/cm: (**a**) 350°C, (**b**) 280°C, (**c**) 265°C, (**d**) 240°C, (**e**) 220°C and (**f**) 25°C. Reprinted with permission from [118]. Copyright [2011], John Wiley and Sons

maximum T_c at 280°C. Below the secondary transition, the dielectric constant can be seen to become strongly frequency dispersive near 130°C, somewhat analogous to that of relaxor ferroelectrics [121]. Upon increasing the field, four observations can be made. First, the temperature of the secondary dielectric constant maximum was increased: from ~130°C for $E = 0$ kV/cm to ~150°C for $E = 12$ kV/cm. Second, the magnitude of the dielectric constant near this second maximum increased dramatically: from ~4,000 for $E = 0$ kV/cm to ~12,000 for $E = 12$ kV/cm. Third, for $E \geq 12$ kV/cm, the secondary transformation sharpened dramatically, becoming frequency independent. Fourth, for $E \geq 8$ kV/cm, a tertiary dielectric anomaly was found near 105°C, indicating an additional step in the phase transformational sequence. Taken together, these data under different E indicate the following general trends. Under zero and moderate biases, the secondary phase transformation is diffuse. With increasing field, the transformation becomes gradually sharper, and a tertiary step in the structural sequence becomes apparent. Near a critical bias, the diffuse characteristics are overridden, and a sharp transition is induced: please note that there are similarities between this induced transition and the relaxor-to-normal transformation in relaxor ferroelectrics [34, 122].

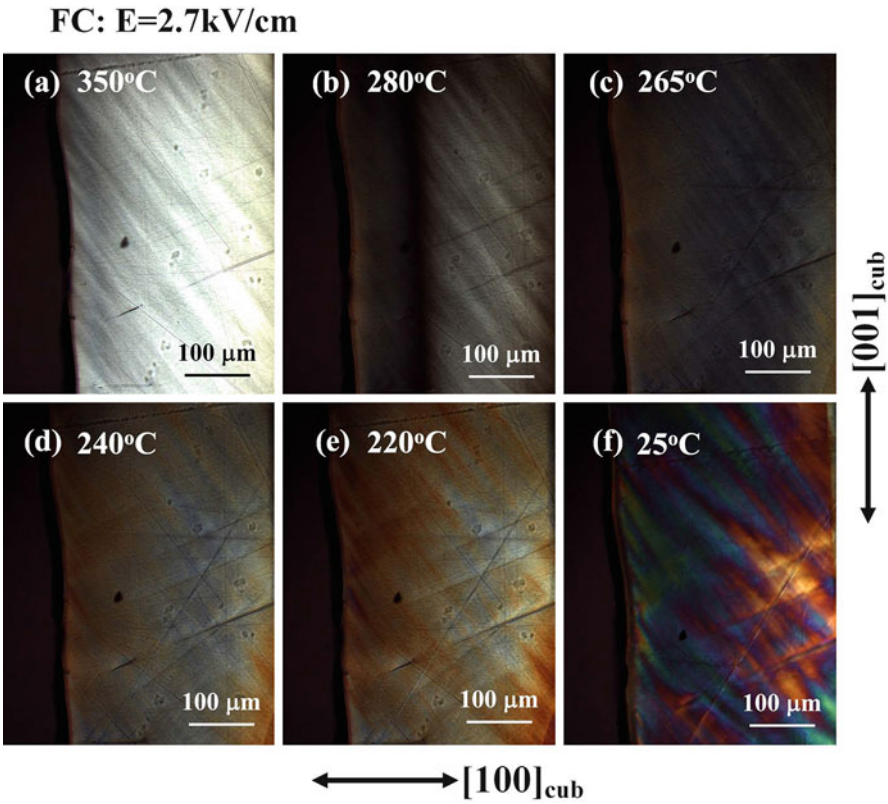

Fig. 1.36 Temperature dependent domain structures for <001> oriented Mn:NBT crystal under FC condition of $E = 2.7$ kV/cm: (**a**) 350°C, (**b**) 280°C, (**c**) 265°C, (**d**) 240°C, (**e**) 220°C and (**f**) 25°C. Reprinted with permission from [118]. Copyright [2011], John Wiley and Sons

Structural studies by XRD were performed about the (200) and (220) zones at room temperature for as-grown Mn:NBT-5.6BT%. Then the crystal was annealed at 600°C for 1 h and cooled to room temperature at a rate of 2°C/min, and (200) and (220) scans were again obtained at room temperature. Finally, the crystal was heated to 200°C and recooled to room temperature at a rate of 2°C/min under dc biases of $E = 6$ and 12 kV/cm, after which (200) and (220) scans were again obtained at room temperature. All of the XRD scans are given together in Fig. 1.38 [120]. The intensity is plotted on a logarithmic scale, so that small peaks with low intensity can be clearly seen.

Along the pseudocubic (200) zone, an intense diffraction peak was found at $2\theta = 46.51^{o}$, and a much weaker one was observed near $2\theta = 46.01^{o}$, as can be seen in the left hand column of Fig. 1.38. Along the pseudocubic (220) zone, an intense peak was found at $2\theta = 67.88^{o}$, which had two shoulders at $2\theta = 67.68^{o}$ and 68.13^{o}, as can be seen in the right hand column of Fig. 1.38. Different rows show the results for different histories. The top row is for the as-grown condition;

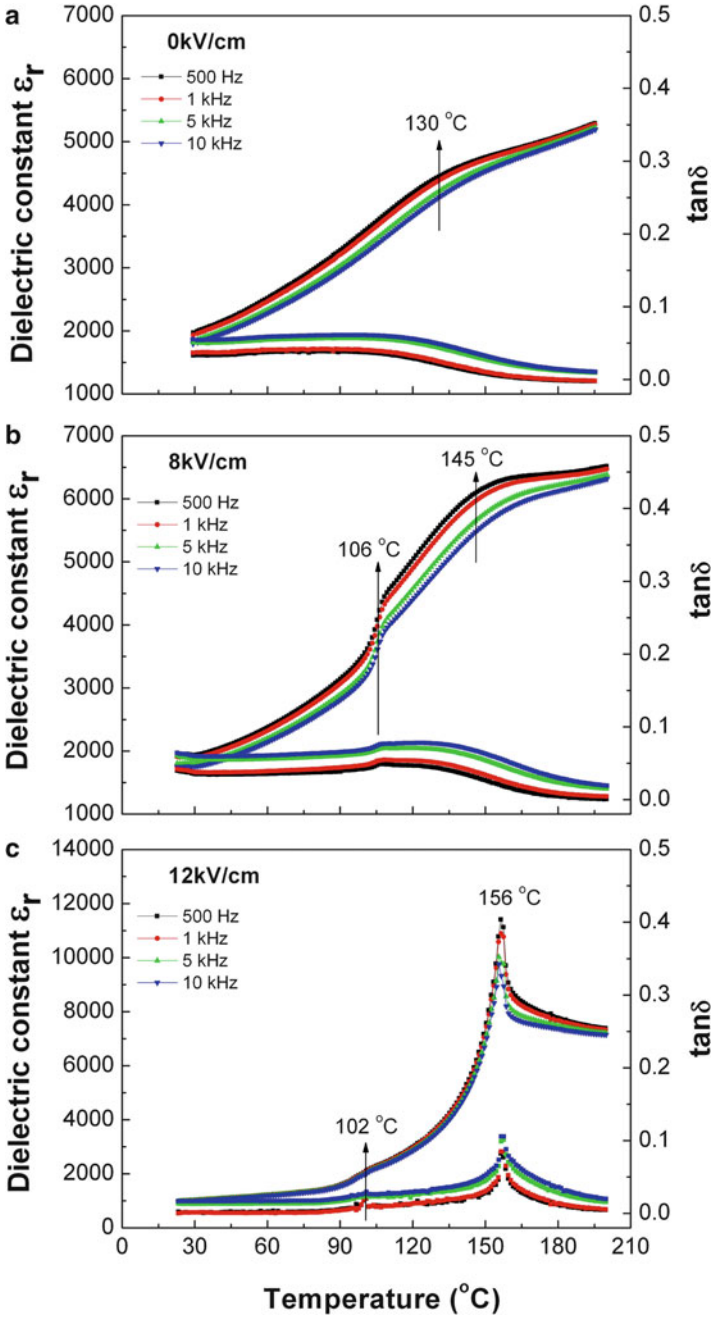

Fig. 1.37 Temperature dependent dielectric constant ε_r and loss factor tanδ for <100> oriented Mn:NBT-5.6%BT crystals taken heating under $E =$ (**a**) 0, (**b**) 8, and (**c**) 12 kV/cm. Reprinted with permission from [119]. Copyright [2009], American Institute of Physics

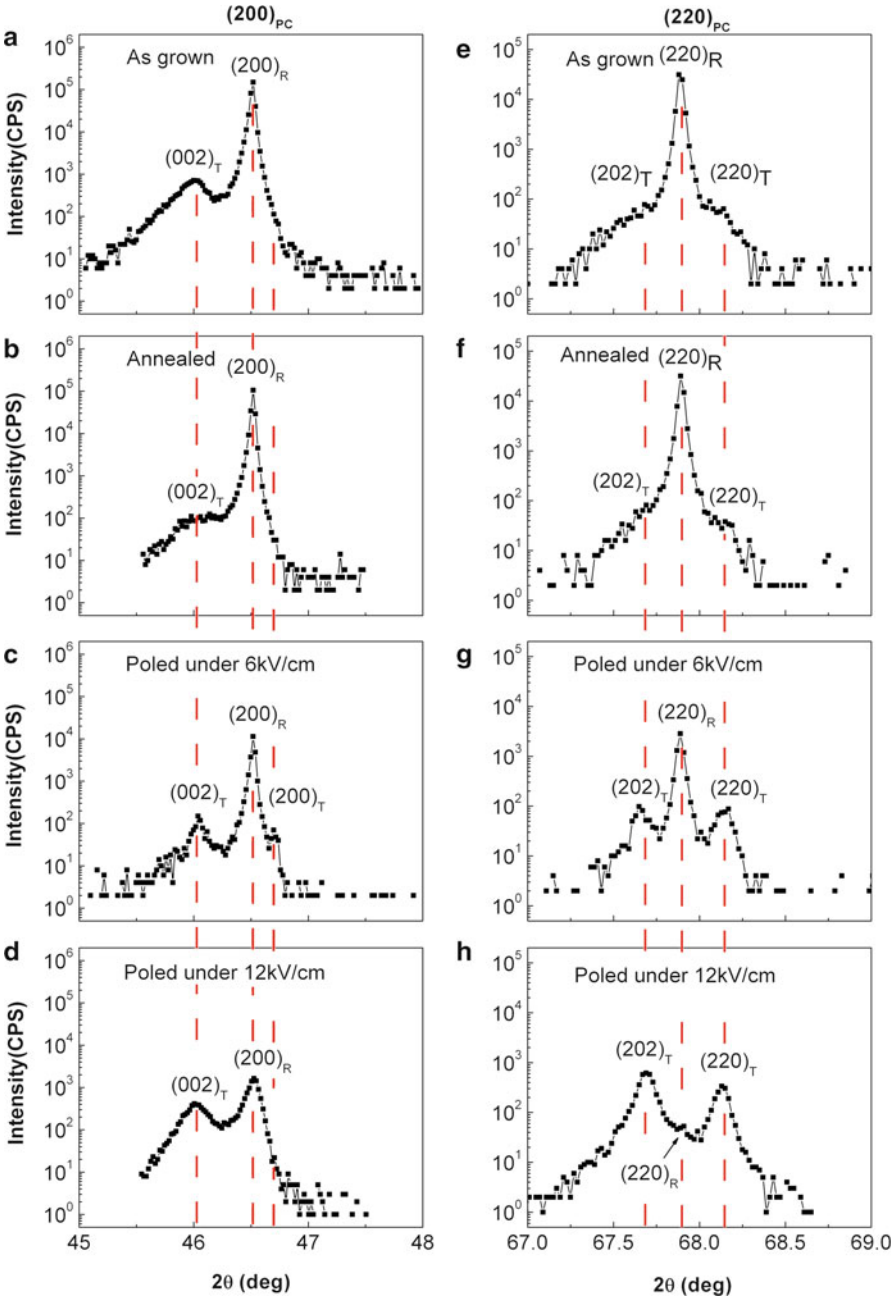

Fig. 1.38 (200) and (220) X-ray line scans for Mn:NBT-5.6%BT crystals at room temperature: (**a**, **e**) as-grown crystal; (**b**, **f**) after annealing at 600°C for 1 h; (**c**, **g**) after poling under dc $E = 6$ kV/cm applied along <100> direction; (**d**, **h**) after poling under dc $E = 12$ kV/cm applied along <100> direction. Reprinted with permission from [119]. Copyright [2009], American Institute of Physics

the second row for annealed; the third and final rows for the field cooled conditions under $E = 6$ kV/cm and $E = 12$ kV/cm, respectively. Comparisons of the various (200) and (220) scans will reveal that none of the diffraction peak positions were changed by thermal/electrical history. However, the intensity of the diffraction peaks was notably changed.

We assign the intense peaks at $2\theta = 46.51^{o}$ and $2\theta = 67.88^{o}$ to the *R* phase. This is consistent with previously published phase diagrams [58], where Mn:NBT-5.6%BT can be expected to lie on the *R* side of the MPB ($6 < x < 7$at%). Generally, there should be both (220) and (111) splittings for the *R* phase. However, the rhombohedral distortion is very weak in NBT crystal [118, 123], and thus its structure is very close to Cubic. Accordingly, we could not find any splittings along (220) and (111) for either pure NBT or Mn:NBT-5.6BT% within the experimental accuracy of our system: perhaps high energy synchrotron XRD studies are needed in the future. The other diffraction peaks in Fig. 1.38 can be assigned to the *T* phase. The lattice parameters were determined to be $(a_r, \alpha) = (3.9020$ Å, $89.98^{o})$ and $(a_t, c_t) = (3.8897, 3.9421)$Å for the *R* and *T* phases, respectively; it must be noted that these lattice constants were determined using both (200) and (220) scans, and that they were consistent with each other. These results show that the *T* and *R* phases coexist in Mn:NBT-5.6at%BT: the composition lies close to the MPB ($6 < x < 7$at%) between *R* and *T* phases, but the *R* phase is dominant. Furthermore, from the lattice parameters, we calculated that a huge volume change of 0.39% must occur at the $R \rightarrow T$ phase stability change.

Interestingly, the (200) pseudocubic reflection exhibited a large increase in the $(200)_r/(002)_t$ intensity ratio from 212 before annealing to 974 after annealing. This may result from one of two reasons. First, the *R*/*T* phase volume ratio might be increased by annealing. Since Mn:NBT-5.6%BT lies close to the MPB, the *T* and *R* phases should be energetically close, and thus there might be some metastability with thermal/electrical history. Second, the domain population might be altered by annealing; if this is the case, then we can conclude that the a-domain state is favored by annealing. Such a 90° domain switching by annealing might be explained by a "symmetry-conforming principle" of point defects, which was first proposed in ferroeleastic/martensite [124–126]. This model was later extended to $BaTiO_3$-based ferroelectrics and used to explain reversible ferroelectric domain-switching in aged samples, in particular Mn-doped perovskite [127–129]. Also, near the MPB that the conforming–symmetry of the internal fields of point defects might slightly alter the relative *R*/*T* phase stability.

After field-cooling under $E = 6$ kV/cm applied along the (001), the intensity for the *T* peaks was notably increased, whereas that of the *R* peaks was decreased: as can be seen in Fig. 1.38c, g. With the increase of *E* to 12 kV/cm, the intensity of the $(200)_r$ peak was further notably decreased, whereas that for the $(220)_r$ had nearly disappeared, as can be seen in Fig. 1.38d, h. These results clearly demonstrate a change from *R* to *T* phase stability between as-grown and field-cooled conditions: although *T* was clearly present in both conditions.

Figure 1.39 shows the temperature dependence of the crystal lattice parameters under $E = 0$ and 11.4 kV/cm applied along the (001) [120]. The investigations

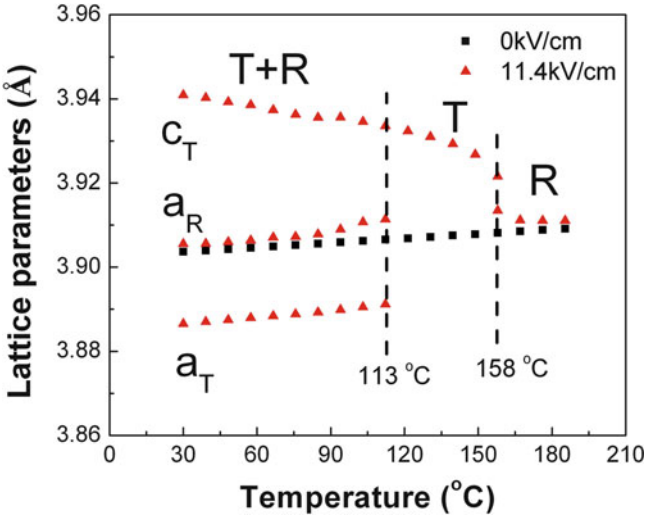

Fig. 1.39 Temperature dependence of the crystal lattice parameters for Mn:NBT-5.6%BT under field of $E = 0$, and 11.4 kV/cm. Reprinted with permission from [119]. Copyright [2009], American Institute of Physics

began from the annealed condition. For $E = 0$ kV/cm, an intense (200) peak for the *R* phase was observed, whose lattice parameter increased near linearly with temperature. Under zero-field, the *R* phase was dominant, whereas the peak for the *T* phase was so weak that its position could not be determined with accuracy, thus the lattice parameters for the *T* phase under zero-field are not shown in Fig. 1.39. However, in the field heating condition between 30 and 113°C under $E = 11.4$ kV/cm, the (200) and (220) reflections exhibited an obvious *T* splitting. Both *T* and *R* phases were found on heating in this temperature range, with lattice parameters as given in Fig. 1.39. On heating between 113 and 158°C under $E = 11.4$ kV/cm, the (200) pseudocubic reflection exhibited only the (002) peak for the *T* phase. This indicates that Mn:NBT-5.6%BT transforms into a near single c-domain *T* state under $E \geq 11.4$ kV/cm in this temperature range. The lattice parameter a_t was not given in the temperature range of 113–158°C because we could not obtain a_t along the zones we had access to for a single c-domain Mn:NBT-5.6%BT wafer with thickness of 0.7 mm. Clearly, the tertiary phase transition observed in the dielectric constant (see Fig. 1.37b, c) is related to contributions from *T* domain realignment. In addition, near 158°C, an abrupt phase transition occurred, and the lattice parameters were equivalent to that for the *R* phase under $E = 0$. This indicates that the Mn:NBT-5.6%BT crystal may have undergone a phase transition from single domain *T* ferroelectric to antiferroelectric, as previously suggested [58].

In summary, the relative phase stability of Mn:NBT-5.6%BT crystals was investigated under dc electrical bias. Tetragonal and rhombohedral phases were found to coexist in the as-grown condition, with the *R* phase being dominant. With increasing temperature, an induced relative phase stability change from *R*

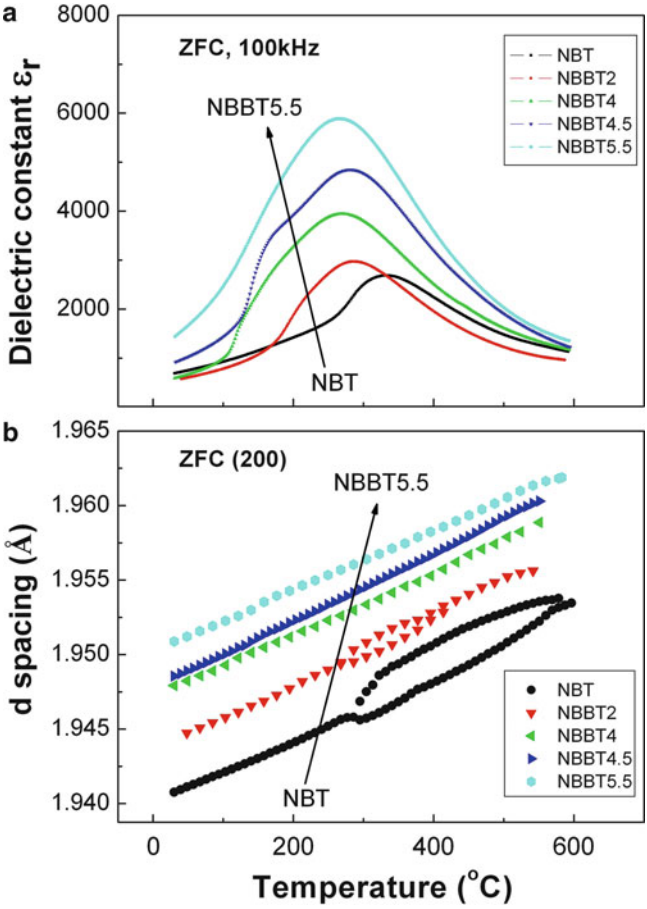

Fig. 1.40 (**a**) Dielectric constant and (**b**) d-spacing for (200) as a function of temperature for various NBT-*x*%BT crystals in the ZFC state

to *T* phases was observed for an *E*-field applied along <001>. These results demonstrate that this *T* phase remains stable after the removal of *E* in the field-cooled state.

1.2.2.4 Domain Structure Evolution in $Na_{0.5}Bi_{0.5}TiO_3$-*x*%$BaTiO_3$ (NBT-*x*%BT, $x = 0$, 4.5 and 5.5) Single Crystals

Figure 1.40a shows the dielectric constant as a function of temperature in the ZFC state for various NBT-*x*%BT crystals, using a measurement frequency of 100 kHz [130]. These data clearly demonstrate a phase transformation between

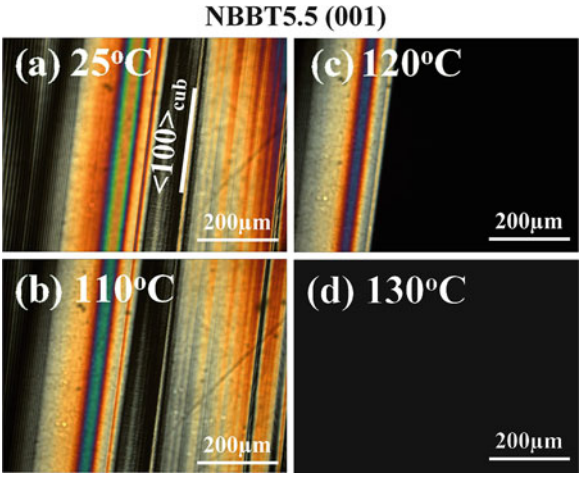

Fig. 1.41 Domain structure for NBBT5.5 at various temperatures (**a**) 25°C, (**b**) 110°C, (**c**) 120°C, and (**d**) 130°C

high temperature paraelectric and low temperature polar phases in the vicinity of 300°C. The phase transformation temperature T_c was not notably dependent on the BT content in the range of $0 < x < 5.5$. However, the magnitude of the dielectric constant exhibited a clear trend of increase with increasing x in this compositional range.

Figure 1.40b shows the d spacing of (200) diffraction plane as a function of temperature. For $0 < x < 2$, XRD data revealed that the $C \rightarrow T$ transition temperature drops dramatically with BT-content increasing from 0 to 2 and T phase only exists a narrow temperature range for NBBT2 (see Fig. 1.40b) [130]. However, for $x = 4$–5.5, XRD data did not reveal any T or R splitting from (111), (200), and (220) diffraction zones and the d-spacing linearly changed with the decrease of temperature (see Fig. 1.40b). Thus the phase below $T_{AF\text{-}F}$ is referred to here as rhombohedral phase for NBT-x%BT ($x = 0 \sim 5.5$).

Figure 1.41 shows PLM images for (001)-oriented NBBT5.5 taken at (a) 25°C, (b) 110°C, close but lower than $T_{F\text{-}AF}$, (c) 120°C, equal to $T_{F\text{-}AF}$ and (d) 130°C, higher than $T_{F\text{-}AF}$ [130]. Interestingly, the domain wall observed by PLM in NBBT5.5 oriented along $<100>_{cub}$ directions (see Fig. 1.41a). These results are quite different from that observed in NBT (see Fig. 1.25): the domain wall oriented along $<110>_{cub}$. This can be explained by the tetragonal phase, which results in the ferroelastic domains with domain wall oriented along $<110>_{cub}$ in NBT crystal, disappearing in NBBT5.5 single crystal (see Fig. 1.40b), i.e., the domain wall observed in Fig. 1.41 results from the ferroelectric domains not from ferroelastic domains. The domain structures in NBBT5.5 were stable below $T_{F\text{-}AF}$, as shown in Fig. 1.41b. With temperature increasing to $T_{F\text{-}AF}$ (see Fig. 1.41c), part of area shows optical extinction. The whole optical extinction was obtained when temperature is higher than $T_{F\text{-}AF}$ (see Fig. 1.41d). No birefringence phenomena could be seen again in NBBT5.5 crystals when temperature reached the range of 130–600°C.

1.2.3 Monoclinic M_C Phase in [001] Field Cooled $BaTiO_3$ Single Crystals

$BaTiO_3$ is the classic perovskite and is a lead-free ferroelectric. It undergoes a sequence of ferroelectric transitions: $C \rightarrow T \rightarrow O \rightarrow R$ upon cooling with the polarization oriented in the [001], [110], and [111] directions in the T, O, and R phases [131]. Under an electric field (E) applied along orientations that are different than that of the spontaneous polarization (P_s) directions, enhanced piezoelectricity has been reported by Wada et al. [40, 92]. Based on the first principle calculations of the R phase of $BaTiO_3$ single crystals as a E function applied along [001], Fu and Cohen [39] proposed a polarization rotation mechanism during an E-field induced R-to-T phase transformation which takes a path of $R \rightarrow M_A \rightarrow T$ and gives high piezoelectric response similar to that found in domain-engineered PMN-x%PT and PZN-x%PT crystals [3]. X-ray diffraction investigations revealed that Moniclinic phase not only can be found in lead-based solid solutions with MPB, but also can be induced under E-field in $BaTiO_3$ near polymorphic phase boundary (PPB) [132].

Upon ZFC, $BaTiO_3$ is known to have the sequence of phase transitions of $C \rightarrow T \rightarrow O \rightarrow R$, which occur at 393, 283, and 183 K, respectively. In the ZFC state, $BaTiO_3$ has a multitude of domain states with a complicated domain configuration in area or mesh scans of reciprocal space. However, application of E-field can simplify the domain configurations, as the field can fix an axis. Figure 1.42 shows mesh scans taken around the (002) and (200) reflections at 300 and 263 K for [001] $BaTiO_3$ under $E = 1$ kV/cm in the FC condition [132]. In the tetragonal or T phase region, E//[001] fixes the c-axis stabilizing a single-domain T state, as can be seen in the mesh scans of Fig. 1.44. At 300 K, both the (200) and (002) scans exhibit a well-defined sharp contour: the (200) peak at higher H has a lattice parameter of $a_t = 3.992$ Å and the (002) peak at lower L of $c_t = 4.038$ Å. These data clearly demonstrate that upon cooling under $E = 1$ kV/cm applied along the [001] that the system transforms from a cubic phase into a single domain tetragonal one.

Upon further cooling below room temperature under an E//[001] of 1 kV/cm, the crystal undergoes a secondary phase transition near the $T \rightarrow O$ phase boundary of the ZFC state. Figure 1.42 show mesh scans taken about the (200) and (002) at 263 K, respectively. The (200) reflection at 263 K was found to split into three peaks: two (200) peaks and a single (020) one, whereas the (002) reflection remained as a single peak. Clearly, the (200) and (002) mesh scans at 263 K have the signature of the M_C phase, similar to that previously reported for PMN-x%PT and PZN-x%PT for compositions close to the MPB. The lattice parameters of this monoclinic phase of $BaTiO_3$ were (a_m, b_m, c_m; β_m) = (4.167 Å, 3.988 Å, 4.168 Å; 89.8°). The limiting case of this M_C phase is the orthorhombic (O) phase, which has been known for many years in $BaTiO_3$ [131].

Figure 1.43 shows a mesh scan taken about the (200) reflection at 263 K upon removal of the electric field after field cooling [132]. This scan reveals that the signatures of the M_C phase remained after removal of field; the M_C phase is stable once induced.

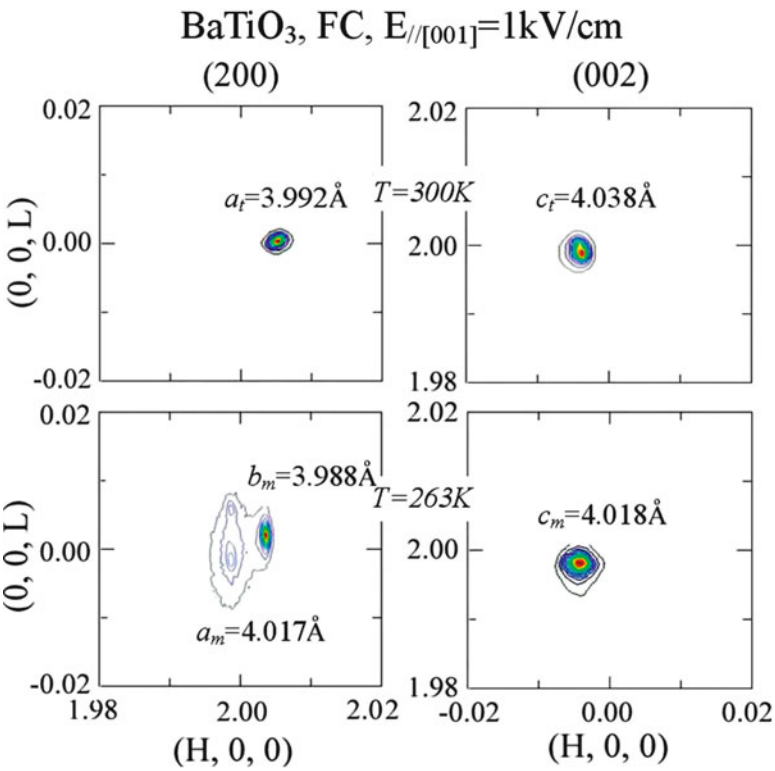

Fig. 1.42 Mesh scans taken around (002) and (200) reflections of $BaTiO_3$ with $E = 1$ kV/cm applied along the [001] at 300 and 263 K in the FC condition. Reprinted with permission from [131]. Copyright [2009], American Institute of Physics

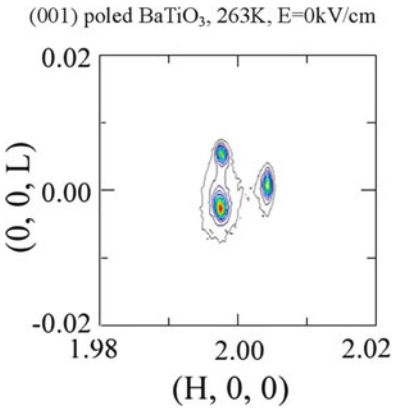

Fig. 1.43 Mesh scan taken around (200) of $BaTiO_3$ at 263 K under an electric field of $E = 0$ kV/cm after a prior FC under $E = 1$ KV/cm. Reprinted with permission from [131]. Copyright [2009], American Institute of Physics

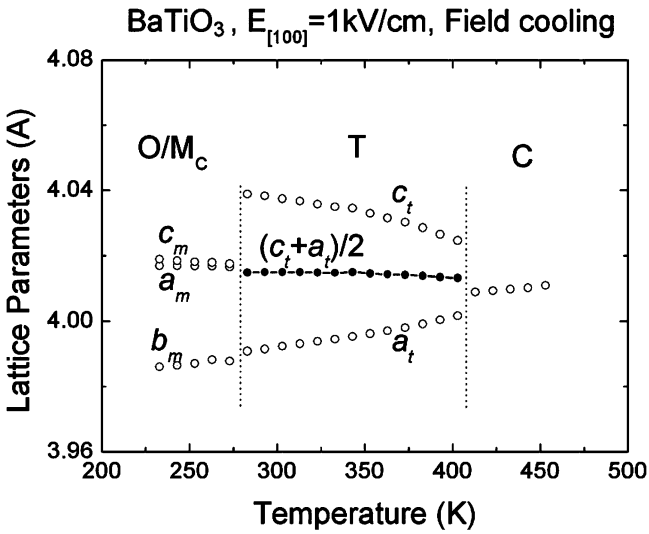

Fig. 1.44 Temperature dependence of lattice parameter for BaTiO3 with $E = 1$ kV/cm applied along [001]. Reprinted with permission from [131]. Copyright [2009], American Institute of Physics

Figure 1.44 shows the temperature dependence of the lattice parameters for $BaTiO_3$ under $E = 1$ kV/cm applied along the [001] direction [132]. At 450 K, a sharp change in the lattice parameter can be seen on cooling, corresponding to the $C \rightarrow T$ transition. Below this temperature, the lattice constant c_t (a_t) gradually increased (decreased) as the temperature was decreased in the tetragonal region. Near 283 K, a sharp change was found corresponding to the $T \rightarrow M_C$ transformation where cm was decreased with respect to c_t, a_m increased with respect to a_t, and b_m was nearly equal to a_t. The temperature dependent lattice parameters are quite similar to the corresponding one in the ZFC condition, which exhibits a $T \rightarrow O$ transition. The main difference for M_C was that $c_m > a_m$ under $E = 1$ kV/cm. This indicates that application of E//[001] results in a slight polarization rotation away from the [110] toward the [001], which is the pathway of $O \rightarrow T$, as previously reported for PZN-0.08PT [21].

In Fig. 1.44, it can be seen on crossing the $T \rightarrow M_C$ phase boundary that $a_t \approx b_m$ and $a_t + c_t \approx a_m + c_m$. Both b_m and a_t were calculated from the same (200) reflection; the continuity of these parameters demonstrates that one of the d-spacing in the unit cell of $BaTiO_3$ remains unchanged by the $T \rightarrow M_C$ transition. These are the same geometrically invariant conditions of the lattice parameters recently predicted by the adaptive phase theory and experimentally reported at the $T \rightarrow M_C$ transition for PMN-xPT and PZN-xPT crystals [41, 42]. This model is based on the concept that the M_C phase consists of conformably miniaturized tetragonal nanodomains with very low domainwall energies. It is interesting to note that enhanced piezoelectricity has also recently been reported in <111> field $BaTiO_3$

crystals, where the value of the transversal piezoelectric coefficient (d_{31}) and electromechanical coupling coefficient (k_{31}) was shown to increase dramatically with decreasing domain size [92].

In summary, a monoclinic M_C phase was induced in $BaTiO_3$ crystals when FC under $E = 1$ kV/cm applied along the [001] direction. The M_C phase is a domain engineered state, which consists of four monoclinic domains. This monoclinic phase is stable upon removal of electric field. This is an interesting finding because domain engineered states are key to enhanced piezoelectricity in Pb-based crystals. It opens up the possibility that many classic perovskite systems may have intermediate structurally bridging phases, by which enhanced piezoelectricity can be achieved.

References

1. Jaffe B, Cook WR, Jaffe H (1971) Piezoelectric ceramics. Academic, New York
2. Berlincourt D (1971) Ultrasonic transducer materials: piezoelectric crystals and ceramics. Springer, London
3. Park SE, Shrout TR (1997) Ultrahigh strain and piezoelectric behavior in relaxor based ferroelectric single crystals. J Appl Phys 82:1804–1811
4. Kuwata J, Uchino K, Nomura S (1981) Phase-transitions in the $Pb(Zn_{1/3}nb_{2/3})O_3$-$PbTiO_3$ system. Ferroelectrics 37:579–582
5. Kuwata J, Uchino K, Nomura S (1982) Dielectric and piezoelectric properties of $0.91Pb(Zn_{1/3}nb_{2/3})O_3$-$0.09PbTiO_3$ single-crystals. Jpn J Appl Phys Pt 1 21:1298–1302
6. Choi SW, Shrout TR, Jang SJ, Bhalla AS (1989) Morphotropic phase-boundary in $Pb(Mg_{1/3}Nb_{2/3})O_3$-$PbTiO_3$ system. Mater Lett 8:253–255
7. Singh AK, Pandey D (2001) Structure and the location of the morphotropic phase boundary region in (1-x)$[Pb(Mg_{1/3}Nb_{2/3})O_3]$-x$PbTiO_3$. J Phys Condens Matter 13:L931–L936
8. Noheda B, Cox DE, Shirane G, Gao J, Ye ZG (2002) Phase diagram of the ferroelectric relaxor (1-x)$PbMg_{1/3}Nb_{2/3}O_3$-x$PbTiO_3$. Phys Rev B 66:054104
9. Ye ZG, Dong M (2000) Morphotropic domain structures and phase transitions in relaxor-based piezo-/ferroelectric (1-x)$Pb(Mg_{1/3}Nb_{2/3})O_3$-x$PbTiO_3$ single crystals. J Appl Phys 87:2312–2319
10. Guo YP, Luo HS, Ling D, Xu HQ, He TH, Yin ZW (2003) The phase transition sequence and the location of the morphotropic phase boundary region in (1-x)$[Pb(Mg_{1/3}Nb_{2/3})O_3]$-x $PbTiO_3$ single crystal. J Phys Condens Matter 15:L77–L82
11. Service RF (1997) Materials science: shape-changing crystals get shiftier. Science 275:1876–1878
12. Damjanovic D (2005) Contributions to the piezoelectric effect in ferroelectric single crystals and ceramics. J Am Ceram Soc 88:2663–2676
13. Noheda B, Cox DE, Shirane G, Gonzalo JA, Cross LE, Park SE (1999) A monoclinic ferroelectric phase in the $Pb(Zr_1$-xTix$)O_3$ solid solution. Appl Phys Lett 74:2059–2061
14. Noheda B, Gonzalo JA, Cross LE, Guo R, Park SE, Cox DE, Shirane G (2000) Tetragonal-to-monoclinic phase transition in a ferroelectric perovskite: the structure of $PbZr_{0.52}Ti_{0.48}O_3$. Phys Rev B 61:8687–8695
15. Noheda B, Cox DE, Shirane G, Guo R, Jones B, Cross LE (2001) Stability of the monoclinic phase in the ferroelectric perovskite $PbZr_1$-x$TixO_3$. Phys Rev B 63:014103
16. Vanderbilt D, Cohen M (2001) Monoclinic and triclinic phases in higher-order Devonshire theory. Phys Rev B 63:094108

17. Bellaiche L, Garcia A, Vanderbilt D (2000) Finite-temperature properties of $Pb(Zr_1\text{-}xTix)O_3$ alloys from first principles. Phys Rev Lett 84:5427–5430
18. Noheda B, Cox DE, Shirane G, Park SE, Cross LE, Zhong Z (2001) Polarization rotation via a monoclinic phase in the piezoelectric 92% $PbZn_{1/3}Nb_{2/3}O_3$-8% $PbTiO_3$. Phys Rev Lett 86:3891–3894
19. Noheda B, Zhong Z, Cox DE, Shirane G, Park SE, Rehrig P (2002) Electric-field-induced phase transitions in rhombohedral $Pb(Zn_{1/3}Nb_{2/3})(1\text{-}x)TixO_3$. Phys Rev B 65:224101
20. La-Orauttapong D, Noheda B, Ye ZG, Gehring PM, Toulouse J, Cox DE, Shirane G (2002) Phase diagram of the relaxor ferroelectric $(1\text{-}x)Pb(Zn_{1/3}Nb_{2/3})O_3\text{-}xPbTiO_3$. Phys Rev B 65:144101
21. Ohwada K, Hirota K, Rehrig PW, Fujii Y, Shirane G (2003) Neutron diffraction study of field-cooling effects on the relaxor ferroelectric $Pb[(Zn_{1/3}Nb_{2/3})0.92Ti_{0.08}]O_3$. Phys Rev B 67:094111
22. Noheda B (2002) Structure and high-piezoelectricity in lead oxide solid solutions. Curr Opin Solid St M 6:27–34
23. Yao JJ, Cao H, Ge WW, Li JF, Viehland D (2009) Monoclinic M-B phase and phase instability in [110] field cooled $Pb(Zn_{1/3}Nb_{2/3})O_3$-4.5%$PbTiO_3$ single crystals. Appl Phys Lett 95:052905
24. Ye ZG, Noheda B, Dong M, Cox D, Shirane G (2001) Monoclinic phase in the relaxor-based piezoelectric/ferroelectric $Pb(Mg_{1/3}Nb_{2/3})O_3\text{-}PbTiO_3$ system. Phys Rev B 64:184114
25. Xu G, Luo H, Xu H, Yin Z (2001) Third ferroelectric phase in PMNT single crystals near the morphotropic phase boundary composition. Phys Rev B 64:020102
26. Lu Y, Jeong DY, Cheng ZY, Zhang QM, Luo HS, Yin ZW, Viehland D (2001) Phase transitional behavior and piezoelectric properties of the orthorhombic phase of $Pb(Mg_{1/3}Nb_{2/3})O_3\text{-}PbTiO_3$ single crystals. Appl Phys Lett 78:3109–3111
27. Kiat J-M, Uesu Y, Dkhil B, Matsuda M, Malibert C, Calvarin G (2002) Monoclinic structure of unpoled morphotropic high piezoelectric PMN-PT and PZN-PT compounds. Phys Rev B 65:064106
28. Singh A, Pandey D (2003) Evidence for MB and MC phases in the morphotropic phase boundary region of $(1\text{-}x)[Pb(Mg_{1/3}Nb_{2/3})O_3]\text{-}xPbTiO_3$: a Rietveld study. Phys Rev B 67:064102
29. Bai FM, Wang NG, Li JF, Viehland D, Gehring PM, Xu GY, Shirane G (2004) X-ray and neutron diffraction investigations of the structural phase transformation sequence under electric field in $0.7Pb(Mg_{1/3}Nb_{2/3})\text{-}0.3PbTiO_3$ crystal. J Appl Phys 96:1620–1627
30. Cao H, Bai FM, Li JF, Viehland D, Xu GY, Hiraka H, Shirane G (2005) Structural phase transformation and phase boundary/stability studies of field-cooled $Pb(Mg_{1/3}Nb_{2/3}O_3)$-32% $PbTiO_3$ crystals. J Appl Phys 97:094101
31. Cao H, Bai FM, Wang NG, Li JF, Viehland D, Xu GY, Shirane G (2005) Intermediate ferroelectric orthorhombic and monoclinic M-B phases in [110] electric-field-cooled $Pb(Mg_{1/3}Nb_{2/3})O_3$-30%$PbTiO_3$ crystals. Phys Rev B 72:064104
32. Cao H, Li JF, Viehland D, Xu GY, Shirane G (2006) Monoclinic MC vs orthorhombic in [001] and [110] electric-field-cooled $Pb(Mg_{1/3}Nb_{2/3}O_3)$-35%$PbTiO_3$ crystals. Appl Phys Lett 88:072915
33. Cao H, Li JF, Viehland D (2006) Electric-field-induced orthorhombic to monoclinic MB phase transition in [111] electric field cooled $Pb(Mg_{1/3}Nb_{2/3}O_3)$-30%$PbTiO_3$ crystals. J Appl Phys 100:084102
34. Cao H, Li JF, Viehland D (2006) Structural origin of the relaxor-to-normal ferroelectric transition in $Pb(Mg_{1/3}Nb_{2/3}O_3)\text{-}xPbTiO_3$. J Appl Phys 100:034110
35. Cao H, Li JF, Viehland D, Xu GY (2006) Fragile phase stability in $(1\text{-}x)Pb(Mg_{1/3}Nb_{2/3}O_3)\text{-}x$ $PbTiO_3$ crystals: a comparison of [001] and [110] field-cooled phase diagrams. Phys Rev B 73:184110

36. Cao H, Stock C, Xu GY, Gehring PM, Li JF, Viehland D (2008) Dynamic origin of the morphotropic phase boundary: soft modes and phase instability in $0.68Pb(Mg_{1/3}Nb_{2/3}O_3)$-$0.32PbTiO_3$. Phys Rev B 78:104103
37. Bai FM (2006) Materials science and engineering. Virginia Polytechnic Institute and State University, Blacksburg
38. Cao H (2008) Materials science and engineering. Virginia Polytechnic Institute and State University, Blacksburg
39. Fu HX, Cohen RE (2000) Polarization rotation mechanism for ultrahigh electromechanical response in single-crystal piezoelectrics. Nature 403:281–283
40. Wada S, Suzuki S, Noma T, Suzuki T, Osada M, Kakihana M, Park SE, Cross LE, Shrout TR (1999) Enhanced piezoelectric property of barium titanate single crystals with engineered domain configurations. Jpn J Appl Phys Pt 1 38:5505–5511
41. Viehland D (2000) Symmetry-adaptive ferroelectric mesostates in oriented $Pb(BI_{1/3}BII_{2/3})O_3$-$PbTiO_3$ crystals. J Appl Phys 88:4794–4806
42. Jin YM, Wang YU, Khachaturyan AG, Li JF, Viehland D (2003) Conformal miniaturization of domains with low domain-wall energy: monoclinic ferroelectric states near the morphotropic phase boundaries. Phys Rev Lett 91:197601
43. Jin YM, Wang YU, Khachaturyan AG, Li JF, Viehland D (2003) Adaptive ferroelectric states in systems with low domain wall energy: tetragonal microdomains. J Appl Phys 94:3629–3640
44. Wechsler MS (1974) On theory of formation of martensite. JOM 5(1953):1503–1515
45. Syutkina VI, Yakovleva ES (1967) The mechanism of deformation of the ordered CuAu alloy. Physica Status Solidi B 21:465–480
46. Wang YU (2006) Diffraction theory of nanotwin superlattices with low symmetry phase. Phys Rev B Condens Matter 74:104109–104101
47. Wang YU (2006) Three intrinsic relationships of lattice parameters between intermediate monoclinic Mc and tetragonal phases in ferroelectric $Pb[(Mg_{1/3}Nb_{2/3})1\text{-}xTiO_3$ and $Pb[(Zn_{1/3}Nb_{2/3})1\text{-}xTix]O_3$ near morphotropic phase boundaries. Phys Rev B Condens Matter 73:14113–14111
48. European Union (2003) Directive 2002/95/Ec of the European Parliament and of the Council of 27 January 2003 on the restriction of the use of certain hazardous substances in electrical and electronic equipment (ROHS). Official J Eur Union L37:19–23
49. European Union (2003) Directive 2002/96/Ec of the European Parliament and of the Council of 27 January 2003 on waste electrical and electronic equipment (WEEE). Official J Eur Union L37:24–38
50. Von Hippel A (1946) High dielectric constant ceramics. Ind Eng Chem 38:1097–1109
51. Roberts S (1947) Dielectric and piezoelectric properties of barium titanate. Phys Rev 71:890
52. Buhrer CF (1962) Some properties of bismuth perovskites. J Chem Phys 36:798–803
53. Smolenskii G, Isupov V, Agranovskaya A, Krainik N (1960) New ferroelectrics of complex composition. Sov Phys Solid State 2:2651–2654
54. Suchanicz J, Roleder K, Kania A, Hanaderek J (1988) Electrostrictive strain and pyroeffect in the region of phase coexistence in $Na_{0.5}Bi_{0.5}TiO_3$. Ferroelectrics 77:107–110
55. Sakata K, Masuda Y (1974) Ferroelectric and antiferroelectric properties of $(Na_{0.5}Bi_{0.5})TiO_3$-$SrTiO_3$ solid solution ceramics. Ferroelectrics 7:347–349
56. Nagata H, Takenaka T (1997) Lead-free piezoelectric ceramics of $(Bi_{1/2}Na_{1/2})TiO_3$-1/2 (Bi_2O_3 center dot Sc_2O_3) system. Jpn J Appl Phys Pt 1 36:6055–6057
57. Nagata H, Takenaka T (1998) Lead-free piezoelectric ceramics of $(Bi_{1/2}Na_{1/2})TiO_3$-$KNbO_3$-1/2(Bi_2O_3-Sc_2O_3) system. Jpn J Appl Phys Pt 1 37:5311–5314
58. Takenaka T, Maruyama K, Sakata K (1991) $Na_{0.5}Bi_{0.5}TiO_3$-$BaTiO_3$ system for lead-free piezoelectric ceramics. Jpn J Appl Phys 30:2236–2239
59. Sasaki A, Chiba T, Mamiya Y, Otsuki E (1999) Dielectric and piezoelectric properties of $(Bi_{0.5}Na_{0.5})TiO_3$-$(Bi_{0.5}K_{0.5})TiO_3$ systems. Jpn J Appl Phys Pt 1 38:5564–5567

60. Matthias BT, Remeika JP (1951) Dielectric properties of sodium and potassium niobates. Phys Rev 82:727–729
61. Nakamura K, Kawamura Y (2000) Orientation dependence of electromechanical coupling factors in $KNbO_3$. Ieee T Ultrason Ferr 47:750–755
62. Wada S, Seike A, Tsurumi T (2001) Poling treatment and piezoelectric properties of potassium niobate ferroelectric single crystals. Jpn J Appl Phys Pt 1 40:5690–5697
63. Ishii H (2001) Morphotropic phase boundary and electrical properties of bismuth sodium titanate-potassium niobate solid-solution ceramics. Jpn J Appl Phys 40:5660–5663
64. Matsuo K, Xie R-J, Akimune Y, Sugiyama T (2002) Lead-free $Sr_2.xCaxNaNb_5O_{15}$(x=0.1) based PTZ with tungsten bronze. J Ceram Soc Jpn 110:491–494
65. Simon A (2003) Lead-free relaxors with "TTB" structure containing either lanthanum or bismuth. Physica Status Solidi A Appl Res 199:541–545
66. Vondermuhll R, Simon A, Elissalde C, Villesuzanne A (2004) Dielectric investigation of a new TKWB lead free relaxor. J Phys Chem Solids 65:1039–1043
67. Patro P (2004) Dielectric and ferroelectric behavior of SBN50 synthesized by solid-state route using different precursors. Ceram Int 30:1405–1409
68. Jiang WJ, Cao WW, Yi XJ, Chen HC (2005) The elastic and piezoelectric properties of tungsten bronze ferroelectric crystals $(Sr_{0.7}Ba_{0.3})(2)NaNb_5O_{15}$ and $(Sr_{0.3}Ba_{0.7})(2)NaNb_5O_{15}$. J Appl Phys 97:094106
69. Subbarao EC (1962) Crystal chemistry of mixed bismuth oxides with layer-type structure. Am Ceram Soc J 45:166–169
70. Armstrong RA (1972) Bismuth titanate solid solutions. Mater Res Bull 7:1025–1034
71. Cross LE (1971) Ferroelectricity in bismuth oxide type layer structure compounds. Mater Res Bull 6:939–949
72. Ikegami S (1974) Piezoelectricity in ceramics of ferroelectric bismuth compound with layer structure. Jpn J Appl Phys 13:1572–1577
73. Takeuchi T (1999) Piezoelectric properties of bismuth layer-structured ferroelectric ceramics with a preferred orientation processed by the reactive templated grain growth method. Jpn J Appl Phys 38:5553–5556
74. Dorrian JF (1971) Crystal structure of $Bi_4Ti_3O_{12}$. Ferroelectrics 3:17–27
75. Cummins SE (1968) Electrical and optical properties of ferroelectric $Bi_4Ti_3O_{12}$ single crystals. J Appl Phys 39:2268
76. Villegas M (1999) Factors affecting the electrical conductivity of donor-doped $Bi_4Ti_3O_{12}$ piezoelectric ceramics. J Am Ceram Soc 82:2411–2416
77. Noguchi Y (2001) Large remanent polarization of vanadium-doped $Bi_4Ti_3O_{12}$. Appl Phys Lett 78:1903
78. Nanao M, Hirose M, Tsukada T (2001) Piezoelectric properties of Bi_3TiNbO_9-$BaBi_2Nb_2O_9$ ceramics. Jpn J Appl Phys Pt 1 40:5727–5730
79. Shibata K (2001) Sr_1-xCax$Bi_2Ta_2O_9$ piezoelectric ceramics with high mechanical quality factor. Jpn J Appl Phys 40:5719–5721
80. Chiang YM, Farrey GW, Soukhojak AN (1998) Lead-free high-strain single-crystal piezoelectrics in the alkaline-bismuth-titanate perovskite family. Appl Phys Lett 73:3683–3685
81. Zhang ST, Kounga AB, Aulbach E, Ehrenberg H, Rodel J (2007) Giant strain in lead-free piezoceramics $Bi_{0.5}Na_{0.5}TiO_3$-$BaTiO_3$-$K_{0.5}Na_{0.5}NbO_3$ system. Appl Phys Lett 91:112906
82. Teranishi S, Suzuki M, Noguchi Y, Miyayama M, Moriyoshi C, Kuroiwa Y, Tawa K, Mori S (2008) Giant strain in lead-free $(Bi_{0.5}Na_{0.5})TiO_3$-based single crystals. Appl Phys Lett 92:182905
83. Hiruma Y, Imai Y, Watanabe Y, Nagata H, Takenaka T (2008) Large electrostrain near the phase transition temperature of $(Bi_{0.5}Na_{0.5})TiO_3$-$SrTiO_3$ ferroelectric ceramics. Appl Phys Lett 92:262904

84. Zhang QH, Zhang YY, Wang FF, Wang YJ, Lin D, Zhao XY, Luo HS, Ge WW, Viehland D (2009) Enhanced piezoelectric and ferroelectric properties in Mn-doped $Na_{0.5}Bi_{0.5}TiO_3$-$BaTiO_3$ single crystals. Appl Phys Lett 95:102904
85. Saito Y, Takao H, Tani T, Nonoyama T, Takatori K, Homma T, Nagaya T, Nakamura M (2004) Lead-free piezoceramics. Nature 432:84–87
86. Saito Y, Takao H (2006) High performance lead-free piezoelectric ceramics in the (K,Na) NbO_3-$LiTaO_3$ solid solution system. Ferroelectrics 338:1433–1448
87. Guo YP, Kakimoto K, Ohsato H (2004) Phase transitional behavior and piezoelectric properties of $(Na_{0.5}K_{0.5})NbO_3$-$LiNbO_3$ ceramics. Appl Phys Lett 85:4121–4123
88. Hollenstein E, Davis M, Damjanovic D, Setter N (2005) Piezoelectric properties of Li- and Ta-modified $(K_{0.5}Na_{0.5})NbO_3$ ceramics. Appl Phys Lett 87:182905
89. Matsubara M, Kikuta K, Hirano S (2005) Piezoelectric properties of $(K_{0.5}Na_{0.5})(Nb_1-xTax)O_3-K_{5.4}CuTa_{10}O_{29}$ ceramics. J Appl Phys 97:114105
90. Zhang SJ, Xia R, Shrout TR, Zang GZ, Wang JF (2006) Piezoelectric properties in perovskite $0.948(K_{0.5}Na_{0.5})NbO_3$-$0.052LiSbO_3$ lead-free ceramics. J Appl Phys 100:104108
91. Park SE, Wada S, Cross LE, Shrout TR (1999) Crystallographically engineered $BaTiO_3$ single crystals for high-performance piezoelectrics. J Appl Phys 86:2746–2750
92. Wada S, Yako K, Kakemoto H, Tsurumi T, Kiguchi T (2005) Enhanced piezoelectric properties of barium titanate single crystals with different engineered-domain sizes. J Appl Phys 98:014109
93. Wada S, Takeda K, Muraishi T, Kakemoto H, Tsurumi T, Kimura T (2007) Preparation of [110] grain oriented barium titanate ceramics by templated grain growth method and their piezoelectric properties. Jpn J Appl Phys 46:7039–7043
94. Takahashi H, Numamoto Y, Tani J, Tsurekawa S (2007) Domain properties of high-performance barium titanate ceramics. Jpn J Appl Phys 46:7044–7047
95. Karaki T, Yan K, Miyamoto T, Adachi M (2007) Lead-free piezoelectric ceramics with large dielectric and piezoelectric constants manufactured from $BaTiO_3$ nano-powder. Jpn J Appl Phys 2(46):L97–L98
96. Liu WF, Ren XB (2009) Large piezoelectric effect in Pb-free ceramics. Phys Rev Lett 103:257602
97. Takenaka T, Nagata H (2005) Current status and prospects of lead-free piezoelectric ceramics. J Eur Ceram Soc 25:2693–2700
98. Shrout TR, Zhang SJ (2007) Lead-free piezoelectric ceramics: alternatives for PZT? J Electroceram 19:111–124
99. Rodel J, Jo W, Seifert KTP, Anton EM, Granzow T, Damjanovic D (2009) Perspective on the development of lead-free piezoceramics. J Am Ceram Soc 92:1153–1177
100. Pronin IP, Syrnikov PP, Isupov VA, Egorov VM, Zaitseva NV (1980) Peculiarities of phase transitions in sodium-bismuth titanate. Ferroelectrics 25:395–397
101. Vakhrushev SB, Isupov VA, Kvyatkovsky BE, Okuneva NM, Pronin IP, Smolensky GA, Syrnikov PP (1985) Phase transitions and soft modes in sodium bismuth titanate. Ferroelectrics 63:153–160
102. Avramenko VP (1995) Peculiarities of electrophysical properties of $Na_{0.5}Bi_{0.5}TiO_3$ single crystals. Ferroelectrics 174:71–75
103. Tu CS, Siny IG, Schmidt VH (1994) Sequence of dielectric anomalies and high-temperature relaxation behavior in $Na_{1/2}Bii_{1/2}TiO_3$. Phys Rev B 49:11550–11559
104. Suchanicz J, Roleder K, Kwapulinski J, Jankowska-Sumara I (1996) Dielectric and structural relaxation phenomena in $Na_{0.5}Bi_{0.5}TiO_3$ single crystal. Phase Transitions 57:173–182
105. Zvirgzds JA, Kapostins PP, Zvirgzde JV, Kruzina TV (1982) X-ray study of phase-transitions in ferroelectric $Na_{0.5}Bi_{0.5}TiO_3$. Ferroelectrics 40:75–77
106. Suchanicz J, Kwapulinski J (1995) X-ray diffraction study of the phase transitions in $Na_{0.5}Bi_{0.5}TiO_3$. Ferroelectrics 165:249–253
107. Kusz J, Suchanicz J, Bohm H, Warczewski J (1999) High temperature x-ray single crystal study of $Na_{1/2}Bi_{1/2}TiO_3$. Phase Transitions 70:223–229

108. Suchanicz J (1997) Time evolution of the phase transformation in $Na_{0.5}Bi_{0.5}TiO_3$. Ferroelectrics 200:319–325
109. Jones GO, Thomas PA (2000) The tetragonal phase of $Na_{0.5}Bi_{0.5}TiO_3$ – a new variant of the perovskite structure. Acta Crystallogr B 56:426–430
110. Yao JJ, Ge WW, Luo L, Li JF, Viehland D, Luo HS (2010) Hierarchical domains in $Na_{1/2}Bi_{1/2}TiO_3$ single crystals: Ferroelectric phase transformations within the geometrical restrictions of a ferroelastic inheritance. Appl Phys Lett 96:222905
111. Ge WW, Li JF, Viehland D, Luo HS (2010) Influence of Mn doping on the structure and properties of $Na_{0.5}Bi_{0.5}TiO_3$ single crystals. J Am Ceram Soc 93:1372–1377
112. Kruzina TV, Duda VM, Suchanicz J (2001) Peculiarities of optical behaviour of $Na_{0.5}Bi_{0.5}TiO_3$ single crystals. Mat Sci Eng B Solid 87:48–52
113. Balke N, Bdikin I, Kalinin SV, Kholkin AL (2009) Electromechanical imaging and spectroscopy of ferroelectric and piezoelectric materials: state of the art and prospects for the future. J Am Ceram Soc 92:1629–1647
114. Syutkina VI (1967) The mechanism of deformation of the ordered CuAu alloy. Physica Status Solidi 21:465–480
115. Raymond MV (1996) Defects and charge transport in perovskite ferroelectrics. J Phys Chem Solids 57:1507–1511
116. Smyth DM (1994) Ionic transport in ferroelectrics. Ferroelectrics 151:115–124
117. Nagata H, Takenaka T (2001) Additive effects on electrical properties of $(Bi_{1/2}Na_{1/2})TiO_3$ ferroelectric ceramics. J Eur Ceram Soc 21:1299–1302
118. Park SE, Chung SJ, Kim IT (1996) Ferroic phase transitions in $(Na_{1/2}Bi_{1/2})TiO_3$ crystals. J Am Ceram Soc 79:1290–1296
119. Ge W, Yao J, Luo L, Devreugd CP, Li J, Viehland D, Zhang Q, Luo H (2011) Nucleation of rhombohedral regions within a tetragonal matrix in Mn-doped $Na_{0.5}Bi_{0.5}TiO_3$ crystals: origins of a diffuse transformation, thermal hysteresis, and isotropization. J Am Ceram Soc 94:478–481
120. Ge WW, Cao H, Li JF, Viehland D, Zhang QH, Luo HS (2009) Influence of dc-bias on phase stability in Mn-doped $Na_{0.5}Bi_{0.5}TiO_3$-5.6 at. %$BaTiO_3$ single crystals. Appl Phys Lett 95:162903
121. Viehland D, Jang SJ, Cross LE, Wuttig M (1990) Freezing of the polarization fluctuations in lead magnesium niobate relaxors. J Appl Phys 68:2916–2921
122. Dai XH, Xu Z, Viehland D (1994) The spontaneous relaxor to normal ferroelectric transformation in La-modified lead-zirconate-titanate. Philos Mag B 70:33–48
123. Park SE, Chung SJ, Kim IT, Hong KS (1994) Nonstoichiometry and the long-range cation ordering in crystals of $(Na_{1/2}Bi_{1/2})TiO_3$. J Am Ceram Soc 77:2641–2647
124. Ren XB, Otsuka K (1997) Origin of rubber-like behaviour in metal alloys. Nature 389:579–582
125. Ren XB, Otsuka K (2000) Universal symmetry property of point defects in crystals. Phys Rev Lett 85:1016–1019
126. Ren X (2002) The interaction of point defects with the martensitic transformation: a prototype of exotic multiscale phenomena. Mrs Bull 27:115–120
127. Ren XB (2004) Large electric-field-induced strain in ferroelectric crystals by point-defect-mediated reversible domain switching. Nat Mater 3:91–94
128. Zhang LX, Ren XB (2006) Aging behavior in single-domain Mn-doped $BaTiO_3$ crystals: implication for a unified microscopic explanation of ferroelectric aging. Phys Rev B 73:094121
129. Zhang LX, Chen W, Ren X (2004) Large recoverable electrostrain in Mn-doped (Ba,Sr) TiO_3 ceramics. Appl Phys Lett 85:5658
130. Ge W, Cao H, Devreugd CP, Li J, Viehland D, Zhang Q, Luo H (2011) Influence of $BaTio_3$ Content on the Structure and Properties of $Nao_{.5}Bio_{.5}Tio_3$ Crystals. J Am Ceram Soc. doi: 10.1111/j.1551-2916.2011.04433.x
131. Jona F, Shirane G (1962) Ferroelectric crystals. Pergamon press, Oxford
132. Cao H, Devreugd CP, Ge WW, Li JF, Viehland D, Luo HS, Zhao XY (2009) Monoclinic MC phase in (001) field cooled $BaTiO_3$ single crystals. Appl Phys Lett 94:032901

Chapter 2
Ferroelectric Domains and Grain Engineering in $SrBi_2Ta_2O_9$

H. Amorin, I. Coondoo, M.E.V. Costa, and A.L. Kholkin

2.1 Introduction

In recent years, there has been a tremendous interest in ferroelectric materials from perspective of their potential applications in electronic devices such as high-temperature piezoelectric transducers, pyroelectric infrared detectors, optical switches, and nonvolatile random access memories (NVRAMs) [1–4]. Advances in processing, including single-crystal growth, epitaxial thin-film growth, and chemical processing, have led to materials with such controlled structure and properties that now new classes of devices are envisioned. Future applications necessarily rely on domain control at small length scales. To realize the full potential of ferroelectric compounds in this context, one needs to consider several factors: patterning ferroelectric domains at small scales, the stability limits of small domains, and the domain dependence of surface reactivity [5]. In simple words, the quality of the device of which the material is an integral part, is directly governed by the potential to expertly engineer the domains within the material.

The Aurivillius family of bismuth layer structured ferroelectrics (BLSFs) encompasses many ferroelectric compounds which are seen as the promising candidates for use in microelectronic applications owing to their high Curie temperature and being lead free [6]. In particular, $SrBi_2Ta_2O_9$ (SBT) which is an $n = 2$ member of the Aurivillius family of layered compounds, has proved to be a versatile material for multiple applications such as fatigue-free memory [7–12] and high-temperature piezoelectric materials [6]. The crystal structure of SBT is characterized by an orthorhombic distortion in the ferroelectric state (space group

H. Amorin
Instituto de Ciencia de Materiales de Madrid, Cantoblanco 28049, Madrid, Spain

I. Coondoo • M.E.V. Costa • A.L. Kholkin (✉)
Center for Research in Ceramics and Composite Materials (CICECO), Department of Ceramics and Glass Engineering, University of Aveiro, 3810-193 Aveiro, Portugal
e-mail: kholkin@ua.pt

S. Priya and S. Nahm (eds.), *Lead-Free Piezoelectrics*,
DOI 10.1007/978-1-4419-9598-8_2, © Springer Science+Business Media, LLC 2012

$A2_1am$) of the high-symmetry tetragonal prototype structure ($I4/mmm$) [13]. The P_s is directed along the orthorhombic *a*-axis and originates mainly from the displacements of the Sr–Ta–O layers relative to Bi–O layers [14].

A large amount of works on SBT ceramics and more importantly on thin films reports improved ferroelectric properties when using modern processing techniques [15–18]. However, the knowledge of the single crystal anisotropy and detailed investigations of the domain configurations are two prerequisites for the understanding of distinct effects observed to date [19]. Besides, from the fundamental point of view, single crystal data are required for the thermodynamic analysis of the phase transitions in these technologically important materials. Therefore the study of single crystal (intrinsic) properties may contribute to further development of memory devices and to improving functionality of SBT films. To carry out such measurements, large single crystals of sufficiently high quality should be grown with a single domain state or at least a controlled domain configuration.

In view of this, the present chapter first discusses processing and characterization of large and high-quality SBT single crystals grown by a high-temperature self-flux solution method. In this process the material to be crystallized is dissolved at high temperature in a suitable solvent, and crystallization is achieved by a slow cooling process, which makes the solution critically supersaturated. This technique is very suitable for growing ferroelectric single crystals [20], namely, for producing Pb-based perovskites and some BLSF materials using lead and bismuth oxide fluxes, respectively [21]. Such fluxes at high temperature are advantageous, because their constituent elements are also part of the desired final composition and, therefore, the incorporation of foreign ions into the lattice of the crystals is avoided. Moreover, the melting point may be conveniently reduced by adding another component to the flux, i.e., B_2O_3 [22]. The main disadvantage of this method is the slow growth rate and the excessive power consumed for the growth of large crystals.

On the other hand, the as-sintered polycrystalline SBT ceramics suffer from a critical disadvantage which hinders its applicability as piezoelectric material. It is difficult to obtain highly dense bulk ceramics and polarize the material to achieve high piezoelectric response. The highly anisotropic crystallographic structure and the limited number of permissible orientations for the spontaneous polarizations are the major causes for low piezoelectric activity [23–25]. Nevertheless, their piezoelectric performance can be improved by texturing, since it enables much more efficient alignment of the polar vector, increasing the poling efficiency and allowing improved tailoring of the piezoelectric properties [26].

In general, controlled development of texture in electroceramics is a topic of current interest in ceramic processing, since it allows improved tailoring of physical properties such as: piezoelectric, electrical or mechanical properties, approaching them to those of single crystals and enhancing in this way the functionality of the various devices. Texture engineering was first applied on SbSI [27] and has been recently utilized for ferroelectric ceramics with not only simple perovskite structure [28–31] but BLSFs and tungsten bronze structure [27, 32–44]. The increase in the piezoelectric response of textured ceramics appears to be more significant in systems with fewer possible orientations for P_s [45]. Thus, ferroelectrics where

the polarization is confined to an axis (e.g., $Sr_{1-x}Ba_xNb_2O_6$) or to a plane (e.g., BLSF materials) show larger property improvements on fiber texturing than do the 3-dimensional ferroelectrics such as perovskites. The main advantage of this kind of processing is the higher values of piezoelectric coefficients (e.g., two times higher d_{33}) achieved in textured ceramics with respect to the randomly oriented sample.

One of the promising routes for the controlled texture development is the templated grain growth (TGG) [45]. Briefly, this process consists of the ceramic sintering mediated by a small amount of well-oriented anisometric template particles distributed in a fine-grained matrix. The template particles grow at the expense of the fine randomly oriented powder ensuring a large volume fraction of highly oriented grains. Being based on a standard powder processing and sintering, TGG achieves texture at a significantly lower cost as compared to other techniques used for texturing like hot forging [46–48] or hot pressing [49–52]. An obstacle to the low-cost processing of TGG-derived materials is the difficulty of producing large amounts of template particles with controlled particle size and aspect ratio, e.g., the anisotropic seeds that control texture development.

It is well known that the selection and preparation of the template particles is a subject of special interest in TGG, since the texture development and the template growth during ceramics annealing strongly depends on the liquid phase content as well as on the number, size, distribution, and initial orientation of the template particles [45]. Usually, template particles with suitable dimensions to be used as seeds for TGG are obtained by molten salt or hydrothermal synthesis methods. However, it is difficult to produce large amounts of SBT templates with controlled particle size and aspect ratio, i.e., the anisotropic seeds of the same material that control texture development by the above mentioned methods. Thus, the large SBT single crystals grown by us via a high-temperature self-flux solution method were used as anisometric templates (seeds) for TGG. In view of this, the present chapter also reports on processing and detailed characterization of textured SBT ceramics with improved performance by TGG.

2.2 SBT Single Crystals: Flux Growth and Characterization

Single crystals are indispensable for studying the anisotropy of ferro/piezoelectric and dielectric properties in BLSF systems. However, in contrast to other BLSF compounds, there were only few attempts to grow and to characterize SBT crystals of sufficient quality [53–55], mainly due to the difficulties in their synthesis. In the last years, efforts were mainly focused on obtaining SBT single crystals by self-flux solution method using a Bi_2O_3 flux [53]. These attempts resulted in crystals too small to be used for structural and electrical characterization. More recently large SBT single crystals have been successfully synthesized using a modified self-flux solution method [54, 55]. In our case, SBT single crystals were grown using a 60/40 molar ratio of SBT to flux (35 wt.% Bi_2O_3 and 5 wt.% B_2O_3) by using

Fig. 2.1 Top view of as-grown and acid cleaned $SrBi_2Ta_2O_9$ crystals

an optimized thermal profile that included a gradually accelerated slow cooling process in order to create the required supersaturation for crystals nucleation and growth [56]. Figure 2.1 shows the large, colorless, and translucent SBT crystals with sizes around 7×5 mm^2 and thickness of 50 μm, showing layered habit and faceted surfaces obtained using a boron-modified flux.

X-ray diffraction (XRD) measurements were carried out on crystals with rectangular platelet morphology and dimensions of $2 \times 1 \times 0.1$ mm^3 using a SIEMENS D500 diffractometer and CuK_α radiation ($\lambda = 1.5418$ Å). Crystals were scanned in reflection and transmission geometries, in the 2θ range from 4 to 130° with a step length of 0.02°, while the rocking curve was recorded for the $(00\underline{18})$ plane reflection. The evaluation of the structural quality of the grown crystals was performed by X-ray angular $\theta - 2\theta$ and θ scanning topography methods on a standard DRON-2 diffractometer (CuK_α radiation), and using the $(00\underline{18})$ reflection for θ–2θ scanning in reflection geometry and the (110) and (200) reflections for θ scanning in transmission geometry. Furthermore, in order to establish the possibility of twinning planes in SBT single crystals, related to the exchange between *a*- and *b*-axes along the *ab*-plane, the extinction rules for the space group $A2_1am$ were investigated using rocking curves in a wide scanning range (WSR) of the $(20\underline{18})$, $(02\underline{18})$, $(10\underline{15})$, and $(01\underline{15})$ plane reflections.

For electrical characterization, naturally rectangular shaped SBT single crystals were polished flat in two directions: parallel to the *ab* plane for measurements along the [001] direction (*c*-axis direction), and perpendicular to the *ab* plane for measurements along the [110] direction. The oriented crystals were polished to the desired thickness and a mirror polishing was performed only for the domain studies. The final surface area of the polished crystals used in this study varied from 3×3 mm^2 for measurements along *c*-axis to 3×0.2 mm^2 for measurements along *ab*-plane, while the final thicknesses were about 100–200 μm in both cases. Gold electrodes were sputtered onto the whole area of the parallel polished facets using a vacuum sputtering system. Dielectric properties were measured using an HP4284A precision LCR Meter and ferroelectric hysteresis loops were obtained by using a Sawyer-Tower circuit. The piezoelectric characterization was carried out using a double-beam (Mach-Zender) laser interferometer on crystals previously embedded in araldite and polished to optical quality for both the top and bottom facets [57].

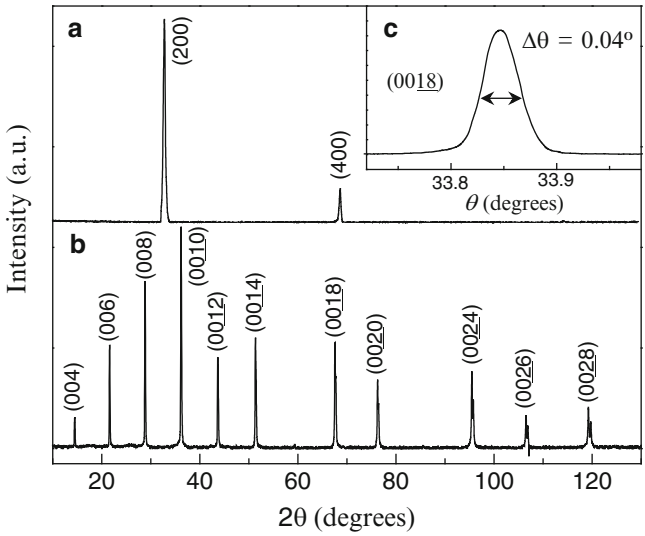

Fig. 2.2 X-ray diffraction (XRD) spectra along the (**a**) [100] and (**b**) [001] directions for a perfectly *c*-axis oriented SBT single crystal platelet. (**c**) Rocking curve of the (0018) reflection, where $\Delta\theta$ is the full-width at the half-maximum (FWHM). The Miller indexes for the orthorhombic SBT phase are included

For domain observation only one facet (top one) of the single crystal was polished similar to the method described above. The crystal was first annealed at 750°C for 10 h to eliminate stresses and domain deformation during preparation steps. Then, the bottom facet of the crystal was electroded by sputtering a gold layer. Ferroelectric domain structure was studied by the piezoresponse force microscopy (PFM). The vertical and lateral vibrations due to the longitudinal (d_{33}) and the shear (d_{15}) piezoelectric effects, respectively, were detected by using a commercial Multimode AFM setup (Veeco, Nanoscope IIIa) equipped with a standard doped silicon conductive tip-cantilever system (FMR, Nanosensors, spring constant 3 N/m, resonance frequency 80 kHz). The ac voltage signal (with amplitude of 10–20 V and frequency of 3 kHz) was applied using a functional generator and an amplifier. The amplitude and phase of the induced deflection of the cantilever was detected using a lock-in amplifier (SR830, Stanford Research Systems).

2.2.1 Crystal Structure and Morphology

XRD spectra in reflection and transmission geometries for a rectangular SBT crystal platelet are shown in Fig. 2.2a, b, where only (h00) and (00l) plane reflections are observed in the directions parallel and perpendicular to the major

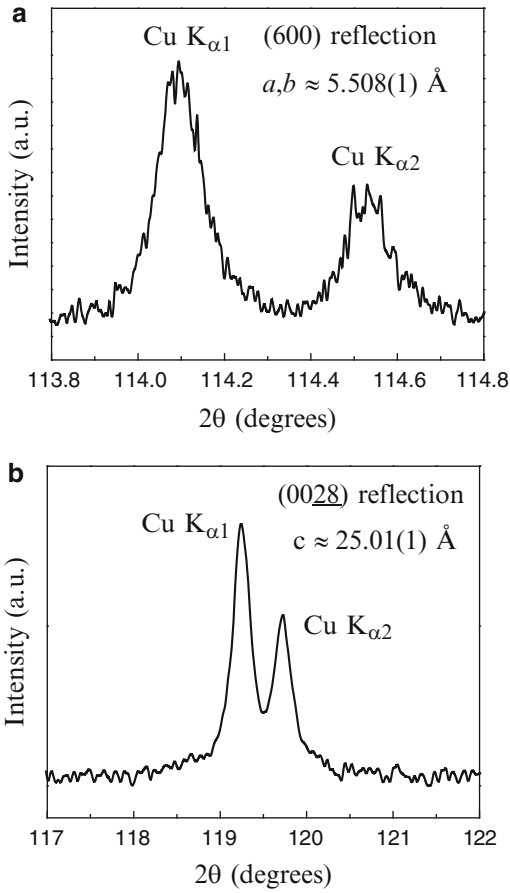

Fig. 2.3 XRD profiles of the reflections (**a**) (600) and (**b**) (0028). Pseudo-tetragonal lattice parameters were estimated and are included in the graphs

face, respectively. The result suggests the higher growth rate of this system in the *ab*-plane, as compared to that in the *c*-axis direction perpendicular to the major face. From the viewpoint of the SBT structure (an orthorhombic distorted structure in which pseudo-perovskite blocks $(SrTa_2O_7)^{2-}$ interleave with $(Bi_2O_2)^{2+}$ layers) [58] growing in a homogeneous flux medium, the easy growth of the single crystal in the *a*, *b*-axis directions is well understood, since all the ions needed are available at the same time. In the *c*-axis, however, this growth is much more complex because both the pseudo-perovskite $(SrTa_2O_7)^{2-}$ blocks and the $(Bi_2O_2)^{2+}$ layers should not be delivered at the same time. The crystal quality is demonstrated through the rocking curves (see Fig. 2.2c), where the full-width at the half-maximum (FWHM) for the (0018) reflection was $\Delta\theta = 0.04°$, indicating very high quality of the crystals. Pseudo-tetragonal lattice parameters were estimated using the space group $A2_1am$ and the reflections (600) and (0028), where the $CuK_{\alpha 1}$ can be completely isolated, as shown in Fig. 2.3. The results obtained [a, b ~ 5.508(1) Å and c ~ 25.01(1) Å] are in a good agreement with the reported data [58, 59].

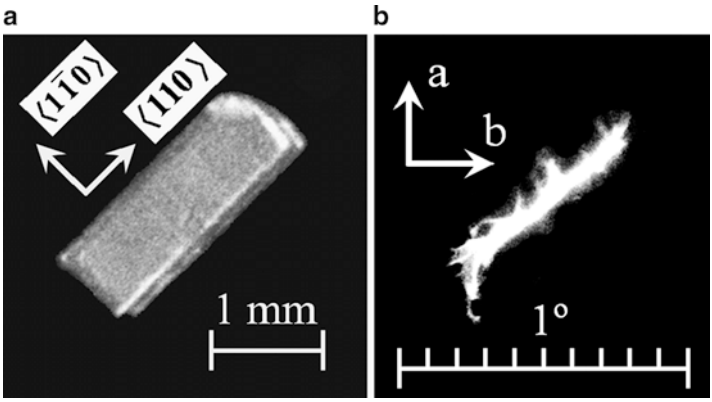

Fig. 2.4 X-ray (**a**) θ-scanning and (**b**) θ–2θ-angular scanning topographies, using the (110) and (0018) reflections, respectively, for a small, rectangular shaped SBT single crystal

2.2.1.1 X-Ray Topography Analysis

X-ray topography is an imaging technique widely used for the verification of the quality of single crystals, which gives information about crystal defects, lattice misorientation, crystallographic orientation of the crystal edges, etc. [60]. In this study, measurements were performed on a small and rectangular shaped SBT crystal with size of ~$2 \times 1 \times 0.02$ mm^3. The θ- and θ–2θ-angular scanning topographies are represented in Fig. 2.4a, b, respectively. The image in Fig. 2.4a was obtained using the (110) reflection. Uniform contrast was observed over the entire sample surface confirming its perfect orientation. The intensity of this image depends on the thickness of the sample and extinction (defect) crystal conditions. Figure 2.4b represents the diffraction image for θ–2θ-angular scanning topography using the (0018) reflection. For an ideal crystal this image should correspond to the shape of the sample with a linear transformation governed by the geometry of the experimental setup [61, 62]. In this case, the small deviation of the diffraction image in Fig. 2.4b from the real shape in Fig. 2.4a can be due to small bending of the crystal surface along its major face. Indeed, this deviation is determined by the magnitude of the misorientation, being smaller than 1°.

The crystallographic orientation of the SBT single crystal facets can also be deduced from X-ray topography. Figure 2.4a illustrates the directions of the main crystallographic axes, where the narrow sides of the rectangular shaped crystals are oriented along the [110] and [1$\bar{1}$0] directions with the [001] direction (c-axis) lying perpendicular to the major face. As a matter of fact, the shape of the crystals should be determined by the high symmetry tetragonal phase (space group $I4/mmm$, $a = b \cong 3.85$ Å) [58] since they were grown at high temperature (far above 1,000°C). It is believed that, when cooled down to room temperature, the symmetry of the single crystal transforms from tetragonal into orthorhombic one but its original shape formed at high temperature is retained. Apparently, during this

transformation, *a*- and *b*-axes rotate by 45° relative to tetragonal axis and [100] direction in the tetragonal phase becomes [110] direction in the orthorhombic phase. It can be concluded that the edges of the crystals (directed along [110] and $[1\bar{1}0]$ directions at room temperature) originate from the [100] and [010] directions of the parent tetragonal structure.

2.2.2 *Ferroelectric Domains, Twinning and Effective Disclinations*

On cooling from high temperatures, SBT first experiences an improper ferroelastic phase transition at $T_{C1} \sim 550°C$ from the parent tetragonal phase ($I4/mmm$) to the intermediate orthorhombic phase ($Amam$), and then at $T_{C2} \sim 350°C$ undergoes the proper ferroelectric transition to the low-temperature orthorhombic phase ($A2_1am$) [63]. The structure of the intermediate orthorhombic phase ($Amam$) permits the formation of ferroelastic domains or twins [64]. Below the Curie temperature T_{C2}, both ferroelastic/ferroelectric 90° domains and purely ferroelectric 180° domains can coexist. In this section, the existence of twins (using rocking curves in a WSR) and measurements of the domain structure in high-quality SBT single crystals using PFM are presented.

2.2.2.1 Rocking Curves in a Wide Scanning Range

Ferroelastic domains (twins) in SBT single crystals are related to the interchange of the crystallographic *a*- and *b*-axes in the *ab*-plane. In order to prove the existence of these twins, the extinction rules for the space group $A2_1am$ were investigated using the XRD profiles at room temperature for a couple of parent reflections, e.g., $(20\underline{18})$, $(02\underline{18})$, $(01\underline{15})$, and $(10\underline{15})$ reflections. For this space group, the extinction rules of possible reflections are [69]: $k + l = 2n$ (n is an integer) for the (h, k, and l) reflections, and $h = 2n$, $l = 2n$ for the (h, 0, l) reflections; which are the same rules as those for the intermediate orthorhombic phase $Amam$. Accordingly, if the SBT single crystal is free of twinning in the *ab*-plane, it can be positioned and rotated in such a way that reflections from the $(20\underline{18})$, $(02\underline{18})$, and $(01\underline{15})$ planes are possible, but the $(10\underline{15})$ plane reflection is not possible since it is forbidden for this space group. Therefore, the occurrence of the $(10\underline{15})$ reflections by rotating the crystal by 90° about the *c*-axis must indicate the presence of multiple twins in the SBT single crystal.

Figure 2.5 displays the rocking curves in a WSR (θ-scanning) for the above mentioned reflections obtained when the crystal is rotated about the [010] direction and considering that reflections $(20\underline{18})$ and $(10\underline{15})$ can be obtained by rotating the crystal by 90° about the *c*-axis from the position where the reflections $(02\underline{18})$ and $(01\underline{15})$, respectively, were obtained. The same peaks were observed in both pairs of

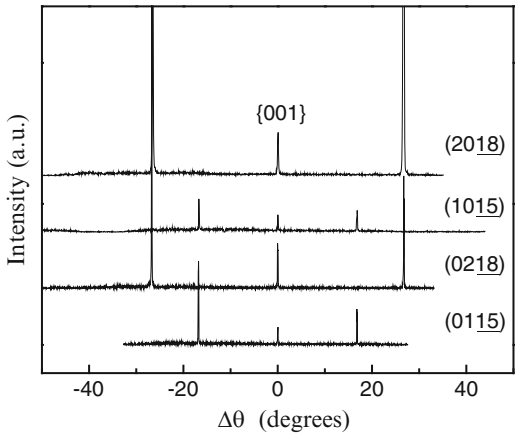

Fig. 2.5 Rocking curves in a WSR (θ-scanning) for the (20$\underline{18}$), (02$\underline{18}$), (01$\underline{15}$), and (10$\underline{15}$) reflections obtained by rotating the crystal by 90° about the [010] direction

parent reflections after the 90° rotation of the crystal about the *c*-axis. Thus, the presence of the pair of (01$\underline{15}$) and (10$\underline{15}$) reflections in both cases, before and after 90° rotation, indicates that in the studied SBT single crystal the *a*- and *b*-axes alternate along two possible directions corresponding to the diagonals of the (001)-oriented face of the unit cell in the parent tetragonal phase. Therefore, twin walls separating ferroelastic 90° domains should exist in the crystal. However, the orientation and density of twin walls cannot be determined from the XRD experiment.

2.2.2.2 Piezoresponse Force Microscopy: 180 and 90° Domains

The examination of the domain structure was carried out by PFM, which is capable of detecting out-of-plane domains (polarization normal to the crystal surface) as well as in-plane domains (polarization lies within the crystal plane) [65]. Measurements were first carried out on small areas of a polished SBT single crystal without thermal treatments, in which the stress induced during polishing might affect the domain structure on the surface. Two different configurations were used to visualize 180° domains, i.e., when the cantilever is parallel to *ab*-plane (major face) of the single crystal and when it is positioned normal to *ab*-plane. In the first case, the in-plane component of polarization vector was observed following the *lateral* deflection of the cantilever. Since only the in-plane component orthogonal to the cantilever contributes to the measured signal, the cantilever was positioned parallel to one of the crystal edges ⟨110⟩ and the crystal surface was scanned by moving the tip at a small rate of 1 μm/s.

Figure 2.6a, b show the topography and piezoresponse images, respectively, using the first configuration (cantilever parallel to the *ab*-plane). The straight lines in the topography image are scratches appearing onto the crystal surface due to the polish. The domain patterns are not greatly influenced by these scratches and can be clearly visualized in the piezoresponse image. The bright and dark stripes observed in

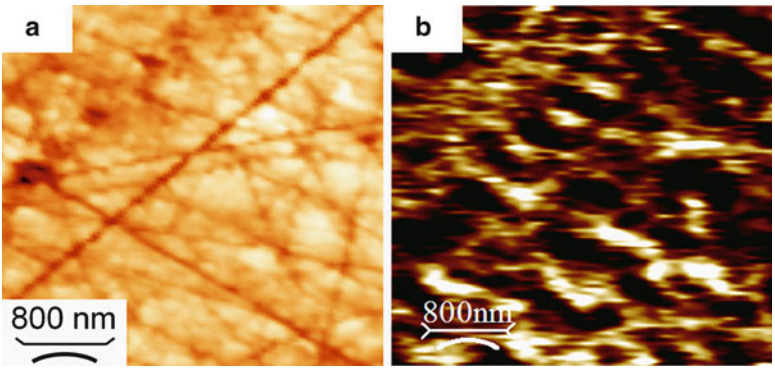

Fig. 2.6 PFM images on the [001] face of a SBT single crystal: (**a**) topography and (**b**) lateral piezoresponse images obtained with the cantilever parallel to *ab*-plane

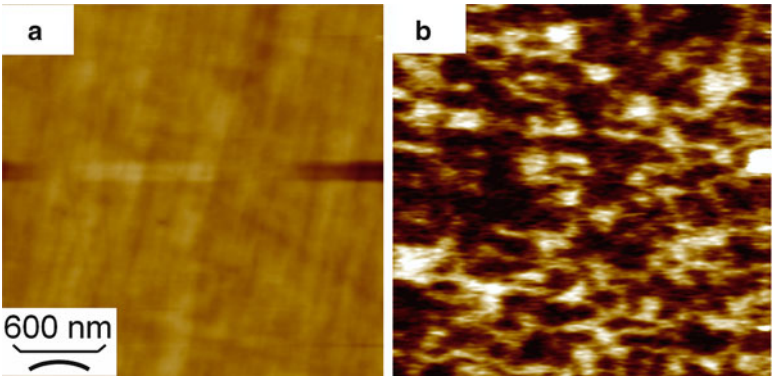

Fig. 2.7 PFM images on the [100] face of a SBT single crystal: (**a**) topography and (**b**) vertical piezoresponse images obtained the cantilever normal to *ab*-plane

the piezoresponse image correspond to ferroelectric 180° domains. These domains are visualized as antiparallel stripes with a periodicity of about 350 nm. As expected, the polarization is oriented along the [100] direction (*a*-axis direction), that is, inclined at 45° from the crystal edges ⟨110⟩ (the crystal edges ⟨110⟩ match with the vertical and horizontal sides of these images).

Figure 2.7a, b show topography and piezoresponse images, respectively, using the second configuration (cantilever normal to the *ab*-plane). In this case, the measured signal corresponds to the *vertical* deflection of the cantilever and reflects the distribution of out-of-plane component of the polarization. Bright/dark contrast corresponds to opposite polarization vectors oriented parallel to the *a*-axis. The observed domain pattern is much less regular in this view than in the first configuration. It is understood that these 180° domains correspond to the domain structure presented in Fig. 2.6b but seen from the *bc*-plane. From this first examination of

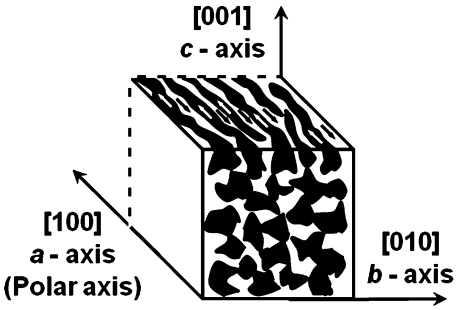

Fig. 2.8 Schematic illustration of the 3D arrangement of 180° domains as suggested by the PFM measurements in a typical *c*-axis oriented SBT single crystal

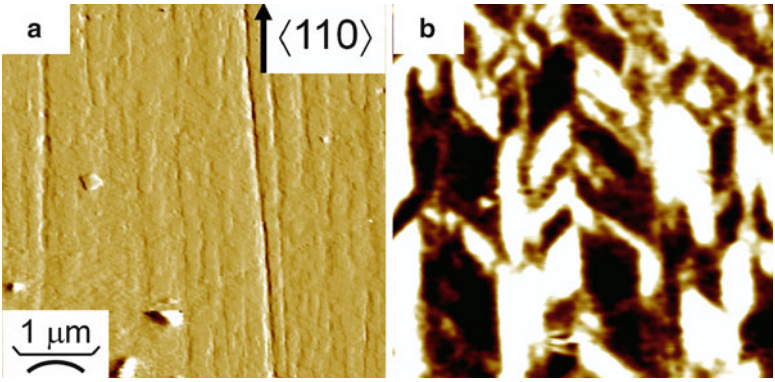

Fig. 2.9 PFM images on the (001) face of SBT single crystal: (**a**) topography and (**b**) lateral piezoresponse images obtained with the cantilever parallel to *ab*-plane

ferroelectric domains, it is believed that a 3D domain image should consist of rod-like shaped 180° domains oriented along *a*-axis, as schematically shown in Fig. 2.8.

In order to further investigate the possibility of 90° domain walls, corresponding to twinning planes, the same SBT single crystal was annealed at 750°C for 10 h, that is, above both ferroelastic and ferroelectric phase transitions, and then cooled down very slowly to room temperature at ~60°C/h. Subsequently, a greater area of the crystal surface was scanned following the first configuration, i.e., the cantilever positioned parallel to one of the crystal edges ⟨110⟩ and to the crystal major face. Topography and piezoresponse images are shown in Fig. 2.9a, b, respectively. On the piezoresponse image, the regions with bright/dark contrast correspond to ferroelectric domains with the in-plane polarization having upward and downward vertical component, respectively. To fully ascertain the polarization orientation inside domains, the sample was rotated by 90° about the *c*-axis and then scanned again. The images of similar domains obtained at the initial position (Fig. 2.10a) and after rotation by 90° (Fig. 2.10b) are complementary. This observation shows that the vertical and horizontal components of the polarization are comparable in magnitude, which agrees with the expected orientation of the polarization, that is,

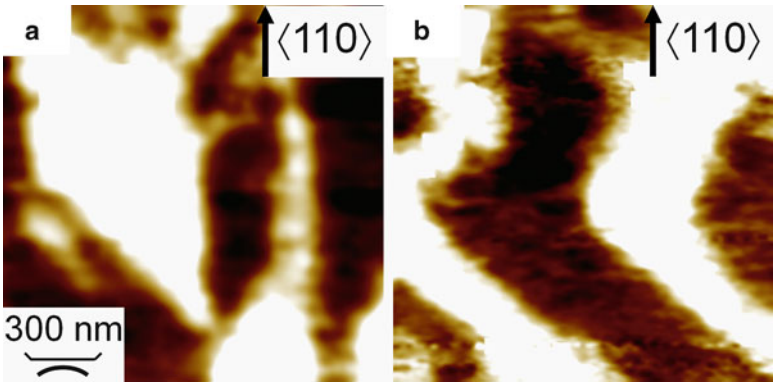

Fig. 2.10 Lateral piezoresponse images on the (001) facet. The image (**b**) was acquired after rotating the sample by 90° the *c*-axis relative to the initial position in (**a**)

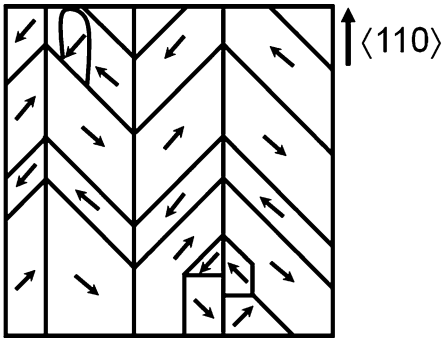

Fig. 2.11 Reconstructed domain structure of the SBT single crystal. The cross-section of domain pattern in the *ab*-plane is depicted. *Arrows* show polarization directions

inclined at 45° from the crystal edges ⟨110⟩. Therefore, the extended vertical domain boundaries seen in Fig. 2.9b may be attributed to 90° domain walls separating domains with orthogonal directions of the polar axis.

Such ferroelastic/ferroelectric walls tend to be parallel to the (100) or (010) plane of the parent tetragonal phase (*I*4/*mmm*), which agrees with the observed preferential orientation. The twin boundaries are slightly inclined due to a small angle between the crystal edge and the scanning direction. By analyzing several images taken at different locations, we found that the widths of 90° domains (twins) forming laminar structures that lie in the range of 0.7–1.5 μm. Alternating bright and dark stripes inside these twins correspond to the ferroelectric 180° domains with the boundaries parallel to the *a*-axis, as mentioned above. The width of these 180° domains varies from 250 to 500 nm. It should be noted that individual 90° domains were also observed inside some laminar twins. The comparison with previous observation of the *ac*(*bc*)-plane of the SBT crystal (see Figs. 2.6 and 2.7) allows us to confirm that 180° domain walls have rod-like shape parallel to *a*-axis. Remarkably, the coexisting domains of two types form a well-known *herringbone* structure (see Fig. 2.11 for the schematic illustration).

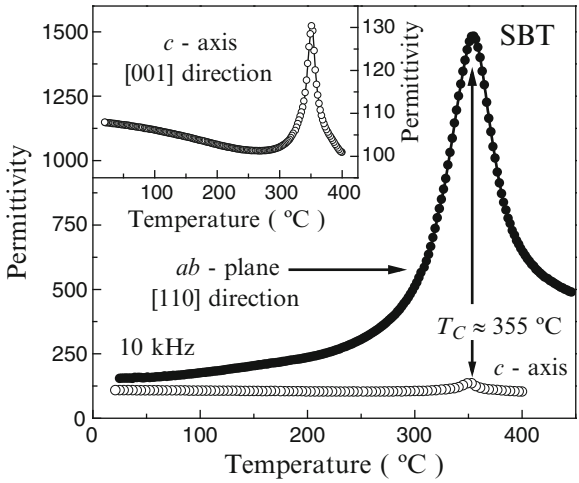

Fig. 2.12 Temperature dependence of the relative permittivity upon cooling at 1 MHz along the [110] (*ab*-plane) and the [001] (*c*-axis) directions in SBT single crystals

In contrast to the previously reported observations of irregular 90° domain patterns with curved boundaries [66–68] the 90° walls were found to be mostly flat in the studied SBT crystals. This is an unexpected result, because the bending of ferroelastic walls should be easy in SBT due to a very small spontaneous strain $S_o = b/a - 1$ (about 7×10^{-4} at room temperature, as calculated by Rae et al. [58]). Indeed, the energy associated with the wall bending is proportional to S_o^2 [69]. Accordingly, this energy must be much smaller in SBT than that in conventional perovskite ferroelectrics (by a factor of 100 as compared with $BaTiO_3$). This feature explains the earlier observations [66–68] of highly curved 90° walls but apparently excludes the existence of flat walls. However, the wall bending produces elastic fields of very long range in the surrounding material since it leads to the appearance of effective *disclinations* with a density directly proportional to the wall curvature [69]. Therefore, even $S_o \sim 10^{-3}$ may be sufficient to stabilize flat walls in high-quality SBT crystals (in contrast to ceramics, films, and imperfect crystals) [19].

2.2.3 Anisotropy in the Ferroelectric and Piezoelectric Properties

2.2.3.1 Dielectric Characterization

Figure 2.12 shows the temperature dependence of the relative permittivity upon cooling in the *ab*-plane (along the [110] direction) and along *c*-axis (the [001] direction) in SBT single crystals at 1 MHz. In both cases, the maximum of dielectric permittivity corresponding to the ferro-paraelectric phase transition is clearly observed at $T_C \approx 355$°C (Curie temperature), in good agreement with previous reports using other techniques on SBT crystals [64, 70, 71]. It is worth noting that

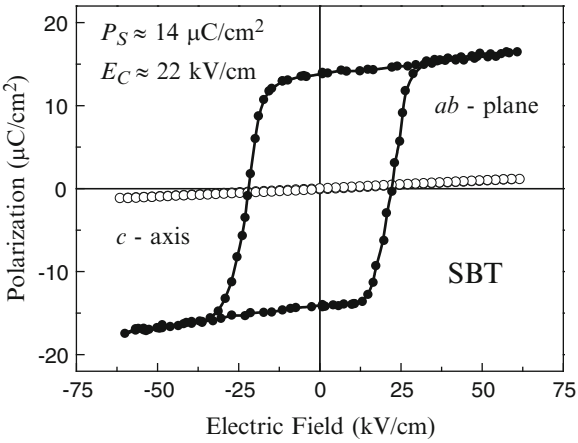

Fig. 2.13 Room temperature *P–E* hysteresis loops measured along the [110] (*ab*-plane) and the [001] (*c*-axis) directions in the SBT single crystal. The values for the spontaneous polarization (P_s) and the coercive field (E_c) are indicated

the T_Cs reported for SBT ceramics (~300°C [9, 72]) are somewhat lower than that obtained for single crystals. Besides, neither a frequency dispersion of the transition temperature nor thermal hysteresis upon heating and cooling was observed in the permittivity curves along both directions. The maximum permittivity in the *ab*-plane (~1,500) was about an order of magnitude greater than that along *c*-axis (~135) in line with results reported in other BLSF single crystals [73, 74]. Besides, the values of the permittivity in the *ab*-plane exceed significantly those of bulk ceramics (~600 at T_C) [9, 72].

It should be noted that the present measurements in the *ab*-plane were performed along the [110] direction. As such, this corresponds to a dielectric permittivity averaged for both *a*- (ferroelectric polarization direction) and *b*-axes (non-polar direction), e.g., $\varepsilon_{[110]} = (\varepsilon_a + \varepsilon_b)/2$. The in-plane anisotropy (ε_a and ε_b) could not be measured due to the ferroelastic twinning observed in the entire ferroelectric phase. From a crystallographic point of view for SBT there should be no coupling between the order parameter lying in the *ab*-plane and the out-of-plane (along *c*-axis) dielectric displacement. The dielectric behavior along *c*-axis should be mainly determined by the paraelectric bismuth oxide layers and the small peak observed around T_C is of the extrinsic character due to, probably, a slight inclination from the [001] direction during the crystal preparation for electrical characterization.

2.2.3.2 Ferroelectric Characterization

To confirm the anisotropy in the ferroelectric properties of the SBT single crystal, the room temperature *P–E* hysteresis loop was measured both along *c*-axis ([001] direction) and in the *ab*-plane (parallel to [110] direction). Anisotropy in the *P–E* hysteresis loops can be clearly observed by comparing the two plots in Fig. 2.13. Well-saturated hysteresis loop was observed in the *ab*-plane (solid circles), from which the values of the spontaneous polarization (P_s) and the coercive field (E_c)

were estimated as ~14 μC/cm^2 and ~22 kV/cm, respectively. On the other hand, only a linear *P–E* behavior with vanishing P_s and E_c was obtained for the measurements along the [001] direction (open circles). The results confirm that the P_s vector in the SBT structure lies *entirely* in the *ab*-plane and no polarization is obtained perpendicular to the bismuth oxide layers. This finding is consistent with that expected for BLSF materials with even number (*m*) of BO_6 octahedra, where dipole moment caused by ionic displacements along *c*-axis is canceled out due to the presence of a mirror plane perpendicular to it [25].

For SBT crystal, the macroscopic P_s, which is directed along the *a*-axis, has been reported to be ~18 μC/cm^2 calculated from ionic displacements [9]. In our crystals, the hysteresis loop was measured along the [110] direction, i.e., the P_s vector is oriented at 45° with respect to the measurement direction. The existence of a combination of ferroelastic twins filled with 180° domains was confirmed by PFM measurements. Thus, P_s along the polar *a*-axis could be determined as $P_s^a = P_s \cos(45°)$, considering that all 180° domains are switched under saturation. In this way, the P_s along the polar direction was estimated to be ~20 μC/cm^2, in good agreement with the above calculations [9]. We believe this value can be considered as a reference one as it is reported for the crystals of high quality.

2.2.3.3 Piezoelectric Characterization

Piezoelectric characterization of SBT crystals was performed along two directions in the *ab*-plane (along [110] and [100] directions) and along the *c*-axis ([001] direction), to confirm the anisotropy in the longitudinal piezoelectric coefficient (d_{33}). In the present study, SBT crystals were embedded in araldite and poled at $E_P = 60$ kV/cm.

Figure 2.14a shows the behavior of the d_{33} coefficient measured under swept dc poling field (piezoelectric hysteresis loop), which is obtained by poling the SBT crystal along the [110] direction and then measuring the d_{33} coefficient using a low ac voltage of 100 V at 1 kHz. The hysteretic behavior of the calculated d_{33} coefficient with the dc poling field is confirmed, and the electric field value at which d_{33} vanishes should be close to E_c (the effects from individual domains cancel each other and the crystal is piezoelectrically inactive). The E_c was estimated from this experiment as $E_c \sim 20$ kV/cm, in good agreement with the result of the *P–E* hysteresis measurements along the [110] direction (see Fig. 2.13).

Figure 2.14b shows the comparison between the dc poling field dependence of d_{33} coefficient measured along the [100] (loop with solid circles) and the [001] (loop with open circles) directions. In both cases, the hysteretic behavior of d_{33} coefficient is also observed, and the value of poling field at which d_{33} vanishes along the [100] direction was also estimated as $E_c \sim 20$ kV/cm. The value for d_{33} when the measuring frequency extrapolates to zero ($f \rightarrow 0$) was estimated to be $d_{33} \sim 30$ pm/V along the [100] direction, which is very close to the value previously obtained along the [110] direction.

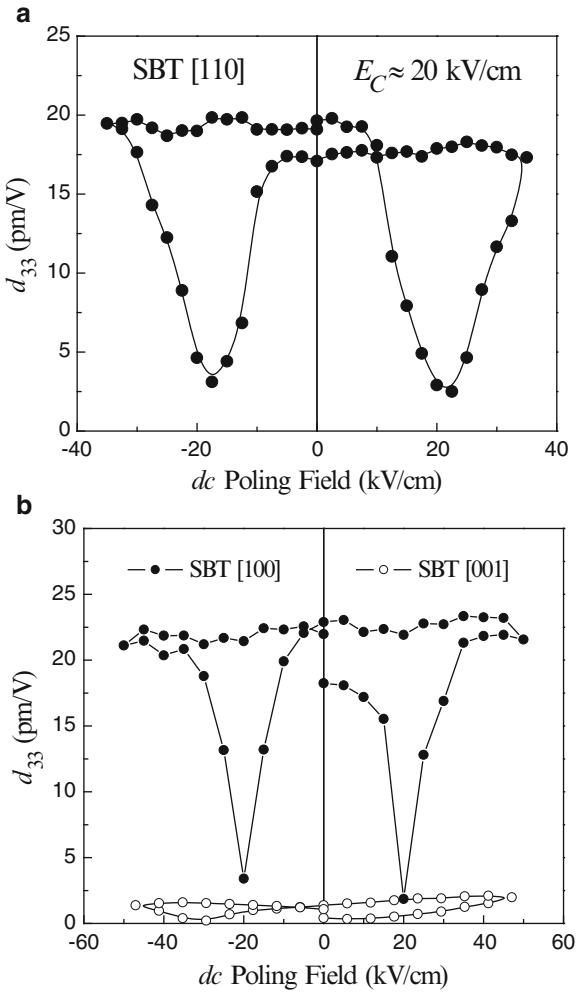

Fig. 2.14 Dependence of the piezoelectric coefficient d_{33} measured at 1 kHz with the dc poling field along the (**a**) [110] direction and (**b**) [100] and [001] directions in SBT crystals. The estimated E_c is indicated

At first view, this result suggests a negligible anisotropy of the d_{33} coefficient when the [100] and the [110] directions are compared, contrary to that expected in BLSF single crystals, where the P_s vector is oriented along the [100] direction (*a*-axis), and thus, at 45° with respect to the [110] direction. A possible explanation of this result may be found on the experimental setup used for the piezoelectric measurements. The SBT crystals were rigidly embedded in an araldite, and thus they were not free to expand or contract in the direction perpendicular to the applied ac voltage, specifically, in the [010] direction (non-polar direction) for the crystals measured along the [100] direction. As a result, due to the effect of the lateral stress induced in the crystal by the rigid araldite, the measured d_{33} coefficient is smaller than the real value for the crystal free of any stress. In other words, the clamping (zeroing) of d_{31} coefficient modifies the real d_{33} coefficient of

the unclamped crystal [75]. A correction factor should be introduced to obtain the true d_{33} coefficient of SBT crystals (i.e., this correction factor has been reported to be about a 10% of the measured clamped d_{33} in piezoelectric $LiNbO_3$ and $LiTaO_3$ crystals) [75].

However, a significant anisotropy in the d_{33} coefficient is clearly observed between the [100] and the [001] directions of the SBT crystal in Fig. 2.14b. In the second case, very small values of d_{33} coefficient were obtained for all poling fields (see open circles), thus confirming that the P_s vector in the SBT structure lies entirely in the *ab*-plane and neither polarization, nor piezoelectric activity, is obtained along the *c*-axis (perpendicular to the bismuth oxide layers), as previously discussed in the *P*–*E* hysteresis measurements.

2.3 Grain Oriented SBT Ceramics by Templated Grain Growth

Textured SBT ceramics were prepared by TGG using the grown SBT single crystals as anisometric templates. The selection and preparation of the templates is a subject of special interest for TGG experiments, since the texture development and the template growth during annealing strongly depends on their number, size, distribution, and initial orientation [45]. Usually, template particles with suitable dimensions to be used as seeds are obtained by molten salt or hydrothermal synthesis. Enhancements in electromechanical properties of various textured ceramic materials via TGG [76–84] have been recently reported. Soller et al. [76] have achieved Lotgering factors up to 81% and strain enhancements by a factor 1.5 with large-signal values of d_{33} up to 550 pm/V in the textured samples of undoped (K,Na,Li)(Nb,Ta)O_3 ceramics. Sabolsky et al. [80] prepared ⟨001⟩ oriented $Ba(Zr_{0.085}Ti_{0.915})O_3$ (BZT) ceramics with d_{33} coefficients at least three times greater than randomly oriented BZT ceramics and equally greater than many lead-free piezoelectric ceramics reported in literature. Highly preferentially [00l] oriented $Bi_{3.25}La_{0.75}Ti_{2.97}V_{0.03}O_{12}$ (BLTV) ceramics with grain-orientation factor (Lotgering factor 83%) were obtained by Ahn et al. [83]. Ogawa et al. obtained ⟨00*l*⟩ oriented ceramics of $SrBi_2Nb_2O_9$ (SBN) by TGG method having a Lotgering factor of 95% [84].

However, because of the complexity of SBT single crystal synthesis, this technique has not been extensively used for SBT and not often reported [85]. In our case, the large plate-like SBT crystals grown by self flux were used to prepare the required seeds for TGG after crushing and sieving procedures. Figure 2.15 shows thus obtained anisometric templates with an average size of ~40 × 40 × 8 μm^3, which preserve the plate-like morphology of the original crystals. 5 wt.% of templates was dispersed in a matrix of relatively fine and equiaxed particles containing a 3 wt.% of Bi_2O_3 excess [86]. Pellets were uniaxially pressed at 150 and 300 MPa followed by cold isostatic pressing at 200 MPa. Two different uniaxial pressures were used to evaluate their effects on the texture development. Unseeded SBT ceramics with 3 wt.% of Bi_2O_3 excess were also prepared under similar sintering conditions for comparison.

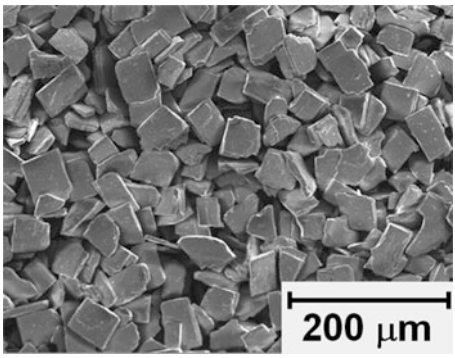

Fig. 2.15 SEM micrographs of SBT template particles used as seeds for TGG

Table 2.1 Relative density (ρ_r)[a] and degree of texture (*Lotgering factor*) of seeded and unseeded SBT ceramics under different pressing and sintering conditions

		Unseeded SBT 150 MPa		Seeded SBT 150 MPa		Seeded SBT 300 MPa	
Sintering temperature (°C)	Sintering time (h)	ρ_r (%)	Lotgering factor (%)	ρ_r (%)	Lotgering factor (%)	ρ_r (%)	Lotgering factor (%)
1,250	0	94	8.4	94	11	93	13
1,250	0.25	94	8.4	95	13	94	19
1,250	1	96	8.5	97	15	94	27
1,250	2	97	8.6	97	17	93	36
1,250	24	96	8.9	95	25	91	46

[a]Theoretical density of SBT is 8.78 g/cm^3

Table 2.1 summarizes densification results for the unseeded and seeded SBT samples processed under different sintering conditions. Densification levels above 90% of theoretical density were achieved in all sintered ceramics. The presence of templates in seeded ceramics does not significantly affect the final density of the samples, although higher densification levels were achieved for unseeded ceramics. The maximum density is observed after sintering for 2 h, and then decreases for longer sintering time. This behavior is tentatively attributed to the presence of liquid phase that increases the boundary mobility of templates throughout the matrix during sintering, promoting matrix grain rearrangement and mass transfer processes for short sintering times. However, after the template impingement, trapped porosity between platelets becomes thermodynamically stable and difficult to be removed afterwards.

The crystalline phases and degree of texture were studied by XRD in the 2θ scan between 4 and 80° with steps of 0.02°, scanning polished cross-sections parallel ($\parallel P$) and perpendicular ($\perp P$) to the uniaxial pressing direction. The degree of (00l) orientation was evaluated by the Lotgering factor, which is based in the relative intensities of the peaks [87]. In this procedure, the degree of $\langle 00l \rangle$-orientation of a sample is defined as $f = (P - P_o)/(1 - P_o)$, where $P = \Sigma I(00l)/I(hkl)$ and

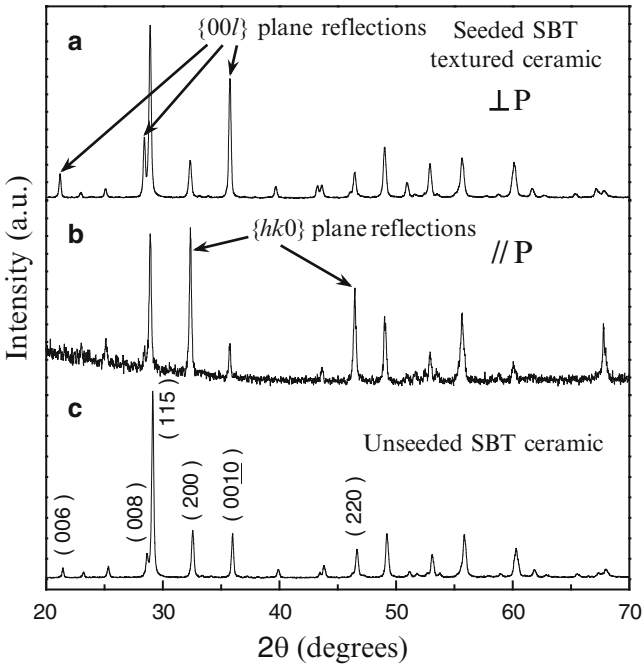

Fig. 2.16 XRD patterns scanned on the cross-sections (**a**) $\perp P$ and (**b**) $\parallel P$ in the seeded SBT ceramic uniaxially pressed at 150 MPa and sintered at 1,250°C during 24 h. (**c**) XRD pattern for the unseeded SBT ceramic processed under similar conditions

I are the integrated intensities of the peaks, whereas P_o is P for the randomly oriented powder. Although f should not be directly used for quantifying texture, it is considered an estimation of the degree of grain orientation in a textured material.

The microstructure was examined on polished and etched cross-sections parallel ($\parallel P$) to the pressing direction by scanning electron microscopy and a stereological analysis was carried out using image analysis [88]. The volume fraction, f_v, of the oriented material was determined by measuring the total area fraction of platelet grains, which was multiplied by an appropriate stereological correction factor [89]. For calculating f_v, the large anisometric grains were considered as textured material while the remaining small ones were considered as randomly oriented matrix grains. For dielectric measurements, the samples were cut and polished in two plates, parallel ($\parallel P$) and perpendicular ($\perp P$) to the pressing direction, and then electroded with sputtered gold.

2.3.1 X-Ray Characterization: Lotgering Factor

Figure 2.16a, b shows XRD patterns on cross-sections $\perp P$ and $\parallel P$, respectively, in the seeded SBT ceramic uniaxially pressed at 150 MPa and sintered at 1,250°C for 24 h. The pattern of the unseeded ceramic is included for comparison in Fig. 2.16c.

The lattice planes (*hkl*) associated with the reflections whose relative intensity changes significantly among the patterns are also pointed out. It can be observed that the diffractions from the {00l} planes of the SBT structure have a meaningful intensity in the XRD pattern on the cross-section $\perp P$, while the diffraction peaks from the {*hk0*} planes, specifically the (200) and (220) lattice planes, are stronger in the XRD pattern scanned on the cross-section $\parallel P$. This result confirms a crystallographic texture in the seeded SBT ceramics.

Table 2.1 also summarizes the calculated f obtained on cross sections $\perp P$ of seeded and unseeded SBT ceramics. Whereas unseeded ceramics show a Lotgering factor lower than 10% even after 24 h of sintering time, seeded ceramics reach a maximum of $f \approx 25\%$ for samples uniaxially pressed at 150 MPa and of $f \approx 46\%$ for 300 MPa. For short sintering time (0 h) a similar degree of orientation was obtained in seeded samples corresponding to both pressure conditions, very close to that observed in the early stage of the TGG process (seeded SBT sintered at 1,000°C for 1 h, $f \approx 10\%$). When the sintering time increases, the seeded ceramics exhibit an initial fast texturing rate which tends to saturate after 2 h. The higher the uniaxial pressure in the green samples, the higher seems to be the initial orientation of the templates, resulting in a higher degree of texture in the sintered samples. Nevertheless, the *f* values obtained in this work are lower than those typically reported for textured ceramics produced by other more elaborated texturing techniques such as tape casting or hot-pressing [30, 90, 91]. Therefore, by using these techniques, higher degrees of texture are expected.

2.3.2 Microstructure Evolution and Texture Analysis

In most BLSF materials, grains grow in an anisotropic form showing platelet morphology to minimize the energy associated with the grain boundaries [90]. Also, in SBT ceramics, (00*l*) facets develop more extensively during the sintering process, thus indicating these facets as the ones possessing the lower surface energy. As a result, plate-like grain morphology develops with major faces parallel to the (00*l*) crystal planes.

Figure 2.17 shows the development of the textured microstructure during sintering at 1,250°C of seeded SBT ceramics. A bimodal microstructure dominated by large anisometric grains is clearly observed at the final stage of the TGG process. These large grains display a plate-like morphology with the dimensions about twice of the initial seeds. With increasing sintering time, template particles grow significantly along the length direction until template impingement occurs, while the matrix grains coarsen gradually. This is in good agreement with the results reported in alumina, in which TGG was proposed to occur in three stages [92–94]: densification, rapid radial growth of individual template particles until impingement, and slower growth by template thickening.

The time evolution of the microstructure in Fig. 2.17 also reveals an increasing amount of oriented grains with their major faces perpendicular to the uniaxial pressing

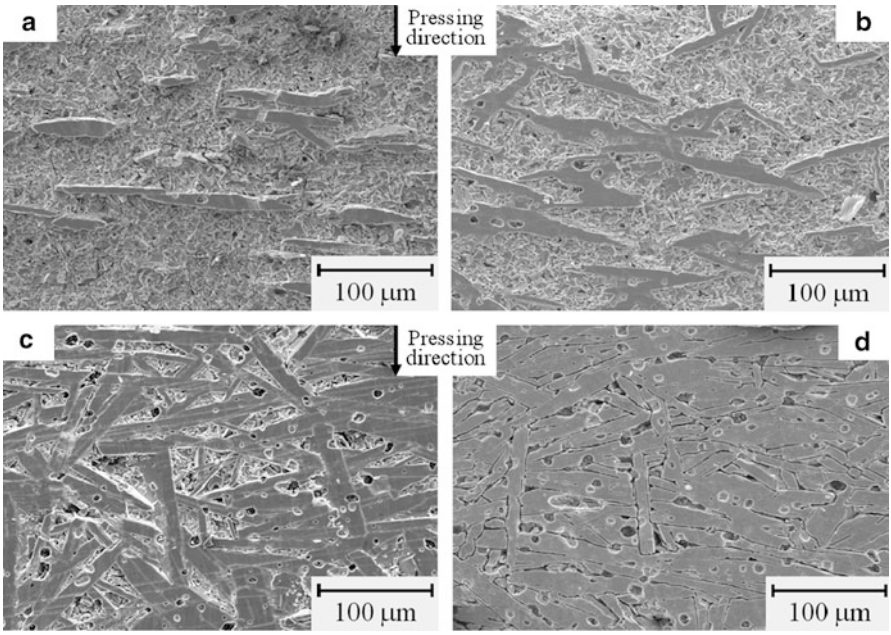

Fig. 2.17 SEM micrographs of cross-section ||*P* of seeded SBT ceramic uniaxially pressed at 300 MPa and sintered at 1,250°C for (**a**) 0 h, (**b**) 1 h, (**c**) 2 h and, (**d**) 24 h

direction. This result may account for the observed increase of crystallographic texture with sintering time. After sintering at 1,250°C for 0 h the microstructure shows few large grains that correspond roughly to the initial concentration of seed crystals. Their average size has significantly increased to ~74 × 9 μm^2 and has been accompanied by the corresponding increase (about 60%) of the aspect ratio (AR) from AR ≈ 5 (initial stage) to AR ≈ 8. Similar to textured ceramics of $Bi_4Ti_3O_{12}$ prepared by TGG, the template growth morphology may be ascribed to the anisotropy of grain boundary energies [90]. Thus, the preferred lateral growth of the templates maximizes the area of the faces perpendicular to the *c*-axis, which appear to be those with lower surface energy. Although slowed down by matrix coarsening, the template lateral growth continues until templates impinge each other after sintering for 2 h (see also Table 2.2). At this point the average size of the large anisometric grains is ~88 × 11 μm^2, while the aspect ratio is still AR ≈ 8. Respecting the matrix grains, those growing too large to be consumed start impinging upon the large anisometric grains too. For longer sintering times, due to impingement, the large anisotropic grains stop growing along the length direction and get thicker, giving place to a decrease of the aspect ratio until AR ≈ 6.7. Their average size was ~91 × 13.5 μm^2 for the samples sintered 24 h. At this stage, some porosity concentrated at the template particle boundary limits grain growth.

The measured values of the average length, thickness, and the calculated aspect ratio for large and small anisotropic grains in seeded SBT samples sintered at

Table 2.2 Microstructural parameters of the seeded SBT ceramics sintered under different conditions: average length, thickness, aspect ratio, and volume fraction corresponding to the large anisometric grains, determined by stereological analysis

Sintering temperature (°C)	Sintering time (h)	Volume fraction, f_v	Large grains (μm)		Aspect ratio
			Length	Thickness	
1,000	1	0.05	42	8.4	5.0
1,250	0	0.09	74	9.1	8.1
1,250	0.25	0.14	77	9.2	8.3
1,250	1	0.21	80	10.1	7.9
1,250	2	0.53	88	11.2	7.8
1,250	24	0.62	91	13.5	6.7

1,250°C for 0–24 h are shown in Table 2.2. The volume fraction of textured material (f_v) increases from ~9% for 0 h to ~62% for 24 h of sintering time. Due to template growth, a fast increase in the volume fraction of large anisometric grains from ~9% after 0 h to ~53% after 2 h is observed, followed then by a scarce increase for 24 h. The anisotropic TGG occurs mainly in the first 2 h of sintering time when sintered at 1,250°C. Although a small amount of this volume fraction corresponds to misaligned grains with respect to the texture plane, that is, the plane $\perp P$, most of these grains are expected to contribute to the improvement of the piezoelectric and ferroelectric properties measured along any direction $\perp P$.

2.3.2.1 Nucleation of Anisometric Grains

In general, texture development during TGG is due to the growth of large, anisometric, and oriented templates consuming the small and randomly arranged matrix grains [94, 95]. Accordingly, the limits of template growth and texture development should be controlled by the geometry, concentration, and alignment of the original seeds. Such assumption predicts the volume fraction of textured material (considering only templates) to be directly related to the number of original seeds: $f_v = NV_T$, in which N is the initial number of templates in 1 cm^3 and V_T the average volume of a single template particle in cm^3.

Figure 2.18 shows the dependence of f_v on V_T, which was calculated using the average length and thickness of large anisotropic grains reported in Table 2.2 and assuming plate-like morphology for the large grains. As observed, instead of a continuous linear relation between the volume fraction of textured material and the calculated average volume for a single large grain, two distinct slopes are identified in this plot, one for short sintering times up to 1 h and a higher slope for longer sintering times. This result suggests that the number of large grains per 1 cm^3 in the final stage of the TGG process increased with respect to the number of original templates. The number of large grains per 1 cm^3 obtained from this plot is $N_o \approx 2.7 \times 10^6$ cm^{-3} for short sintering times and $N_f \approx 1 \times 10^7$ cm^{-3} for longer

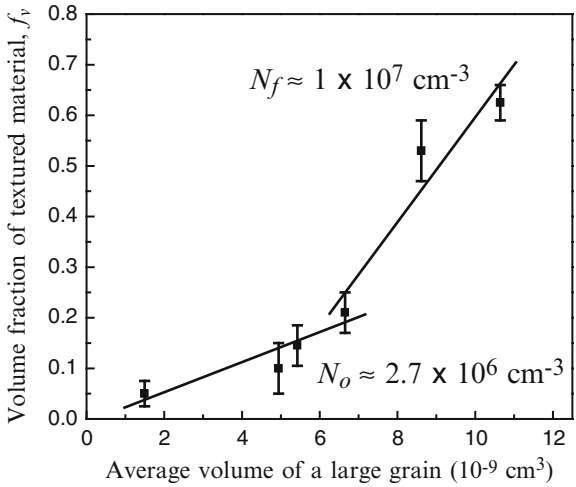

Fig. 2.18 Correlation between the volume fraction of textured material and the calculated average volume of large anisometric grains in seeded SBT ceramics. *N* is the number of large grains per 1 cm^3

sintering times (both with correlation coefficient greater than 0.96). Thus, the number of large anisometric grains at the late stage of the TGG process is almost 4 times greater than that in the early stage.

Therefore, besides the growth of original seeds, new large anisometric grains evolve from the matrix after 1 h of sintering time, acquiring similar platelet morphology with a fast growth along the *ab*-plane and similar alignment with their major face nearly $\perp P$. In this case, a mechanism other than the growth of the original templates should operate. Small matrix grains having face-to-face contact can bond each other to form new large anisometric grain inside the matrix [96]. This matrix grain alignment may have been originally induced by the pressing process itself or by rearrangement of the small matrix grains. It is suggested that the aligned templates induce the alignment of the matrix grains, probably by rotation during the early stage of the TGG process [97]. Those small grains situated closer to the templates rotate to share the low-energy surface, that is, the major surface, thus influencing the rotation of other matrix grains that are more distant from the template [90].

The previously reported results concerning [98]: (1) the effect of the presence of Bi_2O_3 excess as liquid phase, (2) the effect of the increasing sintering temperature and time, and (3) the effect of the increase of the uniaxial pressure, indicate that the template alignment and the liquid phase characteristics are important parameters governing the nucleation of secondary anisometric grains from the matrix. The used experimental conditions seemed to be adequate for improving the initial template alignment and inducing matrix grain rearrangement, which, assisted by a liquid phase of suitable viscosity, allowed the nucleation of new large anisometric grains. These findings are in line with the proposals of Hong et al. [92] for exploring the nucleation of large grains from the matrix in textured mullite, and with suggestions of Suvaci et al. [93] that liquid phase promotes the rearrangement and alignment of the matrix grains in textured alumina.

2.3.2.2 Quantitative Texture Analysis

The texture analysis using the simplest technique (*Lotgering factor*) does not provide enough information about the distribution of platelet orientations in the material, which can be fundamental in understanding processing-texture relationships [99]. A more complete description of texture may quantify the occurrence probability of given crystalline orientations with respect to the reference sample coordinate axes, i.e., the so-called orientation distribution function (ODF) [100]. The knowledge of the distribution of grain orientation, as disclosed from ODF, is very important since the grains with small misorientation relatively to the texture axis also contribute to P_s, thus enhancing ferro/piezoelectric properties along a specific direction. Furushima et al. have correlated the orientation index (Lotgering factor) with the orientation distribution for particle-oriented bismuth titanate ($Bi_4Ti_3O_{12}$), both theoretically and experimentally [101].

The orientation distribution of large anisotropic grains was obtained from the stereological analysis by measuring the number frequency of large grains with their major axis oriented at a given angle ω with respect to the texture plane, and fitted using the March-Dollase equation [102, 103]: $F(1, r, \omega) = (r^2\cos^2\omega + (\sin^2\omega/r))^{-(3/2)}$. In this case, f_v was set $= 1$ to quantify the degree of alignment of the large grains by the r parameter (texture factor).

Figure 2.19a shows the normalized orientation distribution of large anisometric grains for seeded SBT ceramics uniaxially pressed at 300 MPa and sintered at 1,250°C for 0 and 2 h. Each distribution is normalized to unity by dividing it by the number frequency of large grains with orientation equal to zero, i.e., $\omega = 0$. Solid lines are the best fitting curves of the normalized March function to the experimental values. Figure 2.19b shows the r values obtained as a function of the sintering time. A step increase from ~0.49 for short sintering times to ~0.58 for 2 and 24 h of sintering times is clearly observed. The relatively high r values obtained reflect mainly the effectiveness of the used processing technique for template alignment. If texture development during TGG was controlled uniquely by the growth of templates consuming matrix grains, then a nearly constant r value should have been obtained for different sintering times. The sudden increase in the r value after 2 h of sintering time is most likely related to the nucleation and growth of new large grains in the final stage of the TGG process.

2.3.3 Anisotropy of the Ferro/Piezoelectric Properties

In general, seeding induces anisotropy in dielectric, piezoelectric, and ferroelectric properties. The differently oriented grains in the textured ceramics give rise to properties anisotropy between the directions parallel and perpendicular to the pressing axis. Majhi et al. reported anisotropy in the dielectric and pyroelectric properties of textured $SrBi_2Nb_2O_9$ ceramics [79]. They observed superior dielectric constant and pyroelectric coefficient along the direction perpendicular to the melt

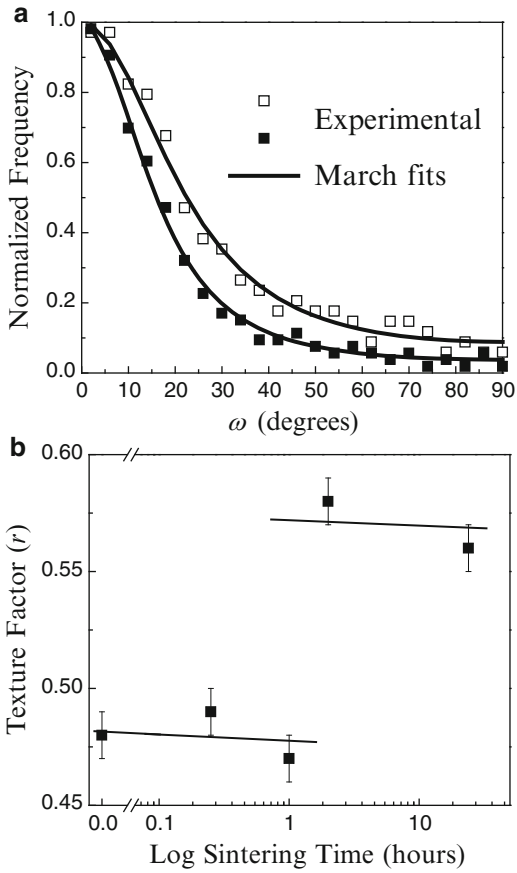

Fig. 2.19 (**a**) Normalized orientation distribution of large anisometric grains corresponding to seeded SBT ceramics pressed at 300 MPa and sintered at 1,250°C for (*filled square*) 0 h and (*open square*) 2 h (*solid lines* represent March-Dollase fits). (**b**) Texture factor (*r*) for different sintering times

pressing axis as compared to that of the direction parallel to the pressing axis at room temperature. Dielectric anisotropy has been observed in textured $Ba_4Nd_{9.33}Ti_{18}O_{54}$ by Wada et al. [104]. Similar results were reported in textured $BaLa_4Ti_4O_{15}$ ceramics with layered perovskite structure [44].

Anisotropy in the dielectric properties has been observed in our seeded samples as well. Figure 2.20 shows the temperature dependence of the permittivity at 10 kHz observed in seeded SBT ceramics sintered at 1,250°C for 0 and 24 h, when the electric field is applied $E \| P$ and $E \perp P$. For comparative purposes, the curve obtained for the unseeded ceramic is also included. The permittivity measured for the ceramic sintered at 1,250°C/24 h along the texture direction ($E \perp P$) exceeds that of the unseeded SBT ceramic which is roughly isotropic and does not depend on the electric field direction.

To date, there exist very few reports on the anisotropy of ferroelectric properties in textured SBT ceramics [85]. Figure 2.21 shows the *P–E* hysteresis loops of seeded SBT ceramics sintered at 1,250°C for different sintering times, and

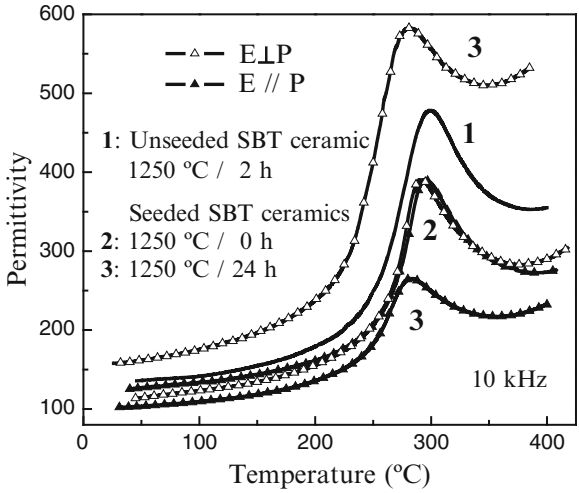

Fig. 2.20 Anisotropy in the temperature dependence of the permittivity measured with $E \| P$ and $E \perp P$ for seeded SBT ceramics sintered at 1,250°C for 0 and 24 h. For comparison, the unseeded randomly oriented SBT ceramic sintered at 1,250°C/2 h is included

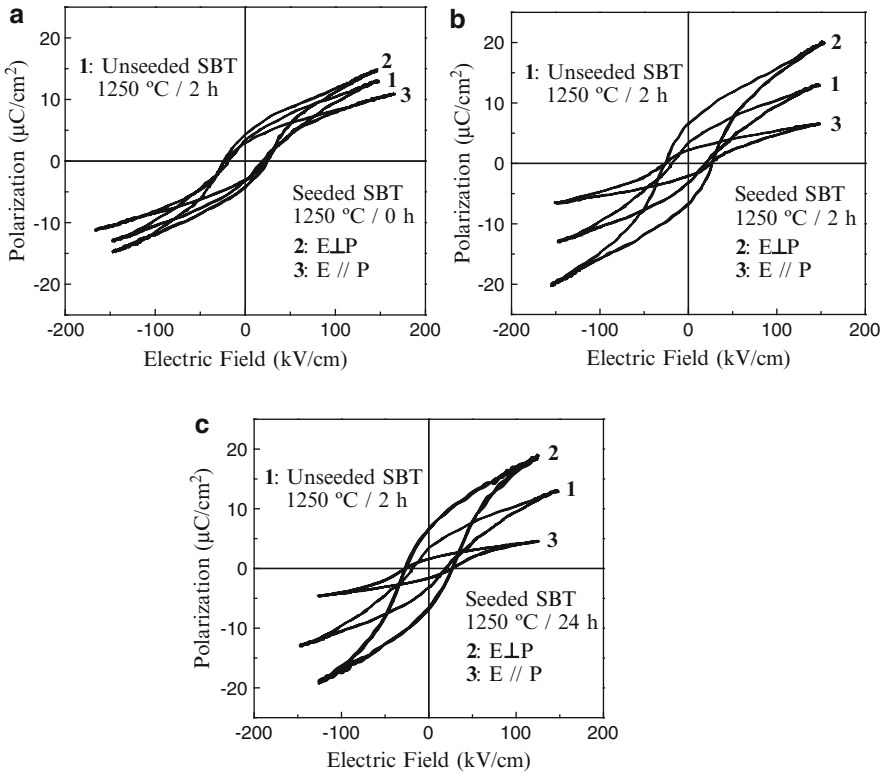

Fig. 2.21 Room temperature P–E hysteresis loops obtained with $E \perp P$ and $E \| P$ in seeded SBT ceramics sintered at 1,250°C during (**a**) 0, (**b**) 2, and (**c**) 24 h. The hysteresis loop obtained for the unseeded ceramic sintered at 1,250°C is also included for comparison

measured with $E \| P$ and $E \perp P$. The ferroelectric characterization was performed on samples uniaxially pressed at 300 MPa, since they demonstrate the best texture feature. For a comparative purpose, the loop corresponding to the unseeded SBT ceramic is also included. Anisotropy of the remnant (P_r) polarization is revealed by $E \| P$ and $E \perp P$ hysteresis curves, P_r being higher for the samples with higher degree of texture. The polarization vector in the SBT structure lies entirely along *a*-axis [58]. Accordingly, the observed increase of permittivity and P_r values for the textured ceramics, when $E \perp P$ is used, may be explained as an increased contribution from the highly polarizable *ab*-plane, allowed by the favorable alignment of the large grains in the direction of the electric field. This contribution is expected to be further increased upon increasing the texture degree in the ceramics. For the sample where $E \| P$, the above mentioned contribution is partly lost and the permittivity and polarization values decrease.

E_c anisotropy is not found when using $E \| P$ and $E \perp P$, but E_c increases from 20 to 27 kV/cm with increasing sintering time. It is important to emphasize that the E_c observed for the unseeded SBT sample (20 kV/cm) is very close to that obtained in SBT single crystals. The maximum P_s of 8.9 μC/cm^2 measured with $E \perp P$ for 24 h of sintering time is lower than that estimated for the SBT single crystal ($P_s \approx 20$ μC/cm^2). These results indicate that ferroelectric properties are considerably improved in the textured SBT ceramics when measured with $E \perp P$, as compared to the unseeded SBT samples, and that highly anisotropic properties can be thus achieved.

2.4 Conclusions

In summary, this chapter was dedicated to the processing and characterization of textured SBT ceramics using the high-quality single crystals processed by the modified high-temperature self–flux method. A detailed analysis of the phase formation, microstructural, and electrical studies on unseeded and seeded SBT ceramics and single crystals was presented.

SBT single crystals were produced by a high-temperature self-flux solution method using a Bi_2O_3 flux added with a small amount of B_2O_3. The largest SBT crystals with sizes of ~7 × 5 × 0.2 mm^3 were obtained under an optimized thermal profile that included a gradually accelerated slow cooling process. The anisotropic morphology of the grown crystals with layered habit was correlated with its crystallographic structure. XRD and X-ray topography analyses revealed highly oriented single crystal platelets with the [001] direction (*c*-axis) lying perpendicular to the major face, whereas the lateral sides of the rectangular shaped crystals were oriented along the [110] and [110] directions (45° to both *a*- and *b*-axes) of the orthorhombic $A2_1am$ phase. Domain imaging of high-quality SBT single crystals was performed by PFM. A domain system of coexisting 90 and 180° domains in SBT single crystals, forming a well-defined "herringbone" structure with mostly flat 90° domain walls oriented along the [110] direction, was

clearly observed. The widths of 90° domains (twins) forming laminar structures lied in the range 0.7–1.5 μm, whereas 180° domain walls, oriented parallel to the [100]-direction (polar axis), exhibited a periodicity 250–500 nm. Formation of the observed complex domain pattern was attributed to a two-stage phase transition process involving separate ferroelastic and ferroelectric phase transitions in SBT. High quality of SBT single crystals was confirmed by ferroelectric and piezoelectric measurements, which were conducted in the *ab*-plane (along the [110] direction) and along the *c*-axis (the [001] direction), demonstrating the expected strong anisotropy in the intrinsic properties. Saturated hysteresis loops were obtained along the [110] direction for SBT crystals, from which the values of P_s and E_c were estimated as ~14 μC/cm^2 and ~22 kV/cm, respectively, thus allowing estimation of P_s ~20 μC/cm^2 along the polar axis in this material. The longitudinal piezoelectric coefficient d_{33} measured along the [100] direction (polar axis) was estimated to be ~30 pm/V.

Seeded SBT ceramics were prepared by TGG using 3 wt.% of Bi_2O_3 excess in liquid phase using 5 wt.% of anisometric SBT templates. The effects of the processing and sintering conditions including uniaxial pressure, the sintering temperature and time on the final density, degree of texture, and microstructure evolution of both seeded and unseeded SBT ceramics were studied and discussed. The texture development examined by XRD and pole figure analyses confirmed a crystallographic texture in seeded SBT samples. Lotgering factor was shown to increase with increasing sintering temperature and time, whereas the higher uniaxial pressure used for shaping the green samples resulted in ceramics with higher degree of texture. A bimodal microstructure with a high amount of large anisometric grains was obtained after sintering the seeded SBT ceramics at 1,250°C for 2 h. Large grains were similar in shape to the original templates but two times larger than the initial seeds. Most of the large grains with *c*-axis ⊥ to the major face were preferentially oriented with the normal to the major face within ~20° about the texture axis (the pressing direction). The volume fraction of oriented material increased from ~9 to ~62% when increasing sintering time from 0 to 24 h. The alignment of the template particles induces alignment of the matrix grains, giving rise to nucleation of new large anisometric grains from the matrix. The number of large anisometric grains per cm^3 increases from 2.7×10^6 cm^{-3} for short sintering times up to 1×10^7 cm^{-3} for longer sintering times. Anisotropy in the ferroelectric properties of the seeded SBT specimens at room temperature is observed. Enhanced ferroelectric properties were measured perpendicularly to the uniaxial pressing direction for the seeded samples sintered at 1,250°C for 2 and 24 h, with polarization values exceeding those of the unseeded SBT ceramics.

Acknowledgments The authors wish to acknowledge Drs. Igor Bdikin and Vladimir Shvartsman for their help with XRD and PFM measurements, respectively. Most of the work was performed within the PhD grant of H. Amorin supported by the Portuguese Science and Technology Foundation (FCT). The work was partly supported by the FCT project PTDC/FIS/108025/2008.

References

1. Noguchi Y, Miyayama M, Oikawa K, Kamiyama T, Osada M, Kakihana M (2002) Defect engineering for control of polarization properties in $SrBi_2Ta_2O_9$. Jpn J Appl Phys 41:7062
2. Bonapasta A, Giannozzi P (2000) Effects of strain and local charge on the formation of deep defects in III-V ternary alloys. Phys Rev Lett 84:3923
3. Connell SH, Siderashaddad E, Bharuthram K, Smallman CG, Sellschop JPF, Bossenger MG (1994) Perturbed angular distribution studies in natural, synthetic CVD and HPHT diamond. Nucl Inst Meth Phys Res B85:508
4. Derry TE, Spits RA, Sellschop JPF (1992) Ion beam studies of the static and dynamic properties of dopants in diamond. Mater Sci Eng B 11:249
5. Li D, Bonnell DA (2008) Controlled patterning of ferroelectric domains: fundamental concepts and applications. Annu Rev Mater Res 38:351
6. Damjanovic D (1998) Materials for high temperature piezoelectric transducers. Curr Opin Solid State Mater Sci 3:469
7. Noguchi T, Hase T, Miyasaka Y (1996) Analysis of the dependence of ferroelectric properties of strontium bismuth tantalate (SBT) thin films on the composition and process temperature. Jpn J Appl Phys 35:4900
8. Tsai HM, Lin P, Tseng TY (1999) Effect of bismuth content on the properties of $Sr_{0.8}BixTa_{1.2}Nb_{0.9}O_{9+y}$ ferroelectric thin films. J Appl Phys 85:1095
9. Shimakawa Y, Kubo Y, Nakagawa Y, Kamiyama T, Asano H, Izumi F (1999) Crystal structure and ferroelectric properties of $SrBi_2Ta_2O_9$ and $Sr_{0.8}Bi_{2.2}Ta_2O_9$. Appl Phys Lett 74:1904
10. Noguchi Y, Miyayama M, Kudo T (2001) Direct evidence of A-site-deficient strontium barium tantalate and its enhanced ferroelectric properties. Phys Rev B 63:214102
11. Kamura SO, Takaoka M, Nishida T, Shiosaki T (2000) Increase in switching charge of ferroelectric $SrBi_2Ta_2O_9$ thin films with polarization reversal. Jpn J Appl Phys 39:5481
12. Aizawa K, Tokumitsu E, Okamoto K, Ishiwara H (2000) Impact of face-to-face annealing in preparation of sol-gel-derived $SrBi_2Ta_2O_9$ thin films. Appl Phys Lett 76:2609
13. Coondoo I, Jha AK, Agarwal SK (2009) Ferroelectric and piezoelectric properties of tungsten substituted $SrBi_2Ta_2O_9$ ferroelectric ceramics. Mater Res Bull 44:1288
14. Coondoo I, Jha AK, Agarwal SK (2007) Enhancement of dielectric characteristics in donor doped Aurivillius $SrBi_2Ta_2O_9$ ferroelectric ceramics. J Eur Ceram Soc 27:253
15. Gruverman A, Ikeda Y (1998) Characterization and control of domain structure in $SrBi_2Ta_2O_9$ thin films by scanning force microscopy. Jpn J Appl Phys 37:L939
16. Harnagea C, Pignolet A, Alexe M, Hesse D, Gosele U (2000) Quantitative ferroelectric characterization of single submicron grains in Bi-layered perovskite thin films. Appl Phys A Mater Sci Proc 70:261
17. Gruverman A, Pignolet A, Satyalakshmi KM, Alexe M, Zakharvo ND, Hesse D (2000) Nanoscopic switching behavior of epitaxial $SrBi_2Ta_2O_9$ films deposited by pulsed laser deposition. Appl Phys Lett 76:106
18. Jiménez R, Calzada ML, Gonza´lez A, Mendiola J, Shvartsman VV, Kholkin AL, Vilarinho PM (2004) Nanoscale properties of ferroelectric ultrathin SBT films. J Eur Ceram Soc 24:319
19. Amorín H, Shvartsman VV, Bdikin IK, Costa MEV, Kholkin AL, Pertsev NA (2006) Ferroelectric domains and twinning in high-quality $SrBi_2Ta_2O_9$ single crystals. Appl Phys Lett 88:062903
20. Almeida A, Chaves MR, Amorin H, Costa MEV, Kholkin AL (2005) Lattice dynamics of high-quality strontium bismuth tantalate single crystals. J Phys Condens Matter 17:7605
21. Yi X, Chen H, Cao W, Zhao Z, Yang D, Ma G, Yang C, Han J (2005) Flux growth and characterization of lead-free piezoelectric single crystal $[Bi_{0.5}(Na_{1-x}K_x)_{0.5}]TiO_3$. J Crys Growth 281:364
22. Wang L, Li Q, Zhang Y (2008) Flux growth of La-doped lead zirconate stannate titanate antiferroelectric crystals. Cryst Res Technol 43:1011

23. Subbarao EC (1962) Crystal chemistry of mixed bismuth oxides with layer-type structure. J Am Ceram Soc 45:166
24. Ikegami S, Ueda I (1974) Piezoelectricity in ceramics of ferroelectric bismuth compound with layer structure. Jpn J Appl Phys 13:1572
25. Newnham RE, Wolfe RW, Dorrian JF (1971) Structural basis of ferroelectricity in the bismuth titanate family. Mater Res Bull 6:1029
26. Takenaka T, Sakata K (1980) Grain orientation and electrical properties of hot-forged $Bi_4Ti_3O_{12}$ ceramics. Jpn J Appl Phys 19:31
27. Kimura T (2006) Application of texture engineering to piezoelectric ceramics – a review. J Ceram Soc Jpn 114:15
28. Yilmaz H, Messing GL, McKinstry ST (2003) (Reactive) templated grain growth of textured sodium bismuth titanate $Na_{1/2}Bi_{1/2}TiO_3$ – $BaTiO_3$) ceramics – I processing. J Electroceram 11:207
29. Yilmaz H, Messing GL, McKinstry ST (2003) (Reactive) templated grain growth of textured sodium bismuth titanate $Na_{1/2}Bi_{1/2}TiO_3$ – $BaTiO_3$) ceramics – II processing. J Electroceram 11:217
30. Takeuchi T, Tani T, Saito Y (1999) Piezoelectric properties of bismuth layer-structured ferroelectric ceramics with a preferred orientation processed by the reactive templated grain growth method. Jpn J Appl Phys 38:5553
31. Duran C, McKinstry ST, Messing GL (2002) Dielectric and piezoelectric properties of textured $Sr_{0.53}Ba_{0.47}Nb_2O_6$ ceramics prepared by templated grain growth. J Mater Res 17:2399
32. Kimura T, Motohashi T (2009) Effect of template particle formation on texture development in $Bi_{0.5}Na_{0.5}TiO_3$ ceramics. Key Eng Materials 388:209
33. Zhao W, Ya J, Xin Y, Lie E, Zhao D, Zhou H (2009) Fabrication of $Na_{0.5}Bi_{0.5}TiO_3$–$BaTiO_3$-textured ceramics templated by plate-like $Na_{0.5}Bi_{0.5}TiO_3$ particles. J Am Ceram Soc 92:1607
34. Sabolsky EM, Maldonado L, Seabaugh MM, Swartz SL (2009) Textured-Ba(Zr, Ti)O_3 piezoelectric ceramics fabricated by templated grain growth (TGG). J Electroceram 25:77
35. Zhao W, Ya J, Xin Y, Liu Z, Lei E, Zhao D (2008) Fabrication of lead-free piezoelectric ceramics by (reactive) templated grain growth. Recent Patents Mater Sci 1:241
36. Andreeta ERM, dos Santos HFL, Andreeta MRB, Lente MH, Garcia D, Hernandes AC, Eiras JA (2007) Anisotropy on $SrTiO_3$ templated textured PMN–PT monolithic ceramics. J Eur Ceram Soc 27:2463
37. Tani T, Kimura T (2006) Reactive-templated grain growth processing for lead free piezoelectric ceramics. Adv Appl Ceram 105:55
38. Li FX, Rajapakse RKND (2007) Analytical saturated domain orientation textures and electromechanical properties of ferroelectric ceramics due to electric/mechanical poling. J Appl Phys 101:054110
39. Leontsev SO, Eitel RE (2010) Progress in engineering high strain lead-free piezoelectric ceramics. Sci Technol Adv Mater 11:044302
40. Saito Y, Takao H, Tani T, Nonoyama T, Takatori K, Homma T, Nagaya T, Nakamura M (2004) Lead-Free Piezoceramics. Nature 432:84
41. Sato T, Yoshida Y, Kimura T (2007) Preparation of <110>-textured $BaTiO_3$ ceramics by the reactive-templated grain growth method using needlelike TiO_2 particles. J Am Ceram Soc 90:3005
42. Tam WK, Kwok KW, Zeng JT, Chan HLW (2008) Fabrication of textured BNKLT ceramics by reactive templated grain growth using NBT templates. J Phys D Appl Phys 41:045402
43. Saito Y, Takao H, Wada K (2008) Synthesis of platelike $CaTiO_3$ particles by a topochemical microcrystal conversion method and fabrication of textured microwave dielectric ceramics. Ceram Int 34:745
44. Wada K, Fukami Y, Kakimoto K, Ohsato H (2005) Microwave dielectric properties of textured $BaLa_4Ti_4O_{15}$ ceramics with layered perovskite structure. Jpn J Appl Phys 44:7094

45. Messing GL, Trolier-McKinstry S, Sabolsky EM, Duran C, Kwon S, Brahmaroutu B, Park P, Yilmaz H, Rehrig PW, Eitel KB, Suvaci E, Seabaugh MM, Oh KS (2004) Templated grain growth of textured piezoelectric ceramics. Crit Rev Solid State Mater Sci 29:45
46. Takenaka T, Shoji K, Takai H, Sakata K (1976) Ferroelectric and dielectric properties of press forged bismuth titanate ceramics. Proc Jpn Congr Mater Res 19:230
47. Takenaka T, Shoji K, Sakada K (1977) Grain orientation and microstructure of hot-forged $Bi_4Ti_3O_{12}$ ceramic. Proc Jpn Congr Mater Res 20:212
48. Takenaka T, Sakada K (1980) Grain orientation and electrical properties of hot-forged $Bi_4Ti_3O_{12}$ ceramics. Jpn J Appl Phys 19:31
49. Takenaka T, Sakada K (1984) Grain orientation effects on electrical properties of bismuth layer-structured ferroelectric $Pb_{(1-x)}(NaCe)_{x/2}$ Bi_4 Ti_40_{15} solid solution. J Appl Phys 55:1092
50. Seth VK, Schulze WA (1989) Grain-oriented fabrication of bismuth titanate ceramics and its electrical properties. IEEE Trans Ultrason Ferroelectr Freq Control 36:41
51. Kimura T, Yoshimoto T, Iida N, Fujita Y, Yamaguchi T (1989) Mechanism of grain-orientation during hot-pressing of bismuth titanate. J Am Ceram Soc 72:85
52. Inoue Y, Kimura T, Yamaguchi T, Nagata K, Okazaki K (1984) Grain orientation and electrical properties of hot-pressed bismuth titanate ceramics. Yagyo-Kyokai-Shi 92:416
53. Machida A, Nagasawa N, Ami T, Suzuki M (1999) Domain motion of ferroelectricity of $Bi_2SrTa_2O_9$ single crystals under an ac-voltage electric field. Jpn J Appl Phys 38:795
54. Sih B, Tang J, Dong M, Ye ZG (2001) Ferroelectric $SrBi_2Ta_2O_9$ single-crystal growth and characterization. J Mater Res 16:1726
55. Amorin H, Costa MEV, Kholkin AL, Baptista JL (2003) Electrical properties of $SrBi_2Ta_2O_9$ single crystals grown by self-flux solution. J Eur Ceram Soc 24:1535
56. Amorin H, Shvartsman VV, Kholkin AL, Costa MEV (2004) Ferroelectric and dielectric anisotropy in high-quality $SrBi_2Ta_2O_9$ single crystals. Appl Phys Lett 85:5667
57. Amorin H, Shvartsman VV, Trolliard G, Manier M, Mercurio JP, Kholkin AL, Costa MEV (2004) Investigation of domain structure of $SrBi_2Ta_2O_9$ single crystals via optical and piezoresponse force microscopy. Integr Ferro 62:215
58. Rae AD, Thompson JG, Withers RL (1992) Structure refinement of commensurately modulated bismuth strontium tantalate, $Bi_2SrTa_2O_9$. Acta Crystallogr B 48:418
59. Shimakawa Y, Kubo Y, Nakagawa Y, Goto S, Kamiyama T, Asano H, Izumi F (2000) Crystal structure and ferroelectric properties of $ABi_2Ta_2O_9$ (A = Ca, Sr and Ba). Phys Rev B 61:6559
60. Amorin H, Bdikin IK, Shvartsman VV, Costa MEV, Kholkin AL (2004) X-ray characterization and domain structure of high-quality $SrBi_2Ta_2O_9$ single-crystals grown by self-flux solution method. Integr Ferro 68:259
61. Bdikin IK, Shmytko IM, Balbashov AM, Kazansky AV (1993) Twinning of $LaGaO_3$ single-crystals. J Appl Crystallogr 26:71
62. Bdikin I, Maljuk A, Watauchi S, Tanaka I, Emel'chenko G (2000) X-ray topography investigation of $La_{2-x}Sr_xCuO_4$ single crystals. Physica C 336:244
63. Hervoches CH, Irvine JTS, Lightfoot P (2001) Two high-temperature paraelectric phases in $Sr_{0.85}Bi_{2.1}Ta_2O_9$. Phys Rev B 64:100102
64. Kamba S, Pokorny J, Porokhonsky V, Petzelt J, Moret MP, Garg A, Barber ZH, Zallen R (2002) Ferroelastic phase in $SrBi_2Ta_2O_9$ and study of the ferroelectric phase-transition dynamics. Appl Phys Lett 81:1056
65. Abplanalp M, Eng LM, Gunter P (1998) Mapping the domain distribution at ferroelectric surfaces by scanning force microscopy. Appl Phys A 66:S231
66. Ding Y, Liu JS, Wang YN (2001) Ferroelectric switching mechanism in $SrBi_2Ta_2O_9$. Appl Phys Lett 79:1015
67. Zhu X, Zhu J, Zhou S, Li Q, Liu Z, Ming N (2001) Domain structures and planar defects in $SrBi_2Ta_2O_9$ single crystals observed by transmission electron microscopy. Appl Phys Lett 78:799
68. Su D, Zhu JS, Wang YN, Xu QY, Liu JS (2003) Different domain structures and their effects on fatigue behaviour in Bi_3TiTaO_9 and $SrBi_2Ta_2O_9$ ceramics. J Appl Phys 93:4784

69. Pertsev NA, Novak J, Salje EKH (2000) Long-range elastic interactions and equilibrium shapes of curved ferroelastic domain walls in crystals. Philos Mag A 80:2201
70. Onodera A, Yoshio K, Yamashita H (2003) Structural study of intermediate phase in layered perovskite $SrBi_2Ta_2O_9$ single crystal. Jpn J Appl Phys 42:6218
71. Ko JH, Hushur A, Kojima S, Sih BC, Ye Z-G (2002) Acoustic anomalies and central peak in $SrBi_2Ta_2O_9$ single crystals studied by micro-Brillouin scattering. Appl Phys Lett 81:4043
72. Subbarao EC (1962) A family of ferroelectric bismuth compounds. J Phys Chem Solids 23:665
73. Irie H, Miyayama M, Kudo T (2000) Electrical properties of a bismuth layer-structured $BaBi_4Ti_5O_{18}$ single crystal. J Am Ceram Soc 83:2699
74. Irie H, Miyayama M (2001) Dielectric and ferroelectric properties of $SrBi_4Ti_4O_{15}$ single crystals. Appl Phys Lett 79:251
75. Royer D, Kmetik V (1992) Measurement of piezoelectric constants using an optical heterodyne interferometer. Electron Lett 28:1828
76. Soller T, Bathelt R, Benkert K, Bodinger H, Schuh C, Schlenkrich F (2010) Textured and tungsten-bronze-niobate-doped (K, Na, Li)(Nb, Ta)O_3 piezoceramic materials. J Kor Phys Soc 57:942
77. Nagata H, Saitoh M, Hiruma Y, Takenaka T (2010) Fabrication and piezoelectric properties of textured $(Bi_{1/2}K_{1/2})TiO_3$ ferroelectric ceramics. Jpn J Appl Phys 49:09MD08
78. Ma S, Fuh JYH, Zhang YF, Lu L (2010) Synthesis of anisotrpic lead titanate powders for template grain growth of textured piezoelectric ceramics. Surf Rev Lett 17:159
79. Majhi K, Varma KBR (2010) Textured ferroelectric $SrBi_2Nb_2O_9$ phase obtained by melt-quenching the $SrBi_2B_2O_7$-Nb_2O_5 system and its anisotropic dielectric and pyroelectric properties. J Electroceram 25:70
80. Sabolsky EM, Maldonado L, Seabaugh MM, Swartz SL (2010) Textured-Ba(Zr, Ti)O_3 piezoelectric ceramics fabricated by templated grain growth (TGG). J Electroceram 25:77
81. Chang YF, Poterala SF, Yang ZP (2010) Microstructure development and piezoelectric properties of highly textured CuO-doped KNN by templated grain growth. J Mater Res 25:687
82. Hussain A, Ahn CW, Lee HJ et al (2010) Anisotropic electrical properties of $Bi_{0.5}(Na_{0.75}K_{0.25})_{0.5}TiO_3$ ceramics fabricated by reactive templated grain growth (RTGG). Curr Appl Phys 10:305
83. Ahn CW, Jeong ED, Kim YH, Lee JS, Chung GS, Lee JY, Kim IW (2009) Piezoelectric properties of textured $Bi_{3.25}La_{0.75}Ti_{2.97}V_{0.03O12}$ ceramics fabricated by reactive templated grain growth method. J Electroceram 23:392
84. Ogawa H, Kawada S, Kimura M, Higuchi Y, Takagi H (2009) High-power characteristics of thickness shear mode for textured $SrBi_2Nb_2O_9$ ceramics. Jpn J Appl Phys 48:09KD05
85. Amorin H, Kholkin AL, Costa MEV (2005) Texture development and dielectric properties of $SrBi_2Ta_2O_9$ ceramics processed by templated grain growth. J Eur Ceram Soc 25:2453
86. Amorin H, Kholkin AL, Costa MEV (2008) Templated grain growth of $SrBi_2Ta_2O_9$ ceramics: Mechanism of texture development. Mater Res Bull 43:1412
87. Lotgering FK (1959) Topotactical reactions with ferrimagnetic oxides having hexagonal crystal structures I. J Inorg Nucl Chem 9:113
88. Software AnalySIS 3.2 (2004) Soft Imaging System, Olympus Company. http://www.soft-imaging.com
89. Wejrzanowski T, Kurzydłowski KJ (2003) Stereology of grains in nano-crystals. Solid State Phenomena 94:221
90. Horn JA, Zhang SC, Selvaraj U, Messing GL, Trolier-McKinstry S (1999) Templated grain growth of textured bismuth titanate. J Am Ceram Soc 82:921
91. Hong SH, Trolier-McKinstry S, Messing GL (2000) Dielectric and electromechanical properties of textured niobium-doped bismuth titanate ceramics. J Am Ceram Soc 83:113
92. Hong SH, Messing GL (1999) Development of textured mullite by templated grain growth. J Am Ceram Soc 82:867

93. Suvaci E, Seabaugh MM, Messing GL (1999) Reaction-based processing of textured alumina by templated grain growth. J Eur Ceram Soc 19:2465
94. Suvaci E, Messing GL (2000) Critical factors in the templated grain growth of textured reaction-bonded alumina. J Am Ceram Soc 83(8):2041
95. Seabaugh MM, Messing GL, Vaudin MD (2000) Texture development and microstructure evolution in liquid-phase-sintered alpha-alumina ceramics prepared by templated grain growth. J Am Ceram Soc 83:3109
96. Sato H, Otsuka N, Liedl GL, Mansour S (1986) Formation of elongated particles in beta-SiC compacts. Mater Lett 4:136
97. Watanabe H, Kimura T, Yamaguchi T (1991) Sintering of plate-like bismuth titanate powder compacts with preferred orientation. J Am Ceram Soc 74:139
98. Amorin H (2005) PhD thesis, University of Aveiro, p 149
99. Jones JL, Slamovich EB, Bowman KJ (2004) Critical evaluation of the Lotgering degree of orientation texture indicator. J Mater Res 19:3414
100. Kocks UF, Tomé CN, Wenk H-R (2000) Texture and anisotropy: preferred orientations in polycrystals and their effect on material properties. Cambridge University Press, Cambridge, UK, pp 126–177
101. Furushima R, Tanaka S, Kato Z, Uematsu K (2010) Orientation distribution–Lotgering factor relationship in a polycrystalline material – as an example of bismuth titanate prepared by a magnetic field. J Ceram Soc Jpn 118:921
102. Dollase WA (1986) Correction of intensities for preferred orientation in powder diffractometry: application of the March model. J Appl Crystallogr 19:267
103. Brosnan KH, Poterala SF, Meyer RJ, Misture S, Messing GL (2009) Templated grain growth of <001> textured PMN-28PT using $SrTiO_3$ templates. J Am Ceram Soc 92:S133
104. Wada K, Kakimoto K, Ohsato H (2006) Dielectric anisotropy and sinterability improvement of Ba4Nd9.33Ti18O54 textured ceramics. J Eur Ceram Soc 26:1899

Part II
Alkali: Niobate-Based Ceramics

Chapter 3
Development of KNN-Based Piezoelectric Materials

Shashaank Gupta, Deepam Maurya, Yongke Yan, and Shashank Priya

3.1 Introduction

Piezoelectric materials are technologically important because of their application in various kinds of devices including ultrasonic medical imaging, ultrasonic nondestructive testing, speakers, resonators, gas igniters, gyroscope, pressure sensors etc [1–3]. Piezoelectrics are finding applications in new emerging areas as well such as micromotors, energy harvesting devices, magnetoelectric sensors, and high power transformers [4–6]. Owing to their excellent piezoelectric and ferroelectric properties, $PbZr_xTi_{(1-x)}O_3$ (PZT) and other lead-based materials such as $Pb(Mg_{1/3}Nb_{2/3})O_3$ (PMN), $Pb(Mg_{1/3}Nb_{2/3})O_3$–$PbTiO_3$ (PMN-PT) and $Pb(Zn_{1/3}Nb_{2/3})O_3$–$PbTiO_3$ (PZN-PT) have been dominating the defense and civilian applications in the past few decades [7, 8]. But with increasing concern about environment, it is the need of the hour to develop new eco-friendly piezoelectric materials with properties comparable to lead-based piezoelectrics. Extensive research has been conducted on the development of lead-free piezoelectric materials with high piezoelectric coefficient and electromechanical coupling factor. Out of the various possible choices, most widely investigated lead-free systems are $K_xNa_{(1-x)}NbO_3$ (KNN), $Na_{0.5}Bi_{0.5}TiO_3$ (NBT) and $BaTiO_3$ (BT) based materials. In recent past, there have been a number of articles published reviewing the current status of research focused on these lead-free piezoelectric compositions [9–16]. Potassium sodium niobate is considered as a leading lead-free candidate among these options with high Curie temperature and good piezoelectric properties [17, 18]. Crystal structure of KNN is studied by many groups and lacks consistency [3, 19–21]. The composition near $x = 0.5$ is of greater interest because of superior piezoelectric and ferroelectric properties. Superior properties of this composition are often attributed to the presence of polymorpic phase boundary (PPB) between two orthorhombic

S. Gupta • D. Maurya • Y. Yan • S. Priya (✉)
CEHMS, Virginia Tech, Blacksburg, VA 24061, USA
e-mail: spriya@vt.edu

S. Priya and S. Nahm (eds.), *Lead-Free Piezoelectrics*,
DOI 10.1007/978-1-4419-9598-8_3, © Springer Science+Business Media, LLC 2012

phases present on either side [3]. Two end compositions of KNN, $KNbO_3$ and $NaNbO_3$ are well studied in the past for their crystal structure, processing and properties including dielectric, ferroelectric and piezoelectric characterization [3, 22–28]. KNN having orthorhombic crystal structure at room temperature exhibits two phase transitions at higher temperatures, orthorhombic to tetragonal (T_{o-t}) at 200°C and tetragonal to cubic (T_c) at 420°C respectively [29]. In this chapter we review the significant research conducted on KNN ceramic and its derivatives, covering random and textured polycrystalline ceramics, single crystals and thin films.

3.2 Processing of KNN-Based Ceramics

Solid state reaction route is the most common and convenient way to synthesize KNN [29–33]. Generally sodium carbonate (Na_2CO_3, Molecular Weight – 105.99), potassium carbonate (K_2CO_3, Molecular Weight – 138.21) and niobium oxide (Nb_2O_5, Molecular Weight – 265.81) are used as starting materials. The melting points of these precursors are 851, 891 and 1,520°C respectively. Since the normal calcination temperature of KNN is close to the melting point of two alkali precursors, they always have the problem of volatilization during calcination and hence deficiency of A site ions [30, 34, 35]. Effect of calcination temperature, dwell time and excess of alkali carbonates on phase formation and microstructure of KNN is studied extensively [30, 36, 37]. Bomlai and coworkers [30] studied the effect of calcination temperature and dwell time on the phase formation of KNN. Authors found that perovskite phase can be achieved at temperatures as low as 600°C but broad X-ray Diffraction (XRD) peaks without orthorhombic splitting suggested the absence of compositional homogeneity. Authors tried different combinations of dwell time and temperature and found the samples calcined at 900°C for 6 h to have pure perovskite phase with orthorhombic splitting. They also found that similar single phase orthorhombic perovskite KNN can be formed at only 800°C, if 5% excess of alkali carbonates is used. Scanning electron micrographs (SEM) showed that the samples with excess of alkali precursors 3% or less had submicron grain size with equiaxed geometry, while on the other hand samples with 5% excess had cubical shape grains with size increasing with calcination temperature and reaching to about 2.5 μm at 900°C. This kind of grain growth was due to secondary crystallization involving consumption of small grains by large ones. Excess of alkali precursors left after volatilization gave rise to liquid phase which help in getting this kind of secondary crystallization.

Effect of Na/K ratio on the properties of sodium potassium niobate was studied by Wu et al. [31]. They prepared the $K_xNa_{(1-x)}NbO_3$ [38] compositions with $0.1 \leq x \leq 0.8$ and noticed a sharp change in lattice parameters of KNN at $x = 0.35$, in contrast to many other reports suggesting the presence of MPB at $x = 0.5$. According to the authors, the broad peak present in piezoelectric properties at $0.4 \leq x \leq 0.6$ is not because of the presence of any MPB, but because of unimodal grain size distribution in this range [31]. Hagh and coworkers [33] synthesized the

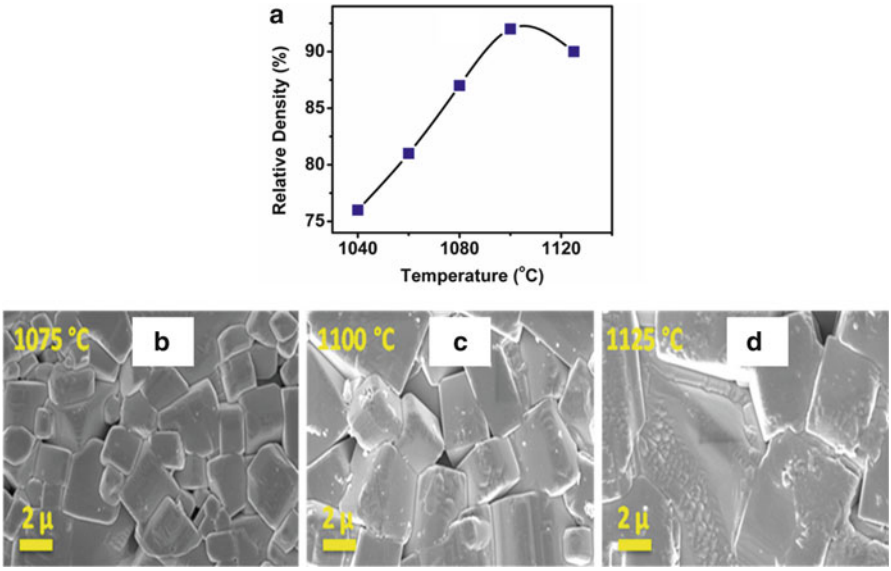

Fig. 3.1 (**a**) Variation of relative density of KNN with sintering temperature (**b–d**) Microstructure of samples sintered at 1,075, 1,100 and 1,125°C respectively

$K_{0.5}Na_{0.5}NbO_3$–$LiSbO_3$–$LiTaO_3$ (KNN–LS–LT) system by two possible routes, namely perovskite and mixed oxides route and studied the effect of humidity and oxygen flow rate during sintering. It was found that piezoelectric properties of ceramic samples synthesized by both processing routes are sensitive to humidity and for best results precursors need to be preheated in inert atmosphere before formulation of desired composition. They concluded that mixed oxide route is more suitable technique to synthesize KNN-based ceramics, followed by sintering in oxygen atmosphere [33].

The biggest setback in the way of any commercial application of KNN ceramic is its low sinterability. Lower relative density of piezoelectric ceramics not only leads to poor electromechanical coupling factor but also gives rise to high conductivity which makes it difficult to pole. This problem is mainly attributed to high volatilization of alkali elements at sintering temperature, which is higher than 1,100°C for normal solid state sintering [34, 35]. Cubical shape of KNN grains also contributes to this problem as high packing density is difficult to achieve with such particle shape [39]. Figure 3.1a shows the variation of relative density of KNN ceramic as a function of sintering temperature. It can be seen that by conventional sintering method, maximum achievable density is about only 91% of theoretical density at temperature about 1,100°C. This temperature is quite close to melting temperature of KNN (1,150°C) and leads to even severe problem of evaporation of alkali elements.

Partial melting and deformation of cubical grains is evident from the microstructure of samples sintered at 1,100 and 1,125°C, as shown in Fig. 3.1c, d. Also abrupt

increase in grain size at temperatures higher than 1,075°C is indicating the domination of coarsening process instead of densification [40]. The volatile nature of constituent elements also gives rise to phase instability of perovskite phase at high temperature and results in secondary tungsten bronze phase [41]. All these factors result in diminishing of piezoelectric and ferroelectric properties of KNN. For example the samples sintered at temperatures 1,125 and 1,075°C and having microstructures shown in Fig. 3.1b, d, are found to have piezoelectric coefficient value to be 48 and 104 pc/N respectively. Jenko et al. [34] studied the effect of sintering temperature on the microstructure, composition and phase formation of KNN ceramic. They found that samples sintered at 1,100°C for 24 h have the presence of niobium-rich second phase having Na/K and (Na + K)/Nb atomic ratios to be 0.3 and 0.6 respectively. This analysis clearly indicates that volatilization of sodium is faster than that of potassium.

Significant amount of research is done to understand the problem of nonsinterability in KNN and other members of family [35, 42]. Ahn and coworkers have recently reported an extensive study on the sintering mechanism of KNN-based ceramics [35]. In their work three stages of sintering were identified. Microstructures of these samples at each stage of sintering along with schematics are shown in Fig. 3.2. In the first step of the process, random shaped ball-milled particles rearranged to form cubical particles consisting of stacks of plate-like particles. Presence of plate-like particles was attributed to non-isotropic interfacial energy for lower liquid content. This stage of sintering lasts until the cross-section of neck reaches a threshold after which further thermal activation energy is required for densification. Presence of liquid phase is also evident from the microstructure shown in Fig. 3.2c. According to the authors, formation of liquid phase is critical for the densification of KNN-based ceramics due to non-uniform cubical shape of the particles. The presence of liquid phase at grain boundaries not only provided a medium for the transportation of mass, leading to a more effective packing but also wetting of the plates resulted in bridging of the porosity. EDX analysis was done to identify the composition of this liquid phase and results showed it to be sodium deficient. Based on the EDX results, authors proposed a chemical reaction (3.1) leading to the formation of liquid phase due to evaporation of Na_2O.

$$\begin{aligned} &0.995(K_{0.48}Na_{0.48}Li_{0.04})NbO_3 - 0.005BaTiO_3 \\ &\rightarrow 0.995(K_{0.48}Na_{0.025}Li_{0.04})NbO_{2.7725} - 0.005BaTio_3 + 0.226Na_2O \uparrow \end{aligned} \tag{3.1}$$

In the second stage of sintering rapid grain growth takes place, which is assisted by presence of liquid phase. Elongated plate-like structure observed at the end of second stage of sintering (Fig. 3.2c, d) can be attributed to the grain accommodation process. According to authors insufficient amount of liquid phase is responsible for this kind of morphology as in these circumstances grains tend to undergo a considerable change in shape in order to flatten their contact region with neighboring grains. In the final stage of sintering, coarsening becomes the dominant process. As is evident from Fig. 3.2e, f, rate of coarsening is higher at higher

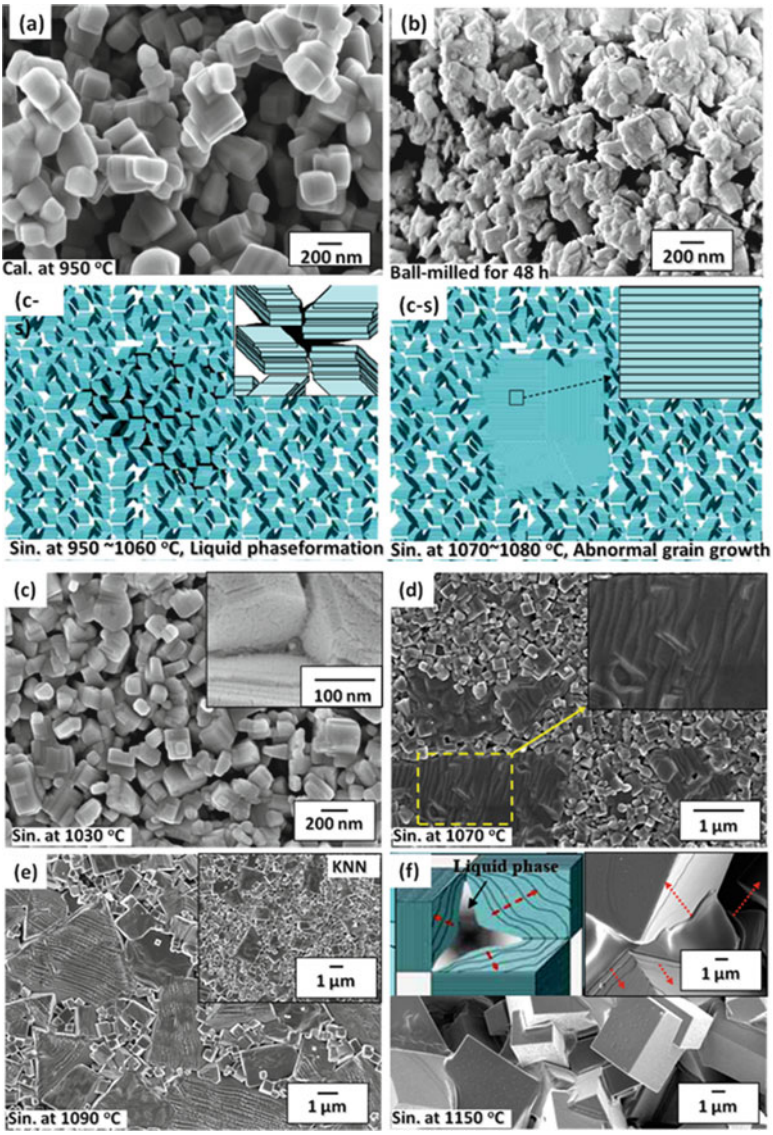

Fig. 3.2 Microstructures of KNN-based ceramic samples at different stages of processing (**a**) calcined powders at 950°C for 180 min (**b**) ball-milled powder for 48 h after calcination (**c**) sintered at 1,030°C, 0 min (**d**) sintered at 1,070°C, 0 min (**e**) sintered at 1,090°C, 0 min, inset of figure (**e**) shows KNN specimen sintered at 1,100°C for 0 min (**f**) sintered at 1,150°C, 0 min; left inset: schematic diagram. Two figures marked with "c-s" are showing the proposed sintering model in KNN-based ceramics

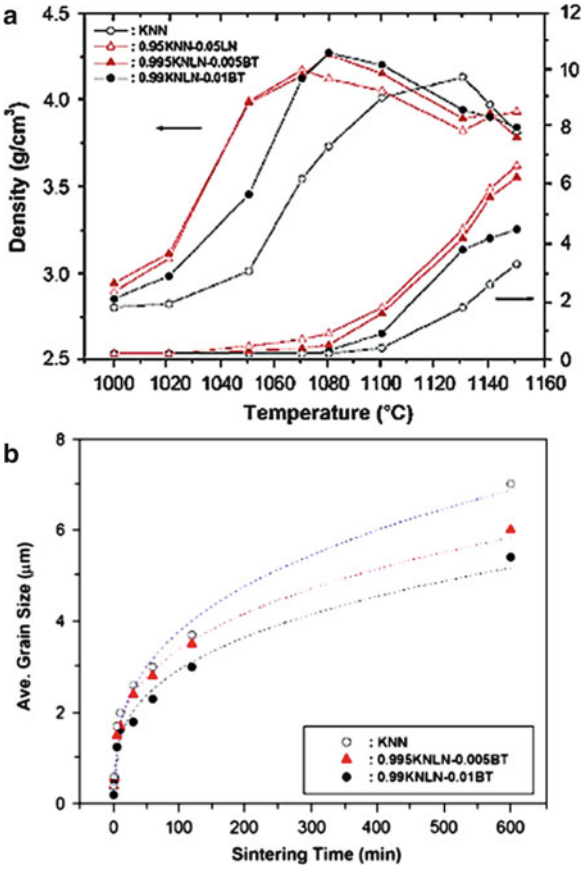

Fig. 3.3 (**a**) Variation of density and average grain size with sintering temperature for various KNN-based ceramics (**b**) Average grain size plotted as a function of sintering time at 1,080°C. *Dashed line* shows fitting to data points according to (3.2) with $m = 3$

temperatures as solubility of solute as well as its diffusion increases with temperature.

Variation of density and average grain size were plotted as a function of sintering temperature and are shown in Fig 3.3a. Variation of density with sintering temperature is similar to what is reported for liquid-assisted sintering and is consistent with microstructures showing presence of liquid phase at grain boundaries. Grain size variation with sintering temperature was modeled for Ostwald ripening mechanism. Lifshitz, Slyozov and Wagner equation relating the grain size with sintering time and temperature was used for this purpose and can be given as in (3.2).

$$G^{\mathrm{m}} = G_{\mathrm{o}}^{\mathrm{m}} + K_{\mathrm{t}} \tag{3.2}$$

where G_o is the initial grain size, K and m are respectively temperature and coarsening mechanism dependent parameters. Figure 3.3b shows the variation of grain size for different compositions with sintering time. The value of parameter m was found to be 3 for all three compositions indicating the diffusion controlled mechanism of coarsening for all of them.

A significant fraction of research done on KNN-based ceramics is focused on rectifying the problem of low sinterability [27, 32, 43–46]. This work includes the application of different nonconventional sintering techniques as well as use of different sintering additives. Ruzhong et al. studied the effect of particle size on the sintering of KNN as driving force for sintering is higher for smaller particle size. They achieved about 98.5% density at 1,100°C by attrition milled powder of size 70 nm, in contrast to 94% density achieved for traditionally ball-milled powder at the same temperature [47]. Problem of volatility can also be controlled up to some extent by performing sintering in sealed crucible with muffling of samples by the same composition powder [41, 46, 48]. Mechano-chemical activation or synthesis by high-energy ball milling can reduce processing temperature resulting in reduction in loss of volatile constituents. However, there is increased possibility of contamination during processing [49].

Spark plasma sintering (SPS) is another common technique used for sintering KNN [50]. Density up to 99% of theoretical density could be achieved with grains of size 200–500 nm. Samples sintered by SPS method required annealing at 900°C to eliminate the oxygen vacancies to get good saturated ferroelectric loops. But due to very small grain size, samples had relatively low saturation polarization value of about 6.5 $\mu C/cm^2$ [50]. The piezoelectric coefficient and coupling factor were found to be 148 pC/N and 0.389 respectively for spark plasma sintered KNN samples. KNN samples synthesized by hot pressing (HP) and hot forging are also found to exhibit improved piezoelectric properties due to better densification [27, 51, 52].

Kosec et al. [53] studied the effect of A site vacancies on sintering of KNN. These vacancies were created in two ways, by doping higher valance Mg^{+2} ions on A site and by using the excess of Nb_2O_5. The shrinkage measurements done at Mg^{+2} doped samples revealed that A site vacancies not only lower the initial sintering temperature but also improve the final density. Similar effects were seen in samples prepared with excess of Nb_2O_5.

Ruzhong et al. [47] and Smelter et al. [54] studied the effect of different oxide additives on sintering of KNN. In Ruzhong's study, ZnO and SnO_2 proved to be best additives but in different ways. SnO_2 on the one hand helped in getting higher density at the same temperature (1,100°C), while on the other hand ZnO decreased the sintering temperature by 100°C for the same relative density. Decrease in Curie point of SnO_2-doped KNN samples indicated the change in lattice parameters of KNN and hence diffusion of Sn^{+4} ions in KNN lattice. Significant increase in the coercive field of these samples suggested the formation of oxygen vacancies by substitution of lower valance Sn^{+4} ions to Nb^{+5} sites. According to the authors these oxygen vacancies helped in getting higher density when sintering was done in air. In the case of ZnO, no change was observed in lattice parameters and coercive field

and lowering of sintering temperature was attributed to the liquid phase sintering. The advantages of ZnO doping are also confirmed by the number of other studies as well [55, 56].

Copper-based sintering additives such as $K_4CuNb_8O_{23}$ (KCN) and $K_{5.4}Cu_{1.3}Ta_{10}O_{29}$ (KCT) are also found to be very effective in improving the sinterability of KNN-based ceramics [57, 58]. Matsubara et al. used the sintering aid KCT and found that only 0.38 mol% of it can help in achieving high density at sintering temperature 1,120°C [58]. X-ray diffraction analysis showed no peaks belonging to KCT suggesting the formation of complete solid solution of it with KNN. KNN-KCT solid solution was found to have decreased T_{o-t} and T_c as compared to KNN. This helped in getting improved piezoelectricity with d_{33} value about 190 pC/N. Copper ions going to Nb sites act as an acceptor and along with higher density, helped in achieving higher mechanical quality factor. According to authors, Q_M value found to be 1,300 was at least 14 times higher than that for pure KNN. Because of improved density, there was also a significant improvement in electromechanical coupling coefficient. Copper oxide is another common sintering aid in this category [59–62]. Lin studied the effect of it on sintering as well as piezoelectric properties of KNN [60]. Authors prepared the ceramic KNN–*x*CuO by normal sintering route with *x* varying between 0 and 2 mol%. Samples with pure orthorhombic perovskite structure and improved density were found to have slightly smaller bimodal grains as compared to pure KNN. CuO doping also lead to significant decrease in piezoelectricity and orthorhombic to tetragonal transition temperature T_{o-t}. In another study CuO was used as the sintering additive for 0.95KNN-0.05ST composition [63]. XRD analysis revealed the change in lattice parameters indicating the occupation of Nb^{+5} and Ti^{+4} sites by Cu^{+2} ions for the addition of 1 mol% of CuO. Samples sintered at 960°C with 1.5 mol% of CuO were found to have larger grain size due to the liquid phase sintering. Owing to the larger grain size, the samples with 1–2% CuO doping were found to exhibit optimum piezoelectric properties with d_{33} and k_p values of 200 pC/N and 0.35 respectively. Anti-ferroelectric like *P-E* hysteresis loops were found in 1 mol% Cu-doped KNN ceramics which was attributed to the presence of defect dipoles. In a recent report, Eichel et al. have performed multi-frequency and multi-pulse electron paramagnetic resonance (EPR) spectroscopy on Cu-doped KNN system and confirmed the substitution of Cu^{2+} on B-site as acceptor [64]. Park et al. have reported enhanced $Q_m \sim 3{,}053$ in KNN ceramics by co-doping of KCT and CuO [65].

Liang et al. studied the effect of poling conditions on the piezoelectric properties of KNN ceramic [38]. They studied the variation of poling field, time and temperature on longitudinal piezoelectric coefficient and concluded that samples poled at fields of 4 kV/mm for 20 min at 140°C had the best piezoelectric properties. Zheng et al. studied the effect of humidity on the piezoelectric properties of KNN and concluded that small amount of $ScTaO_4$ improves the stability of piezoelectric properties in humid environment [66].

3.3 Dopant Engineering

A large number of dopants on both A and B sites as well as different solid solutions are studied in order to improve the piezoelectric properties of KNN [67–79]. To understand the structure – property correlation in KNN-based ceramics Ahn et al. studied the interdependence of piezoelectric coefficient d_{33}, tetragonal to orthorhombic transition temperature (T_{o-t}) and fraction of tetragonality [80]. This analysis was conducted for three different systems namely KNN–$BaTiO_3$ (KNN–BT), KNN–$LiNbO_3$ (KNN–LN) and (K,Na,Li)NbO_3-$BaTiO_3$ (KNLN–BT). Figure 3.4 shows the variation of d_{33} with T_{o-t}, clearly indicating that for KNN-based systems piezoelectric response is almost linearly dependent on T_{o-t} transition temperature and higher values can be achieved by dropping the T_{o-t} close to room temperature. Figure 3.5a shows the XRD pattern of different compositions of KNLN–BT system sintered at 1,080°C for 2 h. Inset of the figure depicts the increase in tetragonality with increasing BT content. The fraction of tetragonal phase was determined by using the equation $F_T = SI_T/(SI_T + SI_o)$, where SI_T and SI_o are the sums of peak intensities for tetragonal and orthorhombic phases. From Fig. 3.5b, which shows the variation of d_{33} and tetragonality with fraction of KNN, it is evident that for all the three studied systems optimum piezoelectric properties are found for a composition having about 93–94% of KNN. Interestingly in all three systems this composition had about 70%

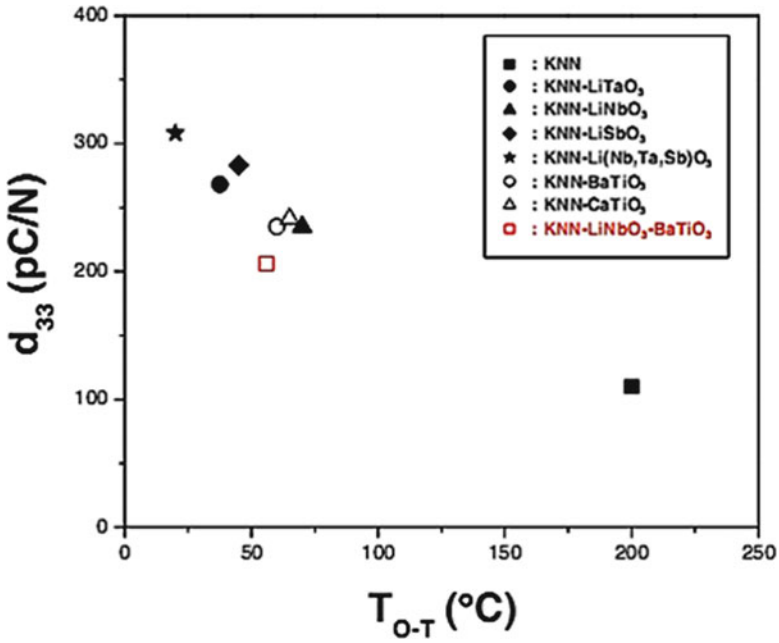

Fig. 3.4 Piezoelectric coefficient of different KNN-based piezoelectric compositions as a function of orthorhombic to tetragonal phase transition temperature

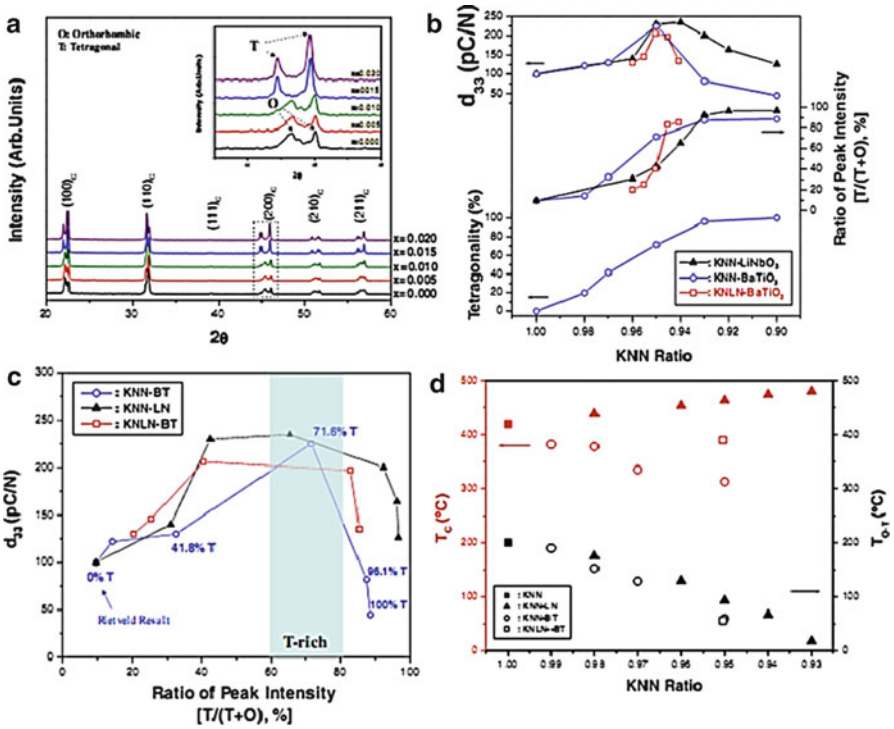

Fig. 3.5 (**a**) X-Ray diffraction patterns of KNLN–BT samples for different amounts of BT, inset of the figure is showing the variation of tetragonality in samples (**b**) Variation of d_{33}, ratio of peak intensities and tetragonality with fraction of KNN for all the three systems studied (**c**) Variation of d_{33} with tetragonality of samples (**d**) T_c and T_{O-t} as a function of KNN fraction

of tetragonality. Variation of T_c and T_{o-t} shown in Fig. 3.5d indicates that for all the three systems, higher amount of doping to KNN shifts the T_{o-t} toward room temperature.

Guo et al. [70] studied the effect of lithium doping on the piezoelectric properties of KNN by synthesizing the samples $Li_x(Na_{0.5}K_{0.5})_{(1-x)}NbO_3$ (KNLN), for x varying between 0.0 and 0.2. They observed the presence of MPB between orthorhombic and tetragonal phases in the range $0.05 < x < 0.07$. A sharp peak in piezoelectric properties (d_{33}–235 pC/N, k_p–44%) observed in this composition range also confirmed the presence of MPB. Temperature dependent dielectric response analysis conducted at MPB compositions revealed the shift of T_c and T_{o-t} to higher and lower temperatures respectively. Du studied the effect of poling temperature on the same lithium-doped MPB compositions ($x = 0.05, 0.06, 0.07$) and found that a significant improvement in piezoelectric properties can be achieved if poling is done at orthorhombic to tetragonal transition temperature T_{o-t} [81]. Zhang et al. [82] extended this work of Guo [70] and studied the effect of antimony doping on B site while the lithium doping at A site was fixed at 0.058 mol%.

For the doping range 2–8 mol%, no MPB could be found and crystal structure remained to be orthorhombic. But the sample with 6 mol% antimony doping had the largest grains and hence best piezolelectric properties (d_{33}–298 pC/N, k_p–34.5% and dielectric constant – 945). The biggest disadvantage of antimony doping is the drastic decrease in the T_{o-t} to 60°C, in contrast to only lithium-doped samples. Zang et al. also studied the solid solution of $LiSbO_3$ with KNN by synthesizing the composition $(Na_{0.5}K_{0.5}Nb)_{(1-x)}(LiSb)_xO_3$ for x lies between 0.048 and 0.056 [83]. Authors found the composition with $x = 0.052$ to have the best piezoelectric properties with d_{33}, dielectric constant and k_p values to be 286 pC/N, 1,372 and 51% respectively. According to authors, this improvement of properties can be attributed to decrease in $T_{o\text{-}t}$ transition temperature. Lin et al. also conducted similar kind of studies on KNN-LS system and found the presence of MPB between orthorhombic and tetragonal phases at $x = 0.06$ and hence the optimum piezoelectric properties.

Wang and coworkers synthesized the $0.95[(K_{0.5}Na_{0.5})_{0.94}Li_{0.06}]NbO_3$–$0.05AETiO_3$ (AE = Alkali Earth elements such as Mg, Ba, Sr and Ca) compositions and found that only $CaTiO_3$ (CT) makes solid solution with $(K_{0.5}Na_{0.5})_{0.94}Li_{0.06}NbO_3$ [84]. These KNLN–CT samples with large grain size and highest density among all samples (>98%), were found to have tetragonal crystal structure at room temperature. Temperature dependent dielectric response study reveals the existence of T_{o-t} below room temperature. Like the work of Du et al. [85], conditions were optimized for poling and KNLN–CT samples were found to have highest piezoelectric properties with d_{33} and k_p values to be 172 pC/N and 0.43 respectively. These properties can be attributed to high density, bigger grain size and near RT existence of orthorhombic to tetragonal phase transition temperature T_{o-t}. Temperature dependent piezoelectric measurements also reveal the excellent stability with only 4% variation in d_{33} value in the range 10–70°C. Li and coworkers [86] studied the effect of silver doping on KNN. Single phase orthorhombic perovskite structure could be achieved for $x \leq 0.3$. For this composition range, both T_c and T_{o-t} were found to be decreasing linearly with x and sample with $x = 0.18$ was found to have best piezoelectric properties with $d_{33} = 186$ pC/N and $k_p = 0.425$. According to the authors, this improvement in properties could be because of decrease in T_{o-t}. The sample with $x = 0.18$ was also found to have temperature independent nature of k_p from RT to T_{o-t}.

Cho and coworkers studied the effect of deficiency of sodium on the microstructure and piezoelectric properties of $0.95KNN–0.05SrTiO_3$ (0.95KNN–0.05ST) ceramic which was found to have high porosity and hence poor piezoelectric properties [87]. The small deficiency (1.0%) of Na_2O lead to denser microstructure due to the formation of liquid phase at sintering temperature 1,080°C. These samples with density about 96% were found to have d_{33} and k_p values to be 220 pC/N and 40% respectively. However Kosec et al. [88] achieved a density higher than 95% for $(1-x)$KNN–xST samples for $0.1 \leq x \leq 0.33$. The samples with $0.15 \leq x \leq 0.25$ were found to have pseudo-cubic crystal structure with submicron sized grains. Temperature dependent dielectric response study conducted on $x = 0.2$ sample revealed the relaxor behavior of this composition with giant dielectric constant values with broad dispersive maxima.

Ahn and other members of his group synthesized the KNN–$BaTiO_3$ (KNN–xBT) [89, 90] solid solution and studied the piezoelectric and dielectric properties of the system. The system was found to have three morphotropic phase boundaries at room temperature, orthorhombic to tetragonal at $0.0 \leq x \leq 0.1$, tetragonal to cubic at $x = 0.2$ and finally cubic to tetragonal at $x > 0.94$. Among these MPBs, orthorhombic to tetragonal one at $0.0 \leq x \leq 0.1$ was found to have best piezoelectric properties. Rietveld refinement of X-ray diffraction patterns revealed the coexistence of Bmm2 and P4mm space groups in the composition range $0.02 \leq x \leq 0.07$. Sintering conditions were optimized for 0.95KNN–0.05BT samples and it was found that muffled samples sintered at 1,060°C for 2 h have the optimum grain size and hence best piezoelectric properties [91]. Different amounts of sintering additives CuO and MnO_2 were also tried to suppress the volatilization of Na_2O by decreasing the sintering temperature and hence to reduce the leakage current [61]. It was found that addition of 2 mol% CuO and 0.5 mol% MnO_2 reduces the sintering temperature to 950°C and improves the piezoelectric properties with increased d_{33} value from 220 pC/N to 248 pC/N. Effect of small amount of doping of BT ($0.0 \leq x \leq 0.20$) was also studied on the piezoelectric properties of $(K_{0.5}Na_{0.5})_{0.96}Li_{0.04}NbO_3$ composition [80].

Saito et al. have shown that KNN-based composition LF4 [$(K_{0.44}Na_{0.52}Li_{0.04})(Nb_{0.84}Ta_{0.10}Sb_{0.06})O_3$] has longitudinal piezoelectric coefficient as high as 300 pC/N [92]. They further improved the piezoelectric properties of this composition by developing a new processing route leading to (100) oriented ceramic. Patents filed by Murata Manufacturing Co. describe processing and piezoelectric properties of modified KNN compositions $(1-n)(K_{1-x-y}Na_xLi_y)_m(Nb_{1-z}Ta_z)O_3 - nM_1M_2M_3O_3$ (M_1, M_2, M_3 being the trivalent, monovalent and tetravalent metal ions) [93]. Different possible combinations of M_1, M_2, M_3, m, n, x, y, and z were investigated revealing the effect on Curie temperature, electromechanical coupling coefficient and dielectric constant.

High temperature applications of piezoelectric materials require not only high Curie temperature, but also good thermal stability between room temperature and Curie temperature. From the point of view of high T_c, KNN is an excellent candidate for high temperature applications with T_c being close to 420°C, but at the same time the presence of orthorhombic to tetragonal phase transition at about 200°C gives rise to discontinuity in piezoelectric properties. Figure 3.6 shows the variation of electromechanical coupling factor (k_p) and dielectric constant as a function of temperature for KNN and KNLNS–BT ceramics. The peaks in coupling coefficient (k_p) and dielectric constant can be seen clearly at the phase transition temperatures. Interestingly Ahn et al. noticed that the slopes of variation in k_p are opposite to each other for two compositions shown in Fig. 3.6. This observation encouraged them to combine these two compositions together in order to compensate the effect of fluctuations in piezoelectric properties with temperature. For this purpose they proposed the synthesis of two kinds of ceramics microstructures, namely island – matrix (type I) and layered structure (type II) with compositional nonhomogeneity. Schematics of these two microstructures are illustrated in Fig. 3.7a, b. The gradient in color in these figures indicates the effect of minor

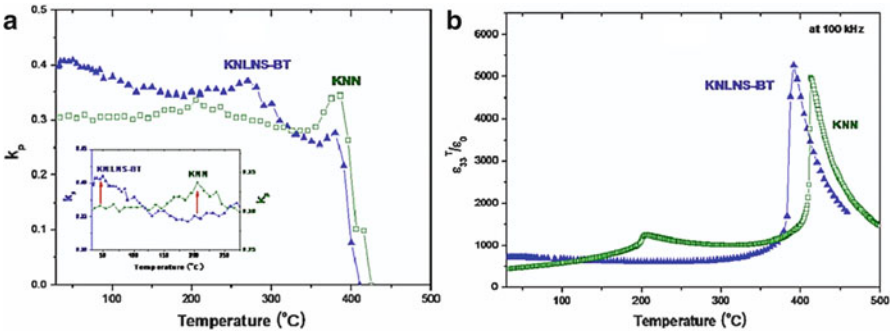

Fig. 3.6 Variation of (**a**) k_p and (**b**) dielectric constant as a function of temperature for KNN and KNLN–BT ceramics

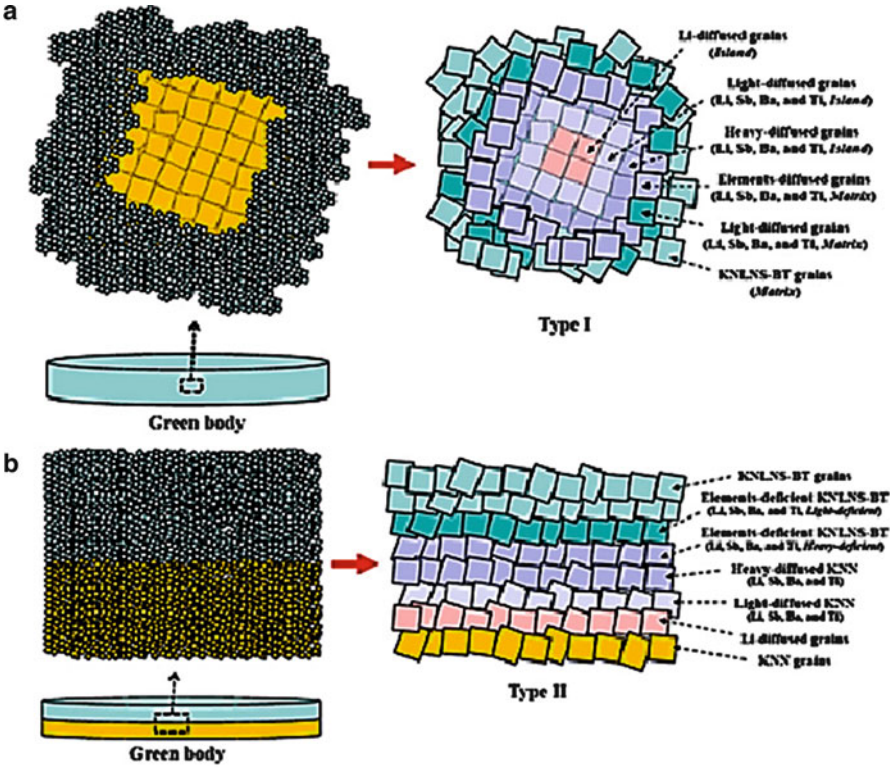

Fig. 3.7 Schematic of microstructures proposed by Ahn et al. for compensating the variation of piezoelectric properties of KNN-based ceramics (**a**) island-matrix (type I) and (**b**) layered structure (type II)

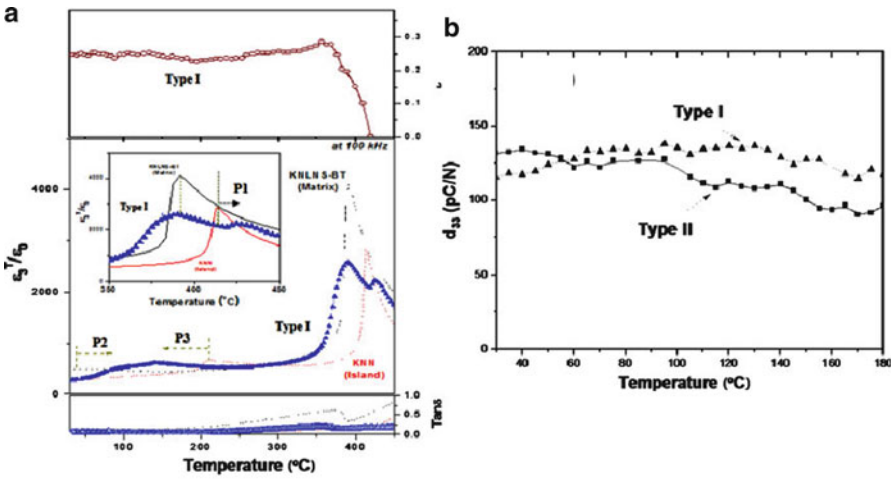

Fig. 3.8 Variations of (**a**) k_p and dielectric constant for type I microstructure (**b**) d_{33} as a function of temperature in type I and II microstructures

elemental diffusion between the two compositions occurred during the high temperature sintering.

Figure 3.8a shows the variation of dielectric constant and k_p as a function of temperature for ceramic sample having type I microstructure along with the contributions from individual components. As compared to its components KNN and KNLNS–BT, island-matrix structure shows a better stability in k_p vs. temperature up to 360°C. The change in dielectric behavior was explained on the basis of elemental diffusion. The T_c of KNN was found to shift to higher temperature while T_{o-t} moved to lower temperature. Since most of the dopants other than lithium decrease the T_c, the increase in Curie temperature was attributed to higher diffusion rate of lithium ions as compared to others. Figure 3.8b shows the variation of d_{33} as a function of temperature for both type I and II microstructures. It clearly demonstrates the differences in the behavior of these two microstructures related to changes in phase transitions. Type I microstructure shows almost no variation of d_{33} in the temperature range of 30–180°C, which again was attributed to elemental diffusion occurred over the whole volume of specimen (interface of island and matrix) leading to the compensation of slope of KNLNS–BT component.

3.4 Textured KNN Ceramics

Since the piezoelectric properties of lead-free piezoelectric materials are far inferior to those of lead-based materials, it is important to utilize the anisotropy in elastic, dielectric and piezoelectric properties in order to achieve desired performance. In the case of relaxor ferroelectrics such as PMN-PT and BNT-BT, [001] oriented

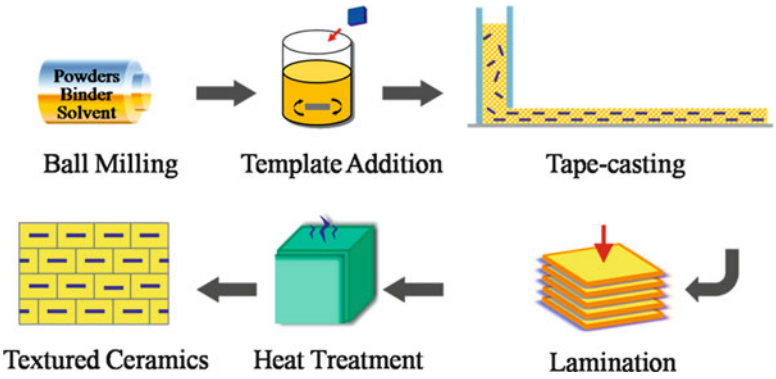

Fig. 3.9 Schematic of template grain growth (TGG) process

crystals exhibit enhanced piezoelectric response for compositions near the MPB. But high cost of production, inflexibility in shape and size of grown crystals and non-uniformity in properties due compositional heterogeneity limits the application of piezoelectric single crystals in commercial devices. It has been demonstrated that crystallographic texturing of polycrystalline ceramics offers an effective way of achieving significant enhancement in the piezoelectric response. Templated grain growth (TGG) and reactive templated grain growth (RTGG) are cost-effective ways to fabricate highly textured ceramics with enhanced properties comparable to those for single crystals. In TGG process, nucleation and growth of the desired crystals take place on aligned single crystal template particles during the heat treatment, resulting in an oriented or textured microstructure. Figure 3.9 shows the schematic of the TGG process.

To maintain favorable thermodynamic and kinetic condition for TGG, synthesis of appropriate templates is one of the most important steps in the TGG process. Suitable template usually has four basic characteristics [94]: (1) same crystallographic structure as matrix and a small lattice mismatch ($< 15\%$) to reduce the activation energy for nucleation and growth (2) an anisotropic morphology like a whisker or platelet so that can be oriented under an applied shear force during tape casting (3) a suitable size because the driving force in TGG process depends upon the size difference between templates and matrix particles (4) Good thermodynamic stability in matrix.

According to the four basic characteristics described above, the most appropriate template for any piezoelectric matrix would be the whisker or platelet shaped particles of the same composition. However due to the complex nature of piezoelectric compositions, it is always not easy to synthesize the homogeneous anisotropic shaped templates of the same composition as matrix. In these circumstances, use of heterogeneous template particles can result into poor piezoelectric properties. To overcome the problem of template heterogeneity, in the RTGG process anisotropic particles of simpler composition are used with matrix composition being complementary to it, in order to achieve desired composition at the end

Table 3.1 Dielectric, ferroelectric and piezoelectric properties of textured lead-free ferroelectric ceramics prepared by TGG/RTGG method

Composition	Template	Parameters	Random ceramics	Textured ceramics	References
Bismuth layered structured					
$Bi_4Ti_{2.96}Nb_{0.04}O_{12}$	$Bi_4Ti_3O_{12}$	P_r(μC/cm^2)	12	24.5	[95]
		d_{33}(pC/N)	20	30	
Bi_3NbTiO_9	$Bi_4Ti_3O_{12}$	d_{33}(pC/N)	15	30	[96]
$CaBi_4Ti_4O_{15}$	$Bi_4Ti_3O_{12}$	k_t(%)	16.2	53.4	[97]
		d_{33}(pC/N)	15	45	
$Na_{0.475}Ca_{0.05}Bi_{4.475}Ti_4O_{15}$	$Bi_4Ti_3O_{12}$	k_t(%)	13.3	49	[98]
		d_{33}(pC/N)	13	44	
		g_{33}(10^{-3}Vm/N)	9.1	33.5	
Tungsten bronze structured					
$Sr_{0.53}Ba_{0.47}Nb_2O_6$	$KSr_2Nb_5O_{15}$	P_r(μC/cm^2)	15	20.3	[99]
		d_{33}(pC/N)	30	83	
Perovskite structured					
$Na_{0.5}Bi_{0.5}TiO_3$–5.5$BaTiO_3$	$Bi_4Ti_3O_{12}$	d_{33}(pC/N)	110	200	[100]
$Na_{0.5}Bi_{0.5}TiO_3$–6$BaTiO_3$	$Bi_4Ti_3O_{12}$	d_{33}(pC/N)	125	299	[101]
$Bi_{0.5}(Na_{0.85}K_{0.15})_{0.5}TiO_3$	$Bi_4Ti_3O_{12}$	k_p(%)	29.5	40.2	[102]
		$-d_{31}$(pC/N)	36.7	57.4	
		$-g_{31}$(10^{-3}Vm/N)	7.21	11.2	
$(K_{0.44}Na_{0.52}Li_{0.04})(Nb_{0.84}Ta_{0.10}Sb_{0.06})O_3$	$NaNbO_3$	S_m/E_m(pm/V)	400	750	[92]
		d_{33}(pC/N)	300	416	
		T_c(°C)	253	253	
$(K_{0.5}Na_{0.5})NbO_3$–1.0 mol% CuO	$NaNbO_3$	k_p	0.38	0.54	[103]
		d_{33}(pC/N)	86	123	
		$-d_{31}$	28	47	
$(K_{0.476}Na_{0.524})NbO_3$–1.0 mol%CuO	$NaNbO_3$	k_p	0.31	0.58	[104]
		d_{33}(pC/N)	85	146	
		k_{31}	0.17	0.33	
$(K_{0.5}Na_{0.5})(Nb_{0.97}Sb_{0.03})O_3$	$NaNbO_3$	k_p	0.43	0.64	[105]
		d_{33}(pC/N)	148	208	
		k_{31}	–	0.37	

of processing. During their reaction with matrix, these templates preserve their crystallographic orientation and lead to the texturing of resultant composition. Using TGG and RTGG processes, several lead-free piezoelectric ceramics have been fabricated in the past few years (Table 3.1).

<001> textured KNN-based ceramic prepared by TGG process was firstly reported by Saito et al. in 2004 [92]. They used $NaNbO_3$ platelets as reactive template for texturing KNN based ceramic. Figure 3.10a, b shows the scanning electron micrograph (SEM) and X-ray diffraction (XRD) profile of textured $(K_{0.44}Na_{0.52}Li_{0.04})(Nb_{0.84}Ta_{0.10}Sb_{0.06})O_3$ ceramic (LF4T) in comparison to that of the random

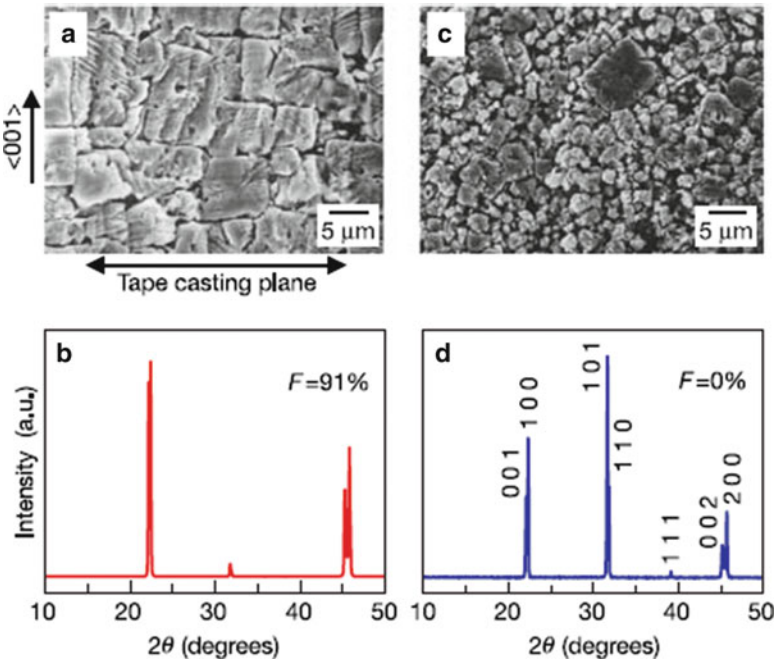

Fig. 3.10 Microstructures (a & c) and XRD patterns (b & d) of <100> textured (LF4T) and random (LF4) ceramics respectively

Table 3.2 Comparison of different piezoelectric properties of LF4T and PZT4 ceramics [92]

Piezoelectric property		LF4T	PZT4
Curie temperature	T_c (°C)	253	250
Piezoelectric coupling constant	k_p	0.61	0.60
Piezoelectric charge sensor constant	d_{31} (pC/N^{-1})	152	170
	d_{33} (pC/N^{-1})	416	410
Piezoelectric voltage constant	g_{31} (10^{-3} V m N^{-1})	11.0	8.3
	g_{33} (10^{-3} V m N^{-1})	29.9	20.2
Dielectric constant	$\varepsilon_{33}{}^T/\varepsilon_0$	1,570	2,300
Normalized strain	S_{max}/E_{max} (pm V^{-1})	750	700

ceramic (LF4) with the same composition. It can be seen in figure 3.10a that the textured ceramic exhibits brick-wall-type microstructure with grains aligned parallel to the tape-casting direction. As shown in Table 3.2, the overall performance of the textured KNN-based ceramic (LF4T) is comparable to the lead-based PZT ceramic (PZT4).

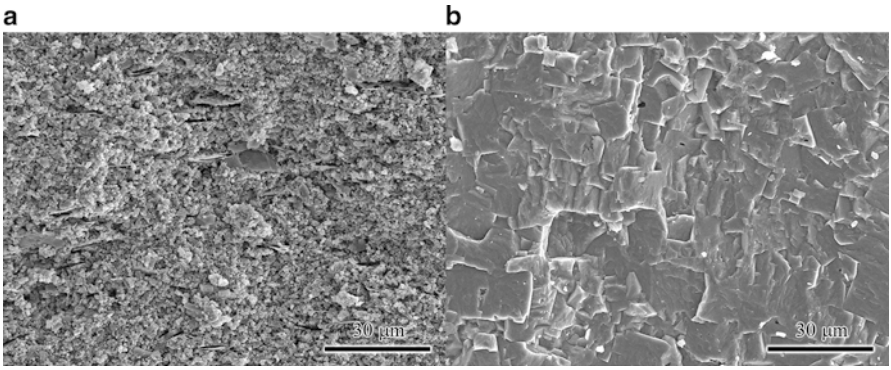

Fig. 3.11 SEM images of KNN-LN samples (**a**) green tape (**b**) after sintering and annealing at 1,100°C for 1 h

For texturing KNN ceramics using TGG or RTGG process, high relative density is desired as density below 90% of theoretical density inhibits the formation of texture. To improve the sinterability, a number of sintering additives and non-conventional sintering techniques described earlier can be used. Use of some appropriate sintering additive such as CuO and KCT is the most economical method to achieve high density and texture in KNN-based ceramics. Another effective way of achieving high density for KNN based compositions is by using non conventional sintering techniques like hot pressing (HP) and spark plasma sintering (SPS), however these techniques are very costly as compared to conventional technique. In another approach RTGG method was used to achieve textured KNN-LN ceramics by using 5 mol% $NaNbO_3$ seeds. Figure 3.11a shows the green sample after binder burnout at 600°C. This sample was sintered at 900°C for 5 min using SPS. During this process, heating rate and pressure values were 100°C/min and 50 MPa respectively. SPS was followed by annealing of samples at 1,100 C for one hour, which accelerated the oriented grain growth. Figure 3.11b shows the cross-sectional SEM image of the textured sample. The texture degree was calculated from XRD pattern (Fig. 3.12) using Logtering factor and was found to be 86%.

In both TGG and RTGG processes, the matrix grains should remain small to maintain enough kinetic force for oriented grain growth. Usually, cold isostatic press (CIP) can be used to increase the density of green sample. This step is called pre-densification process. The purpose is to accelerate the densification rate during the sintering. But for KNN ceramics with poor sinterability, this is also not sufficient. In contrast, SPS has been found to be much more efficient due to (1) fast densification at low temperature due to applied external pressure and (2) limited matrix grain growth due to fast heating rate.

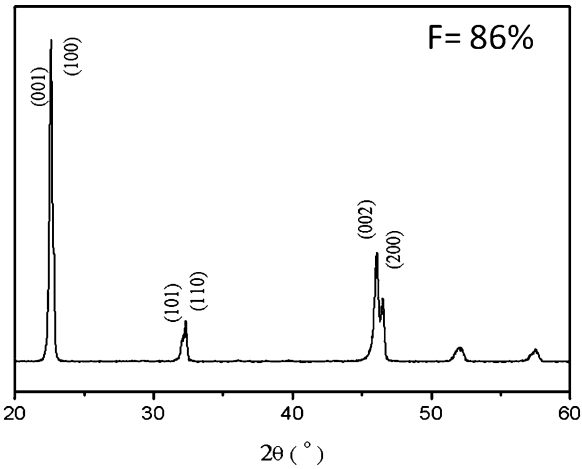

Fig. 3.12 XRD pattern of textured KNN ceramic showing the lotgering factor to be about 86%

3.5 KNN-Based Thin Films

Demand of thin film processing of ferroelectric and piezoelectric materials has increased significantly because of their possible application in small devices for different kinds of applications such as sensors and small scale energy harvesting. Thin films of piezoelectric materials are attractive for MEMS and ultrasonic transducers providing lower operating voltages and higher frequencies than bulk ceramic samples. KNN and KNN-based thin films have been fabricated by several thin film deposition techniques. They are described in this section one by one.

3.5.1 RF Magnetron Sputtering

Radio-frequency (RF) magnetron sputtering onto $Pt_{0.8}Ir_{0.2}$ substrate is shown to provide single phase perovskite films with about 30% deficiency of the alkali metal elements [106]. Processing under reduced pressure and temperature suggested that the deficiency is not a consequence of volatilization due to heat treatment but as a result of different sputtering rates. Films of KNN without metal deficiency can be achieved by adjusting the ratio K: Na: Nb in the target material to 1.5:1.5:1. As a drawback of alkali compensation, long-term stability and resistance to humidity are adversely affected. Shibata et al. measured the piezoelectric properties of high-quality KNN films deposited by RF magnetron sputtering. The piezoelectric properties of KNN films were determined from the tip displacement of KNN/Pt/MgO or KNN/Pt/Ti/SiO_2/Si unimorph cantilevers. The transverse piezoelectric coefficients e_{31}^{*} (d_{31}/s_{11}^{E}) of KNN films on Pt/MgO and Pt/Ti/SiO_2/Si were calculated to be −3.6 and −5.5 C/m^2 respectively [106].

3.5.2 Pulsed Laser Deposition

Pulsed laser deposition can provide thin films of KNN with near stoichiometric composition. Cho et al. have reported that the presence of high oxygen pressure (400 mTorr) during deposition helps in achieving single phase KNN thin films [107]. On the other hand, the films deposited at low oxygen pressure (10 mTorr) were found to be sodium deficient. According to the authors, at low oxygen partial pressure the ablation of two alkali elements from target is not same. The authors found remnant and spontaneous polarization values to be 10 and 17.5 $\mu C/cm^2$ respectively with loss tangent and coercive field values to be 2.5% and 2 kV/mm. Resistivity of thin films was found to be about 10^{12} Ωm, which is almost same as for bulk KNN. Conductivity of (Li, Ta, Sb)-modified KNN thin films could be reduced by three orders of magnitude with manganese doping.

3.5.3 Chemical Deposition

Early attempts to synthesize KNN thin films via three different sol–gel routes namely alkoxide route, oxalate and Pechini methods did not result in single-phase perovskite films even at sintering temperature of 900°C. Stability of the precursor solutions and porosity of films were also the points of concern. Tanaka et al. [108] further investigated the alkoxide route and fabricated single-phase perovskite films. Thin films by CSD needed 15–50% excess alkali metals to form single-phase KNN and showed dielectric constants up to 900. Chemical vapor deposition is also known to produce single-phase films but avoiding Nb deficiency is still a challenge. For chemical solution deposition (CSD) method, another problem with KNN films is high leakage current resulting in poor ferroelectric properties. KNN thick films with improved performance were prepared by polyvinylpyrrolidone (PVP) modified CSD method, but the KNN films with thicknesses less than 2 μm did not show well-saturated ferroelectric hysteresis loops. This indicates that introduction of PVP is not sufficient to improve the performance of KNN thin films. Many studies have suggested that oxygen or the alkali-ion vacancies in perovskite oxides significant contribute towards leakage current. Doping these materials can effectively decrease the vacancy concentration, hence can significantly improve the electrical properties.

Table 3.3 compares the ferroelectric and piezoelectric properties of the KNN thin films synthesized by different techniques. Values of ferroelectric polarization and piezoelectric coefficient are far inferior as compared to bulk KNN. Abazari et al. studied the domain structure of epitaxial KNN-LT-LS lead-free piezoelectric thin films deposited on $SrTiO_3$ substrate and measured the effective longitudinal piezoelectric coefficient d_{33} using PFM [109]. They found that films possessed tetragonal crystal structure with predominantly c-axis oriented domains and d_{33} value was about 45 pmV^{-1} for 500 nm Mn-doped films.

Table 3.3 Ferroelectric and piezoelectric properties of KNN thin films prepared by different deposition methods

Methods	P_r (μC/cm^2)	E_c (kV/cm)	d_{33} (pm/V)	References
CSD	7	70	46	[110]
CSD	16.4	42	61	[111, 112]
CSD	–	–	74	[113]
CSD	10	35	40	[114]
RF magnetron sputtering	22.5	90	45	[115]
Aerosol deposition	15.5	50	50	[116]
Pulse laser deposition	10	30	53	[117]

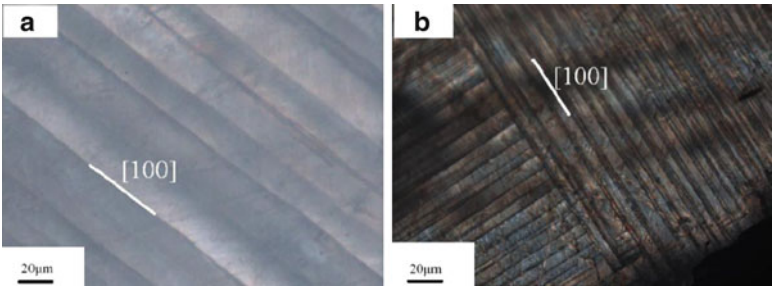

Fig. 3.13 Domain structure of (**a**) pure and (**b**) 5 mole % Mn doped KNN single crystals

3.6 KNN-Based Single Crystal

As compared to the amount of research done on random KNN ceramics, there are very few published reports on the synthesis and characterization of KNN single crystals. Because of the presence of volatile components it is difficult to grow good quality single crystals of KNN and derived compositions. Recently Kizaki et al. [118] have reported the synthesis of KNN single crystals of size $2 \times 2 \times 2$ mm^3. In their work molten salt method was used to grow these crystals and mixture of NaF and KF salts was used as a flux. But due to high conductivity of crystals, they could not be characterized for ferroelectric and piezoelectric properties. According to the authors, this high conductivity was due to charge fluctuation of niobium ions (Nb^{+4} instead of Nb^{+5}). By doping 5 mol% Manganese ions at B site, significant improvement in resistivity of crystals was achieved with remanent polarization value of 40 μC/cm^2. Recently in another work Mn-doped KNN single crystals are reported to show significant improvement in piezoelectric and dielectric properties [119]. The domain structures of two crystals are shown in Fig. 3.13 and improvement in piezoelectric and dielectric responses were attributed to the presence of higher domain density (lower domain size) in Mn-doped crystals.

Solid state single crystal growth (SSCG) method is an effective crystal growth technique to grow compositionally homogeneous single crystals of complex compositions. The main principle of SSCG method is based on abnormal grain

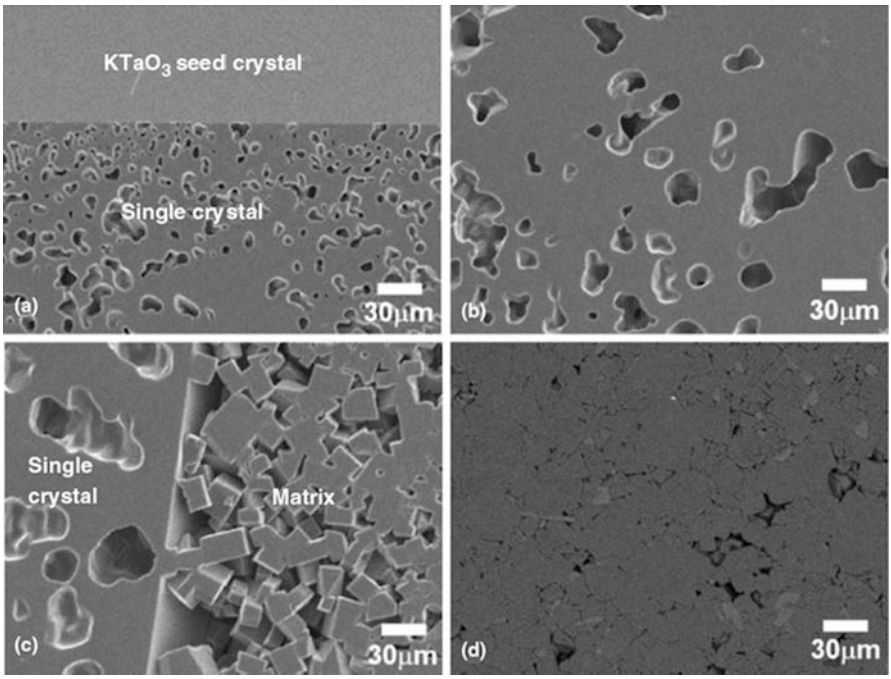

Fig. 3.14 SEM images of $(K_{0.5}Na_{0.5})NbO_3$ single crystal grown in conventional furnace at 1,100°C for 100 h (**a**) Secondary electron image of the seed crystal/single crystal boundary (**b**) secondary electron image of the single crystal (**c**) secondary electron image of the single crystal/matrix boundary (**d**) backscattered electron image of the matrix

growth in ceramics and is suitable for growing single crystals containing volatile components. Uršič et al. [120–122] synthesized the KNN single crystal by SSCG method using (110) oriented $KTaO_3$ crystal as seed. The crystals had largest dimension up to 4 mm but did not exhibit full density as shown in Fig. 3.14. HP instead of conventional sintering reduced the porosity of the grown crystals as shown in Fig. 3.15. Dielectric response as a function of temperature showed T_{o-t} and T_c to be 193 and 410°C respectively, being consistent with reported values for ceramics [120]. Crystals were found to have higher dielectric constant values in $[1\bar{3}1]$ direction as compared to $[3\bar{2}3]$ direction. Ferroelectric properties measured in $[1\bar{3}1]$ direction exhibited P_r value of 17 μC/cm^2 at applied field of 60 kV/cm. Crystals were found to possess d_{33} value of about 80 pC/N at 2 Hz which was attributed to the presence of nano size (<300 nm) domains. According to the authors, decrease in piezoelectricity of samples at higher frequencies was because of the inability of 180° domains in reorienting in such small response time.

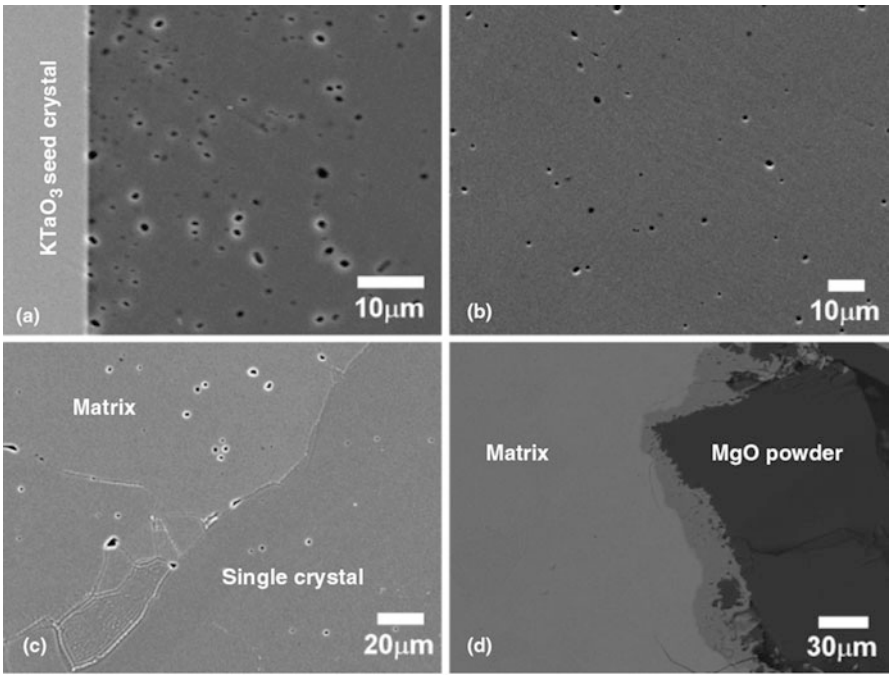

Fig. 3.15 Scanning electron microscopy images of a single crystal of $(K_{0.5}Na_{0.5})NbO_3$ grown in a hot press using a two-stage treatment: 975°C/50 MPa for 2 h followed by 1,100°C/50 MPa for 100 h (**a**) Secondary electron image of the seed crystal/single crystal boundary (**b**) backscattered electron image of the single crystal (**c**) secondary electron image of the single crystal/matrix boundary (**d**) backscattered electron image of the edge of the sample

Bencan et al. [121] investigated the chemical composition and structure of KNN single crystal prepared by SSCG method. No compositional inhomogeneities, typically encountered in single crystals prepared by the conventional flux synthesis method were observed. According to XRD and TEM analysis, KNN single crystals had monoclinic symmetry. The structure of domains and domain walls play an essential role in the ferroelectric behavior of perovskites. KNN single crystals grown by SSCG method were found to have large 90° domains of size about 100 mm along with smaller 180° domains having width few tens of nm. Lin et al. [123] also studied the domain structure of KNN crystals by polarized light microscopy. At room temperature he found the presence of 90° domains in poled crystals while unpoled crystals were found to have 60°, 90° and 120° domains. Temperature dependent study done on poled crystals was found to be consistent with the known transition temperatures of KNN. Domain structures of poled crystal at different temperatures are shown in Fig. 3.16.

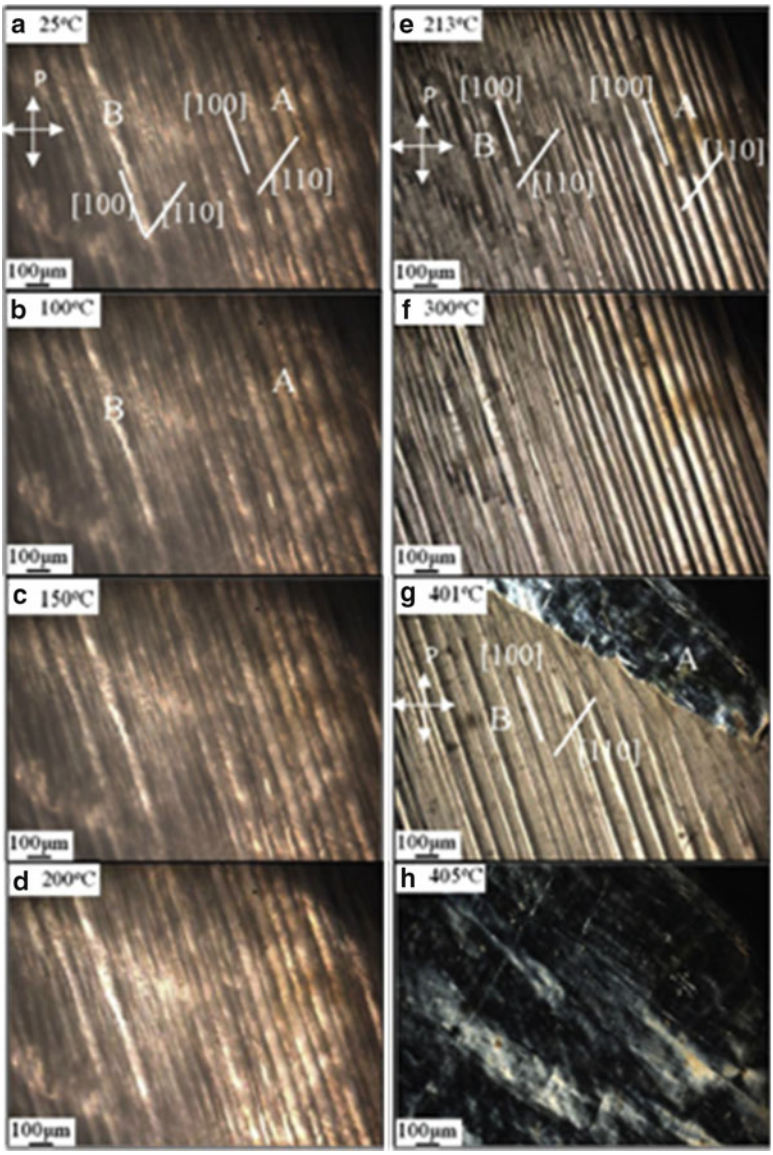

Fig. 3.16 Domain structure of [001] oriented KNN single crystal at different temperatures (**a**) 25°C (**b**) 100°C (**c**) 150°C (**d**) 200°C (**e**) 213°C (**f**) 300°C (**g**) 401°C (**h**) 405°C

3.7 Relationship Between Weight Ratio and Piezoelectric Response in Perovskites: A Guiding Path to Design New Piezoelectric Material

In their recent work Ahn et al. have reported an interesting trend by studying the variation of longitudinal piezoelectric constant d_{33} with respect to atomic weight ratio R_W of A and B site atoms ($R_W = W_A/W_B$) for different piezoelectric perovskite compositions [124]. The plot obtained by them can be seen in Fig. 3.17a, which clearly indicates that piezoelectric compositions having weight ratio (R_W) either less than 0.5 or greater than 2 show comparatively higher longitudinal piezoelectric response (d_{33}). A forbidden zone $0.5 \leq R_W \leq 2.0$ can easily be observed, showing the absence of piezoelectric response in the range. This observation indicates that good piezoelectric properties can only be achieved in perovskites if one of the cations is at least twice heavier than the other. This observation is important and can be used as a generalized rule for achieving high piezoelectric response in perovskites.

This concept was further elaborated by studying the variation of d_{33} with respect to R_W for various compositions in the same system. As can be seen in Fig. 3.17b that lead-based systems with high piezoelectric response have heavier lead ion at A site and lighter ions such as Mg, Ti, Zn, Zr, etc. on B site. While on the other hand in lead-free systems like KNN, high piezoelectric response is achieved by having heavier B site ions (e.g. Nb and Ta) and lighter A site ions (e.g. Li). The materials with mixed distribution of heavier and lighter ions such as BNT have averaging effect. The value of $1/R_W$ for KNN ceramics is similar to R_W for PZT ceramics at MPB compositions and both these materials exhibit high piezoelectric response. The variation in d_{33} with R_W in PZT-based ceramics is shown in Fig. 3.17c. A large d_{33} magnitude of the order of 600 pC/N is evident for composition having R_W higher than 2.89. For lead-free materials a similar trend is presented in Fig. 3.17d. Using these observations, it was proposed that high values of d_{33} can be obtained when R_W (or $1/R_W$) is higher than 2.9 in perovskite piezoelectric ceramics indicating unified nature of correlation between the *weight* ratio of A and B site atoms in perovskite lattice with piezoelectric response. Empirical expressions were proposed for piezoelectric coefficients outside forbidden zone ($0.5 \leq R_W \leq 2.0$) for both lead-based and KNN-based perovskite compositions.

$$d \propto \frac{1}{\mathrm{mRw} + 1} \,(\text{KNN based})$$

$$\propto \frac{1}{1 + n/R_w} \,(\text{PZT based}),$$

where m and n are the system dependent constants.

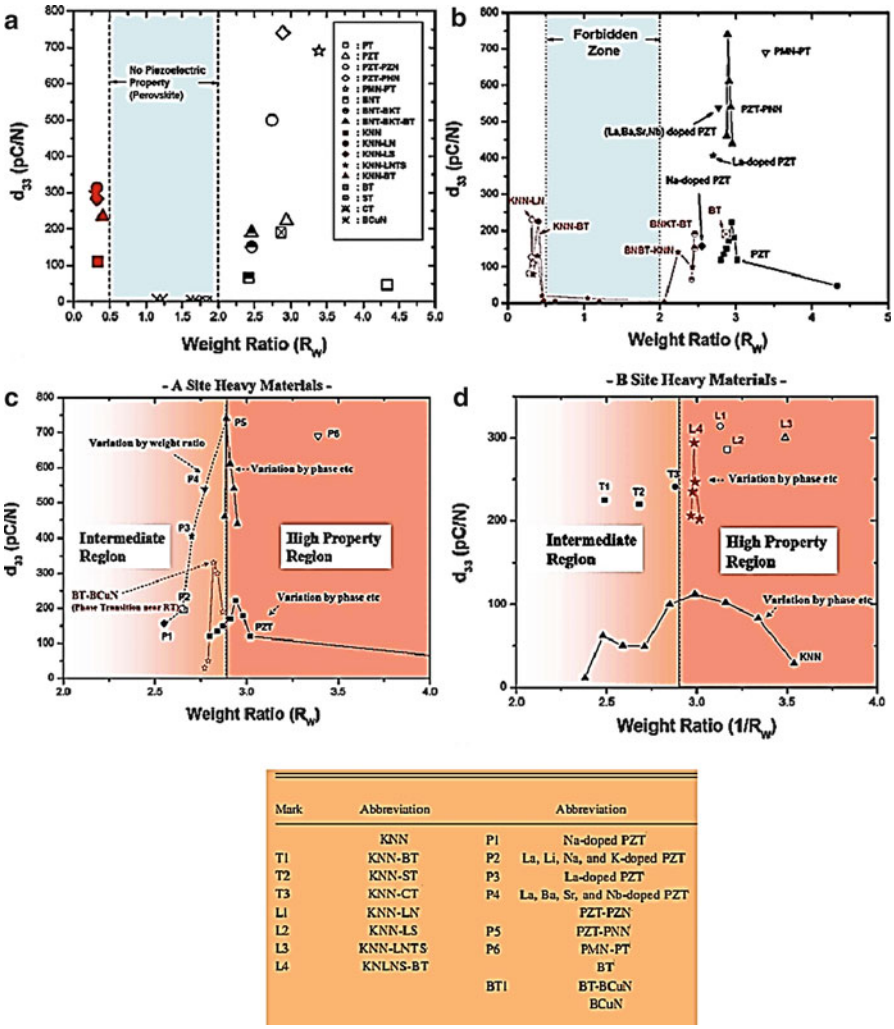

Mark	Abbreviation		Abbreviation
	KNN	P1	Na-doped PZT
T1	KNN-BT	P2	La, Li, Na, and K-doped PZT
T2	KNN-ST	P3	La-doped PZT
T3	KNN-CT	P4	La, Ba, Sr, and Nb-doped PZT
L1	KNN-LN		PZT-PZN
L2	KNN-LS	P5	PZT-PNN
L3	KNN-LNTS	P6	PMN-PT
L4	KNLNS-BT		BT
		BT1	BT-BCuN
			BCuN

Fig. 3.17 Longitudinal piezoelectric constant (d_{33}) as a function of R_W or $1/R_W$ in perovskite piezoelectric ceramics (**a**) MPB compositions in PZT and BNT based compositions, two-phase-polymorphic compositions in KNN and BT based ceramics (**b**) various compositions in perovskite piezoelectric ceramics (**c**) *A*-site heavy materials (**d**) *B*-site heavy materials

References

1. Rosen CZ, Hiremath BV, Newnham R (1992) Key papers in physics piezoelectricity. American Institute of Physics, New York
2. Uchino K (2009) Ferroelectric devices, 2nd edn. CRC Press, New York
3. Jaffe B, Cook WR, Jaffe H (1971) Piezoelectric ceramics. Academic Press, New York

4. Kim H, Tadesse Y, Priya S (2009) In: Priya S, Inman DJ (eds) Piezoelectric energy harvesting, energy harvesting technologies. Springer, New York, pp 3–39
5. Priya S (2007) Advances in energy harvesting using low profile piezoelectric transducers. J Electroceram 19(1):167–184
6. Hollenstein E, Damjanovic D, Setter N (2007) Temperature stability of the piezoelectric properties of Li-modified KNN ceramics. J Eur Ceram Soc 27(13–15):4093–4097
7. Park S-E, Shrout TR (1997) Ultrahigh strain and piezoelectric behavior in relaxor based ferroelectric single crystals. J Appl Phys 82(4):1804–1811
8. Herklotz A et al. (2010) Electrical characterization of PMN–28%PT(001) crystals used as thin-film substrates. J Appl Phys 108(9):094101
9. Takenaka T, Nagata H (2005) Current status and prospects of lead-free piezoelectric ceramics. J Eur Ceram Soc 25(12):2693–2700
10. Takenaka T et al. (2007) Lead-free piezoelectric ceramics based on perovskite structures. J Electroceram 19(4):259–265
11. Panda P (2009) Review: environmental friendly lead-free piezoelectric materials. J Mater Sci 44(19):5049–5062
12. Rödel J et al. (2009) Perspective on the development of lead-free piezoceramics. J Am Ceram Soc 92(6):1153–1177
13. Maeder MD, Damjanovic D, Setter N (2004) Lead free piezoelectric materials. J Electroceram 13(1):385–392
14. Kosec M et al. (2008) KNN-based piezoelectric ceramics. In: Safari A, Akdoğan EK (eds) Piezoelectric and acoustic materials for transducer applications. Springer, New York, pp 81–102
15. Zhang S, Xia R, Shrout T (2007) Lead-free piezoelectric ceramics vs. PZT? J Electroceram 19(4):251–257
16. Shrout T, Zhang S (2007) Lead-free piezoelectric ceramics: alternatives for PZT? J Electroceram 19(1):113–126
17. Ringgaard E, Wurlitzer T, Wolny WW (2005) Properties of lead-free piezoceramics based on alkali niobates. Ferroelectrics 319(1):97–107
18. Egerton L, Dillon DM (1959) Piezoelectric and dielectric properties of ceramics in the system potassium—sodium niobate. J Am Ceram Soc 42(9):438–442
19. Tellier J et al. (2009) Crystal structure and phase transitions of sodium potassium niobate perovskites. Solid State Sci 11(2):320–324
20. Baker DW et al. (2009) A comprehensive study of the phase diagram of $K_xNa_{1-x}NbO_3$. Applied Physics Letters 95(9)
21. Kodre A et al. (2009) Extended x-ray absorption fine structure study of phase transitions in the piezoelectric perovskite $K_{0.5}Na_{0.5}NbO_3$. J Appl Phys 105(11):113528
22. Satoshi W et al. (2001) Poling treatment and piezoelectric properties of potassium niobate ferroelectric single crystals. Jpn J Appl Phys 40:5690–5697
23. Shirane G, Newnham R, Pepinsky R (1954) Dielectric properties and phase transitions of NaNbO3 and (Na, K)NbO3. Phys Rev 96(3):581
24. Matthias BT (1949) New ferroelectric crystals. Phys Rev 75(11):1771
25. Kakimoto K, Masuda I, Ohsato H (2005) Lead-free $KNbO_3$ piezoceramics synthesized by pressure-less sintering. J Eur Ceram Soc 25(12):2719–2722
26. Yamanouchi K et al. (2001) Single crystal growth of $KNbO_3$ and application to surface acoustic wave devices. J Eur Ceram Soc 21(15):2791–2795
27. Jaeger RE, Egerton L (1962) Hot pressing of potassium-sodium niobates. J Am Ceram Soc 45(5):209–213
28. Dubernet P, Ravez J (1998) Dielectric study of $KNbO_3$ ceramics over a large range of frequency (10^{2-9}Hz) and temperature (300-800 K). Ferroelectrics 211(1):51–66
29. Ahn C-W et al. (2010) Effect of elemental diffusion on temperature coefficient of piezoelectric properties in KNN-based lead-free composites. J Mater Sci Lett 45(14):3961–3965

30. Bomlai P et al. (2007) Effect of calcination conditions and excess alkali carbonate on the phase formation and particle morphology of $Na_{0.5}K_{0.5}NbO_3$ powders. J Am Ceram Soc 90(5):1650–1655
31. Wu L et al. (2008) Influence of compositional ratio K/Na on physical properties in $(K_xNa_{1-x})NbO_3$ ceramics. J Appl Phy 103(8)
32. Bernard J et al. (2008) Low-temperature sintering of $(Na_{0.5}K_{0.5})$NbO3 ceramics. J Am Ceram Soc 91(7):2409–2411
33. Hagh M, Jadidian NB, Safari A (2007) Property-processing relationship in lead-free (K, Na, Li) NbO_3 solid solution system. J Electroceram 18(3):339–346
34. Jenko D et al. (2005) Electron microscopy studies of potassium sodium niobate ceramics. Microsc Microanal 11(06):572–580
35. Ahn C-W et al. (2009) Sintering behavior of lead-free (K, Na)NbO_3-basedpiezoelectric ceramics. J Am Ceram Soc 92(9):2033–2038
36. Skidmore TA, Milne SJ (2007) Phase development during mixed-oxide processing of a $[(Na_{0.5}K_{0.5})NbO_3]_{1-x}$-$[LiTaO_3]$ x powder. J Mater Res 22(08):2265–2272
37. Wang Y et al. (2007) Compositional Inhomogeneity in Li- and Ta-Modified (K, Na)NbO_3 Ceramics. J Am Ceram Soc 90(11):3485–3489
38. Du Hl et al. (2006) Effect of poling condition on piezoelectric properties of $(Na_{0.5}K_{0.5})NbO_3$ ceramics. Transactions of Nonferrous Metals Society of China 16(Suppl 2):s462–s465
39. German RM (1996) Sintering theory and practice. Wiley, New York
40. Rahaman MN (2007) Ceramic processing. CRC/Taylor & Francis, Boca Raton
41. Wang Y et al. (2008) High-temperature instability of Li- and Ta-modified (K, Na)NbO3 piezoceramics. J Am Ceram Soc 91(6):1962–1970
42. Pang X et al. (2011) Study on the sintering mechanism of KNN-based lead-free piezoelectric ceramics. J Mater Sci Lett 46(7):2345–2349
43. Ahn C-W et al. (2008) Low temperature sintering and piezoelectric properties of CuO-doped $(Na_{0.5}K_{0.5})NbO_3$ ceramics. Ferroelectrics Lett Sec 35(3-4):66–72
44. Lin DM, Kwok KW et al. (2008) Piezoelectric and ferroelectric properties of Cu-doped $Na_{0.5}K_{0.5}NbO_3$ lead-free ceramics. J Phys Appl Phys 41(4)
45. Du H et al. (2006) Preparation and piezoelectric properties of $(Na_{0.5}K_{0.5})NbO_3$lead-free piezoelectric ceramics with pressure-less sintering. Mater Sci Eng B 131(1-3):83–87
46. Zhao P, Zhang B-P, Li J-F (2008) Enhanced dielectric and piezoelectric properties in LiTaO3-doped lead-free (K, Na)NbO3 ceramics by optimizing sintering temperature. Scripta Mater 58(6):429–432
47. Zuo R et al. (2006) Sintering and electrical properties of lead-free $Na_{0.5}K_{0.5}NbO_3$ piezoelectric ceramics. J Am Ceram Soc 89(6):2010–2015
48. Zhen Y, Li J-F (2006) Normal sintering of (K, Na)NbO3-based ceramics: influence of sintering temperature on densification, microstructure, and electrical properties. J Am Ceram Soc 89(12):3669–3675
49. Castro A et al. (2004) Sodium niobate ceramics prepared by mechanical activation assisted methods. J Eur Ceram Soc 24(6):941–945
50. Li JF et al. (2006) Ferroelectric and piezoelectric properties of fine-grained $Na_{0.5}K_{0.5}NbO_3$ lead-free piezoelectric ceramics prepared by spark plasma sintering. J Am Ceram Soc 89 (2):706–709
51. Bieling LE et al. (1968) Isostatically hot-pressed sodium–potassium niobate transducer material for ultrasonic devices. Ceram. Bull 47(1151)
52. Haertling GH (1967) Properties of hot-pressed ferroelectric alkali niobate ceramics. J Am Ceram Soc 50(6):329–330
53. Kosec M, Kolar D (1975) On activated sintering and electrical properties of $NaKNbO_3$. Mater Res Bull 10(5):335–339
54. Smeltere I et al. (2009) Sintering of lead-free $(K_{0.5}Na_{0.5})NbO_3$ based solid solution. Integr Ferroelectr 108(1):46–56

55. Park S-H, Ahn C-W, Nahm S, Song J-S (2004) Microstructure and piezoelectric properties of ZnO-added $(Na_{0.5}K_{0.5})NbO_3$ ceramics. Jpn J Appl Phys 43:L1072
56. Li Z et al. (2010) Dielectric and piezoelectric properties of ZnO and SnO_2 co-doping $Na_{0.5}K_{0.5}NbO_3$ceramics. Phys B Condens Matter 405(1):296–299
57. Matsubara M et al. (2004) Sinterability and piezoelectric properties of $(K,Na)NbO_3$ ceramics with novel sintering aid. Jpn J Appl Phys 1 43(10):7159–7163
58. Matsubara M et al. (2005) Sintering and piezoelectric properties of potassium sodium niobate ceramics with newly developed sintering aid. Jpn J Appl Phys 1 44(1A):258–263
59. Li E et al. (2007) Influence of CuO on the structure and piezoelectric properties of the alkaline niobate-based lead-free ceramics. J Am Ceram Soc 90(6):1787–1791
60. Lin D et al. (2008) Piezoelectric and ferroelectric properties of Cu-doped $K_{0.5}Na_{0.5}NbO_3$ lead-free ceramics. J Phys D Appl Phys 41(4):045401
61. Ahn C-W et al. (2008) Effect of CuO and MnO_2 on sintering temperature, microstructure, and piezoelectric properties of $0.95(K_{0.5}Na_{0.5})NbO_3$-$0.05BaTiO_3$ ceramics. Mater Lett 62(20):3594–3596
62. Yan K et al. (2010) Microstructure and piezoelectric properties of $(K_{0.5}Na_{0.5})NbO_3$–$BaTiO_3$ lead-free piezoelectric ceramics modified by B_2O_3–CuO. J Am Ceram Soc 93(11): 3823–3827
63. Seo IT et al. (2008) Effect of CuO on the sintering and piezoelectric properties of 0.95 $(Na_{0.5}K_{0.5})NbO_3$-$0.05SrTiO_3$ lead-free piezoelectric ceramics. J Am Ceram Soc 91(12): 3955–3960
64. Eichel R-A et al. (2009) Local variations in defect polarization and covalent bonding in ferroelectric Cu^{2+}-doped PZT and KNN functional ceramics at the morphotropic phase boundary. Phys Chem Chem Phys 11(39):8698–8705
65. Park B-C et al. (2010) Highly enhanced mechanical quality factor in lead-free $(K_{0.5}Na_{0.5})$ NbO_3 piezoelectric ceramics by co-doping with $K_{5.4}Cu_{1.3}Ta_{10}O_{29}$ and CuO. Mater Lett 64(14):1577–1579
66. Li-Mei Z et al. (2009) Thermal stability and humidity resistance of $ScTaO_4$ modified $(K_{0.5}Na_{0.5})NbO_3$ ceramics. Chinese Phys Lett 26(12):127701
67. Guo YP, Kakimoto K, Ohsato H (2005) (Na0.5K0.5)NbO3-LiTaO3 lead-free piezoelectric ceramics. Mater Lett 59(2–3):241–244
68. Guo YP, Kakimoto K, Ohsato H (2004) Structure and electrical properties of lead-free $(Na_{0.5}K_{0.5})NbO_3$-$BaTiO_3$ ceramics. Jpn J Appl Phys 1 43(9B):6662–6666
69. Guo YP, Kakimoto K, Ohsato H (2004) Dielectric and piezoelectric properties of lead-free (Na0.5K0.5)NbO3-SrTiO3 ceramics. Solid State Commun 129(5):279–284
70. Guo Y, Kakimoto P, Ohsato H (2004) Phase transitional behavior and piezoelectric properties of $(Na_{0.5}K_{0.5})NbO_3$-$LiNbO_3$ ceramics. Appl Phys Lett 85(18):4121–4123
71. Zuo R, Ye C (2007) Structures and piezoelectric properties of $(NaKLi)_{1-x}(BiNaBa)_xNb_{1-x}$ Ti_xO_3 lead-free ceramics. Appl Phys Lett 91(6):062916
72. Zuo R, Ye C, Fang X (2008) $Na_{0.5}K_{0.5}NbO_3$-$BiFeO_3$ lead-free piezoelectric ceramics. J Phys Chem Solids 69(1):230–235
73. Zuo R, Fang X, Ye C (2007) Phase structures and electrical properties of new lead-free $(Na_{0.5}K_{0.5})NbO_3$ -$(Bi_{0.5}Na_{0.5})TiO_3$ ceramics. Appl Phys Lett 90(9):092904
74. Saito Y, Takao H (2006) High performance lead-free piezoelectric ceramics in the $(Na_{0.5}K_{0.5})$ NbO_3 -$LiTaO_3$ solid solution system. Ferroelectrics 338(1):17–32
75. Ming B-Q et al. (2007) Piezoelectric properties of (Li, Sb, Ta) modified (Na, K)NbO3 lead-free ceramics. J Appl Phys 101(5):054103
76. Park H-Y et al. (2007) Microstructure and piezoelectric properties of lead-free (1 - x) $(Na_{0.5}K_{0.5})NbO_3$-$xCaTiO_3$ ceramics. J Appl Phys 102(12):124101
77. Lang SB, Zhu W, Cross LE (2006) Piezoelectric and Pyroelectric Properties of $(K_{0.5}Na_{0.5})_{1-x}$ $(Nb_{1-y}Ta_y)O_3$ Ceramics. Ferroelectrics 336(1):15–21
78. Dai Y, Zhang X, Zhou G (2007) Phase transitional behavior in $(Na_{0.5}K_{0.5})NbO_3$ -$LiTaO_3$ ceramics. Appl Phys Lett 90(26):262903

79. Zuo R, Fu J (2011) Rhombohedral–tetragonal phase coexistence and piezoelectric properties of (NaK)(NbSb)O_3–$LiTaO_3$–$BaZrO_3$ lead-free ceramics. J Am Ceram Soc 94(5):1467–1470
80. Ahn CW, Park C-H, Viehland D, Nahm S, Kang DH, Bae K-S, Priya S (2008) Correlation between phase transitions and piezoelectric properties in lead-free (K,Na,Li)NbO_3–$BaTiO_3$ ceramics. Jpn J Appl Phys 47:8880
81. Du H et al. (2007) An approach to further improve piezoelectric properties of($Na_{0.5}K_{0.5}$) NbO_3 -based lead-free ceramics. Appl Phys Lett 91(20):202907
82. Zhang Q et al. (2010) Effects of Sb content on electrical properties of lead-free piezoelectric $(Na_{0.535}K_{0.480})_{0.942}Li_{0.058}(Nb_{1-x}Sb_x)O_3$ ceramics. J Alloy Comp 490(1-2):260–263
83. Zang GZ et al. (2006) Perovskite $(Na_{0.5}K_{0.5})_{(1-x)}(LiSb)_xNb_{1-x}O_3$ lead-free piezoceramics. Appl Phys Lett 88(21)
84. Wang Y et al. (2008) Electrical properties and temperature stability of a new kind of lead-free piezoelectric ceramics. J Phys D Appl Phys 41(24):245401
85. Du HL et al. (2007) An approach to further improve piezoelectric properties of 0.95 $(Na_{0.5}K_{0.5})NbO_3$ based lead-free ceramics. Appl Phys Lett 91(20)
86. Lei C, Ye ZG (2008) Lead-free piezoelectric ceramics derived from the $Na_{0.5}K_{0.5}NbO_3$-$AgNbO_3$ solid solution system. Appl Phys Lett 93(4)
87. Cho K-H et al. (2007) Microstructure and Piezoelectric Properties of $0.95(Na_{0.5}K_{0.5})NbO_3$-$0.05SrTiO_3$ Ceramics. J Am Ceram Soc 90(6):1946–1949
88. Kosec M et al. (2004) New lead-free relaxors based on the $K_{0.5}Na_{0.5}NbO_3$–$SrTiO_3$ solid solution. J Mater Res 19(6):1849–1854
89. Ahn CW et al. (2008) Dielectric and piezoelectric properties of (1-x) $(Na_{0.5}K_{0.5})NbO_3$-x $BaTiO_3$ ceramics. J Mater Sci Lett 43(20):6784–6797
90. Choi C-H et al. (2007) (1 - x)$BaTiO_3$ - x($(Na_{0.5}K_{0.5})NbO_3$ ceramics for multilayer ceramic capacitors. Appl Phys Lett 90(13):132905
91. Park HY et al. (2006) Microstructure and piezoelectric properties of $0.95(Na_{0.5}K_{0.5})NbO_3$-$0.05BaTiO_3$ ceramics. Appl Phys Lett 89(6)
92. Saito Y et al. (2004) Lead-free piezoceramics. Nature 432(7013):84–87
93. Ando, M et al. (1999) Piezoelectric Ceramic composition. US Patent 6,083,415, Murata Manufacturing Co
94. Messing GL et al. (2004) Templated grain growth of textured piezoelectric ceramics. Crit Rev Solid State Mater Sci 29:45–96
95. Hong S-H, Trolier-McKinstry S, Messing GL (2000) Dielectric and Electromechanical Properties of Textured Niobium-Doped Bismuth Titanate Ceramics. J Am Ceram Soc 83 (1):113–118
96. Zhang Z et al. (2004) Grain orientation effects on the properties of a bismuth layer-structured ferroelectric (BLSF) Bi_3NbTiO_9 solid solution. J Am Ceram Soc 87(4):602–605
97. Takeuchi T et al. (2000) Unidirectionally textured $CaBi_4Ti_4O_{15}$ ceramics by the reactive templated grain growth with an extrusion. Jpn J Appl Phys 39:5577
98. Takeuchi T et al. (1999) Piezoelectric Properties of Bismuth Layer-Structured Ferroelectric Ceramics with a Preferred Orientation Processed by the Reactive Templated Grain Growth Method. Jpn J Appl Phys 38:5553
99. Cihangir D et al. (2002) Dielectric and piezoelectric properties of textured $Sr_{0.53}Ba_{0.47}Nb_2O_6$ ceramics prepared by templated grain growth. J Mater Res 17(9)
100. Yilmaz H, Trolier-McKinstry S, Messing GL (2003) (Reactive) Templated Grain Growth of Textured Sodium Bismuth Titanate ($Na_{1/2}Bi_{1/2}TiO_3$-$BaTiO_3$) Ceramics—II Dielectric and Piezoelectric Properties. J Electroceram 11(3):217–226
101. Zhao W et al. (2009) Fabrication of $Na_{0.5}Bi_{0.5}TiO_3$–$BaTiO_3$ textured ceramics templated by plate-like $Na_{0.5}Bi_{0.5}TiO_3$ particles. J Am Ceram Soc 92(7):1607–1609
102. Tani T (1998) Crystalline-oriented Piezoelectric Bulk Ceramics with a Perovskite-type Structure. J Korean Phys Soc 32
103. Takao H et al. (2006) Microstructural evolution of crystalline-oriented $(K_{0.5}Na_{0.5})NbO_3$ piezoelectric ceramics with a sintering aid of CuO. J Am Ceram Soc 89(6):1951–1956

104. Chang Y et al. (2010) Microstructure development and piezoelectric properties of highly textured CuO-doped KNN by templated grain growth. J Mater Res 25(4)
105. Chang Y et al. (2009) <001> textured $(K_{0.5}Na_{0.5})Nb_{0.97}Sb_{0.03}O_3$ piezoelectric ceramics with high electromechanical coupling over a broad temperature range. Appl Phys Lett 95(23):232905
106. Shibata K et al. (2008) Crystalline structure of highly piezoelectric (K, Na)NbO3 films deposited by RF magnetron sputtering. Jpn J Appl Phys 47:8909–8913
107. Cho C-R, Grishin A (2000) Background oxygen effects on pulsed laser deposited $K_{0.5}Na_{0.5}NbO_3$ films: From superparaelectric state to ferroelectricity. J Appl Phys 87(9): 4439–4448
108. Tanaka K, Nishizawa K, Miki T, Kato K (2005) Microstructure control and dielectric/piezoelectric properties of alkoxy-derived $Ba(Ti,Zr)O_3$ thin films. Jpn J Appl Phys 44
109. Abazari M et al. (2010) Nanoscale characterization and local piezoelectric properties of lead-free KNN-LT-LS thin films. J Phys D Appl Phys 43(2):025405
110. Nakashima Y, Hiroshi M, Tetsuo S, Toshinobu Y (2007) Lead-Free Piezoelectric (K,Na) NbO_3 Thin Films Derived from Metal Alkoxide Precursors. Jpn J Appl Phys 46
111. Wang X et al. (2002) Growth and Characterization of $K_{0.5}Na_{0.5}NbO_3$Thin Films on Polycrystalline $Pt_{80}Ir_{20}$ Substrates. J Mater Res 05:1183–1191
112. Wang L, Yao K, Ren W (2008) Piezoelectric $K_{0.5}Na_{0.5}NbO_3$ thick films derived from polyvinylpyrrolidone-modified chemical solution deposition. Appl Phys Lett 93(9)
113. Goh PC, Yao K, Chen Z (2010) Lead-free piezoelectric $(K_{0.5}Na_{0.5})NbO_3$ thin films derived from chemical solution modified with stabilizing agents. Appl Phys Lett 97(10):102901
114. Ahn C-W et al. (2009) The effect of K and Na excess on the ferroelectric and piezoelectric properties of $K_{0.5}Na_{0.5}NbO_3$ thin films. J Phys D Appl Phys 42(21):215304
115. Lee HJ et al. (2009) Ferroelectric and piezoelectric properties of $Na_{0.52}K_{0.48}NbO_3$ thin films prepared by radio frequency magnetron sputtering. Appl Phys Lett 94(9):092902
116. Ryu J et al. (2008) Ferroelectric and piezoelectric properties of $0.948((K_{0.5}Na_{0.5})NbO_3$-$0.052LiSbO_3$ lead-free piezoelectric thick film by aerosol deposition. Appl Phys Lett 92(1):012905
117. Abazari M, Safari A (2010) Leakage current behavior in lead-free ferroelectric (K, Na)NbO3-LiTaO3-LiSbO3 thin films. Appl Phys Lett 97(26):262902
118. Kizaki Y, Noguchi Y, Miyayama M (2006) Defect control for low leakage current in $(K_{0.5}Na_{0.5})NbO_3$single crystals. Appl Phys Lett 89(14):142910
119. Lin D et al. (2010) Influence of MnO_2 Doping on the Dielectric and Piezoelectric Properties and the Domain Structure in $(K_{0.5}Na_{0.5})NbO_3$ Single Crystals. J Am Ceram Soc 93(4): 941–944
120. Ursi CH et al. (2010) Dielectric, ferroelectric, piezoelectric, and electrostrictive properties of $K_{0.5}Na_{0.5}NbO_3$ single crystals. J Appl Phys 107(3):033705
121. Bencan A et al. (2009) Compositional and Structural Study of a $(K_{0.5}Na_{0.5})NbO_3$ Single Crystal Prepared by Solid State Crystal Growth. Microsc Microanal 15(5):435–440
122. Bencan A et al. (2006) Electron microscopy studies of alkali niobate single crystals using the solid state crystal growth method. Scanning 28(2):123–124
123. Lin D et al. (2009) Dielectric/piezoelectric properties and temperature dependence of domain structure evolution in lead free single crystal. Solid State Comm 149(39–40):1646–1649
124. Ahn C-W et al. (2009) A generalized rule for large piezoelectric response in perovskite oxide ceramics and its application for design of lead-free compositions. J Appl Phys 105(11): 114108

Chapter 4
Low Temperature Sintering of the Alkali-Niobate Ceramics

Hwi-Yeol Park and Sahn Nahm

4.1 Introduction

$Pb(Zr,Ti)O_3$ (PZT)-based ceramics have outstanding dielectric and piezoelectric properties and have been widely used in piezoelectric devices [1]. However, they contain 60 wt.% PbO, which presents an environmental problem. Therefore, extensive studies have been conducted to find lead-free piezoelectric materials for the replacement of PZT-based ceramics. In particular, $(Na_{1-x}K_x)NbO_3$ (NKN) lead-free ceramics, which are the solid solutions of ferroelectric $KNbO_3$ and antiferroelectric $NaNbO_3$, have been extensively investigated because of their high piezoelectric properties ($d_{33} = 80$ pC/N and $k_p = 36 \sim 40\%$) and high Curie temperature ($T_c = 420°C$) [2–5]. However, $(Na_{1-x}K_x)NbO_3$ ceramics (NKNCs) are difficult to sinter and they decompose when exposed to moisture. To solve these problems, sintering aids, such as CuO, $K_4CuNb_8O_{23}$, and ZnO have been used [6–8]. Moreover, various processing methods have been used to improve the sinterability.

NKN-based ceramics have generally been sintered at high temperatures ($\geq$1,050°C) [9, 10]. Such high sintering temperatures cause the Na_2O to evaporate during the sintering process, resulting in the formation of a liquid phase, which assists in the densification of the specimens [5, 9, 11]. Therefore, NKN-based ceramics have been sintered using a liquid phase-assisted process and the liquid phase formed at temperatures above 1,000°C due to the Na_2O evaporation. On the other hand, Na_2O evaporation decreases the polling efficiency by reducing the resistivity of the specimen as well as degrades the piezoelectric properties [5]. Furthermore, Na_2O evaporation considerably changes the microstructure and eventually affects the piezoelectric properties of the NKN-based ceramics. Therefore, it

H.-Y. Park • S. Nahm (✉)
Department of Materials Science and Engineering, Korea University,
1-5 Ka, Anam-Dong, Sungbuk-Ku, Seoul 136-701, Korea
e-mail: vantage@korea.ac.kr; snahm@korea.ac.kr

S. Priya and S. Nahm (eds.), *Lead-Free Piezoelectrics*,
DOI 10.1007/978-1-4419-9598-8_4, © Springer Science+Business Media, LLC 2012

is necessary to control the Na_2O evaporation to obtain stable piezoelectric properties in the specimens. Double crucible muffling has been previously used to minimize Na_2O evaporation [5]. Although this was found to improve the piezoelectric properties by increasing the polling efficiency, it is very difficult to control the Na_2O evaporation by muffling. Therefore, it is necessary to develop a method to decrease the sintering temperature of NKNCs to below 1,000°C in order to obtain stable piezoelectric properties.

Sintering NKN-based ceramics at low temperatures also facilitates their use in multilayers. Multilayer devices are required to achieve low driving forces, miniaturization, and hybridization in electronic components. A multilayer consists of alternating piezoelectric ceramic layers and internal metallic electrode layers. Ag has been used as the metallic electrode of multilayer devices because of its high conductivity and low cost. For the application to multilayer devices, the sintering temperature of the NKN-based ceramics should be reduced to below 950°C, because the melting temperature of Ag is 961°C. In order to reduce the sintering temperature of the NKN-based ceramics, the following methods have generally been used (1) addition of a small amount of sintering aids, for example, low melting point oxides, and (2) spark plasma sintering (SPS). In this chapter, the research, which has been performed to reduce the sintering temperature of the NKN-based ceramics, is discussed in detail.

4.2 Low Temperature Sintering of the NKN-Based Ceramics Using Sintering Aids

4.2.1 Low Temperature Sintering Mechanism and Piezoelectric Properties of the CuO-Added NKN-Based Ceramics

Sintering Mechanism of the CuO-Added NKN-Based Ceramics

The 0.95NKN-0.05$BaTiO_3$ ceramics sintered at 950°C had a porous microstructure with small grains, as shown in Fig 4.1a [12]. In the specimen containing 1.0 mol% CuO, a dense microstructure with enlarged grains was developed and a liquid phase was found as indicated by the arrow in Fig. 4.1b. The liquid phase was also observed in the NKN and 0.95NKN-0.05$ATiO_3$ (A = Sr and Ca) ceramics, as shown in Figs. 4.2a, b. The liquid phase formed in the CuO-added NKN-based ceramics could be a CuO-related phase.

Grain growth was also observed for the 0.95NKN-0.05$BaTiO_3$ ceramics containing 1.0 mol% CuO sintered at 925°C for 10 h, as shown in Fig. 4.3a. However, the grain size decreased for the specimen sintered at 975°C (see Fig. 4.3b). A small amount of the liquid phase was considered to be formed for the specimens sintered at 925°C, and this liquid phase aided the densification and grain growth to thereby produce a large-grained microstructure. However, for the

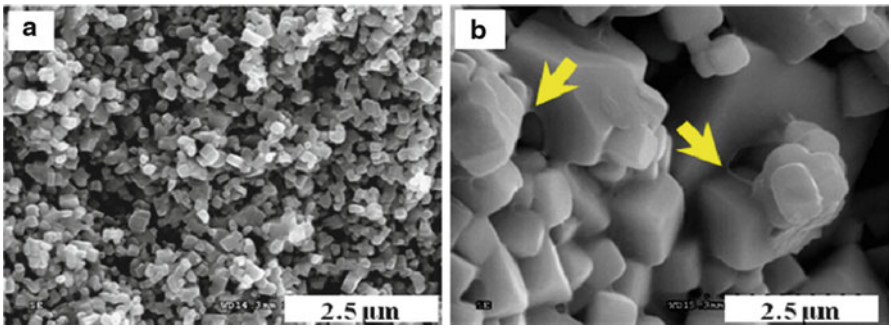

Fig. 4.1 SEM images of (**a**) pure 0.95NKN-0.05BT ceramics and (**b**) 0.95NKN-0.05BT ceramics containing 1.0 mol% of CuO sintered at 950°C for 10 h [12]

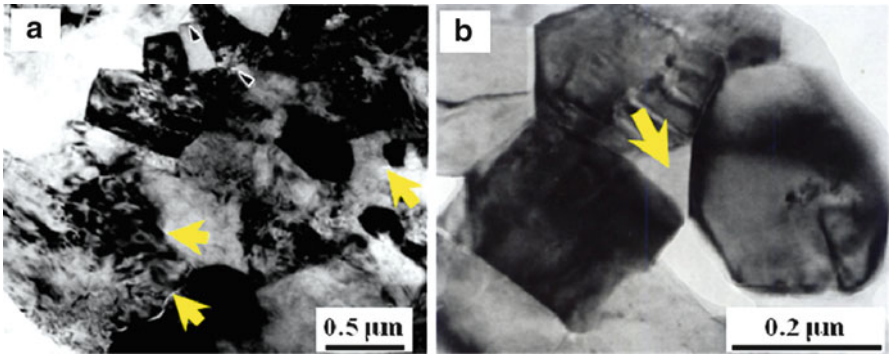

Fig. 4.2 TEM bright field image of (**a**) the 0.95NKN-0.05ST ceramic containing 5.0 mol% CuO and (**b**) the 0.95NKN-0.05CT ceramic containing 1.0 mol% CuO (The liquid phase, indicated by the *arrows*, existed in the grain boundary of the specimens) [13, 14]

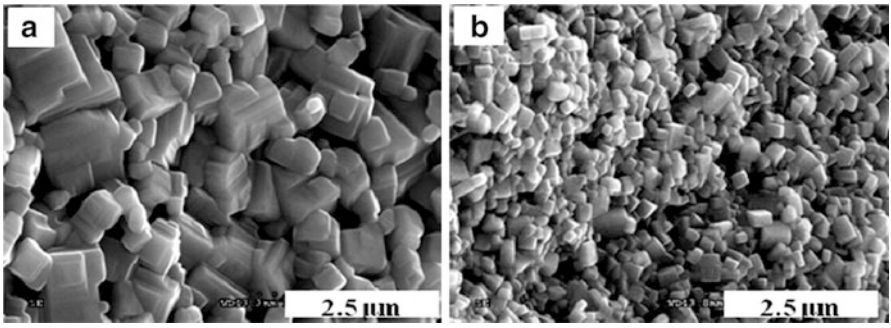

Fig. 4.3 SEM images of the fracture surface of 0.95NKN-0.05BT ceramics containing 1.0 mol% of CuO sintered at (**a**) 925°C (**b**) 975°C for 10 h[12]

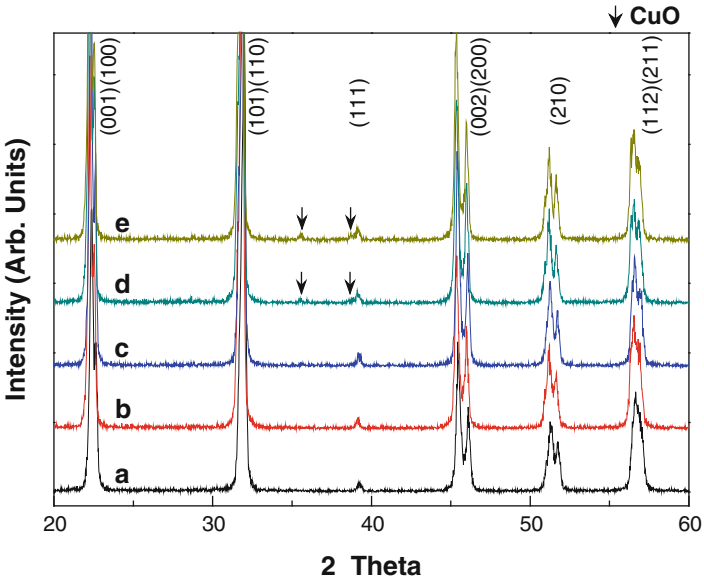

Fig. 4.4 XRD patterns of the NKN ceramics containing (**a**) 0.0, (**b**) 0.5, (**c**) 1.0, (**d**) 1.5, (**e**) 3.0 mol% of CuO sintered at 960°C for 10 h [15]

specimens sintered at 975°C, a large amount of the liquid phase was expected to be formed. Moreover, many grains can grow abnormally from the beginning and then impinge upon each other at the early stage of growth, thereby preventing grain growth and producing a microstructure with small grains. The small grain size of the specimens sintered at 975°C could be attributed to the increased liquid phase. Similar results were also observed in the NKN and 0.95NKN-0.05ATiO_3 (A = Sr and Ca) ceramics [13, 14]. Therefore, it can be concluded that the increased sinterablity and grain growth that occurred in the CuO-added NKN-based ceramics sintered at approximately 950°C were explained by the liquid phase sintering mechanism.

Piezoelectric Properties of the CuO-Added NKN-based Ceramics

A homogeneous orthorhombic NKN phase was well developed without a second phase when the amount of CuO addition was $\leq$1.0 mol%, as shown in Fig. 4.4 [15]. However, when the CuO content exceeded 1.0 mol%, peaks for the CuO second phase indicated by the arrows, were observed. This indicates that only a small amount of Cu^{2+} ions enter the NKNC matrix. Moreover, when a small amount of CuO was added, the Curie temperature (T_c) slightly increased from 400 to 406°C for the 2.0 mol% CuO-added NKNC, as shown in Fig. 4.5. However, the T_c did not

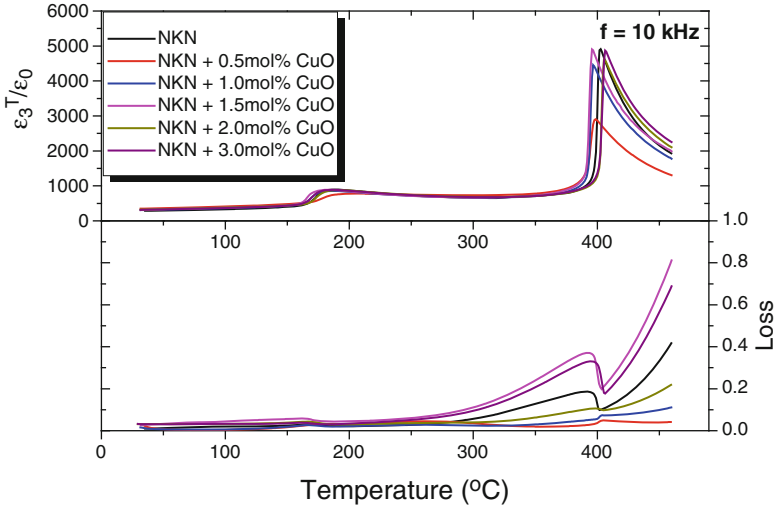

Fig. 4.5 Temperature dependence of $\varepsilon_3^T/\varepsilon_0$ and dielectric loss for the NKNC sintered at 1,070°C for 2 h and the NKN + x mol% CuO ceramics, with $0.5 \leq x \leq 3.0$, sintered at 960°C for 2 h [15]

increase further as the CuO addition increased, indicating that only a small amount of Cu ion was incorporated into the NKNC matrix. Since the radius of the Cu^{2+} ion (0.73 Å) is similar to that of the Nb^{5+} ion (0.64 Å), the Cu^{2+} ion is thought to replace the Nb^{5+} ions and transform the NKNCs into hard ceramics. Figure 4.6 shows the polarization versus electric field (P-E) hysteresis curves of the NKNC sintered at 1,070°C for 2 h and of the CuO-added NKNCs sintered at 960°C for 2 h. The coercive field (E_c) of the NKNC was approximately 1.05 kV/mm and slightly increased to 1.24 kV/mm as the CuO content increased to 1.5 mol% CuO-added NKNC, indicating that the NKNC was transformed into a hard piezoelectric ceramic with the CuO addition. Similar results were also obtained in the CuO-added 0.95NKN-0.05ATiO$_3$ (A = Ba, Sr and Ca) ceramics.

The relative density of the NKNC sintered at 960°C was very low, but considerably increased as the CuO content increased and reached a saturated value of 92.0% of the theoretical value for the specimen containing 1.5 mol% CuO, as shown in Fig. 4.7. The k_p and $\varepsilon_3^T/\varepsilon_0$ values increased as the CuO content increased in a trend that was similar to that of the relative density (see Fig. 4.7). The Q_m value also increased to 844 as the CuO content increased to 1.5 mol% CuO for the NKNCs. The Q_m value of the NKNC sintered at 1,070°C was low, approximately 100, despite its high relative density of 95%. Therefore, the increased Q_m value may have been due to the hardening effect of the Cu^{2+} ions. Similar results were obtained for the CuO-added $(Na_{0.5}K_{0.5})(Nb_{0.97}Sb_{0.03})O_3$[16] and 0.95NKN-0.05ATiO$_3$ (A = Ba, Sr and Ca) ceramics, as listed in Table 4.1.

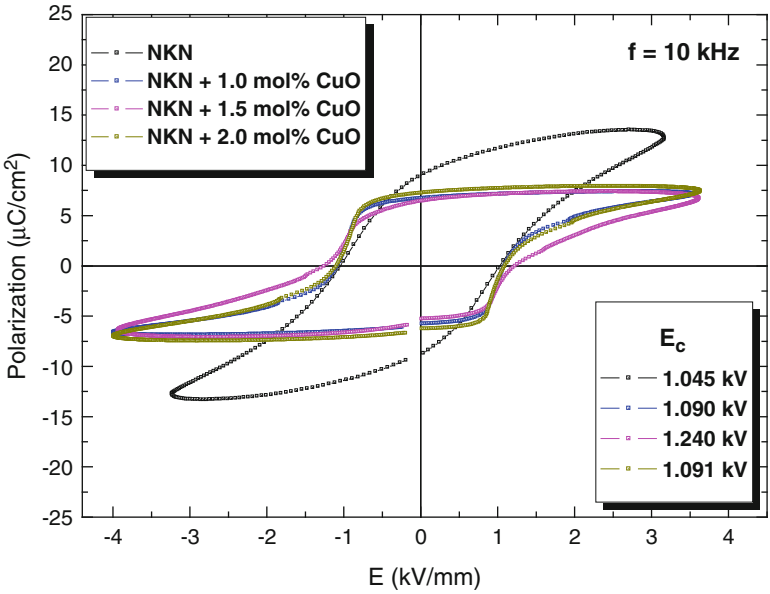

Fig. 4.6 Polarization vs. electric field curves for the NKNC sintered at 1,070°C for 2 h and the NKN + x mol% CuO ceramics, with $0.5 \leq x \leq 3.0$, sintered at 960°C for 2 h [15]

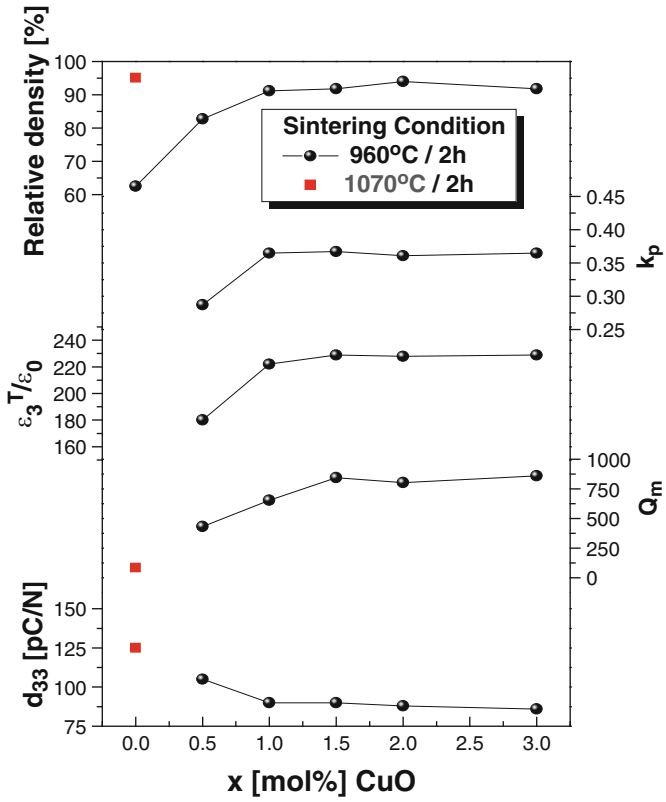

Fig. 4.7 Variations of the relative density, d_{33}, k_p, $\varepsilon_3^T/\varepsilon_0$, and Q_m values for the NKNCs sintered at 1,070°C for 2 h and the NKN + x mol% CuO ceramics, with $0.0 \leq x \leq 3.0$ sintered at 960°C for 2 h.[15]

Table 4.1 Relative density, k_p, d_{33}, $\varepsilon_3^T/\varepsilon_0$, Q_m, and phase angle values of the CuO-added $(Na_{0.5}K_{0.5})(Nb_{0.97}Sb_{0.03})O_3$, and 0.95NKN-0.05ATiO$_3$ (A = Ba, Sr, and Ca) ceramics sintered at 950 and 960°C for various times [12–14, 16]

Composition	x	Relative density (%)	k_p	d_{33}(pC/N)	$\varepsilon_{33}^T/\varepsilon_0$	Q_m	Phase angle (degree)
NK($N_{0.97}S_{0.03}$)	0	72.2					
+ xmol% CuO	0.5	89.8	0.38	122	385	371	85.7
960°C/8 h	1.0	94.2	0.40	111	315	1,256	89.0
	2.0	94.9	0.41	111	324	1,333	89.3
	3.0	94.7	0.39	107	305	1,131	88.6
	5.0	94.3	0.36	106	363	546	85.5
0.95NKN-	0.3	59.7	0.21	180	497	41	
0.05BT +	0.6	85.1	0.31	185	885	129	
x mol% CuO	1.0	94.5	0.37	230	1,148	183	
950°C/10 h	2.0	94.2	0.36	225	1,206	186	
	3.0	95.6	0.36	215	1,178	213	
	4.0	95.3	0.36	215	1,194	189	
	10.0	94.3	0.30	185	1,179	160	
0.95NKN-	0	55					
0.05CT +	0.5	84	0.26	145	787	137	
x mol% CuO	1.0	93.2	0.38	185	1,108	322	
960°C/10 h	1.5	94.9	0.37	185	1,100	316	
	2.0	95.4	0.37	200	1,173	253	
	4.0	90	0.33	195	949	231	
0.95NKN-	0	64.2	0.20	150			
0.05ST +	0.5	85.3	0.23	140	1,266	90	
x mol% CuO	1	95.9	0.31	196	1,281	234	
960°C/10 h	1.5	96	0.35	200	1,235	286	
	2	94.2	0.27	170	1,357	180	
	5	96	0.31	184	1,267	38	

4.2.2 Low Temperature Sintering of the ZnO and CuO Co-doped and V_2O_5-Added NKNCs

Low Temperature Sintering of the ZnO and CuO Co-doped NKNCs

The 1.5 mol% CuO-added NKNC ($NKNC_{1.5}C$) sintered at 900°C exhibited a porous microstructure with small grains, as shown in Fig. 4.8a [17]. However, when a small amount of ZnO was added to the $NKNC_{1.5}C$, a dense microstructure developed and some grains were abnormally grown, as indicated by the arrows in Fig. 4.8b. The liquid phase was observed in the ZnO-added $NKNC_{1.5}C$, as shown in Fig. 4.8c. According to the EDS analysis, the liquid phase contains a large amount of Cu ions and a small amount of Zn ions, as listed in Table 4.2. Therefore, CuO is a major component of the liquid phase and the incorporation of Zn ions in the liquid phase decreased its melting temperature. The transition temperatures for the orthorhombic to tetragonal (T_{O-T}) and tetragonal to cubic (T_C) transitions of the $NKNC_{1.5}C$ were 200 and 393°C, respectively, and they did not change with the increasing additions of ZnO,

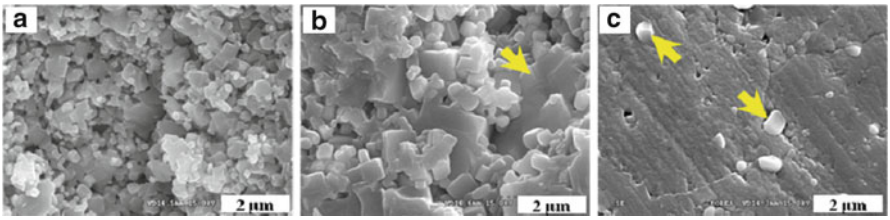

Fig. 4.8 SEM images of the fractured surface of $NKNC_{1.5}C + x$ mol% ZnO ceramics: (**a**) $x = 0.0$, (**b**) $x = 0.5$ and (**c**) polished surface of 1.5 mol% ZnO-added $NKNC_{1.5}C$ sintered at 900°C for 2 h. In (**b**) the *arrow* indicates abnormally grown grain, and (**c**) the *arrows* indicate a second phase at the grain boundaries of the specimens [17]

Table 4.2 Chemical composition of the matrix and the liquid phase of the 1.5 mol% ZnO-added $NKNC_{1.5}C$ sintered at 900°C for 2 h.[17]

Element	Matrix (at. %)	Liquid Phase (at. %)
Na	22.47	13.75
K	26.35	16.90
Cu	0.35	29.15
Zn	0.51	6.59
Nb	50.32	33.61
Total	100.00	100.00

as shown in Fig. 4.9a. The remnant polarization of the $NKNC_{1.5}C$ sintered at 900°C was low at approximately 3.1 μC/cm^2, and it increased to 14.4 μC/cm^2 for the specimen containing 0.5 mol% ZnO, as shown in Fig. 4.9b, which is probably due to the increased density. The E_c of the specimen also increased with the addition of ZnO (see Fig. 4.9b). In particular, the 0.5 mol% ZnO-added $NKNC_{1.5}C$ exhibited a high E_c of 2.1 kV/mm, which was higher than that of the $NKNC_{1.5}C$ sintered at 960°C (1.2 kV/mm).

The relative density of all the $NKNC_{1.5}C$ considerably increased to a saturated value of 95% of the theoretical density with the addition of 0.5 mol% ZnO for the specimens sintered at 900 and 920°C, as shown in Fig. 4.10. However, the relative densities of all the specimens sintered at 880°C were very low, which suggested melting temperatures of approximately 900°C for the liquid phase formed in the ZnO-added $NKNC_{1.5}C$. The k_p and Q_m values increased with the addition of ZnO due to the increased density. High k_p and Q_m values of 0.37 and 755, respectively, were obtained for the specimen containing 1.0 mol% ZnO, despite the low sintering temperature of 900°C. In particular, the 1.0 mol% ZnO-added $NKNC_{1.5}C$ sintered at 920°C exhibited a very high Q_m value of 1,000, which is higher than those of the $NKNC_{1.5}C$ ceramics with high densities sintered at 960°C. All the ZnO-added specimens sintered at 900 and 920°C exhibited similar d_{33} values, ranging between 100 and 110 pC/N. The $\varepsilon_3^T/\varepsilon_0$ values of the $NKNC_{1.5}C$ sintered at 900°C were small, due to their low density; these value slightly increased with the addition of ZnO, but their variation with ZnO was not significant, ranging between 268 and 327 for the specimens sintered at 900°C.

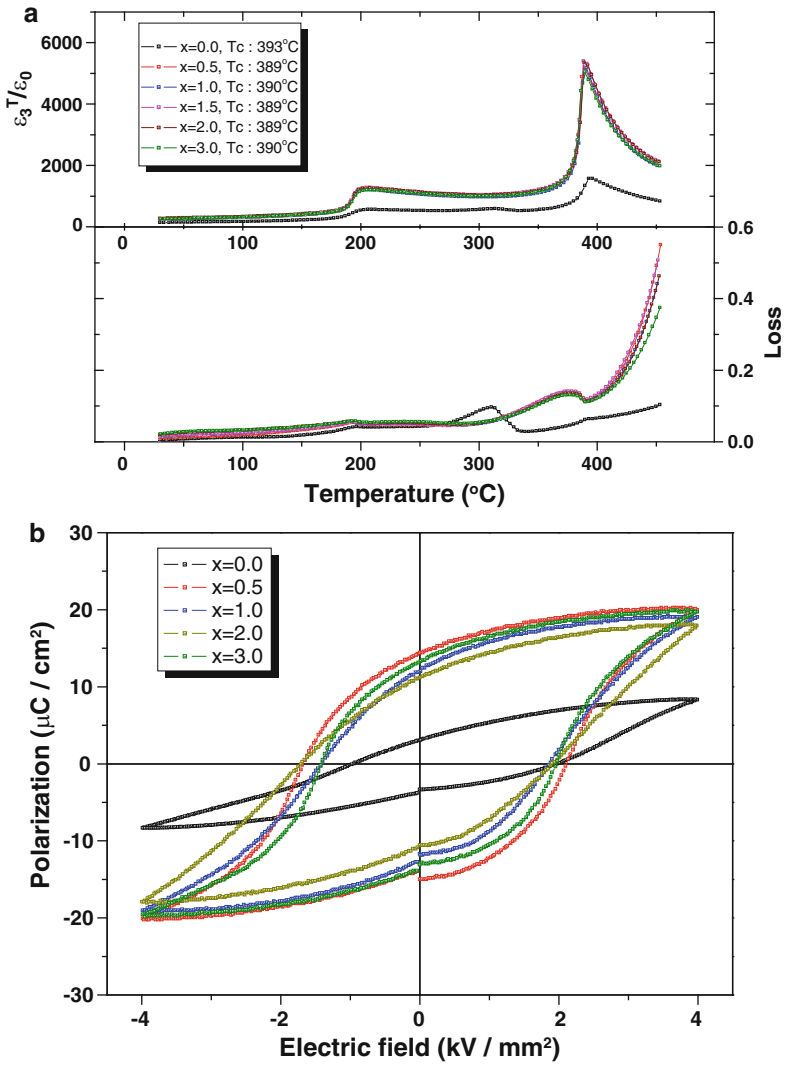

Fig. 4.9 (**a**) Variations in the $\varepsilon_3^T/\varepsilon_0$ and dielectric loss according to temperature and (**b**) polarization vs. electric field (P-E) hysteresis curves for the $NKNC_{1.5}C + x$ mol% ZnO ceramic with $0.0 \leq x \leq 3.0$ sintered at 900°C for 2 h [17]

Low Temperature Sintering of the V_2O_5-Added NKNCs

When a small amount of the Nb_2O_5 was substituted by V_2O_5, all the NKN specimens were well sintered but the KVO_3 and $NaNbO_3$ secondary phases were formed.[18] Since the melting temperature of the KVO_3 phase is 510°C, it melted during the sintering and assisted the densification of the specimen.[19, 20] It is also possible that the V_2O_5 melted during the sintering and that the KVO_3 and $NaNbO_3$

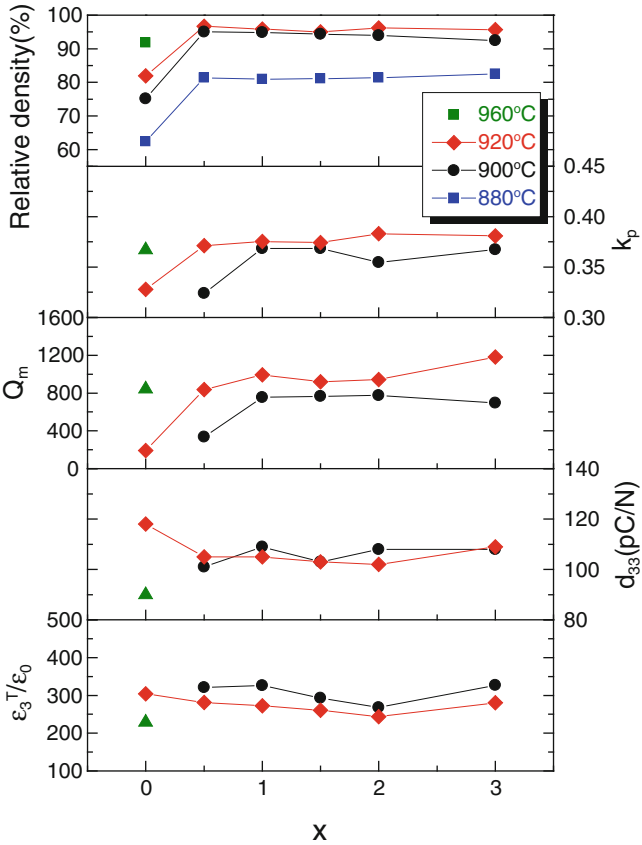

Fig. 4.10 Relative density, d_{33}, k_p, Q_m, and $\varepsilon_3^T/\varepsilon_0$ values of the NKNC + x mol% ZnO ceramics, with $0.0 \leq x \leq 3.0$, sintered at various temperatures for 2 h [17]

second phases formed during the cooling. The T_c decreased from 400 to 328°C but T_{O-T} increased from 178 to 200°C with the addition of 3.0 mol% of V_2O_5. In addition, the V_2O_5-containing specimens exhibited a new transition peak at around 380°C, corresponding to the T_{O-T} of the $NaNbO_3$ ceramic [21].

The relative densities of the NKNCs reached a saturated value of 95% of the theoretical density for the specimens containing 7.0 mol% V_2O_5. The k_p value increased as the V_2O_5 content increased, exhibiting a maximum value of 32 for the specimen with 5.0 mol% V_2O_5. The variation of $\varepsilon_{33}^T/\varepsilon_0$ with the V_2O_5 content was similar to that of the relative density. The $\varepsilon_{33}^T/\varepsilon_0$ value of the specimen containing 5.0 mol% V_2O_5, which exhibited the maximum k_p value, was 245. The value of d_{33} also increased when V_2O_5 was increased from 1.0 to 3.0 mol%. However, the variation of d_{33} with V_2O_5 was negligible, ranging between 115 and 121 pC/N for the specimens containing more than 3.0 mol% V_2O_5 [22]. The maximum Q_m value of 232 was obtained for the specimen containing 5.0 mol% V_2O_5.

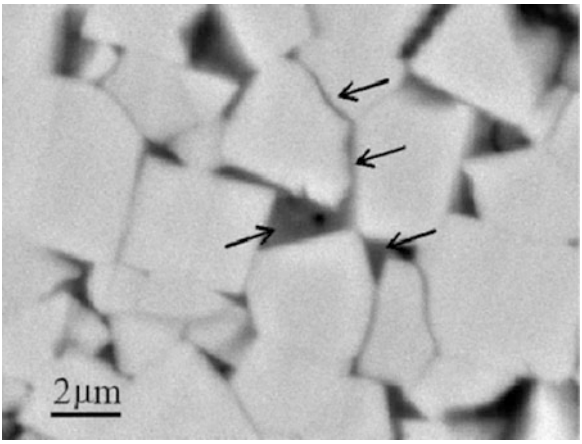

Fig. 4.11 Scanning electron microscope–BEI image of $K_{0.5}Na_{0.5}NbO$ (KNN) ceramics with 4 mass% alkaline germanate after sintering at 1,000°C for 2 h. The germanium-rich liquid phase around KNN matrix grains is marked with *arrows* [23]

4.2.3 Low Temperature Sintering of the NKNCs Using (K, Na)-Germanate, $LiBO_2$, or Li_2O Additives

Low Temperature Sintering of NKNCs Modified by (K, Na)-Germanate [23]

(K, Na)-germanate, which melts at around 700°C, was added to the NKNCs to reduce their sintering temperatures. The (K, Na)-germanate-added NKNCs were well sintered at 1,000°C. The germanium-rich liquid phase, which is shown in Fig. 4.11, was responsible for the densification of the NKNCs at 1,000°C. The 1.0 wt (K,Na)-germanate-modified NKNCs sintered at 1,000°C exhibited the high piezoelectric properties: $\varepsilon_{33}^{T}/\varepsilon_0 = 397$, tan $\delta = 0.02$, $d_{33} = 120$ pC/N, $k_p = 0.4$, and $Q_m = 77$. These values are comparable with the NKNCs sintered at 1,100°C.

Low temperature Sintering of NKN-Based Ceramics using a $LiBO_2$ Additive [24]

$LiBO_2$ is added to reduce the sintering temperature of the $(Li_{0.04}\ K_{0.52}Na_{0.44})(Nb_{0.84}Ta_{0.1}Sb_{0.06})O_3$ (LF4) ceramics because it has a low melting temperature of 845°C and addition of Li has been known to reduce the sintering temperature of NKN-based ceramics. The LF4 ceramics were well sintered at 950°C with a relative density of 95% due to the formation of the liquid phase during the sintering, as shown in Fig 4.12. However, the Li content in the LF4 changed the LF4 to a tetragonal phase, which degraded the piezoelectric properties of the LF4 ceramics. To avoid this problem, 2.0 mol% Na was added to the 3.0 wt $LiBO_2$-added LF4 ceramics.

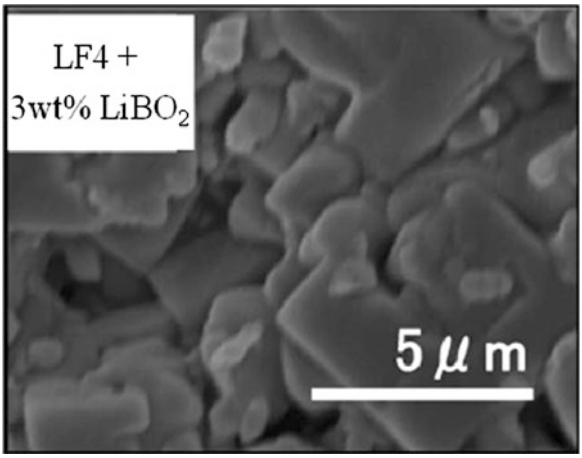

Fig. 4.12 SEM images of fracture surfaces of LF4 ceramics added with 3 wt% $LiBO_2$ and sintered at 1,050°C [24]

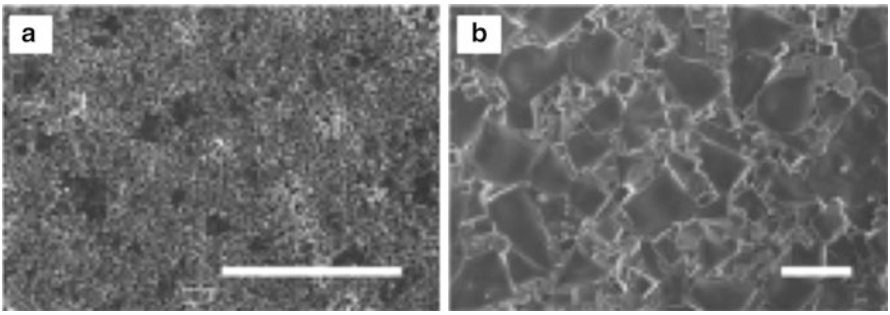

Fig. 4.13 Microstructures of Li_2O-excess $0.95(Na_{0.5}K_{0.5})NbO_3$–$0.05LiTaO_3$ samples sintered for 4 h in air at 1,000°C: (**a**) Li_2O-excess = 0 mol%, (**b**) Li_2O-excess = 1.0 mol%. Twenty micrometer—scale bars were included [25]

The specimen sintered at 950°C exhibited good piezoelectric properties: $\varepsilon_r = 723$, $d_{33} = 138$ pC/N, $k_{31} = 16.3$, and $T_c = 362$°C.

Low temperature Sintering of NKN-Based Ceramics using a Li_2O Additive [25]

The sintering temperature of the $0.95NKN\text{-}0.05LiTaO_3$ (NKN-5LT) ceramics was lowered to 1,000°C by adding Li_2O as a sintering aid. The NKN-5LT ceramics sintered at 1,000°C consisted of mostly submicrometer-sized equiaxed grains, as shown in Fig. 4.13a. When Li_2O was added to the NKN-5LT ceramics, the driving

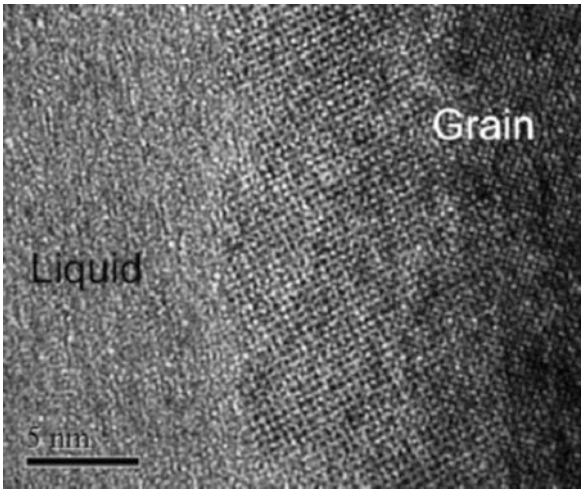

Fig. 4.14 A high-resolution transmission electron microscopy image of the junction area of $(1-x)(Na_{0.535}\ K_{0.48})NbO_3$–$xLiNbO_3$ ($x = 0.08$) sintered at 950°C for 1 h, showing the presence of liquid phase embedded in the grain matrix [26]

force for the rapid grain growth decreased, leading to a microstructure consisting of abnormally grown grains, as shown in Fig. 4.13b. Moreover, 1.0 mol% Li_2O excess NKN-5LT ceramics sintered at 1,000°C for 4 h exhibited good piezoelectric properties of $k_p = 0.37$ and $d_{33} = 250$ pC/N.

4.2.4 Low Temperature Sintering of the NKN-Based Ceramics Using Excess Na_2O Additive

Low Temperature Sintering of the Li-Modified NKN Lead-Free Ceramics [26]

The addition of excess Na_2O could effectively reduce the sintering temperature of the Li-modified NKNCs to 950°C due to the formation of the liquid phase, as shown in Fig. 4.14. The liquid phase formed in these ceramics may be eutectic phases formed between any combination of A_2O (A = Li, Na, and K) and Nb_2O_5 or remnant carbonates A_2CO_3 (A = Li, Na, and K).

The $(1–x)(Na_{0.535}K_{0.48})NbO_3$-$xLiNbO_3$ ($x = 0.058 \sim 0.08$) ceramics sintered at 950°C for 1–8 h exhibited a dense microstructure with a uniform grain size distribution of 20–40 μm, as shown in Fig. 4.15a. However, when the Li content reaches as much as 8.5 mol%, a loose microstructure with reduced grain sizes of <20 μm was formed, as shown in Fig. 4.15b, probably due to the reduced amount of the liquid phase, indicating that the Li element is also relevant to the liquid phase. The density and grain sizes exhibited no significant changes during the long-time

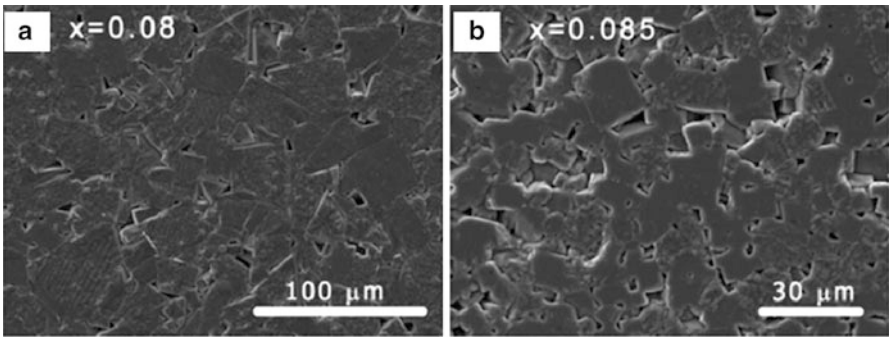

Fig. 4.15 Scanning electron micrographs of thermally etched surfaces of $(1-x)(Na_{0.535}K_{0.48})NbO_3$–$xLiNbO_3$ sintered at 950°C with different Li contents [26]

Table 4.3 Various properties of $(1-x)(Na_{0.535}K_{0.48})NbO_3$-$xLiNbO_3$ ceramics sintered at 950°C for 8 h with different Li contents [26]

Li Content (x)	ρ (g/cm^3)	d_{33} (pC/N)	k_p (%)
0.058	4.32	125	42.7
0.065	4.30	130	42.6
0.070	4.35	170	43.4
0.075	4.32	230	41.8
0.080	4.36	280	48.3
0.085	4.11	145	34.4
0.090	4.10	117	31.6

sintering, but the piezoelectric and ferroelectric properties were greatly influenced by the soaking time. Table 4.3 shows the density, d_{33} and k_p values of the $(1-x)(Na_{0.535}K_{0.48})NbO_3-xLiNbO_3$ ($x = 0.058 \sim 0.08$) ceramics sintered at 950°C for 8 h with different Li contents.

4.3 Low Temperature Sintering of the NKN-Based Ceramics Using SPS

SPS, which has a rapid heating rate and short soaking time, has been increasingly used to reduce the sintering temperature of NKN-based ceramics. The NKNCs were sintered at 920°C under 50 MPa, and subsequently annealed at 900°C for 4 h. The density of a specimen was 4.47 g/cm, which was 99% of the theoretical density. The grain sizes of this specimen were in the range of 200 ~ 500 nm, as shown in Fig. 4.16a [27]. The E_c and P_r of this specimen were 1.3 kV/mm and 6.49 μC/cm^2, respectively. The T_c, d_{33}, and k_p of this specimen were 395°C, 148 pC/N, and 38.9 %, respectively [27].

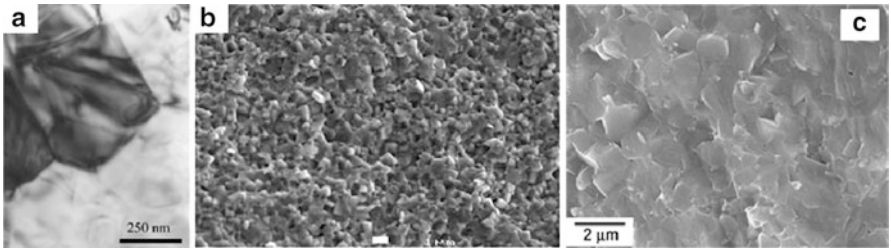

Fig. 4.16 (**a**) Transmission electron microscopy micrographs of the $Na_{0.5}K_{0.5}NbO_3$ ceramics spark plasma sintered at 920°C for 5 min and then annealed at 900°C for 4 h, (**b**) Scanning electron microscopy (SEM) image of fractured surface of the NKNCs consolidated at 850°C for 5 min and (**c**) SEM image of SPS-processed NKL_xNT ceramics with $x = 0.05$ [27–29]

Commercial NKN powders with an initial particle size of ~ 260 nm were consolidated by SPS at 850°C under a pressure of 100 MPa and subsequently annealed at 750°C for 4 h. This specimen also had a dense microstructure with an average grain size of ~ 0.6 μm, as shown in Fig. 4.16b. Moreover, this specimen exhibited high E_c, P_r and d_{33} values of 10 kV/mm, 30 μC/cm^2 and 146 pC/N respectively [28]. The improved ferroelectric properties were explained by the homogeneous, dense, and submicron grained microstructure.

Dense and fine-grained $(Na_{0.535}K_{0.48})_{1-x}$–$Li_x(Nb_{0.8}Ta_{0.2})O_3$ ($x = 0.02 \sim 0.08$) (abbreviated as NKL_xNT) ceramics were also fabricated by SPS at temperatures between 850 and 900°C, followed by postannealing in air at 900°C. These specimens had a dense microstructure with submicron-sized grains, as shown in Fig. 4.16c. In particular, The NKL_xNT ceramic with $x = 0.05$ exhibited good piezoelectric properties: $d_{33} = 243$ pC/N, $k_p = 46.1\%$, and $Q_m = 85$ [29]. In addition, the NKL_xNT ceramics prepared by SPS had a better fracture strength than of that prepared by normal sintering, due to the enhanced densification and refined microstructure.

4.4 Concluding Remarks

The NKN-based lead-free ceramics have been extensively investigated because of their high piezoelectric properties and high Curie temperatures. Moreover, the NKN-based ceramics have generally been sintered at high temperatures (≥1,050°C), which causes the Na_2O to evaporate during the sintering process, resulting in the formation of a liquid phase, which assists the densification of the specimens. Na_2O evaporation, which occurs at temperatures above 1,000°C, decreases the polling efficiency and considerably changes the microstructure and eventually degrades the piezoelectric properties of the NKN-based ceramics. Therefore, it is necessary to develop a method to decrease the sintering temperature of the NKNCs to below 1,000°C in order to obtain stable piezoelectric properties.

In addition, sintering of the NKN-based ceramics at low temperatures also facilitates their use in multilayers. The addition of CuO reduced the sintering temperatures of the NKN-based ceramics to approximately 950°C. The Cu^{2+} ions transformed the NKNCs to good, hard piezoelectric materials. The sintering temperature of the NKN-based ceramics was further reduced to 900°C by the co-doping of CuO and ZnO, or by the addition of V_2O_5. The addition of $LiBO_2$ or excess Na_2O decreased the sintering temperature of the NKN-based ceramics to 950°C and 1.0 mol% Li_2O excess NKN-5LT ceramics were sintered at 1,000°C. The SPS sintering can also reduce the sintering temperature to below 900°C. Therefore, even though more investigations into the low temperature sintering of NKN-based ceramics are needed, the methods to sinter the NKN-based ceramics at approximately 900°C have been established. However, for the application to multilayer devices, the interaction between NKN-based ceramics and metal electrode should be investigated. Moreover, the tape casting processes for NKN-based ceramics need to be developed.

References

1. Jaffe B, Cook WR, Jaffe H (1971) Piezoelectric Ceramics. New York, Academic, p 140
2. Saito Y, Takao H, Tani T, Nonoyama T, Takatomi K, Homma T, Nagaya T, Nakamura M (2004) Lead-free piezoceramics. Nature 432:84–86
3. Guo Y, Kakimoto K, Oshato H (2004) Phase transition behavior and piezoelectric properties of $(Na_{0.5}\ K_{0.5})NbO_3$-$LiNbO_3$ ceramics. Appl Phys Lett 85:4121–4123
4. Zang GZ, Wang JF, Chen HC, Su WB, Wang CM, Qi P, Ming BQ, Du J, Zheng LM, Zhang S, Shrout TR (2006) Perovskite $(Na_{0.5}\ K_{0.5})_{1\text{-}x}(LiSb)_xNb_{1\text{-}x}O_3$ lead-free piezoceramics. Appl Phys Lett 88(212908):1–3
5. Park HY, Ahn CW, Song HC, Lee JH, Nahm S, Uchino K, Lee HG, Lee HJ (2006) Microstructure and piezoelectric properties of $0.95(Na_{0.5}\ K_{0.5})NbO_3$-$0.05BaTiO_3$ ceramics. Appl Phys Lett 89(062906):1–3
6. Matsubara M, Yamaguchi Y, Sakamoto W, Kikuta K, Yogo T, Hirano S (2005) Processing and piezoelectric properties of lead-free (K, Na)(Nb, Ta)O3 ceramics. J Am Ceram Soc 88:1190–1196
7. Matsubara M, Kikuta K, Hirano S (2005) Piezoelectric properties of $(K_{0.5}Na_{0.5})\ (Nb_{1-x}Ta_x)O_3$-$K_{5.4}CuTa_{10}O_{29}$ ceramics. J Appl Phys 97:114105–114111
8. Park SH, Ahn CW, Nahm S, Song JS (2004) Microstructure and piezoelectric properties of ZnO-added $(Na_{0.5}K_{0.5})NbO_3$ ceramics. Jpn J Appl Phys 43:L1072–L1074
9. Song HC, Cho KH, Park HW, Ahn CW, Nahm S, Uchino K, Lee HG (2007) Microstructure and piezoelectric properties of $(1 - x)(Na_{0.5}K_{0.5})NbO_3$-$xLiNbO_3$ ceramics. J Am Ceram Soc 90:1812–1816
10. Zhen Y, Li JF (2006) Normal sintering of (K, Na)NbO3-based ceramics: influence of sintering temperature on densification, microstructure, and electrical properties. J Am Ceram Soc 89:3669–3675
11. Ahn C-W, Park H-Y, Nahm S, Uchino K, Lee H-G, Lee H-J (2007) Structural variation and piezoelectric properties of $0.95(Na_{0.5}K_{0.5})NbO_3$-$0.05BaTiO_3$ ceramics. Sensors and Actuat A 136:255–260
12. Park HY, Ahn CW, Cho K-H, Nahm S, Lee HG, Kang H-W, Lee D-H, Park K-S (2007) Low temperature sintering and piezoelectric properties of CuO-added $0.95(Na_{0.5}\ K_{0.5})NbO_3$-$0.05BaTiO_3$ ceramics. J Am Ceram Soc 90:4066–4069

13. Park S-J, Park H-Y, Cho K-H, Nahm S, Lee HG, Lee D-H, Choi B-H (2008) Effect of CuO on the sintering temperature and piezoelectric properties of lead-free $0.95(Na_{0.5}\ K_{0.5})NbO_3$-$0.05CaTiO_3$ ceramics. Mater Res Bull 43:3580–3586
14. Seo I-T, Cho K-H, Park H-Y, Park S-J, Choi M-K, Nahm S, Lee HG, Kang H-W, Lee H-J (2008) Effect of CuO on the sintering and piezoelectric properties of $0.95(Na_{0.5}\ K_{0.5})NbO_3$-$0.05SrTiO_3$ lead-free piezoelectric ceramics. J Am Ceram Soc 91:3955–3960
15. Park HY, Choi J-Y, Cho K-H, Nahm S, Lee HG, Kang H-W (2008) Effect of CuO on the sintering temperature and piezoelectric properties of $(Na_{0.5}\ K_{0.5})NbO_3$ lead-free piezoelectric ceramics. J Am Ceram Soc 91:2374–2377
16. Park H-Y, Seo I-T, Choi M-K, Nahm S, Lee HG, Kang H-W, Choi B-H (2008) Microstructure and piezoelectric properties of the Cuo-added $(Na_{0.5}\ K_{0.5})(Nb_{0.97}Sb_{0.03})O_3$ lead-free piezoelectric ceramics. J Appl Phys 104:034103
17. Park H-Y, Seo I-T, Choi J-H, Nahm S, Lee HG (2010) Low-temperature sintering and piezoelectric properties of $(Na_{0.5}\ K_{0.5})NbO_3$ lead-free ceramics. J Am Ceram Soc 93:36–39
18. Seo I-T, Park H-Y, Dong NV, Choi M-K, Nahm S, Lee HG, Choi B-H (2009) Microstructure and piezoelectric properties of (Na0.5 K0.5)NbO3 lead-free piezoelectric ceramics with V2O5 addition. IEEE Trans Ultrason Ferroelectr Freq Control 56:2337
19. Holtzberg F, Reisman A, Berry M, Berkenblit M (1956) Reactions of the group VB pentoxides with alkali oxides and carbonates. 11. Phase diagram of the system K_2CO_3-V_2O_5. J Am Chem Soc 78:1536–1540
20. Irle E, Blachnik R, Gather B (1991) The phase diagrams of Na_2O and K_2O with Nb_2O_5 and the ternary system Nb_2O_5-Na_2O-Yb_2O_3. Thermochim Acta 179:157–169
21. Shirane G, Newnham R, Pepinsky R (1954) Dielectric properties and phase transitions of NaNbO3 and (Na, K)NbO3. Phys Rev 96:581–588
22. Zuo R, Rodel J (2006) Sintering and electrical properties of lead-free $Na_{0.5}\ K_{0.5}NbO_3$ piezoelectric ceramics. J Am Ceram Soc 89:2010–2015
23. Bernard J, Bečan A, Rojac T, Holc J, Malič B, Kosec M (2008) Low-temperature sintering of $K_{0.5}Na_{0.5}NbO_3$ ceramics. J Am Ceram Soc 91:2409–2411
24. Sasaki R, Suzuki R, Uraki S, Kakemoto H, Tsurumi T (2008) Low-temperature sintering of alkaline niobate based piezoelectric ceramics using sintering aids. J Ceram Soc Jpn 116:1182–1186
25. Kim MS, Jeong SJ, Song JS (2007) Microstructure and piezoelectric properties in the Li_2O-Excess $0.95(Na_{0.5}\ K_{0.5})NbO_3$-$0.05LiTaO_3$ Ceramics. J Am Ceram Soc 90:3338–3340
26. Wang K, Li JF (2010) Low-temperature sintering of Li-modified (K, Na)NbO_3 lead-free ceramics: sintering behavior, microstructure, and electrical properties. J Am Ceram Soc 93:1101–1107
27. Li JF, Wang K, Zhang BP, Zhang LM (2006) Ferroelectric and piezoelectric properties of fine-grained $Na_{0.5}\ K_{0.5}NbO_3$ lead-free piezoelectric ceramics prepared by spark plasma sintering. J Am Ceram Soc 89:706–709
28. Eriksson M, Yan H, Nygren M, Reece MJ, Shen Z (2010) Low temperature consolidated lead-free ferroelectric niobate ceramics with improved electrical properties. J Mater Res 25:240–247
29. Shen ZY, Li JF, Wang K, Xu S, Jiang W, Deng Q (2010) Electric and mechanical properties of fine-grained Li/Ta-modified (Na, K)NbO3-based piezoelectrics prepared by spark plasma sintering. J Am Ceram Soc 93:1378–1383

Chapter 5
Lead-Free KNN-Based Piezoelectric Materials

Ahmad Safari and Mehdi Hejazi

5.1 Polycrystalline KNN-Ceramics

5.1.1 Pure $K_{1-x}Na_xNbO_3$ System

Sodium potassium niobate with the general chemical formula of $K_{1-x}Na_xNbO_3$ (KNN hereafter) is one of the most attractive lead-free materials which have been extensively investigated throughout the last decade.

KNN is a solid solution of $NaNbO_3$ (NN) and $KNbO_3$ (KN) compounds. A KNN phase diagram comprised of the tetragonal, orthorhombic, and monoclinic ferroelectric regions and an orthorhombic antiferroelectric region is depicted in Fig. 5.1.

The phase transitions and variations of dielectric properties of pure KNN vs. temperature resemble those of $BaTiO_3$ (BT), but every transition occurs at a higher temperature compared to BT ceramics. Figure 5.2 displays variations of the dielectric constant and loss tangent of KNN over a wide temperature range, with the orthorhombic lattice at room temperature.

The substitution of K ions in pure KN with Na ions, does not change the phase transition temperatures (except for the orthorhombic-rhombohedral transition), as demonstrated in Fig. 5.1. Two nearly horizontal lines can be noted at about 220°C and 420°C showing that the phase transition temperatures (i.e., transition from orthorhombic to tetragonal phase and transition from ferroelectric tetragonal to paraelectric cubic phase) are almost independent of chemical composition. The antiferroelectric phase is found in NN-rich compositions since NN is an orthorhombic antiferroelectric itself (with unit cell dimensions of $a = 5.512^{o}$A, $b = 5.577^{o}$A, $c = 15.54^{o}$A) [1]. NN shows metastable ferroelectricity upon the application of a

A. Safari (✉) • M. Hejazi
Glenn Howatt Electroceramics Laboratory, Department of Materials Science and Engineering, Rutgers, The State University of New Jersey, Piscataway, NJ, USA
e-mail: safari@rci.rutgers.edu; mmhejazi@eden.rutgers.edu

S. Priya and S. Nahm (eds.), *Lead-Free Piezoelectrics*,
DOI 10.1007/978-1-4419-9598-8_5, © Springer Science+Business Media, LLC 2012

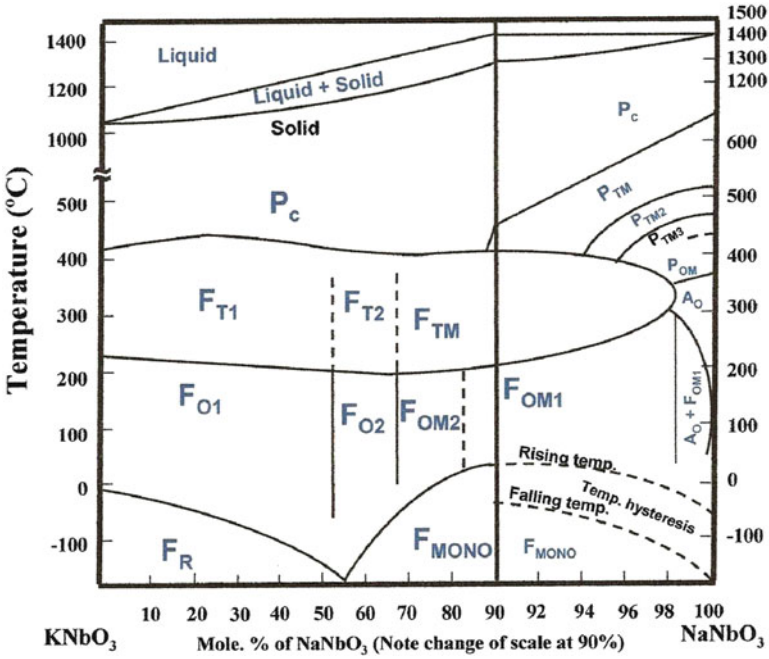

Fig. 5.1 Phase diagram of binary $KNbO_3$–$NaNbO_3$ (KNN) system. F, P, and A stand for ferroelectric, paraelectric, and antiferroelectric phases, respectively. C, T, O, R, and MONO denote cubic, tetragonal, orthorhombic, rhombohedral, and monoclinic structures [1]

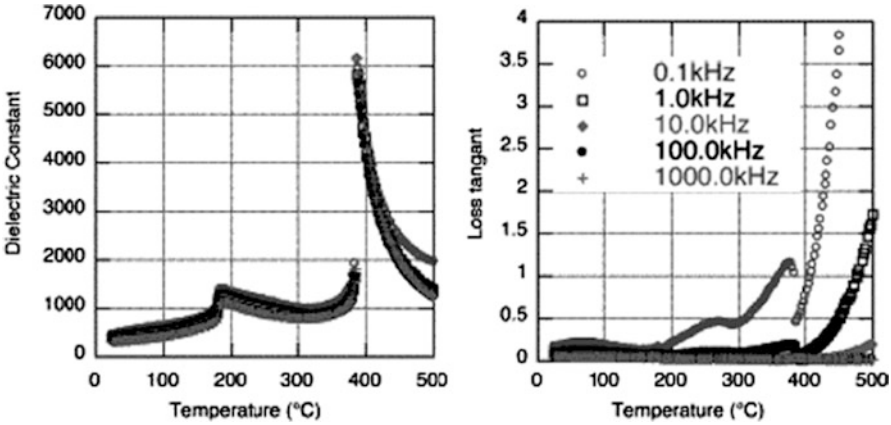

Fig. 5.2 Variations of dielectric constant and loss tangent vs. temperature in stoichiometric $K_{0.5}Na_{0.5}NbO_3$ ceramic [9]

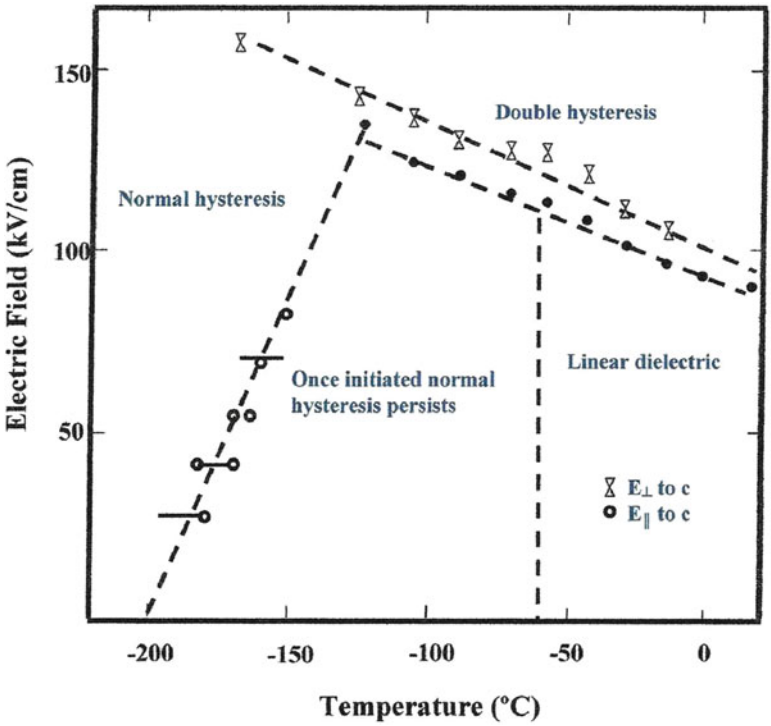

Fig. 5.3 Effect of applying DC electric field on electrical behavior of $NaNbO_3$ single crystals. Metastable field-induced ferroelectricity is observed at adequately high applied fields and low temperatures [1]

very high electric field. Two field-enforced phases with a rhombohedral and a monoclinic structure showing normal hysteresis behavior also exist at low temperatures. Figure 5.3 summarizes the low temperature response of a NN single crystal to an applied DC electric field. The addition of KN to NN decreases the amount of the required field to stabilize the ferroelectric phase and hinders the formation of metastable secondary phases [1].

KN, on the other hand, is a perovskite ferroelectric material with an orthorhombic unit cell ($a = 5.697^{o}$A, $b = 3.971^{o}$A, $c = 5.721^{o}$A) at room temperature [2]. One of the problems associated with KN processing is difficulty in making a dense ceramic due to the volatility of K_2O at the sintering temperature and the formation of secondary phases. Figure 5.4 shows the permittivity-temperature behavior of a KN single crystal with a Curie point of 420°C. A KN crystal has a large thickness extension mode coupling factor ($k_t = 0.69$) along a certain crystallographic direction (49.5° from polar axis) [3]. Poled ceramics of KN show a relative permittivity of about 430 (at 1 MHz), dielectric loss of 2%, planar coupling coefficient (k_p) of 0.3, and polarization of 22 μC cm^{-2} [1, 4]. It has been suggested that leaching the calcined powder with a 2% K_2CO_3 solution, doping with Na, or adding $Bi_{0.5}Na_{0.5}TiO_3$ enhances the relative density, coupling factor, and mechanical quality factor of KN ceramics [1, 5, 6].

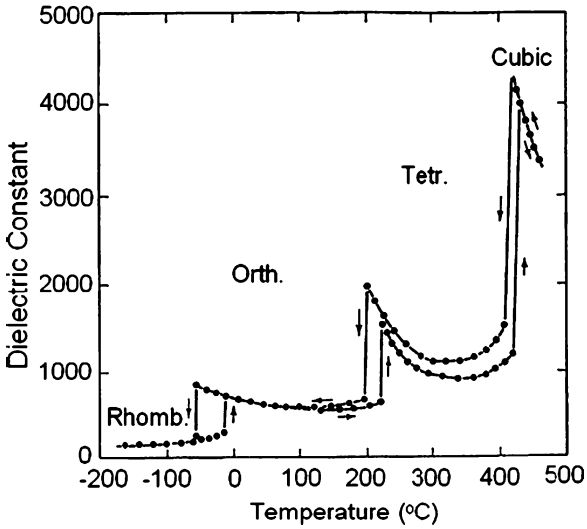

Fig. 5.4 Variation of dielectric constant vs. temperature (upon heating and cooling) in a $KNbO_3$ single crystal [1]

Table 5.1 Properties of a typical KNN ceramic compared with KN and NN compounds [10]

Material	T_C (°C)	ε_r	k_p (%)
KNN	400	230–475	23–40
KN	416–434	>1,000	15
NN	480	20–200	–

An in-depth study by D. Baker et al. showed that the classic KNN phase diagram needs a minor modification around the $K_{0.3}Na_{0.7}NbO_3$ composition since a phase coexistence region was identified for the monoclinic to tetragonal first order phase transition in a temperature range of 200–210°C [7].

It has been shown that a $K_{0.5}Na_{0.5}NbO_3$ composition has the highest piezoelectric properties among different compositions in a KN-NN system. Contrary to a PZT system, there is no evidence of the formation of an MPB (morphotropic phase boundary) in the vicinity of a $K_{0.5}Na_{0.5}NbO_3$ composition [8]. Deviation from a stoichiometric composition (K/Na ratio of 1) leads to the frequency dependence of the loss tangent and dielectric constant vs. temperature (dispersion phenomenon) [9].

Table 5.1 shows the piezoelectric and dielectric properties of a typical KNN ceramic along with its end member constituents [10].

5.1.2 Modified KNN Ceramics

KNN ceramics have been chemically modified to obtain high quality materials with higher piezoelectric response and more established properties. Many scientists have carried out extensive research to find binary, ternary, and quaternary KNN-based

systems with a possible MPB where the material shows an enhanced polarizability. However, it has been found that improvement in electromechanical properties is due to shifting the tetragonal-orthorhombic polymorphic phase transition (PPT) from 200°C down to around room temperature as well as the possible MPB in some compositions.

Some other additives have also been utilized as a sintering aid to ameliorate the density of KNN materials mainly through the formation of a liquid phase during the sintering stage without shifting the PPT or forming the MPB. Some of the most important dopants and modifiers belonging to the aforementioned categories will be briefly discussed here.

A relatively large d_{33} of 235 pC N^{-1} with a high k_p of 44% is reported for $(1 - x)$KNN–$x$$LiNbO_3$ (LN) ceramics at $x = 0.06$. A $K_3Li_2Nb_5O_{15}$ phase with tungsten bronze structure begins to appear at $x = 0.08$ and becomes dominant with the increasing content of $LiNbO_3$. The addition of Li causes T_C to shift to higher temperatures, and T_{T-O} to lower temperatures [11–13]. The MPB for the $(1 - x)$KNN–xLBT ($Li_{0.5}Bi_{0.5}TiO_3$) ceramics reported in the vicinity of $x = 0.02$ with a T_C of about 381°C where d_{33}, k_p, and ε_r (relative permittivity) were found to be 172 pC N^{-1}, 0.37, and 1,480, respectively [14]. The MPB in KNN-BNT ($Bi_{0.5}Na_{0.5}TiO_3$) ceramics exists in the vicinity of 3 mol% BNT with a d_{33} of 195 pC N^{-1} and k_p of 0.43 [15]. The addition of BNT decreases the grain size and improves the densification of KNN ceramics. The translucence was observed in relaxor 0.94KNN–0.06BNT ferroelectrics with T_m of about 320°C [16]. Modification of KNN ceramic with BZT ($Bi(Zn_{0.5}Ti_{0.5})O_3$) changes the room temperature structure from orthorhombic to rhombohedral ($0.01 \leq BZT \leq 0.03$) and increases the dielectric constant up to 1,200 while the rhombohedral-cubic phase transition temperature is about 390°C [17].

KNN-LT ($LiTaO_3$) and KNN-LS ($LiSbO_3$) ceramics are some of the other compositions of interest which then resulted to the advent of the KNN-LT-LS ternary system with noticeable properties ($d_{33} = 300$ pC N^{-1}) [18]. The higher electronegativities of Ta^{5+} and Sb^{5+} compared to Nb^{5+} increase covalency of the bonds and hence, the resultant Sp^3 hybridization of covalency over the ionic bond leads to further improvement in the piezoelectric properties of KNN-LT-LS. This composition has been shown to be a good candidate for high frequency transducer applications [19]. The MPB in KNN-LT ceramics was claimed to exist at about 5–6 mol% of LT (ε_r of 570, d_{33} ~200 pC N^{-1}, and k_p ~36%) [20]. Saito et al. also reported a dielectric constant of 1,255, d_{33} of 230 pC N^{-1}, and k_p of 50.5% for $\{(K_{0.5}Na_{0.5})_{0.97}Li_{0.03}\}(Nb_{0.8}Ta_{0.2})O_3$ ceramics [21]. Later on, Raman spectroscopy data provided direct evidence of coexistence of the tetragonal and orthorhombic phases at room temperature and the high properties for KNN-LT system was attributed to the shifting in transition temperatures not to the formation of the MPB [22]. It has been suggested that pre-reacting Nb and Ta to form a $(Nb_x,Ta_{1-x})_2O_5$ solid solution, is an effective way to decrease the compositional inhomogeneity in KNN-LT ceramics and to obtain improved and reproducible electrical properties [23]. The volatilization of the alkali metal elements during high temperature annealing of these ceramics results in the abnormal grain growth,

and the compositional segregation along with the formation of secondary phases with a tetragonal tungsten bonze structure [24]. The simultaneous addition of Li and Sb via $LiSbO_3$ also decreases T_{T-O} while not reducing T_C significantly. Shifting T_{T-O} to room temperature causes this material to show high properties particularly when the LS amount is 5.2 mol% with ε_r of 1,380, coupling factors of k_p ~50%, k_{33} ~62%, and k_{31} ~30%, and piezoelectric coefficients of d_{33} ~265 pC N^{-1} and d_{31} approximately −116 pC N^{-1}. The T_{T-O} was shifted from 195°C for pure KNN to 35°C in KNN-LS [25–28]. Relaxor ferroelectric behavior with the PPT around room temperature was reported in $0.982(K_{0.5}N_{0.5})NbO_3$–$0.018BiScO_3$ ceramics with d_{33}, k_p, T_C, Q_m, and ε_r values of 224 pC N^{-1}, 0.40, 331°C, 288, and 1,217, respectively [29].

Recently $(1 - x)(0.98K_{0.5}Na_{0.5}NbO_3$–$0.02LiTaO_3)$–$x(0.96Bi_{0.5}Na_{0.5}TiO_3$–$0.04BaTiO_3)$, ceramics prepared by the mixed oxide route were found to show an improved sintering behavior. There is coexistence of orthorhombic-tetragonal phases near room temperature in this composition which indicated the presence of a polymorphism behavior. The remnant polarization of 24 μC cm^{-2}, coercive field of 20 kV cm^{-1}, and d_{33} of 155 pC N^{-1} were obtained at $x = 0.02$ where T_C and T_{T-O} were reported to be about 340 and 25°C, respectively [30].

The relaxor-type behavior with broad dispersive variation of the relative permittivity with temperature was reported in the $(1 - x)K_{0.5}Na_{0.5}NbO_3$–$xSrTiO_3$ system with a, very high dielectric constant of about 3,000 at room temperature (at 1 kHz) for composition of $0.85K_{0.5}Na_{0.5}NbO_3$–$0.15SrTiO_3$ [31]. The combination of $SrTiO_3$ and $BiFeO_3$ enhances the piezoelectric performance and improves the temperature dependency of electromechaical properties in KNN-LN ceramics [32].

It has been proposed that the sinterability of materials with perovskite structure (with ABO_3 formula) can be enhanced by the formation of A-site vacancies [1] which can be created by either having excess B-site ions or substituting the A-site cations with an element of higher valence. For example, the incorporation of excess Nb^{+5} in the B-site or Mg^{+2} in the A-site improves the sinterability of KNN materials [33]. The substitution of Ca^{2+} and Sr^{2+} also improves densification and increases the permittivity and piezoelectric charge coefficient while decreasing both T_C and T_{T-O}. When KNN is doped with 0.5 mol% Mg^{2+}, transition temperatures stay the same [34]. Moreover, Ba^{2+} and Sr^{+2} can improve the planar coupling coefficient as well as the permittivity and the piezoelectric coefficient of KNN ceramics [35]. For high power applications where a high coercive field, high mechanical quality factor, and low loss tangent are needed to prevent the overheating of the part, Cu-doped KNN-LT-LS composition can be used. The addition of Cu^{2+} to KNN-LT-LS ceramics stabilizes the orthorhombic phase at room temperature by shifting the orthorhombic-tetragonal phase transition to higher temperatures while the T_C remains constant at about 264°C. The addition of Cu^{2+} drastically lowers the room temperature dielectric loss and significantly improves the mechanical quality factor of KNN-LT-LS [36] as well as KNN-LN ceramics (with a Q_m value of 414–1,400) [37, 38]. Takao et al. reported a high Q_m value of 2,280 for KNN-1 mol % CuO ceramic [39]. The addition of Ba^{+2} as a donor dopant induces soft characteristics in KNN-LT-LS ceramics by increasing the remnant polarization

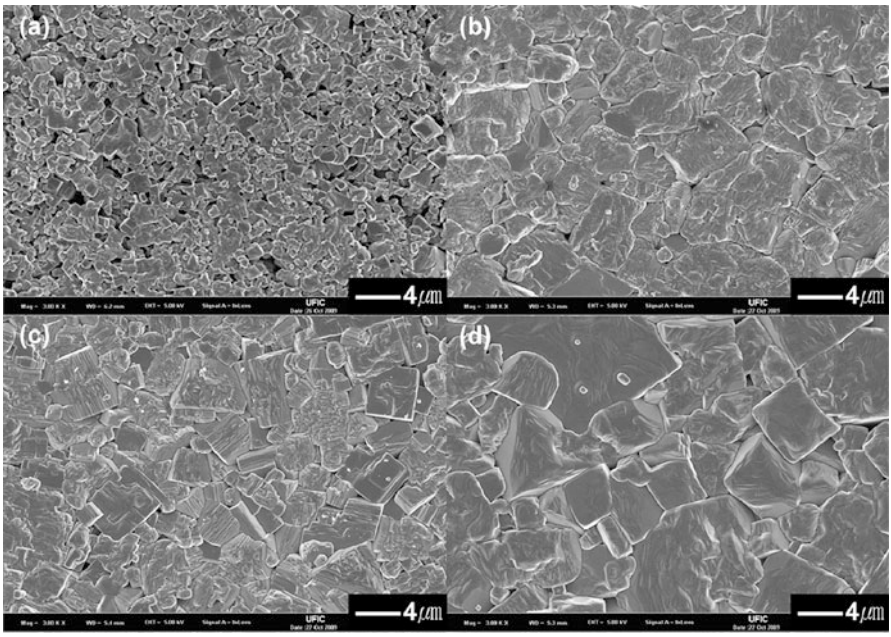

Fig. 5.5 SEM images of fractured surfaces of KNN-LS-xFeO ceramics sintered at 1,050°C for 2 h: (**a**) $x = 0$, (**b**) $x = 0.005$, (**c**) $x = 0.01$, and (**d**) $x = 0.03$ [41]

along with reducing the coercive field. The composition with 1 mol% Ba with a permittivity of 1,173, exhibits 36% and 58% higher values of d_{33} (210 pC N^{-1}) and k_{33} (0.491) than the undoped composition. Furthermore, the incorporation of Ba^{2+} up to 1.5 mol% increases the bulk resistivity. The conductivity of the base composition doped with more than 1.5 mol%, increases with barium concentration, In this case, the donor electron concentration exceeds the amount of electrons needed to compensate for the intrinsic hole concentration. The incorporation of Ba^{+2} lowers the Curie temperature, increases the room temperature relative permittivity, and slightly decreases the mechanical quality factor. This is accompanied by a broadening of the relative permittivity-temperature peak [40].

A small amount of FeO addition ($x = 0.01$) to KNN-LS ceramics (0.95KNN–0.05LS + x FeO) was found to effectively enhance the densification and the grain size (Fig. 5.5). It has been suggested that the abnormal grain growth is due to a liquid phase sintering. The 1 mol% FeO-doped KNN-LS ceramics exhibited a relative permittivity of 1,200, d_{33} of 311 pC N^{-1}, and k_p of 0.42. It has been reported that a small variation in sintering temperature has a remarkable effect on the properties of these materials [41].

The modification of KNN-LS ceramics with 1 wt% $CaTiO_3$ (CT) shifts the $T_{T–O}$ to well below room temperature (−15°C) while T_C is reported to be about 300°C. The shifting of this PPT to lower temperatures improves the temperature and domain stability of the KNN-LS composition. For instance, the change of d_{15} of the

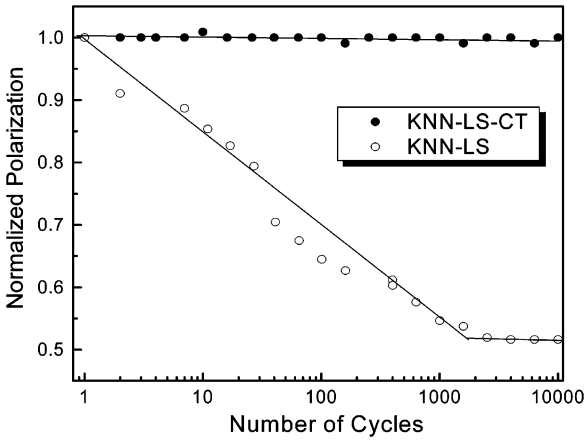

Fig. 5.6 Normalized polarization as a function of switching cycle, for pure and CT-modified KNN-LS materials [43]

unmodified composition in the temperature range of −50°C to 200°C is in the order of 55% while that for CT-modified KNN is less than 10% [42]. Figure 5.6 shows the normalized polarization as a function of switching cycles, where no polarization degradation is observed for KNN-LS-CT ceramics. It should be noted that the values of saturated polarization for base and CT-doped ceramics are 39 and 11 μC cm^{-2}, respectively. Bi-polar fatigue generates microscopic defect clusters which effectively pin 90° domain wall motion and result in a gradual loss of polarization during the repetitive application of the electric field. However, in CT-modified KNN-LS ceramics, due to defect generation, no more 90° domain can be pinned which results in a consistent polarization manner under cyclic switching [43].

Doping of KNN with 1 mol% ZnO leads to the enhancement of the piezoelectric charge coefficient, permittivity and planar coupling coefficient by expediting the densification through the formation of a liquid phase during sintering [44]. At higher doping levels, secondary phase formation and abnormal grain growth has been reported [45]. ZrO_2 addition hinders the abnormal grain growth in KNN ceramics and enhances the relative permittivity up to 905 at 10 kHz [46].

Figure 5.7 displays the piezoelectric constant of different KNN-based compositions as a function of the orthorhombic-tetragonal phase transition temperature. Although the piezoelectric properties of KNN ceramics depend on various intrinsic and extrinsic parameters, this figure indicates that lowering the T_{T-O} has a remarkable effect on enhancing the electromechanical properties of KNN-based ceramics.

Besides developing KNN solid solutions, other additives have been employed to aid in sintering and to obtain high density ceramics without using pressure-assisted sintering. $K_{5.4}Cu_{1.3}Ta_{10}O_{29}$ (KCT), $K_4CuNb_8O_{23}$ (KCN), and $K_{1.94}Zn_{1.06}Ta_{5.19}O_{15}$ (KZT) are some examples of these additives [47–52]. In the case of KCT, adding

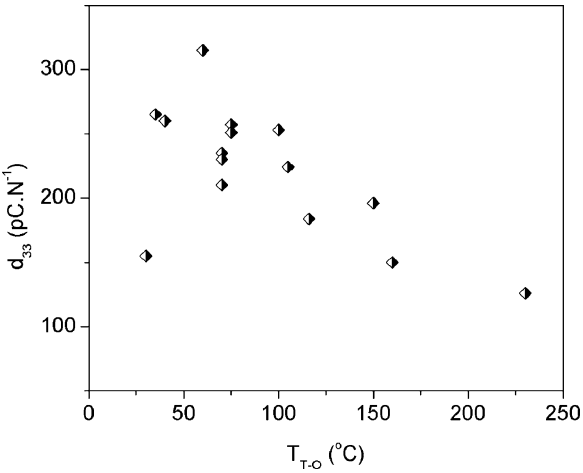

Fig. 5.7 The correlation between the piezoelectric constant (d_{33}) and the orthorhombic-tetragonal phase transition temperature (T_{T-O}) in KNN-based ceramics. The data points were obtained from refs. [11, 12, 20, 21, 25, 26, 29, 30, 36, 40, 53, 55]. No MPB exists in these compositions

0.38 mol% KCT to KNN increased the density of pure KNN by almost 12%. Adding KCT hinders the abnormal grain growth and forms a liquid phase during sintering of KNN. The reduction of the porosity volume fraction of pure KNN by adding a sintering aid noticeably suppresses the leakage current and increases the mechanical quality factor to about 14 times its original value [47]. Incorporating 0.5 mol% KCN into KNN provides similar results to the addition of KCT. In both cases, the Curie temperature decreases by about 20–40°C [48]. These materials with high Q_m value of about 1,500 can be regarded as hard piezoceramics [51]. In KCT-containing KNN, the introduction of Li^+ to the A-site increases the Curie temperature and decreases T_{T-O} and results in a high planar coupling factor of 0.43 and mechanical quality factor of 1,270. Lithium substitution also increases the piezoelectric charge coefficient and electric-field-induced strain. A higher amount of Li (6 mol%) stabilizes the tetragonal structure at room temperature [11].

Table 5.2 lists the electrical properties of some KNN-based solid solutions as well as doped KNN ceramics.

5.1.3 Processing of KNN Ceramics

The main obstacle in the development of KNN ceramics is the difficulty of powder processing. Difficulty in obtaining fully dense samples and poor reproducibility are some of the general problems associated with the processing of KNN. Many papers written in the past years have been focused on optimizing the chemical composition and processing of KNN with the goal of obtaining reliable samples. Using the

Table 5.2 Typical properties of KNN ceramics modified with various additives and dopants

Composition	ε_r	Tan δ	P_r (μC cm^{-2})	E_c (kV cm^{-1})	T_c (°C)	T_{T-O} (°C)	d_{33} (pC N^{-1})	k_p%	Q_m
KCN-modified KNN [48, 51]	220–330	0.002–0.01	20	12–13	410	185–200	100–180	33–39	1,200–1,500
KZT-modified KNN [50]	590		18	10	390		126	42	58
KCT-modified KNN [47]	–	0.003	20	9.8	390	180	190	42	1,300
Bi_2O_3-doped KNN [118]	1,309	0.058	23.6	21	373		127	28.3	
$LiSbO_3$-doped KNN-0.005BF [119]	1,556	0.02			365	~75	257	52	45
KNN + excess K and Na [55]	361	0.096	33.6	8.5	425	230	126	34.1	116
KNN-$Bi(Sc_{0.5}Fe_{0.5})O_3$ [120]			33.9	18.1	372		255	44	
KNN-0.24$AgNbO_3$ [121]	550		20	6.4	340	150	160	37.5	
KNN-$CaTiO_3$ [122]	411 (10 kHz)	0.024	15.7	8	397	184	116	39	176
KNN-$BiScO_3$ [123]	~1,100 (10 kHz)				351	~100	253	48	
CuO-doped KNN-$BiScO_3$ [29]	1,217 (10 kHz)	0.017	19	15	331	105	224	40	288
Mn_3O_4-doped KNNT [124]	1,290	0.017			193	23	240	45	280

Table 5.2 (continued)

Composition	ε_r	Tan δ	P_r (μC cm^{-2})	E_c (kV cm^{-1})	T_C (°C)	T_{T-O} (°C)	d_{33} (pC N^{-1})	k_p%	Q_m
KNN-LN [12]					~470	~70	235	42	
KCT-modified KNN-LN [11]	340		16	16	415	151	196 (pm V^{-1})	43	1,270
KNN-BLT [14]	1,480	0.015			381		172	37	102
KNN-BKT [125]	1,260	0.03			376	75	251		
KNN-LT [20, 21]	540–1,256		9	12.5	323	~70	200–230	36–51	73
(KNN-LT)-(BNT-BT) [30]			24	20	340	~30	155		
KNN-LS [25, 26]	1,380	0.02	25	18.5	368	35	265	50	40
KNN-LS, FeO doped [41]	1,200	0.022			350		311	42	
CT-modified KNN-LS [42]	1,170	0.02			330	−15	210	49	
KNN-LT-LS [40, 53]	665–1,865	0.01–0.035	18–22	8.2	265–290	~60	315	48.4	50
KNN-LT-LS [19]	644	0.02					175	25	
KNN-LT-LS, Ba-doped [40]	1,173	0.026	21	9.8	266	70	210	34.8	72
MnO_2-doped KNN-LT-LS [126]	1,528	0.018	8.3	5.8	250	~70	331 (pm V^{-1})		
CuO-doped KNN-LT-LS [36]	1,230	0.008	13.5	6.9	264	~40	260	48	225

conventional mixed oxide route is a common way to produce KNN polycrystalline ceramics. The perovskite method has also been used to synthesize KNN-based compositions. Both processing routes are very sensitive to processing variables such as sintering atmosphere (air or oxygen, and flow rate of oxygen) and humidity [53, 54]. To exemplify, KNN-LT-LS powders can be prepared by the perovskite route in which the binary compositions of sodium niobate ($NaNbO_3$; NN), potassium niobate ($KNbO_3$; KN), potassium tantalate ($KTaO_3$; KT), sodium antimonate ($NaSbO_3$; NS), and lithium antimonite ($LiSbO_3$; LS) are first synthesized at 800°C and then the appropriate molar ratio of the calcined powders are mixed, ball milled, and dried in order to form the final composition of $(K_{0.44}Na_{0.52}Li_{0.04})(Nb_{0.84}Ta_{0.10}Sb_{0.06})O_3$. Transgranular fracture has been observed to be the dominant fracture mechanism in KNN ceramics made by either the mixed oxide or perovskite method. Higher relative permittivity and dielectric loss along with lower remnant polarization were observed in the perovskite route. It is concluded that the mixed-oxide route is a suitable technique to prepare KNN-LT-LS ceramics [53].

The electrical properties of these materials are very sensitive to variations in chemical composition. Therefore, precaution should be taken to assure obtaining samples with the desired stoichiometric composition. Since alkaline elements have a high saturated vapor pressure, they are prone to volatilization during any high temperature processing stage such as calcination and sintering. Similar to the procedures utilized in Pb-based materials, one can use an excess amount of alkaline sources in raw materials to compensate for any probable loss of A-site elements [55, 56]. Volatile mass of potassium is approximately two times greater than that of sodium [55]. Lowering the processing temperature can help in minimizing the volatilization extent. Using high-energy ball milling, for instance, reduces the calcination temperature [10]. The purity of the raw materials is also of great importance for attaining high quality samples. Alkaline materials have a high tendency to absorb environmental moisture (hygroscopic effect). The precursors used to synthesize KNN powders (such as K_2CO_3, Na_2CO_3, and Li_2CO_3) are also moisture sensitive. Therefore, the processing of this material under a controlled atmosphere (e.g., using glove box with Ar protective atmosphere) becomes an important issue [53]. It has been reported that by pre-heating the as-received raw materials, the substantial improvement in properties can be achieved. The importance of preheating is mainly in acquiring the right stoichiometry by removing the excess absorbed moisture [53].

Many researchers have emphasized the role of utilizing non-conventional densification routes (pressure-assisted methods such as cold isostatic press (CIP), hot isostatic press (HIP), sinter forging, spark plasma sintering (SPS), and hot press) in achieving dense and high performance KNN ceramics with a relative density up to 99.4% [57–60]. Table 5.3 compares the dielectric and piezoelectric properties of some KNN ceramics densified by different methods, confirming the correlation between high density samples and higher electromechanical properties.

Table 5.3 Comparison of the properties of KNN ceramics made by different consolidation techniques. Hot pressed samples show superior properties [9]

Consolidation	Air-sintered	Hot-pressed
Composition	$K_{0.5}Na_{0.5}NbO_3$	$K_{0.5}Na_{0.5}NbO_3$
ρ_{rel} (%)	94.2	98.9
ε_r	290	420
Tan δ	0.02	0.014
d_{33} (pC N^{-1})	80	160
$-d_{31}$ (pC N^{-1})	32	49
k_p	0.36	0.45

Note: Dielectric properties were measured at 100 kHz

5.2 Textured KNN-Based Ceramics

An important approach to enhancing the properties of piezoelectric ceramics is to control the grain orientation without decreasing the Curie temperature. There are several processing techniques to make directionally oriented bulk ceramics including: (1) hot forging and pressing, and (2) oriented consolidation of anisometric particles such as particles with plate-like or needle shaped morphology. The seed materials can be made by molten salt synthesis (MSS) and topochemical microcrystal conversion (TMC). Tape casting and extrusion are usually used to homogenously align anisometric particles in a fine green matrix of the desired ceramic powder. In templated grain growth (TGG), highly dense and oriented ceramics can be produced by using a small amount of anisometric seeds (usually less than 5 vol%) dispersed in a fine matrix powder. Templates usually have a different composition than matrices and are made of materials which are easily fabricated in anisometric shapes. $Bi_4Ti_3O_{12}$ compound with a bismuth layer structure is considered as an excellent example of a template material. It is obvious that higher electrical properties can be achieved if a template with the same composition as a matrix is used. However, it is difficult to make perovskite ceramics in high aspect ratio morphologies due to the isotropic properties of perovskite structure. Reactive-templated grain growth (RTGG) is a type of TGG in which templates are aligned in the matrix and the final composition forms as a result of some consecutive in situ reactions [61]. Y. Saito et al. used RTGG method to make <001> oriented $(K,Na)NbO_3$–$LiTaO_3$–$LiSbO_3$ ceramics. This process comprises three successive stages. First, $Bi_{2.5}Na_{3.5}Nb_5O_{18}$ (designated as $BiNN_5$) particles with a bismuth layer structure, are synthesized by the MSS method. Then, $NaNbO_3$ plate-like particles with <001> crystallographic orientation are formed by the exchange of Na ions for Bi ions existing in the BiNN5 compound via a topochemical reaction. Finally, $NaNbO_3$ platelets as a reactive template are mixed with complementary reactants – $KNbO_3$, $NaNbO_3$, $KTaO_3$, $LiSbO_3$, and $NaSbO_3$ particles – in a proper solvent, with sufficient amounts of a binder and a plasticizer to form slurry needed for tape casting. A textured $(K,Na)NbO_3$–$LiTaO_3$–$LiSbO_3$ ceramic is then formed by sintering the stacked tape at about 1,135°C. This material with a $(K_{0.44}Na_{0.52}Li_{0.04})(Nb_{0.084}Ta_{0.10}Sb_{0.06})O_3$ composition exhibited a high d_{33} of 416 pC N^{-1}, ε_r of 1,570, k_p of 0.61, with T_C about 253°C [18].

Table 5.4 Dielectric and piezoelectric properties of textured KNN ceramics

Material	T_C (°C)	T_{T-O} (°C)	Electromechanical properties	ε_r	Tan δ	Method
KNN [63]	420	209	$d_{33} = 135$ (pC N^{-1}) $k_p = 0.45$ $Q_m = 144$	285	0.044	TGG
KNN-1% CuO [63]	415	183	$d_{33} = 146$ $k_p = 0.58$ $Q_m = 382$	202	0.016	TGG
KNN-LT-LS [18]	253	–	$d_{33} = 416$ $g_{33} = 29.9$ $k_p = 0.61$	1,570	–	RTGG
KNN-1% CuO [39]	–	–	$d_{33} = 123$ $k_p = 0.54$ $g_{33} = 66$ $Q_m = 523$	211	0.02	RTGG

Textured KNN-LT ceramics were also prepared by the same research group with a d_{33} of 373 pC N^{-1} and T_C of 323°C. Plate-like NN particles synthesized by TMC have also been used for making highly textured 1 mol% CuO-KNN [62].

TGG method has been utilized to prepare (001)-oriented CuO-doped KNN ceramics by using NN templates. The best electromechanical properties ($k_p = 0.58$, $k_{31} = 0.33$, $d_{33} = 146$ pC N^{-1}) are achieved in 1 mol% CuO-doped KNN with a Lotgering factor of 99% and a relative density of 96.3% [63]. Table 5.4 shows the dielectric and piezoelectric properties of some of the KNN textured ceramics.

5.3 KNN-Based Single Crystals

KNN-based single crystals have been processed by different crystal growth techniques such as the Bridgeman, flux, slow cooling, solid state growth, and top-seeded solution growth (TSSG) methods [64–76].

Single crystals of 0.95KNN–0.05LN ($LiNbO_3$) with a relatively high Curie temperature of 426°C and d_{33} of 405 pC N^{-1} have been grown using the Bridgman method. The crystal, however, showed a lossy hysteresis loop with a remnant polarization of 9 μC cm^{-2} and low dielectric constant of 185 at room temperature which was attributed to the high concentration of potassium and oxygen vacancies as well as unoptimized processing conditions [64]. The addition of Mn ($x = 0.005$) followed by a moderate annealing of the crystal has been proposed to be effective for suppressing the leakage current of KNN crystals prepared by the flux method [65]. Both as-grown pure and Mn-modified crystals exhibited a high value of leakage current (over 10^{-4} A cm^{-2}) which was attributed to the electrical conduction through the 4*d* electrons of Nb^{4+}. The leakage current density (J) is sensitive to the oxidation degree which is dictated by annealing temperature and atmosphere.

During the first-stage oxidation (annealing temperature of lower than 1,100°C, in air atmosphere), the as-grown crystals are oxidized gradually and J drops sharply due to the valence increase of niobium from Nb^{4+} to Nb^{5+} through the following reaction: [65]

$$\frac{1}{2}O_2 + 2Nb'_{Nb} + V^{\circ\circ}{}_{O} \rightarrow O^{*}{}_{O} + 2Nb^{*}{}_{Nb}$$

After the oxidation of all Nb^{4+} ions to Nb^{5+}, second-stage oxidation happens which results in the formation of holes $h^{\cdot}$ (p-type conductivity) and hence an increase in the leakage current of KNN crystals annealed in an O_2 atmosphere (at 750°C for 10 h) [65].

$$V^{\circ\circ}{}_{O} + \frac{1}{2}O_2 \rightarrow O^{*}{}_{O} + 2h^{o}$$

On the other hand, electron spin resonance (ESR) spectroscopy confirms that in as-grown crystals, Mn substitutes at the B-site as Mn^{2+}, which is accompanied by the formation of oxygen vacancies:

$$2MnO \rightarrow 2Mn'''_{Nb} + 2O^{*}{}_{O} + 3\,V^{\circ\circ}{}_{O}$$

In Mn-doped crystals, therefore, Mn^{2+} transforms to higher valent states by absorbing some of the generated electron holes and decreases the conductivity compared to the pure crystals annealed under the same conditions. The highest resistivity is achieved in the Mn-KNN crystal grown by flux method and annealed at 1,100°C in an air atmosphere which shows a well-saturated hysteresis loop with a remanent polarization of 40 μC cm^{-2} and coercive field of 12 kV cm^{-1} [65].

KNN crystals by flux method have also been grown by some other groups [69, 71, 73]. Figure 5.8 shows the P–E hysteresis loop of a 0.5 mol% Mn-doped KNN single crystal grown by the flux method with remnant polarization of 52 μC cm^{-2} which is one of highest values reported for KNN-based materials [71]. Mn-substitution in $K_{0.14}Na_{0.86}NbO_3$ single crystals also provides superior polarization and reduces the leakage current [73].

Mn-doped KNN single crystals have been also grown by the high-temperature solution method using a K_2CO_3–Na_2CO_3 eutectic composition as a flux. It has been shown that a small amount of MnO_2-addition noticeably enhances the dielectric and piezoelectric properties of KNN crystals as the 0.5% MnO_2-doped crystals show a dielectric constant of 730, d_{33} of 270 pC N^{-1} and T_C of 416°C [66]. This beneficial effect was attributed to the suppression of the leakage current and increase of the domain wall density. The domain size is observed to decrease from 25 μm for pure KNN to 9 μm for 0.5% MnO_2-doped crystals [66].

KNN single crystals with a homogenous chemical composition were prepared by solid-state crystal growth (SSCG) by embedding <110> oriented $KTaO_3$ seed in KNN powder followed by hot-pressing at 1,100°C for 100 h. The dielectric

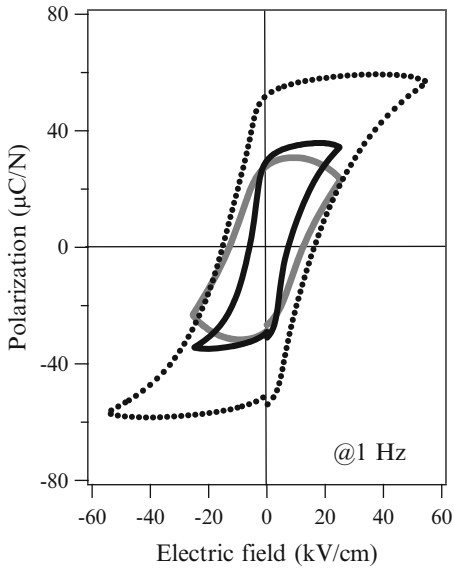

Fig. 5.8 *P–E* hysteresis loops of Mn-doped KNN crystal made by the flux method. Dotted line: Mn-doped KNN crystal, *black line*: undoped KNN crystal, *gray line*: Mn-doped KNN ceramics [71]

constant, dissipation factor, remanent polarization, and coercive field in the [131] direction are 1,015, 1%, 17 μC cm^{-2}, and 24 kV cm^{-1}, respectively [67]. The combination of SSCG and hot pressing is an effective way of reducing the porosity and growing dense KNN single crystals [75]. Electric field-induced strain shows a frequency-dependent behavior where the slope of the displacement-voltage plot decreases with the increase of the frequency applied by an AFM tip. The displacement exhibits both linear (piezoelectric effect) and nonlinear (electrostrictive effect) portions with the measured coefficient of d_{33} ~67 pm V^{-1} and M_{33} ~2.39×10^{-14} m^2 V^{-2}. It has been suggested that fine 180° domains mostly contribute to the displacement response and the observed d_{33} decline with frequency can be explained by the inability of 180° domains to re-orientate fast enough at higher frequencies [68]. A systematic study on the evolution of the domain structure of poled and unpoled [001]-oriented KNN single crystals in a temperature range of −195 to 405°C can be found in ref. [69]. Table 5.5 summarizes the electrical properties of some of the KNN single crystals.

5.4 KNN-Based Films

KNN thin films have been processed by both chemical and physical deposition techniques. The chemical processing methods include sol–gel, chemical solution deposition (CSD), metalorganic solution deposition (MOSD), and metalorganic chemical vapor deposition [77–86]. The physical deposition methods include RF magnetron sputtering, [87–97]] pulsed laser deposition (PLD) [98–109], and

Table 5.5 Dielectric and ferroelectric properties of pure and doped KNN single crystals

Composition	T_C (°C)	T_{T-O} (°C)	d_{33} (pC N^{-1}) Other coefficients	ε_r	Tan δ	P_r (μC cm^{-2})	E_c (kV cm^{-1})	Method
KNN-0.5% Mn [71]	407	170	$d_{33} = 161$ $k_{33} = 0.64$	424	–	52	13	Flux
KNN-0.5% Mn [65]	–	–	–	–	–	40	12	Flux
KNN [67]	410	192	$d_{33} = 80$[a]	1,015	0.01	17	24	SSCG
KNN-0.5% Mn [66]	416	193	$d_{33} = 270$	730	0.03	–	–	High temperature solution
KNN [66]	423	208	$d_{33} = 160$	240	0.02	–	–	High temperature solution
0.95 KNN- 0.05LN [64]	426	190	$d_{33} = 405$ $k_t = 0.61$	185	0.011	9	22	Bridgeman
KNN [69]	393	205	$d_{33} = 160$ $k_t = 0.45$	240	0.02	–	–	Flux
$Li_{0.02}(Na_{0.5}K_{0.5})_{0.98}NbO_3$ [70]	–	–	$d_{33} = 0.59$ $p = 52$ $k_t = 0.70$	164	0.025		–	TSSG
KNN [72]	433	214	$d_{33} = 130$	–	–	–	–	Slow cooling

Note: Dielectric constant and dissipation factor are measured at different frequencies
p: Pyroelectric coefficient
[a]Unit: pm V^{-1}. Measured by AFM

Table 5.6 Effect of excess amount of K and Na elements on the final chemical composition of KNN thin films prepared by CSD method. (Composition is measured by electron microprobe analysis) [78]

	(K + Na)/Nb	Na/(K + Na)	O/Nb
KNN-00	0.85	0.36	2.92
KNN-10	0.97	0.49	2.98
KNN-20	1.03	0.50	3.04
KNN-30	1.08	0.49	3.04

aerosol deposition (AD) [110]. The volatility of alkaline elements, deviation from stoichiometric composition, formation of secondary phases, and high leakage current density are some of the challenges encountered in the processing of KNN-based thin films. In this section, the activities regarding the deposition and dielectric and piezoelectric properties of KNN-based thin and thick films have been reviewed to shed light on the possible application opportunities for lead-free films in the near future.

5.4.1 KNN Films Prepared by Chemical Deposition Techniques

Due to the volatility of sodium and potassium, adding an excess amount of these elements in precursors can compensate for the loss of A-site elements and result in films with improved properties [77–82, 86]. Excess sources of Na and K largely suppress the formation of cation and anion vacancies in the films, eliminate the formation of secondary phases such as $K_4Nb_6O_{17}$, and improve the surface roughness. With hindering the formation of K and Na vacancies, the concentration of oxygen vacancies decreases accordingly which results in the improvement of the leakage current of the films by about three orders of magnitude [77, 78]. Anh et al. added 0–30 mol% excess amounts of alkaline chemicals to the precursor solutions to compensate for the loss of Na and K and found that 20 mol% (KNN-20) was an optimum amount of excess A-site elements in KNN thin films on $Pt/Ti/SiO_2/Si$ substrates [78]. The leakage current is reduced by more than one order of magnitude with a saturated *P–E* hysteresis loop and a remnant polarization, and coercive field of 10 μC cm^{-2} and 35 kV cm^{-1}, respectively [78]. KNN-20 films with a d_{33} value of about 40 pm V^{-1} did not show serious polarization degradation when subjected to bipolar voltage pulses up to 10^{10} switching cycles [78]. Table 5.6 shows the chemical composition of deposited films with different concentrations of A-site elements in primary solutions, confirming that the films with 20 mol% excess Na and K have a composition very close to stoichiometric KNN film after the deposition.

The optimization of the annealing temperature has a vital influence on the properties and microstructure of KNN films produced by chemical methods. At low annealing temperatures, it is difficult to acquire the perovskite phase and

the film is liable to suffer from cracking. At high temperatures, on the other hand, the volatilization of alkaline elements leads to the formation of pores, pinholes, and secondary phases or decreases the tendency for preferential grain growth [79].

The KNN thick films (3.5 μm) prepared by the polyvinylpyrrolidone (PVP)-modified CSD technique, annealed at 600°C showed improved piezoelectric and ferroelectric properties ($P_r = 16.4$ μC cm^{-2}, $P_{sat} = 36$ μC cm^{-2}) compared to the films annealed at other temperatures (500, 650, and 700°C). The d_{33} value for the optimized film was found to be 61 pm V^{-1} while that for the films annealed at different temperatures was lower than 32 pm V^{-1} [79].

One of the other secondary phases observed in KNN thin films is $K_2Nb_4O_{11}$ which is detrimental for electromechanical properties of the films [80, 86]. According to the phase diagram of K_2O–Nb_2O_5, this compound forms when the ratio of Nb_2O_5 to K_2O is larger than 1.5. The volatilization of the potassium element, therefore, causes the formation of a $K_2Nb_4O_{11}$ phase in KNN thin films. The addition of 30% excess source of potassium to the precursor eliminates any redundant phase in sol–gel-derived films and decreases the minimum annealing temperature necessary for the formation of the single perovskite phase. Such thin films on ZrO_2 and Pt-coated silicon substrates exhibited high P_r values of about 16–38 μC cm^{-2} [80, 86].

Schroeter et al. [81] launched a high throughput experimentation (HTE) for the production of KNN, $KNbO_3$ (KN), and $NaNbO_3$ (NN) thin films by CSD with an automated sample preparation and characterization method. It has been shown that the optimum excess amount of alkaline elements for KNN films with 450 nm thickness on Pt/SiO_2/Si substrates is about 35%. In stoichiometric films, Nb-rich phases form which deteriorate the electrical properties of the film. The hygroscopic nature of the films causes the environmental moisture to be absorbed into the porosities available in the film which then increases the leakage current and dissipation factor of the films. It has been suggested that drying the films at 50°C is beneficial to reducing the loss tangent from 20% down to 5% [81].

The optimization of CSD-derived KNN films by the addition of proper amounts of K and Na sources to the precursor solutions improves the ferroelectric and leakage current behavior of the films by eliminating secondary phases (K_4NbO_{17}) and decreasing the concentration of charge carriers [82]. The volatilization of A-site elements triggers the formation of oxygen vacancies to maintain charge neutrality in the film. By applying voltage during the measurement of the leakage current, oxygen vacancies, which are positive charge carriers, flow toward the cathode and accumulate near the interface between the film and the electrode, leading to an asymmetric *I*–*V* curve. The addition of 10 mol% excess A-site elements (5% for each) compensates for the loss of Na and K during the high-temperature processing of chemically deposited thin films. Exposing the films to the excessively high annealing temperature or time facilitates the condition for further loss of alkaline elements and hence, deteriorates the electrical properties [82].

There have been controversial results concerning the effect of Li addition to KNN thin films. Lai et al. [83] reported that the addition of 0.06 $LiNbO_3$ (LN) to sol–gel-derived KNN thin films remarkably enhances the piezoelectric constant and

remnant polarization of the film. The d_{33} and P_r of the base film were measured to be 45 pm V^{-1} and 1.4 μC cm^{-2}, respectively, while those of the Li substituted films were 192 pm V^{-1} and 9.7 μC cm^{-2}. Lithium facilitated the (001) preferential growth of the KNN films on Pt/Ti/SiO_2/Si substrates due to the stronger anisotropy of the surface energy and the lowering of the crystallization temperature in the presence of lithium. The enhanced electrical properties of films containing Li were attributed to the shift in the orthorhombic-tetragonal phase transition and larger grain size of the film which increases the extrinsic piezoelectric contribution by facilitating non-180° domain switching. However, Anh et al. [84] reported that Li addition leads to a decreased (001) preferential growth in KNN films made by CSD. A concentration of Li higher than 6 mol% results in the formation of surface pinholes or secondary phases (such as $K_3Li_2NbO_{15}$) due to the volatility and the limited solubility of Li in KNN films. While Anh et al. [84] suggested the addition of 5 mol% Li to decrease the leakage current density of KNN films, Lai et al. [83] indicated that lithium substitution makes the film leakier due to the increased number of point defects existing in the films. It should be noticed that due to the porous structure of the film, the saturated current density in thin films made by Anh et al. is about four orders of magnitude higher than that of the films made by Lai et al.

5.4.2 KNN Films Prepared by Physical Deposition Techniques

KNN-based films on various substrates prepared by RF magnetron sputtering have been reported by several research groups [87–97].

In 1989, Margoline et al. deposited KNN films on stainless steel substrates [96]. Some years later, several papers concerning with deposition of the KNN films by sputtering were reported including the articles by Wang et al. [96] Kim et al. [89] and Lee et al. [90]. The saturation polarization, remnant polarization, and coercive field of $K_{0.48}Na_{0.52}NbO_3$ thin films with 300 nm thickness on Pt/Ti/SiO_2/Si substrates were 42 μC cm^{-2}, 22.5 μC cm^{-2}, and 90 kV cm^{-1} respectively [89, 90]. The phase transition temperatures for these films with a d_{33} of 45 pm V^{-1}, were measured to be 200 and 430°C [90]. Lee at al. [87, 88] showed that post-annealing of KNN films on Pt/Ti/SiO_2/Si substrates increases the remnant polarization. The optimum post-annealing temperature was identified to be 700°C (for 1 h in the O_2 atmosphere) and the films showed a well-saturated hysteresis loop with a remnant polarization and coercive field of 25 μC cm^{-2} and 90 kV cm^{-1} [88]. The annealed films exhibit better crystallinity and a smoother surface compared to the as-deposited films. Thin films with reduced surface roughness and denser grain structure show better insulative and fatigue properties due to the good quality of contact between the film and the top electrode.

Wu et al. [91] deposited (001)-oriented KNN films on a $SrTiO_3$ substrate with the remnant polarization and dielectric constant of 12 μC cm^{-2} and 452 (at 1 kHz), respectively. The films showed higher values of dielectric constant and lower

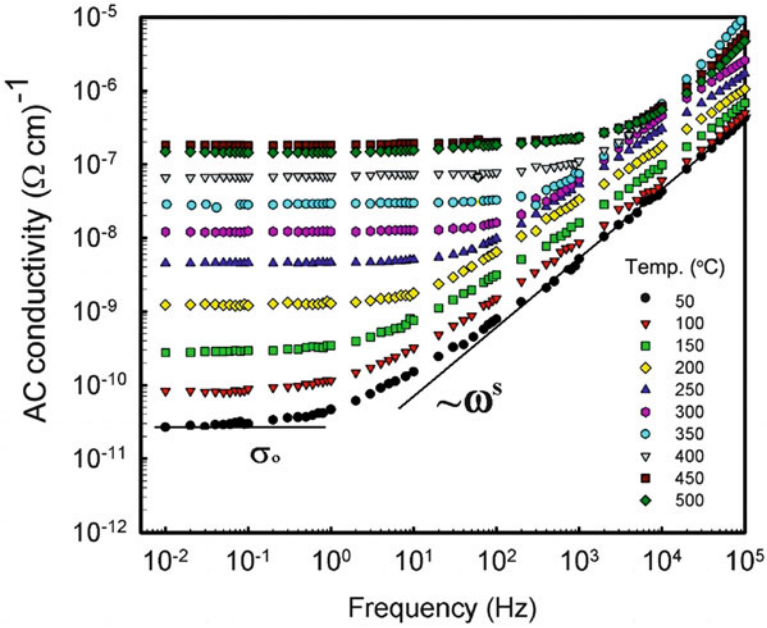

Fig. 5.9 Frequency dependency of AC conductivity of $K_{0.48}Na_{0.52}NbO_3$ thin films on Pt/Ti/SiO_2/Si at various temperatures [89]

values of dissipation factor and AC conductivity in comparison to the bulk KNN ceramic made by the same research group. They also reported that the KNN film possesses good fatigue endurance with a consistent polarization up to 10^9 switching cycles. The phase transition temperature for the orthorhombic-tetragonal and the tetragonal-cubic are reported to be 120°C and 310°C, respectively [91].

Shibata et al. reported e_{31} in the range of −3.6 to −5.5 C m^{-2} for the KNN thick films of 3 μm on (100)Pt/MgO and (111)Pt/Ti/SiO_2/Si substrates [92]. While KNN films were epitaxially grown on (100)Pt/MgO substrates, they showed a columnar structure on (111)Pt/Ti/SiO_2/Si substrates. Since the thermal expansion coefficient of a MgO substrate is higher than that of a KNN film, compressive stress is developed in the film during cooling to room temperature, which manifests itself as lattice defects [92, 94]. For KNN/Pt/Ti/SiO_2/Si films, on the other hand, the stress is relaxed through the formation of grain boundaries and only a few defects are present within the grains.

By using the optical lever method, the biaxial elastic modulus and thermal expansion coefficient of 3 μm KNN thick films made by RF magnetron sputtering were found to be 92 GPa and 8×10^{-6} (°C^{-1}), respectively. The film's Curie temperature was about 360°C while the tetragonal-orthorhombic transition temperature was 210°C [97].

Figure 5.9 demonstrates the AC conductivity of KNN thin films as a function of frequency at different temperatures. The frequency-independent portion of the

graph, which is almost equal to DC conductivity, infers that DC conductivity is dominant at higher temperatures as the plateau portion is spread over a wider range of frequencies with increasing temperature [89].

According to Jonscher's power law, AC conductivity can be expressed as a function of frequency: $\sigma = \sigma_0 + A\omega^s$, where σ_0 is the DC conductivity in a certain temperature, A is a temperature-dependent parameter, and s is a temperature-dependent exponent having value of $0 \leq s \leq 1$. Based on the graphs shown in Fig. 5.9, the values of s were extracted to be in the range of 0.72–0.90 as the temperature changes from 25°C to 500°C. The activation energy of AC conductivity was also calculated to be 0.57 eV at 10 Hz [89].

The optical properties of KNN films have also been explored for the possibility of making lead-free electro-optical devices [93, 95]. The refractive indices for 2 μm KNN thick films on sapphire substrates were determined to be $n_{TE} = 2.247$ and $n_{TM} = 2.216$, assuming a homogenous film with a rectangular refractive index profile. Thinner films show fewer waveguide modes and the values of n_{TE} and n_{TM} for a film with 1 μm thickness were determined to be 2.265 and 2.423, respectively. The difference between the values of refractive indices for two orthogonal polarizations shows that the films are birefringent with a birefringence of about −0.031 for the 2 μm thick film [93].

Pulsed laser deposition is one of the other widespread procedures for making KNN-based thin films [98–108]. PLD processing parameters should be carefully optimized and controlled in order to deposit thin films with enhanced ferroelectric properties. In the late nineties, Cho et al. [98] reported the deposition of [89] oriented KNN thick films of 1.2 μm on $Pt/SiO_2/Si$ substrates with a remnant polarization of 10 μC cm^{-2} and a coercive field of 20 kV cm^{-1}. The dielectric constant was about 450 at 1 kHz. The optimum oxygen pressure was 350 mTorr at a laser repetition rate of 7 Hz and laser fluence of 4–5 J cm^{-2}. They [100] demonstrated 2 μm KNN/quartz (Y + 36° cut single crystal) interdigital capacitors with high values of tunability (23.1% at 40 V bias). $KNN/SiO_2/Si$ thin films, also, were investigated as a planar interdigital variable reactance (varactor) and it was found that the films possess an electrical tunability of 3.1% at 20 V and low dissipation factor of 0.8% at 1 MHz [99].

Early work on $(K_{0.44}Na_{0.52}Li_{0.04})(Nb_{0.84}Ta_{0.10}Sb_{0.06})O_3$ (KNN-LT-LS hereafter) films on SRO/STO substrates was published by Saito et al. at 2004. The remnant polarization and coercive field of these films (2.7 μm in thickness) were 3.7 μC cm^{-2} and 10.5 kV cm^{-1}, respectively, while the dielectric constant and loss tangent were reported to be 824 and 8% at 1 kHz. The rough surface of the film and the deviation of the film composition from the stoichiometric composition (which was shown to be intensified with decreasing the thickness of the film) can be reasons for the film's low ferroelectric properties [101, 102].

Processing parameters have vital effects on the structure and properties of KNN films prepared by PLD. Abazari et al. studied the effect of the substrate temperature and oxygen background pressure as well as different dopants (Mn, Ba, and Ti) on the ferroelectric properties of KNN-LT-LS thin films deposited on $SrRuO_3$ (SRO) coated $SrTiO_3$ (STO) substrates [103–107].

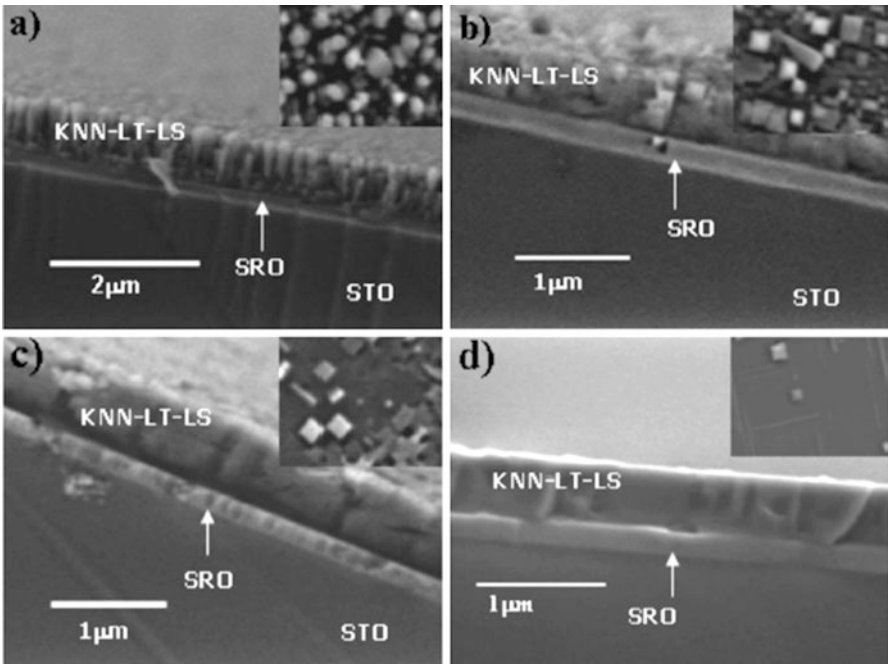

Fig. 5.10 SEM micrographs showing the effect of deposition temperature on the microstructure of KNN-LT-LS/SRO/STO films, deposited at (**a**) 600°C, (**b**) 650°C, (**c**) 700°C, and (**d**) 750°C [105]

Figure 5.10 depicts the evolution of the microstructure of the KNN-LT-LS thin films at different deposition temperatures. As can be observed, at low temperatures (600°C), the film exhibits a columnar structure along the [001] direction pointing out of the surface of the film with a grain size of about 200 nm. By increasing the deposition temperature, the columnar grains coalesce and form a uniform dense structure with a smooth surface [105].

Figure 5.11 shows the XRD spectra and phi-scans of the (011) pole of KNN-LT-LS films deposited at different temperatures. For the films deposited at 750°C, a single perovskite phase with intense (001) oriented peaks is observed in the θ–2θ scan. The phi-scan of the (011) pole consists of four peaks separated by 90° which indicates the locking of in-plane orientational symmetry and confirms that the films are grown epitaxially [105].

The assessment of the chemical compositions of thin films by Rutherford backscattering spectroscopy (RBS) shows that composition of the film deposited at 750°C, is very close to the simulated stoichiometric composition. At lower temperatures, the RBS profile shows a considerable discrepancy between the experimental and simulated data caused by low atomic mobility and higher surface roughness of the film [105].

The oxygen pressure used during the deposition of the film can control the stoichiometry and microstructure of the film through altering the mechanism,

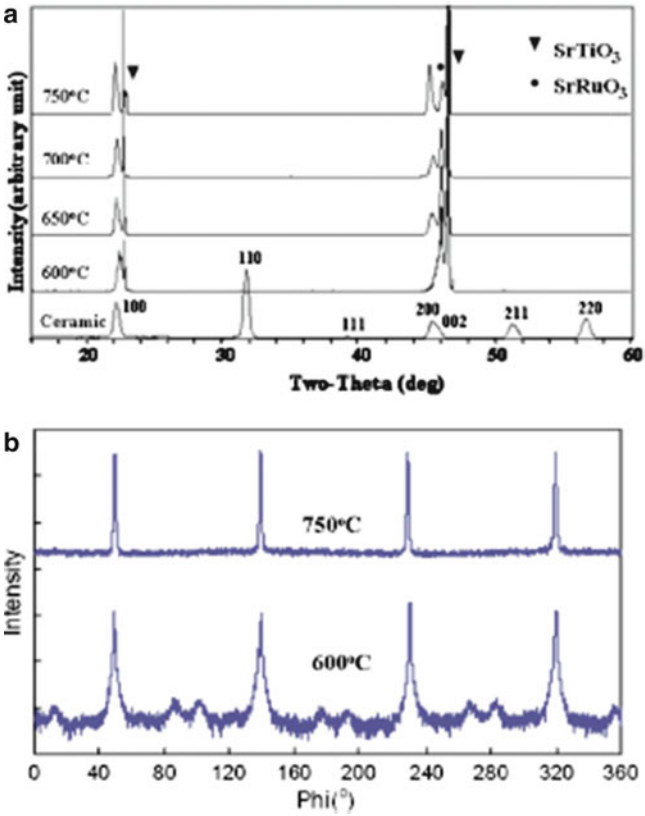

Fig. 5.11 XRD pattern of (**a**) the KNN-LT-LS bulk ceramic and KNN-LT-LS/SRO/STO films deposited at 600–750°C and (**b**) scans of the (110) pole of KNN-LT-LS for 600 and 750°C deposited films. A <001> oriented epitaxial thin film with single perovskite phase is achieved at 750°C [105]

flow pattern, or interaction of the plume and the substrate. The dielectric constant of the KNN-LT-LS films linearly increases from 220 to 450 as the oxygen pressure changes from 100 to 400 mTorr. Figure 5.12 depicts the influence of P_{O_2} on the *P–E* hysteresis loops of these films. At $P_{O_2} = 100$ mTorr, the loops have a saturation and remnant polarization of 10 and 3 μC cm^{-2}, while the coercive field is 20 kV cm^{-1}. Spontaneous polarization is enhanced in return of P_{O_2}, as the saturated and remnant polarization in 400 mTorr deposited films are found to be 7.5 and 16.5 μC cm^{-2}, along with an E_c of 15 kV cm^{-1}. Looking at hysteresis loops, it can be inferred that an increasing P_{O_2} leads to films with softer characteristics as the E_c decreases from 20 to 15 kV cm^{-1} with P_{O_2} increasing from 100 to 400 mTorr. Furthermore, by decreasing the oxygen pressure, the shape of the hysteresis loop deviates more from an ideal shape (which has a 90° slope at the intercept with *x* axis) implying that the films deposited at lower pressures have more defect-driven internal fields. With increasing the oxygen pressure, the domain wall mobility is made higher and the

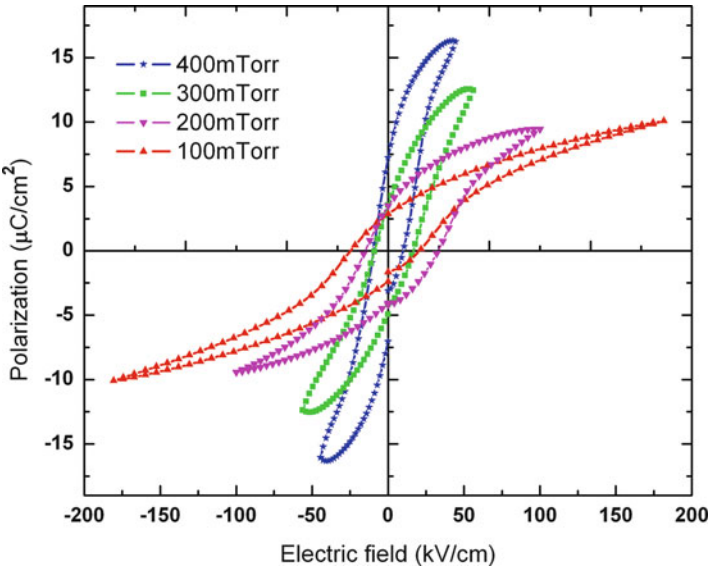

Fig. 5.12 Comparison of hysteresis loops of KNN-LT-LS/SRO/STO thin films at various background oxygen pressures, showing the improvement of polarization with increasing oxygen pressure (film thickness = 450 nm) [106]

closer the A-site cation concentration comes to its ideal stoichiometry which results in a higher dielectric constant and spontaneous polarization [106].

Abazari et al. reported that 1 mol% doping of KNN-LT-LS films increases the remnant polarization from 4 to 10 μC cm^{-2}, and at the same time decreases the leakage current by about three orders of magnitude as shown in Fig. 5.13a. The donor doping of these films with manganese introduces excess electrons to the perovskite structure which can annihilate p-type conductivity originating from the volatilization of A-site elements. Figure 5.13b compares the *P–E* hysteresis loops for undoped and Mn-doped films of 400 nm in thickness. Well-saturated loops can be achieved for Mn-doped thin films due to the higher resistivity of this film in comparison to the base film. The dielectric constant and dissipation factor of Mn-modified films were measured to be 600 and 10% at 100 kHz [103]. It has been suggested that multivalent Mn with different ionic radii substitutes both A-sites and B-sites. The creation of oxygen vacancies as a result of Mn^{+4} ions sitting on the B-site can be a reason for the increased coercive field of the film [103, 104] as shown in Fig. 5.13b. The hardening effect of Mn has been also confirmed by the measurement of the piezoelectric coefficient (d_{33}) of base and Mn-doped films which shows that Mn-addition is accompanied by a decline in the d_{33} value from 53 pm V^{-1} in an undoped film to 45 pm V^{-1} in an Mn-doped film [107].

Yamazoe et al. [109] reported that the introduction of a NN buffer layer (150 nm thick) on Pt/(001)MgO substrates had a noticeable effect on the improvement of the ferroelectric properties of KNN-LT-LS films. As illustrated in Fig. 5.14, the films

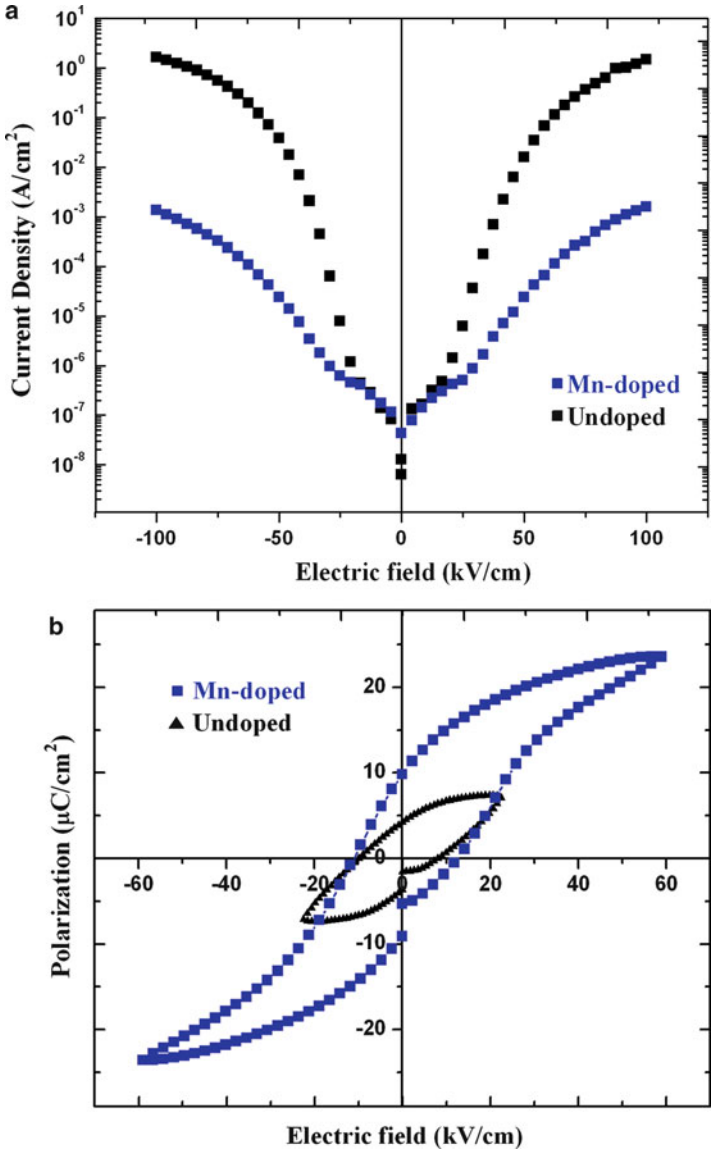

Fig. 5.13 (**a**) leakage current density and (**b**) hysteresis loops of undoped and 1 mol% Mn-doped KNN-LT-LS/SRO/STO thin films, showing an improvement in electrical resistance and remanent polarization by manganese doping (film thickness = 400 nm) [103]

show saturated polarization loops with an outstanding value of remnant polarization (26.3 μC cm^{-2}) which is much higher than that of similar films in the absence of the NN buffer layer. The dielectric constant and dissipation factor were measured to be 398 and 0.22 at 1 kHz.

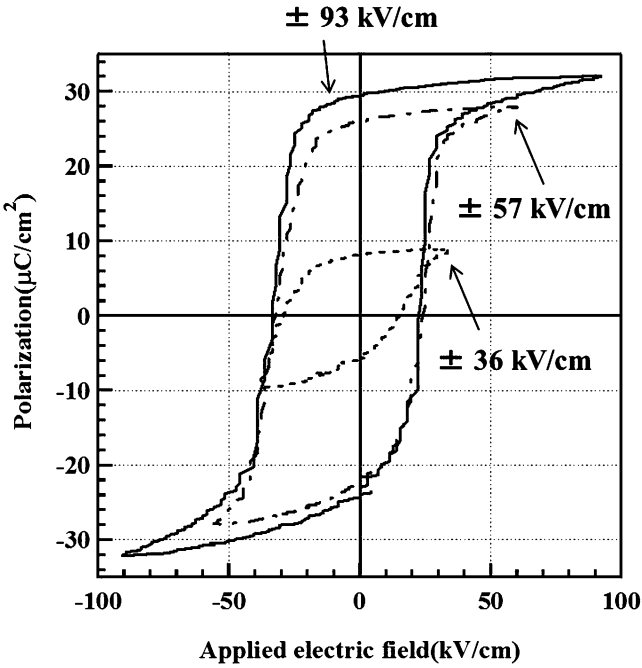

Fig. 5.14 *P–E* hysteresis loops of KNN-LT-LS films on NN/Pt/(001)MgO substrates. The large P_r value of 26.3 mC cm^{-2}, and the E_c of 28.6 kV cm^{-1} were obtained at applied electric field of 93 kV cm^{-1} (film thickness = 1.4 μm) [109]

KNN-LT-LS films with columnar structure have been deposited on platinized Si substrates without using any barrier layer. An Nb-rich $K_2Nb_6O_{16}$ pyrochlore phase was detected in the film and no hysteresis loop could be measured unless the thickness of the film was above 3.2 μm, where the remnant polarization and coercive field were measured to be 3.8 μC cm^{-2} and 20 kV cm^{-1}, respectively [108].

5.4.3 Electrical Conduction Mechanisms in KNN Thin Films

The leakage current is one of the most important characteristics of ferroelectric thin films which directly affects the applicability of the film. Thin films with high current densities are known for their lossy hysteresis loops with rounded corners. Underlying conduction mechanisms in thin films have been identified to fall into three major categories:

1. Poole-Frenkel (P-F) model: This mechanism, which operates through the bulk of the material, is a thermal emission of charge carriers from trapped centers under

high electric fields [111–113]. The quantitative equation for current density created via this mechanism can be expressed by the following equation:

$$J = J_0 \exp\left(\frac{\beta_{\mathrm{PF}} E^{1/2} - \phi_{\mathrm{PF}}}{k_{\mathrm{B}} T}\right)$$
$$\beta_{\mathrm{PF}} = \left(e^3/\pi\varepsilon_0\varepsilon\right)^{1/2}, \quad J_0 = \sigma_0 E, \tag{5.1}$$

where β_{PF} is the Poole-Frenkel coefficient, Φ_{PF} is the trapped level, e is the unit electrical charge, E is the applied electric field, ε is the dielectric constant in the infrared region, ε_0 is the permittivity of the free space, k_{B} is the Boltzmann's constant, T is the absolute temperature, and σ_0 is a constant.

If conductivity (J/E) is plotted vs. E on a logarithmic scale, a linear line can be fitted.

2. Schottky emission: This is an interface controlled mechanism operating at the electrode-film interface [111–113]. The current density can be estimated by (5.2):

$$J = A^* T^2 \exp\left(\frac{\beta_{\mathrm{s}} E^{1/2} - \phi_{\mathrm{s}}}{k_{\mathrm{B}} T}\right)$$
$$\beta_{\mathrm{s}} = \left(e^3/4\pi\varepsilon_0\varepsilon\right)^{1/2}, \tag{5.2}$$

where β_{s} is the Schottky coefficient, A is a constant, and Φ_{s} is the barrier height at the interface. Log J vs. $E^{0.5}$ will show a linear behavior if this mechanism is operating.

3. Space-charge limited current (SCLC): When large numbers of charge carriers exist in the film, the current density caused by space charges increases rapidly with the electric field [111–113]. The Log J–Log E plot, in this case, would show a linear relationship with a slope theoretically equal to two:

$$J_{\mathrm{SCLC}} = C\mu_{\mathrm{p}}\varepsilon_{\mathrm{i}} \frac{E^2}{d} \exp\left[\frac{-qW_{\mathrm{t}}}{k_{\mathrm{B}} T}\right], \tag{5.3}$$

where C is a constant, d is the film thickness, W_{t} is the trapping level, and μ_{p} is the hole mobility.

Figure 5.15 demonstrates the Ln J vs. $E^{0.5}$ plot for pure KNN and Li-modified (6 mol%) KNN films. The measured dielectric constant and β values are presented in Table 5.7, accordingly.

β_{expt} is calculated based on the slope of the graph (slope $= \beta/k_{\mathrm{B}}T$) at low and high electric fields. For pure KNN films at lower voltages, β_{expt} is closer to β_{s} showing that the dominant conduction mechanism is the interface-controlled injection current [83]. At higher voltages, the mechanism changes to the bulk-controlled P-F mechanism. For Li-doped films, the same mechanisms as pure films are predominant at high voltages. At lower voltages, as indicated in the inset (Fig. 5.15), there is a linear relationship between Log J and Log E having a slope value of 3 which indicates the presence of traps in the film and the rapid increase of the leakage current with applied voltage, which can be explained by the SCLC mechanism.

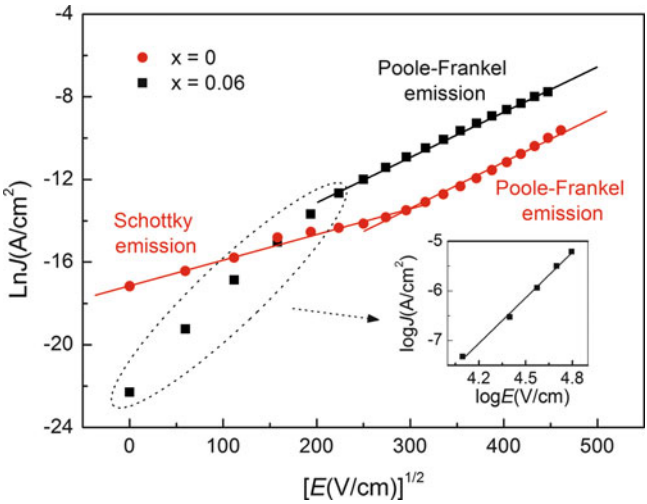

Fig. 5.15 Ln J vs. $E^{0.5}$ for pure KNN and Li-modified (6 mol%) KNN thin films on a Pt/Ti/SiO_2/Si substrates [83]

Table 5.7 The measured dielectric constant and β values of pure KNN and Li-modified films [83]

Li content	Dielectric constant	β_s	β_{PF}	β_{expt} at low E (<80 kV/cm)	β_{expt} at high E (>80 kV/cm)
$x = 0$	563	5.15	10.30	5.01	9.12
$x = 0.06$	625	5.42	10.84	...	9.04

Abazari et al. carried out a similar analysis to find the leakage current mechanism in pulsed laser deposited KNN-LT-LS and Mn-doped KNN-LT-LS films on STO substrates. The conduction mechanisms were identified to be P-F and Schottky for the base film and the Mn-doped film, respectively. At low electric fields, ohmic conduction contributes to the leakage current of Mn-modified thin films. Ohmic conduction has also been reported to be the prevailing mechanism for KNN films made by the sputtering technique [91]. At higher electric fields, the mechanism changes to modified Child's conduction, followed by a steep rise in the Log J–Log E plot where the trap-field limit (TFL) operates after the complete filling of deep traps [91].

The temperature dependency of DC conductivity can be expressed by an Arhenius type equation:

$$\sigma_{dc} = \sigma_o \exp(-E_a/k_B T), \tag{5.4}$$

where σ_o and k_B are constants and E_a is the activation energy of conduction.

Wu et al. calculated the activation energy of a KNN thin film to be about 0.93 eV, which is near the activation energy for the motion of oxygen vacancies in oxide thin films. This suggests that oxygen vacancies have a main role in the conduction process

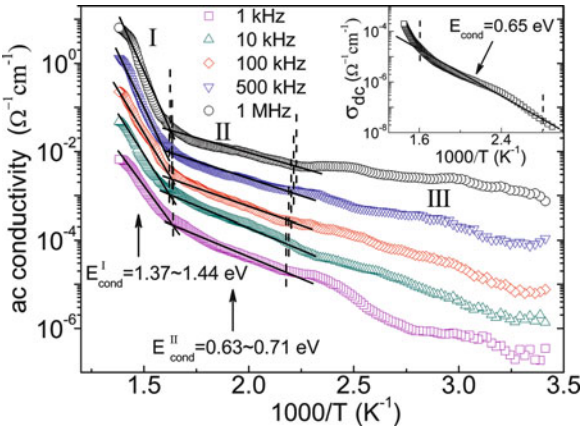

Fig. 5.16 Inverse temperature dependence of AC conductivity of the KNN/LSM/LAO heterostructure at various frequencies. The inset shows the plot of DC conductivity vs. 1,000 T^{-1} in the films (film thickness = 220 nm) [114]

of KNN films [91]. Miao et al. [114] reported epitaxial KNN/LSM ($La_{0.67}Sr_{0.33}MnO_3$) heterostructures on $LaAlO_3$ (LAO) substrates with a high remnant polarization of 21.3 μC cm^{-2}. A relaxation phenomenon exists in the temperature range of 200–350°C, meaning that increasing the frequency decreases the dielectric constant and shifts the maximum temperature (T_m) to higher temperatures. Considering the relaxation behavior as a thermally activated process, the activation energy for that is estimated to be 1.87 eV which is close to the activation energy for the diffusion of ionized oxygen vacancies in many oxides [115, 116].

The temperature dependence of AC conductivity at different frequencies for KNN/LSM heterostructures on LAO substrates is shown in Fig. 5.16.

The activation energy for the temperature range (200–350°C) in which the relaxation phenomenon occurs is about 0.63–0.71 eV, which is the same as the activation energy for DC conductivity as shown in the inset, implying that an identical activation process is responsible for both DC and AC conductivities in the mentioned temperature region. Lee et al. also calculated the activation energy for DC conductivity to be 0.59 eV for KNN films on $Pt/Ti/SiO_2/Si$ substrates [90]. Since the activation energy for relaxation is larger than the activation energy for conduction, it can be concluded that the relaxation process is dominated by a dipolar conduction process (V_O^{oo}-Nb^{+4} dipoles in this case) [114]. In the case that E_{relax} is lower than E_{cond}, it has been suggested that the relaxation is governed by the trapped control or hopping conduction processes [117].

5.5 Summary

In this chapter, the piezoelectric and ferroelectric properties of the most important KNN-based ceramics, crystals, and thin films have been reviewed. The novel compositions with the highest electromechanical properties along with their processing challenges have been introduced.

The hygroscopic nature of the precursors, volatilization of K and Na elements during high temperature processing, formation of secondary phases, low relative density, and high leakage current are some of the challenges facing the development of lead-free KNN-based compositions. The electrical properties can be improved by modification of the microstructure or chemical composition through targeting the sintering behavior, formation of the MPB, or shifting the PPT temperature downward to around room temperature.

The preparation of high quality thin films requires an optimization of processing condition to control the microstructure and achieve the stoichiometric composition. The low electrical resistivity in KNN-based thin films prevents achieving saturated *P–E* hysteresis loops. This high leakage current can be reduced by adding an appropriate dopant or utilizing a buffer layer.

Despite the enormous studies on KNN materials during the last decade, still more research is needed to address the preparation of KNN-based compositions for sensor, actuator, and microelectromechanical systems (MEMS) applications.

References

1. Jaffe B, Cook WR, Jaffe H (1971) Piezoelectric ceramics. Academic, London
2. Katz L, Megaw HD (1967) The structure of potassium niobate at room temperature: the solution of a pseudosymmetric structure by Fourier methods. Acta Crystallogr 22:639–648
3. Nakamura K, Kawamura Y (2000) Orientation dependence of electromechanical coupling factors in $KNbO_3$. IEEE Trans Ultrason Ferroelectr Freq Control 47:750–755
4. Kakimoto K, Masuda I, Ohsato HJ (2005) Lead-free $KNbO_3$ piezoceramics synthesized by pressure-less sintering. J Eur Ceram Soc 25:2719–2722
5. Tashiro S, Nagamatsu H, Nagata K (2002) Sinterability and piezoelectric properties of $KNbO_3$ ceramics after substituting Pb and Na for K. Jpn J Appl Phys 41:7113–7118
6. Ishii H, Nagata H, Takenaka T (2001) Morphotropic phase boundary and electrical properties of bismuth sodium titanate-potassium niobate solid-solution ceramics. Jpn J Appl Phys 40:5660–5663
7. Baker DW, Thomas PA, Zhang N et al (2009) Structural study of $K_xNa_{1-x}NbO_3$ (KNN) for compositions in the range x = 0.24-0.36. Acta Crystallogr B 65:22–28
8. Wu L, Zhang JL, Wang CL et al (2008) Influence of compositional ratio K/Na on physical properties in $K_xNa_{1-x}NbO3$ ceramics. J Appl Phys 103:084116
9. Ringgaard E, Wurlitzer T (2005) Properties of lead-free piezoceramics based on alkali niobates. J Eur Ceram Soc 25:2701–2706
10. Rodel J, Jo W, Seifert KTP et al (2009) Perspective on the development of lead-free piezoceramics. J Am Ceram Soc 92:1153–1177

11. Matsubara M, Yamaguchi T, Kikuta K (2005) Effect of Li substitution on the piezoelectric properties of potassium sodium niobate ceramics. Jpn J Appl Phys 44:6136–6142
12. Guo Y, Kakimoto K, Ohsato H (2004) Phase transitional behavior and piezoelectric properties of $(Na_{0.5}\ K_{0.5})NbO_3$-$LiNbO_3$ ceramics. Appl Phys Lett 85:4121–4123
13. Ahn CW, Park CS, Viehland D et al (2008) Correlation between phase transitions and piezoelectric properties in lead-free (K, Na, Li)NbO3-BaTiO3 ceramics. Jpn J Appl Phys 47:8880–8883
14. Jiang XP, Yang Q, Yu ZD et al (2010) Microstructure and electrical properties of $Li_{0.5}Bi_{0.5}TiO_3$-modified $(Na_{0.5}\ K_{0.5})NbO_3$ lead-free piezoelectric ceramics. J Alloy Compd 493:276–280
15. Zuo R, Fang X, Ye C (2007) Phase structures and electrical properties of new lead-free $(Na_{0.5}\ K_{0.5})NbO_3$-$(Bi_{0.5}Na_{0.5})TiO_3$ ceramics. Appl Phys Lett 90:092904
16. Du H, Zhou W, Zhu D et al (2008) Sintering characteristic, microstructure, and dielectric relaxor behavior of $(K_{0.5}Na_{0.5})NbO_3$-$(Bi_{0.5}Na_{0.5})TiO_3$ lead-free ceramics. J Am Ceram Soc 91:2903–2909
17. Sutapun M, Huang CC, Cann D et al (2009) Phase transitional behavior and dielectric properties of lead free $(1\text{-}x)(K_{0.5}Na_{0.5})NbO_3$-$xBi(Zn_{0.5}Ti_{0.5})O_3$ ceramics. J Alloy Compd 479:462–466
18. Saito Y, Takao H, Tani T et al (2004) Lead-free piezoceramics. Nature 432:84–87
19. Jadidian B, Marandian Hagh N, Winder AA et al (2009) 25 MHz ultrasonic transducers with lead-free piezoceramic, 1–3 PZT fiber-epoxy composite, and PVDF polymer active elements. IEEE Trans Ultrason Ferroelectr Freq Control 56:368–378
20. Guo Y, Kakimoto K, Ohsato H (2004) $(Na_{0.5}\ K_{0.5})NbO_3$-$LiTaO_3$ lead-free piezoelectric ceramics. Mater Lett 59:241–244
21. Saito Y, Takao H (2003) High performance lead-free piezoelectric ceramics in the (K, Na) NbO3-LiTaO3 solid solution system. Ferroelectrics 338:17–32
22. Dai Y, Zhang X, Zhou G (2007) Phase transitional behavior in $K_{0.5}Na_{0.5}NbO_3$-$LiTaO_3$ ceramics. Appl Phys Lett 90:262903
23. Wang Y, Damjanovic D, Klein N et al (2007) Compositional inhomogeneity in Li- and Ta-modified (K, Na)NbO_3 ceramics. J Am Ceram Soc 90:3485–3489
24. Wang Y, Damjanovic D, Klein N et al (2008) High-temperature instability of Li- and Ta-modified (K, Na)NbO3 Piezoceramics. J Am Ceram Soc 91:1962–1970
25. Zhang S, Xia R, Shrout TR et al (2007) Characterization of lead free $(K_{0.5}Na_{0.5})NbO_3$-$LiSbO_3$ piezoceramic. Solid State Commun 141:675–679
26. Zhang S, Xia R, Shrout TR et al (2006) Piezoelectric properties in perovskite 0.948 $(K_{0.5}Na_{0.5})NbO_3$-$0.052LiSbO_3$ lead-free ceramics. J Appl Phys 100:104108
27. Wu J, Wang Y, Xiao D et al (2007) Piezoelectric properties of $LiSbO_3$-modified $(K_{0.48}Na_{0.5})NbO_3$ lead-free ceramics. Jpn J Appl Phys 46:7375–7377
28. Wu J, Xiao D, Wang Y et al (2007) Compositional dependence of phase structure and electrical properties in $K_{0.42}Na_{0.58}NbO_3$-$LiSbO_3$ lead-free ceramics. J appl Phys 102:114113
29. Li X, Jiang M, Liu J et al (2009) Phase transitions and electrical properties of $(1\text{-}x)(K_{0.5}Na_{0.5})NbO_3$-$xBiScO_3$ lead-free piezoelectric ceramics with a CuO sintering aid. Phys Status Solidi A 206:2622–2626
30. Dai Y, Zhang X (2008) Phase transition behavior and electrical properties of lead-free $(1\text{-}x)(0.98\ K_{0.5}Na_{0.5}NbO_3\text{-}0.02LiTaO_3)\text{-}x(0.96Bi_{0.5}Na_{0.5}TiO_3\text{-}0.04BaTiO_3)$ piezoelectric ceramics. J Eur Ceram Soc 28:3193–3198
31. Kosec M, Bobnar V, Hrovat M et al (2004) New lead-free relaxors based on the $K_{0.5}Na_{0.5}NbO_3$-$SrTiO_3$ solid solution. J Mater Res 19:1849–1854
32. Li E, Suzuki R, Hoshina T et al (2009) Dielectric, piezoelectric, and electromechanical phenomena in $K_{0.5}Na_{0.5}NbO_3$-$LiNbO_3$-$BiFeO_3$-$SrTiO_3$ ceramics. Appl Phys Lett 94:132903
33. Kosec M, Kolar D (1975) On activated sintering and electrical properties of $KNaNbO_3$. Mater Res Bull 10:335–340
34. Malic B, Bernard J, Holc J et al (2005) Alkaline-earth doping in (K, Na)NbO3 based piezoceramics. J Eur Ceram Sco 25:27072711

35. Maeder MD, Damjanovic D, Setter N (2004) Lead free piezoelectric materials. J Electroceram 13:385–392
36. Hagh NM, Kerman K, Jadidian B (2009) Dielectric and piezoelectric properties of Cu^{2+}-doped alkali Niobates. J Eur Ceram Soc 29:2325–2332
37. Li E, Kakemoto H, Wada S et al (2008) Enhancement of Q_m by Co-doping of Li and Cu to potassium sodium niobate lead-free ceramics. IEEE Trans Ultrason Ferroelectr Freq Control 55:980–987
38. Li E, Kakemoto H, Hoshina T et al (2008) A shear-mode ultrasonic motor using potassium sodium niobate-based ceramics with high mechanical quality factor. Jpn J Appl Phys 47:7702–7706
39. Takao H, Saito Y, Aoki Y et al (2006) Microstructural evolution of crystalline-oriented $(K_{0.5}Na_{0.5})NbO_3$ piezoelectric ceramics with a sintering aid of CuO. J Am Ceram Soc 89:1951–1956
40. Hagh NM, Jadidian B, Ashbahian E et al (2008) Lead-free piezoelectric ceramic transducer in the donor-doped $K_{0.5}Na_{0.5}NbO_3$ solid solution system. IEEE Trans Ultrason Ferroelectr Freq Control 55:214–224
41. Ji HN, Ok YP, Tai WP et al (2010) Preparation of lead-free (K, Na)NbO3-LiSbO3 ceramics with high piezoelectric constants by FeO doping. J Korean Phys Soc 56:1156–1159
42. Zhang S, Xai R, Shrout TR (2007) Modified $(K_{0.5}Na_{0.5})NbO_3$ based lead-free piezoelectrics with broad temperature usage range. Appl Phys Lett 91:132913
43. Zhang S, Xia R, Hao H et al (2008) Mitigation of thermal and fatigue behavior in $K_{0.5}Na_{0.5}NbO_3$-based lead free piezoceramics. Appl Phys Lett 92:152904
44. Park SH, Ahn CW, Nahm S et al (2004) Microstructure and piezoelectric properties of ZnO-added $(Na_{0.5}\ K_{0.5})NbO_3$ Ceramics. Jpn J Appl Phys 43:L1072–L1074
45. Rubio-Marcos F, Romero JJ, Navarro-Rojero MG et al (2009) Effect of ZnO on the structure, microstructure and electrical properties of KNN-modified piezoceramics. J Eur Ceram Soc 29:3045–3052
46. Malic B, Bernard J, Bencan A et al (2008) Influence of zirconia addition on the microstructure of K0.5Na0.5NbO3 ceramics. J Eur Ceram Soc 28:1191–1196
47. Matsubara M, Yamaguchi T, Kikuta K et al (2005) Sintering and piezoelectric properties of potassium sodium niobate ceramics with newly developed sintering aid. Jpn J Appl Phys 44:258–263
48. Matsubara M, Yamaguchi T, Kikuta K et al (2004) Sinterability and piezoelectric properties of (K, Na)NbO3 ceramics with novel sintering aid. Jpn J Appl Phys 43:7159–7163
49. Matsubara M, Kikuta K, Hirano S (2005) Piezoelectric properties of $(K_{0.5}Na_{0.5})(Nb_{1-x}Ta_x)O_3$-$K_{5.4}CuTa_{10}O_{29}$ ceramics. J Appl Phys 97:114105
50. Ryu J, Choi JJ, Hahn BD et al (2007) Sintering and piezoelectric properties of KNN ceramics doped with KZT. IEEE Trans Ultrason Ferroelectr Freq Control 54:2510–2515
51. Lim JB, Zhang S, Jeon JH et al (2010) (K, Na)NbO3-based ceramics for piezoelectric hard lead-free materials. J Amer Ceram Soc 93:1218–1220
52. Matsubara M, Yamaguchi WT, Sakamoto W et al (2005) Processing and piezoelectric properties of lead-free (K, Na)(Nb, Ta)O3 ceramics. J Am Ceram Soc 88:1190–1196
53. Hagh NM, Jadidian B, Safari A (2007) Property-processing relationship in lead-free (K, Na, Li)NbO3-solid solution system. J Electroceram 18:339–346
54. Safari A, Abazari M, Kerman K et al (2009) $(K_{0.44}Na_{0.52}Li_{0.04})(Nb_{0.84}Ta_{0.10}Sb_{0.06})O_3$ ferroelectric ceramics. IEEE Trans Ultrason Ferroelectr Freq Control 56:1586–1594
55. Leel YH, Cho JH, Kim B et al (2008) Piezoelectric properties and densification based on control of volatile mass of potassium and sodium in $(K_{0.5}\ Na_{0.5})NbO_3$ ceramics. Jpn J Appl Phys 47:4620–4622
56. Acker J, Kungl WH, Hoffmann MJ (2010) Influence of alkaline and niobium excess on sintering and microstructure of sodium-potassium niobate $(K_{0.5}Na_{0.5})NbO_3$. J Am Ceram Soc 93:1270–1281

57. Haertling GH (1967) Properties of hot-pressed ferroelectric alkali niobate ceramics. J Am Ceram Soc 50:329–330
58. Jaeger RE, Egerton L (1962) Hot-pressing of potassium sodium niobates. J Am Ceram Soc 45:209–213
59. Wang R, Xie R, Sekiya T et al (2004) Fabrication and characterization of potassium-sodium niobate piezoelectric ceramics by spark-plasma-sintering method. Mater Res Bull 39:1709–1715
60. Wang R, Xie R, Sekiya T et al (2002) Piezoelectric properties of spark-plasma-sintered $(Na_{0.5}\ K_{0.5})NbO_3$-$PbTiO_3$ ceramics. Jpn J Appl Phys 41:7119–7122
61. Tani T, Kimura T (2006) Reactive-templated grain growth processing for lead free piezoelectric ceramics. Adv Appl Ceram 105:55–63
62. Saito Y, Takao H (2010) Synthesis of polycrystalline platelike $NaNbO_3$ particles by the topochemical micro-crystal conversion from $K_4Nb_6O_{17}$ and fabrication of grain-oriented $(K_{0.5}Na_{0.5})NbO_3$ ceramics. J Electroceram 24:39–45
63. Chang YF, Poterala SF, Yang ZP et al (2010) Microstructure development and piezoelectric properties of highly textured CuO-doped KNN by templated grain growth. J Mater Res 25:687–694
64. Chen K, Xu G, Yang D et al (2007) Dielectric and piezoelectric properties of lead-free 0.95 $(K_{0.5}Na_{0.5})NbO_3$-0.05$LiNbO_3$ crystals grown by the Bridgeman method. J Appl Phys 101:044103
65. Kizaki Y, Noguchi Y, Miyayama M (2006) Defect control for low leakage current in $K_{0.5}Na_{0.5}NbO_3$ single crystals. Appl Phys Lett 89:142910
66. Lin D, Li Z, Zhang S et al (2010) Influence of MnO_2 doping on the dielectric and piezoelectric properties and the domain structure in $(K_{0.5}Na_{0.5})NbO_3$ single crystals. J Am Ceram Soc 93:941–944
67. Ursic H, Bencan A, Skarabot M et al (2010) Dielectric, ferroelectric, piezoelectric, and electrostrictive properties of $K_{0.5}Na_{0.5}NbO_3$ single crystals. J Appl Phys 107:033705
68. Bencan A, Tchernychova E, Godec M et al (2009) Compositional and structural study of a $(K_{0.5}Na_{0.5})NbO_3$ single crystal prepared by solid state crystal growth. Microsc Microanal 15:435–440
69. Lin D, Li Z, Zhang S et al (2009) Dielectric-piezoelectric properties and temperature dependence of domain structure evolution in lead free $(K_{0.5}Na_{0.5})NbO_3$ single crystal. Solid State Commun 149:1646–1649
70. Davis M, Klein N, Damjanovic D et al (2007) Large and stable thickness coupling coefficients of [001]C-oriented KNbO3 and Li-modified (K, Na)NbO3 single crystals. Appl Phys Lett 90:062904
71. Inagaki Y, Kakimoto K (2008) Dielectric and piezoelectric properties of Mn-doped $Na_{0.5}$ $K_{0.5}NbO_3$ single crystals grown by flux method. Appl Phys Express 1:061602
72. Lin D, Li Z, Xu Z et al (2009) Characterization of KNN single crystals by slow-cooling technique. Ferroelectr 381:1–8
73. Noguchi Y, Miyayama M (2010) Effect of Mn doping on the leakage current and polarization properties in $K_{0.14}Na_{0.86}NbO_3$ ferroelectric single crystals. J Ceramic Soc Jpn 118:711–716
74. Kimura H, Tanahashi R, Maiwa K et al (2009) Potassium-sodium-rubidium niobate single crystals and electric properties. Int J Mod Phys B 23:3631–3636
75. Fisher JG, Bencan ZA, Kosec M et al (2008) Growth of dense single crystals of potassium sodium niobate by a combination of solid-State crystal growth and hot pressing. J Am Ceram Soc 91:1503–1507
76. Fisher JG, Bencan A, Holc J et al (2007) Growth of potassium sodium niobate single crystals by solid state crystal growth. J Cryst Growth 303:487–492
77. Nakashima Y, Sakamoto W, Maiwa H et al (2007) Lead-free piezoelectric (K, Na)NbO3 thin films derived from metal alkoxide precursors. Jpn J Appl Phys 46:L311–L313
78. Anh CW, Lee SY, Lee HJ et al (2009) The effect of K and Na excess on the ferroelectric and piezoelectric properties of $K_{0.5}Na_{0.5}NbO_3$ thin films. J Phys D Appl Phys 42:215304

79. Wang L, Yao K, Ren W (2008) Piezoelectric $K_{0.5}Na_{0.5}NbO_3$ thick films derived from polyvinylpyrrolidone-modified chemical solution deposition. Appl Phys Lett 93:092903
80. Lai F, Li JF (2007) Sol-Gel processing and characterization of (Na, K)NbO3 lead-free ferroelectric films. Ferroelectr 358:181–187
81. Schroeter C, Wessler B, Eng LM (2007) High throughput method for $K_{0.5}Na_{0.5}NbO_3$ thin films preparation by chemical solution deposition. J Eur Ceram Soc 27:3785–3788
82. Nakashima Y, Sakamoto W, Shimura T et al (2007) Chemical processing and characterization of ferroelectric (K, Na)NbO3 thin films. Jpn J Appl Phys 46:6971–6975
83. Lai F, Li JF, Zhu ZX et al (2009) Influence of Li content on electrical properties of highly piezoelectric (Li, K, Na)NbO3 thin films prepared by sol-gel processing. J Appl Phys 106:064101
84. Ahn CW, Jeong ED, Lee SY et al (2008) Enhanced ferroelectric properties of $LiNbO_3$ substituted $Na_{0.5}$ $K_{0.5}NbO_3$ lead-free thin films grown by chemical solution deposition. Appl Phys Lett 93:212905
85. Tanaka K, Kakimoto K, Ohsato H (2006) Fabrication of highly oriented lead-free (Na, K) NbO3 thin films at low temperature by sol-gel process. J Cryst Growth 294:209–213
86. Lai F, Li JF (2007) Sol-gel processing of lead-free (Na, K)NbO3 ferroelectric films. J Sol-Gel Sci Technol 42:287–292
87. Lee H, Ahn CW, Kang SH et al (2006) The ferroelectric properties of $(Na_{0.5}$ $K_{0.5})NbO_3$ thin films fabricated by rf-magnetron sputtering. Ferroelectrics 335:227–232
88. Lee JS (2008) Preparation and evaluation of lead-free $Na_{0.5}$ $K_{0.5}NbO_3$ ferroelectric thin films. J Korean Phys Soc 52:1109–1113
89. Kim JS, Lee HJ, Lee SY et al (2010) Frequency and temperature dependence of dielectric and electrical properties of radio-frequency sputtered lead-free $K_{0.48}Na_{0.52}NbO_3$ thin films. Thin Solid Films 518:6390–6393
90. Lee HJ, Kim IW, Kim JS et al (2009) Ferroelectric and piezoelectric properties of $Na_{0.52}$ $K_{0.48}NbO_3$ thin films prepared by radio frequency magnetron sputtering. Appl Phys Lett 94:092902
91. Wu J, Wang J (2009) Phase transitions and electrical behavior of lead-free $(K_{0.50}Na_{0.50})NbO_3$ thin film. J Appl Phys 106:066101
92. Shibata K, Oka F, Ohishi A et al (2008) Piezoelectric properties of (K, Na)NbO3 films deposited by RF magnetron sputtering. Appl Phys 1:011501
93. Blomqvist M, Khartsev S, Grishin A (2003) Optical waveguiding in magnetron-sputtered $Na_{0.5}$ $K_{0.5}NbO_3$ thin films on sapphire substrates. Appl Phys Lett 82:439–441
94. Shibata K, Oka F, Nomoto A et al (2008) Crystalline structure of highly piezoelectric (K, Na) NbO3 films deposited by RF magnetron sputtering. Jpn J Appl Phys 47:8909–8913
95. Khartsev I, Grishin MA, Grishin AM (2005) Characterization of heteroepitaxial $Na_{0.5}$ $K_{0.5}NbO_3/La_{0.5}Sr_{0.5}CoO_3$ electro-optical cells. Appl Phys Lett 86:062901
96. Wang X, Helmersson U, Olafsson S et al (1998) Growth and field dependent dielectric properties of epitaxial $Na_{0.5}$ $K_{0.5}NbO_3$ thin films. Appl Phys Lett 73:927–929
97. Shibata K, Suenaga K, Nomoto A et al (2009) Curie temperature, biaxial elastic modulus, and thermal expansion coefficient of (K, Na)NbO3 piezoelectric thin films. Jpn J Appl Phys 48:121408
98. Cho CR, Grishina A (1999) Self-assembling ferroelectric $Na_{0.5}$ $K_{0.5}NbO_3$ thin films by pulsed-laser deposition. Appl Phys Lett 75:268–270
99. Cho CR, Koh JH, Grishin A (2000) $Na_{0.5}$ $K_{0.5}NbO_3/SiO_2/Si$ thin film varactor. Appl Phys Lett 76:1761
100. Cho CR, Katardjiev I (2002) $Na_{0.5}$ $K_{0.5}NbO_3$ thin films for voltage controlled acoustoelectric device applications. Appl Phys Lett 80:3171–3173
101. Saito T, Wada T, Adachi H et al (2004) Pulsed laser deposition of high-quality (K, Na)NbO3 thin films on SrTiO3 substrate using high-density ceramic targets. Jpn J Appl Phys 43:6627–6631

102. Saito T, Adachi H, Wada T (2005) Pulsed laser deposition of ferroelectric ($Na_{0.5}$ $K_{0.5}$) NbO_3-based thin films. Jpn J Appl Phys 44:L573–L575
103. Abazari M, Akdogan EK, Safari A (2008) Effect of manganese doping on remnant polarization and leakage current in (K0.44, Na0.52, Li0.04)(Nb0.84, Ta0.10, Sb0.06)O3 epitaxial thin films on SrTiO3. Appl Phys Lett 92:212903
104. Abazari M, Safari A (2009) Effects of doping on ferroelectric properties and leakage current behavior of KNN-LT-LS thin films on $SrTiO_3$ substrate. J Appl Phys 105:094101
105. Abazari M, Akdogan EK, Safari A (2008) Dielectric and ferroelectric properties of strain-relieved epitaxial lead-free KNN-LT-LS ferroelectric thin films on $SrTiO_3$ substrates. J Appl Phys 103:104106
106. Abazari M, Akdogan EK, Safari A (2008) Effects of background oxygen pressure on dielectric and ferroelectric properties of epitaxial (K0.44, Na0.52, Li0.04)(Nb0.84, Ta0.10, Sb0.06)O3 thin films on SrTiO3. Appl Phys Lett 93:192910
107. Abazari M, Choi T, Cheong SW et al (2010) Nanoscale characterization and local piezoelectric properties of lead-free KNN-LT-LS thin films. J Phys D: Appl Phys 43:025405
108. Harada S, Muralt P (2009) Pulsed laser deposition of KNN-based ferroelectric thin films on platinised Si substrates. IOP Conf Ser: Mater Sci Eng 8:012004
109. Yamazoe S, Miyoshi Y, Komaki K et al (2009) Ferroelectric properties of ($Na_{0.5}$ $K_{0.5}$)NbO_3-based thin films deposited on Pt/(001)MgO Substrate by pulsed laser deposition with $NaNbO_3$ buffer layer. Jpn J Appl Phys 48:09KA13
110. Ryu J, Choi JJ, Hahn BD et al (2007) Fabrication and ferroelectric properties of highly dense lead-free piezoelectric $K_{0.5}Na_{0.5}NbO_3$ thick films by aerosol deposition. Appl Phys Lett 90:152901
111. Sze SM (1981) Physics of semiconductor devices. Wiley, New York
112. Ohring M (1992) The materials science of thin films. Academic, New York
113. Kao KCH (2004) Dielectric phenomena in solids. Elsevier Academic, London
114. Miao J, Xu XG, Jiang Y et al (2009) Ionized-oxygen vacancies related dielectric relaxation in heteroepitaxial $K_{0.5}Na_{0.5}NbO_3/La_{0.67}Sr_{0.33}MnO_3$ structure at elevated temperature. Appl Phys Lett 95:132905
115. Wang ZY, Chen TG (1998) Evidence for the weak domain wall pinning due to oxygen vacancies in $SrBi_2Ta_2O_9$ from internal friction measurements. Phys Status Solidi A 167: R3–R4
116. Paladino AE (1965) Oxidation kinetics of single-crystal $SrTiO_3$. J Am Ceram Soc 48:476–478
117. Morii K, Kawano H, Fujii I et al (1995) Dielectric relaxation in amorphous thin films of $SrTiO_3$ at elevated temperatures. Appl Phys 78:1914–1919
118. Wang Y, Li Y, Kalantar-zadeh K et al (2008) Effect of Bi^{3+} ion on piezoelectric properties of $K_xNa_{1-x}NbO_3$. J Electroceram 21:629–632
119. Jiang M, Liu X, Chen G et al (2009) Dielectric and piezoelectric properties of $LiSbO_3$ doped 0.995 $K_{0.5}Na_{0.5}NbO_3$-0.005$BiFeO_3$ piezoelectric ceramics. Mater Lett 63:1262–1265
120. Ding A, Wang H (2010) Phase transitions and electrical properties of ($Na_{0.5}$ $K_{0.5}$)NbO_3-Bi ($Sc_{0.5}Fe_{0.5}$)O_3 lead-free piezoelectric ceramics. J Ceram Process Res 11:44–46
121. Lei C, Ye ZG (2008) Lead-free piezoelectric ceramics derived from the $K_{0.5}Na_{0.5}NbO_3$-$AgNbO_3$ solid solution system. Appl Phys Lett 93:042901
122. Chang Y, Yang Z, Wei L et al (2006) Effects of $AETiO_3$ additions on phase structure, microstructure and electrical properties of ($K_{0.5}Na_{0.5}$)NbO_3 ceramics. Mater Sci Eng A 437:301–305
123. Du H, Zhou W, Luo F et al (2008) Design and electrical properties' investigation of $K_{0.5}Na_{0.5}NbO_3$-$BiMeO_3$ lead-free piezoelectric ceramics. J Appl Phys 104:034104
124. Watanabe Y, Sumidal K, Yamadal S et al (2008) Effect of Mn-doping on the piezoelectric properties of ($K_{0.5}Na_{0.5}$)($Nb_{0.67}Ta_{0.33}$)O_3 lead-free ceramicsm. Jpn J Appl Phys 47:3556–3558

125. Du H, Zhou W, Lou F et al (2008) Polymorphic phase transition dependence of piezoelectric properties in $(0.5Na_{0.5})NbO_3$-$(Bi_{0.5}\ K_{0.5})TiO_3$ lead-free ceramics. J Phys D: Appl Phys 41:115413
126. Mgbemere HE, Herber RP, Schneider GA (2009) Effect of MnO_2 on the dielectric and piezoelectric properties of alkaline niobate based lead free piezoelectric ceramics. J Eur Ceram Soc 29:1729–1733

Chapter 6
Alkali Niobate Piezoelectric Ceramics

Akira Ando

6.1 Introduction

Piezoelectric ceramic materials are widely used in various electronic equipments [1–26]. Lead-based perovskite materials such as Pb(Ti, Zr)O_3 (PZT), or $PbTiO_3$-based materials are commonly used there. Piezoelectric properties of these lead-containing materials have been studied by a large number of researchers. On the other hand, environmental conscious (ECO) consideration grew up in the middle of 1990s especially in Europe. Alternatives for toxic lead-based piezoelectric ceramics have been studied by many researchers recently.

Bismuth layer structured ferroelectrics (BLSF) have been studied mainly for resonator applications [27–41], because of their relatively small electromechanical coupling, high mechanical quality factor (Q_m), and very flat temperature characteristics of resonance frequencies. Bi-perovskites such as $(Bi_{1/2}Na_{1/2})TiO_3$-based ceramics have also been studied for many years [42–53], and recently have been used for practical application of ultrasonic vibrators [42]. There have not been significant problems of degradations of the ceramics originating from the relatively low phase transition temperature around 200°C at which the ferroelectric phase changes to the antiferroelectric phase, and their piezoelectricity disappears. Alkaline niobate perovskite ceramic materials have been studied by a number of researchers [53–143, 146–150], because of their attractive properties such as high acoustic vibration velocities, high Curie temperatures, and relatively high electromechanical coupling properties. One of the earliest studies on the alkali niobate ceramics was done by Shirane, Newnham, and Pepinsky on ferroelectric properties of $KNbO_3$–$NaNbO_3$ (KNN) binary system [58]. Egarton and Dillon reported the piezoelectric properties of KNN binary system [61]. Nitta's pioneer work [66, 67] revealed the fundamental piezoelectric properties of pseudo binary system

A. Ando (✉)
Murata Mfg. Co., 1-10-1 Kotari, Nagaokakyo, Kyoto 617-8555, Japan
e-mail: a_ando@murata.co.jp

S. Priya and S. Nahm (eds.), *Lead-Free Piezoelectrics*,
DOI 10.1007/978-1-4419-9598-8_6, © Springer Science+Business Media, LLC 2012

$LiNbO_3$–$NaNbO_3$ (LNN). LNN-based ceramics had practically been used for transducers for delay line applications, because sound velocity of LNN is precisely high for these applications. Yonezawa and Ohno indicated poor reproducibility of these pseudo binary systems, and pointed out that it was improved by taking $LiNbO_3$–$NaNbO_3$–$KNbO_3$ ternary system [68]. Piezoelectric properties of these ternary system alkali niobate ceramic materials were detailed.

In spite of these great pioneers' works, the piezoelectric properties of the alkaline niobate-based materials at that days were not comparable to those of PZTs.

However, ECO technologies have increased their importance in 1990s especially in Europe, a number of studies on nontoxic electroceramics have been carried out [70–143, 146–150]. Current R&D situation of the lead-free piezoelectric ceramic materials is summarized by several researchers, and they give us good reviews on this research field [70–73]. On the other hand, recent studies revealed that alkali niobate ceramic material could show comparable piezoelectric properties to those of PZTs under certain given conditions. Kimura and Ando reported that alkali niobate-based ceramics show high dielectric permittivity above 1,500 with relatively high electromechanical coupling coefficient and relatively high Curie point with their developed materials of solid solutions between alkali niobates and other perovskite systems such as $CaTiO_3$ [76, 77, 81].

Matsubara and coresearchers reported large electric-field-induced strain over 0.1% with Ta modified KNN ceramics [83, 92–95]. Takenaka and coresearchers also showed that $KNbO_3$-based ceramics can generate a strain over 0.1% at a high electric field [84, 137]. These studies revealed that alkali niobate-based ceramics potentially have possibilities to compete with PZT as high strain piezoelectric ceramics. Saito and coresearchers applied the RTGG method to their alkali niobate ceramics in order to prepare oriented ceramics, and reported very large piezoelectric strain characteristics comparable to those of PZT ceramics which are practically used in large displacement actuator applications [85]. Furthermore, Wang and coreseachers also reported high d_{33} value around 450 pm/V, with their developed alkali niobate-based ceramics very recently [143]. However, for ordinarily sintered (nontextured) ceramics, alkali niobate ceramics did not show large d_{33} as PZTs until now.

There have also been many improvements for ceramic sample preparations of alkali niobate ceramics. Well-sintered ceramic samples for a wide composition region of alkali niobate-based materials have become possible by compositional designs [95, 138] or precise sintering aid additions such as Bi_2O_3, or CuO [122–125], or complex oxide materials such as $K_4CuNb_8O_{23}$ [83, 91–95, 138].

On the other hand, recently Kawada and coresearchers successfully obtained cofired multilayered ceramics of alkali niobate ceramics with Ni inner electrodes [142]. The multilayered ceramics showed comparable displacement characteristics with the PZT-based multilayered ceramics.

Furthermore, among a large number of piezoelectric application fields, high power characteristics of the alkali niobate ceramics attract the attention of many researchers. Kimura showed very high Q_m value around 3,000 for LNN-based alkali niobate ceramics by thermal annealing [80, 81], and maximum vibration velocity of the annealed LNN is much higher than those of PZT-based ceramic materials [82].

Matsubara and his coresearchers reported high Q_m characteristics of KNN-based ceramics by conventional fabrication process, and showed an electromechanical coupling coefficient around 40% (planer mode) and Q_m value above 1,000 [91]. Li, Tsurumi, and their coresearchers recently reported good high power characteristics of KNN-based alkali niobate ceramics for a piezoelectric motor application [135]. These high power properties are expected to exceed those of PZT materials, and lead to new piezoelectric application fields.

In this chapter, the authors give a historical review on the studies on alkali niobate family piezoelectric ceramics, and describe recent topical works on these ceramic materials.

6.2 Historical Review

Several years later after the discovery of ferroelectricity of $BaTiO_3$, ferroelectricity of alkali niobate materials such as $KNbO_3$ was discovered by Matthias [54]. Single crystalline samples were prepared by the molten salt method in order to reveal their electrical properties, such as dielectric permittivity and electric polarization. Dielectric anomalies were observed at around 200°C and around 400°C as shown in Fig. 6.1D–E hysteresis characteristics were also reported there. The ferroelectric phase transition temperature was determined to be 400°C, because the D–E hysteresis

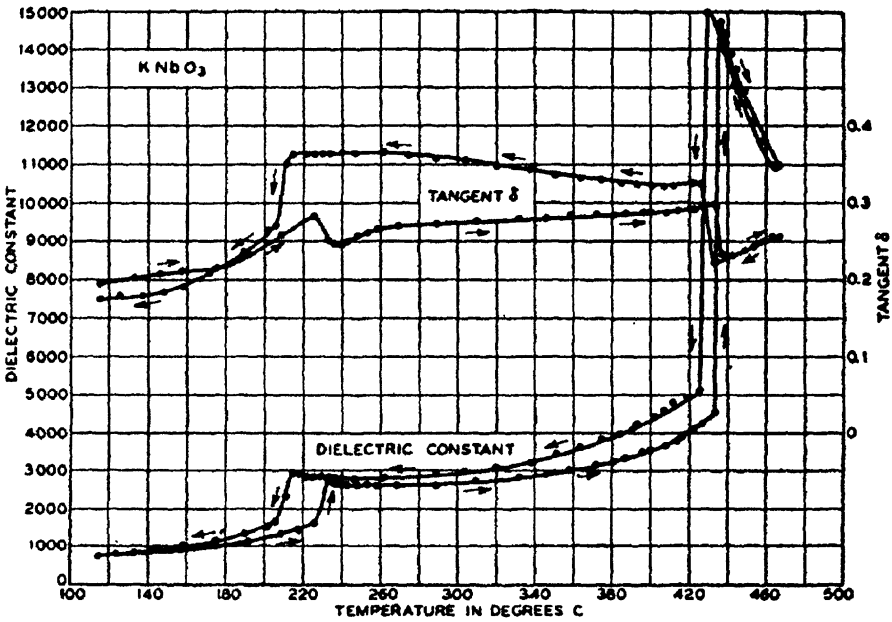

Fig. 6.1 Dielectric properties of single crystal of $KNbO_3$ above room temperature (After Matthias [55])

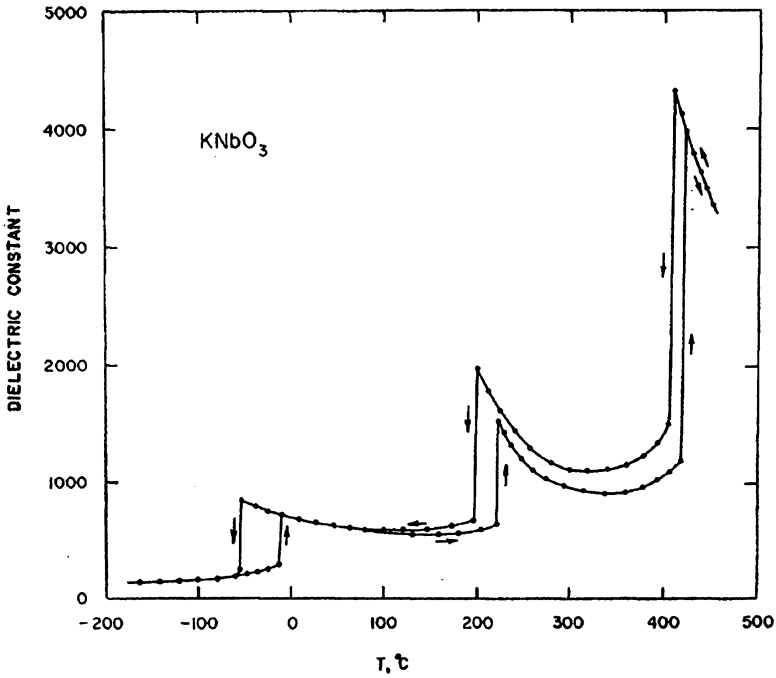

Fig. 6.2 Dielectric properties of $KNbO_3$ ceramics (After Shirane et al. [57])

disappears above 400°C. These phase transition properties were analyzed by Triebwasser [60] on the basis of the Devonshire's phenomenological treatment.

Further study of dielectric properties of $KNbO_3$ was done by Shirane and coresearchers [57], They investigated dielectric properties of $KNbO_3$ in a wide range of temperatures from −150 to 450°C and showed another dielectric anomaly below room temperature as shown in Fig. 6.2.

On the other hand, the antiferroelectric model for $NaNbO_3$ was suggested by detailed studies by Vousden [56]. At that time, Cross also described that no evidence was found for the ferroelectricity of $NaNbO_3$ [59]. A binary system of alkali niobates $KNbO_3$–$NaNbO_3$ (KNN) was studied at that time by Shirane et al. [58].

They fabricated ceramic samples of KNN, and investigated their dielectric properties. Dielectric characteristics of $NaNbO_3$ were also reported there as shown in Fig. 6.3.

The phase diagram of KNN binary system is shown in Fig. 6.4. They revealed the temperature dependences of their dielectric properties and clearly showed the successive phase transition of this binary system by using X-ray structural analysis data. They also showed ferroelectric characteristics of this binary system by measurements of D–E hysteresis.

Piezoelectric properties of the KNN binary system were discussed in detail by Egerton [61]. They made ceramic plate samples, and measured the temperature

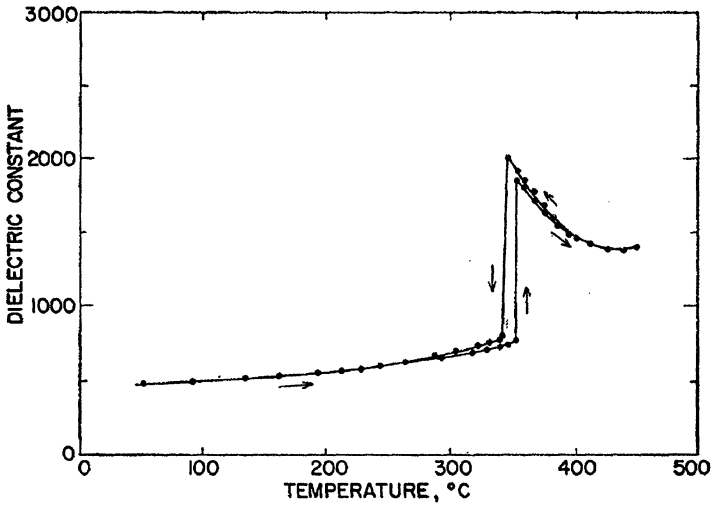

Fig. 6.3 Dielectric permittivity of $NaNbO_3$ ceramics (After Shirane et al. [58])

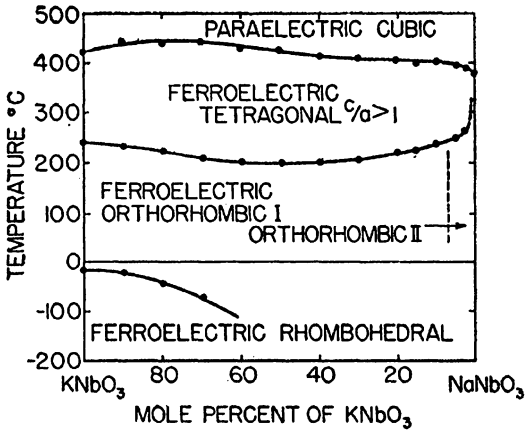

Fig. 6.4 Phase diagram of $K_xNa_{1-x}NbO_3$ (After Shirane et al. [58])

dependence of the resonance frequency as shown in Fig. 6.5. It showed some discontinuous changes according to the successive structural phase transitions.

Ceramic samples of KNN-based ceramics are difficult to make, because suitable firing temperature range is very narrow, i.e., less than 10°C. Jaeger and Egerton reported that the hot press technique is effective to obtain well-sintered ceramic samples of the alkali niobate materials and showed much improved piezoelectric properties for $K_{0.5}Na_{0.5}NbO_3$ composition [62]. Haertling also showed piezoelectric properties of hot pressed ceramics of KNN solid solution by changing their K:Na ratio [68]. Figure 6.6 shows the dielectric and piezoelectric properties of KNN binary system.

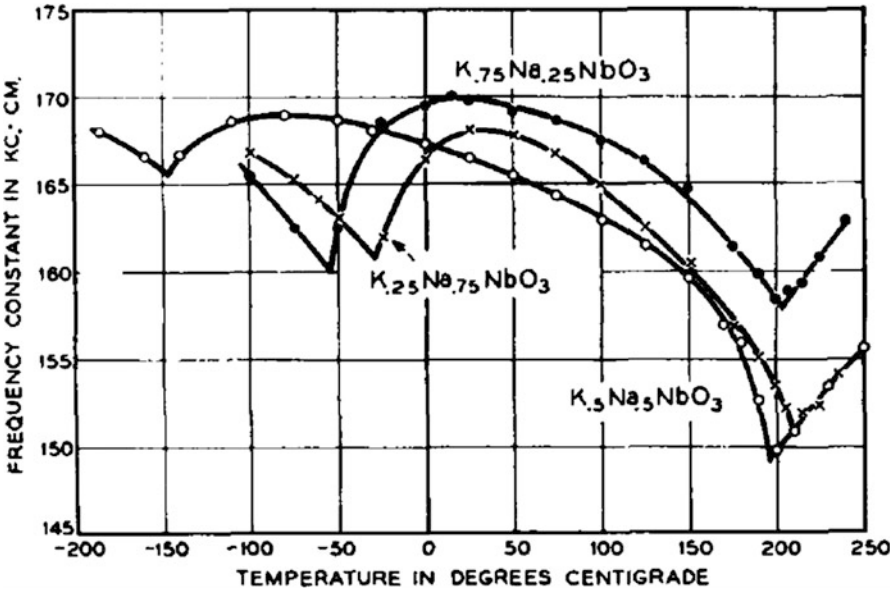

Fig. 6.5 Temperature dependence of piezoelectric resonance frequency of $(K_{0.5}Na_{0.5})NbO_3$ ceramics (planer mode) (After Egerton et al. [61])

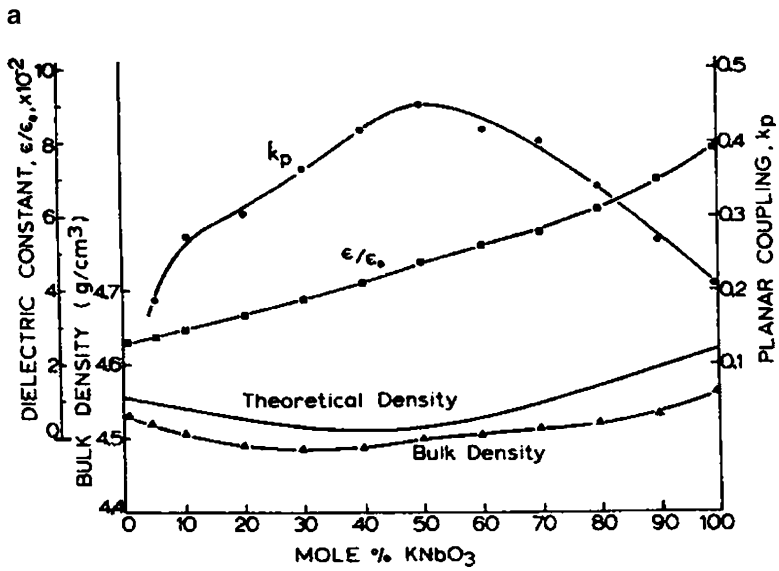

Fig. 6.6 Dielectric and piezoelectric properties of $K_xNa_{1-x}NbO_3$ ceramics with changing x (After Haertling [65]). Dielectric permittivity and planer electromechanical coupling coefficient k_p(a), remanent polarization P_r, and coercive field E_c(b)

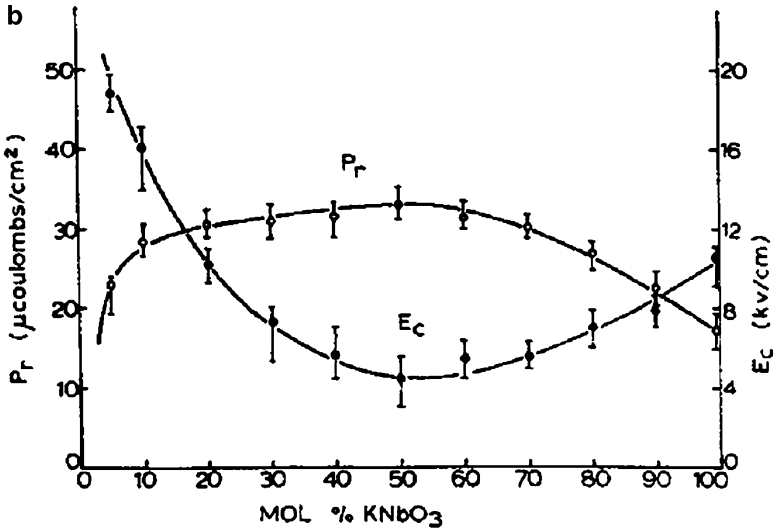

Fig. 6.6 (continued)

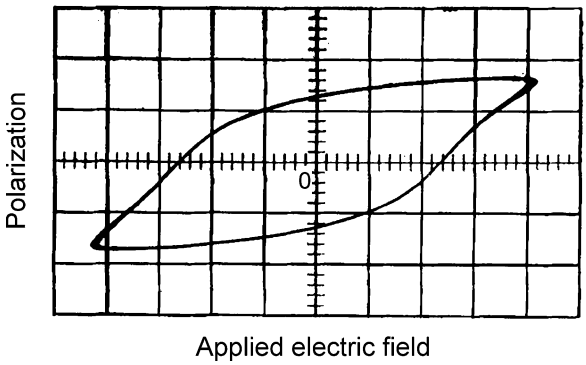

Fig. 6.7 D–E hysteresis observed for ceramic sample of $Li_xNa_{1-x}NbO_3$ ($x = 0.12$) (After Nitta [66]). Horizontal axis: 1 division = 14.4 kV/cm, Vertical axis: 1 division = 10mC/cm^2, Data taken at 60 Hz

The remanent polarizations of KNN are large among other ferroelectric material families. This means that electrically induced strains of KNN-based materials are supposed to be intrinsically large. This study on the KNN materials by Haertling is one of the epochs in the history of lead-free ceramic R&D.

Ferroelectric properties of another important binary system LNN were firstly reported by Nitta [66, 67]. The fraction of $LiNbO_3$ of the binary system was up to 0.14. A beautiful D–E hysteresis curve was observed for the composition with $LiNbO_3$ of 0.12 molar fraction as shown in Fig. 6.7. Henson and coresearchers pointed out that LNN has MPB-like phase change at vicinity of 0.12 of $LiNbO_3$, and observed dielectric permittivity maximum at that composition [69].

Table 6.1 Piezoelectric properties of alkali niobate ternary system (K, Na, Li)NbO_3 ceramics (After Yonezawa and Ohno [68])

Composition			Electrical properties				
$KNbO_3$	$NaNbO_3$	$LiNbO_3$	k_p (%)	Q_m	$\varepsilon_{33}^T/\varepsilon_0$	Tan δ (%)	fr·D (m/s)
0.1	0.88	0.02	22	360	128	2.9	3,440
0.1	0.86	0.04	21	490	138	2.9	3,490
0.1	0.84	0.06	22	290	140	2.8	3,470
0.09	0.82	0.08	27	220	122	2.1	3,400
0.09	0.81	0.1	29	340	106	2	3,420
0.09	0.79	0.12	30	400	99	2	3,400
0.09	0.77	0.14	30	440	99	1.9	3,440
0.09	0.75	0.16	27	490	91	2	3,400
0.08	0.74	0.18	21	520	104	2.2	3,410
0.19	0.76	0.05	29	400	160	1.9	3,380
0.18	0.72	0.1	34	290	136	2.5	3,280
0.17	0.68	0.15	31	330	133	2.5	3,290
0.16	0.64	0.2	20	350	133	1.5	3,310
0.285	0.665	0.05	30	160	276	3.6	3,360
0.27	0.63	0.1	32	220	232	2.8	3,270
0.475	0.475	0.05	38	160	357	3.1	3,190

k_p: Planer electromechanical coupling coefficient; Q_m: Mechanical quality factor; $\varepsilon_{33}^T/\varepsilon_0$: Relative dielectric permittivity along the poling direction; tan δ: Dielectric dissipation factor; fr·D: Frequency constant (D is the diameter of the disc-shaped specimen, and fr is the resonance frequency)

Though intensive studies on alkali niobate ceramics were carried out by these great frontiers, alkali niobate-based materials did not attract much attention as piezoelectric materials, because of the discovery of the superior piezoelectric ceramic material i.e. PZT. Piezoelectric ceramic materials and their application have been made mainly on the PZT materials for 50 years or more from the discovery of their piezoelectricity [144].

After 20 years from these frontier works on alkali niobate ceramics, in the middle of 1970s, nontoxic piezoelectric materials were required as alternatives for PZT which consists of lead as their main composition. Since alkali niobate system was considered as the good candidate for the alternates, its piezoelectric properties were re-examined. Ternary system (Li, Na, K)NbO_3 was studied by several researchers. Yonezawa and Ohno widely investigated the piezoelectric characteristics of this alkali niobate ternary system [68]. They showed the dielectric permittivity around 300, and the electromechanical coupling coefficient ranging from 0.2 to 0.3 for its planner vibration mode. These piezoelectric characteristics are summarized in Table 6.1.

Even though much effort was paid to obtain good lead-free piezoelectric materials in the ternary system (Li,Na,K)NbO_3, there were no materials which could compete PZT. At that time, one of the main application fields for piezoelectric ceramics is resonator device application such as acoustic wave filters. Then large temperature dependence of resonance frequency of the ternary system (Li, Na, K)

Table 6.2 Typical piezoelectric alkali niobate ceramics and their piezoelectric properties taken before 1980

Composition	$\varepsilon_{33}^T/\varepsilon_0$	k_p (%)	Q_m	fr·D (m/s)
$(Li_{0.04}Na_{0.96})NbO_3$ [66]	160	14.6	948	3,657
$(Li_{0.12}Na_{0.88})NbO_3$ [66]	220	23.2	720	3,352
$(K_{0.12}Na_{0.88})NbO_3$ hot-pressed [69]	110	39.5	755	1,760
$(K_{0.5}Na_{0.5})NbO_3$ [61]	290	34–39	130	1,670
$(K_{0.5}Na_{0.5})NbO_3$ hot-pressed [62]	420	45	240	1,700
$(K_{0.08}Na_{0.74}Li_{0.18})NbO_3$ [68]	104	21	520	3,410
$(K_{0.475}Na_{0.475}Li_{0.05})NbO_3$ [68]	357	38	160	3,190

k_p: Planer electromechanical coupling coefficient
Q_m: Mechanical quality factor
$\varepsilon_{33}^T/\varepsilon_0$: Relative dielectric permittivity along the poling direction
fr·D: Frequency constant (D is the diameter of the disc-shaped specimen, and fr is the resonance frequency)

NbO_3 is inconvenient for the practical resonator applications. It is very difficult to obtain very flat temperature characteristics of resonance frequency without a typical morphotoropic phase boundary [145]. Furthermore, their fabrication processes are more difficult than those for $BaTiO_3$ or lead-based perovskite materials, because of their water soluble composition, and their very narrow process windows for the conventional sintering. The motivation for alternating the lead-containing piezoelectric ceramics such as PZT by some lead-free material had been shrunk. However, on the data of piezoelectric properties of alkali niobate materials taken in this era, we can find still very important information for our recent R&D activities.

Piezoelectric properties of alkali niobates reported in this era are summarized in Table 6.2.

6.3 Recent Progress

ECO consideration grew up in the middle of 1990s especially in Europe as mentioned above. Alternatives for lead-based piezoelectric ceramics have been intensively investigated again. Here recent progresses on research and development of alkali niobate piezoelectric ceramics are reviewed.

6.3.1 Sample Preparation of Alkali Niobate Ceramics

The conventional powder processing is taken in order to make the sintered ceramic samples of alkali niobate ceramics. Typical fabrication process for alkali niobate-based ceramics is introduced here. Starting materials were carbonate salts such as Li_2CO_3, Na_2CO_3, K_2CO_3, and metal oxides such as Nb_2O_5. High purities above 99.9% are recommended for various starting materials. These materials are weighed and mixed in 2-propanol to make desired compositions. The mixtures of the starting

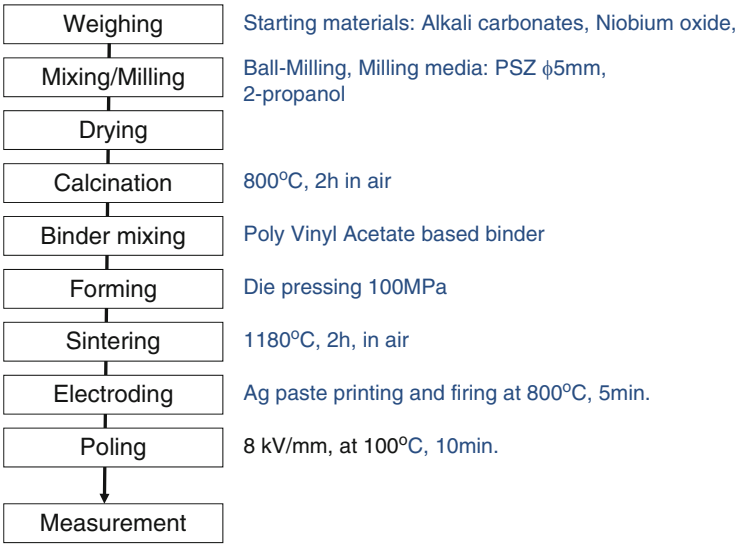

Fig. 6.8 Ceramic sample preparation procedure chart for alkali niobate-based materials

materials are ball-milled with partially stabilized zirconia (PSZ) balls (ϕ 5 mm), and the mixed powder is dried and calcined at 850°C for 2 h to obtain perovskite-structured crystalline powder. The calcined powder is mixed with an appropriate binder. Both organic- and water-based binder systems are possible to use. For example, a poly-vinyl acetate-based binder is added to the calcined powder by an amount of 5 wt%, and they are well mixed by the ball-milling in water for 10 h. The powder is dried and pulverized after a filtration. The pulverized powder is die-pressed into disk-shaped samples. These samples are fired at temperatures between 1,100 and 1,250°C. The calcination temperature can be roughly set; however, the sintering temperature for each composition should be carefully chosen to make well-sintered ceramic bodies. At higher temperatures the sample would melt, and at lower temperatures dense ceramic samples cannot be obtained. The process window for firing temperature is very narrow i.e., less than 10°C.

Silver electrodes are formed by paste printing on the main surfaces of the disk-shaped ceramic samples and firing at 850°C. A poling treatment is carried out at 100°C in silicone oil with electric fields between 5 and 8 kV/mm for 10 min. Then their dielectric and piezoelectric characteristics are evaluated. Fabrication process for the alkali niobate ceramics is shown in Fig. 6.8

6.3.2 Sinterability of Ceramics of $KNbO_3$–$NaNbO_3$–$LiNbO_3$ Ternary System

Since these pseudo ternary system materials are difficult to sinter, good piezoelectric characteristics were obtained at limited composition areas. Firing temperature should be controlled within 10°C of fluctuation to obtain good sintered samples.

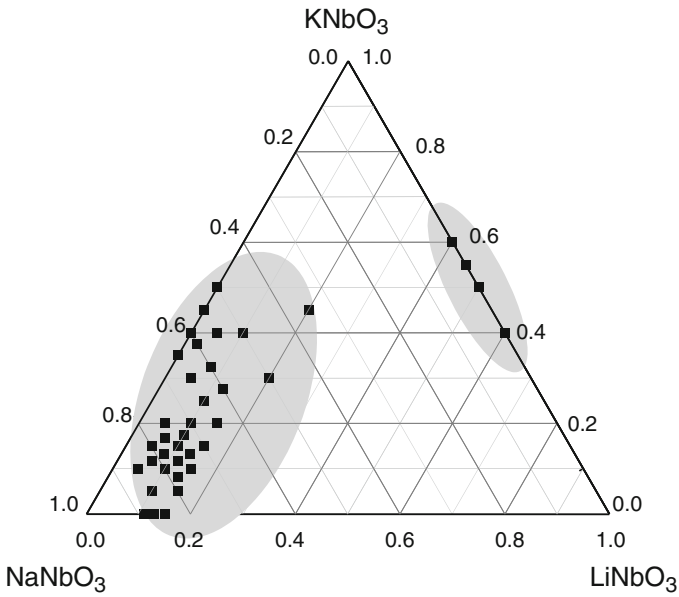

Fig. 6.9 Sinterability of ceramics of alkali niobate ternary system (Li, Na, K)NbO_3

Ceramic samples of the $KNbO_3$-rich compositions or $LiNbO_3$-rich compositions showed poor sinterability in the author's study. Well-sintered ceramics were obtained in the $NaNbO_3$-rich compositional region as shown in Fig. 6.9. The mark (black spot) in Fig. 6.9 represents a composition where the well-sintered ceramic samples were obtained, and their piezoelectric properties could be measured.

In order to improve their poor sinterability, special techniques such as a hot pressing have been employed. Recent study shows that by choosing appropriate additives as sintering aids, such as Bi_2O_3 or CuO [122–125] or complex oxides such as $K_4CuNb_8O_{23}$ [91–95], well-sintered alkali niobate ceramics can be obtained. Compositional modifications to alkali niobate ceramics were also proven to be effective in order to obtain well-sintered materials. Matsubara et al. showed good sinterability of KNN ceramics with alkali site-deficient compositions [95], and Aoyagi reported good sinterability of LNN also by alkali site-deficient modifications [141]. Matsubara et al. reported that the molar fraction of alkali ions between 0.9 and 0.99 led to the well-sintered ceramics. Optimal firing temperature is plotted against the composition as shown in Fig. 6.10.

These sintering process technologies will be increasing their importance in order to achieve the practical applications of lead-free piezoelectric ceramics.

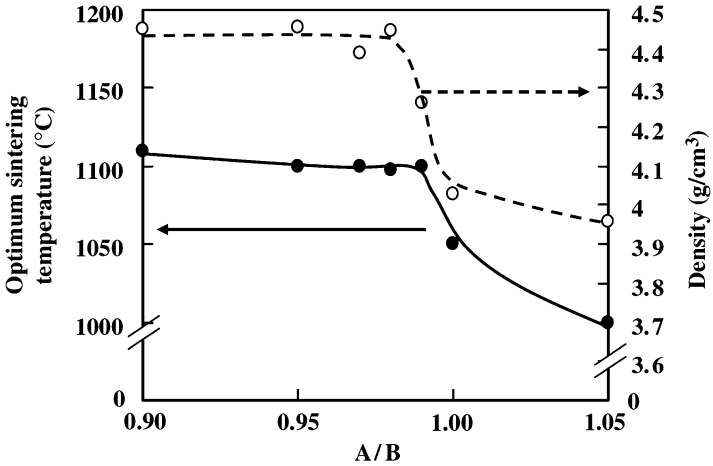

Fig. 6.10 Density of sintered ceramics of $KNbO_3$-based ceramics with changing A:B ratio (= K:Nb ratio) (After Matsubara et al. [95])

6.3.3 Dielectric and Piezoelectric properties of $KNbO_3$–$NaNbO_3$–$LiNbO_3$ Ternary System

Figure 6.11 shows dielectric permittivity of the ternary system. Relatively high values above 500 are obtained for the composition of which $KNbO_3$ fraction is above 0.3 and of which $LiNbO_3$ fraction is around 0.1. There is a tendency that dielectric permittivity increases with $KNbO_3$ fraction increase up to 0.3, and relatively low permittivity around 100 was observed with low $KNbO_3$ fraction.

Figure 6.12 shows the electromechanical coupling coefficient of the planer mode (k_p) of the ternary system. There are several compositions which show the electromechanical coupling coefficient more than 40%. Curie temperatures T_c of most of the obtained ceramics samples are more than 300°C.

Figure 6.13 shows the dielectric permittivity and the electromechanical coupling coefficient against $KNbO_3$ fraction while fixing the $LiNbO_3$ fraction at 0.1. Drastic changes are observed at around 0.25 of $KNbO_3$ fraction. The dielectric permittivity change against the $KNbO_3$ fraction shows an opposite trend to the electromechanical coupling coefficient change.

Spontaneous polarization is considered to be relatively unstable in the composition region with high dielectric permittivity, because unstable spontaneous polarizations mean that dielectric response against an electric field becomes large. Moreover, smaller spontaneous polarizations exhibit lower electromechanical couplings. Therefore, the dielectric permittivity and electromechanical coupling coefficient show opposite trends.

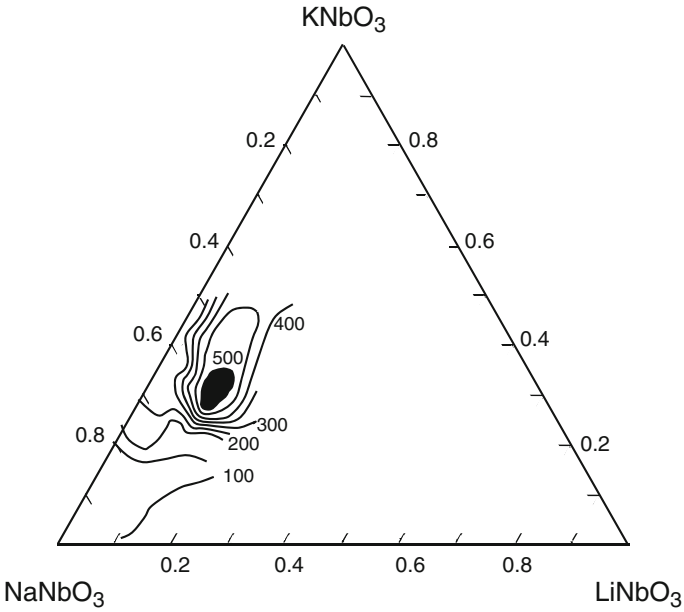

Fig. 6.11 Dielectric permittivity of ceramics of alkali niobate ternary system (Li, Na, K)NbO_3

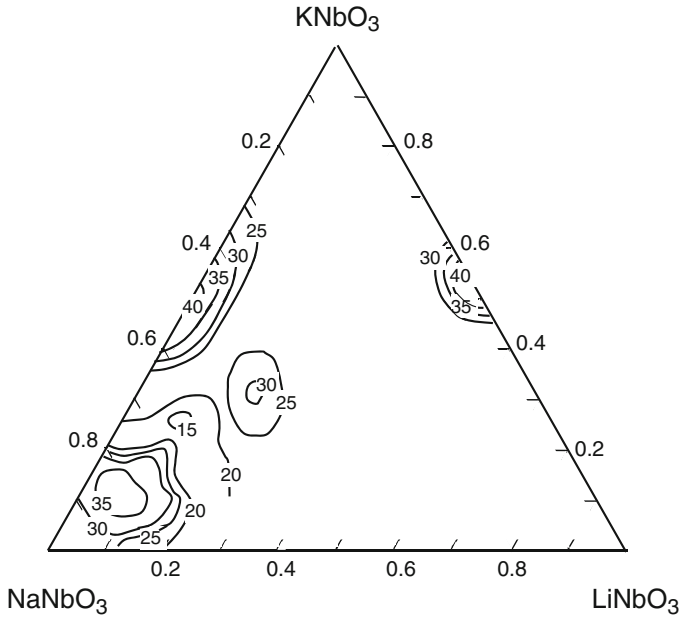

Fig. 6.12 Electromechanical coupling coefficient of ceramics of alkali niobate ternary system (Li, Na, K)NbO_3

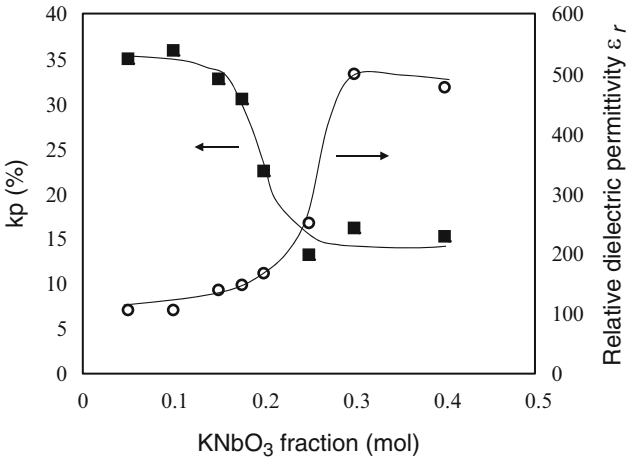

Fig. 6.13 Dielectric permittivity and electromechanical coupling coefficient of $(Li_{0.1}Na_{1-x}K_x)NbO_3$ ceramics

6.3.4 Solid Solutions Between Alkaline Niobates and Other Perovskite Materials

As mentioned above, $NaNbO_3$-rich composition shows its relative dielectric permittivity around 150; however, the dielectric permittivity increases up to around 500 with increasing $KNbO_3$ amount. For both the cases, high dielectric permittivity is difficult to obtain. On the other hand, the dielectric properties of their solid solutions with CaTiO3 were investigated [81]. Dielectric permittivity of x•$CaTiO_3$ – $(1 - x)$ • $(Na_{0.5}K_{0.5})NbO_3$ is shown in Fig. 6.14. It increases with increasing $CaTiO_3$ fraction and becomes higher than 1,500 with $CaTiO_3$ higher than 0.08.

A few materials have been reported to show high dielectric permittivity higher than 1,000, besides the $BaTiO_3$-based materials or lead-based perovskite materials. Large piezoelectric constant is obtained for high dielectric permittivity materials. Therefore, high dielectric permittivity observed in this material system is noteworthy. Temperature dependences of dielectric permittivity and resonance frequency (planer mode) of the pseudo binary system x • $CaTiO_3$ – $(1 - x)$ • $(Na_{0.5}K_{0.5})NbO_3$ are shown with changing x in Figs. 6.15 and 6.16.

A phase transition temperature T_{t-m} between monoclinic (orthorhombic) and tetragonal phases and a Curie temperature T_c change with the $CaTiO_3$ fraction. The two transition temperatures lowered with the increase of the $CaTiO_3$ fraction within 0.06 (mol). The T_{t-m} was here decided from the temperature dependence of the resonance frequency. The temperature T_{t-m} slightly increased for the $CaTiO_3$ fraction above 0.06. The transition temperature T_{t-m} lies around room temperatures for the composition with the $CaTiO_3$ fraction of 0.06. However, the dielectric permittivity does not make a clear peak at T_{t-m} as shown in Fig. 6.15. The obtained phase diagram is shown in Fig. 6.17.

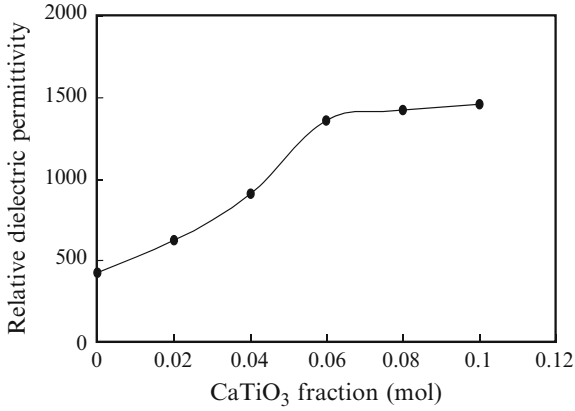

Fig. 6.14 Dielectric permittivity of $(1 - x)$ $(K_{0.5}Na_{0.5})NbO_3 - x$ $CaTiO_3$ ceramics

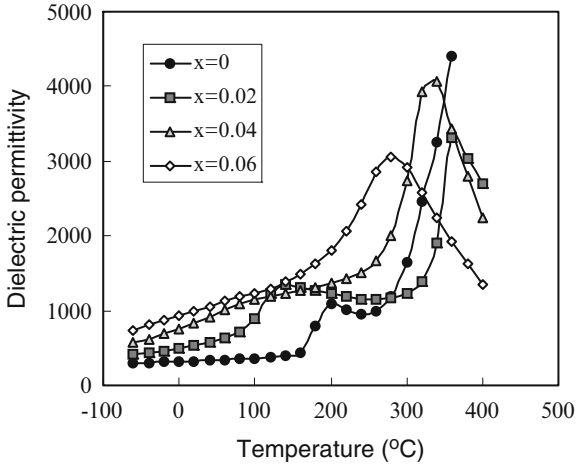

Fig. 6.15 Temperature dependence of dielectric permittivity of $(1 - x)$ $(K_{0.5}Na_{0.5})NbO_3 - x$ $CaTiO_3$ ceramics

6.3.5 High Q_m Characteristics of Alkali Niobate Ceramics

Alkali niobate piezoelectric ceramics were firstly studied for the resonance application such as the wave filters for broadcasting systems [68]. As mentioned above, since alkali niobate piezoelectric ceramic materials have successive phase transitions, the resonance frequency of the ceramic resonator largely changes with temperature. There have been limited applications such as the vibrator of the delay line devices, where LNN-based ceramics have been used once.

Adequate additives for Q_m heightening of alkali niobate ceramics had not been known for long time.

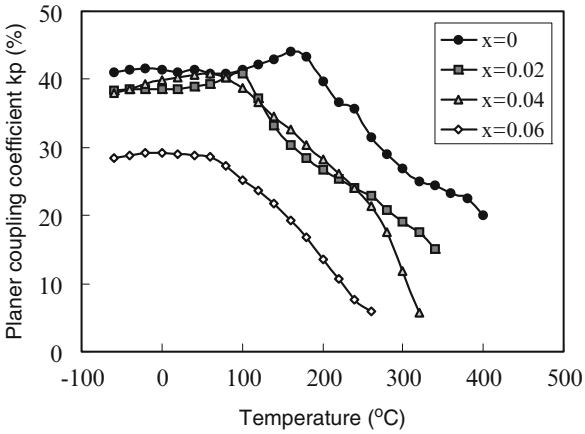

Fig. 6.16 Temperature dependence of planer electromechanical coupling coefficient of $(1 - x)$ $(K_{0.5}Na_{0.5})NbO_3 - x\ CaTiO_3$ ceramics

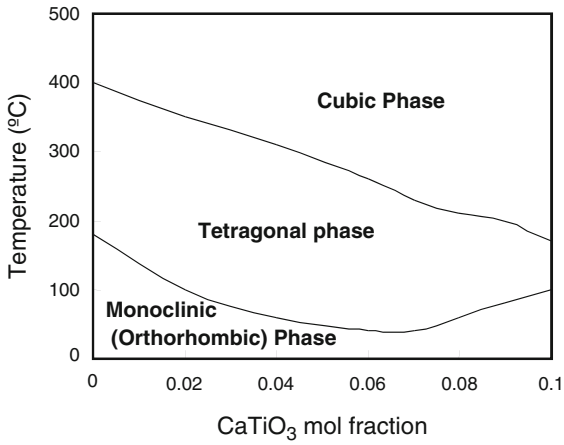

Fig. 6.17 Phase diagram of $(1 - x)$ $(K_{0.5}Na_{0.5})NbO_3 - x\ CaTiO_3$

For example, Mn doping to the alkali niobate ceramics does not show significant Q_m heightening effects [126], while it shows great effects of Q_m heightening for PZT materials. One of the earliest reports for Q_m heightening of alkali niobate ceramics was given by Kimura et al. [80]. They discovered the high Q_m characteristics of the LNN ceramics by a heat treatment after the poling procedure. Sample preparation procedure taken in this experiment is summarized in Fig. 6.18.

Ceramic disk samples of $(Li_{0.12}Na_{0.88})NbO_3$ were prepared, and the poling was done at 100°C (in the rhombohedral phase), and the annealing was done at 400°C (in the tetragonal phase). The Q_m value was significantly increased from 500 to 3,000. It was the earliest discoveries of lead-free piezoelectric ceramic materials

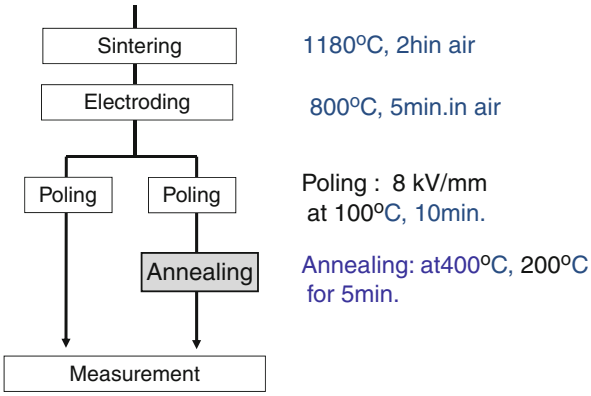

Fig. 6.18 Sample preparation chart for high Q_m ceramics of (Li, Na)NbO_3. Samples show high Q_m characteristics after annealing

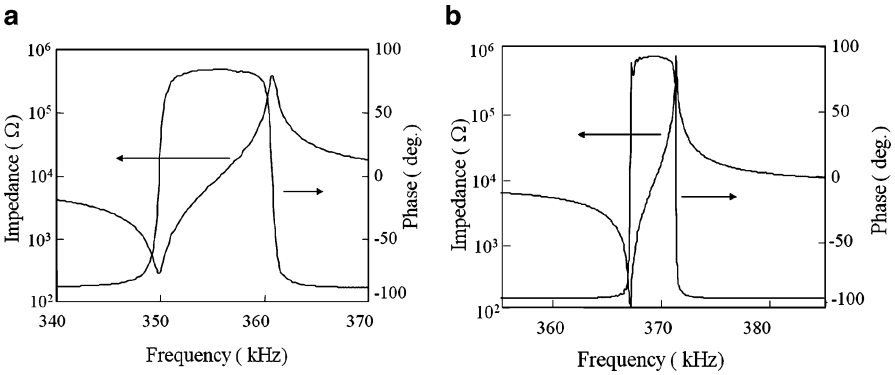

Fig. 6.19 Impedance resonance characteristics of (Li, Na)NbO_3-based ceramics before annealing (**a**) and after annealing (**b**)

which possess such high Q_m values for planer vibration mode with a relatively high electromechanical coupling coefficient more than 20%.

The change in resonance characteristic after the annealing is shown in Fig. 6.19.

Resonance characteristics of a sample annealed at 200°C (in the monoclinic phase) were also measured; however, there were no significant changes.

The origin of this Q_m heightening is considered to be the poling direction against the normal direction of the sample plate. Once a poling procedure was taken for the samples (111), direction (of cubic denotation) is normal to the plate. The crystalline structure after the annealing is observed as monoclinic, then the poling direction is (110) and it has an angle of 35.3° against the normal direction. There are three equivalent directions to (110) direction around the (111) directions, and they make angles of 60°. Since these directions are also energetically equivalent, when an electric field is applied along the (111) direction, 60° domain rotations are restricted.

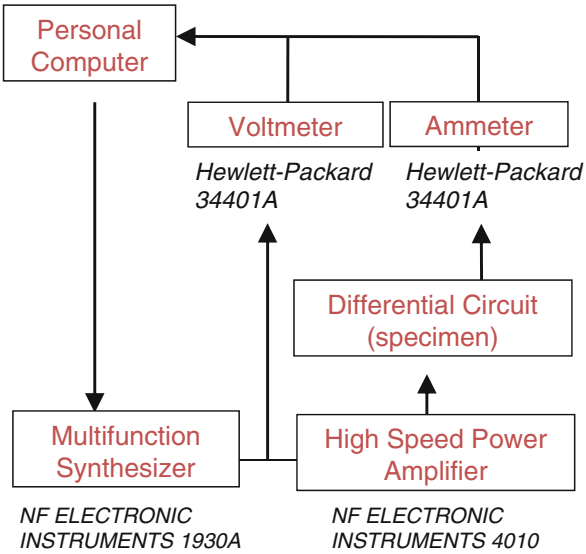

Fig. 6.20 Measurement circuit diagram for high power characteristics of piezoelectric plate with the constant current method. This setup measures a voltage between terminal electrodes of specimen with keeping a constant electric current by a feedback control

The Q_m value is much heightened without the non-180° domain rotation. This situation is considered to be quite the same as the $Pb(Zn_{1/3}Nb_{2/3})$–$PbTiO_3$ single crystals with the engineered domain structures [129, 146]. On the other hand, the reason why the monoclinic phase appears only for the samples which experiences the tetragonal phase at the annealing is still unclear. Detailed studies on successive phase transitions are necessary from both theoretical and experimental aspects.

Unlike BLSF, Alkaline niobate-based material shows good lateral piezoelectric effects. It is preferable to design the structure of high power devices, such as ultrasonic vibrators, ultrasonic motors, piezoelectric transformers, and so on. High power characteristics of the Q_m heightened LNN with the annealing are measured by the constant current method developed by Hirose [129]. The measuring setup is schematically shown in Fig. 6.20. The measured vibration mode is the length expansion mode of the lateral effect.

Q_m value against the vibration velocity is shown in Fig. 6.21 while comparing to a typical hard PZT.

The annealed alkali niobate $(Li_{0.12}Na_{0.88})NbO_3$ shows approximately 2 times higher maximum velocity than the hard PZT.

Even though the high Q_m lead-free piezoelectric ceramic LNN was obtained, it requires additional fabrication procedures to the conventional process. If high Q_m lead-free piezoelectric ceramics could be obtained by the conventional fabrication process, it is very convenient for the practical applications. Furthermore, KNN-based material is considered to be better than LNN-based materials, because of its higher density and electromechanical coupling. Higher density is considered to be suitable for high power applications when a vibration maximum velocity is

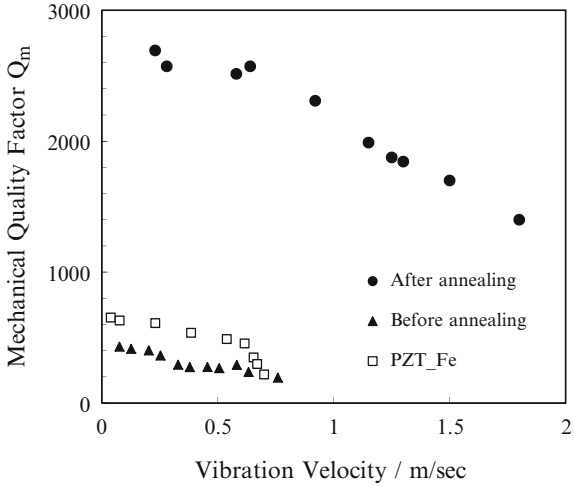

Fig. 6.21 Mechanical quality factor Q_m of piezoelectric plates with changing vibration velocity

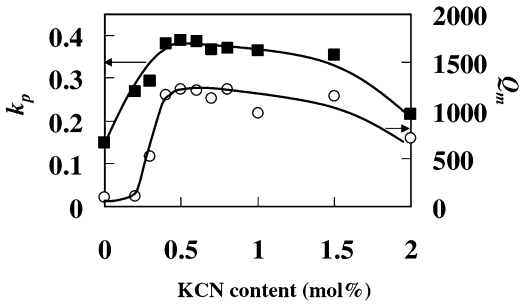

Fig. 6.22 Piezoelectric properties of (K, Na)NbO_3-based ceramics with sintering aid $K_4CuNb_8O_{23}$ (After Matsubara [91])

constant. Matsubara and coresearchers reported that KNN ceramic showed high Q_m values and high electromechanical coupling coefficients by using complex oxide additives such as $K_4CuNb_8O_{23}$ [91]. The planer electromechanical coupling coefficient around 40%, and high Q_m values above 1,000 are reported. The results are shown in Fig. 6.22.

Now, there are several studies on high power characteristics for alkaline niobate family materials. Li et al. reported characteristics of a shear mode ultrasonic motor with an Alkaline niobate (K, Na, Li) NbO_3 + Cu [135]. This material shows excellent piezoelectric high power characteristics. Its piezoelectric constant d_{15} is 207, and its mechanical quality factor is 1,400.

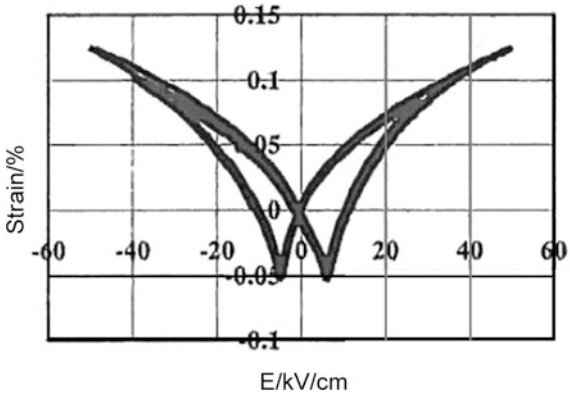

Fig. 6.23 Electrically induced large strain of alkali niobate ceramics observed by Matsubara et al. [83]. Similar data is shown in references [91–94]. This is one of the earliest reports on large strain of alkali niobate ceramics

6.3.6 Large d_{33} Alkali Niobate Piezoelectric Ceramics

Kimura and Ando widely studied the alkali niobate ceramic systems as ECO benign piezoelectric materials in the early 1990s, and showed a high dielectric permittivity over 1,500 for $(K,Na)NbO_3$–$CaTiO_3$ system as shown in Fig. 6.14. Relatively good piezoelectric properties were also presented. Their work on this alkali niobate ceramics is one of the earliest studies of alkali niobates for high strain piezoelectric materials. Matsubara and coresearchers observed a large strain more than 0.1% at a high electric field 5 kV/mm for their developed $(K, Na)NbO_3$ ceramics as shown in Fig. 6.23 [83].

They employed a mixed oxide such as $K_4CuNb_8O_{23}$ as a sintering aid in order to obtain dense ceramics. Calculated d_{33} value at the high field is 180 pm/V. Yoshida and coresearchers also showed large strain characteristics of $KNbO_3$-based ceramics over 0.1% [84]. Considering that ceramic materials which show high electrically induced strain are limited besides $BaTiO_3$ or lead-based perovskite, the above studies are very important in the history of lead-free piezoelectric ceramic materials, because these studies meant that alkali niobate-based lead-free ceramics have good possibility to be used as actuator applications. However, in spite of the generated large strain of the above alkali niobate ceramics, piezoelectric constant d_{33} is much lower than that of PZT.

On the other hand $(K, Na, Li)(Nb, Ta, Sb)O_3$, system materials were developed by Saito et al. [85]. One of these ceramic materials exhibits d_{33} values at low and high electric fields of around 300 pC/N and 470 pm/V, respectively. Grain oriented ceramics were made by using the RTGG method, and they showed high piezoelectric constant of around 750 pm/V at a high electric field. This value is attractive to replace the Pb-based piezoelectric ceramics. However, recently developed PZT shows a higher strain characteristic, and further improvements on strain

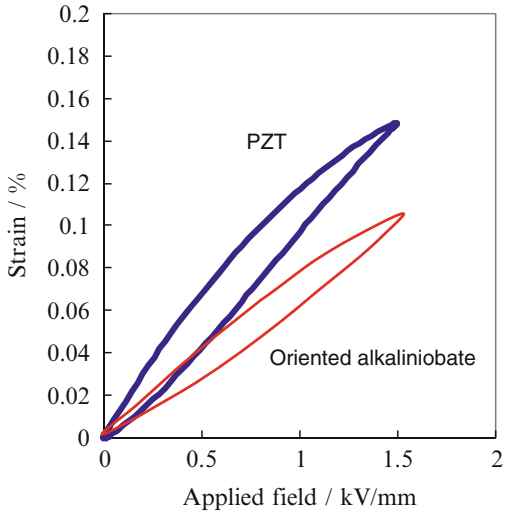

Fig. 6.24 Strain characteristics of large strain piezoelectric ceramics. PZT is still superior to any lead-free piezoelectric ceramics at present in terms of electrically induced strain characteristics

characteristics are still necessary for the alkali niobate ceramic materials in order to replace the PZT. The comparison for induced strain between their developed alkali niobate ceramics (oriented) and PZT is shown in Fig. 6.24.

Moreover, the alkali niobate ceramic materials still have several problems to be solved for practical applications. For example, compositional reproducibility seems to be low, because there have been no reports of success to trace their achieved high piezoelectricity. Relatively low T_c might be required to improve, and process cost for the oriented ceramic fabrication should be preferably decreased.

Recently, Tanaka et al. show good piezoelectric properties of an alkaline niobate-based piezoelectric materials, the composition of which is represented by

$$(K_{0.359}Na_{0.539}Li_{0.047}Ba_{0.005}Sr_{0.005})(Nb_{0.855}Ta_{0.095}Zr_{0.005})O_3 + 0.5\text{wt\%}MnCO_3.$$

It shows piezoelectric constants d_{33} at low and high electric fields of around 300 pC/N and 470 pm/V, respectively [140]. These properties are good for several practical applications of actuators.

Wang and coresearchers reported very recently that alkali niobate-based ceramic, the composition of which is expressed as

$$0.92(K_{0.5}Na_{0.5})NbO_3 - 0.02(Bi_{0.5}Li_{0.5})TiO_3 - 0.06BaZrO_3$$

shows good piezoelectric properties, for example, d_{33} value at low electric field around 400 pm/V [143]. Its piezoelectric properties are similar to those of PZT for actuator applications except its Curie temperature.

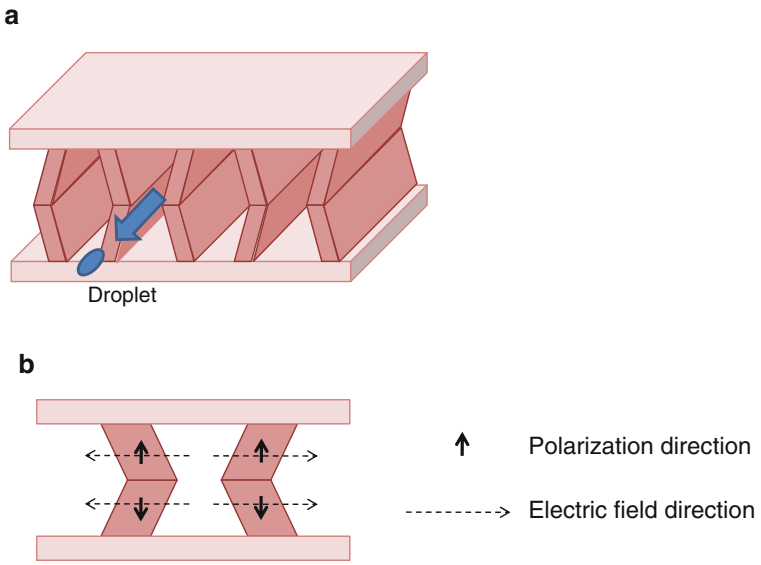

Fig. 6.25 Side-wall-type actuator for ink-jet printing heads developed by Uraki et al. [113] Schematic view of actuator (**a**), Schematically drawn shear deformation (**b**)

From the viewpoints of practical applications, Uraki et al. proposed shear deformation type (side wall type) actuator for ink jet printings, because larger piezoelectric constant is generally obtained for shear strain. Piezoelectric constant for shear deformation d_{15} is larger than that of longitudinal one in many kinds of piezoelectric ceramic materials. They used a material the composition of which is expressed as

$$(K_{0.46}, Na_{0.50}Li_{0.04})(Nb_{0.84}Ta_{0.10}Sb_{0.06})O_3,$$

and showed relatively high piezoelectric constants for shear deformation d_{15} around 280 pC/N [113]. The structure of the side wall type actuator for the ink-jet printing head is schematically shown in Fig. 6.25.

Matsumoto and coresearcher recently reported very large strain around 0.22% at an electric field of 8 kV/mm on $KNbO_3$-based ceramics [137]. Figure 6.26 shows the very large electrically induced strain of Mn-doped $KNbO_3$ ceramics. Strain more than 0.2% was observed in this material system.

Recent studies on lead-free piezoelectric ceramics, as seen above, reveal that alkali niobate perovskite materials has intrinsically good potential to be used in high strain actuator application in the future. Piezoelectric characteristics reported in recent papers are partly tabulated in Table 6.3.

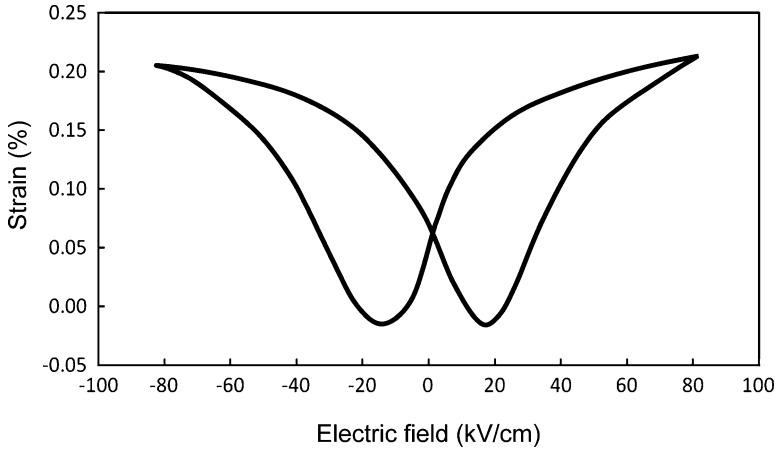

Fig. 6.26 Electrically induced strain characteristic of $KNbO_3$-based ceramics. (0.4 wt% of $MnCO_3$ was added to $KNbO_3$ in raw material mixing process) (Data is taken from the paper by Matsumoto et al. [137])

Table 6.3 Recently developed alkali niobate based piezoelectric ceramic materials (for actuator applications) and their piezoelectric properties

	$\varepsilon_{33}{}^T/\varepsilon_0$	k_p (%)	Q_m	d_{33} (pC/N)	S/E (pm/V)	T_c (°C)
ANSZ [140]	1,610	45.5	84	295	466	278
KNN-BZ [143]	2,000	57.4	48	400	~600?	240
KNN-BT [146, 150]	1,060	36.0	–	225	–	310
KNN-ST [129, 150]	1,450	40.0	70	220	–	280
KNN-CT [147]	1,320	41.0	–	241	–	310
LNKN [148]	~700	41.2	–	314	–	490
KNN-LS [149]	1,380	50.0	–	270	355	368
LF4 [85]	1,570	–	–	300	470	253
Oriented LF4 [85]	1,570	61.0	–	416	750	253
PZT	2,000–5,000	60–80	40–60	500–700	700–1,100	200–300

k_p: Planer electromechanical coupling coefficient, Q_m: Mechanical quality factor; $\varepsilon_{33}{}^T/\varepsilon_0$: Relative dielectric permittivity along the poling direction; T_c: Curie temperature; ANSZ: $(K_{0.359}Na_{0.539}Li_{0.047}Ba_{0.005}Sr_{0.005})(Nb_{0.855}Ta_{0.095}Zr_{0.005})O_3$ + 0.5wt%$MnCO_3$; KNN-BZ: 0.92 $(K_{0.5}Na_{0.5})NbO_3$–0.06$BaZrO_3$–0.02$(Bi_{0.5}Li_{0.5})TiO_3$; KNN: $(K_{0.5}Na_{0.5})NbO_3$, KNN-BT: 0.95KNN–0.05$BaTiO_3$; KNN-ST: 0.95KNN–0.05$SrTiO_3$, KNN-CT: 0.95KNN–0.05$CaTiO_3$; LNKN: 0.942 $(K_{0.480}Na_{0.535})NbO_3$–0.058$LiNbO_3$, KNN-LS: 0.948KNN–0.052$LiSbO_3$; LF4: $(K_{0.44}Na_{0.52}Li_{0.04})(Nb_{0.86}Ta_{0.10}Sb_{0.04})O_3$

Piezoelectric constant d_{33} is measured with Berlincourt type d_{33} meter; S/E is obtained by strain-field characteristic measured at high electric field more than 20 kV/cm

6.3.7 Multilayering

Another solution to obtain large displacement of alkali niobate ceramics is a layering technique. Kawada et al. attempted to make multilayered cofired ceramics of alkali niobates with nickel inner electrodes [142]. Lead-based piezoelectric

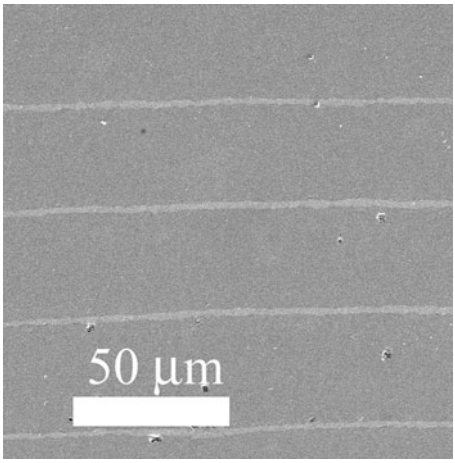

Fig. 6.27 Cross-sectional view of multilayered alkali niobate-based ceramics by scanning electron microscopy [142]

ceramics cannot be cofired with nickel inner electrodes. Lead in these lead-based ceramics is easily reduced at the reductive atmosphere, which is necessary to keep the nickel at the metal state preventing from the oxidation. On the other hand, alkaline metals are easily oxidized, which means alkali metal in the oxide state is much more stable than lead in the oxide state at reductive atmosphere. Following composition was selected and multilayered ceramics were prepared by using a conventional tape casting method.

$$0.96(K_{0.5}Na_{0.5})NbO_3 - 0.04CaZrO_3 - 0.03ZrO_2 - 0.05Mn_2O_3.$$

Starting materials are K_2CO_3, Na_2CO_3, $CaCO_3$, Nb_2O_5, ZrO_2, and Mn_2O_3 of high purity grade (>99%). These are weighed to make the above composition, and mixed in ethanol. The mixed compact is dried and calcined at alumina crucible at around 900°C. The calcined powder is mixed with poly acetate binder and water-based ceramic slurry is prepared for the tape casting. The inner nickel electrodes are formed by the screen printing method. The printed tapes are stacked and pressed to make a ceramic green body, which is fired with a heating rate of 3°C/min to 1,080°C and held for 2 h in a reducing atmosphere (oxygen partial pressure of 1×10^{-11} to 1×10^{-10} MPa).

Figure 6.27 shows a cross-sectional view of the cofired sample.

The electric field strain characteristics is shown in Fig. 6.28.

This multilayered ceramics achieve high strain more than 0.1% at high electric fields.

Roughly speaking, d_{33} value of this alkali niobate ceramics at a high electric field is around half the value of d_{33} of PZT-based ceramics which have been practically used as large displacement actuators such as fuel injection actuators for automobile engines. However, when an applied electric field can be raised by thinning the ceramic layers, the alkali niobate-based ceramic might show similar displacement

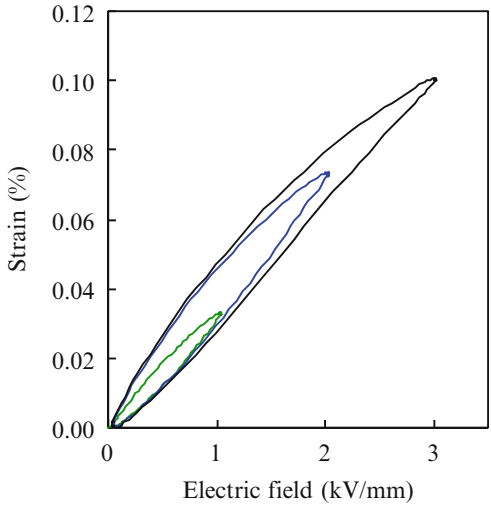

Fig. 6.28 Strain characteristics of multilayered alkali niobate-based ceramics observed by Kawada et al. [142]

characteristics to those of the PZT-based materials. In that case, the layer number of the actuator is twice that of PZT actuator. If dielectric permittivity were the same for both alkali niobate- and PZT-based ceramics, capacitance of the alkai niobate-based multilayered ceramic would be 4 times larger than that of PZT-based one. This situation is quite inconvenient for the practical applications. However, fortunately, dielectric permittivity of the alkali niobate-based materials is much lower than that for PZT at a high electric field. Then we can expect that similar piezoelectric actuator characteristics to that of the PZT-based material can be realized by applying this multilayering technique to the alkali niobate ceramic materials.

Furthermore, Ni inner electrode is suitable for the applications from the viewpoint of migration of the electrode material into the piezoelectric materials. Ag-Pd-based inner electrodes have usually been used in the PZT multilayered actuator. When an high electric field is applied to those actuators at high temperatures or humid atmosphere, silver metal easily migrates into the ceramics from the inner electrodes, and causes significant insulation degradations. Nickel is a suitable metal as for migration, however, PZT cannot be co-fired with nickel inner electrode. On the other hand, alkali niobate ceramic materials can be co-fired with nickel inner electrode, and they have good advantages for the actuator applications from the viewpoint of the reliability at harsh environments.

6.4 Conclusions

The history of R&D activities for piezoelectric alkali niobate ceramic materials was reviewed in this article by picking up the topical works in this research field. From the discovery of the ferroelectricity of $KNbO_3$, a large number of researches have

been carried out on piezoelectric properties of alkali niobate ceramic materials for more than half century.

Moreover, the R&D on the alkali niobate materials has been promoted with a follow wind of ECO trend. As a result of efforts paid by a large number of researchers, piezoelectric properties of the recently developed alkali niobate materials have become close to those of PZT with some discrepancies.

On the other hand, it has been already found that the alkali niobate ceramic materials which exhibit superior high power characteristics, and the alkali niobate ceramics are expected to be used in ultrasonic applications such as piezoelectric motors more preferably than high Q_m PZTs. Superior high power characteristic of the alkali niobate ceramic materials is one of the most important discoveries in the current lead-free piezoelectric material R&D.

Another important work of the current lead-free piezoelectric material R&D is the multilayered alkali niobate ceramic. It allows us to obtain highly reliable actuators for harsh environment use such as high temperature use in the future automotive application.

These two examples do not mean simple alternates for lead-based piezoelectric ceramics. In both of these cases, using alkali niobate-based piezoelectric ceramic materials is better than using the lead-based ones. In the future R&D, lead-free materials which show superior piezoelectric properties than the lead-based ones should be aimed. High Q_m characteristics, high temperature stability (high Curie temperature), high frequency constant (high elastic stiffness), and high reduction-proof properties and so on are good advantageous properties of the alkali niobate ceramic materials. With these advantageous properties, we can broaden the piezoelectric application field which makes our society more communicative, more comfortable, and more convenient.

References

1. Tanaka T (1982) Piezoelectric devices in Japan. Ferroelectrics 40:167–187
2. Kawabata A, Ichinose N, Takahashi S (1998) Yasasii. Ultrasonic engineering [in Japanese] revised version. Kougyou Chousakai, Tokyo
3. Royer D, Dieulsaint E (2000) Elastic waves in solids II generation, acousto-optic interaction, applications, Chap. 4: Signal processing components and Chap. 5: Sensor and instrumentation. Springer, Berlin, translated from Ondes elastiques dans les solides. In: Tome 2 generation, interaction acousto-optique, applications, Masson, Paris, 1999
4. Ichinose N (ed) Atsuden seramikkusu shin-gijutsu [in Japanese] (New piezoelectric ceramic technologies) Ohmu-sha, Tokyo
5. Nihon Zairyou Kagaku Kai (ed) (1993) Kyou-Yuudensei to Kouon Choudendou (Ferroelectrics and high temperature superconductors). Shoukabou, Tokyo
6. Takahashi S (1993) Multilayer piezo-ceramic actuators and their applications. In: Setter N, Colla EL (eds) Ferroelectric ceramics. Birkhäuser, Basel, pp 349–362
7. Nomura S, Uchino K (1985) Electrostrictive effect in $Pb(Mg_{1/3}Nb_{2/3})O_3$-type materials. In: Taylor GW, Gagnepain JJ, Meeker TR, Nakamura T, Shuvalov LA (eds) Piezoelectricity. McGraw-Hill, New York, pp 151–166
8. Uchino K (1986) Electrostrictive actuators: materials and applications. Am Ceram Soc Bull 65:647–652
9. Vazquez A, Uchino K (2001) Novel piezoelectric-based power supply for driving piezoelectric actuators designed for active vibration damping applications. J Electroceramics 7:197–210

10. Keeling MR (1981) Ink jet printing. Phys Technol 12:196–203
11. Wersing W (2002) Applications of piezoelectric materials: an introductory review. In: Setter N (ed) Piezoelectric materials in devices. EPFL, Lausanne, pp 29–66
12. Komai H, Hirata T, Inada T, Nakano T, Kadonaga M (1992) Ink jet recording device. Japan Patent 2957683
13. Sonehara H (1992) Ink jet type printing head. Japan Patent 2987944
14. Schuh C, Lubitz K, Steinkopff TH, Wolff A (2000) Piezoelectric components for technical applications. In: Galassi C, Dinescu M, Uchino K, Sayer M (eds) Piezoelectric materials. Kluwer, Dordrecht, pp 391–399
15. Lubitz K, Schuh C, Steinkopff T, Wolff A (2002) Material aspects for reliability and life time of PZT multilayer actuators. In: Setter N (ed) Piezoelectric materials in devices. EPFL, Lausanne, pp 183–194
16. Claeyssen F, Le Letty R (2002) Performance and applications of actuators based on multi-layered piezo ceramics and shell structures. In: Setter N (ed) Piezoelectric materials in devices. EPFL, Lausanne, pp 103–122
17. Zhu W, Wang Z, Yao K, Yao X (2002) Piezoelectric multilayer microactuators for high track density hard disk drives. Key Eng Mater 228–229:31–36
18. Kurihara K, Hida M, Umeyama S, Kondo M, Koganezawa S (2006) Rotating symmetrical piezoelectric microactuators for magnetic head drives. Jpn J Appl Phys 45(9B):7471–7474
19. Fuda Y, Ono H, Shiotani F, Kumasaka K (1995) Multilayer piezoelectric ceramic vibrator with internal electrodes. Jpn J Appl Phys 34:5270–5272
20. Fuda Y, Ono H, Kumasaka K, Katsuno T (1995) Multilayer ceramic transformer using transverse effect. Extended Abstract of the 7th US–Japan seminar on dielectric and piezoelectric ceramics, Tsukuba, Japan, November, pp. 129–136
21. Takami A (1999) Knocking sensor [in Japanese]. Mater Integr 12(9):23–27
22. Wakatsuki N (1999) Gyroscope for direction sensor and angular velocity sensor in automotives. Mater Integr 12(9):65–70
23. Ogiura M (1995) Surface mount type shock sensor [in Japanese]. Nyu Seramikkusu 8(6):39
24. Face BR, Boyd CD (2000) Self-powered trainable switching network. International patent WO-02/42873 (priority date: Nov 21, 2000)
25. Kymissis J, Kendall C, Paradiso J, Gershenfeld N (1998) Parasitic power harvesting in shoes. In: Proc. the Second IEEE International Conference on Wearable Computing (ISWC) October, IEEE Computer Society, pp. 132–139
26. Paradiso JA, Feldmeier M (2001) A compact, wireless, self-powered pushbutton controller. Ubicomp 2001: Ubiquitous computing. In: Abowd GD, Brumitt B, Shafer SACM (eds). UBICOMP conference proceedings, Atlanta GA, Sept 2001, Springer, Berlin, pp. 299–304
27. Ikegami S, Ueda I (1974) Piezoelectricity in ceramics of ferroelectric bismuth compound with layer structure. Jpn J Appl Phys 13:1572
28. Takenaka T, Shoji K, Takai H, Sakata K (1976) Ferroelectric and dielectric properties of press forged $Bi_4Ti_3O_{12}$ ceramics. In: Proc. 19th Jpn. Cong. Mat. Res, Tokyo, March 1976, pp. 230–233
29. Takenaka T, Sakata K (1981) Liquid phase sintering of grain-oriented ferroelectric ceramics in the bismuth layer structure oxides. Jpn J Appl Phys 20(Suppl 20–4):189–192
30. Ando A, Kimura M, Sakabe Y (1999) Energy trapping phenomenon of piezoelectric $SrBi_2Nb_2O_9$ ceramics. Proc. The 11th IEEE Intl. Symp. Appl. Ferroelectrics, Montreux 1998, pp. 303–306
31. Ando A, Kimura M, Sawada T, Hayashi K, Sakabe Y (2002) Piezoelectric and ferroelectric properties of the modified $SrBi_2Nb_2O_9$ ceramics. Ferroelectrics 268:65–70
32. Takenaka T (2002) Grain orientation effects on electrical properties of bismuth layer-structured ferroelectric ceramics. J Ceram Soc Jpn 110:215–224
33. Ando A, Sawada T, Ogawa H, Kimura M, Sakabe Y (2002) Fine-tolerance resonator applications of bismuth-layer-structured ferroelectric ceramics. Jpn J Appl Phys 41:7057–7061
34. Ando A, Kimura M, Sakabe Y (2003) Piezoelectric resonance characteristics of $SrBi_2Nb_2O_9$-based ceramics. J Appl Phys 42:520–525

35. Hirose M, Suzuki T, Oka H, Itakura K, Miyauchi Y, Tsukada T (1999) Piezoelectric properties of $SrBi_4Ti_4O_{15}$-based ceramics. Jpn J Appl 38:5561
36. Oka H, Hirose M, Tsukada T, Watanabe Y, Nomura T (2000) Thickness-shear vibration mode characteristics of $SrBi_4Ti_4O_{15}$-based ceramics. Jpn J Appl Phys 39:5613
37. Nanao M, Hirose M, Tukada T (2001) Piezoelectric properties of Bi_3TiNbO_9–$BaBi_2Nb_2O_9$ ceramics. Jpn J Appl Phys 40:5727–5730
38. Shibata K, Shoji K, Sakata K (2001) $Sr_{1-x}CaxBi_2Ta_2O_9$ piezoelectric ceramics with high mechanical quality factor. Jpn J Appl Phys 40:5719–5721
39. Noguchi Y, Shimizu H, Miyayama M, Oikawa K, Kamiyama T (2001) Ferroelectric properties and structure distortion in a-site-modified $SrBi_2Ta_2O_9$. Jpn J Appl Phys 40:5812–5815
40. Yokosuka M (2002) Dielectric and piezoelectric properties of Mn-Modified $Bi_4CaTi_4O_{15}$ based ceramics. Jpn J Appl Phys 41:7123–7126
41. Demartin M, Damjanovic D (2002) Lead free piezoelectric materials. In: Setter N (ed) Piezoelectric materials in device. EPFL, Lausanne, pp 389–412
42. Sakata K, Masuda Y (1974) Ferroelectric and antiferroelectric properties of $(Na_{0.5}Bi_{0.5})TiO_3$–$SrTiO_3$ solid solution ceramics. Ferroelectrics 7:347–349
43. Takenaka T, Sakata K (1989) Dielectric, piezoelectric and pyroelectric properties of $(BiNa)_{1/2}TiO_3$-based ceramics. Ferroelectrics 95:153–156
44. Takenaka T, Sakata K (1988) Grain-oriented and Mn-Doped $(NaBi)_{(1-x)/2}Ca_xBi_4Ti_4O_{15}$ ceramics for piezo- and pyrosensor materials. Sens Mater 1:35–46
45. Takenaka T, Sakata K, Toda K (1990) Piezoelectric properties of $(Bi_{1/2}Na_{1/2})Ti_3$ – based ceramics. Ferroelectrics 106:375–380
46. Takenaka T, Maruyama K, Sakata K (1991) $(Bi_{1/2}Na_{1/2})TiO_3$-$BaTiO_3$ system for lead-free piezoelectric ceramics. Jpn J Appl Phys 30:2236–2239
47. Herabut A, Safari A (1997) Processing and electromechanical properties of $(Bi_{0.5}Na_{0.5})_{(1-1.5x)}La_xTiO_3$ ceramics. J Am Ceram Soc 80:2954–2958
48. Sasaki A, Chiba T, Mamiya Y, Otsuki E (1999) Dielectric and piezoelectric properties of $(Bi_{0.5}Na_{0.5})TiO_3$–$(Bi_{0.5}K_{0.5})TiO_3$ systems. Jpn J Appl Phys 38:5564–5567
49. Nagata H, Koizumi N, Takenaka T (1999) Lead-free piezoelectric ceramics of $(Bi_{1/2}Na_{1/2})TiO_3$–$BaTiO_3$–$BiFeO_3$ system. Ferroelectrics 229:273–278
50. Nagata H, Koizumi N, Takenaka T (1999) Lead-free piezoelectric ceramics of $(Bi_{1/2}Na_{1/2})TiO_3$-$BiFeO_3$ system. In: Key engineering materials, vols. 169–170. Trans Tech, Switzerland, pp. 37–40
51. Lee J, Hong K, Kim C, Park S (2002) Phase transitions and dielectric properties in A-site ion substituted $(Na_{1/2}Bi_{1/2})TiO_3$ ceramics (A=Pb and Sr). J Appl Phys 91:4538–4542
52. Tani T, Fukuchi E, Kimura T (2002) Relationship between pre-sintering conditions and sintering behavior of Bi0.5(Na, K)0.5TiO_3 ceramics textured by reactive templated grain growth method. Jpn Soc Powder Powder Metall 49:198–202
53. Tou T, Hamaguti Y, Maida Y, Yamamori H, Takahashi K, Terashima Y (2009) Properties of $(Bi_{0.5}Na_{0.5})TiO_3$–$BaTiO_3$–$(Bi_{0.5}Na_{0.5})(Mn_{1/3}Nb_{2/3})O_3$ Lead-free piezoelectric ceramics and its application to ultrasonic cleaner. Jpn J Appl Phys 48:07GM03
54. Matthias BT (1949) New ferroelectric crystals. Phys Rev 75:1771
55. Matthias BT, Remeika JP (1951) Dielectric properties of sodium and potassium niobates. Phys Rev 82:727–729
56. Vousden P (1951) A study of the unit-cell dimensions and symmetry of certain ferroelectric compounds of niobium and tantalum at room temperature. Acta Cryst 4:373–376; Vousden P (1951) The structure of ferroelectric sodium niobate at room temperature Acta Cryst 4:545–551
57. Shirane G, Danner H, Pavlovic A, Pepinsky R (1954) Phase transitions in ferroelectric $KNbO_3$. Phys Rev 93:672–673
58. Shirane G, Newnham R, Pepinsky R (1954) Dielectric properties and phase transitions of $NaNbO_3$ and (Na, K)NbO_3. Phys Rev 96:581–588
59. Cross LE, Nicholson BJ (1955) The optical and electrical properties of single crystals of sodium niobate. Philos Mag 46(4):53–466
60. Triebwasser S (1956) Behavior of ferroelectric $KNbO_3$ in the vicinity of the cubic-tetragonal transition. Phys Rev 101:993–997

61. Egarton L, Dillon DM (1959) Piezoelectric and dielectric properties of ceramics in the system potassium-sodium niobate. J Am Ceram Soc 42:438–442
62. Jaeger RE, Egerton L (1962) Hot pressing of potassium-sodium niobates. J Am Ceram Soc 45:209–213
63. Dungan RH, Golding RD (1964) Metastable ferroelectric sodium niobate. J Am Ceram Soc 47:73–76
64. Dungan RH, Golding RD (1965) Golding polarization of $NaNbO_3$-$KNbO_3$ ceramic solid solutions. J Am Ceram Soc 48:601
65. Haertling GH (1967) Properties of hot-pressed ferroelectric alkali niobate ceramics. J Am Ceram Soc 50:329–330
66. Nitta T (1968) Properties of sodium-lithium niobate solid solution ceramics with small lithium concentrations. J Am Ceram Soc 51:626–629
67. Nitta T, Miyazawa T (1971) You have full text access to this content X-ray and thermal-expansion study of an $(Na_{0.88}Li_{0.12})NbO_3$+6 mol% Li_2O ceramic. J Am Ceram Soc 54:636–637
68. Yonezawa M, Ohno T (1975) Piezoelectric properties of $KNbO_3$–$NaNbO_3$–$LiNbO_3$ ternary system ceramics [in Japanese]. Annual Report of Study Group on Applied Ferroelectrics in Japan, vol. 21, pp. 65–71
69. Henson RM, Zeyfang RR, Kiehl KV (1977) Dielectric and electromechanical properties of (Li, Na)NbO_3 ceramics. J Am Ceram Soc 60:15–17
70. Takenaka T, Nagata H (2005) Current status and prospects of lead-free piezoelectric ceramics. J Eur Ceram Soc 25:2693–2700
71. Shrout TR, Zhang SJ (2007) Lead-free piezoelectric ceramics: Alternatives for PZT? J Electroceram 19:111–124
72. Takenaka T, Nagata H, Hiruma Y, Oshii K, Matsumoto K (2007) Lead-free piezoelectric ceramics based on Pervskite structures. J Electroceram 19:259–265
73. Takenaka T, Nagata H, Hiruma Y (2008) Current developments and prospective of lead-free piezoelectric ceramics. Jpn J Appl Phys 47:3787–3801
74. Pardo L, Duran-Martin P, Millar CE, Wolny WW, Jimenez B (1996) High temperature electromechanical behaviour of sodium substituted lithium niobate ceramics. Ferroelectrics 186:281–285
75. Pardo L, Durán-Martin P, Mercurio JP, Nibou L, Jiménez B (1997) Temperature behaviour of structural, dielectric and piezoelectric properties of sol-gel processed ceramics of the system $LiNbO_3$-$NaNbO_3$. J Phys Chem Solid 58:1335–1339
76. Kimura M, Ogawa T, Ando A (1998) Piezoelectric ceramic composition. Japan Patent Application 1998–35713 (equivalent to US Patent 6093339)
77. Kimura M, Ando A (1998) Piezoelectric ceramic composition. Japan Patent Application 1998–35714 (equivalent to US patent 6083415)
78. DiAntonio CB, Pilgrim SM (2001) Processing, characterization, and dielectric studies on $K(Ta_{1-x}Nb_x)O_3$ for use at cryogenic temperatures. J Am Ceram Soc 84:2547–2552
79. Reznitchenko LA, Turik AV, Kuznetsova EM, Sakhnenko VP (2001) Piezoelectricity in $NaNbO_3$ ceramics. J Phys Condens Matter 13:3875–3881
80. Kimura M, Ogawa T, Ando A, Sakabe Y (2003) Piezoelectric properties of metastable (Li, Na)NbO_3 ceramics. In: Proc. 13th IEEE international symposium on applications of ferroelectrics, Nara, Japan 2002, pp. 339–342
81. Kimura M, Ando A, Shiratsuyu K, Sakabe Y (2004) Piezoelectric properties of alkaline niobate perovskite ceramics. Trans Mater Res Soc Jpn 29:1049–1054
82. Kimura M, Kawada S, Shiratsuyu K, Ando A, Tamura H, Sakabe Y (2004) Piezoelectric properties and applications of high Qm (Li, Na)NbO_3 ceramics after heat treatment. Key Eng Mater 269:3–6
83. Matsubara M, Yamaguchi T, Kikuta K, Hirano S (2003) Processing and characterization of newly piezoelectric (K,Na)(Nb,Ta)O_3 ceramics [in Japanese]. In: Proc. Annual Meeting of the Ceramic Society of Japan, p. 133
84. Yoshida T, Hiruma Y, Aoyagi R, Nagata H, Takenaka T (2004) Optimized fabrication process and electrical properties of $KNbO_3$ ceramics [in Japanese]. In: Proc. The 17th Autumn Symposium of Ceramic society of Japan

85. Saito Y, Takao H, Tani T, Nonoyama T, Takatori K, Homma T, Nagaya T, Nakamura M (2004) Lead-free piezoceramic. Nature 432:84–87
86. Guo Y, Kakimoto K, Ohsato H (2004) Phase transitional behavior and piezoelectric properties of $(Na_{0.5}K_{0.5})NbO_3$–$LiNbO_3$ ceramics. Appl Phys Lett 85:4121–4123
87. Guo Y, Kakimoto K, Ohsato H (2004) Structure and electrical properties of lead-free $(Na_{0.5}K_{0.5})NbO_3$-$BaTiO_3$ ceramics. Jpn J Appl Phys 43:6662–6666
88. Sundarakannan B, Kakimoto K, Ohsato H (2004) Ti and V substitutions on the $KNbO_3$ ceramics: dielectric study. Ferroelectrics 302:175–179
89. Masuda I, Kakimoto K, Ohsato H (2004) Ferroelectric property and crystal structure of $KNbO_3$ based ceramics. J Electroceram 13:555–559
90. Kakimoto K, Masuda I, Ohsato H (2004) Solid-solution structure and piezoelectric property of $KNbO_3$ ceramics doped with small amounts of elements. Jpn J Appl Phys 43:6706–6710
91. Matsubara M, Yamaguchi T, Kikuta K, Hirano S (2004) Sinterability and piezoelectric properties of (K, Na)NbO_3 ceramics with novel sintering aid. Jpn J Appl Phys 43:7159–7163
92. Matubara M, Yamaguchi T, Kikuta K, Hirano S (2005) Sintering and piezoelectric properties of potassium sodium niobate ceramics with newly developed sintering aid. Jpn J Appl Phys 44:258–263
93. Matubara M, Yamaguchi T, Kikuta K, Hirano S (2005) Effect of Li substitution on the piezoelectric properties of potassium sodium niobate ceramics. Jpn J Appl Phys 44:6136–6142
94. Matubara M, Yamaguchi T, Kikuta K, Hirano S (2005) Synthesis and characterization of $(K_{0.5}Na_{0.5})(Nb_{0.7}Ta_{0.3})O_3$ piezoelectric ceramics sintered with sintering aid $K_{5.4}Cu_{1.3}Ta_{10}O_{29}$. Jpn J Appl Phys 44:6618–6623
95. Matsubara M, Yamaguchi T, Sakamoto W, Kikuta K, Yogo T, Hirano S (2005) Processing and piezoelectric properties of lead-free (K, Na)(Nb, Ta) O_3 ceramics. J Am Ceram Soc 88:1190–1196
96. Hollenstein E, Davis M, Damjanovic D, Setter N (2005) Piezoelectric properties of Li- and Ta-modified $(K_{0.5}Na_{0.5})NbO_3$ ceramics. Appl Phys Lett 87:182905
97. Guo Y, Kakimoto K, Ohsato H (2005) $(Na_{0.5}K_{0.5})NbO_3$-$LiTaO_3$ lead-free piezoelectric ceramics. Mater Lett 59:241–244
98. Birol H, Damjanovic D, Setter N (2005) Preparation and characterization of $KNbO_3$ ceramics. J Am Ceram Soc 88:1754–1759
99. Kakimoto K, Masuda I, Ohsato H (2005) Lead-free $KNbO_3$ piezoceramics synthesized by pressure-less sintering. J Euro Ceram Soc 25:2719–2722
100. Ringgaard E, Wurlitzer T (2005) Lead-free piezoceramics based on alkali niobates. J Euro Ceram Soc 25:2701–2706
101. Malic B, Bernard J, Holc J, Jenko D, Kosec M (2005) Alkaline-earth doping in (K, Na)NbO_3 based piezoceramics. J Euro Ceram Soc 25:2707–2711
102. Bobnar V, Malic B, Holc J, Kosec M, Steinhausen R, Beige H (2005) Electrostrictive effect in lead-free relaxor $K_{0.5}Na_{0.5}NbO_3$–$SrTiO_3$ ceramic system. J Appl Phys 98:024113
103. Matsubara M, Kikuta K, Hirano S (2005) Piezoelectric properties of $(K_{0.5}Na_{0.5})(Nb_{1-x}Ta_x)O_3-K_{5.4}CuTa_{10}O_{29}$ ceramics. J Appl Phys 97:114105
104. Zang GZ, Wang JF, Chen HC, Su WB, Wang CM, Qi P, Ming BQ, Du J, Zheng LM, Zhang S, Shrout TR (2006) Perovskite $(Na_{0.5}K_{0.5})_{1-x}(LiSb)_xNb_{1-x}O_3$ lead-free piezoceramics. Appl Phys Lett 88:212908
105. Lang SB, Zhu W, Cross LE (2006) Piezoelectric and pyroelectric properties of $(K_{0.5}Na_{0.5})_{1-x}(Nb_{1-y}Ta_y)O_3$ ceramics. Ferroelectrics 336:15–21
106. Saito Y, Takao H (2006) High performance lead-free piezoelectric ceramics in the (K, Na) NbO_3-$LiTaO_3$ solid solution system. Ferroelectrics 338:17–32
107. Wang R, Tachibana N, Miura N, Hanada K, Matsusaki K, Bando H, Itoh M (2006) Effects of vacancies on the dielectric and piezoelectric properties of $(Na_{0.5}K_{0.5})NbO_3$-$SrTiO_3$ solid solution. Ferroelectrics 331:135–139
108. Li JF, Wang K, Zhang BP, Zhang LM (2006) Ferroelectric and piezoelectric properties of fine-grained $Na_{0.5}K_{0.5}NbO_3$ lead-free piezoelectric ceramics prepared by spark plasma sintering. J Am Ceram Soc 89:706–709

109. Zhen Y, Li JF (2006) Normal sintering of (K, Na)NbO_3-based ceramics: influence of sintering temperature on densification, microstructure, and electrical properties. J Am Ceram Soc 89:3669–3675
110. Zuo R, Rödel J, Chen R, Li L (2006) Sintering and electrical properties of lead-free $Na_{0.5}K_{0.5}NbO_3$ piezoelectric ceramics. J Am Ceram Soc 89:2010–2015
111. Birol H, Damjanovic D, Setter N (2006) Preparation and characterization of $(K_{0.5}Na_{0.5})NbO_3$ ceramics. J Euro Ceram Soc 26:861–866
112. Matsumoto K, Hiruma Y, Nagata H, Takenaka T (2006) Piezoelectric properties of pure and Mn-doped potassium niobate ferroelectric ceramics. Jpn J Appl Phys 45:4479–4483
113. Uraki S (2006) Shear mode-type piezoelectric actuator and liquid droplet delivery head. International Patent WO-2008029573 (priority date: Sept 8 2006)
114. Pithan C, Shiratori Y, Magrez A, Mi SB, Dornseiffer J, Waser R (2006) Consolidation, microstructure and crystallography of dense $NaNbO_3$ ceramics with ultra-fine grain size. J Ceram Soc Jpn 114:995–100
115. Hagh NM, Jadidian B, Safari A (2007) Property-processing relationship in lead-free (K, Na, Li)NbO_3-solid solution system. J Electroceram 18:339–346
116. Matsumoto K, Hiruma Y, Nagata H, Takenaka T (2007) Piezoelectric properties of $KNbO_3$ ceramics prepared by ordinary sintering. Ferroelectrics 358:169–174
117. Li E, Kakemoto H, Wada S, Tsurumi T (2007) Effect of small amount CuO doping on microstructure and properties of the alkaline niobate-based lead-free ceramics. Ferroelectrics 358:153–160
118. Zhang BP, Zhang LM, Li JF, Ding XN, Zhang HL (2007) Effect of sintering temperature on electrical properties of $Na_{0.5}K_{0.5}NbO_3$ lead-free piezoelectric ceramics prepared by normal sintering. Ferroelectrics 358:188–195
119. Zuo R, Fang X, Ye C, Li L (2007) Phase transitional behavior and piezoelectric properties of lead-free $(Na_{0.5}K_{0.5})NbO_3$–$(Bi_{0.5}K_{0.5})TiO_3$ ceramics. J Am Ceram Soc 90:2424–2428
120. Chang Y, Yang Z, Wei L (2007) Microstructure, density, and dielectric properties of lead-free $(K_{0.44}Na_{0.52}Li_{0.04})(Nb_{0.96-x}Ta_xSb_{0.04})O_3$ piezoelectric ceramics. J Am Ceram Soc 90:1656–1658
121. Lin D, Kwok KW, Tian H, Chan HWL (2007) "Phase transitions and electrical properties of $(Na_{1-x}K_x)(Nb_{1-y}Sb_y)O_3$ lead-free piezoelectric ceramics with a MnO_2 sintering aid. J Am Ceram Soc 90:1458–1462
122. Li E, Kakemoto H, Wada S, Tsurumi T (2007) Influence of CuO on the structure and piezoelectric properties of the alkaline niobate-based lead-free ceramics. J Am Ceram Soc 90:1787–1791
123. Kim MS, Jeong SJ, Song JS (2007) Microstructures and piezoelectric properties in the Li_2O-excess $0.95(Na_{0.5}K_{0.5})NbO_3$–$0.05LiTaO_3$ ceramics. J Am Ceram Soc 90:3338–3340
124. Park HY, Ahn CW, Cho KH, Nahm S, Lee HG, Kang HW, Kim DH, Park KS (2007) Low-temperature sintering and piezoelectric properties of CuO-Added $0.95(Na_{0.5}K_{0.5})NbO_3$–$0.05BaTiO_3$ ceramics. J Am Ceram Soc 90:4066–4069
125. Du H, Liu D, Tang F, Zhu D, Zhou W, Qu S (2007) Microstructure, piezoelectric, and ferroelectric properties of Bi_2O_3-added $(K_{0.5}Na_{0.5})NbO_3$ lead-free ceramics. J Am Ceram Soc 90:2824–2829
126. Li E, Kakemoto H, Wada S, Tsurumi T (2007) Effects of manganese addition on piezoelectric properties of the (K, Na, Li)(Nb, Ta, Sb)O_3 lead-free ceramics. J Ceram Soc Jpn 115:250–253
127. Song HC, Cho KH, Park HY, Ahn CW, Nahm S, Uchino K, Park SH, Lee HG (2007) Microstructure and piezoelectric properties of $(1-x)(Na_{0.5}K_{0.5})NbO_3$–$xLiNbO_3$ ceramics. J Am Ceram Soc 90:1812–1816
128. Li H, Shih WY, Shih WH (2007) Effect of antimony concentration on the crystalline structure, dielectric, and piezoelectric properties of $(Na_{0.5}K_{0.5})_{0.945}Li_{0.055}Nb_{1-x}Sb_xO_3$ solid solutions. J Am Ceram Soc 90:3070–3072
129. Cho KH, Park HY, Ahn CW, Nahm S, Uchino K, Park SH, Lee HG, Lee HJ (2007) Microstructure and piezoelectric properties of $0.95(Na_{0.5}K_{0.5})NbO_3$–$0.05SrTiO_3$ ceramics. J Am Ceram Soc 90:1946–1949

130. Hollenstein E, Damjanovic D, Setter N (2007) Temperature stability of the piezoelectric properties of Li-modified KNN Ceramics. J Euro Ceram Soc 27:4093–4097
131. Higashide K, Kakimoto K, Ohsato H (2007) Temperature dependence on the piezoelectric property of (1-x)$(Na_{0.5}K_{0.5})NbO_3$-x$LiNbO_3$ ceramics. J Euro Ceram Soc 27:4107–4110
132. Nagata H, Matsumoto K, Hirosue T, Hiruma Y, Takenaka T (2007) Fabrication and electrical properties of potassium niobate ferroelectric ceramics. Jpn J Appl Phys 46:7084–7088
133. Wu J, Peng T, Wang Y, Xiao D, Zhu J, Jin Y, Zhu J, Yu P, Wu L, Jiang Y (2008) Phase structure and electrical properties of $(K_{0.48}Na_{0.52})(Nb_{0.95}Ta_{0.05})O_3$-$LiSbO_3$ lead-free piezoelectric ceramics. J Am Ceram Soc 91:319–321
134. Bomlai P, Sinsap P, Muensit S, Milne SJ (2008) Effect of MnO on the phase development, microstructures, and dielectric properties of $0.95Na_{0.5}K_{0.5}NbO_3$–$0.05LiTaO_3$ ceramics. J Am Ceram Soc 91:624–627
135. Li E, Kakemoto H, Hoshina T, Tsurumi T (2008) A shear-mode ultrasonic motor using potassium sodium niobate-based ceramics with high mechanical quality factor. Jpn J Appl Phys 47:7702–7706
136. Aoyagi R, Takeda A, Iwata M, Maeda M, Nishida T, Shiosaki T (2008) Depolarization temperature shift of $Li_{0.08}Na_{0.92}NbO_3$ lead-free piezoelectric ceramics by high-electric-field poling. Jpn J Appl Phys 47:7689–7692
137. Matsumoto K, Hiruma Y, Nagata H, Takenaka T (2008) Electric-field-induced strain in Mn-doped $KNbO_3$ ferroelectric ceramic. Ceram Int 34:787–791
138. Sasaki R, Suzuki R, Uraki S, Kakemoto H, Tsurumi T (2008) Low-temperature sintering of alkaline niobate based piezoelectric ceramics using sintering aids. J Ceram Soc Jpn 116:1182–1186
139. Suzuki R, Uraki S, Li E, Hoshina T, Tsurumi T (2008) Influence of Bi-perovskites on the piezoelectric properties of $(K_{0.5}Na_{0.5})NbO_3$-based lead free ceramics. J Ceram Soc Jpn 116:1199–1203
140. Tanaka D, Tsukada T, Furukawa M, Wada S, Kuroiwa Y (2009) Thermal reliability of alkaline niobate-based lead-free piezoelectric ceramics [in Japanese]. In: Proc. 26th Meeting on Ferroelectric materials and their application, Kyoto, Japan, pp. 33–34
141. Aoyagi R, Ohashi T, Iwata M, Maeda M (2009) Influence of (Li,Na)/Nb ratio in Electrical Properties of $(Li,Na)NbO_3$ Lead-free Piezoelectric Ceramics [in Japanese]. In: Proc. the 22th Autumn Symposium of Ceramic society of Japan, p. 21
142. Kawada S, Kimura M, Higuchi Y, Takagi H (2009) (K, Na)NbO_3-based multilayer piezoelectric ceramics with nickel inner electrodes. Appl Phys Expr 2:111401
143. Wang R, Bando H, Itoh M (2009) Formation of tetrogonal-rhombohedral morphotropic phase boundary in perovskite niobate. In: Proc. the 22th autumn symposium of the Ceramic Society of Japan, p. 20
144. Jaffe B, Roth RS, Marzullo S (1954) Piezoelectric properties of lead zirconate-lead titanate solid solution ceramics. J Appl Phys 25:809–810
145. Boudys M (1991) Relations between temperature coefficients of permittivity and elastic compliances in PZT ceramics near the morphotropic phase boundary. IEEE Trans Ultrason Ferroelectrics Freq Contr 38:569–571
146. Park HY, Ahn CW, Song HC, Lee JH, Nahm S, Uchino K, Lee HG, Lee HJ (2006) Microstructure and piezoelectric properties of $0.95(Na_{0.5}K_{0.5})NbO_3$–$0.05BaTiO_3$ ceramics. Appl Phys Lett 89:062906
147. Park HY, Cho KH, Paik DS, Nahm S, Lee HG, Kim DH (2007) Microstructure and piezoelectric properties of lead-free $(1-x)(Na_{0.5}K_{0.5})NbO_3$-x$CaTiO_3$ ceramics. J Appl Phys 102:124101
148. Zhao P, Zhang BP, Li JF (2007) High piezoelectric d33 coefficient in Li-modified lead-free (Na, K)NbO_3 ceramics sintered at optimal temperature. Appl Phys Lett 90:242909
149. Zhang S, Xia R, Shrout TR, Zang G, Wang J (2006) Piezoelectric properties in perovskite $0.948(K_{0.5}Na_{0.5})NbO_3$–$0.052LiSbO_3$ lead-free ceramics. J Appl Phys 100:104108
150. Ahn C, Priya S (2009) KNN based lead-free piezoelectrics. Extended Abstract of the 14th US-Japan Seminar on Dielectric and Piezoelectric Materials, Welches, OR, pp. 288–291

Chapter 7
Influence of the A/B Stoichiometry on Defect Structure, Sintering, and Microstructure in Undoped and Cu-Doped KNN

Michael J. Hoffmann, Hans Kungl, Jérôme Acker, Christian Elsässer, Sabine Körbel, Pavel Marton, Rüdiger-A. Eichel, Ebru Erünal, and Peter Jakes

7.1 Introduction

Development of ceramics based on the alkaline niobate (KNN) system is one of the major lines of current research pointing to substitution of the lead containing ferroelectrics by lead-free materials. Sodium potassium niobate $(K_{0.5}Na_{0.5})NbO_3$ is a prototype material of lead-free alkaline-transition metal ferroelectrics with $A^{1+}B^{5+}O_3^{2-}$ perovskite structure. Processing procedures for KNN-based ceramics are however challenging due to the hygroscopic behavior of sodium- and potassium carbonates and the evaporation of alkalines at the elevated processing temperatures, which make it difficult to control the stoichiometry of the ceramics. Alkaline (A-site) or niobium (B-site) excess results in pronounced qualitative differences of the microstructure in KNN ceramics.

Similar to many other perovskite ceramics, the functional characteristics are only moderate for pure KNN, but attempts to improve both performance and processing stability by the addition of dopants are underway. Hereby one line of development is the addition of copper or copper containing sintering additives. Discussion of the effects of Cu additions to KNN has to distinguish according to the level of Cu addition and to face the interrelationship between Cu content and A/B stoichiometry. When adding small amounts of Cu, remaining well below the solubility limit, Cu will be incorporated into the KNN lattice by definition. Substituting type of incorporation of Cu in the KNN lattice however implies

M.J. Hoffmann (✉) • H. Kungl • J. Acker
Institute for Ceramics in Mechanical Engineering, Karlsruhe Institute of Technology, Haid-und-Neu-Strasse 7, 76131 Karlsruhe, Germany

C. Elsässer • S. Körbel • P. Marton
Fraunhofer-Institut für Werkstoffmechanik IWM, Wöhlerstrasse 11, 79108 Freiburg, Germany

R.-A. Eichel • E. Erünal • P. Jakes
Institut für Physikalische Chemie I, Albertstrasse 21, 79104 Freiburg, Germany

S. Priya and S. Nahm (eds.), *Lead-Free Piezoelectrics*,
DOI 10.1007/978-1-4419-9598-8_7, © Springer Science+Business Media, LLC 2012

consequences for stoichiometry and therefore requires anticipation of the site of occupancy when preparing the powder mixtures in order to fabricate ceramics with a well-defined A/B stoichiometry. Consequently, information on site occupancy and the charge compensation mechanisms are the preconditions for controlling A/B stoichiometry when doping KNN. The effects of the Cu-dopants in the KNN lattice on electromechanical properties are governed by the type of point defects. Along with Cu-additions exceeding the solubility limit, secondary phase formation will result. Alkaline polyniobates and compounds from the quarternary (Na_2O, K_2O, Nb_2O_5, CuO) system may be formed depending on stoichiometry and processing conditions. Therefore at higher Cu-additions, in addition to the dopant effects from Cu in the KNN lattice, the secondary phase formation has to be analyzed and its consequences with respect to processing behavior and the properties of the ceramics have to be taken into account.

Consequently, in the paper a methodological framework for an analysis of the influence of dopants, considering the effects from lattice defects, the influence of the secondary phase formation, and their interrelationship with the A/B stoichiometry is developed. The methods are applied to copper additions in KNN ceramics, since for this type of material improvement of densification has been proved, enhancement of mechanical quality factors has been found and development of devices such as ultrasonic motors is already underway. Corresponding to the features and their interrelationships described above, the paper is organized as follows: First, the processing, the sintering behavior, and the development of microstructure in undoped KNN ceramics focusing the effects of A/B stoichiometry are concerned. Second, the substitution of Cu into the KNN lattice is discussed from different points of view. After some introductory remarks on the relations between substitution, charge compensation mechanisms, and their consequences for the stoichiometry and defect structure, an analysis of these issues on an atomic scale is presented. Results from a theoretical approach based on density functional theory (DFT) calculating the energetically favorable types of defect formation are described and corresponding experimental work from electron paramagnetic resonance (EPR), which monitors the local environment of the Cu cations in the KNN lattice is reported. Information on the effects of copper substitution on a larger length scales by experimental results on the microstructure and the macroscopic electromechanical properties of Cu-doped KNN is provided thereafter. The third subject to be discussed are the effects of Cu additions at concentrations higher than the solubility limit. An approach to evaluate the consequences of high level Cu-doping for secondary phase formation and stoichiometry is presented. Then, experimental results on microstructure and electromechanical properties for KNN ceramics with niobium excess and higher Cu content are reported and discussed with respect to the role of the secondary phases. The results are summarized in a final part.

7.2 Undoped KNN Ceramics

7.2.1 Challenges for Processing and Sintering

Ceramics based on the sodium-potassium niobate system have been investigated since the 1950s [32, 14]. It was pointed out already in the early research work that the hygroscopic behavior of alkaline carbonate raw materials and the volatility of alkalines during sintering are the major challenges for the processing in order to develop stable procedures [12, 14, 30, 33, 40, 41, 52]. Fluctuation in the humidity content of the alkaline carbonates, which are commonly used as raw materials for preparation by a solid-state route, affects the stoichiometry of the KNN. If a high water content of the alkaline carbonates is not correctly anticipated, it will result in niobium excess KNN. Powder preparation therefore requires to account for the humidity content by weighting dried powders or by determination of the humidity content by heating experiments and appropriate adjustment of the required alkaline carbonate weights. However, care has to be taken to choose the appropriate temperatures for obtaining water-free alkaline carbonates because temperatures too low may lead to an incomplete removal of humidity, whereas temperatures too high may lead to additional mass losses because carbonate decomposition starts. Experimental routine uses temperatures of approximately 200°C [7, 52]. Alternative routes for the preparation of KNN powders are under investigation. Processing KNN from sodium niobate and potassium niobate precursors [53, 78], which may be favorable with respect to calcination behavior, homogeneity and suppress secondary phase formation [78], is shifting the problems related to humidity only toward the previous stage of the preparation of $KNbO_3$ and $NaNbO_3$. Attempts to circumvent the problems of humidity were made by using organic sodium- and potassium tartrate tetrahydrate, but this procedure involves the use of the expensive metallorganic precursor [51]. Consequences of variations in alkaline or niobium content for powder processing are different calcination behavior and powder properties [1]. Calcination temperatures of more than 800°C or double calcinations [30] are required to obtain homogeneity of KNN perovskite solid solutions in stoichiometric KNN. With B-site excess, the temperatures necessary for a homogenization are even higher. In contrast to that, KNN powders with alkaline excess require lower calcination temperatures and dwell time to obtain homogenous solid solutions. Drawback from the A-site excess modification in stoichiometry is particle coarsening during calcinations [1, 8].

Challenges for sintering KNN are complete densification and control of the volatilization of alkalines [30, 40]. Under atmosphere pressure stoichiometric KNN was sintered to densities from 3.9 to 4.3 g/cm^3 ($\rho_{th} = 4.51$ g/cm^3) [4, 12, 14, 31, 34, 40, 92]. Higher densification was obtained by hot pressing or spark plasma sintering (SPS) [31, 83, 87]. These procedures, when carried out with carbon equipment, cause strong reduction of the KNN ceramics which involves electrical conductivity from oxygen vacancies. The vacancies have to be eliminated by means of a subsequent oxidizing treatment [84]. Moreover, the small grain size at the low SPS sintering

temperatures may not be favorable with respect to piezoelectric properties. For industrial applications the sintering technology has to remain within low cost atmospheric pressure sintering conditions. The gas atmosphere [76] and its humidity content [24] during sintering affect the volatility of the alkalines at high temperatures, and also play an important role in the microstructural development. They may change local stoichiometry, in particular at the grain boundaries [91] or even lead to the formation of secondary phase [82]. Atmospheric control by powder bed was suggested to stabilize the evaporation of alkalines [30, 76, 90, 91], but involves corresponding waste disposal of the powders for atmospheric control. For sintering under atmospheric pressure Kosec and Kolar suggested an activation by B-site excess in order to obtain enhanced diffusion by creation of A-site vacancies. By this method the densities could be increased from 3.90 g/cm^3 for the stoichiometric to 4.19 g/cm^3 of the KNN with 1.0 wt% B-site excess [40]. A similar approach was pursued for the B-site excess design modification of (Li,K,Na)(Nb,Ta,Sb)O_3 ceramics, originally suggested by Saito et al. [69, 70], to $(K_{0.44}Na_{0.52}Li_{0.04})_{0.998}(Nb_{0.84}Ta_{0.10}Sb_{0.06})O_3$ by the Penn. State group. The A/B stoichiometry on the one hand appears to be an efficient leverage to control densification behavior and microstructure, on the other hand it may provide an important tool for the microstructural tailoring [3, 42] of KNN ceramics.

7.2.2 Influence of A/B Stoichiometry in Undoped KNN Ceramics

7.2.2.1 Sintering

Preparation of KNN from alkali carbonates and niobium oxide results in pronounced differences in sintering behavior and microstructure between stoichiometric KNN, KNN with alkaline-, and KNN with niobium excess [1]. The characteristics of the shrinkage behavior for KNN with different A/B ratios under a heating rate of 5°C/min are shown in Fig. 7.1. The stoichiometric, undoped KNN 50/50 densifies within a narrow sintering interval with a pronounced maximum of the shrinkage rate at 950°C. In the presence of alkaline- or niobium excess, a completely different shrinkage behavior of KNN ceramics was found. KNN ceramics with alkaline excess are starting to shrink at much lower temperatures, whereby the shrinkage rate shows two pronounced maxima. The first shrinkage maximum occurs at 820°C, the second one at 890°C. At 971°C the shrinkage stops before the densification is completed. In contrast to that, in KNN with Nb-excess the shrinkage is shifted to much higher temperatures beyond 1100°C close to the solidus.

Sintering at 1105°C in air results in different levels of densification and different effects of varying dwell time depending on the A/B stoichiometry of the KNN ceramics [1]. The densities for ceramics sintered at 1105°C are plotted as a function of the dwell times (t_d) between 0.05 and 8 h in Fig. 7.2. For all dwell times from

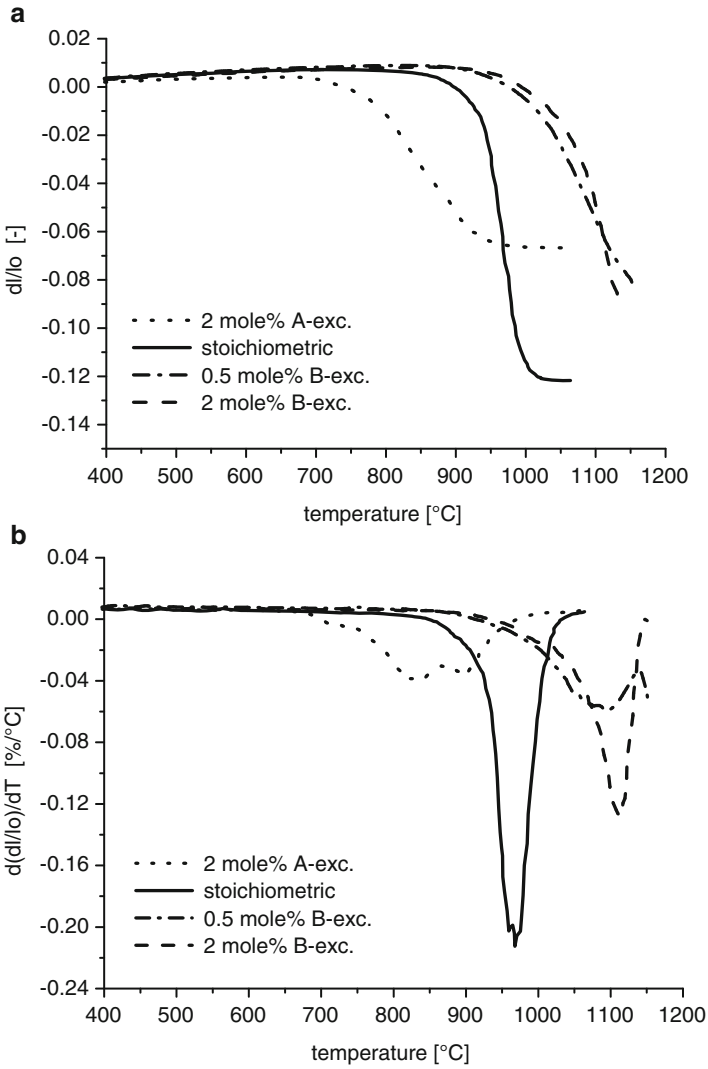

Fig. 7.1 Dilatometric curves when sintering the KNN ceramics. **(a)** Shrinkage. **(b)** Shrinkage rate

0.05 to 8 h the stoichiometric KNN ceramics sinter to high densities up to 4.34 g/cm^3, corresponding to 96.2% relative density. A slight trend toward an inverse relation between dwell time and density is indicated for the stoichiometric KNN ceramics. Under the same conditions the densities of KNN A-site excess are significantly lower, ranging from 3.85 to 3.97 g/cm^3 (relative densities 85.4–88.0%). For A-site excess KNN ceramics the densities are slightly increasing at longer dwell time. A more marked influence of dwell time on density was found in KNN ceramics with B-site excess. While short sintering times at 1105°C result in relatively low densities

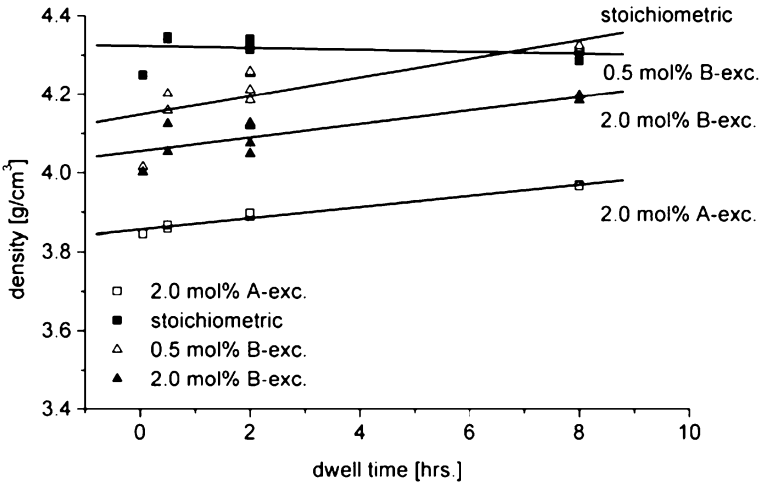

Fig. 7.2 Densities ρ after sintering KNN ceramics at 1105°C with varying dwell time t_s including linear fits of densities ρ vs. dwell time t_s

(4.0–4.1 g/cm^3, relative densities 88.7–90.9 %), the densification is enhanced when 8 h dwell time is applied, reaching densities of 4.20 g/cm^3 (relative density 93.1%) in the 2 mol% B-site excess KNN ceramics. Longer sintering time has still more pronounced effects for 0.5 mol% B-site excess KNN ceramics. With 8 h dwell time at 1105°C the densities of 0.5 mol% B-excess KNN reach 4.32 g/cm^3, which is approximately the same level as for the stoichiometric KNN. The weight losses for KNN with A-site excess (0.93–0.97%) are markedly higher than for the stoichimetric KNN (0.40–0.44%) and the compositions with B-site excess (0.17% and 0.21% at 2 mol% B-exc. and 0.11–0.20 % at 0.5 mol% B-exc.). However, a significant influence of dwell time on weight losses could not be detected from mass losses during sintering.

7.2.2.2 Structure and Microstructure

The XRD patterns of the sintered KNN (1105°C/2 h) match the $KNbO_3$ structure types with orthorhombic or monoclinic symmetry. The structure of these materials is currently under discussion: While originally considered to be orthorhombic (*Amm*2) [28, 32] recent work of Tellier et al. [78] and Baker et al. [6] demonstrated that monoclinic patterns with space group *Pm* provide excellent fits to the diffraction patterns. Probably, the diffraction patterns of the KNN ceramics are also affected by effects of the real structure, i.e., coherent scattering from the domain structure [9] and diffuse scattering from domain walls [10] similar to those in morphotropic PZT ceramics [29, 35, 36, 71, 72, 80]. Peaks of B-site excess KNN and stoichiometric compositions are evolving during sintering from broadened peaks after calcinations to sharp peaks (Fig. 7.3), due to a homogenization from a mixture of KNN solid solutions in the calcined powders to ceramics with largely uniform composition.

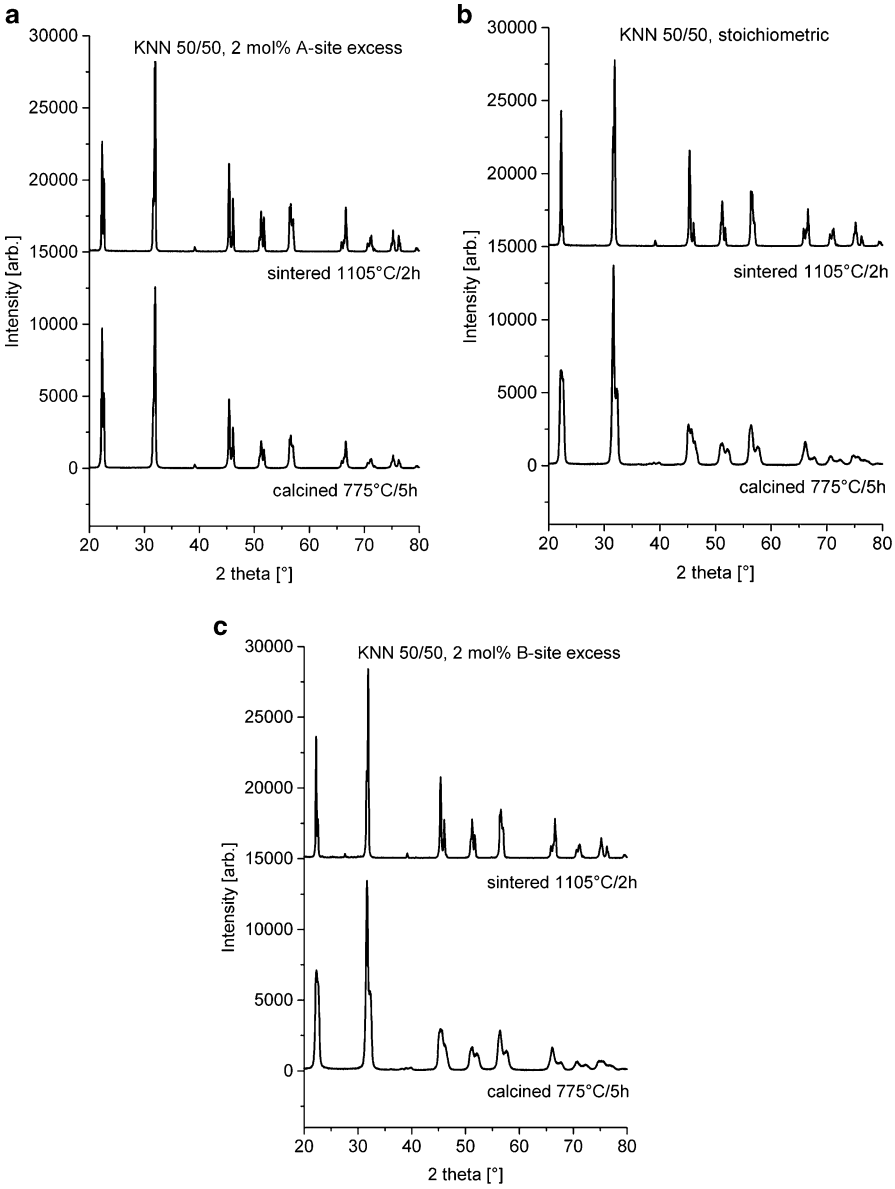

Fig. 7.3 X-ray diffraction (XRD) Patterns of KNN after calcinations at 775°C and after sintering at 1105°C/2 h. (**a**) KNN with 2 mol% A-site excess. (**b**) Stoichiometric KNN. (**c**) KNN with 2 mol% B-site excess

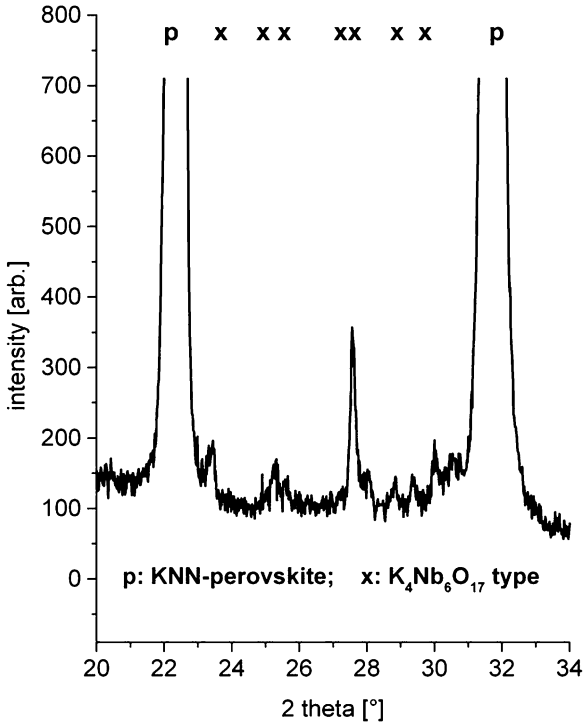

Fig. 7.4 Part of XRD pattern of KNN ceramics with 2 mol% B-site excess (1105°C/2 h) and the attribution of its major secondary phase peaks to $K_4Nb_6O_{17}$ type phase (JCPDS 076-0977)

In addition to that, size effects may sustain the sharpening of the peaks. The diffraction patterns of the A-site excess composition, which is already highly homogeneous in composition after calcinations, show no marked difference after sintering compared to the calcined powder. Additional peaks of secondary phases appear in the diffraction patterns of the sintered KNN ceramics with 2 mol% B-site excess (Fig. 7.4). These low intensity peaks can be attributed to the structure of the polyniobate phase $K_4Nb_6O_{17}$ (JCPDS 076-0977) [25, 49], compatible with the K_2CO_3-Nb_2O_5 phase diagram, which predicts the formation of this polyniobate phase for $KNbO_3$ in the presence of Nb_2O_5 excess [65]. Presently it is not clear, if the $K_4Nb_6O_{17}$ type phase tends to form $(K,Na)_4Nb_6O_{17}$ solid solutions with significant sodium content, and what conditions are necessary to promote the formation of other alkaline-polyniobate phases [34, 51, 52].

SEM micrographs of the undoped KNN ceramics sintered at 1105°C/2 h in air, which indicate a marked influence of the A/B ratio on the microstructure, are shown in Fig. 7.5. Alkaline excess, stoichiometric and niobium excess in KNN result in

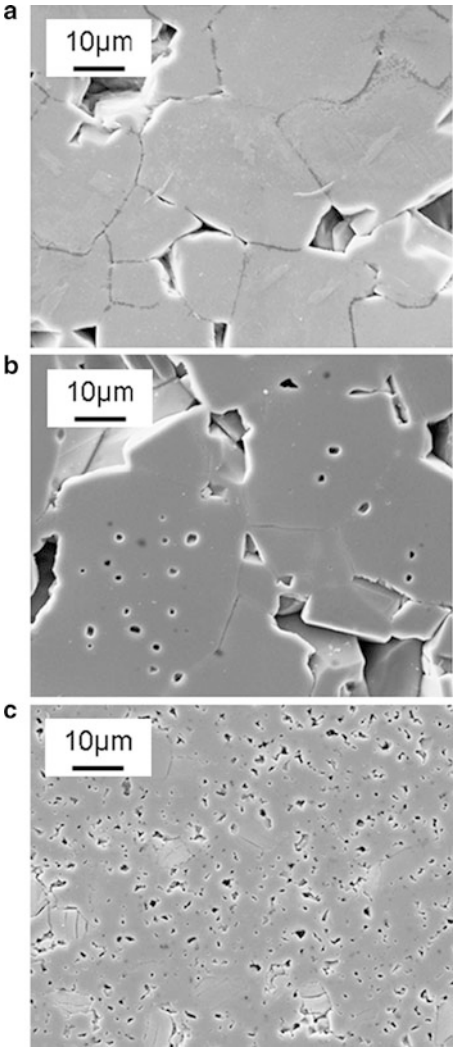

Fig. 7.5 Microstructure of the polished and chemically etched KNN ceramics sintered at 1105°C/2 h with (**a**) 2 mol% excess on A-site, (**b**) Stoichiometric, (**c**) 2 mol % excess on B-site

ceramics with completely different microstructures. In the stoichiometric materials the grain size ranges between 30 and 50 μm. In all grains considerable intragranular porosity is present (Fig. 7.5b). The large grains develop via a transient stage of abnormal grain growth. Nb-excess drastically reduces grain growth to a size between 3 and 5 μm (Fig. 7.5c and 7.6). The microstructures of KNN with 2.0 and 0.5 mol% Nb-excess are largely similar. In the fine-grained matrix of the 0.5 mol% Nb-excess KNN occasionally stray larger grains were detected. The KNN ceramics with alkaline excess are completely different from both (Fig. 7.5a). The shape of the grains tends to be more rectangular with mean grain size 20–30 μm. No intragranular porosity was found in this material [1].

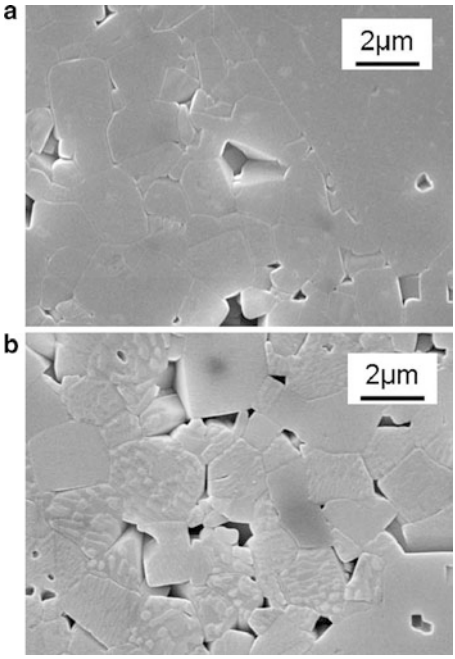

Fig. 7.6 Microstructure of the polished and thermally etched samples of KNN ceramics sintered at 1105°C/2 h with (**a**) 0.5 mol% B-site excess, (**b**) 2 mol% B-site excess

7.2.2.3 Mechanisms of Interaction Between Densification and Formation of Microstructure

Depending on stoichiometry, the mechanisms governing and limiting the sintering behavior are different. In the stoichiometric KNN, the evolution of the microstructure plays an important role for the sintering behavior and the limits for densification. Densification of these ceramics in the initial stages of sintering is fast, as long as the grain size remains small. The reduction in shrinkage rate can be related to the onset of abnormal grain growth. Abnormal grain growth on the one hand results in the formation of grains with internal porosity, on the other hand in large size pores resulting from the dissolution of fine-grained matrix grains. Both mechanisms are hindering complete densification in the late stage of sintering. At elevated temperatures no further densification occurs and extension of dwell time at high temperature rather reduces than increase the densities. In the A-site excess KNN a liquid/solid solution is formed at temperatures above 845°C and 987°C respectively according to the phase diagrams of K_2CO_3/Nb_2O_5 and Na_2CO_3/Nb_2O_5. The onset of sintering in the A-site excess KNN ceramics is even lower, at 750°C, but premelting grain boundary wetting films may reduce the temperatures required for liquid phase formation. Pronounced grain growth, the formation of cuboid grain morphology indicating the formation of low energy grain boundaries, and changes of the grain boundary films may result in the slowdown of the sintering rate. An increase in temperature from 970°C to 1105°C results in mass losses rising from 0.72 to 0.88%, which most probably indicates enhanced evaporation of alkalines.

While a standstill of the densification for temperatures higher than 970°C is indicated by the dilatometric data, at much higher temperature (1105°C) there is enhanced densification at longer dwell time. At these high temperatures, the activation of volume diffusion or changes in grain boundary state may promote a resurgence of the sintering process. With B-site excess the K_2CO_3/Nb_2O_5 and Na_2CO_3/Nb_2O_5 phase diagrams [65, 73] also predict the formation of liquid phase, although at higher temperatures than for A-site excess. However, for the B-site excess KNN no effects from liquid phase formation were detected by the dilatometer up to temperatures of 1100°C. Probably, the $K_4Nb_6O_{17}$ formation occurs at grain boundaries and acts as impediment for grain boundary diffusion and grain growth by a solute drag mechanism [1].

7.3 KNN with Cu Additions

In spite of recent improvements in the preparation of undoped KNN ceramics, current trends in research activity point to improve the materials by adding dopants. Major objectives of the doping are to stabilize the processing, improve the densification behavior, and to enhance the electromechanical properties. Recent research was concerned with the effects of Cu dopant on KNN ceramics as well as on the Li-, Ta-, Sb- modified versions of this system. Several forms of Cu-addition were developed and various types of effects were identified. Extensive work on various forms of Cu-addition to alkaline-based ferroelectric was reported by Matsubara et al. [55–58]. They touched the core of the problem of interrelationship between dopant addition, stoichiometry, and secondary phase formation when analyzing the effects of Cu-dopants in alkaline excess and niobium excess materials, which results in significant differences on the properties of the KNN ceramics. Addition of Cu leads to deliquescent ceramics when applied to A-site excess or stoichiometric material, whereas stable ceramics containing a secondary $K_4CuNb_8O_{23}$ phase are formed when doping B-site excess KNN. At the same time they identified addition of $K_4CuNb_8O_{23}$ or $K_{5.4}Cu_{1.3}Ta_{10}O_{29}$ after calcination as the most effective way to improve the properties of KNN. Therefore, no details on phase formation under doping by adding CuO to the K_2CO_3 -Na_2CO_3 - Nb_2O_5 powder mixture were published. With 0.2 and 0.5 mol% $K_4CuNb_8O_{23}$ addition they found an optimum sintering temperature at 1090°C [55, 56]. Under these conditions, large size grains with internal porosity developed [56, 57] and high strain and Q_m up to 180 pm/V and 1200 respectively were obtained. Park et al. [61] as well as Azough et al. [5], when adding CuO to KNN ceramics measured a reduction of the sintering temperature required for densification and an improvement in mechanical quality factor Q_m for KNN-Cu. At the same time they recognized the formation of secondary phase. Park et al. [61] found an increase in grain size, whereas Azough et al. [5] observed a trend to reduced abnormal grain growth by CuO-additions. From the secondary phase present in these ceramics they concluded that liquid phase formation was the origin for the enhanced densification. Park et al. [61] attributed the changes in piezo electric properties to the formation of defect

dipoles consisting of Cu^{2+} cations and oxygen vacancies. Similar trends for the electrical properties they found for the Sb-modified KNN variant [62]. Ahn et al. [2] analyzed the high field polarization behavior in KNN-Cu prepared by a similar route. An improved polarization behavior leading to a square-shaped polarization vs. electric field ($P - E$) curve, most marked for 1.5 mol% CuO additions was reported and correlated with the enhanced densities. In contrast to that, KNN with Cu additions prepared by Lin et al. [48] showed constricted double loop characteristics with Cu content increasing, which was attributed to dipole formation. The constriction of the $P - E$ loops also occurred when the Cu was added in the form of $K_{5.4}Cu_{1.3}Ta_{10}O_{29}$ sintering aid [48]. Li et al. [44] were investigating Cu-additions to $(Li_{0.04}Na_{0.44}K_{0.52})(Nb_{0.86}Ta_{0.1}Sb_{0.04})O_3$. They observed hardening of the piezoelectric properties with increasing Cu-additions. It was suggested that with low copper additions Cu substitutes on A-site, whereas along with higher copper addition Cu is incorporated on B-sites. Furthermore they found the formation of $K_4CuNb_8O_{23}$ secondary phase. Zuo et al. [93] observed grain coarsening by Cu in $(Na_{0.5}K_{0.5})_{0.96}Li_{0.04}(Ta_{0.1}Nb_{0.9})_{1-x}Cu_xO_{3-3x/2}$ ceramics and piezoelectric softening at low (<0.25 mol% Cu) doping but hardening at higher Cu-contents. The increase in the loss tangent with higher Cu-content, which in first instance seems contrary to hardening characteristics, was attributed to the presence of Cu cations with different charge states. While many of the modifications in properties of KNN ceramics appear to depend on the specifics of composition and processing, a common feature of most investigations of Cu-doping seems to be the high mechanical quality factor Q_m [47]. This may give rise to applications of this type of ceramics in specific fields [11]. Recent reports announced the fabrication of an ultrasonic shear mode motor prototype based on KNN-Li-Cu ceramic drive elements [45, 46]. Moreover, Cu additions may play an important role when tailoring [3, 23, 42] or texturing [77] the microstructure of the KNN-based ceramics.

In general, the results on Cu addition to KNN found in experimental work, are a combination of the direct effects of Cu substitution in the KNN lattice, the formation of secondary phase, and a shift in A/B stoichiometry. The approach pursued in the present analysis is to attempt to discuss the effects from lattice contributions by Cu-defects, the effects via the A/B ratio and the influence of the secondary phase formation on the KNN-Cu ceramics and their interrelationship. The type of substitution and the compensation mechanism of the dopant do not only influence the conditions for diffusion and the piezoelectric properties, but the A/B stoichiometry of the KNN base material will depend on the resulting defect structure. Consequently, the identification of the defect structure of Cu in KNN and its implications for stoichiometry are the first point to be discussed. Second, the conditions for the formation of secondary phases and its influence on the properties will be considered. When the solubility limit of the dopant in the KNN structure is exceeded, only part of the Cu will be substituted into the KNN lattice. The Cu-excess does not necessarily appear in the form of CuO, but may tend to arrange in other copper containing KNN compounds. Again, the formation of secondary phases will affect conditions for the stoichiometry of the KNN-based material. Effects from the secondary phase on densification behavior and the electromechanical properties of the materials may be depending on their microstructural characteristics. Related to these issues,

preliminary results on the secondary phase formation under high level Cu additions in B-site excess KNN and its consequences for the properties will be presented.

7.3.1 *Effects of Cu-Substitution in the KNN Lattice Substitution Mechanisms, Charge Compensation, and Their Consequences*

The charge state of the dopant ion, the lattice site which the dopant cation occupies, and the type of charge compensation mechanism that prevails in order to accomplish an overall charge balance directly influence the stoichiometry of the material. The basic cases of Cu-substitution in KNN for a Cu^{2+} charge state are shown in Fig. 7.7. Cu substituting in the form of Cu^{2+} for K^{+} or Na^{+} on the A-site will provide an additional positive charge to the lattice and has to be compensated by free electrons (Fig. 7.7a) or formation of A-site vacancies (Fig. 7.7b) [27]. In case Cu^{2+} goes to the B-site, replacing Nb^{5+}, oxygen vacancies or holes are required for charge balance [27]. Site occupancy and the type of charge compensation mechanism for the Cu-dopant are affecting the A/B stoichiometry of the base material. An intended A/B stoichiometry is realized in the ceramics only, if the site occupancy and charge compensation mechanism anticipated for calculation of the batch composition are correct. In general, the site occupancy cannot be determined by the molar ratios of the batch composition, but is governed by thermodynamics. Assuming Cu occupying A-sites when calculating the batch composition will result in a shift of the A/B ratio toward B-excess, if the Cu actually substitutes for the B-site

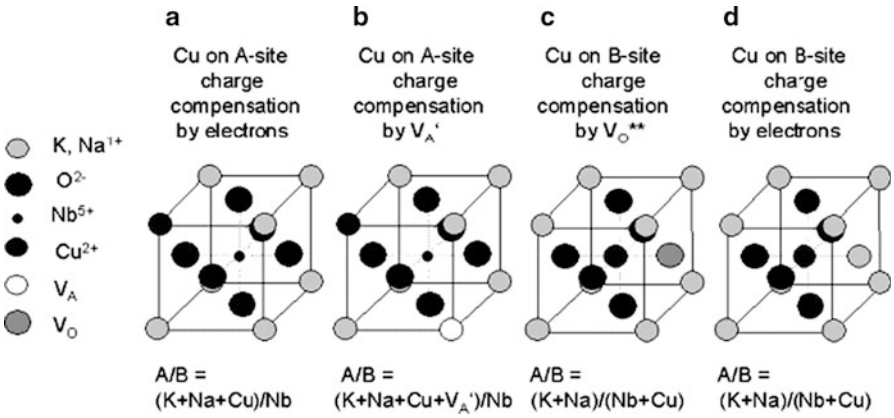

Fig. 7.7 Types of sites occupancy and charge compensation mechanisms and their implications for the calculation of the A/B ratio **(a)** Cu on A-site charge compensation by electrons **(b)** Cu on A-site charge compensation by V_A^* **(c)** Cu on B-site charge compensation by V_O^{**} **(d)** Cu on B-site charge compensation by electrons

and vice versa. The type of charge compensation mechanism also plays a role. Theoretically, under A-site occupancy of the Cu, less alkaline is required for a stoichiometric composition, when charge balance is accomplished by A-site vacancies than for charge compensation by electrons. In the case of B-site substitution, the type of charge compensation - formation of oxygen vacancies ($\frac{3}{2}V_{O}^{\bullet\bullet}$ for each Cu_{Nb}''') or compensation by free defect electrons - results in the same A/B ratio, because neither $V_{O}^{\bullet\bullet}$ nor $2e'$ affects the concentration [A] or [B] (Fig. 7.7c).

Theoretical and experimental results for the site occupancy and charge compensation mechanisms scale are obtained on an atomistic scale from DFT calculations and by the investigation of the local environment of the Cu-dopants using EPR. On a macroscopic scale, the influence of the A/B ratio on sintering behavior and microstructure was evaluated for Cu-doped KNN and undoped KNN reference. From the A/B stoichiometry, which markedly influences the microstructure and the sintering behavior, and its interdependence with Cu-site occupancy, conclusions with respect to the substitution of Cu in the KNN lattice are derived.

7.3.2 Ab Initio Thermodynamics of Cu Substitutionals in KNN

With ab initio DFT calculations it is possible to study crystal defects on the atomic level. DFT is a standard method for accurately calculating structural and energetical properties of materials and has been extensively applied to perovskites and/or defects in the literature (cf., e.g., the review articles [79, 85], and references therein). In Ref. [74] and [75] DFT was used to determine the formation energies of vacancies in $NaNbO_3$ and $KNbO_3$ as function of the chemical potentials, which are related to the processing conditions. According to these studies, Nb vacancies have a high formation energy regardless of the processing conditions and are therefore unlikely to form. In Section 7.3.2.1, we use DFT to determine the preferred lattice site of Cu substitutionals in KNN as function of the processing conditions.

Experiments presented in [22, 66] show that defect dipoles in an aged ferroelectric sample can act as a restoring force for the polarization after the external electric field is switched off, enabling reversible switching by 90° which is accompanied by a large strain already at comparatively low electric fields, and therefore interesting for actuator applications. On the other hand, such a polarization restoring mechanism is undesirable in memory applications. With DFT Erhart *et al.* showed that in $PbTiO_3$ the defect dipole ($Fe_{Ti} - V_O$) is energetically stable and tends to orient parallel to the spontaneous polarization of the surrounding bulk crystal [20]. Marton and Elsässer investigated the energy barriers for reorienting the ($Fe_{Ti} - V_O$) dipole and conclude that it "provides a pinning center for domain wall propagation" [54]. In Section 7.3.2.2 we apply DFT to investigate the stability of two possible defect configurations of Cu substitutionals and oxygen vacancies in KNN, one of them analoguous to the ($Fe_{Ti} - V_O$) defect in $PbTiO_3$.

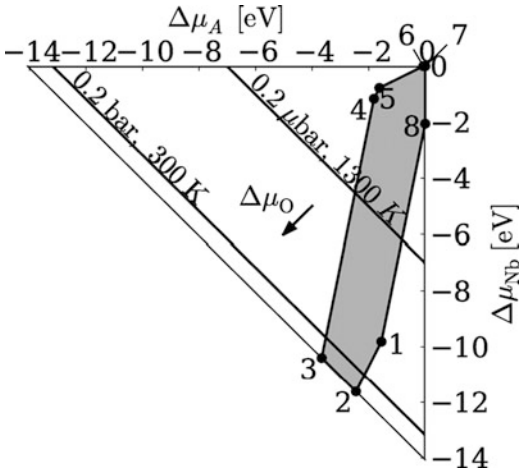

Fig. 7.8 Phase stability diagram for KNN. The areas of chemical potentials of alkali atoms ($\Delta\mu_A$) and Nb atoms ($\Delta\mu_{Nb}$) for which the perovskite phase is stable with respect to other competing phases is shaded in gray. The chemical potentials that correspond to the metallic phases are set to zero

7.3.2.1 On Which Lattice Sites Do Cu Dopants Substitute?

In principle, Cu substitutionals may be incorporated either on alkaline (*A*) sites, where they could act as donors, or as acceptors on the Nb (*B*) sites in the KNN lattice. DFT calculations can predict which lattice site is thermodynamically most stable for dopants. An appropriate description of the doping process is that of an open thermodynamic system that exchanges atoms and electrons with reservoirs, in which the atoms and electrons have certain chemical potentials (grand canonical ensemble). While for crystalline solids the effect of temperature and pressure on the chemical potentials of the atoms is rather small, for gases (oxygen) the chemical potentials depend strongly on temperature and pressure. Reuter and Scheffler [67] used the ideal gas equation to correlate the oxygen chemical potential with the temperature and the oxygen partial pressure, an approach we adopted for the present study. In experiments, mainly the temperature and the oxygen partial pressure are controlled, i.e., the chemical potential of oxygen. In the case of a metal-oxide like KNN, the chemical potentials of the metals are correlated to that of oxygen. Therefore the oxygen content in the processing atmosphere and the temperature can influence which lattice site is most stable for a dopant.

The chemical potentials of the atoms are confined to certain ranges for which the respective compound is stable. If those ranges are exceeded, other phases with different chemical compositions become more favorable. The gray area in Fig. 7.8 marks such ranges of possible chemical potentials for the example of KNN. Lines of constant chemical potential of oxygen in air (with about 20% oxygen content) at about room temperature (300 K) and at atmospheric pressure (about 0.2 bar oxygen

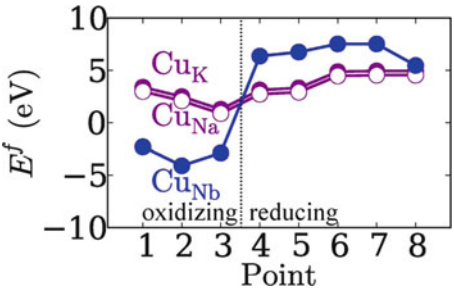

Fig. 7.9 Defect formation energy E^f for Cu on K, Na, and Nb sites for the points 1–8 in Fig. 7.8. The electronic chemical potential is assumed to lie at the center of the band gap

partial pressure), as well as for air at 10^{-6} bar at 1300 K (which is in the range of typical sintering temperatures for this material), show the relation between chemical potentials and chemical environment.

The upper right region corresponds to an oxygen-poor and metal-rich environment (for instance, in an Ar atmosphere at high temperature). The region down left corresponds to an oxygen-rich atmosphere, and to metal oxides as reservoirs. The black circles labeled by the numbers 1–8 form a representative set of chemical conditions for further analysis. The most stable one of a set of several possible defect types is the one with the lowest defect formation enthalpy, which is for crystalline solids often approximated by the defect formation energy (e.g., the energy needed to replace a host atom by a dopant). The formation energies for Cu substitutionals on alkali and Nb sites depend on the chemical conditions during processing (via the chemical potential of oxygen). The formation energies further depend on the electronic chemical potential, if the defect is charged (in the defect formation reaction electrons are removed from the electron reservoir and added to the defective crystal, or vice versa). For an electronic chemical potential at the center of the bandgap, we calculated the defect formation energies for Cu dopants on K, Na, and Nb sites in KNN for the chemical conditions corresponding to the points 1–8 in the phase stability diagram in Fig. 7.8. The resulting defect formation energies are depicted in Fig. 7.9. For oxygen-rich conditions (points 1–3) Cu preferentially substitutes on Nb sites (the defect formation energy on this site is lowest), in an oxygen-poor environment (points 4–8) the alkali substitution becomes energetically favorable. The present study shows that Cu is likely to substitute for Nb in the KNN lattice when processed in air, but may be driven to substitute on alkali sites by a reducing atmosphere [39].

7.3.2.2 Which Defect Complexes of Cu Substitutionals and Oxygen Vacancies Are Stable?

The total energy of the system can possibly be lowered if two or more defects form a defect complex. For instance, two defects with opposite effective charges in an ionic crystal are attracted toward each other by Coulomb interaction. In lead

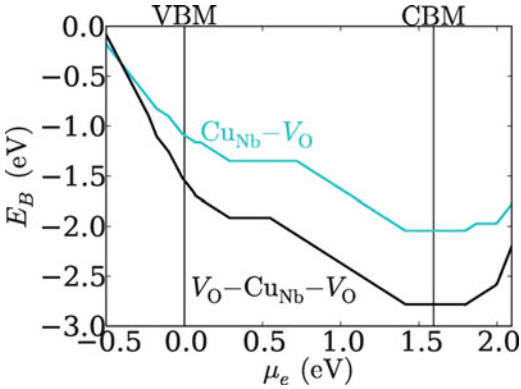

Fig. 7.10 Binding energies E_b of the defect complexes ($Cu_{Nb} - V_O$) and ($V_O - Cu_{Nb} - V_O$) in $KNbO_3$ as function of the electronic chemical potential μ_e in the LDA band gap. VBM and CBM denote the valence-band maximum and the conduction-band minimum, respectively

titanate, such defect complexes were investigated by means of density functional calculations, and binding energies (the energy gain with respect to the isolated single defects) up to about 2.3 eV were found [20]. For $KNbO_3$-Cu two different types of defect complexes, ($Cu_{Nb} - V_O$) and ($V_O - Cu_{Nb} - V_O$), are considered. Figure 7.10 shows the binding energies of these two defect complexes calculated with DFT. Because the energies of the isolated defects and that of each complex depend on the electronic chemical potential, the binding energies do so as well. For electronic chemical potentials throughout the LDA band gap, both defect complexes are stable with respect to the isolated defects (their binding energies are negative). Oxygen vacancies can thus be trapped by isolated Cu impurities to form ($Cu_{Nb} - V_O$) complexes, and for the ($Cu_{Nb} - V_O$) defect dipole it is energetically favorable to trap a second oxygen vacancy and form a ($V_O - Cu_{Nb} - V_O$) complex. Very similar binding energies were obtained for the same complexes in KNN [38].

The concentration of a defect type can be estimated by a Boltzmann factor $\exp - \frac{E^f}{k_B T}$ multiplied with the number of possible configurations of the defect [79], where E^f is the formation energy of a defect complex, k_B is Boltzmann's constant, and T is the temperature. Such an estimate of the relative concentrations of the dimer ($Cu_{Nb} - V_O$) and the trimer ($V_O - Cu_{Nb} - V_O$) in $KNbO_3$ reveals that although the dimer is energetically more favorable and the equilibrium concentration of the dimer should be several orders of magnitude lower than that of the trimer at room temperature, it could exceed that of the dimer at the sintering temperature [21].

Summarizing, the DFT calculations show that Cu dopants are likely to be incorporated on Nb sites in the KNN lattice if the samples are processed in air but may be driven toward the alkali sites in a reducing environment. If Cu ions substitute on Nb sites, they can form stable defect complexes with one or two neighboring oxygen vacancies, which then presumably interact with the ferroelectric polarization.

7.3.3 Experimental Evidence of Defect Centers from EPR

7.3.3.1 Theoretical Background and Experimental Methods

EPR spectroscopy may be used to study two main aspects - i.e., (i) the charge state of the copper functional center and (ii) the coordination of copper in the KNN lattice [15, 16]. Concerning the charge state, EPR principally allows distinguishing between Cu^{+}, which is diamagnetic and thus does not contribute to the EPR signal, and Cu^{2+} that is paramagnetic ($S = 1/2$) and gives rise to a characteristic EPR signal. The corresponding finger-print type EPR pattern originates from the copper hyperfine interaction with the two naturally abundant isotopes ^{63}Cu and ^{65}Cu, both of which have a nuclear spin of $I = 3/2$. Accordingly, the EPR resonances occur as quartets. There are four "*allowed*" transitions ($\Delta m_s = \pm 1$ and $\Delta m_I = 0$) between the corresponding energy levels, which appear as four resonances in the derivative-type continuous-wave EPR spectra. These quartets are centered about the electronic g-value and separated by the copper hyperfine interaction. Because the $3d$-shell is more than half filled in case of Cu^{2+} ($3d^9$), the main values of the g-matrix in its eigen-system are found to be larger than the free electron g-value ($g_e = 2.0023$). The observed EPR spectra may also be quantitatively analyzed. Electronic g-values and copper hyperfine interaction parameters can be evaluated by numerically fitting the experimentally obtained spectra to a spin Hamiltonian. In addition to that, the intensity of the continuous-wave EPR spectra that reflect the second derivative of the paramagnetic susceptibility need to be double integrated and compared to the susceptibility of a standard with known number of electron spins. Such investigations are helpful when analyzing the amount of impurity ions or when determining the solubility limit of an ion in the KNN lattice. With respect to an analysis of the coordination of the copper functional centers, recently a semiempirical model has been developed to distinguish between different defect-structural models [18]. This model is based on an analysis of the relative values of electronic g-values versus copper hyperfine interaction. Correspondingly, an incorporation of Cu^{2+} on the A-site may be distinguished from incorporation at the B-site. Furthermore, the formation of defect complexes with charge-compensating oxygen vacancies may be distinguished from "*free*" Cu^{2+}-centers - i.e., Cu^{2+} in a complete oxygen octahedron without any oxygen vacancy in the first coordination sphere.

7.3.3.2 EPR-Analysis of the Defect Structure

The cw-measurement of stoichiometric KNN with 0.25 mol% Cu shows two types of Cu-centers, indicated by their quartet hyperfine patterns as depicted in Fig. 7.11. For both centers, copper in the form of Cu^{2+} occupies the B-site in the perovskite structure. In centers type 1 there is one oxygen vacancy associated with the Cu^{2+} cation, whereas for centers type 2 there are two next neighbour oxygen vacancies aligned along opposite sides of the Cu^{2+} cation. Thus, the centers 1 and 2 can be

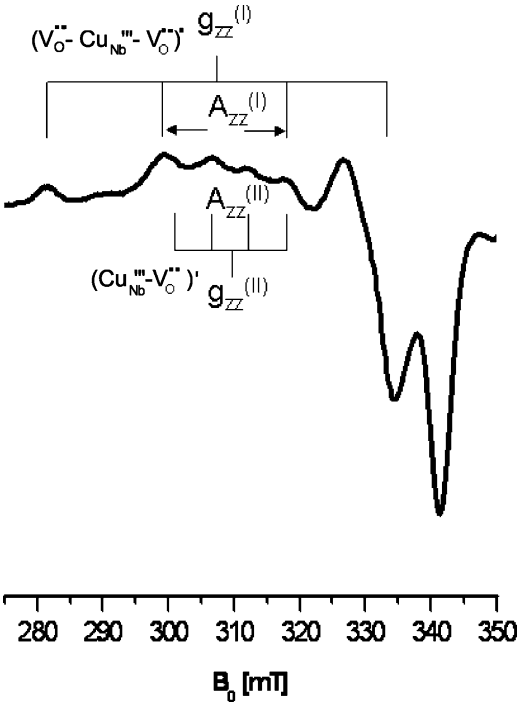

Fig. 7.11 X-band (9.8 GHz) EPR spectrum of 0.25 mol% CuO-doped KNN 50/50 ceramics

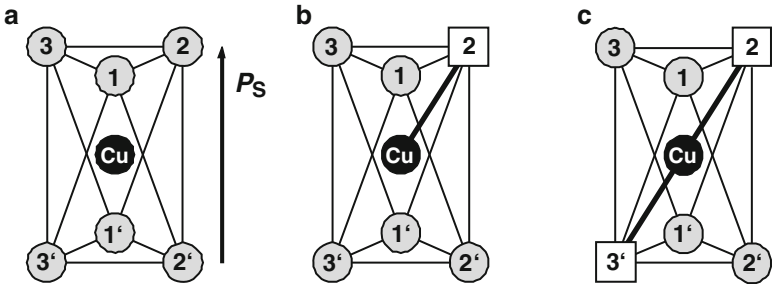

Fig. 7.12 Schematic representation of the defect structure for the Cu^{2+}-functional centers and their truncated oxygen octahedra. The direction of spontanous polarization, P_s, in KNN is indicated by an arrow. Oxygen vacancies are represented by open squares. **(b)** - $\left(\mathrm{Cu}_{\mathrm{Nb}}''' - V_{\mathrm{O}}^{\bullet\bullet}\right)'$ defect complex. **(c)** - $\left(V_{\mathrm{O}}^{\bullet\bullet} - \mathrm{Cu}_{\mathrm{Nb}}''' - V_{\mathrm{O}}^{\bullet\bullet}\right)^{\bullet}$ defect complexes

attributed to $\left(\mathrm{Cu}_{\mathrm{Nb}}''' - V_{\mathrm{O}}^{\bullet\bullet}\right)'$ and $\left(V_{\mathrm{O}}^{\bullet\bullet} - \mathrm{Cu}_{\mathrm{Nb}}''' - V_{\mathrm{O}}^{\bullet\bullet}\right)^{\bullet}$ defect complexes [19, 21]. Schematically, these defect complexes are illusrated in Fig. 7.12.

The corresponding incorporation reaction can then be given as

$$2\mathrm{CuO} \xrightarrow{\mathrm{Nb_2O_5}} 2\mathrm{Cu}_{\mathrm{Nb}}''' + 3V_{\mathrm{O}}^{\bullet\bullet} + 2\mathrm{O}_{\mathrm{O}}^{\times} \tag{7.1}$$

Accordingly, each copper atom brings in 3/2 oxygen vacancies into the KNN lattice. Because at temperatures below T_C the copper centers form $(Cu_{Nb}''' - V_O^{\bullet\bullet})'$ and $(V_O^{\bullet\bullet} - Cu_{Nb}''' - V_O^{\bullet\bullet})^{\bullet}$ defect complexes, the net result of doping with CuO can be written as:

$$2CuO \xrightarrow{Nb_2O_5} (Cu_{Nb}''' - V_O^{\bullet\bullet})' + (V_O^{\bullet\bullet} - Cu_{Nb}''' - V_O^{\bullet\bullet})^{\bullet} + 2O_O^{\times} \tag{7.2}$$

and overall charge neutrality will be established by

$$[(Cu_{Nb}''' - V_O^{\bullet\bullet})'] \approx [(V_O^{\bullet\bullet} - Cu_{Nb}''' - V_O^{\bullet\bullet})^{\bullet}] \tag{7.3}$$

This would ultimately lead to equal concentrations of dimeric, $(Cu_{Nb}''' - V_O^{\bullet\bullet})'$, and trimeric, $(V_O^{\bullet\bullet} - Cu_{Nb}''' - V_O^{\bullet\bullet})^{\bullet}$, defect complexes. The real situation, however, will be a mixture of both. Interestingly, these two defect complexes mutually compensate. The defect structure in CuO-doped KNN is thus considerably different from the one in CuO-doped $PbTiO_3$, where only one electrically neutral $(Cu_{Ti}'' - V_O^{\bullet\bullet})^{\times}$ defect complex is observed [17]. This is owing to the fact that in $PbTiO_3$, Cu^{2+} replaces Ti^{4+} and complexation with one oxygen vacancy results in an electrically neutral complex.

7.3.3.3 Impact of Defect Complexes on Domain Switching

In order to distinguish between the impact of different defect complexes on the material properties, the following arguments have to be considered. Concerning differences in the di- and trimeric defect complexes in KNN, the number of $V_O^{\bullet\bullet}$-jumps about the Cu^{2+}-functional center when interacting with 180° and non 180° domain walls have to be taken into account, as schematically illustrated in Fig. 7.13. For simplicity, the corresponding unit cells are regarded in a quasi tetragonal representation. The movement of 180° and non 180° domain walls from the 'right' side is represented by means of three snapshots, where particularly the hopping of oxygen vacancies is accounted for when the orientation of spontaneous polarization in a unit cell is changed. In this model, the width of the domain wall is restricted to a single unit cell.

First, the interaction of the dimeric $(Cu_{Nb}''' - V_O^{\bullet\bullet})'$ defect complex with non-180° domain walls is considered. More generally, the movement of non 180° domain-walls mainly impacts the electromechanical properties of a piezoelectric compound. Owing to the reorientation of the $(Cu_{Nb}''' - V_O^{\bullet\bullet})'$ defect complex by 90°, the oxygen vacancy has to migrate about the Cu^{2+}-functional center (Fig. 7.13a). With this respect, the 90°-reorientation of the trimeric $(V_O^{\bullet\bullet} - Cu_{Nb}''' - V_O^{\bullet\bullet})^{\bullet}$ defect complex involves a hopping process of two oxygen vacancies (Fig. 7.13b), which necessitates a considerably higher amount of energy as compared to the reorientation of the dimeric complex.

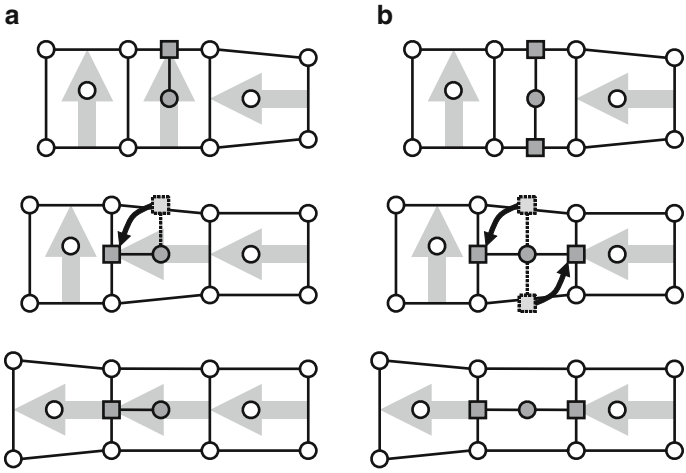

Fig. 7.13 Schematic representation of the interaction between the different defect complexes with 180° and non-180° domain-walls in a pseudo tetragonal representation. **(a)** Interaction with the dimeric defect complex. **(b)** Interaction with the trimeric defect complex. The orientation of spontaneous polarization is represented by a bold blue arrow

The deformation of the lattice by means of the oxygen vacancies and the increased ionic size of $Cu^{2+}(r_{Cu^{2+}} = 73\,\text{pm})$ as compared to $Nb^{5+}(r_{Nb^{5+}} = 64\,\text{pm})$, may be described by an elastic dipole moment [60]. By taking into consideration the elastic moments of the $(Cu''''_{Nb} - V_O^{\bullet\bullet})'$ and $(V_O^{\bullet\bullet} - Cu''''_{Nb} - V_O^{\bullet\bullet})^{\bullet}$ defect complexes together with the involved hopping of $V_O^{\bullet\bullet}$ when the corresponding complexes have to be reoriented by 90°, an enhanced mechanical quality factor is expected. This expectation agrees well with the reported increase of Q_m for CuO-doped and Li-modified KNN [44, 45]. On the other hand, the movement of 180° domain-walls mainly impacts the electric polarization of a piezoelectric compound. Concerning the interaction of the defect complexes with 180° domain walls, the interaction of the dimeric $(Cu''''_{Nb} - V_O^{\bullet\bullet})'$ defect complex necessitates a reorientation by 180°, which involves two hopping processes of the oxygen vacancy about the Cu^{2+}-functional center (Fig. 7.13c). By assuming an additional electric dipole moment for the trimeric defect complex, $p_D = q \times l$, with $q = +2e$ at the oxygen vacancy site and $q = -3e$ at the copper site, both having a distance of about half a lattice constant an additional defect polarization emerges. As a result, the orientation of spontaneous polarization in the neighboring unit cells as well as the domain structure is impacted. The corresponding restoring forces for domain walls that limit domainwall displacements have already been proposed for PZT and $BaTiO_3$ [37, 68, 86, 89]. On the contrary, the trimeric $(V_O^{\bullet\bullet} - Cu''''_{Nb} - V_O^{\bullet\bullet})^{\bullet}$ defect complex induces no such additional polarization. Consequently, there is no need for a reorientation of the defect complex when interacting with a domain wall. Therefore, the impact of the trimeric defect complexes $\left(V_O^{\bullet\bullet} - Cu''''_{Nb} - V_O^{\bullet\bullet}\right)^{\bullet}$ on the motion of 180°-domain walls tends to vanish because no hopping processes of oxygen vacancies are needed.

7.3.4 *Influence of Low Level Cu-Doping on A/B Ratio, Sintering and Microstructure*

7.3.4.1 Method of Analysis

On a macroscopic, phenomenological level the evaluation of site occupancy of the Cu ions in the KNN ceramics can be based on an analysis of the microstructure and sintering behavior. The characteristics of low level Cu-doped KNN ceramics under various stoichiometric conditions with respect to alkaline and niobium excess are analyzed and compared to those of undoped KNN materials with corresponding stoichiometry. From the results of the undoped KNN, it follows, that the alkaline/niobium stoichiometry has drastic influence on microstructure and densification behavior of these materials. Now the idea of the analysis is as follows: if the effects of Cu substitution on densification behavior and microstructure are small compared to those of the A/B ratio, the shrinkage, sintering behavior, and microstructure will be indicating the stoichiometric conditions in these ceramics, i.e., they show if the composition is with A-site excess, stoichiometric or with B-site excess. Consequently, the method of analysis is to compare several types of modifications in KNN and KNN-Cu ceramics. First, the effects of off-stoichiometry with high A- and B-site excess and its changes induced by copper doping are considered. Then the microstructural characteristics and the shrinkage behavior of $(K_{0.5}Na_{0.5})_{0.9975}Cu_{0.0025}NbO_3$ and $(K_{0.5}Na_{0.5})Cu_{0.0025}Nb_{0.9975}O_3$, corresponding to stoichiometric materials in case Cu goes on the A- or Cu goes on the B-site respectively, are analyzed and compared to those of the alkaline- and niobium excess materials. From a combined analysis of the changes, conclusions with respect to the site occupancy of the Cu in KNN ceramics are drawn. The batch compositions of the KNN-Cu materials used for the analysis are listed in Table 7.1.

Corresponding calculations of the real A/B ratio resulting for the KNN-Cu batch compositions with varying scenarios for site occupancy and charge compensation mechanism are reported in Fig. 7.14. The compositions $(K_{0.5}Na_{0.5})_{1.02}$-$Cu_{0.0025}Nb_{0.9975}O_3$ and $(K_{0.5}Na_{0.5})_{0.98}Cu_{0.0025}Nb_{0.9975}O_3$ remain within the alkaline- or niobium excess regime, independent of conditions for site occupancy and charge compensation. In contrast to that, $(K_{0.5}Na_{0.5})_{0.9975}Cu_{0.0025}NbO_3$ represents a stoichiometric material in case Cu goes on the A-site, whereas in case Cu occupies the B-site, the material will exhibit B-site excess. Correspondingly, $(K_{0.5}Na_{0.5})$ $Cu_{0.0025}Nb_{0.9975}O_3$, will be stoichiometric for Cu substituting on B-site, whereas an

Table 7.1 Batch compositions of the alkaline niobate (KNN)-Cu materials with Cu-dopant level of 0.25 mol% and varying A/B-stoichiometry

	Chemical Batch Composition
B-site excess KNN-Cu	$(K_{0.5}Na_{0.5})_{0.98}(Cu_{0.0025}Nb_{0.9975})O_3$
KNN-Cu stoich. for Cu on A-site	$((K_{0.5}Na_{0.5})_{0.9975}Cu_{0.0025})NbO_3$
KNN-Cu stoich. for Cu on B-site	$(K_{0.5}Na_{0.5})Cu_{0.0025}Nb_{0.9975}O_3$
A-site excess KNN-Cu	$(K_{0.5}Na_{0.5})_{1.02}(Cu_{0.0025}Nb_{0.9975})O_3$

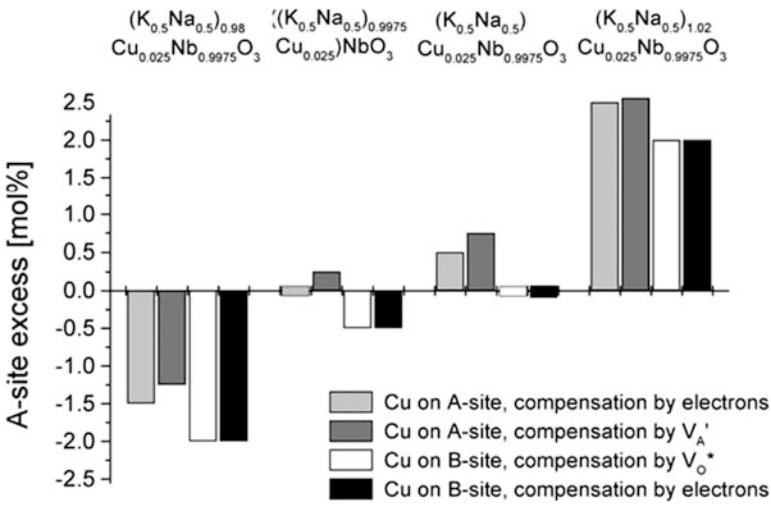

Fig. 7.14 Calculation of the A-excess for the different KNN 0.25 mol% Cu compositions

A-site occupancy will result in A-site excess for this material. Dipole formation of the Cu with oxygen vacancies does not alter the stoichiometric conditions for the KNN materials as long as no additional cation vacancies are involved in the overall charge compensation mechanism. This condition is perfectly met, if the concentrations of dimeric and trimeric defect complexes equal.

7.3.4.2 Sintering Behavior of the KNN-Cu Ceramics

The shrinkage behavior of the 0.25 mol% Cu-doped A-site and B-site excess KNN compared to the undoped materials with corresponding A/B stoichiometry is shown in Fig. 7.15. KNN with 2 mol% A-site excess shows shrinkage already at low temperature, with two pronounced maxima of the shrinkage analogous to the undoped KNN. In KNN-Cu with 2 mol% niobium excess the shrinkage is shifted to the high temperature range. Again the shrinkage characteristics are comparable to those of the undoped KNN with 2 mol% B-site excess. The conclusion from these experiments is that in off-stoichiometric KNN the effects of the alkaline or niobium excess are much more pronounced than those of a small amount of copper dopant. So the shrinkage behavior of the $(K_{0.5}Na_{0.5})Cu_{0.0025}Nb_{0.9975}O_3$ and $(K_{0.5}Na_{0.5})_{0.9975}Cu_{0.0025}NbO_3$ may allow for an evaluation, if there is niobium excess, alkaline excess or if these materials are stoichiometric. Indeed, significant differences in shrinkage behavior were found between the $(K_{0.5}Na_{0.5})Cu_{0.0025}Nb_{0.9975}O_3$ and $(K_{0.5}Na_{0.5})_{0.9975}Cu_{0.0025}NbO_3$ compositions. The former ceramics (corresponding to stoichiometric composition in case of B-site substation by Cu^{2+}) behaves very much like those of the stoichiometric KNN. In contrast to that, the shrinkage rate maxima in $(K_{0.5}Na_{0.5})_{0.9975}Cu_{0.0025}NbO_3$ (corresponding to a stoichiometric composition in case of A-site substitution by Cu^{2+})

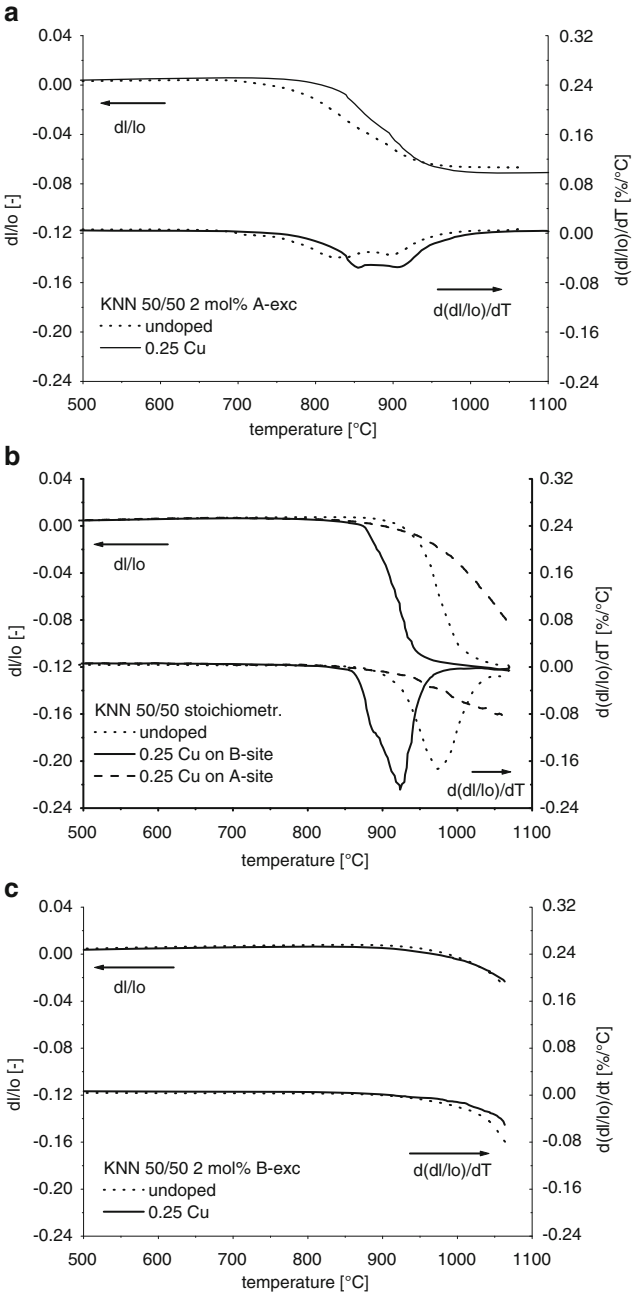

Fig. 7.15 Shrinkage dl/l_0 and shrinkage rate $d(dl/l_0)/dT$ of undoped and 0.25 mol% Cu-doped KNN. **(a)** A-site excess KNN and KNN-Cu. **(b)** stoichiometric KNN vs. $(K_{0.5}Na_{0.5})Cu_{0.0025}Nb_{0.9975}O_3$ and $(K_{0.5}Na_{0.5})_{0.9975}Cu_{0.0025}NbO_3$. **(c)** B-site excess KNN and KNN-Cu

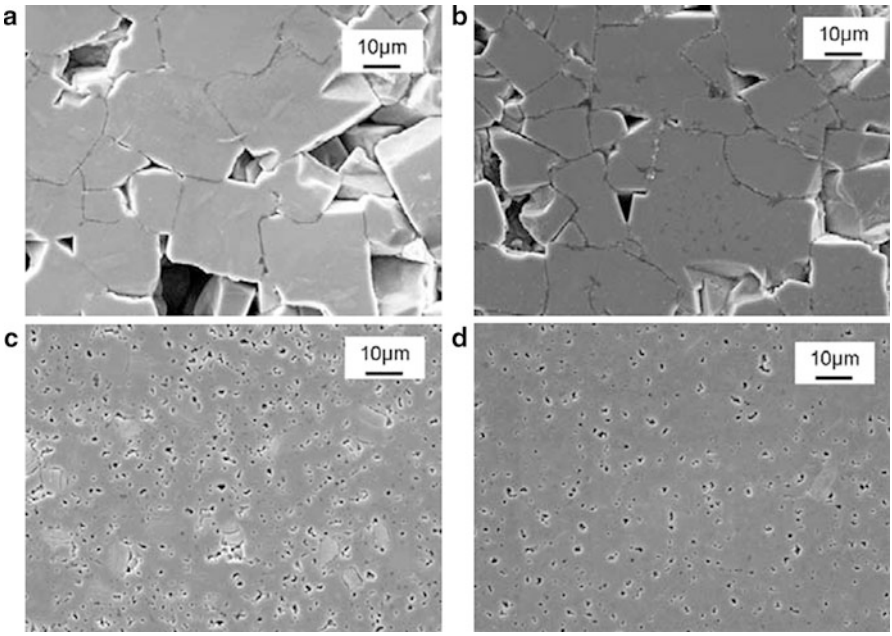

Fig. 7.16 Microstructure of KNN 50/50 undoped and 0.25 mol% Cu-doped, sintered at 1105°C/2 h. **(a)** KNN undoped 2 mol% A-exc. **(b)** KNN 0.25 mol% Cu 2 mol% A-exc. **(c)** KNN undoped 2 mol% B-exc. (**d**) KNN 0.25 mol% Cu 2 mol% B-exc

are shifted toward an elevated temperature range, typical for B-excess KNN. Therefore, the shrinkage behavior indicates that $(K_{0.5}Na_{0.5})_{0.9975}Cu_{0.0025}NbO_3$, which would correspond to stoichiometric material in case Cu^{2+} would occupy the A-site, seems to be in fact a B-site excess KNN. On the other hand, $(K_{0.5}Na_{0.5})Cu_{0.0025}Nb_{0.9975}O_3$, for which the copper was anticipated to substitute on B-site in the batch composition, behaves like a stoichiometric KNN. Overall, the analysis of the shrinkage behavior supports the B-sites substitution by Cu^{2+} in KNN.

7.3.4.3 Microstructure of the KNN-Cu Ceramics

Following the same line of analysis as for the shrinkage, the comparison and analysis of the microstructures were carried out. The microstructures of undoped and Cu-doped A-site excess KNN are shown in in Fig. 7.16a,b. In KNN with A-site excess the microstructure remains largely unaffected by 0.25 mol% copper addition compared to the undoped A-site excess KNN. The grains are cubioid and grain size is between 10 and 30 μm. Similarity to the undoped KNN also holds for the KNN with B-site excess, the grain size of the KNN matrix grain remains much smaller in both the undoped and the 0.25 mol% Cu-doped ceramics (Fig. 7.16c,d). Small amounts of secondary phase

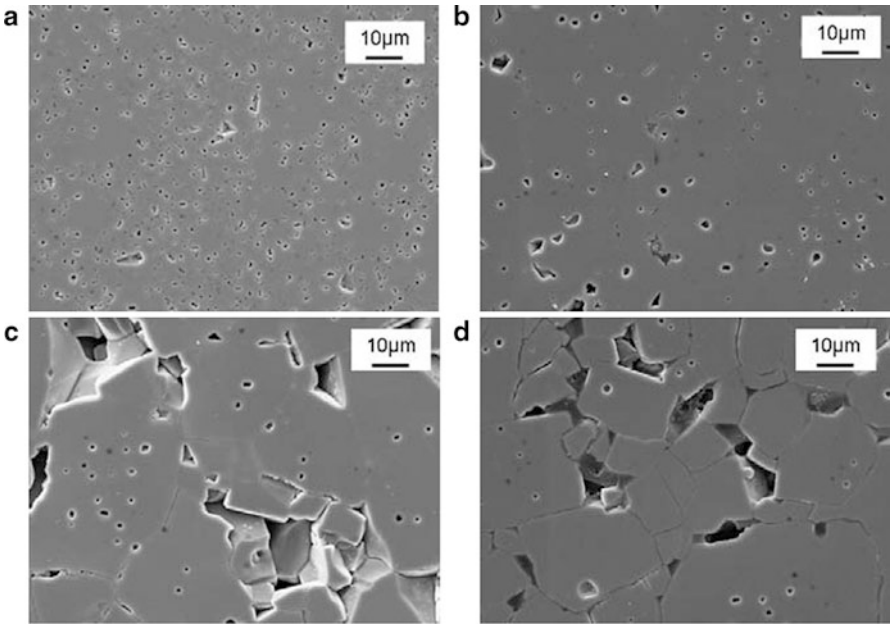

Fig. 7.17 Microstructure of KNN 50/50 undoped and 0.25 mol% Cu-doped, sintered at 1105°C/2 h. **(a)** KNN undoped 0.5 mol% B-exc. **(b)** $(K_{0.5}Na_{0.5})_{0.9975}Cu_{0.0025}NbO_3$. **(c)** KNN undoped, stoichiometric. **(d)** $(K_{0.5}Na_{0.5})Cu_{0.0025}Nb_{0.9975}O_3$

were also found in both undoped and 0.25 mol% Cu doped B-site excess KNN. Therefore, under large A- and B-site excess, the microstructure is subject only to minor changes when adding 0.25 mol% Cu dopant. A microstructure similar to the fine-grained matrix with stray larger-sized grains in the B-site excess KNN and KNN-Cu was found in the $(K_{0.5}Na_{0.5})_{0.9975}Cu_{0.0025}NbO_3$ ceramics (Fig. 7.17a,b). In contrast to that, the $(K_{0.5}Na_{0.5})Cu_{0.0025}Nb_{0.9975}O_3$ ceramics show large grains with intragranular porosity, the characteristic features of stoichiometric KNN ceramics (Fig. 7.17c,d).

The copper doping at 0.25 mol% Cu in the high A-excess and the high B-excess KNN does not lead to marked changes. It is therefore concluded that it is the A/B stoichiometry and not the low level Cu dopant which predominantly influences the microstructure. Based on this approach, an assessment on the A/B ratios in the KNN Cu on A site and the KNN Cu on B-site ceramics can be made, applying the following line of argument: (i) the KNN ceramics with batch composition $(K_{0.5}Na_{0.5})_{0.9975}Cu_{0.0025}NbO_3$ will be stoichiometric (A/B = 1) in case the Cu dopant substitutes for the A-site. In this case one would therefore expect, that Cu-doped stoichiometric KNN will be largely similar to the microstructure of stoichiometric undoped KNN. In case the Cu ions occupy B-sites, the ceramics will be off stoichiometric with a 0.5 mol% B-site excess. As shown in Fig. 7.17b the $(K_{0.5}Na_{0.5})_{0.9975}Cu_{0.0025}NbO_3$ has predominantly fine-grained microstructure which is corresponding to the undoped

KNN 0.5 mol% B-excess KNN (Fig. 7.17a). This indicates that the Cu actually substitutes on B-sites. (ii) in $(K_{0.5}Na_{0.5})Cu_{0.0025}Nb_{0.9975}O_3$ batch composition ceramics the A/B ratio will equal one only in case the Cu occupies the B-sites, whereas Cu substitution on A-sites would result in an A-site excess KNN (A/B = 1.005). Inspection of the microstructure and comparison with the undoped compositions shows that the microstructure of the $(K_{0.5}Na_{0.5})Cu_{0.0025}Nb_{0.9975}O_3$ ceramic (Fig. 7.17d) closely resembles the undoped stoichiometric material (Fig. 7.17c) and is significantly different from an A-site excess KNN (Fig. 7.16a). Therefore, the analysis of the microstructure also indicates that copper occupies the niobium site.

Summarizing the effects of low level Cu doping in KNN on densification behavior and on microstructure, the impact on both is small as long as the stoichiometric regime – A-site excess, stoichiometric conditions or B-site excess – remains unchanged. Batch compositions with additions of Cu which drive the chemical conditions from stoichiometric to the A- or to B-site excess regime or vice versa, however, will result in pronounced changes of the microstructure and shrinkage behavior.

7.3.5 Effects in KNN-Cu from Formation of Secondary Phases

7.3.5.1 Relations Between Secondary Phase Formation and A/B Stoichiometry in KNN

While the formation of defect dipoles in the lattice may result in effects on dielectric and piezoelectric properties owing to dipole formation already at low dopant levels, the densification behavior and the microstructures remain largely unaffected as long as the stoichiometric regime – A-site excess, stoichiometric conditions or B-site excess – is not altered. Doping with small amounts of Cu below the solubility limit does not significantly improve the densities, which remain in the range between 94 and 97% relative density. So the sensitivity of these ceramics to the effects from open porosity on the electrical behavior remains. Significant enhancement of the densification and reduction in sintering temperatures can be obtained only with higher levels of Cu-dopant, exceeding the solubility limit of Cu in KNN along with the formation of liquid phase. Cu-addition above the solubility limit however, implies that not all the Cu can be integrated into the KNN structure. This will lead to the formation of secondary phases and additional shifts in the A/B stoichiometry. The type of secondary phase thereby may depend on the A/B stoichiometry used for the KNN batch composition. Therefore, the conditions of stoichiometry have to be analyzed and the role of the secondary phases on dielectric and piezoelectric properties has to be investigated.

Methodology of Analysis Based on Linear Programming Technique of Mass Balance

Calculation of the quantities for the appropriate raw materials for an intended material containing two phases with defined stoichiometry can be derived from the mass balance of the elements. An example for the calculation of the molar masses M_{Na}, M_K, M_{Cu}, and M_{Nb} for an intended two-phase material $(K_{0.6}Na_{0.4})Cu_{0.02}Nb_{0.98}O_3$ KNN-Cu - $K_4CuNb_8O_{23}$ with molar fractions x_1 of $(K_{0.6}Na_{0.4})Cu_{0.02}Nb_{0.98}O_3$ and x_2 for $K_4CuNb_8O_{23}$ is given in (7.4) to (7.7). No deviations from stoichiometry by alkaline or niobium excess are allowed within the calculation. Assuming that the oxygen stoichiometry will be balanced, the equations governing the mass balance for the cations read:

$$\text{Na}: \ 0.4x_1 + 0.0x_2 = M_{\text{Na}} \tag{7.4}$$

$$\text{K}: \ 0.6x_1 + 4.0x_2 = M_{\text{K}} \tag{7.5}$$

$$\text{Cu}: 0.02x_1 + 1.0x_2 = M_{\text{Cu}} \tag{7.6}$$

$$\text{Nb}: 0.98x_1 + 8.0x_2 = M_{\text{Nb}} \tag{7.7}$$

and result in $M_{Na} = 0.4$, $M_K = 0.68$, $M_{Cu} = 0.04$, and $M_{Nb} = 1.14$ mol, required for stoichiometric compositions of the product combination 1 mol $(K_{0.6}Na_{0.4})Cu_{0.02}Nb_{0.98}O_3$ and 0.02 mol $K_4CuNb_8O_{23}$.

Graphical representation in the $(K_{0.6}Na_{0.4})Cu_{0.02}Nb_{0.98}O_3$ - $K_4CuNb_8O_{23}$ materials space results in linear constrains with respect to each cation species (Fig. 7.18a). The constraint for Na is a vertical line, because $K_4CuNb_8O_{23}$ does not contain sodium, therefore it limits only the $(K_{0.6}Na_{0.4})Cu_{0.02}Nb_{0.98}O_3$ molar fraction. All product combinations inward from a constraint for each cation species toward the origin are feasible with respect to the available quantities of this cation species [26]. When limited by the available molar fractions of the cations only, any product combination $(K_{0.6}Na_{0.4})Cu_{0.02}Nb_{0.98}O_3$ - $K_4CuNb_8O_{23}$ within the field ASB (Fig. 7.18a) can be realized, leaving however residual quantities of at least some cations. Product combinations outward of a constraint cannot be realized because not enough of the cation is available. For product combinations on the constraints of a cation species the complete quantity of this cation species is used in the products. The common point of intersection of the constraints (point S) represents the intended batch molar fractions of $(K_{0.6}Na_{0.4})Cu_{0.02}Nb_{0.98}O_3$ and $K_4CuNb_8O_{23}$ with no excess or deficit of any cation species (Fig. 7.18a). Precondition for the realization of this composition without any excess elements is however the exact adherence to the stoichiometry assumed in (7.4) – (7.7). In particular, differences in the solubility limit of the Cu-dopant and excess of alkalines or niobium in the KNN may lead to deviation from the intended stoichiometry. In practice neither the niobium excess that can be tolerated by the KNN perovskite

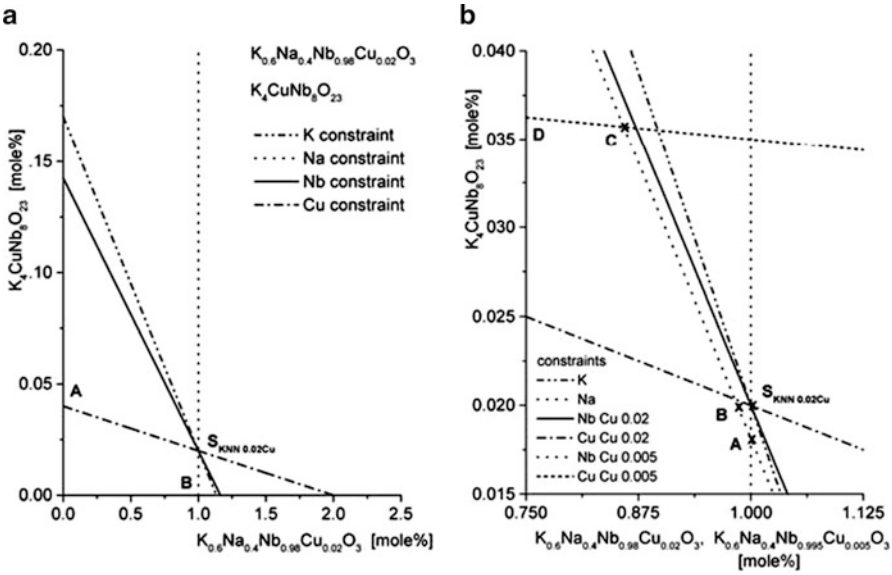

Fig. 7.18 Constraints for the formation of KNN-Cu and $K_4CuNb_6O_{17}$ for a given amount of cations. **(a)** Constraints for $K_{0.6}Na_{0.4}Cu_{0.02}Nb_{0.98}O_3$ and $K_4CuNb_6O_{17}$ with cations available for M ($K_{0.6}Na_{0.4}Cu_{0.02}Nb_{0.98}O_3$) = 1 mol and M($K_4CuNb_6O_{17}$) = 0.02 mol. **(b)** Effects of shift in solubility of Cu for $K_{0.6}Na_{0.4}Cu_{0.02}Nb_{0.98}O_3$ to $K_{0.6}Na_{0.4}Cu_{0.005}Nb_{0.995}O_3$ on constraints and excess cations

before secondary phase formation starts nor the solubility limit for Cu in KNN is known. If the solubility of Cu is less than assumed in the calculations (e.g., 0.5 mol % instead of 2.0 mol% assumed in the calculation above), part of the Cu will not go into the KNN lattice. For a given batch composition the immediate consequences are on the one hand an excess of Cu and on the other hand a lack of available B-site cations (because less Cu than assumed will go to the B-site). Assuming that the KNN-Cu material changes composition from $(K_{0.6}Na_{0.4})Cu_{0.02}Nb_{0.98}O_3$ to $(K_{0.6}Na_{0.4})Cu_{0.005}Nb_{0.995}O_3$ owing to the solubility limit for Cu, at given quantities of the cations available in the batch, the constrains for Cu and Nb will shift (Fig. 7.18b). There is no more common point of intersection of all constraints and any product combination leaves excess of some cation species. So several scenarios can be discussed, assuming defined stoichiometries $(K_{0.6}Na_{0.4})Cu_{0.005}Nb_{0.995}O_3$ and $K_4CuNb_8O_{23}$ for the products (Fig. 7.18b). If the fraction of KNN-Cu shall remain constant (point A), the $K_4CuNb_8O_{23}$ fraction has to be reduced in order to provide the additional niobium. This scenario will result in excess potassium and in excess Cu. If the fraction of $K_4CuNb_8O_{23}$ remains constant (point B), the KNN-Cu fraction has to be reduced. In addition to the K and Cu excess, this kind of change will result also in sodium excess. Finally, the excess Cu may form additional secondary phase $K_4CuNb_8O_{23}$ (in the extreme case until there is no more residual Cu, point C). This however has to withdraw additional niobium and alkalines from

the KNN and results in a pronounced reduction of the KNN-Cu connected with large excess in alkalines. Further modifications will arise, when nonstoichiometries of the KNN-Cu and the $K_4CuNb_8O_{23}$, changes of the K/Na ratio in both compounds or the formation of additional polyniobates are considered. The excess alkalines may change the A/B stoichiometry of both the KNN-Cu and the $K_4CuNb_8O_{23}$ volume fractions.

In general, under conditions when doping involves secondary phase formation, many things may happen. The intended stoichiometries are not necessarily those intended by the batch composition, if these are calculated without precise information on solubility limit of the dopant, permissible excess of alkalines or niobium in the KNN and alkaline solid solution conditions in the secondary phase. In principle, for thermodynamic equilibrium the same problems remain when a Cu containing additive such as $K_4CuNb_8O_{23}$ is added to KNN. In this case, Cu may depart from the $K_4CuNb_8O_{23}$ phase and substitute into the KNN structure leaving residual K and Nb cations. However, kinetics may be more sluggish and make the materials less sensitive to small processing fluctuations. Overall, along with higher Cu-dopant contents, the solubility limit for Cu in KNN and the formation of secondary phases, which may result in a shift in the A/B ratio, have to be taken into account for an analysis of the dopant effects at higher dopant levels.

7.3.5.2 Properties in KNN–Cu Along with Variation of the Cu-Dopant Level

Phase Formation and Sintering

Effects of different amounts of Cu-doping in KNN on the secondary phase formation are demonstrated in Fig. 7.19. Batch compositions, all with B-site excess intended, of these materials are listed in Table 7.2. Their X-ray diffraction patterns show that for undoped KNN with B-site excess $K_4Nb_6O_{17}$ type secondary phase is present. With additions of low amounts of Cu, part of the secondary phase is transformed to $K_4CuNb_8O_{23}$. With increasing amount of Cu, the $K_4Nb_6O_{17}$ type secondary phase vanishes, while the secondary phase $K_4CuNb_8O_{23}$ remains. Essential condition for the formation of this phase is, however, that a sufficiently high niobium supply is present [56], because the stoichiometry of this phase requires twice as much niobium compared to the KNN with an alkaline to niobium ratio of 1:1. Therefore the B-site excess in the batch composition of the KNN-Cu ceramics may favor this type of secondary phase formation.

The formation of the secondary phase has a pronounced impact on densification behavior. The shrinkage onset temperatures decrease with increasing Cu content from 979°C for the undoped KNN to 923°C for KNN with 2 mol% Cu. The shrinkage maxima, which are at temperatures higher than 1100°C for the undoped and 0.25 mol% Cu doped B-site excess KNN, are shifted to 1020°C with the addition of 2 mol% Cu (Fig. 7.20). Densities of the KNN-Cu ceramics with different amounts of Cu and Nb-excess are shown in Fig. 7.21. Densities up to

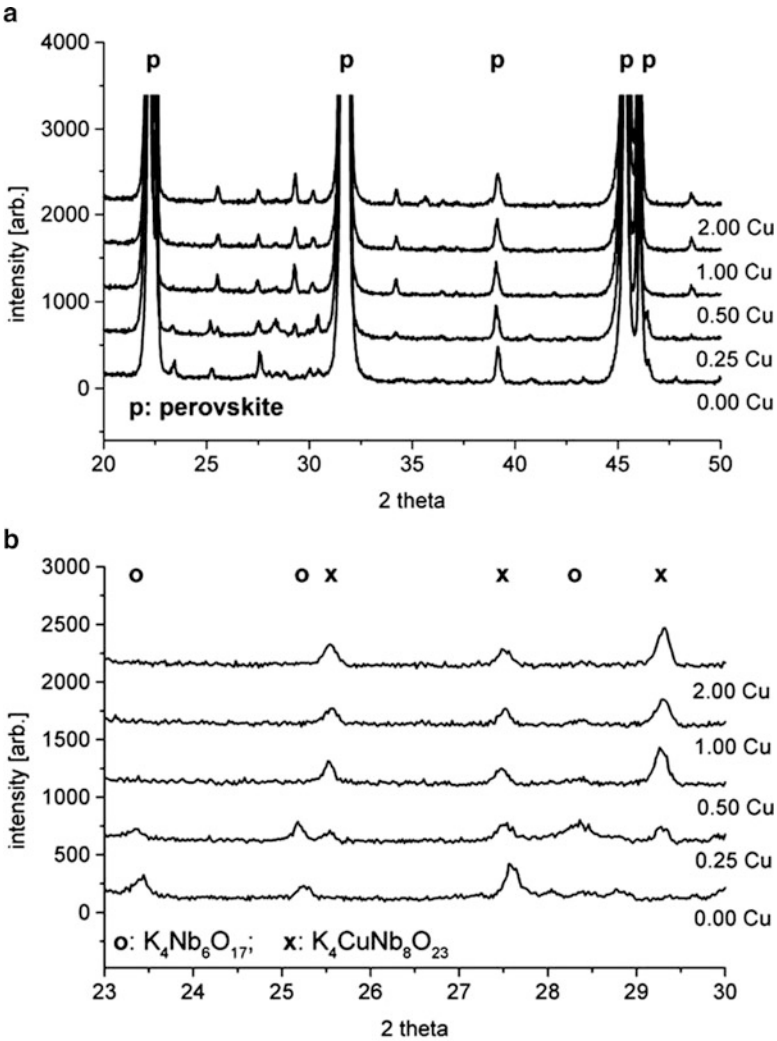

Fig. 7.19 X-ray diffraction patterns of the KNN *x*Cu ceramics. **(a)** Full patterns. **(b)** Detailed view of the secondary phase peaks

Table 7.2 Batch compositions of the KNN-*x*Cu materials with Cu dopant levels from 0.0 to 2.0 mol%

	Chemical Batch Composition
undoped KNN	$(K_{0.5}Na_{0.5})_{0.98}NbO_{2.99}$
KNN 0.25 mol% Cu	$(K_{0.5}Na_{0.5})_{0.9775}Cu_{0.0025}NbO_{2.99125}$
KNN 0.5 mol% Cu	$(K_{0.5}Na_{0.5})_{0.975}Cu_{0.005}NbO_{2.9925}$
KNN 1.0 mol% Cu	$(K_{0.5}Na_{0.5})_{0.97}Cu_{0.01}NbO_{2.995}$
KNN 2.0 mol% Cu	$(K_{0.5}Na_{0.5})_{0.96}Cu_{0.02}NbO_{3}$

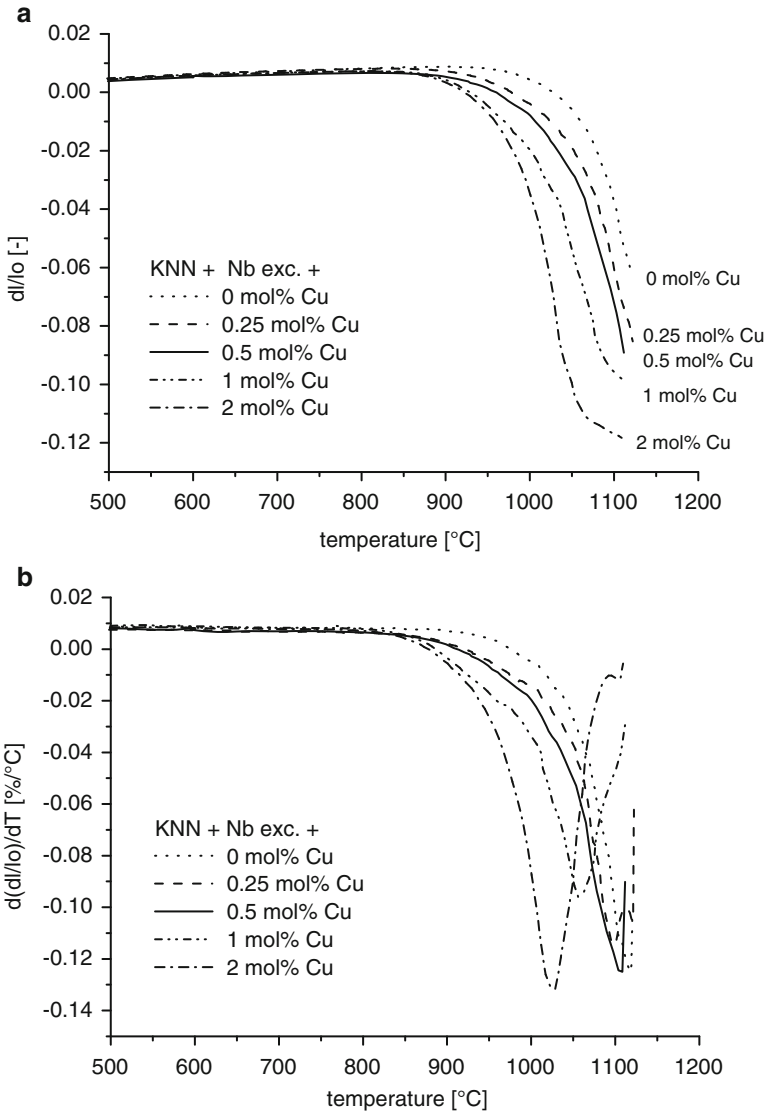

Fig. 7.20 Shrinkage behavior of KNN ceramics with niobium excess at various levels of Cu-dopant additions. (a) Linear shrinkage (dl/l_0). (b) Shrinkage rate $d(dl/l_0)/dT$

4.3 g/cm^3 can be reached already at 1030°C sintering temperature for KNN containing 2 mol% Cu, whereas for similar densities of the undoped KNN and KNN with 0.25 mol% Cu (both with B-site excess) sintering temperatures higher than 1100°C are required. When sintered at 1080°C/2 h grain size in these ceramics remains small and shows a slight increase with higher Cu-content.

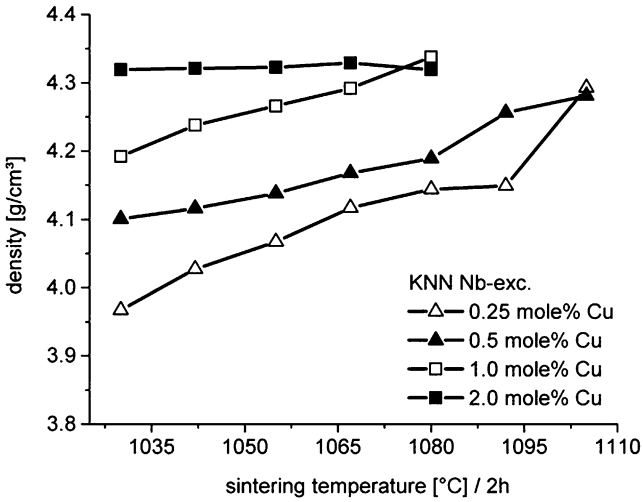

Fig. 7.21 Densities of the KNN ceramics doped with 0.25 – 2.0 mol% Cu for sintering temperatures between 1030 and 1100°C

Microstructure of Secondary Phases

The formation and microstructural development of the secondary phases may play an important role for the densification behavior of KNN. The shrinkage characteristics of the $K_4CuNb_8O_{23}$ and the $K_4Nb_6O_{17}$ secondary phases are shown in Fig. 7.22 in the form of dilatometric curves compared to the shrinkage behavior of undoped KNN with B-site excess. For significant shrinkage of B-site excess KNN temperatures as high as 1100°C are required. In contrast to that, both $K_4CuNb_8O_{23}$ and $K_4Nb_6O_{17}$ show maximum shrinkage rates already at approximately 1000°C. However, while in presence of $K_4CuNb_8O_{23}$ in the KNN ceramics the densification is markedly enhanced, the presence of the $K_4Nb_6O_{17}$ does not lead to a reduction in sintering temperature. There are three possible reasons for these differences. First, the volume fraction of $K_4Nb_6O_{17}$ present in undoped and low level Cu-doped B-site excess KNN might be less than the volume fractions of $K_4CuNb_8O_{23}$ in the B-site excess KNN doped with higher amounts of Cu. However, in the presence of the $K_4Nb_6O_{17}$ type phase along with high B-site excess in undoped KNN ceramics, the densification is rather reduced than promoted (Fig. 7.1). So the small amount of this secondary phase may not be the reason for the lack of effects on sintering. Second, the composition of the secondary phase of $K_4Nb_6O_{17}$ type might contain also sodium in solid solution. As shown in Fig. 7.22, for a sodium containing batch composition of $(K_{0.5}Na_{0.5})_4Nb_6O_{17}$ the shrinkage behavior is low. Although this may be in part due to the formation of other polynibate phase, less pronounced effects promoting the sintering may be expected, if the $(K,Na)_4Nb_6O_{17}$ solutions are formed. Third, the microstructure of the secondary phase may play an important role. In case the secondary phase is distributed in the form of isolated grains, at small volume fractions the impact on the sintering behavior

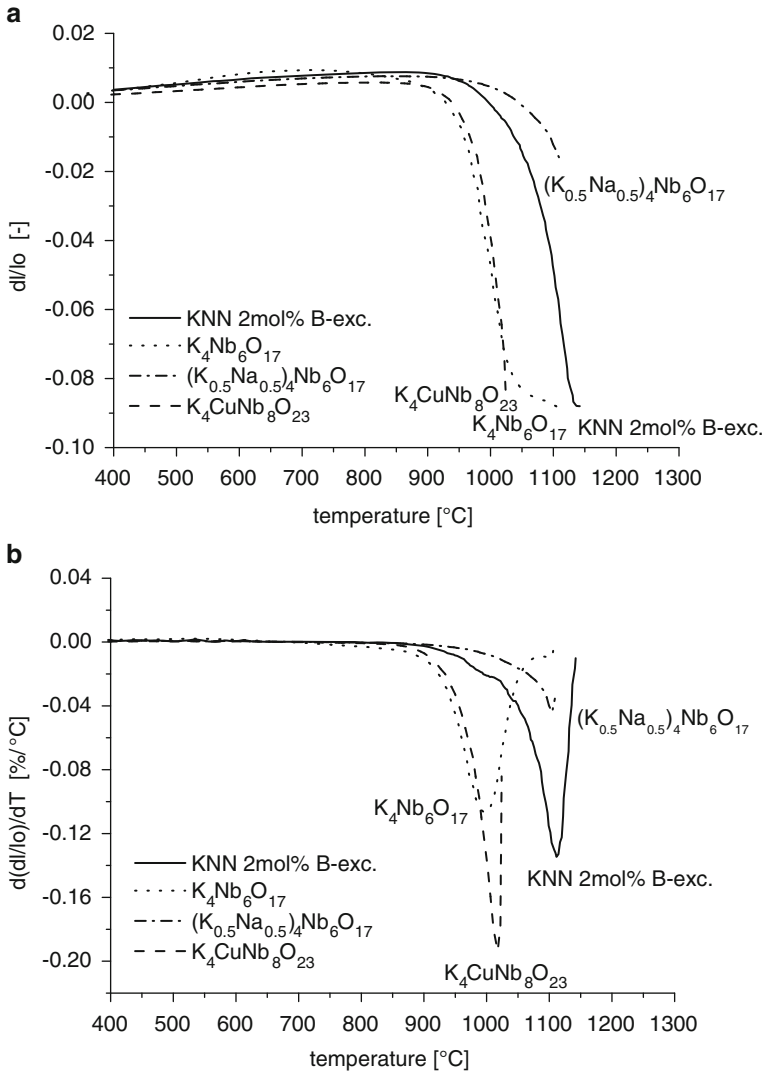

Fig. 7.22 Shrinkage behavior of KNN ceramics with niobium excess compared to the shrinkage behavior of pure secondary phase ceramics $K_4Nb_6O_{17}$, $K_4CuNb_8O_{23}$, and $(K,Na)_4Nb_6O_{17}$. (A) Linear shrinkage (dl/l_0). (b) Shrinkage rate $d(dl/l_0)/dT$

should be low. In contrast to that, if the secondary phase appears as a (probably wetting) grain boundary phase, pronounced effects on the sintering may occur.

Although the microstructures realized by $K_4Nb_6O_{17}$ and $K_4CuNb_8O_{23}$ when present in small amounts of secondary phase in a KNN-based material in general will be

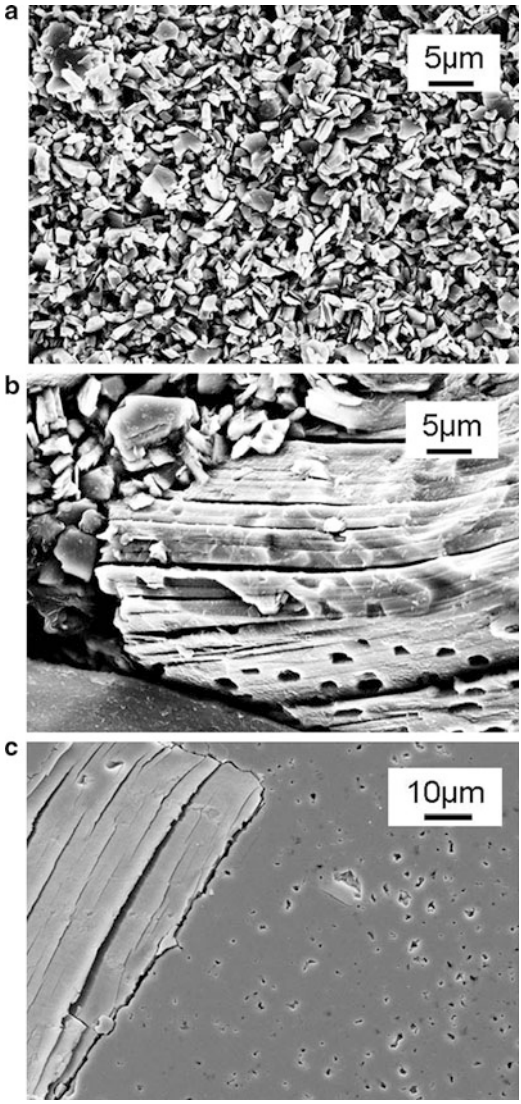

Fig. 7.23 Microstructure of $K_4Nb_6O_{17}$. (**a**) After sintering at 970°C. (b) After sintering at 1000°C/2 h. (**c**) $K_4Nb_6O_{17}$ cluster in a 0.25 mol% Cu 2 mol% B-site excess KNN ceramic matrix sintered at 1105°C

different from those present in the pure phases, investigations on $K_4Nb_6O_{17}$ and $K_4CuNb_8O_{23}$ ceramics may provide insights in the trends for microstructural characteristics of the secondary phases. In both secondary phase materials, the microstructures are subject to significant changes in the temperature range which is relevant for the sintering process for KNN ceramics (Fig. 7.23 and 7.24). Up to 970°C $K_4Nb_6O_{17}$ shows a homogeneous microstructure with grain size of 1 μm approximately (Fig. 7.23a). When increasing the temperature, large 50 μm sized clusters are of mica-like structures with the formation of layered arrangements [49, 59]

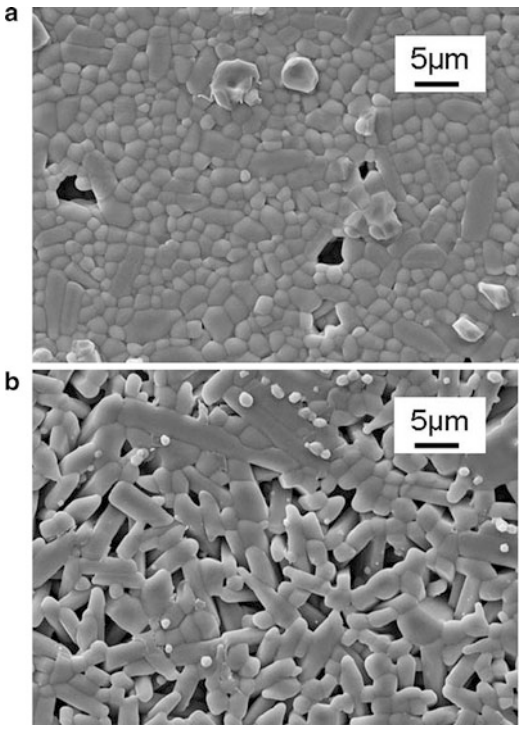

Fig. 7.24 Microstructure of $K_4CuNb_8O_{23}$ after sintering at (**a**) 1055°C/2 h and (**b**) 1105°C/2 h

(Fig. 7.23b) were detected. While this form of microstructure occurs already at 1000°C in the pure material, similar clusters consisting of the $K_4Nb_6O_{17}$ secondary phase in the 0.25 mol%Cu B-site excess KNN ceramics are found after sintering at 1105°C with extended dwell time only (Fig. 7.23c). The $K_4Nb_6O_{17}$ secondary phase is hygroscopic [25]. Therefore, the formation of large clusters may be detrimental to the mechanical stability of the ceramics, in particular in the presence of humidity. The $K_4CuNb_8O_{23}$ ceramics also exhibit changes in the microstrctural characteristics when changing the sintering temperature (Fig. 7.24). Sintering at 1055°C results in dense ceramics consisting of fine equiaxed grains with narrow grain sized distribution in the range of 1 μm (Fig. 7.24a). Similar microstructure was found in these ceramics up to 1080°C. When further increasing the temperatures, these ceramics become less dense and the shape of the grains turns to needle-like structures (Fig. 7.24b). The temperature range of this change in microstructure corresponds to the temperatures considered as the limiting temperatures, for which the $K_4CuNb_8O_{23}$ is considered to be an effective sintering additive [56]. It is not known, if or how the changes in microstructure affect the densification behavior of KNN-Cu ceramics containing $K_4CuNb_8O_{23}$ secondary phase. In the KNN ceramics with 0.5, 1.0, and 2.0 mol% Cu up to sintering temperatures of 1080°C no formation of needle-like structures has been found.

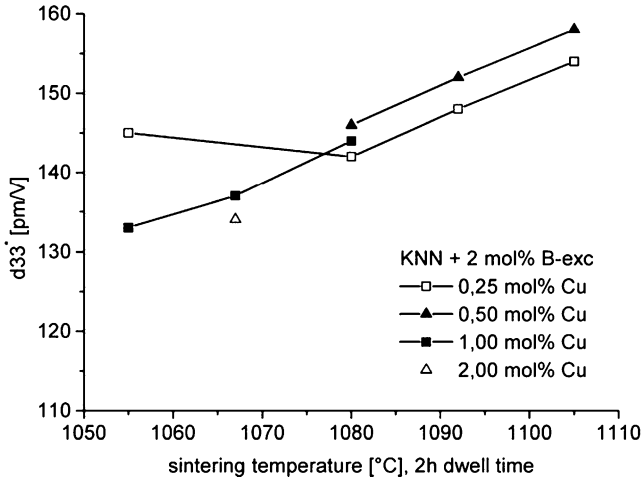

Fig. 7.25 Piezoelectric high-field strain coefficient d^*_{33} measured under fields of 3 kV/mm of the KNN *x*Cu ceramics, sintered for 2 h at various temperatures

Piezoelectric Properties

In undoped KNN piezoelectric strain coefficients between 70 and 125 pm/V [7, 12, 31, 61, 92] for pressureless sintered ceramics were reported. Enhanced piezoelectric strain was found for hot pressed ($d_{33} = 160$ pm/V) [31] or SPS ($d_{33} = 148$ pm/V) sintered [84] ceramics. For KNN with 0.5 mol% $K_4CuNb_8O_{23}$ sintering aid Matsubara et. al found high piezoelectric strain under high field conditions, corresponding to d^*_{33} of 180 pm/V [55]. Piezoelectric properties of undoped KNN with K/Na ratio 45/55 and the same materials with 0.5 mol% $K_4CuNb_8O_{23}$ were investigated by Lim et al. [47] by means of resonance measurements. They measured an increase in d_{33} from 95 pm/V to 110 pm/V and almost constant values for d_{15} ($d_{15} = 158$ pm/V and 162 pm/V) along with the $K_4CuNb_8O_{23}$ addition. Moreover they reported the temperature dependence of the d_{15}, showing an increase of the piezoelectric shear coefficient to approximately 200 pm/V at 160°C. When adding CuO to KNN, a decrease of the d_{33} by approximately 20 % from the undoped KNN to KNN with 1 mol% Cu was observed by Park et al. [61] and Lin et al. [48]. At higher Cu additions the d_{33} tends to stabilize. In KNN with the addition of 0.5–2.0 mol% Cu Ahn et al. [2] measured strain coefficients d_{33} of 100 pm/V, almost independent from the Cu content, by means of a d_{33}-meter. Similar trends for the changes in d_{33} with Cu content hold, if in addition to the CuO 1.5 mol% ZnO sintering aid is added to the KNN ceramics [63].

The influence of varying Cu-content in the KNN ceramics with Nb excess, sintered at temperatures between 1030 and 1100°C on the piezoelectric properties is reported in Fig. 7.25. It shows the high field strain coefficients d^*_{33}, measured at 3 kV/mm and 10 mHz frequency after poling by cycling to 5 kV/mm. In the KNN-Cu ceramics with niobium excess elevated strain is obtained in particular for the

ceramics with low Cu content when sintered at high temperatures. The $(K_{0.5}Na_{0.5})_{0.975}NbCu_{0.005}O_{2.9925}$ ceramics sintered at 1105°C show strain coefficients up to 160 pm/V. For lower sintering temperature, the d_{33}^{*} of the KNN doped with 0.25 and 0.5 mol% Cu decrease to 140 pm/V approximately. For Cu-dopant levels higher than 1 mol%, the strain coefficients are in the range of 135 pm/V.

The effects of the dipole formation, the formation of secondary phases and changes in the alkaline–mobium stoichiometry will play an important part in the effects on the piezoelectric properties of the KNN-Cu ceramics. However, other characteristics which influence the piezoelectric properties in ferroelectric ceramics, such as grain size effects [43, 64], differences in density [2], modification in the Na–K solid solution composition and shifts in the polymorphic phase transition temperature [3, 4, 88] have also to be taken into account.

7.4 Summary

Stoichiometry plays an important role for preparation, densification, and microstructure of KNN ceramics. Densification of stoichiometric undoped KNN occurs within a quite narrow temperature interval and high shrinkage rates. An excess of alkaline is lowering the temperature at which densification occurs whereas densification of the B-site excess compositions requires higher temperatures. Depending on A/B stoichiometry the microstructures show marked differences. In stoichiometric KNN the grains are large with polyhedral shapes and considerable intragranular porosity. KNN with A-site excess also shows large grains, but the grain shapes tend to plane grain boundaries and no internal porosity is present. KNN ceramics with B-site excess show much lower grain size. At low dopant levels, copper substitutes in the perovskite structure. The DFT calculations demonstrate that Cu dopants are likely to be incorporated on Nb sites in the KNN lattice if the samples are processed in air but could be driven toward the alkali sites in a reducing environment. If Cu ions substitute on Nb sites, they can form stable defect complexes with one or two neighboring oxygen vacancies. For stoichiometric KNN doped with 0.25 mol% Cu, two types of defect complexes were identified by EPR and attributed to $(Cu_{Nb}''' - V_O^{\bullet\bullet})'$ and $(V_O^{\bullet\bullet} - Cu_{Nb}''' - V_O^{\bullet\bullet})'$ defect associates. These defect complexes with single and double oxygen vacancies are mutually compensating with respect to the excess charges and show different interaction with the domain walls. When doping at low amounts of Cu, the characteristics in densification behavior and microstructure for the different stoichiometries are largely maintained. Analysis of shrinkage behavior and microstructure of KNN and KNN-Cu with different A/B stoichiometries also indicates that copper substitutes on the B-site. At higher dopant content and with the presence of alkaline or niobium excess, in addition to the changes in the defect structure, the properties of the KNN ceramics are influenced by the formation of secondary phases. Presence of B-site excess results in $K_4Nb_6O_{17}$ secondary phase formation in undoped KNN.

Along with Cu doping there is a trend to form $K_4CuNb_8O_{23}$ phase instead. So the impact of Cu doping of KNN on piezoelectric properties is on the one hand from its effects on amount and type of the lattice defect structure, on the other hand from the influence on the secondary phase formation.

Acknowledgments This work is funded by the German Science Foundation (DFG projects HO 1165/14-2, EI 498/1-2 and EL 155/21-2).

References

1. Acker J, Kungl H, Hoffmann MJ (2010) Influence of the alkaline- and niobium excess on sintering and microstructure of sodium-potassium niobate $(K_{0.5}Na_{0.5})NbO_3$. J Am Ceram Soc 93:1270–1281
2. Ahn CW, Karmarkar M, Viehland D, Kang DH, Bae KS, Priya S (2008) Low temperature sintering and piezoelectric properties of Cu-doped $K_{0.5}Na_{0.5}NbO_3$ ceramics. Ferroelectron Lett 35:55–72
3. Ahn CW, Park CS, Chang CH, Nahm S, Yoo MJ, Lee HG, Priya S (2009) Sintering behavior of lead free (K, Na)NbO3-based piezoelectric ceramics. J Am Ceram Soc 89:2033–2038
4. Ahn CW, Park CS, Priya S (2010) Sintered composites for low temperature coefficient of piezoelectric property in KNN-based lead free materials. Funct Mater Lett 3:35–39
5. Azough F, Wegrzyn M, Freer R, Sharma S, Hall D N. Setter, EPFL, Lausanne, Switzerland (2011) Microstructure and piezoelectric properties CuO added (K, Na, Li)NbO3 lead-free piezoceramics. J Eur Ceram Soc 31:569–576
6. Baker DW, Thomas PA, Zhang N, Glazer AM (2009) Structural study of $K_xNa_{1-x}NbO_3$ (KNN) for compositions in the range x=0.24-0.36. Acta Cryst B65
7. Birol H, Damjanovic D, Setter N (2006) Preparation and characterization of $(K_{0.5}Na_{0.5})NbO_3$ ceramic. J Eur Ceram Soc 26:861–866
8. Bomlai P, Wichianrat P, Muensit S, Milne SJ (2007) Effect of calcination conditions and excess alkali carbonate on the phase formation and particle morphology of $Na_{0.5}K_{0.5}NbO_3$ powders. J Am Ceram Soc 90:1650–1655
9. Boysen H (2007) Coherence effects in the scattering from domain walls. J Phys Condens Matter 88:275206
10. Bruce DA (1981) Scattering properties of ferroelectric domain walls. J Phys C Solid State Phys 14:5195–5214
11. Damjanovic D, Klein N, Li J, Porokhonskyy V (2010) What can be expected from lead-free piezoelectric materials? Funct Mater Lett 3:5–13
12. Demartin Maeder M, Damjanovic D (2002) Lead free ferroelectric materials. In: Setter N (ed) Piezoelectric materials in devices. Lausanne, pp 389–412
13. Demartin Maeder M, Damjanovic D, Setter N (2004) Lead free ferroelectric materials. J Electroceram 13:385–392
14. Egerton L, Dillon DM (1959) Piezoelectric and dielectric properties of ceramics in the system potassium-sodium niobate. J Am Ceram Soc 42:438–442
15. Eichel R-A (2008) Characterization of defect structure in acceptor-modified piezoelectric ceramics by multifrequency and multipulse electron paramagnetic resonance spectroscopy. J Am Ceram Soc 91:691701
16. Eichel R-A (2011) Structural and dynamic properties of oxygen vacancies in perovskite oxides – analysis of defect structure by modern multi-frequency and pulsed EPR techniques. Phys Chem Chem Phys 13:368–384
17. Eichel R-A, Erhart P, Träskelin P, Albe C, Kungl H, Hoffmann MJ (2008) Defect-dipole formation in copper-doped $PbTiO_3$ ferroelectrics. Phys Rev Lett 100:095504

18. Eichel R-A, Drahus MD, Jakes P, Erünal E, Erdem E, Parashar SKS, Kungl H, Hoffmann MJ (2009a) Defect structure and formation of defect complexes in Cu^{2+}-modified metal oxides derived from a spin-Hamiltonian parameter analysis. Mol Phys 107:1981–1986
19. Eichel R-A, Erünal E, Drahus MD, Smyth DM, van Tol J, Acker J, Kungl H, Hoffmann MJ (2009b) Local variations in defect polarization and covalent bonding in ferroelectric Cu^{2+}-doped PZT and KNN functional ceramics at the morphotropic phase boundary. Phys Chem Chem Phys 11:8698–8705
20. Erhart P, Eichel R-A, Träskelin P, Albe K (2007) Association of oxygen vacancies with impurity metal ions in lead titanate. Phys Rev B 76:174116
21. Erünal E, Eichel R-A, Körbel S, Elsässer C, Acker J, Kungl H, Hoffmann MJ (2010) Defect structure of copper doped potassium niobate ceramics. Funct Mater Lett 3:19–24
22. Feng Z, Ren X (2008) Striking similarity of ferroelectric aging effect in tetragonal, orthorhombic and rhombohedral crystal structures. Phys Rev B 77:134115
23. Fisher JG, Bencan A, Godnjavec J, Kosec M (2008) Growth behavior of potassium sodium niobate single crystals grown by solid-state crystal growth using $K_4CuNb_8O_{23}$ as a sintering aid. J Eur Ceram Soc 28:1657–1663
24. Flückiger U, Arend H, Oswald H (1975) Synthesis of $KNbO_3$ powder. J Am Ceram Soc 56:575–577
25. Gasperin M, Le Bihan M (1986) Mécanisme d'hydratation des niobates alcalins lamellaires de formule $A_4Nb_6O_{17}$ (A=K, Rb, Cs). J Solid State Chem 43:346–353
26. Hadley G (1962) Linear programming. Addison-Wesley, Reading
27. Hagh NM, Kerman K, Jadidian B, Safari A (2009) Dielectric and piezoelectric properties of Cu^{2+}-doped alkali niobates. J Eur Ceram Soc 29:2325–2332
28. Hewat AW (1973) Cubic-tetragonal-orthorhombic-rhombohedral ferroelectric transitions in perovskite potassium niobate: neutron powder profile refinement of the structure. J Phys C Solid State Phys 6:2559–2572
29. Hoffmann MJ, Kungl H, Theissmann R, Wagner S (2008) Microstructural analysis based on microscopy and x-ray diffraction. In: Heywang W, Lubitz K, Wersing W (eds) Piezoelectricity – evolution and future of a technology. Springer series in materials science 114. Springer, Berlin, pp 401–423
30. Hollenstein E (2007) Preparation and properties of $KNbO_3$ based piezoceramics. PhD Thesis, EPFL Lausanne
31. Jaeger RE, Egerton L (1962) Hot pressing of potassium-sodium niobates. J Am Ceram Soc 42:209–213
32. Jaffe B, Cook WR, Jaffe H (1971) Piezoelectric ceramics. Academic, Marietta
33. Jenko D, Malic B, Bernard JB, Cilensek J, Kosec M (2003) Synthesis and sintering of KNN 50/50 ceramics. Mater Technol 37:22–28
34. Jenko D, Bencan A, Malic B, Holc J, Kosec M (2005) Electron microscopy studies of potassium-sodium niobate ceramics. Microsc Microanal 11:572–580
35. Jin YM, Wang YU, Khachaturian AG, Li JF, Viehland D (2003a) Conformal miniaturization of domains with low domain wall energy: monoclinic ferroelectric states near the morphotropic phase boundary. Phys Rev Lett 91:197601
36. Jin YM, Wang YU, Khachaturian AG, Li JF, Viehland D (2003b) Adaptive ferroelectric states in systems with low domain wall energy: tetragonal microdomains. J Appl Phys 94:3629–3640
37. Jin L, He Z, Damjanovic D (2009) Nanodomains in Fe^{3+}-doped lead zirconate titanate ceramics at the morphotropic phase boundary do not correlate with high properties. Appl Phys Lett 95:012905
38. Körbel S, Elsässer C (2011) Cu substitutionals and defect complexes in the lead-free ferroelectric KNN. In: Nagel WE et al (eds) High performance computing in science and engineering, 10. Springer, Heidelberg, p 181
39. Körbel S, Marton P, Elsässer C (2010) Formation ofvacancies and copper substitutionals in potassium sodium niobate under various processing conditions. Phys Rev B 81:174115

40. Kosec M, Kolnar D (1975) On activated sintering and electrical properties of $NaKNbO_3$. Mater Res Bull 10:335–340
41. Kosec M, Malic B, Bencan A, Rojas T (2008) KNN-based piezoelectric ceramics. In: Safari A, Akdogan EK (eds) Piezoelectric and acoustic materials for transducer applications. Springer Science and Business Media, New York, pp 81–102
42. Kosec M, Malic B, Golob AB, Rojac T, Tellier J (2010) Alkaline niobate based piezoceramics: crystal structure, synthesis, sintering and microstructure. Funct Mater Lett 3:15–18
43. Kungl H, Hoffmann MJ (2010) Effects of sintering temperature on microstructure and high field strain of niobium-strontium doped morphotropic lead zirconate titanate. J Appl Phys 107:054111
44. Li E, Kakemoto H, Wada S, Tsurumi T (2007) Influence of CuO on the structure and piezoelectric properties of alkaline-niobate based lead-free ceramics. J Am Ceram Soc 90:1787–1791
45. Li E, Kakemoto H, Hoshina T, Tsurumi T (2008a) A shear-mode ultrasonic motor using potassium-sodium niobate based ceramics with high mechanical quality factor. Jpn J Appl Phys 47:7702–7706
46. Li E, Sasaki R, Hoshina T, Takeda H, Tsurumi T (2008) Miniature ultrasonic motor using shear mode of potassium-sodium niobate based lead-free piezoelectric ceramics. Jpn J Appl Phys 48:09KD11
47. Lim JB, Zhang S, Lee HJ, Jeon JH, Shrout TR (2010) (K, Na)NbO3-based ceramics for piezoelectric "hard" lead-free materials. J Am Ceram Soc 93:1218–1220
48. Lin D, Kwok KW, Chan HL (2008) Piezoelectric and ferroelectric properties of Cu-doped $K_{0.5}Na_{0.5}NbO_3$ lead-free ceramics. J Phys D Appl Phys 41:045401
49. Lundberg M, Sundberg M (1986) Studies in the $KNbO_3$-Nb_2O_5 system by high resolution electron microscopy and x-ray powder diffraction. J Solid State Chem 63:216–230
50. Malic B, Jenko D, Bernard JB, Cilensek J, Kosec M (2003) Synthesis and sintering of (K,Na) NbO_3-based ceramics. In: Alario-Franco MA, Greenblatt M, Rohrer G, Whittingham MS (eds) Solid state chemistry of inorganic materials, IV. Materials Research Society, Warrendale, pp 755, 83–88
51. Malic B, Bernard J, Holc J, Jenko D, Kosec M (2005) Alkaline-earth doping in (K, Na)NbO3 based piezoceramics. J Eur Ceram Soc 25:2707–2711
52. Malic B, Jenko D, Holc J, Hrovat M, Kosec M (2008a) Synthesis of sodium potassium niobate: a diffusion couples study. J Am Ceram Soc 91:1916–1922
53. Malic B, Bernard J, Bencan A, Kosec M (2008b) Influence of zirconia addition on the microstructure of $(K_{0.5}Na_{0.5})NbO_3$ ceramics. J Eur Ceram Soc 28:1191–1196
54. Marton P, Elsässer C (2011) Switching of a substitutional-iron/oxygen-vacancy defect complex in ferroelectric $PbTiO_3$ from first principles. Phys Rev B 83:020106(R)
55. Matsubara M, Yamaguchi T, Kikuta K, Hirano S (2004) Sinterability and piezoelectric properties of (K, Na)NbO3 ceramics with novel sintering aid. Jpn J Appl Phys 43:7159–7163
56. Matsubara M, Yamaguchi T, Sakamoto WT, Kikuta K, Yogo T, Hirano S (2005a) Pro-cessing and piezoelectric properties of (K, Na)(Nb, Ta)O3 ceramics. J Am Ceram Soc 88:1190–1196
57. Matsubara M, Yamaguchi T, Kikuta K, Hirano S (2005) Synthesis and characterization of $(K_{0.5}Na_{0.5})(Nb_{0.7}Ta_{0.3})O_3$ piezoelectric ceramics sintered with sintering aid $K_{5.4}Cu_{1.3}Ta_{10}O_{29}$. Jpn J Appl Phys 44:6618–6623
58. Matsubara M, Yamaguchi T, Kikuta K, Hirano S (2005) Piezoelectric properties of $(K_{0.5}Na_{0.5})(Nb_{1-x}Ta_x)O_3$-$K_{5.4}Cu_{1.3}Ta_{10}O_{29}$ ceramics. J Appl Phys 97:114105
59. Nassau K, Shiever JW, Bernstein JL (1969) Crystal growth and properties of mica-like potassium niobates. J Electrochem Soc 116:348–353
60. Nowick AS, Berry BS (1972) Anelastic relaxation in crystalline solids. Academic, New York
61. Park HY, Choi JY, Choi MK, Cho KH, Nahm S (2008a) Effect of CuO on the sintering temperature and piezoelectric properties of $K_{0.5}Na_{0.5}NbO_3$ lead-free piezoelectric ceramics. J Am Ceram Soc 91:2374–2377

62. Park HY, Seo IT, Choi MK, Nahm S, Lee HG, Kang HW, Choi BH (2008b) Microstructure and piezoelectric properties of the CuO added $(Na_{0.5}K_{0.5})(Nb_{0.97}Sb_{0.03})O_3$ lead-free piezoceramics. J Appl Phys 104:034103
63. Park HY, Seo IT, Choi JH, Nahm S, Lee HG (2010) Low temperature sintering and piezoelectric properties of lead free piezoelectric ceramics. J Am Ceram Soc 93:36–39
64. Randall CA, Kim N, Kucera J, Cao W, Shrout TR (1998) Intrinsic and extrinsic size effects in fine grained morphotropic phase boundary lead zirconate titanate ceramics. J Am Ceram Soc 81:677
65. Reisman A, Holtzberg F (1955) Phase equilibria in the system K_2CO_3-Nb_2O_5 by the method of differential thermal analysis. J Am Chem Soc 116:2115–2119
66. Ren X (2004) Large electric-field-induced strain in ferroelectric crystals by point-defect-mediated reversible domain switching. Nat Mater 3:91
67. Reuter K, Scheffler M (2001) Composition, structure, and stability of RuO_2(110) as a function of oxygen pressure. Phys Rev B 65:35406
68. Robels U, Arlt G (1993) Domain wall clamping in ferroelectrics by orientation of defects. J Appl Phys 73:3454–3460
69. Saito Y, Takao H (2006) High performance lead-free piezoelectric ceramics in the (K, Na) NbO3-LiTaO3 solid solution system. Ferroelectronics 338:17–32
70. Saito Y, Takao H, Tani T, Nonoyama T, Takatori K, Homma T, Nagaya T, Nakamura M (2004) Lead-free piezoceramics. Nature 432:84–87
71. Schmitt LA, Schönau KA, Theissmann R, Fuess H, Kungl H, Hoffmann MJ (2007) Composition dependence of the domain configuration and size in PZT ceramics. J Appl Phys 101:074107
72. Schönau KA, Schmitt LA, Knapp M, Fuess H, Eichel R-A, Kungl H, Hoffmann MJ (2007) Nanodomain structures of Pb(Zr, Ti)O3 at its morphotropic phase boundary: investigations from local to average structure. Phys Rev B 75:184117
73. Shafer MW, Roy R (1959) Phase equilibria in the system $NaNbO_3$-Nb_2O_5. J Am Ceram Soc 42:482–485
74. Shigemi A, Wada T (2004) Enthalpy of formation of various phases and formation energy of point defects in pervskite $NaNbO_3$ by first principles calculation. Jpn J Appl Phys 43:6793–6798
75. Shigemi A, Wada T (2005) Evaluation of phases and vacancy formation energy in $KNbO_3$ by first principles calculations. Jpn J Appl Phys 44:8048–8054
76. Stannek W (1968) Characterization of sintering phenomena of $(Na_{0.5}K_{0.5})NbO_3$. Master Thesis, University of California, Berkeley
77. Takao H, Saito Y, Aoki Y, Horibuchi K (2006) Microstructural evolution of crystalline oriented piezoelectric ceramics with a sintering aid of CuO. J Am Ceram Soc 89:1951–1956
78. Tellier J, Malic B, Dkhil B, Jenko D, Cilensek J, Kosec M (2009) Crystal structure and phase transitions of sodium potassium niobate perovskites. Solid State Sci 11:320–324
79. Van de Walle C, Neugebauer J (2004) First-principles calculations for defects and impurities: applications to III-nitrides. J Appl Phys 95:3851
80. Wang U (2006) Diffraction theory of nanotwin superlattices with low symmetry phase. Phys Rev B 74:104109
81. Wang K, Zhang BP, Li JF, Zhang LM (2008) Lead-free $Na_{0.5}K_{0.5}NbO_3$ piezoelectric ceramics fabricated by spark plasma sitnering: annealing effect on electrical properties. J Electroceram 21:251–254
82. Wang J, Damjanovic D (2007) Compositional inhomogeneity in Li and Ta modified (K, Na) NbO_3 ceramics. J Am Ceram Soc 90:3485–3489
83. Wang R, Xie R, Sekiya T, Shimojo Y (2004) Fabrication and characterization of potassium-sodium niobate piezoelectric ceramics by spark-plasma sintering method. Mater Res Bull 39:1709–1715

84. Wang K, Zhang BP, Li JF, Zhang LM (2008) Lead-free $Na_{0.5}K_{0.5}NbO_3$ piezoelectric ceramics fabricated by spark plasma sintering: annealing effect on electrical properties. J Electroceram 21:251–254
85. Zhang SB (2002) The microscopic origin of the doping limits in semiconductors and wide-gap materials and recent developments in overcoming these limits: a review. J Phys Condens Matter 14:R881–R903
86. Zhang L, Ren X (2005) In-situ observation of reversible domain switching in aged Mn-doped $BaTiO_3$ single crystals: implication for unified microscopic explanation of ferroelectric Aging. Phys Rev B 71:174108
87. Zhang BP, Li JF, Wang K, Zhang H (2006) Compositional dependence of piezoelectric properties in $Na_xK_{1-x}NbO_3$ lead-free ceramics prepares spark-plasma sintering. J Am Ceram Soc 89:1605–1609
88. Zhang S, Xia R, Shrout TR (2007) Lead free piezoelectric ceramics vs. PZT. J Electroceram 19:251–257
89. Zhang L, Erdem E, Ren X, Eichel R-A (2008) Reorientation of $(Mn^{T'i}-V^{\bullet\bullet}O)\times$ defect dipoles in acceptor-modified $BaTiO_3$ single crystals: an electron paramagnetic resonance study. Appl Phys Lett 93:202901
90. Zhen Y, Li JF (2006) Normal sintering of (K, Na)NbO_3-based ceramics: influence of sintering temperature on densification, microstructure and electrical properties. J Am Ceram Soc 89:3669–3675
91. Zhen Y, Li JF (2007) Abnormal grain growth and new core-shell structure in (K, Na)NbO3-based lead free piezoelectric ceramics. J Am Ceram Soc 90:3496–3502
92. Zuo R, Rödel R, Chen R, Li L (2006) Sintering and electrical properties of lead-free $Na_{0.5}K_{0.5}NbO_3$ piezoelectric ceramics. J Am Ceram Soc 89:2010–2015
93. Zuo R, Ye C, Fang X, Yue Z, Li L (2008) Processing and piezoelectric properties of $(Na_{0.5}K_{0.5})_{0.96}Li_{0.04}(Ta_{0.1}Nb_{0.9})_{1-x}Cu_xO_{3-3x/2}$. J Am Ceram Soc 91:914–917

Part III
Sodium Bismuth Titanate-Based Ceramics

Chapter 8
Sodium Bismuth Titanate-Based Ceramics

Tadashi Takenaka and Hajime Nagata

8.1 Introduction

Piezoelectric materials play an important role for electronic devices such as actuators, accelerators, piezoelectric motors, transducers, filters and resonators, and microelectromechanical systems (MEMS). The most widely used piezoelectric materials are $PbZrO_3$-$PbTiO_3$ (PZT)-based multicomponent systems (PZT system) [1–4] because of their excellent piezoelectric properties. However, it is recently desired to use lead-free materials for environmental protection during the waste disposal of products. For example, legislation has been enforced in the EU as the draft directives on Waste from Electrical and Electronic Equipment (WEEE) since January 1, 2004, Restriction of Hazardous Substances (RoHS) since July 1, 2006, and end-of-life vehicles (ELV) since July 1, 2003. Therefore, lead-free piezoelectric materials have been attracting attention worldwide [5–8] as new materials in place of PZT-based piezoelectric ceramics.

Lead-free piezoelectric materials, such as piezoelectric single crystals, e.g. langasite [9], and ferroelectric ceramics with a perovskite structure [10–45], a tungsten bronze structure [46, 47], and bismuth layer-structured ferroelectrics (BLSF) [48–53], have been extensively reported for mainly the past 20 years. However, no lead-free materials display more excellent piezoelectric properties than those of PZT-based systems. To replace PZT-based systems, it is necessary that the required piezoelectric properties for various applications are classified and developed for each application. For example, the perovskite-type ceramics seem to be suitable for actuator and high-power applications. On the other hand, BLSF ceramics seem to be candidate materials for ceramic resonator applications. Recently, various perovskite-structured

T. Takenaka (✉) • H. Nagata
Faculty of Science and Technology, Tokyo University of Science,
2641 Yamazaki, Noda, Chiba 278-8510, Japan
e-mail: tadashi@ee.noda.tus.ac.jp

S. Priya and S. Nahm (eds.), *Lead-Free Piezoelectrics*,
DOI 10.1007/978-1-4419-9598-8_8, © Springer Science+Business Media, LLC 2012

ferroelectrics such as $BaTiO_3$ [BT], $(Bi_{1/2}Na_{1/2})TiO_3$ [BNT], $(Bi_{1/2}K_{1/2})TiO_3$ [BKT], $KNbO_3$ [KN], $(K,Na)NbO_3$ [KNN], and their solid solutions have been actively studied [10–45] as candidates for lead-free piezoelectric ceramics. These ceramics have been widely studied and are expected for actuator and high-power applications because of their relatively large piezoelectric constants, d, among many lead-free piezoelectrics. However, there are some problems such as low Curie temperatures, T_c, low depolarization temperatures, T_d, difficulties in poling treatments and/or low relative density ratios because of lower sinterabilities.

In this chapter, the dielectric, ferroelectric, and piezoelectric properties including phase transitions of typical lead-free bismuth perovskite ferroelectric ceramics such as bismuth sodium titanate, BNT, and some BNT-based solid solutions, as compared with bismuth potassium titanate, $(Bi_{1/2}K_{1/2})TiO_3$ [BKT] and BKT-based systems describe from a viewpoint of piezoelectric actuator and high-power applications.

8.2 $(Bi_{1/2}Na_{1/2})TiO_3$ [BNT] [14, 15, 18, 37, 54–56]

Bismuth sodium titanate, BNT, is a perovskite-structured ferroelectric with rhombohedral symmetry ($R3C$) at room temperature (RT) and their phase transitions are complicated. The phase transition temperatures, T_{R-T}, from rhombohedral to tetragonal (the temperature T_m of the maximum dielectric constant), and T_{T-C}, from tetragonal to cubic (Curie temperature, T_C), are approximately 340 and 540°C on heating, respectively, for BNT single crystals.

The BNT ceramic shows the strong ferroelectric properties of a large remanent polarization, $P_r = 38$ μC/cm^2, and relatively high piezoelectric properties compared with other lead-free piezoelectric ceramics. Therefore, the BNT is considered to be an excellent candidate as a key material of lead-free piezoelectric ceramics. However, data on piezoelectric properties of the BNT ceramic are scarce because it is difficult to pole this ceramic due to a large coercive field, E_c (=73 kV/cm) except in specialized work [37]. In the recent 2 decades, BNT-based solid solutions [17, 19–32] and A-site substituted BNT [57–59] that can be poled easily were recently extensively studied.

In the previous reports, the electromechanical coupling factor, k_{33}, of the BNT ceramic was investigated as the end-member of solid solutions. However, the k_{33} values are varied such as $k_{33} = 0.25$–0.40. On the other hand, the BNT ceramic needs a high sintering temperature of more than 1,200°C to obtain a dense body. It is thought that the vaporization of Bi ions occurred during the sintering process at temperatures higher than 1,200°C, resulting in the poor poling treatments because of the low resistivities. From the thermograph (TG, weight loss) measurement, the weight loss caused by the Bi vaporization was carried out at over 1,130°C. Various processes and methods are thought to prevent the Bi vaporization and to obtain the stoichiometric BNT ceramic. Thus, the BNT ceramic should be sintered at 1,100°C and lower.

Two approaches were attempted to sinter the BNT ceramic with the higher density and the higher resistivity as follows [37]: (1) the addition of Bi_2O_3 to the BNT ceramic (BNT + Bi_2O_3 x wt.% [BNT-x]) sintered at 1,225°C for 5 min to 10 h to compensate for the insufficiency of Bi ions and (2) the low sintering temperature process with a long soaking time of 30–100 h in the ordinary firing method and the hot-pressing (HP) method to suppress the Bi vaporization. Furthermore, the dielectric and piezoelectric properties of BNT-x and HP-BNT ceramics were investigated, focusing on estimating the true piezoelectric properties of the BNT ceramic.

The excess Bi_2O_3-add bismuth sodium titanate, BNT, ceramics (BNT + Bi_2O_3 x wt.% [BNT-x]) including no excess Bi_2O_3 (BNT-0) ($x = 0$–2.0) were sintered at 1,225°C for 5 min to 10 h to compensate for the insufficiency of Bi ions. The measured density ratio to the theoretical density as a function of the sintering temperature on the BNT-0 ceramic becomes higher as the sintering temperature increases. The highest density ratio of 98.0% was obtained at 1,225°C for 2 h. At temperatures higher than 1,225°C, the specimen was partially melted. From this result, the optimum sintering temperature was determined to be 1,225°C so as to obtain the highest relative density. The weight loss profile on the BNT-0 ceramic from the measurement of the TG analysis shows the weight loss occurring at temperatures higher than approximately 1,130°C. Therefore, when BNT samples were sintered at 1,225°C, it is assumed that some components evaporated into the air during the sintering process. It is thought that the evaporated component is mainly Bi ions. Therefore, the BNT ceramic sintered at 1,225°C is the Bi-poor composition as compared to the stoichiometric one. From these results, it is believed that the Bi_2O_3 addition and low sintering processes are effective for making the stoichiometric BNT ceramic.

X-ray diffraction patterns for BNT-x [$x = 0$, 0.1, 0.2, 0.3, 0.4, 0.5, 1.0 and 2.0] sintered at 1,225°C show a single phase of a perovskite structure with a rhombohedral symmetry. Lattice parameters, a, of BNT-x ceramics are almost constant ($a = 3.87$ Å). The colors of the BNT-0 and BNT-0.3, -0.5 ceramics are white and those of BNT-1.0 and -2.0 ceramics become yellow with increasing the amount (x) of Bi_2O_3 content. This result indicates that BNT-1.0 and -2.0 ceramics have too excess Bi ions. It is very easy to get the dense ceramics with high density ratios of higher than 95% on BNT-x ceramics. SEM micrographs of BNT-0, -0.3, and -0.5 ceramics show that the grain size of BNT-0 sintered at 1,225°C is extremely large of about 20–50 μm and grains become smaller as increasing the amount of Bi_2O_3 content. The grain sizes of BNT-0.3, -0.5, -1.0, and -2.0 become rapidly smaller (about 1–5 μm) than that of the BNT-0 ceramic. It is assumed that excess Bi ions impede the grain growth and exist on the grain boundaries and triple points for the BNT-0.3, 0.5, 1.0, and 2.0 ceramics.

The temperature, T_m, of maximum dielectric constant measured at 1 MHz of BNT-x ceramics becomes higher with increasing the amount (x) of Bi_2O_3 content and shows the tendency to saturate around the BNT-1.0 and 2.0. According to our previous report [27], it is considered that excess Bi ions occupied the A-site of the perovskite structure on the BNT ceramic up to the amount of 0.5. From the saturation tendency of T_m, a portion of the excess Bi ions for BNT-1.0 and 2.0

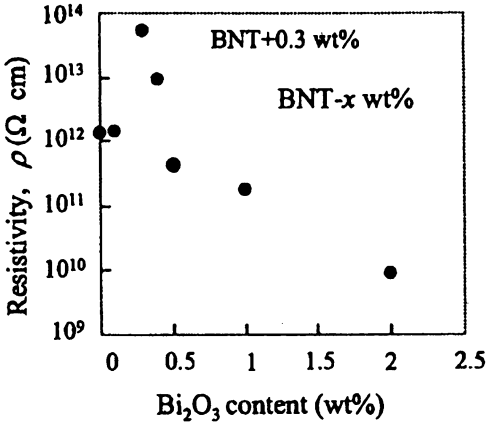

Fig. 8.1 Resistivity, ρ, of BNT-x ceramics as a function of excess Bi_2O_3 content (x) [37]

could not be substituted on the A-site and existed on other places such as grain boundaries and/or triple points. This speculation is consistent with experimental observations of the microstructures and the sample colors.

Figure 8.1 shows the resistivity, ρ, of BNT-x as a function of excess Bi_2O_3 content (x). The ρ shows the largest value of about 10^{14} Ω cm at $x = 0.3$. It is clear that the ρ is improved by adding the excess Bi_2O_3 and the optimum charge neutrality was observed for the BNT-0.3. Therefore, the BNT-0.3 seems to be a stoichiometric neutral state of the BNT.

From the TG measurement, it was clear that the Bi ions were vaporized at above 1,130°C. To suppress the Bi vaporization, it is necessary to prepare the BNT ceramic at below 1,100°C. The density ratio of the ordinarily fired BNT ceramic sintered at 1,100°C for 2 h was 87% whose value is too low to pole sufficiently this ceramic. Two approaches under the low sintering temperature were tried to increase the density. The first one is to keep the longer soaking time at the low temperature during the ordinary sintering process, and the other one is to utilize the HP method to prepare the BNT ceramic with high density. The relative density ratio of the BNT-0 with no excess Bi_2O_3 increases with the increase of the soaking time in the ordinary firing process at 1,100°C. The highest density ratio of 96% was obtained at 100 h. On the other hand, densities of the hot-pressed BNT-0 (HP-BNT-0) ceramics under some conditions were higher than that of non-hot pressed ones. The HP-BNT-0 ceramic pressed at 200 kg/cm^2 under 1,100°C for 30 min showed a highest density ratio of more than 98%, and might be expected to have excellent piezoelectric properties.

Figure 8.2 shows the frequency characteristics of the impedance, Z, for BNT-0 and HP-BNT-0 ceramics both with clear resonance and anti-resonance profiles. The k_{33} of the BNT-0 sintered at 1,100°C for 100 h and the HP-BNT-0 by the HP method at 1,100°C for 30 min were 0.44 and 0.48, respectively.

Table 8.1 summarizes the dielectric and piezoelectric properties of BNT-0.3 and HP-BNT-0 ceramics. The BNT ceramic is superior as a key material for some lead-free piezoelectric applications because of the relatively high electromechanical coupling factor, k_{33}, and the relatively high piezoelectric strain constant, d_{33}.

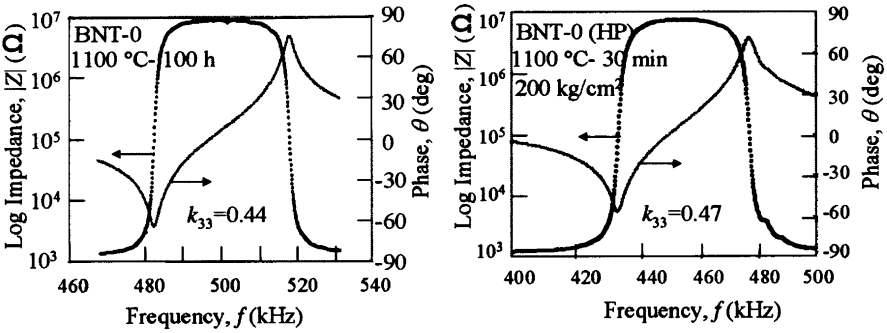

Fig. 8.2 Frequency characteristics of the impedance, Z, for BNT-0 and HP-BNT-0 ceramics [37]

Table 8.1 Dielectric and piezoelectric properties of BNT-0.3 and HP-BNT-0 ceramics [37]

	BNT-0.3 1,225°C for 30 min	BNT-(HP) 1,100°C for 30 min
Curie temperature, T_c (°C)	337	–
Density, ρ_0 (g/cm^3)	5.91	5.96
Dielectric constant, $\varepsilon_{33}^T/\varepsilon_0$	406	422
Coupling factor, k_{33}	0.47	0.48
Mechanical quality factor, Q_m	85	80
Elastic constant, s_{33}^E (pm^2/N)	10.5	10.0
Piezoelectric constant, d_{33} (pC/N)	92	93

The d_{33} was calculated from k_{33}, ε_{33}^T, and s_{33}^E using the (8.1), where ε_{33}^T is the free permittivity and s_{33}^E the elastic compliance constant.

$$d_{33} = k_{33}\sqrt{\varepsilon_{33}^T \cdot s_{33}^E}. \tag{8.1}$$

The k_{33} and the d_{33} of the BNT-0.3 sintered at 1,225°C for 30 min and the HP-BNT-0 by hot-pressed at 1,100°C for 30 min were 0.47 and 92 pC/N; and 0.48 and 93 pC/N, respectively.

The important feature is that the BNT forms an MPB with the other perovskites having a tetragonal symmetry, such as $PbTiO_3$ [PT], $BaTiO_3$ [BT], and $(Bi_{1/2}K_{1/2})TiO_3$ [BKT], and these MPB compositions show excellent piezoelectric properties [22, 31, 33, 39, 41, 42, 60, 61]. Therefore, BNT-based solid solutions have attracted considerable attention as lead-free piezoelectric materials because of the MPBs. Also the easy preparation of the dense BNT-based ceramics is an advantage for manufacture.

However, the BNT presents low depolarization temperature T_d of 185°C, and the MPBs of BNT-based solid solutions show a particularly low T_d of approximately

100°C [39, 41, 42, 62], even though the MPBs have excellent piezoelectric properties. For example, while BNT-BKT-BT system shows a high electromechanical coupling factor, k_{33}, of 0.56 and a high piezoelectric constant, d_{33}, of 181 pC/N at the MPB, the T_d is as low as 113°C [39]. Piezoelectricities disappear at the T_d and higher temperatures and the piezoelectric working temperature range is limited to below the T_d. Therefore, it is important to increase the T_d of the MPB composition to enable its practical use in piezoelectric applications. In order to increase the T_d, it is important to clarify the behavior of the phase transition temperatures, such as T_d, T_{R-T}, and T_C of BNT-based solid solutions. The T_d is thought to be the phase transition temperature from ferroelectric to antiferroelectric [17]; however, the nature of this phase transition is not yet clear until now. Similarly, it is not obvious whether the T_m is a phase transition temperature or not. The ferroelectric properties of the intermediate phase between T_d and T_{R-T} and that at the temperatures higher than T_{R-T} also have not yet been clarified due to the high conductivities at those higher temperatures. Although the detailed studies on the phase transition temperatures have been carried out for BNT single crystals, there are very few studies on the phase transition temperatures of BNT-based solid solutions, because of their low tetragonality ($c/a < 1.002$) at the tetragonal region.

The tetragonal side of the MPB is mainly studied for lead-free piezoelectric actuators owing to its high d_{33} and high T_d. On the other hand, the rhombohedral side of the MPB has received little attention owing to its low T_d and low d_{33} in spite of having the feature of a relatively high Q_m. Recently, we have investigated the variation in phase transition temperatures, such as T_d, rhombohedral-tetragonal phase transition temperature T_{R-T}, and the maximum dielectric temperature T_m, of a BNT-based solid solution to increase the T_d of BNT. As a result, we have clarified that the substitution of small amounts of Li^{1+} and K^{1+} in the A-site of BNT is possible for increasing the T_d to 199 and 209°C, respectively. Moreover, in order to co-substitute Li^{1+} and K^{1+} into the A-site of BNT, T_d can be increased to 221°C at the rhombohedral composition.

Although there have been many studies on the dielectric and piezoelectric properties in the past, very few studies have been reported on the phase transition temperatures of BNT-based solid solutions. For example, most reports on BNT-based solid solutions have regarded the T_m as the T_C, because the dielectric constant is maximum there. Moreover, in the past, the T_{R-T} has not been reported because of the small tetragonality c/a of 1.002. In the case of the T_d, a few studies have demonstrated accurate measurement [39, 42, 61]. In a previous study, we demonstrated how to easily determine the phase transition temperatures of BNT-based solid solutions, and the behaviors of T_d, T_{R-T}, and dielectric maximum temperature T_m of BNT-based solid solutions were clarified [41, 45]. As above, it was realized that the variation in the T_d is strongly dependent on the T_{R-T} near the MPB. Moreover, we investigated the behavior of phase transition temperatures of divalent (Ca, Sr, Ba) and trivalent (La, Nd, Ho, Yb)-ions-substituted BNT-solid solutions, and exhibited the relationship between ionic radius and phase transition temperatures [45, 59].

8.3 $(Bi_{1/2}Na_{1/2})TiO_3 - (Bi_{1/2}K_{1/2})TiO_3 - BaTiO_3$ [BNT-BKT-BT]

Bismuth sodium titanate, BNT, bismuth potassium titanate, $(Bi_{1/2}K_{1/2})TiO_3$ [BKT], and barium titanate, $BaTiO_3$ [BT] are well-known lead-free piezoelectric materials with perovskite structures. Two solid solution systems, that is, $(1 - x)$BNT–xBT (BNBT100x) and $(1 - y)$BNT–yBKT (BNKT100y) have already been reported by Takenaka et al. [22] and Sasaki et al. [31], respectively. It is reported that the MPB existed at $x = 0.06$–0.07 for BNBT100x and $y = 0.16$–0.20 for BNKT100y, respectively. Then, the dielectric and piezoelectric properties of the three-component system, $a(Bi_{1/2}Na_{1/2})TiO_3$–$b(Bi_{1/2}K_{1/2})TiO_3$–$cBaTiO_3$ (BNBK), were investigated [33, 35, 39, 40], focusing on the MPB compositions.

Figure 8.3 shows the phase relation of the BNBK system around the MPB area. The MPBs of both BNBT6 and BNKT16 exist on the rhombohedral side, and the MPBs of both BNBT7 and BNKT20 exist on the tetragonal side around the MPB region, respectively. Prepared compositions are expressed as follows:

$$a\,(\text{BNBT6}) - (1 - a)(\text{BNKT16})\ [\text{BNBK1-}a],\ \text{and}\ a(\text{BNBT7}) - (1 - a)\ (\text{BNKT20})\ [\text{BNBK2-}a],$$

where $a = 0$, 0.2, 0.4, 0.6, 0.8, and 1, for each system.

It was found by X-ray diffraction that the MPB between the rhombohedral and tetragonal phases exists between the two systems of BNBK1 and BNBK2. Figure 8.4 shows the compositional dependence of the piezoelectric constant, d_{33}, for BNBK1 and BNBK2 ceramics. All of the d_{33} values of BNBK2 are higher than those of BNBK1. The d_{33} value showed the maximum value, $d_{33} = 191$ pC/N, at the BNBK2-0.4 which is the tetragonal region around the MPB composition. It is thought that the BNBK2-0.4 (0.852BNT-0.12BKT-0.028BT) ceramic seems to be one of the candidate materials for lead-free actuator applications with a relatively large d_{33}.

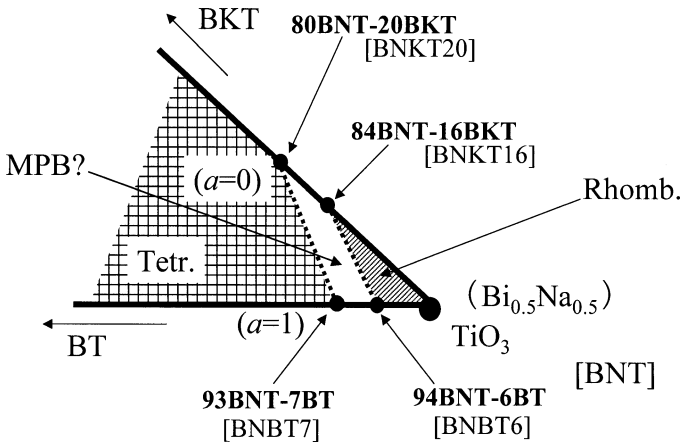

Fig. 8.3 Phase relation of the $(Bi_{1/2}Na_{1/2})TiO_3$ (BNT)–$(Bi_{1/2}K_{1/2})TiO_3$ (BKT)–$BaTiO_3$ (BT) system around the MPBs

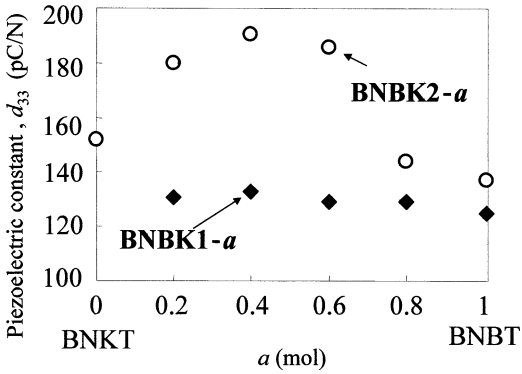

Fig. 8.4 Piezoelectric constant, d_{33}, of BNBK1 and BNBK2 as a function of the amount (a) of BNBT-6 for BNBK1 and BNBT-7 for BNBK2

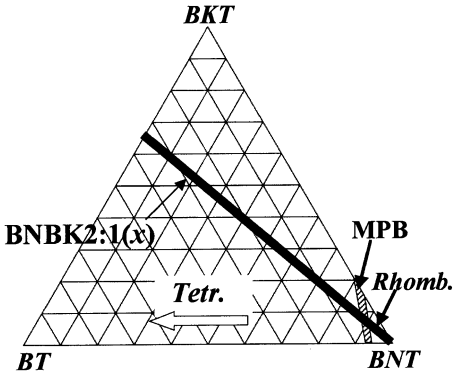

Fig. 8.5 Phase relationship of ternary system between $(Bi_{1/2}Na_{1/2})TiO_3$ (BNT), $(Bi_{1/2}K_{1/2})TiO_3$ (BKT), and $BaTiO_3$ (BT). The *bold solid line* was investigated here as follows: $x(Bi_{1/2}Na_{1/2})TiO_3$-$y(Bi_{1/2}K_{1/2})TiO_3$-$zBaTiO_3$($x + y + z = 1$, y:z = 2:1) [BNBK2:1(x)]

Figure 8.5 also shows the phase relationship between BNT, BT, and BKT. This system has an MPB between rhombohedral (BNT) and tetragonal (BKT and BT) phases, respectively. The three-component solid solution system between BNT, BKT, and BT is expressed by $x(Bi_{1/2}Na_{1/2})TiO_3$-$y(Bi_{1/2}K_{1/2})TiO_3$-$zBaTiO_3$, [$x + y + z = 1$, y:z = 2:1, abbreviated to BNBK2:1(x)]. In this case, compositions near the MPB were mainly investigated. The sintering temperatures shifted to lower temperatures and the sintering temperature range gradually became narrower with increasing ratio of BKT content, owing to the relatively low sintering temperature (<1,060°C) of BKT. Figure 8.6 shows the X-ray diffraction patterns and density ratios of BNBK2:1(x) [x = 0.86–0.92]. The patterns for BNBK2:1 (0.3–0.98) show a single phase of the perovskite structure with rhombohedral, tetragonal or complex rhombohedral, and tetragonal symmetries, where MPB exists in BNBK2:1

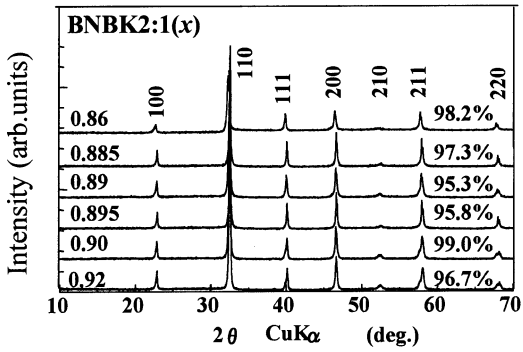

Fig. 8.6 X-ray diffraction patterns and density ratios of the ternary system, $x(Bi_{1/2}Na_{1/2})TiO_3$-$y(Bi_{1/2}K_{1/2})TiO_3$-$zBaTiO_3$ ($x + y + z = 1$, y:z = 2:1) [BNBK2:1(x)]

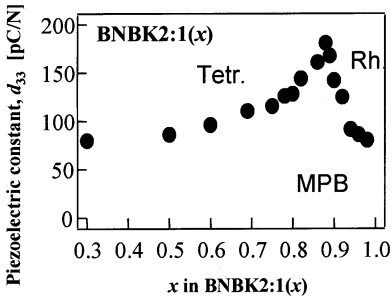

Fig. 8.7 Compositional dependence of the piezoelectric constant, d_{33}, for BNBK2:1(x) as a function of the BNT content (x)

(0.89–0.90). The ceramic measured density ratios were found to be higher than 95% of the theoretical densities and were easily obtained in the BNBK2:1 (0.3–0.98) system.

The compositional dependences of the piezoelectric coefficients, d_{33}, for BNBK2:1(x), as a function of the content (x) of BNT, are shown in Fig. 8.7. High d_{33} values were obtained near the MPB composition being highest just on the tetragonal side. A maximum d_{33} value of 181 pC/N was obtained in BNBK2:1 (0.88). On the tetragonal side, the d_{33} decreased because both the k_{33} and the free permittivity, ε_{33}^{T}, decreased. The d_{33} values of BNBK2:1(0.98) and BNBK2:1(0.30) were found to be 80.3 and 79.9 pC/N, respectively.

It is important for BNT-based solid solutions to investigate the actual working temperature for use in practical applications. For that reason, the depolarization temperature, T_d, was accurately determined from the temperature dependence of piezoelectric properties [39–41]. The temperature dependences of k_{33} are shown in Fig. 8.8 for (a) the rhombohedral side of $x = 0.92$–0.98, (b) the MPB composition of $x = 0.88$–0.90, and (c) the tetragonal side of $x = 0.30$–0.84 in BNBK2:1(x). It is recognized that the rhombohedral and tetragonal sides exhibit more stable k_{33} values with temperature than that for compositions around the MPB. The T_d and the temperature, T_m, with the maximum dielectric constant in the temperature dependence of BNBK2:1(x) are summarized in Fig. 8.9. The T_m was determined by the temperature of the maximum ε_r in the temperature dependence of dielectric

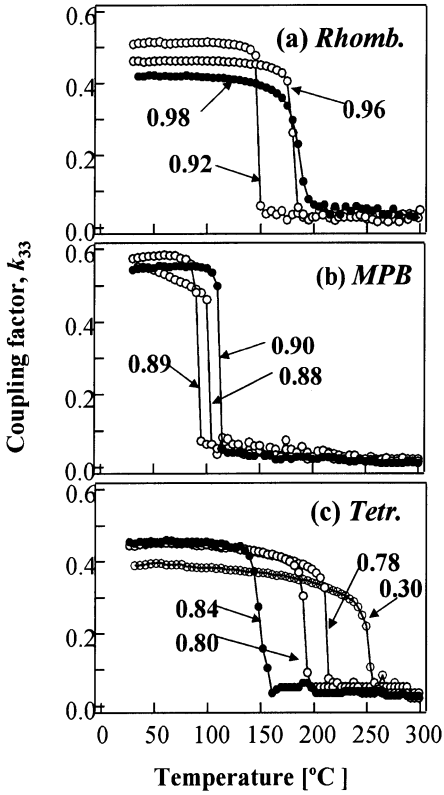

Fig. 8.8 Temperature dependence of electromechanical coupling factor, k_{33}, of (**a**) rhombohedral side of $x = 0.92$–0.98, (**b**) MPB composition of $x = 0.88$–0.90, and (**c**) tetragonal side of $x = 0.30$–0.84 in BNBK2:1(x)

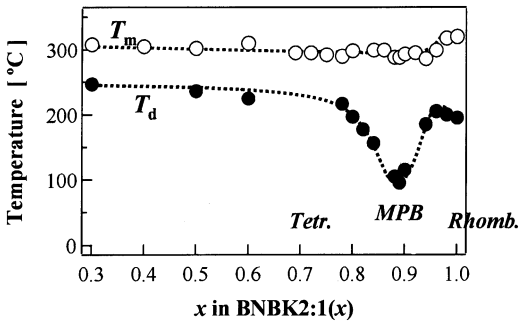

Fig. 8.9 The depolarization temperature, T_d and the T_m, determined by the maximum dielectric constant, ε_r, from the measurement of temperature dependence of ε_r

constant, ε_r. The T_m of BNBK2:1(x) was approximately the same at 300°C; however, T_d was largely decreasing near the MPB composition. T_d increased with decreasing BNT content (x). It is thought that these results indicate that T_d is dependent on lattice anisotropy (tetragonality), c/a. Figure 8.10 demonstrates the relationship between the T_d and the d_{33} of the tetragonal and rhombohedral sides. It is necessary for actual applications to obtain the value in the right upper corner

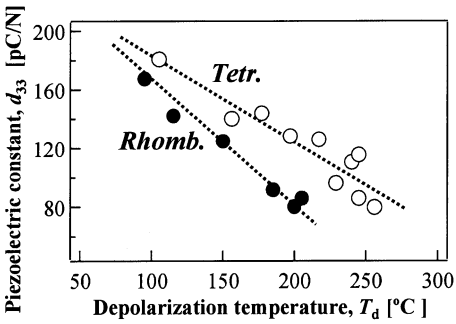

Fig. 8.10 The relationship between the T_d and the d_{33} of the tetragonal side (Tetr.) and the rhombohedral side (Rhomb.)

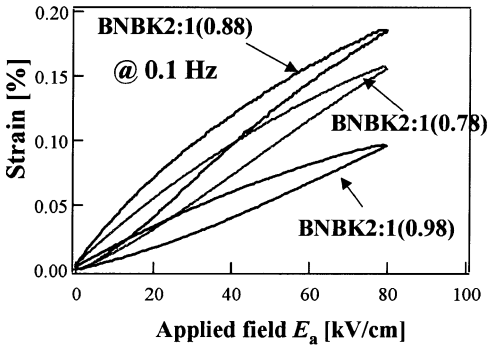

Fig. 8.11 Strain of BNBK2:1 (0.88), BNBK2:1(0.78), and BNBK2:1(0.98) as a function of the applied electric field, E_a

(high d_{33} and high T_d) of this figure. However, d_{33} and T_d indicated a trade-off relationship. The d_{33} as a function of T_d on the tetragonal side is higher than that on the rhombohedral side.

Figure 8.11 [8] shows the strain of BNBK2:1(0.88), BNBK2:1(0.78), and BNBK2:1(0.98) as a function of the applied electric field, E_a, measured at 0.1 Hz. The magnitudes of their strains, S, are S (MPB) $>$ S (tetragonal) $>$ S (rhombohedral) for their compositions. Table 8.2 [8] summarizes the piezoelectric properties of BNBK2:1(x) ($x = 0.78$, 0.88, and 0.98) obtained from the results shown in Fig. 8.11. The normalized strain, d^*_{33}, which corresponds to piezoelectric constant of inverse piezoelectric effects, is defined as (8.2), where S is the maximum strain and E_a is the maximum applied electric field. For example, d^*_{33} is 188 pm/V with relatively high T_d (206°C) in the tetragonal composition ($x = 0.78$).

$$d^*_{33}\ (\text{pm/V}) = \frac{\text{Strain}, S}{E_a\ (\text{kV/mm})} \times 10^6. \tag{8.2}$$

Finally, Table 8.3 [8] summarizes the depolarization temperature, T_d, and piezoelectric properties of rhombohedral, MPB, and tetragonal compositions of the BNBK2:1(x) ternary system.

Table 8.2 Piezoelectric properties of BNBK2:1(x) ($x = 0.78$, 0.88, and 0.98)

x in BNBK2:1(x)		T_d (°C)	k_{33}	d_{33} (pC/N)	d^*_{33}(pm/V) at $E_a = 80$ kV/cm	Strain (%) at 80 kV/cm
0.98	Rhombohedral	200	0.42	80	121	0.097
0.88	MPB	113	0.56	181	240	0.183
0.78	Tetragonal	206	0.45	126	188	0.150

Table 8.3 The depolarization temperature, T_d, and piezoelectric properties of rhombohedral, MPB and tetragonal compositions of BNBK2:1(x) ternary system

	Rhombohedral		MPB		Tetragonal			
Comp. (x)	0.94	0.90	0.89	0.88	0.84	0.82	0.80	0.78
T_d (°C)	185	115	95	113	144	169	182	206
ε_s	844	1,668	1,698	1,786	1,617	1,627	1,058	879
$\varepsilon^T_{33}/\varepsilon_0$	493	756	778	999	1,118	1,081	993	883
$\varepsilon^T_{11}/\varepsilon_0$	652	900	1,010	–	–	1,078	–	–
k_{33}	0.476	0.543	0.579	0.560	0.455	0.473	0.455	0.452
k_{31}	0.153	0.207	0.222	0.217	0.094	0.098	0.097	0.100
k_t	0.443	0.499	0.510	0.501	0.474	0.445	0.450	0.417
k_p	0.253	0.340	0.361	0.319	0.156	0.159	0.170	0.162
k_{15}	0.330	0.449	0.459	–	–	0.316	–	–
d_{33}	91.6	142	168	181	140	144	128	126
d_{31} (pC/N)	−28.5	−48.0	−54.3	−59.2	−27.7	−28.2	−26.8	−26.3
d_{15}	109	184	212	–	–	139	–	–

8.4 $(Bi_{1/2}Na_{1/2})TiO_3$ – $SrTiO_3$ [BNT-ST] [63]

$(1 - x)(Bi_{1/2}Na_{1/2})TiO_3$-$xSrTiO_3$ (abbreviated to BNST100x) ceramics were first reported by Sakata and Masuda [17]. They exhibited the phase diagram of BNST100x obtained from the temperature dependence of dielectric properties; however, the variations of T_d and $T_{R–T}$ have not been clarified yet.

Recently, we investigated the variation of the phase transition temperatures of divalent (Ca, Sr, Ba) and trivalent (La, Nd, Ho, Yb) ions substituted into the A-site of BNT [45, 59]. This result indicated that T_d and/or $T_{R–T}$ for BNST100x shift to RT at approximately $x = 0.26$. Detailed studies on the variation of phase transition temperatures and electrical properties around T_d and/or $T_{R–T}$ for BNST100x have been carried out because BNST100x is thought to be a suitable composition for clarifying the electrical behavior around T_d and/or $T_{R–T}$.

The ratios of the measured densities to the theoretical densities of BNST100x ($x = 0$–0.4) were all higher than 96%, and these ceramics showed a single-phase perovskite structure. X-ray powder diffraction patterns revealed that the crystal structure of BNST100x was rhombohedral ($R3C$) in the x range of 0–0.26. The rhombohedral distortion 90°-α gradually decreased with increasing x, and the crystal structure at $x \geq 0.28$ was pseudocubic.

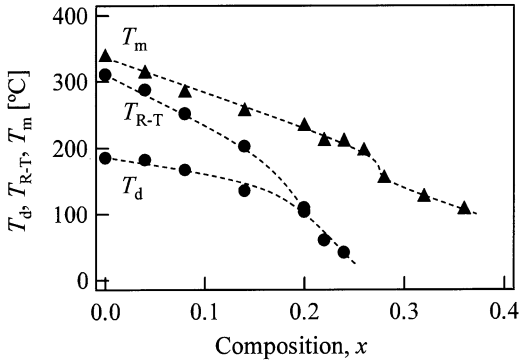

Fig. 8.12 Depolarization temperature, T_d, rhombohedral-tetragonal phase transition temperature T_{R-T}, and the temperature T_m resulting in the maximum dielectric constant for BNST100x

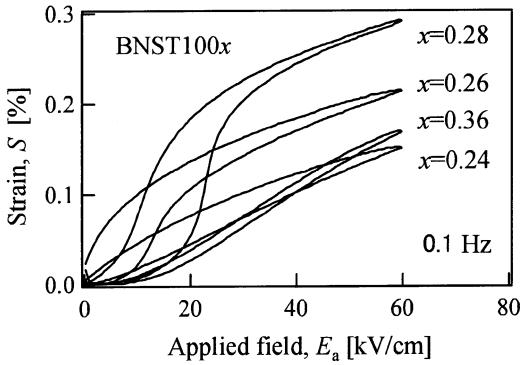

Fig. 8.13 Field-induced strain for BNST100 measured at 0.1 Hz

From temperature dependences of the dielectric properties for poled and unpoled BNST ceramics, it is possible to determine the depolarization temperature T_d, the rhombohedral-tetragonal phase transition T_{R-T}, and the temperature giving the maximum dielectric constant T_m, as discussed in ref. [41]. The phase transition temperatures of BNST100x are summarized in Fig. 8.12. It was found that T_{R-T} decreases rapidly and is equal to T_d at approximately $x = 0.20$. In BNT-BT, BNT-BKT, and BNT-BKT-BT (BNBK) systems, the MPB of rhombohedral ferroelectric and tetragonal ferroelectric phases formed to decrease T_{R-T} [41, 62]. Similarly, the MPB of BNST100x was formed at approximately $x = 0.26$ accompanied by a decrease in T_{R-T}. However, it was not possible to pole at $x > 0.26$, because of the reduction of T_d with T_{R-T}. The phase diagram of BNST100x indicates that the phase for $x > 0.28$ is tetragonal at RT. However, no split of (200) peak was observed in the X-ray diffraction pattern at $x > 0.28$. This is because the tetragonality c/a of the tetragonal phases of BNT is very small ($c/a < 1.002$). Thus, the lattice anisotropy at $x > 0.28$ was undetectable using our X-ray diffractometer.

Field-induced strains were measured using a contact type displacement sensor (Millitron; Model 1240) at 0.1 Hz. Figure 8.13 shows the S–E curves of BNST100x

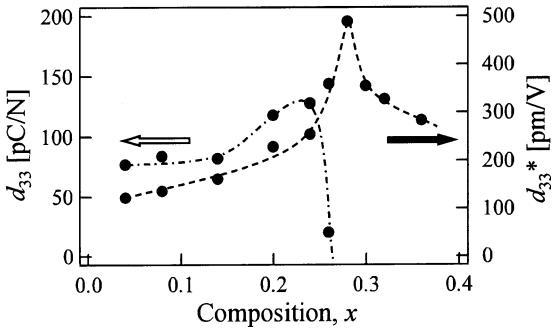

Fig. 8.14 Piezoelectric constant, d_{33} and normalized strain, d^*_{33} for BNST100x

at 60 kV/cm under unipolar driving. Figure 8.14 summarizes the piezoelectric strain constant, d_{33}, and the normalized strain, $d^*_{33} = (S_{max}/E_{max})$, calculated by using (8.2) from Fig. 8.13. The d_{33} gradually increased with increasing x when $x \leq 0.24$ because ε^T_{33} gradually increased due to decreases in T_d and T_{R-T}. Although the maximum d_{33} value of 127 pC/N was obtained at $x = 0.24$, this decreased markedly to 19.7 pC/N at $x = 0.26$, and no piezoelectric response was obtained at $x > 0.26$. Meanwhile, the strain, S, rapidly increased at $x = 0.26$–0.28 for BNST100x. In particular, BNST28 showed a very large strain ($S = 0.29\%$) and the d^*_{33} (=488 pm/V), respectively. Typical piezoelectric S–E curves were obtained at $x \leq 0.24$, and BNST36 showed nonlinear strain with a small hysteresis loop as shown in Fig. 8.13. On the other hand, the S–E curves of BNST28 and BNST30 displayed nonlinear strain with large hysteresis loops. A BNBK ternary system forms an MPB of rhombohedral ferroelectric and tetragonal ferroelectric, and the highest d_{33} of 189 pC/N was obtained at the MPB composition. However, the strain and the d^*_{33} of the MPB composition for the BNBK system [39] were almost half those of BNST28 ($S = 0.14\%$ and $d^*_{33} = 230$ pm/V at 60 kV/cm). On the other hand, BNST100x forms an MPB of rhombohedral ferroelectric and pseudocubic (tetragonal) paraelectric, resulting in the MPB of BNST100x exhibiting no piezoelectric properties. Thus, it is considered that very large strain and the d^*_{33} of the MPB composition of BNST100x are associated with the field-induced phase transition of T_{R-T} and the rotation of the 180° and non-180° domains in the field-induced rhombohedral phase.

From observations of the D–E hysteresis loops of BNST20, -28, -32, and -36 at RT, BNST20 showed a typical ferroelectric hysteresis loop and BNST28 a loop slightly resembling a double hysteresis loop. On the other hand, BNST32 and BNST36 showed hysteresis loops with very small remanent polarizations, P_r, and coercive fields, E_c. The ferroelectric properties of the tetragonal phase of BNT have not been clarified because of the high conductivity due to the high measuring temperature (>300°C). As shown in Fig. 8.12, the phases of BNST32 and BNST36 at RT can be regarded as being the same as the tetragonal phase of BNT, though the X-ray diffraction pattern shows that BNST32 and BNST36 are pseudocubic at RT. In addition, the temperature dependence of dielectric constants for BNST32 and BNST36 displayed a strong frequency dispersion similar to that of relaxor-type ferroelectrics. Therefore, the small hysteresis loops in the intermediate phase between T_{R-T} and T_m can be explained by the micropolar region, resulting in there being no piezoelectric properties in this phase.

8.5 $(Bi_{1/2}Na_{1/2})TiO_3 - (Bi_{1/2}Li_{1/2})TiO_3 - (Bi_{1/2}K_{1/2})TiO_3$ [BNT-BLT-BKT] [43, 67]

To clarify the details of the behavior of phase transition temperatures, and the relationship between phase transition temperatures and electrical properties, the phase transition temperatures and electrical properties of BNT solid solutions substituted by monovalent (Li^+ and K^+) ions were investigated in detail. Two solid solutions, $(1 - x)(Bi_{1/2}Na_{1/2})TiO_3$–$x(Bi_{1/2}K_{1/2})TiO_3$ (abbreviated to BNKT100x) and $(1 - x)(Bi_{1/2}Na_{1/2})TiO_3$–$x(Bi_{1/2}Li_{1/2})TiO_3$ (abbreviated to BNLT100x) ceramics were prepared by the conventional ceramic fabrication process [64]. The ratios of the measured to the theoretical densities of sintered ceramics were all higher than 96%, and the resistivities were all higher than 10^{12} Ω cm. X-ray powder diffraction patterns of BNKT100x and BNLT100x ($x = 0$–0.24) indicated a single phase of perovskite structure. However, a few secondary phases were observed for BNLT28. Therefore, the solubility of Li (x) in the A-site of BNLT100x was limited to 0–0.24 at atmospheric pressure because of its small ionic radius. The lattice constants a and c, rhombohedrality 90°-α and tetragonality c/a of BNKT100x show an MPB between rhombohedral and tetragonal phases at $x = 0.18$–0.2. The 90°-α of BNKT100x was the highest at $x = 0.1$, and then decreased with increasing x. In addition, the tetragonality c/a increased with x at $x > 0.20$.

Figure 8.15 shows the temperature dependences of dielectric constant ε_s and loss tangent tan δ for unpoled and poled BNKT100x at 10 kHz. Phase transition temperatures, T_d, T_{R-T}, and T_m, are summarized in Fig. 8.16.

The T_m of BNT was about 340°C, which is nearly the same as in other reports. The T_m of BNKT100x decreased to 280°C with increasing x, and then was approximately constant at $x = 0.10$–0.30. Although the ε_{max} of BNT was about 3,500 at 10 kHz, the ε_{max} reached up to 8,000 near the MPB ($x = 0.2$; Fig. 8.15e). There are few reports on T_{R-T} of BNT-based solid solutions [23], because it is difficult to determine T_{R-T} from X-ray diffraction patterns. The T_{R-T} of BNKT100x in Fig. 8.16 was determined by comparing the poled and unpoled dielectric properties, as shown in Fig. 8.15 [41]. Siny et al. report that the anomaly peak of dielectric constant is due to T_{R-T} [65]; however, our results indicate that the behavior of T_m is independent of that of T_{R-T}.

The T_d of BNKT100x was determined from the peak of tan δ, as shown in Fig. 8.15 [41]. In addition, the temperature dependences of piezoelectric properties in 33-mode were measured to demonstrate the accuracy of the T_d measured from the peak of tan δ. The peaks of tan δ for BNKT100x were well coincident with the T_d determined from the temperature dependences of piezoelectric properties. The variation in T_d as a function of x for BNKT100x is also summarized in Fig. 8.16. When the trivalent lanthanoid ions (La, Nd, Ho, Yb) were substituted to the A-site of BNT, the T_m increased and the T_d decreased with decreasing ionic radius [28]. This result indicates that the substitution of large ions, such as Ba^{2+} (1.61 Å) and K^{1+} (1.64 Å), to the A-site of BNT is important to increase T_d at the rhombohedral composition. In BNKT100x, it can be seen that the T_d increases to 209°C for BNKT8

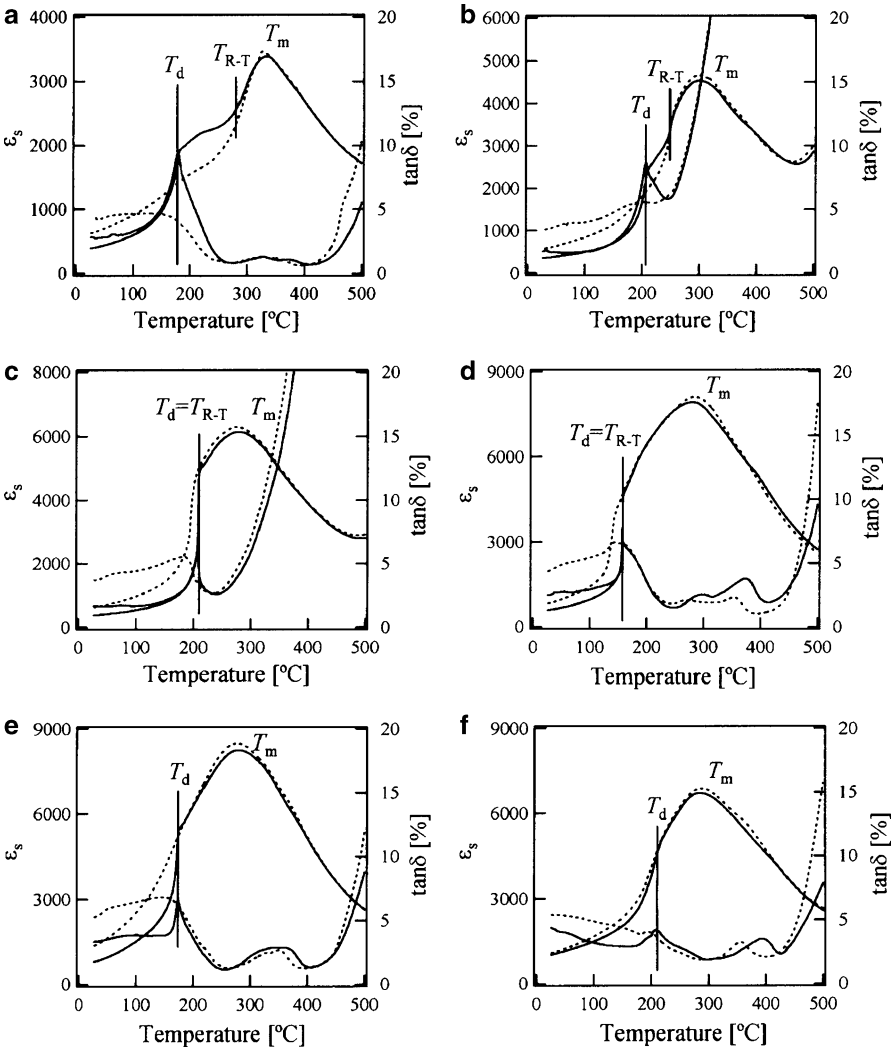

Fig. 8.15 Temperature dependences of poled and unpoled dielectric constants ε_s and loss tangents tan δ for BNKT100x ((**a**) $x = 0.02$, (**b**) $x = 0.06$, (**c**) $x = 0.10$ (**d**) $x = 0.16$ (**e**) $x = 0.20$, and (**f**) $x = 0.30$)

and then decreases with the increasing amount of BKT (x) because it was affected by the behavior of the T_{R-T} near the MPB [41]. The lowest T_d of 130°C was obtained for BNKT18, and the T_d then increased with increasing x for BNKT100x. The behavior of the T_d is still not well understood. However, it is realized that the variation in the T_d is related to the magnitude of the lattice anisotropy, such as the rhombohedrality 90°-α and the tetragonality c/a.

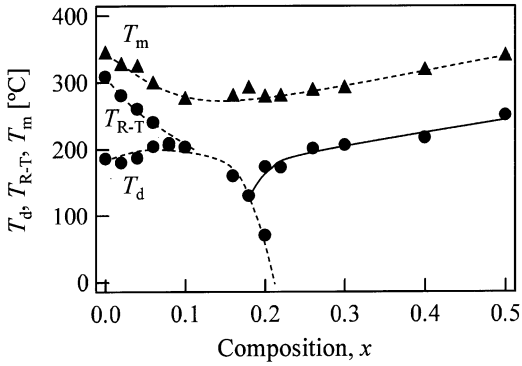

Fig. 8.16 Compositional dependence of phase transition temperatures T_d, T_{R-T}, and T_m as a function of the content (x) of BKT for BNKT100x ceramics

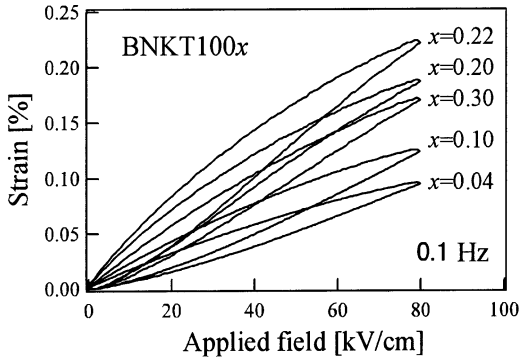

Fig. 8.17 Field-induced strains of BNKT100x ($x = 0.04, 0.10, 0.20, 0.22$, and 0.30) under unipolar driving at 0.1 Hz

The electromechanical coupling factor k_{33}, free permittivity $\varepsilon_{33}^{T}/\varepsilon_0$, and piezoelectric constant d_{33}, measured by the resonance and antiresonance method, of BNKT100x indicate that the ε_{33}^{T} of BNKT100x increases markedly near the MPB composition and the ε_{33}^{T} of the tetragonal compositions ($x = 0.22$–0.30) were approximately three times higher than those of the rhombohedral compositions ($x = 0$–0.10). The highest k_{33} and d_{33} of BNKT100x were obtained at the MPB composition ($x = 0.20$), and these values were 0.56 and 167 pC/N, respectively. In the case of BNKT100x, the k_{33} values of the tetragonal compositions were lower than those of the rhombohedral compositions; however, the d_{33} values of the tetragonal compositions were higher than those of the rhombohedral compositions because of the higher the ε_{33}^{T}. The relationships between the T_d and the d_{33} for BNKT100x demonstrate that the d_{33} linearly increases with the decrease of the T_d. Considering both high d_{33} and high T_d, the tetragonal compositions of BNKT100x are better than those of the rhombohedral and the MPB compositions.

Field-induced strains of BNKT100x under unipolar driving at 0.1 Hz are shown in Fig. 8.17, and the piezoelectric constant, d_{33}, and the normalized strain, $d_{33}^{*}(= S_{max}/E_{max})$, at 80 kV/cm are summarized in Fig. 8.18. The d_{33}^{*} was all higher than the d_{33}, because the d_{33}^{*} includes the domain contribution due to the high applied voltage and the low measuring frequency [66]. The highest value was

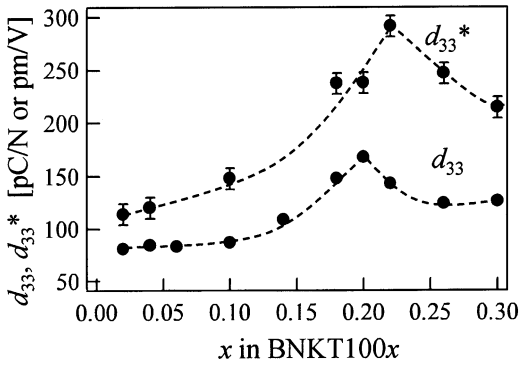

Fig. 8.18 Compositional dependence of the piezoelectric constant d_{33} and the normalized strain, d^*_{33}, for BNKT100x

obtained near the MPB composition for BNKT100x. Moreover, the ratios of the d^*_{33} to the d_{33} are larger for the tetragonal compositions than for the rhombohedral compositions due to the difference in the domain structures.

The typical *D–E* hysteresis loops of a ferroelectric were obtained at RT for BNKT100x ($x = 0$, 0.18, and 0.22). The variation of the *D–E* hysteresis loops for BNKT100x in the temperature range between 80 and 260°C is shown in Fig. 8.19. Double-like hysteresis loops were observed at approximately the T_d to 180°C for BNKT18 and BNKT22. It is considered that a double-like hysteresis loop is due to the mixture phases because of the existence of the intermediate phase near the MPB [41]. On the other hand, weak ferroelectric hysteresis loops were observed at 200°C for BNKT18 and 220°C for BNKT22. There is no discussion about ferroelectricity of the middle phase of T_{R-T}-T_m ($T_{R-T} > T_d$) and T_d-T_m ($T_{R-T} < T_d$) for BNT-based solid solutions. However, the results of this study indicate that those regions are probably very weak ferroelectric.

Recently, an excellent piezoelectric constant d_{33} (d_{33} meter value) of 231 pC/N was obtained at the MPB composition of $(Bi_{1/2}Na_{1/2})TiO_3$-$(Bi_{1/2}Li_{1/2})TiO_3$-$(Bi_{1/2}K_{1/2})TiO_3$ [BNT-BLT-BKT] ternary systems [61] however, the relationship between T_d and d_{33} has not been clarified. From the effects of Li- and K-substitution on the T_d in the A-site of BNT [43], it is seen that the T_d of BNT increases when the small amounts of Li and K are substituted. Thus, it is thought that co-substitution of Li and K is effective in increasing the T_d of BNT-based solid solutions. Therefore, this section describes the phase transition temperatures and the relationship between the T_d and the d_{33}, and also the piezoelectric properties of $x(Bi_{1/2}Na_{1/2})TiO_3$-$y(Bi_{1/2}Li_{1/2})TiO_3$-$z(Bi_{1/2}K_{1/2})TiO_3$ ($x + y + z = 1$) (abbreviated to BNLKT100y-100z) three component system [43, 67]. In order to increase the T_d, a small amount of Li-substitution is probably optimal. In addition, it is important to use the MPB composition to enhance the piezoelectric properties. Thus, BNLKT4-100z and BNLKT8-100z have been studied to clarify the effects of Li and K concentrations. Figure 8.20 shows the phase relation of xBNT-yBLT-zBKT system including BNLT100y (BNT-BLT) and BNKT100z (BNT-BKT).

The ratios of the measured density to the theoretical density of sintered ceramics were all higher than 96%. BNLKT0-100z ($z = 0$–0.26), BNLKT4-100z ($z = 0$–0.28),

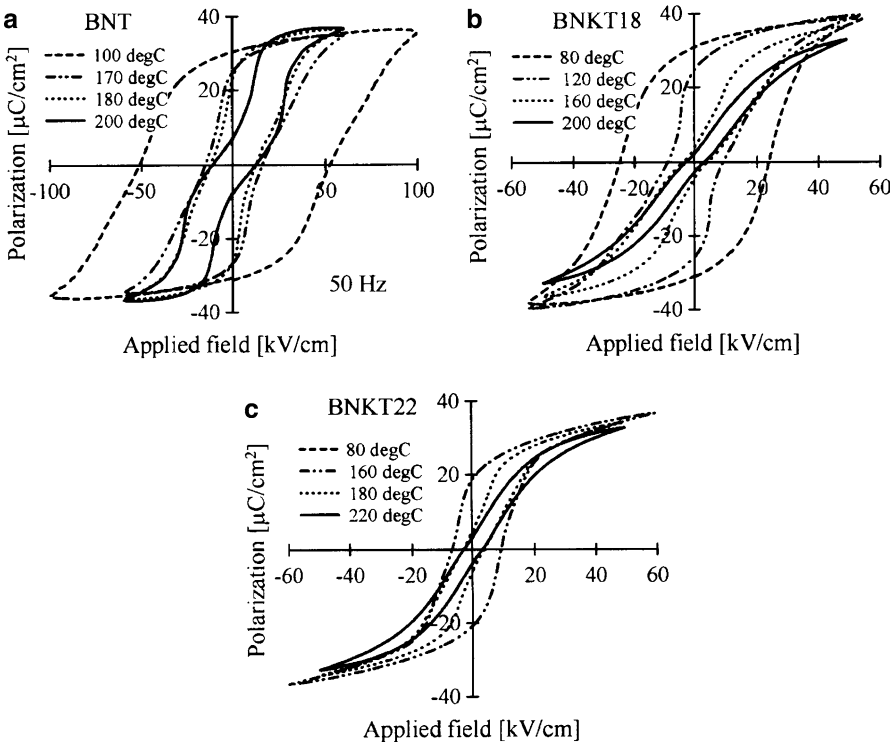

Fig. 8.19 Temperature dependences of *D–E* hysteresis loops for (**a**) BNT, (**b**) BNKT18, and (**c**) BNKT22

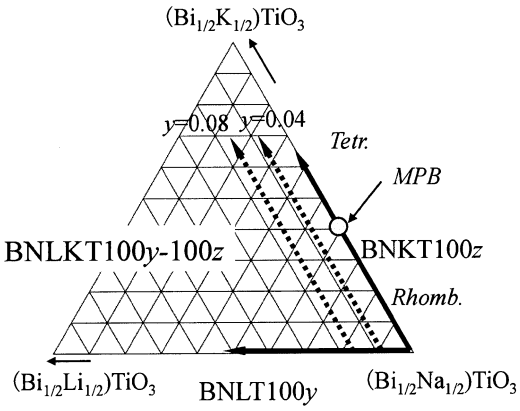

Fig. 8.20 The phase relation of $(Bi_{1/2}Na_{1/2})TiO_3$ [BNT]-$(Bi_{1/2}Li_{1/2})TiO_3$ [BLT]-$(Bi_{1/2}K_{1/2})TiO_3$ [BKT] system

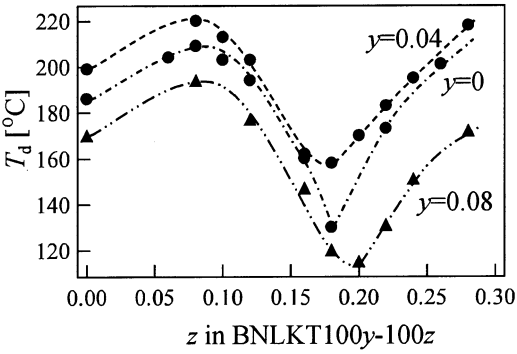

Fig. 8.21 Depolarization temperature, T_d, of BNLKT100y-100z ($y = 0$, 0.04 and 0.08) as a function of the content (z) of BKT

and BNLKT8-100z ($z = 0$–0.28) showed all single phases of perovskite structure. X-ray powder diffraction patterns displayed coexistence of rhombohedral and tetragonal phases at $z = 0.18$–0.20 for BNLKT4-100z and at $z = 0.18$–0.22 for BNLKT8-100z. Therefore, the MPBs exist in these compositions. The rhombohedrality, 90°-α and the tetragonality, c/a of BNLKT4-100z and BNLKT8-100z indicate that the 90°-α of BNLKT4-100z is larger than that of BNLKT8-100z and the 90°-α reached the maximum at $z = 0.08$ and showed the lowest at the MPB. However, the c/a increased significantly near the MPB composition with increasing z, which tendency is similar to the MPB of PZT [1, 2].

The resistivities of the prepared ceramics were all higher than the order of 10^{12} Ω cm. Figure 8.21 shows the variation in the depolarization temperature, T_d, as a function of the content (z) of BKT, for BNLKT0-100z, BNLKT4-100z, and BNLKT8-100z. In order to determine the T_d accurately, it was measured from the temperature dependence of piezoelectric properties using fully poled 33-mode specimens and dielectric loss tangent, tan δ, using fully poled specimens [41]. The T_d of BNLKT4-100z was higher than those of BNLKT0-100z and BNLKT8-100z. On the rhombohedral side ($0 < z < 0.16$), the T_d was the highest (221°C) at $z = 0.08$. Then, the T_d decreased with increasing z and the lowest value of T_d was approximately 160°C for $y = 0.04$ at around the MPB composition of $z = 0.16$–0.18. On the tetragonal side ($0.2 < z < 0.28$), the T_d increased with increasing z, and that of BNLKT4-28 was 218°C. The T_d values of BNLKT0-0 (BNT), BNLKT4-0, and BNLKT8-0 were 185, 196, and 170°C, respectively. This result indicates that a small amount of Li-substitution is effective in increasing T_d of BNT-based solid solution. In addition, T_d of BNLKT4-100z and BNLKT8-100z showed the maximum at $z = 0.08$ at the rhombohedral side as the same as BNLKT0-100z. Although very few data on increased T_d have been reported previously at the rhombohedral composition of BNT-based solid solutions [45], the T_d could be increased up to 221°C for BNLKT4-8.

Recently, piezoelectric ceramics have attracted much attention for high-power devices, such as ultrasonic motors and transducers [68–71]. These devices were mainly composed of PZT-based piezoelectric ceramics with a high mechanical quality factor Q_m, which is called hard PZT. However, the resonant vibration of

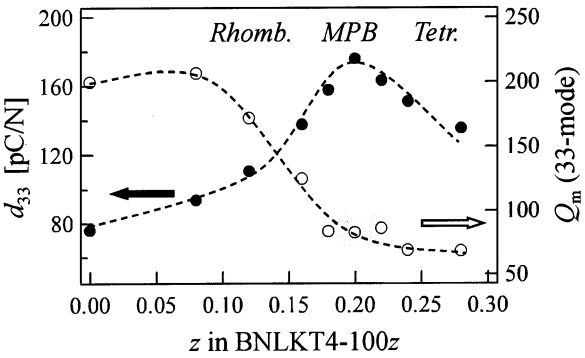

Fig. 8.22 Piezoelectric strain constant, d_{33}, and the mechanical quality factor, $Q_m(33)$, in (33) mode, of BNLKT4-100z as a function of the content (z) of BKT

hard PZT becomes unstable at a vibration velocity of approximately 1.0 m/s, resulting in marked decrease in Q_m and no increase in vibration velocity. Moreover, PZT contains a large amount of PbO; therefore, recently, there has been much interest in lead-free piezoelectric ceramics as a material for replacing PZT-based ceramics. As materials for lead-free high-power applications, $(Sr,Ca)_2NaNb_5O_{15}$ and $SrBi_2Nb_2O_9$ have been reported [47, 72, 73].

The relationship between the T_d and the d_{33}, and also the piezoelectric properties of BNLKT100y-100z system indicates that it has the high possibility of the use for high-power applications. Therefore, in this section, we would like to compare the properties of the rhombohedral and tetragonal sides of MPB composition in the T_d vs. Q_m, and to discuss the optimum composition for high-power applications. In addition, we clarified the effect of Mn doping on the variations in T_d and piezoelectric properties with high-power characteristics of BNLKT100y-100z including w wt.% $MnCO_3$-doped BNLKT100y-100z (abbreviated to BNLKT100y-100zMnw).

Figure 8.22 shows the piezoelectric strain constant, d_{33}, and the mechanical quality factor, $Q_m(33)$, in the 33-mode, of BNLKT4-100z as a function of the content (z) of BKT. The d_{33} reaches about 180 pC/N at the MPB composition ($z = 0.20$). On the other hand, the $Q_m(33)$ was the highest of approximately 200 at $z \leq 0.08$ and decreased to below 90 at $z \geq 0.18$.

Figure 8.23 shows the relationships between the T_d and (a) the d_{33} and (b) the Q_m on the rhombohedral and tetragonal sides. As has already been described, the tetragonal side of the MPB is considered to be an excellent candidate composition for actuator applications with high T_d and high d_{33} compared with the rhombohedral side and the MPB composition. On the other hand, it was found that the relationship between the T_d and the $Q_m(33)$ on the rhombohedral side is higher than those on the tetragonal side and the MPB composition. This indicates that the rhombohedral side is a suitable composition for high-power applications.

$MnCO_3$ was doped into BNLKT4-8 because this seems to be the optimum composition for high-power applications as both a high T_d and a high Q_m.

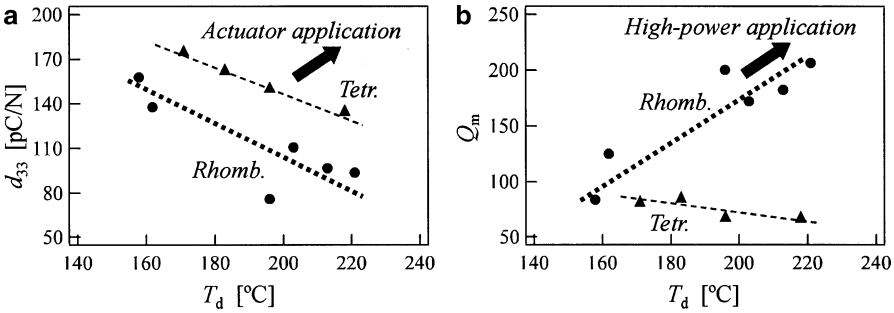

Fig. 8.23 Relationship of the depolarization temperature, T_d, between (**a**) the d_{33} and (**b**) the $Q_m(33)$ for rhombohedral (Rhomb.) and tetragonal (Tetr.) sides

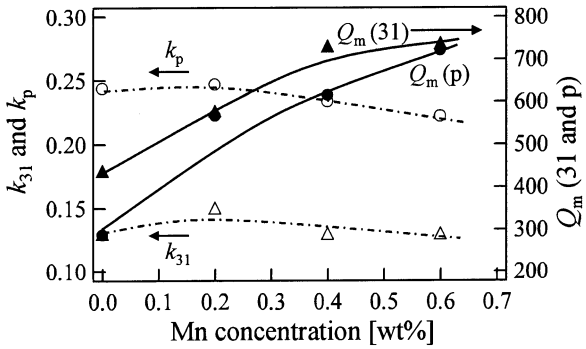

Fig. 8.24 Coupling factors, k, and mechanical quality factors, Q_m, in the (31) and the planar (p) modes as a function of the Mn concentration (w)

BNLKT4-8Mnw (w = 0–0.6) showed high density ratios of more than 97% without any secondary phases. The resistivity, ρ, of these ceramics was higher than the order of 10^{12} Ω cm. The temperature dependences of the dielectric constant, ε_s, and the loss tangent, tan δ, of BNLKT4-8Mnw (w = 0–0.6) show that the maximum dielectric constant, ε_{max}, and tan δ decrease with increasing amount of Mn (w). On the other hand, the dielectric maximum temperature, T_m, was almost constant at approximately 272°C.

Figure 8.24 shows the variations of the k_{31} and the k_p, and the $Q_m(31)$ and $Q_m(p)$ in the (31) and the planar (p) modes of BNLKT4-8 as a function of the Mn concentration (w). Although the k_{31} and the k_p slightly decreased with increasing Mn concentration (w), the $Q_m(31)$ and the $Q_m(p)$ markedly increased with increasing w. The $Q_m(31)$ and the $Q_m(p)$ values were approximately 300 and 400 for BNLKT4-8 (w = 0), and 730 and 720 for BNLKT4-8Mn0.6, respectively. On the other hand, the d_{33} gradually decreased with increasing Mn concentration (w), and the d_{33} values of BNLKT4-8 and BNLKT4-8Mn0.6 were 94 and 85 pC/N, respectively.

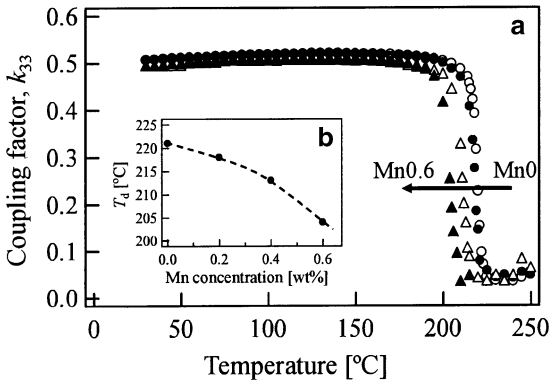

Fig. 8.25 (**a**) Temperature dependence of the coupling factor, k_{33}, for BNLKT4-8Mnw ($w = 0$ and 0.6) and (**b**) the T_d as a function of w

Figure 8.25a shows the temperature dependence of the k_{33} for BNLKT4-8Mnw ($w = 0$ and 0.6). It is found that the k_{33} is almost constant up to the T_d. Moreover, the T_d gradually decreases with increasing Mn concentration (w), as shown in Fig. 8.25b, with $T_d = 204°C$ for BNLKT4-8Mn0.6.

The decrease in the T_d with increasing Mn content (w) indicates that the Mn ion substitution into either the A-site or B-site of BNLKT4-8. According to the previous reports, both ε_{max} and T_m decrease with increasing amount of Mn in BNT and BNT-BT [74, 75]. In BNLKT4-8Mnw, although the temperature dependence of dielectric constant showed that the ε_{max} decreased with increasing w, the T_m was almost constant at 272°C [67].

Previously, we investigated the variations in phase transition temperature for monovalent (Li, K), divalent (Ca, Sr, Ba), and trivalent (La, Nd, Ho, Yb) ions substituted into the A-site of BNT ceramics [45, 64]. Considering the use of an ionic radius of six coordinate by Shannon [76], it is found that the substitution of large ions, such as Ba^{2+}, Sr^{2+}, and K^{1+}, into the A-site of BNT decreases T_m, and other smaller ions and lanthanoid ions increase T_m. Moreover, comparing the same valence, T_m decreases with increasing ionic radius. In particular, the substitution of lanthanoid ions generates vacancies in the A-site of BNT resulting in a decrease in the average ionic radius of the A-site. Therefore, T_m dramatically increases when small amount of lanthanoid ions substituted into A-site of BNT.

On the other hand, there are a few data on the effect of the substitution into the B-site of BNT. The phase transition temperatures of the BNT-$BiScO_3$ and BNT-$BiAlO_3$ systems were reported [24, 77]. In these systems, T_m increases with increasing amount of $BiScO_3$, and decreases with increasing amount of $BiAlO_3$. The ionic radius of Bi^{3+} is similar to that of Na^{1+}; therefore, the variation of T_m is attributed to the B-site of BNT. The ionic radii of Sc^{3+}, Al^{3+}, and Ti^{4+} are 0.745, 0.535, and 0.605 Å, respectively. Thus, the decrease in T_m is due to the substitution of small ions (Al^{3+}) into the B-site of BNT.

Considering the valence state of Mn ions in BNT, the Mn^{4+} substitution into the B-site probably decreases T_m because the ionic radius of Mn^{4+} is 0.530 Å which is similar to that of Al^{3+}. In contrast, the substitution of Mn^{2+} and Mn^{3+} into the A-site

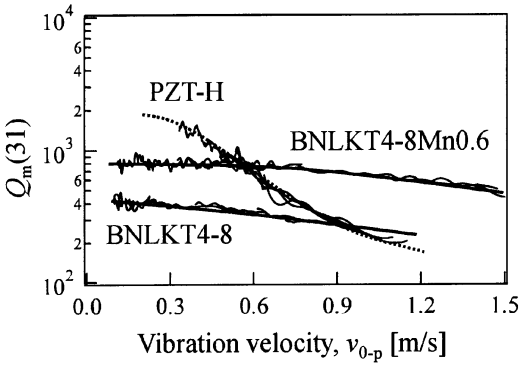

Fig. 8.26 Variations in $Q_m(31)$ as a function of the vibration velocity $v_{0\text{–p}}$ for BNLKT4-8, BNLKT4-8Mn0.6, and PZT-H

or B-site of BNT should increase the T_m of BNT. Therefore, the decay of T_d and the lack of variation in T_m indicate that Mn ions exist in BNLKT4-8, in the mixed state of Mn^{2+} or Mn^{3+}, and Mn^{4+}.

The resistivity was maximum at $w = 0.2$, and then, decreased with increasing Mn concentration w. The vaporization of A-site ions such as Bi, Na, and K occurs during sintering. Therefore, the very small amount of Mn probably compensates for the A-site vacancies as a donor, resulting in an increase in resistivity [74, 75]. In contrast, Mn^{2+} or Mn^{3+} in the B-site works as an acceptor; therefore, resistivity decreases at $w > 0.2$. Generally, acceptor ions associate with oxygen vacancies, and cause domain pinning, thereby increasing in Q_m [78–80]. Therefore, the Q_m of BNLKT4-8Mnw increases with increasing w.

The high-power characteristics of BNLKT4-8, BNLKT4-8Mn0.6, and PZT-H were evaluated by the high-power characteristic measurement [71]. The small amplitude $Q_m(31)$ values of BNLKT4-8, BNLKT4-8Mn0.6, and PZT-H are 440, 740, and 1,770, respectively. Figure 8.26 shows the variation in $Q_m(31)$ as a function of the vibration velocity $v_{0\text{–p}}$. It is found that the $Q_m(31)$ values of BNLKT4-8 and BNLKT4-8Mn0.6 decrease slower than that of PZT-H. Although the small amplitude $Q_m(31)$ of PZT-H was twice higher than that of BNLKT4-8Mn0.6, that of BNLKT4-8Mn0.6 was larger than that of PZT-H at $v_{0\text{–p}} > 0.6$ m/s. Moreover, the $Q_m(31)$ of BNLKT4-8Mn0.6 was higher than 400 even at $v_{0\text{–p}} = 1.5$ m/s.

It is considered that the small decay of $Q_m(31)$ under a high amplitude vibration for BNLKT4-8 and BNLKT4-8Mn0.6 is attributed to the high coercive field E_c. It is known that the E_c at the rhombohedral composition is larger than that at the MPB and on the tetragonal side for BNT-based solid solutions [39]. The BNLKT4-8 has high E_c of 60 kV/cm, which is 4 times larger than that of PZT-H. Moreover, domain wall motion is suppressed by oxygen vacancies associated with the doping of acceptor ions [68]. Therefore, the acceptor-ion-doped rhombohedral composition of BNT-based solid solutions is stable even when vibration velocity is higher than PZT-H.

8.6 $(Bi_{1/2}K_{1/2})TiO_3$ [BKT] [8, 36, 81]

BKT, is a typical lead-free ferroelectric with a perovskite structure of tetragonal symmetry at room temperature and has a relatively high Curie temperature, T_c, of 380°C [15]. This indicates that BKT has a certain promise as a candidate for lead-free piezoelectrics in a wide working temperature range. However, there are few reports about this material owing to its poor sinterability. This problem has restricted extensive activities of researchers in investigations for the BKT-based solid solution systems.

Recently, Hiruma et al. [36, 81] reported the electrical properties of BKT ceramics prepared by the hot-pressing (HP) method. Figure 8.27 shows the density of ordinarily fired (OF) and hot-pressed (HP) BKT ceramics as a function of the sintering temperature. The optimum sintering temperature seems to be 1,060–1,080°C. Figure 8.28 shows the temperature dependences of dielectric constants, ε_s, and dielectric loss tangents, tan δ, for BKT-HP1060°C and BKT-HP1080°C, in the temperature range from room temperature to 600°C, measured at frequencies of 10 kHz, 100 kHz, and 1 MHz. The tan δ curves in Fig. 8.28 show two peaks. High-temperature peaks show frequency dispersions; therefore, it is thought that these peaks are related to the T_c. On the other hand, low-temperature peaks are almost independent of frequencies; therefore, it is considered to indicate the second-phase transition, T_2, between tetragonal and pseudocubic symmetries, whose temperatures of BKT-HP1060°C and BKT-HP1080°C are about 340 and 315°C, respectively. The T_c of Bi_2O_3, La_2O_3 and $MnCO_3$ doped BKT ceramics showed a tendency to decreasing with the increase of the content of dopants.

Figure 8.29 shows *D–E* hysteresis loops of BKT-HP1060°C and BKT-HP1080°C. Well-saturated *D–E* hysteresis loops with low leakage current were obtained for all specimens at RT. Figure 8.30 shows the saturation properties of remanent polarization P_r for (a) BKT-HP1060°C and BKT-HP1080°C, (b) BKT-Bi*x* (c) BKT-La*x* and (d) BKT-Mn*x*. The P_r and the coercive fields E_c were 22.2 μC/cm^2 and 52.5 kV/cm for BKT-HP1080°C, and 14.2 μC/cm^2 and

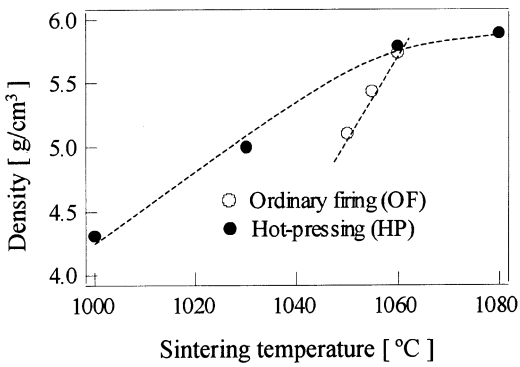

Fig. 8.27 The density of ordinarily fired (OF) and hot-pressed (HP) BKT ceramics as a function of the sintering temperature

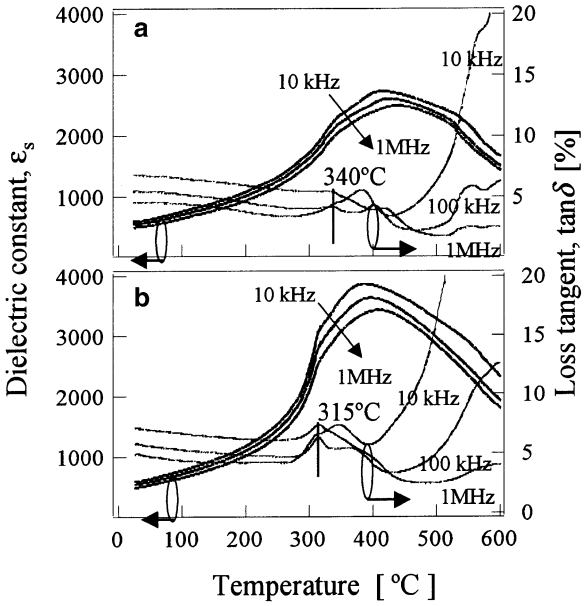

Fig. 8.28 Temperature dependences of dielectric constant ε_s and dielectric loss tangent tan δ for the hot-pressed BKT ceramics sintered at (**a**) 1,060°C and (**b**) 1,080°C

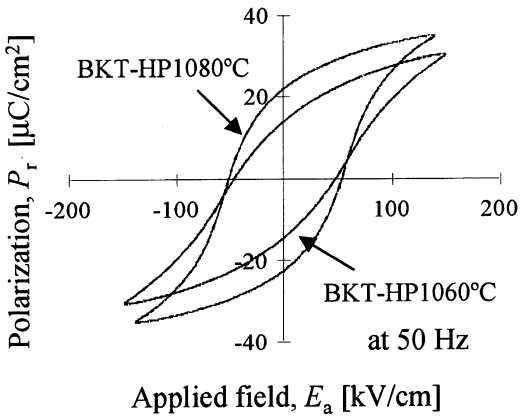

Fig. 8.29 D-E hysteresis loops of the HP-BKT at 1,060 and 1,080°C

47.3 kV/cm for BKT-HP1060°C, respectively. The different tendencies seem to be the difference in grain size 0.2 μm for BKT-HP1060°C and 0.4 μm for BKT-HP1080°C. Compared BKTLax with BKT-HP1060°C in Fig. 8.30(c), the P_r of BKTLax increased and the rising applied field shift lower, and this result imply BKT ceramics become soft such as La-doped PZT ceramics. On the other hand, the P_r of BKTBix and BKTMnx was almost the same as BKT-HP1060°C. The temperature dependence of *D–E* hysteresis loops for BKT-HP1080°C was observed in the temperature range from room temperature to 260°C as shown in Fig. 8.31. The P_r and the E_c gradually decreased with increasing sample temperature, and well-saturated *D–E* hysteresis loops were observed even at 260°C.

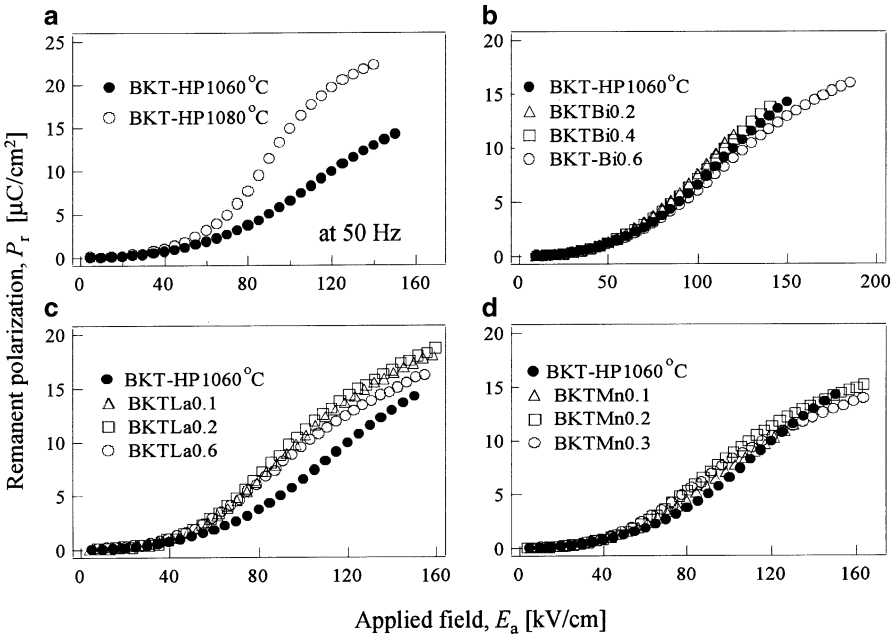

Fig. 8.30 Remanent polarization, P_r, of (**a**) hot-pressed HP-BKT ceramics compared with ordinarily fired (OF) BKT doped (**b**) Bi ion, (**c**) La ion and (**d**) Mn ion in wt.%, respectively, as a function of the applied electric field, E_a

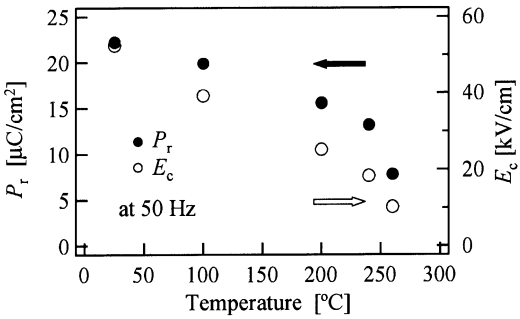

Fig. 8.31 Temperature dependence of the remanent polarization, P_r, and the coercive field, E_c, of HP1060°C-BKT measured at 50 Hz

Figure 8.32 shows the temperature dependence of electromechanical coupling factor, k_{33}, and the phase, θ, in the impedance-frequency characteristics of the (33)-mode for BKT ceramic [36]. This figure indicates that the BKT ceramic seems to be attractive for higher temperature applications compared with the BT ceramic.

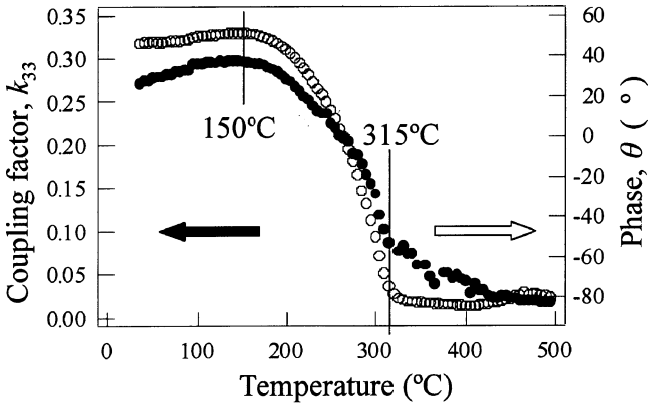

Fig. 8.32 Temperature dependence of electromechanical coupling factor, k_{33}, and the phase, θ, in the impedance-frequency characteristics of the (33)-mode for BKT ceramic

8.7 $(Bi_{1/2}K_{1/2})TiO_3$ – $BaTiO_3$ [BKT-BT] [8, 82, 83]

A solid solution system, $(1 - x)$ $(Bi_{1/2}K_{1/2})TiO_3$–$xBaTiO_3$ (BKT-BT100x) was investigated for evaluating their characterizations and electrical properties by using randomly oriented and grain-oriented samples. Especially, the compositions near the BKT and BKT itself, $x = 0$–0.4, were focused as the lead-free piezoelectric ceramics with the wide working temperature.

X-ray diffraction patterns of BKT-BT100x ceramics with $0 \leq x \leq 1$ show a single phase of perovskite structure with tetragonal symmetry at room temperature. The sintered ceramics of BKT-BT indicated higher relative densities than 95%, even in the compositions of the BKT side as shown in Table 8.4.

Figure 8.33 shows lattice constants, a and c, and lattice anisotropy, c/a, as a function of the amount (x) of BT in BKT–BT100x ceramics. Both BKT ($x = 0$) and BT ($x = 1$) have the same crystal structure of tetragonal symmetry; however, the c/a indicated nonlinear tendency. The c/a shows the maximum (~1.025) at the composition around $x = 0.2$, which is very large value among the lead-free piezoelectric materials. This result corresponds almost to that as shown in Buhrer's report [15].

From temperature dependences of dielectric constant, ε_r and loss tangent, tan δ, for the BKT-BT100x ceramics, the Curie temperature, T_c, linearly shifted to lower temperatures with the increase of the amount of BT content (x), as shown in Fig. 8.34. The T_c of BKT-BT80 ($x = 0.8$) shows still a higher temperature than 200°C. However, both the ε_r at RT and at the T_c decrease with increasing x. The T_2 in Fig. 8.34 shows the second-phase transition temperature from tetragonal to pseudocubic phases, existing near 270°C in BKT. The T_2 of BKT ceramic was reported by Ivanova et al. [84].

Table 8.4 Physical and piezoelectric properties for non-oriented (OF) and grain-oriented (RTGG) BKT-BT10, 20, and 30 prepared by ordinary firing (OF) and RTGG methods [85]

	BKT-BT10		BKT-BT20		BKT-BT30	
	OF	RTGG	OF	RTGG	OF	RTGG
ρ_o/ρ_x (%)	98.5	97.8	99.3	95.4	98.0	94.3
F (%)	–	35	–	72	–	61
k_{33}	0.35	0.37	0.36	0.33	0.38	0.38
$\varepsilon_{33}^{T}/\varepsilon_0$	602	560	532	501	461	426
s_{33}^{E} (pm^2/N)	8.2	10.5	8.2	10.1	7.8	13.0
d_{33} (pC/N)	73.4	84.5	69.3	70.7	67.6	83.3
d_{33}^{*} (pm/V)	103	168	116	143	103	134

ρ_o/ρ_x: relative density ratio; F: orientation factor; k_{33}: electromechanical coupling factor; ε_{33}^{T}: free permittivity; s_{33}^{E}: elastic constant; d_{33}: piezoelectric strain constant obtained by (8.1); d_{33}^{*}: normalized strain calculated by (8.2)

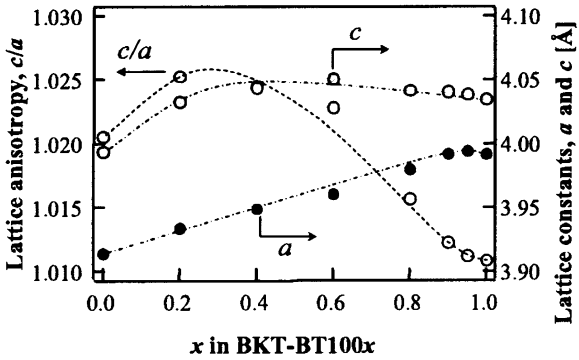

Fig. 8.33 Lattice anisotropy, c/a and lattice constants, a and c, as a function of the amount (x) of BT in BKT–BT100x ceramics

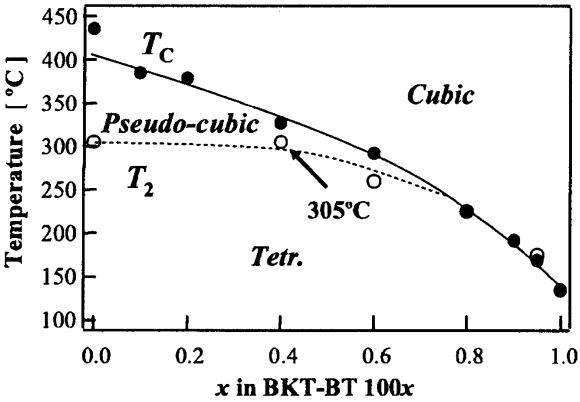

Fig. 8.34 Curie temperature, T_c, and second-phase transition temperature, T_2, of BKT-BT100x ceramics, as a function of the amount (x) of BT, measured at 1 MHz

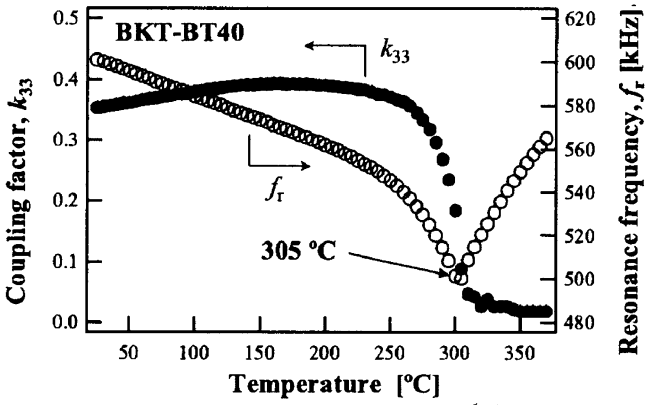

Fig. 8.35 Temperature dependences of the coupling factor, k_{33} and the resonance frequency, f_r, for the BKT-BT40

Figure 8.35 shows temperature dependences of the coupling factor, k_{33}, and the resonance frequency, f_r, for BKT-BT40. The k_{33} (=0.35) at RT maintained the same value up to around 250°C and then almost disappeared at about 300°C. Also, the temperature dependence of the f_r showed the minimum at 305°C. This temperature is not equal to the T_c of BKT-BT40. From this result, we determined the depolarization temperature, T_d, which corresponds to the second-phase transition temperature, T_2, from the tetragonal to pseudocubic phases, as shown in Fig. 8.34. The BKT-BT100x ceramics (x = 0–0.4) indicated high T_d temperatures around 300°C.

Furthermore, grain orientation effects for piezoelectric properties were investigated in BKT-BT100x using a RTGG method [85]. Piezoelectric strain constants, d_{33}, for randomly oriented BKT-BT10, 20, and 30 are 73.4, 69.1 and 67.6 pC/N, respectively. These values are relatively small for the practical use to actuators. So, we tried to prepare the textured samples by the RTGG method to enhance their piezoelectric properties. Textured specimens were prepared using the RTGG method with matrix and templates of plate-like $Bi_4Ti_3O_{12}$ (BiT) particles for BKT-BT. Calcination and sintering temperatures were 900–1,000°C and 1,100–1,400°C, respectively. The piezoelectric properties of the textured and nontextured BKT-BT10, 20, and 30 are summarized in Table 8.4. The measured direction of textured specimens is parallel [//] to the tape stacking direction. The d_{33} in textured specimens were improved as compared with those of nontextured specimens. For example, the d_{33} in BKT-BT10 was improved from 73.4 to 84.5 pC/N. However, the increment was relatively small because the orientation factor, F, was still low of about 35%. Further systematic studies for improving the F may be necessary as a future work. From these results, the BKT-BT system seems to be a superior candidate for lead-free piezoelectric materials at high temperature applications.

8.8 Summary

The dielectric, ferroelectric, and piezoelectric properties of lead-free perovskite-type ceramics were investigated being candidates for lead-free piezoelectric materials to reduce environmental damage during the waste disposal of piezoelectric products. Perovskite ferroelectric ceramics seem to be suitable for high-power applications such as piezoelectric actuators requiring large piezoelectric constants, d_{33} and high Curie temperatures, T_c or high depolarization temperatures, T_d.

The Bi-excess bismuth sodium titanate, $(Bi_{1/2}Na_{1/2})TiO_3$ [BNT] + Bi_2O_3 x wt. % [BNT-x] and hot-pressed BNT [HP-BNT] ceramics were prepared and their piezoelectric properties were investigated. All of BNT-x ceramics sintered at 1,225°C showed a high-density ratio more than 97% to the theoretical density. The BNT-0.3 seems to be a stoichiometry because of the measurement results from the resistivity, ρ, Curie temperature, T_c and microstructure. BNT-0.3 ceramic showed a relatively large electromechanical coupling factor, k_{33} (=0.47) and piezoelectric constant, d_{33} (=93 pC/N). The large piezoelectricity, k_{33} (=0.48) and d_{33} (=98 pC/N), with the high density ratio (98%), could be obtained on the HP-BNT ceramic sintered at 1,100°C for 30 min and pressed at 200 kg/cm^2 as lead-free piezoelectric materials.

In the case of the ternary system $x(Bi_{1/2}Na_{1/2})TiO_3$-$y(Bi_{1/2}K_{1/2})TiO_3$-$zBaTiO_3$ ($x + y + z = 1$), [BNBKy:z (x)], enhanced piezoelectric properties were obtained near the MPB composition, and the highest electromechanical coupling factor, k_{33}, and d_{33} were 0.58 for BNBK2:1(0.89) and 181 pC/N for BNBK2:1(0.88). Nevertheless, the T_d shift to lower temperatures (about 100°C) around the MPB compositions corresponds to BNBK2:1(0.88–0.90). On the tetragonal side, T_d shifts to a value higher than 200°C for $x < 0.78$, with $k_{33} = 0.452$ and $d_{33} = 126$ pC/N for BNBK2:1(0.78). This ternary system shows high potential (with properties such as large $d_{33} > 250$ pC/N and high $T_d > 250$°C) for actuator applications.

It is revealed that $(1 - x)(Bi_{1/2}Na_{1/2})TiO_3$-$xSrTiO_3$ [BNST100x] forms an MPB of rhombohedral ferroelectric and pseudocubic (tetragonal) paraelectric at $x = 0.28$, and very large electrostrain and normalized strain (0.29%) and $d^*_{33} = 488$ pm/V, respectively, were obtained at the MPB composition, although no piezoelectric properties were obtained at $x \geq 0.28$. In addition, it has been clarified that the intermediate phase between T_{R-T} ($\geq T_d$) and T_m shows relaxor behavior.

The phase transition temperatures and piezoelectric properties of $(1 - x)(Bi_{1/2}Na_{1/2})TiO_3$–$x(Bi_{1/2}K_{1/2})TiO_3$ [BNKT100x] and $(1 - x)(Bi_{1/2}Na_{1/2})TiO_3$–$x(Bi_{1/2}Li_{1/2})TiO_3$ [BNLT100x] were investigated in detail. We demonstrated that the T_d of BNKT100x was increased to 209°C at $x = 0.08$. On the other hand, the T_d of BNLT100x anomalously increased to 199°C when a small amount of Li was substituted to the A-site of BNT. In addition, we clarified that the T_d is related to the magnitude of rhombohedrality 90°-α and tetragonality c/a for BNT-based solid solutions. While piezoelectric constant d_{33} decreased near T_d, normalized strain d^*_{33} increased. Double-like hysteresis loops were observed in the middle phase of T_d-T_{R-T} and intermediate phase near the MPB. In addition, we revealed that the middle

phases of T_{R-T}-T_m ($T_{R-T} > T_d$) and T_d-T_m ($T_{R-T} < T_d$) are probably very weak ferroelectric.

A detailed study of the phase transition temperatures, such as T_d, T_{R-T}, and T_d, and the piezoelectric properties of $x(Bi_{1/2}Na_{1/2})TiO_3$-$y(Bi_{1/2}Li_{1/2})TiO_3$-$z(Bi_{1/2}K_{1/2})TiO_3$ [BNLKT100y-100z] was carried out. It was found that the variation of the T_d is related to the variation of lattice distortion, such as rhombohedrality 90°-α and tetragonality c/a. A small amount of Li-substitution was very effective for increasing T_d, and that of BNLKT4-100z increased from 185 to 221°C at the rhombohedral composition. Although excess Li-substitution enhanced the piezoelectric properties, T_d drastically decreased with increasing amount of Li-substitution. Considering both high T_d and high d_{33}, the tetragonal composition of BNLKT4-100z is optimal for piezoelectric actuator applications.

The piezoelectric properties on rhombohedral and tetragonal sides of the MPB compositions were compared. In this study, we clarified that the rhombohedral composition of BNLKT4-8 is considered suitable for high-power application. In addition, a small amount of Mn doping is very effective for improving Q_m. The high-power characteristics of BNLKT4-8Mn0.6 are superior to those of PZT-H at approximately $v_{p-p} > 0.6$ m/s. Therefore, a Mn-doped BNT-based solid solution with rhombohedral symmetry is a promising candidate for lead-free high-power applications.

BKT has a certain promise as a candidate for lead-free piezoelectrics in a wide working temperature range. BKT ceramics were prepared by the hot-pressing (HP) method. The temperature dependences of dielectric constants, ε_s, and dielectric loss tangents, tan δ, for HP-BKT show two peaks. High-temperature peaks are related to the T_c and low-temperature peaks indicate the second-phase transition, T_2, between tetragonal and pseudo-cubic symmetries. Well-saturated D–E hysteresis loops of HP-BKT with low leakage current were obtained at RT and even at 260°C.

A solid solution system, $(1 - x)$ $(Bi_{1/2}K_{1/2})TiO_3$–xBaTiO$_3$ [BKT-BT100x] was investigated on the compositions near the BKT ($x = 0$–0.4). The lattice anisotropy, c/a, indicated nonlinear tendency with the maximum (~1.025) at the composition around $x = 0.2$. The Curie temperature, T_c, linearly shifted to lower temperatures with the increase of the amount of BT content (x) and the $T_c > 200$°C for BKT-BT80 ($x = 0.8$). BKT-BT system elevates the T_c of BT to higher temperatures than 200°C and seems to be a superior candidate for lead-free piezoelectric materials for high temperature applications. Grain-oriented BKT-BT100x by the RTGG method enhanced their piezoelectric properties.

To replace PZT-based systems, it is necessary that special features of each lead-free material correspond to the required piezoelectric properties for each application [86]. Future trends in the research and development of lead-free piezoelectric ceramics seem to be focused on textured grain orientations realized using the TGG and seeded polycrystal conversion (SPC) methods. Also domain controls including engineered domain of lead-free ferroelectric ceramics will be very important to enhance the piezoelectric activities. The trend toward thick and thin films with lead-free piezoelectrics seems to be necessity for FBAW and MEMS applications.

References

1. Sawaguchi E (1953) Ferroelectricity versus antiferroelectricity in the solid solutions of $PbZrO_3$ and $PbTiO_3$. J Phys Soc Jpn 8:615–629
2. Jaffe B, Roth RS, Marzullo S (1954) Piezoelectric properties of lead zirconate-lead titanate solid-solution ceramics. J Appl Phys 25:809–810
3. Jaffe B, Cook WR, Jaffe H (1971) Piezoelectric ceramics. Academic, New York, p 142
4. Yamamoto T (1996) Ferroelectric properties of the $PbZrO_3$-$PbTiO_3$ system. Jpn J Appl Phys 35(9B):5104–5108
5. Takenaka T (1999) Piezoelectric properties of some lead-free ferroelectric ceramics. Ferroelectrics 230:87–98
6. Saito Y, Takao H, Tani T, Nonoyama T, Takatori K, Homma T, Nagaya T, Nakamura M (2004) Lead free piezoceramics. Nature 42:84–87
7. Takenaka T, Nagata H (2005) Current status and prospects of lead-free piezoelectric ceramics. J Eur Ceram Soc 25(12):2693–2700
8. Takenaka T, Nagata H, Hiruma Y (2008) Current developments and prospective of lead-free piezoelectric ceramics. Jpn J Appl Phys 47:3787–3801
9. Shimamura K, Takeda H, Kohno T, Fukuda T (1996) Growth and characterization of lanthanum gallium silicate La3Ga5SiO14 single crystals for piezoelectric applications. J Crystal Growth 163:388–392
10. Von Hippel A (1946) J Ind Eng Chem 28:1097
11. Robert S (1947) Dielectric and piezoelectric properties of barium titanate. Phys Rev 71:890–895
12. Mathias BT, Remeika JP (1951) Dielectric properties of sodium and potassium niobates. Phys Rev 82:727–729
13. Egerton L, Dillon DM (1959) Piezoelectric and dielectric properties of ceramics in the system potassium-sodium niobate. J Am Ceram Soc 42:438–442
14. Smolensky GA, Isupov VA, Agranovskaya AI, Krainic NN (1961) New ferroelectrics of complex composition. IV. Soviet Phys Solid State 2(11):2651–2654
15. Buhrer CF (1962) Some properties of bismuth perovskites. J Chem Phys 36(3):798–803
16. Jaeger RE, Egerton L (1962) Hot pressing of potassium-sodium niobates. J Am Ceram Soc 45 (5):209–213
17. Sakata K, Masuda Y (1974) Ferroelectric and antiferroelectric properties of $(Bi_{1/2}Na_{1/2})TiO_3$-$SrTiO_3$ solid solution ceramics. Ferroelectrics 7:347–349
18. Suchanicz J, Roleder K, Kania A, Handerek J (1988) Electrostrictive strain and pyroeffect in the region of phase coexistence in $Na_{0.5}Bi_{0.5}TiO_3$. Ferroelectrics 77:107–110
19. Takenaka T, Sakata K (1988) New piezo- and pyroelectric sensor materials of $(BiNa)_{1/2}TiO_3$-based ceramics. Sensor Mater 1:123–131
20. Takenaka T, Sakata K (1989) Dielectric, piezoelectric and pyroelectric properties of $(BiNa)_{1/2}TiO_3$-based ceramics. Ferroelectrics 95:153–156
21. Takenaka T, Sakata K, Toda K (1990) Piezoelectric properties of $(Bi_{1/2}Na_{1/2})TiO_3$-based ceramics. Ferroelectrics 106:375–380
22. Takenaka T, Maruyama K, Sakata K (1991) (Bi, Na)TiO_3-$BaTiO_3$ system for lead-free piezoelectric ceramics. Jpn J Appl Phys 30(9B):2236–2239
23. Takenaka T, Hozumi A, Hata T, Sakata K (1993) Mechanical properties of $(Bi_{1/2}Na_{1/2})TiO_3$-based piezoelectric ceramics. Silicate Indus Ceram Sci Technol 58(7–8):136–142
24. Nagata H, Takenaka T (1997) Lead-free piezoelectric ceramics of (Bi1/2Na1/2)TiO3–1/2 (Bi2O3·Sc2O3) system. Jpn J Appl Phys 36:6055–6057
25. Takenaka T, Okuda T, Takegahara K (1997) Lead-free piezoelectric ceramics based on $(Bi_{1/2}Na_{1/2})TiO_3$-$NaNbO_3$. Ferroelectrics 196:175–178
26. Chiang Y-M, Farrey GW, Soukhojak AN (1998) Lead-free high-strain single-crystal piezoelectrics in the alkaline–bismuth–titanate perovskite family. Appl Phys Lett 73:3683–3685

27. Nagata H, Takenaka T (1998) Lead-free piezoelectric ceramics of $(Bi_{1/2}Na_{1/2})TiO_3$-$KNbO_3$-1/2 (Bi_2O_3· Sc_2O_3) System. Jpn J Appl Phys 37:5311–5314
28. Nagata H, Takenaka T (1998) $(Bi_{1/2}Na_{1/2})TiO_3$-based non-lead piezoelectric ceramics. J Korean Phys Soc 32:S1298–S1300
29. Takenaka T, Nagata H (1999) Ferroelectric and piezoelectric properties of lead-free $(Bi_{1/2}Na_{1/2})TiO_3$-$KNbO_3$-1/2(Bi_2O_3·Sc_2O_3) ceramics. In: Proceedings of the 11th IEEE international symposium on the applications of ferroelectrics (ISAF XI '98) (IEEE Catalog No. 98CH36245), pp 559–562
30. Nagata H, Koizumi N, Takenaka T (1999) Lead-free piezoelectric ceramics of $(Bi_{1/2}Na_{1/2})TiO_3$-$BaTiO_3$-$BiFeO_3$ system. Ferroelectrics 229:273–278
31. Sasaki A, Chiba T, Mamiya Y, Otsuki E (1999) Dielectric and piezoelectric properties of (Bi, Na)TiO_3-(Bi, K)TiO_3 systems. Jpn J Appl Phys 38(9B):5564–5567
32. Ishii H, Nagata H, Takenaka T (2001) Morphotropic phase boundary and electrical properties of bismuth sodium titanate-potassium niobate solid-solution ceramics. Jpn J Appl Phys 40 (9B):5660–5663
33. Nagata H, Yoshida M, Makiuchi Y, Takenaka T (2003) Large piezoelectric constant and high curie temperature of lead-free piezoelectric ceramic ternary system based on bismuth sodium titanate-bismuth potassium titanate-barium titanate near the morphotropic phase boundary. Jpn J Appl Phys 42(12):7401–7403
34. Hiruma Y, Aoyagi R, Nagata H, Takenka T (2004) Piezoelectric properties of $BaTiO_3$-$(Bi_{1/2}K_{1/2})TiO_3$ ferroelectric ceramics. Jpn J Appl Phys 43(11A):7556–7559
35. Makiuchi Y, Aoyagi R, Hiruma Y, Nagata H, Takenaka T (2005) $(Bi_{1/2}Na_{1/2})TiO_3$- $(Bi_{1/2}K_{1/2})TiO_3$-$BaTiO_3$-based lead-free piezoelectric ceramics. Jpn J Appl Phys 44(6B):4350–4353
36. Hiruma Y, Aoyagi R, Nagata H, Takenaka T (2005) Ferroelectric and piezoelectric properties of $(Bi_{1/2}K_{1/2})TiO_3$ ceramics. Jpn J Appl Phys 44(7A):5040–5044
37. Nagata H, Shinya T, Hiruma Y, Takenaka T, Sakaguchi I, Haneda H (2005) Piezoelectric properties of bismuth sodium titanate ceramics. Ceram Trans 167:213–222
38. Yoshii K, Hiruma Y, Nagata H, Takenaka T (2006) Electrical properties and depolarization temperature of (Bi1/2Na1/2)TiO3-(Bi1/2K1/2)TiO3 lead-free piezoelectric ceramics. Jpn J Appl Phys 45(5B):4493–4496
39. Hiruma Y, Makiuchi Y, Aoyagi R, Nagata H, Takenaka T (2005) Lead-free piezoelectric ceramics based on $(Bi_{1/2}Na_{1/2})TiO_3$-$(Bi_{1/2}K_{1/2})TiO_3$-$BaTiO_3$ solid solution. Ceram Trans 174:139–146
40. Hiruma Y, Yoshii K, Aoyagi R, Nagata H, Takenaka T (2006) Piezoelectric properties and depolarization temperatures of $(Bi_{1/2}Na_{1/2})TiO_3$-$(Bi_{1/2}K_{1/2})TiO_3$-$BaTiO_3$ lead-free piezoelectric ceramics. Key Eng Materials 320:23–26
41. Hiruma Y, Nagata H, Takenaka T (2006) Phase transition temperatures and piezoelectric properties of $(Bi_{1/2}Na_{1/2})TiO_3$-$(Bi_{1/2}K_{1/2})TiO_3$-$BaTiO_3$ lead-free piezoelectric ceramics. Jpn J Appl Phys 45(9B):7409–7412
42. Zhang S, Shrout TR, Nagata H, Hiruma Y, Takenaka T (2007) Piezoelectric properties in $(K_{0.5}Bi_{0.5})TiO_3$-$(Na_{0.5}Bi_{0.5})TiO_3$-$BaTiO_3$ lead-free ceramics. IEEE Trans Ultrason Ferroelectr Freq Control 54(5):910–917
43. Hiruma Y, Nagata H, Takenaka T (2007) Phase-transition temperatures and piezoelectric properties of $(Bi_{1/2}Na_{1/2})TiO_3$-$(Bi_{1/2}Li_{1/2})TiO_3$-$(Bi_{1/2}K_{1/2})TiO_3$ lead-free ferroelectric ceramics. IEEE Trans Ultrason Ferroelectr Freq Control 54(12):2493–2499
44. Takenaka T, Nagata H, Hiruma Y, Yoshii K, Matsumoto K (2007) Lead-free piezoelectric ceramics based on perovskite structures. J Electroceramics 19:259–265
45. Hiruma Y, Watanabe Y, Nagata H, Takenaka T (2007) Phase transition temperatures of divalent and trivalent ions substituted $(Bi_{1/2}Na_{1/2})TiO_3$ ceramics. Key Eng Materials 350:93–96
46. Kimura M, Minamikawa T, Ando A, Sakabe Y (1997) Temperature characteristics of $(Ba_{1-x}Sr_x)_2NaNb_5O_{15}$ ceramics. Jpn J Appl Phys 36:6051–6054

47. Doshida Y, Kishimoto S, Ishii K, Kishi H, Tamura H, Tomikawa Y, Hirose S (2007) Miniature cantilever-type ultrasonic motor using Pb-free multilayer piezoelectric ceramics. Jpn J Appl Phys 46:4921–4925
48. Ikegami S, Ueda I (1974) Piezoelectricity in ceramics of ferroelectric bismuth compound with layer structure. Jpn J Appl Phys 13(10):1572–1579
49. Takenaka T, Sakata K (1980) Grain orientation and electrical properties of hot-forged $Bi_4Ti_3O_{12}$ ceramics. Jpn J Appl Phys 19(1):31–39
50. Takenaka T, Sakata K (1984) Grain orientation effects on electrical properties of bismuth layer-structured ferroelectric $Pb_{(1-x)}(NaCe)_{x/2}Bi_4Ti_4O_{15}$ solid solution. J Appl Phys 55 (4):1092–1099
51. Takenaka T, Sakata K (1989) Piezoelectric and pyroelectric properties of calcium-modified and grain-oriented $(NaBi)_{1/2}Bi_4Ti_4O_{15}$ ceramics. Ferroelectrics 94:175–181
52. Takenaka T (2002) Grain orientation effects on electrical properties of bismuth layer-structured ferroelectric ceramics. J Ceram Soc Jpn 110(4):215–224
53. Zuo-Guang Ye (ed) (2008) Handbook of advanced dielectric, piezoelectric and ferroelectric materials (Part VII novel processing and new materials, No. 27 "Grain orientation and electrical properties of bismuth layer-structure ferroelectrics"), Woodhead Publishing Limited, CRC Press LLC, pp 818–851
54. Park S-E, Chung S-J (1994) Nonstoichiometry and the long-range cation ordering in crystals of $(Bi_{1/2}Na_{1/2})TiO_3$. J Am Ceram Soc 77(10):2641–2647
55. Pronin IP, Syrnikov PP, Isupov VA, Egorov VM, Zaitseva NV, Ioffe AF (1980) Peculiarities of phase transitions in sodium-bismuth titanate. Ferroelectrics 25:395–397
56. Zvirgzds JA, Kapostis PP, Zvirgzde JV (1982) X-ray study of phase transition in ferroelectric $(Bi_{0.5}Na_{0.5})TiO_3$. Ferroelectrics 40:75–77
57. Yi JY, Lee J-K, Hong K-S (2003) Dependence of the microstructure and the electrical properties of lanthanum-substituted $(Bi_{1/2}Na_{1/2})TiO_3$ on cation vacancies. J Am Ceram Soc 85(12):3004–3010
58. Herabut A, Safari A (1997) Processing and electrochemical properties of $(Bi_{1/2}Na_{1/2})_{1-1.5x}La_xTiO_3$ ceramics. J Am Ceram Soc 80(11)
59. Watanabe Y, Hiruma Y, Nagata H, Takenaka T (2008) Phase transition temperatures and electrical properties of divalent Ions (Ca^{2+}, Sr^{2+} and Ba^{2+}) substituted $(Bi_{1/2}Na_{1/2})TiO_3$ ceramics. Ceram Int 34(4):761–764
60. Wang XX, Tang XG, Chan HLW (2004) Electromechanical and ferroelectric properties of $(Bi_{1/2}Na_{1/2})TiO_3$–$(Bi_{1/2}K_{1/2})TiO_3$–$BaTiO_3$ lead-free piezoelectric ceramics. Appl Phys Lett 85 (1):91–93
61. Lin D, Xiao D, Zhu J, Yu P (2006) Piezoelectric and ferroelectric properties of $(Bi_{1-x-y}K_xLi_y)_{0.5}TiO_3$ lead free piezoelectric ceramics. Appl Phys Lett 88 art. no. 062901
62. Hiruma Y, Yoshii K, Nagata H, Takenaka T (2007) Investigation of phase transition temperatures on $(Bi_{1/2}Na_{1/2})TiO_3$-$(Bi_{1/2}K_{1/2})TiO_3$ and $(Bi_{1/2}Na_{1/2})TiO_3$-$BaTiO_3$ lead-free piezoelectric ceramics by electrical measurements. Ferroelectrics 346:114–119
63. Hiruma Y, Imai Y, Watanabe Y, Nagata H, Takenaka T (2008) Large electrostrain near the phase transition temperature of $(Bi_{0.5}Na_{0.5})TiO_3$-$SrTiO_3$ ferroelectric ceramics. Appl Phys Lett 92:262904
64. Hiruma Y, Yoshii K, Nagata H, Takenaka T (2008) Phase transition temperature and electrical properties of $(Bi_{1/2}Na_{1/2})TiO_3$-$(Bi_{1/2}A_{1/2})TiO_3$ (A = Li and K) lead-free ferroelectric ceramics. J Appl Phys 103:084121
65. Siny IG, Tu C-S, Schmidt VH (1995) Critical acoustic behavior of the relaxor ferroelectric $Na_{1/2}Bi_{1/2}TiO_3$ in the intertransition region. Phys Rev B 51:5659–5665
66. Tsurumi T, Sasaki T, Kakemoto H, Harigai T, Wada S (2004) Domain contribution to direct and converse piezoelectric effects of PZT ceramics. Jpn J Appl Phys 43:7618–7622
67. Hiruma Y, Watanabe T, Nagata H, Takenaka T (2008) Piezoelectric properties of $(Bi_{1/2}Na_{1/2})TiO_3$-based solid solution for lead-free high-power applications. Jpn J Appl Phys 47 (9B):7659–7663

68. Takahashi S, Hirose S (1992) Vibration-level characteristics of lead-zirconate-titanate ceramics. Jpn J Appl Phys 31:3055–3057
69. Hirose S, Magami N, Takahashi S (1996) Piezoelectric ceramic transformer using piezoelectric lateral effect on input and on output. Jpn J Appl Phys 35:3038–3041
70. Tashiro S, Ikehiro M, Igarashi H (1997) Influence of temperature rise and vibration level on electromechanical properties of high-power piezoelectric ceramics. Jpn J Appl Phys 36:3004–3009
71. Umeda M, Nakamura K, Ueha S (1998) The measurement of high-power characteristics for a piezoelectric transducer based on the electrical transient response. Jpn J Appl Phys 37:5322–5325
72. Kawada S, Ogawa H, Kimura M, Shiratsuyu K, Niimi H (2006) High-power piezoelectric vibration characteristics of textured $SrBi_2Nb_2O_9$ ceramics. Jpn J Appl Phys 45:7455–7459
73. Kawada S, Ogawa H, Kimura M, Shiratsuyu K, Higuchi Y (2007) Relationship between vibration direction and high-power characteristics of $<001>$ -textured $SrBi_2Nb_2O_9$ ceramics. Jpn J Appl Phys 46:7079–7083
74. Nagata H, Takenaka T (2001) Effects of substitution on electrical properties of $(Bi_{1/2}Na_{1/2})TiO_3$-based lead-free ferroelectrics. In: Proceedings of the 12th IEEE international symposium on the applications of ferroelectrics (ISAF XII 2000) (IEEE Catalog No. 00CH37076), pp 45–51
75. Zhu M, Liu L, Hou Y, Wang H, Yan H (2007) Microstructure and electrical properties of MnO-doped $(Na_{0.5}Bi_{0.5})_{0.92}Ba_{0.08}TiO_3$ lead-free piezoceramics. J Am Ceram Soc 90:120–124
76. Shannon RD (1976) Revised effective ionic radii and systematic studies of interatomic distances in halides and chalcogenides. Acta Cryst A32(5):751–767
77. Watanabe Y, Hiruma Y, Nagata H, Takenaka T (2009) Fabrication and electrical properties of $(Bi_{1/2}Na_{1/2})TiO_3$-$BiAlO_3$ ferroelectric ceramics. Key Eng Materials 388:229–232
78. Gerthsen P, Härdtl KH, Schmidt NA (1980) Correlation of mechanical and electrical losses in ferroelectric ceramics. J Appl Phys 51:1131–1134
79. Takahashi S (1982) Effects of impurity doping in lead zirconate-titanate ceramics. Ferroelectrics 41:143–156
80. Hayashi K, Ando A, Hamaji Y, Sakabe Y (1998) Study of the valence state of the manganese ions in $PbTiO_3$ ceramics by means of ESR. Jpn J Appl Phys 37:5237–5240
81. Hiruma Y, Nagata H, Takenaka T (2007) Grain-size effect on electrical properties of $(Bi_{1/2}K_{1/2})TiO_3$ ceramics. Jpn J Appl Phys 46:1081–1084
82. Takenaka T, Hiruma Y, Nemoto M, Nagata H (2008) Piezoelectric properties of $(Bi_{1/2}K_{1/2})TiO_3 - BaTiO_3$ ceramics with wide working temperatures. In: Extended abstract of the 17th international symposium on the applications of ferroelectrics (ISAF 2008), PL002
83. Hiruma Y, Nagata H, Takenaka T (2004) Dielectric, ferroelectric and piezoelectric properties of barium titanate and bismuth potassium titanate solid-solution ceramics. J Ceram Soc Jpn 112(5):S1125–S1128
84. Ivanova VV, Kapyshev, AG, Veenevtsev YN, Zhdanov GS (1962) X-Ray Determination of the Symmetry of Elementary Cells of the Ferroelectric Materials $(K_{0.5}Bi_{0.5})TiO_3$ and $(Na_{0.5}Bi_{0.5})TiO_3$ and of High-Temperature Phase Transitions in $(K_{0.5}Bi_{0.5})TiO_3$. Akad Nauk SSSR 26:354
85. Nemoto M, Hiruma Y, Nagata H, Takenaka T (2008) Fabrication and piezoelectric properties of grain-oriented (Bi1/2K1/2)TiO3-BaTiO3 ceramics. Jpn J Appl Phys 47:3829–3832
86. Takenaka T, Nagata H, Hiruma Y (2009) Phase transition temperatures and piezoelectric properties of $(Bi_{1/2}Na_{1/2})TiO_3$ and $(Bi_{1/2}K_{1/2})TiO_3$-based perovskite lead-free ferroelectric ceramics. IEEE Trans Ultrason Ferroelectr Freq Control 56(8):1595–1612

Chapter 9
Perovskite Lead-Free Piezoelectric Ceramics

Hyeong Jae Lee and Shujun Zhang

9.1 Introduction

For more than 50 years, lead zirconate titanate (PZT) and related lead-based perovskite compositions have been the mainstay for a wide range of piezoelectric applications, such as actuators, sensors, and ultrasound transducers, owing to their superior piezoelectric and electromechanical properties. In the last few years, research studies have become more concentrated in the development of lead-free piezoelectric ceramics with properties comparable to those of PZT ceramics due to environmental regulations, for example, the legislation regarding lead-containing equipment will be enforced in the EU as the draft directives on Waste from Electrical and Electronic Equipment (WEEE), Restriction of Hazardous Substances (RoHS), and end-of-life vehicles (ELV). It is expected that the USA and Japan will also have similar regulations in the near future.

The key material properties that are typically considered for piezoelectric applications are electromechanical coupling (k_{ij}), dielectric permittivity (ε_r), and piezoelectric coefficients (d_{ij}). For example, high strain actuators, such as fuel injectors, piezoelectric materials require high strain d_{33} , e.g., >600 pC/N with broad temperature usage range, being operational temperature range from −50 to 150°C [41]. For medical ultrasound transducers, the figure of merit is electromechanical coupling factor, since high coupling factor allows effective energy conversion in both transmitting and receiving energy, improving bandwidth and sensitivity of the transducer response. The dielectric permittivity (ε_r) of a piezoelectric material is an important consideration for the design of transducer since it determines the electrical impedance of the transducer. High permittivity is also beneficial for achieving high piezoelectric response of piezoelectric materials since ε_r is correlated to a piezoelectric constant (d_{ij})

H.J. Lee • S. Zhang (✉)
Material Research Institute, Pennsylvania State University, University Park, PA, USA
e-mail: soz1@psu.edu

S. Priya and S. Nahm (eds.), *Lead-Free Piezoelectrics*,
DOI 10.1007/978-1-4419-9598-8_9, © Springer Science+Business Media, LLC 2012

according to the following equation: $d_{ij} \sim 2Q_{ij}\varepsilon_r\varepsilon_0 P_i$, where Q_{ij} is the electrostrictive constant, ε_0 is the permittivity of free space, ε_r is the relative permittivity, and P_i is the remnant polarization.

Recently, lead-free piezoelectric materials have been reported to offer comparable properties to those of PZTs. Of significant contrast to PZT ceramics, however, they suffer from relatively low polymorphic phase transition temperatures (PPTs) or low depolarization temperature. This limits the implementation of lead-free ceramics into various piezoelectric applications that require wide operational temperature range. In this chapter, recent progress in lead-free piezoelectric ceramics is reviewed with emphasis on perovskite-type ferroelectric materials. The effects of chemical modification on the macroscopic properties of lead-free piezoelectric materials are presented, including enhanced dielectric and piezoelectric properties at morphotropic phase boundary (MPB), and modifications using donor and acceptor dopants, and subsequent improvement of the properties in comparison with donor and acceptor-doped PZTs. Special attention is devoted to demonstrating the thermal stability of these families of lead-free piezoelectric materials in relation to their respective PPTs or depolarization temperature.

9.2 Enhanced Piezoelectricity-PZTs

Piezoelectricity is the linear coupling between mechanical stress, X and polarization, P, or between electric field, E and strain, x ($P = d{\cdot}X$ or $x = d{\cdot}E$). "d" is piezoelectric coefficient, which is a third rank tensor (d_{jkl}), but "d" is frequently expressed using reduced matrix notation (d_{ij}). Currently, the majority of piezoelectric materials are ferroelectric materials, exhibiting a spontaneous polarization (P_s) in the absence of an electric field.

For the vast majority of piezoelectric applications, lead-based ferroelectric materials have been dominant for many years. High piezoelectric properties of PZT are attributed to the existence of an MPB, separating tetragonal and rhombohedral phases, at $x = 0.48$ $PbTiO_3$, as shown in Fig. 9.1. Near the MPB, the increased number of thermodynamically equivalent states can substantially enhance the alignment of randomly oriented ferroelectric domains, allowing optimum polarization under an applied electric field.

The properties of PZT ceramics can be further enhanced with the use of suitable dopant additions. To enhance and optimize the dielectric and piezoelectric properties of PZT ceramics, donor dopants, i.e., higher valency ions than those of host atoms (e.g., La^{3+} for Pb^{2+} or Nb^{5+} for Ti^{4+}/Zr^{4+}), are typically added to pure PZT systems. The addition of these dopants facilitates domain wall movements and leads to the material with enhanced dielectric, piezoelectric, and electromechanical properties, but reduces its mechanical quality factor and increase dielectric loss. These materials are so-called soft PZT (e.g., DoD type II and VI). In contrast, acceptor dopants stabilize the domain wall movement, resulting in the opposite effect of donor-doped PZT; reducing dielectric and piezoelectric properties,

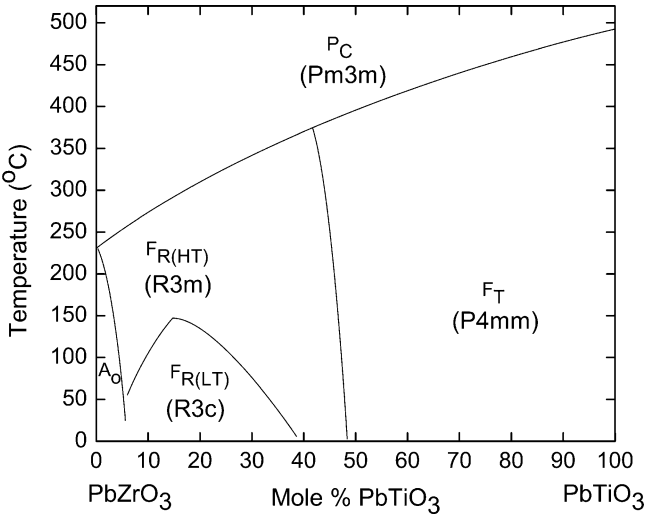

Fig. 9.1 Structural phase diagram for the $(1 - x)PbZrO_3$-$xPbTiO_3$ (P_C – paraelectric cubic phase, F_R ferroelectric rhombohedral phase, and F_T ferroelectric tetragonal phase) [19]

Table 9.1 Typical values for the dielectric, piezoelectric, and electromechanical properties of some selected PZT materials

Material	PZT	DoD II	DoD VI	DoD I	DoD III
T_C (°C)	386	365	190	328	300
ε_r	730	1,700	3,400	1,300	1,000
tan δ	0.004	0.02	0.02	0.004	0.004
d_{33} (pC/N)	223	375	590	289	225
k_{33}	0.67	0.71	0.75	0.7	0.64
E_C (kV/cm)		15	6–8	14	22
Q_m	500	75	65	500	1,000

but increasing mechanical quality factor. These materials are referred to as hard PZT (e.g., DoD type I and III). Although any lowering of dielectric and piezoelectric properties is not desirable for piezoelectric applications, high-power and/or high-voltage applications, such as ultrasonic motors, transformers, and high intensity focused ultrasound (HIFU) therapy, require high mechanical quality factor and low dielectric loss in order to deliver high acoustic power without excessive heat generation [56, 69]. Typical values of the piezoelectric and other properties of soft and hard PZTs are given in Table 9.1.

The origin of enhanced piezoelectric properties of PZT with donor dopants is believed to be due to a reduction in oxygen vacancies. Owing to the high volatility of PbO, there is a high chance of lead loss during the sintering process, followed by the formation of lead vacancies. The created lead vacancies ionize negatively charged lead vacancies and holes, which could act as acceptors, attracting electrons from the surrounding oxygens and leaving oxygen vacancies in the lattice.

The increased number of oxygen vacancies impedes the mobility of domain walls and reduces the dielectric and piezoelectric properties, which will be more discussed in the following paragraph. However, the addition of donor dopants reduces oxygen vacancies, and creates the defect dipoles between the donors and lead vacancies, providing the condition for enhanced domain wall movements.

Hardening of piezoelectric materials can be attributed to the acceptor-oxygen vacancy defect dipoles. When an acceptor dopant is incorporated into PZT, the positively charged oxygen vacancies are created in order to compensate the negatively charged acceptors, forming acceptor-oxygen vacancy defect dipoles. In cubic phase, defect dipoles are randomly oriented via oxygen vacancy diffusion, but when the material is no longer cubic, the oxygen vacancies occupy energetically preferred site in the lattice, and align parallel with spontaneous polarization direction, resulting in the development of internal bias. This internal bias stabilizes domain wall motion, leading to the material with low dielectric and mechanical loss [4, 11, 38, 51].

9.3 Lead-Free Perovskites

Lead-free piezoelectric materials can be categorized as tungsten bronze, aurivillius (bismuth layer structured ferroelectrics), and perovskite families. Among the most researched lead-free compositions, perovskite-type ferroelectrics are of interest as replacements for PZT since relatively high dielectric and piezoelectric properties were found in this crystal structure.

Currently, the most actively studied lead-free piezoelectric compositions are barium titanate, bismuth sodium titanate (BNT), and potassium sodium niobate (KNN) family. Barium titanate, due to its high dielectric ($\varepsilon_r \sim 1{,}900$) and piezoelectric properties ($d_{33} \sim 190$ pC/N) [19], has been used in a wide range of applications from capacitors to piezoelectric applications before the advent of PZT ceramics. The main limitations of barium titanate are its low Curie temperature ($T_C \sim 120°C$) and the occurrence of multiple polymorphic phase transitions. The low T_C of barium titanate limits its upper use temperature, and the multiple polymorphic phase transitions cause significant temperature-dependent properties. BNT and potassium sodium niobate, on the other hand, have high T_C (>300°C), but have moderate dielectric and piezoelectric properties, with $\varepsilon_r < 500$, and $d_{33} < 100$ pC/N.

The property comparisons of various piezoelectric materials, including non-perovskite and perovskite lead- and lead-free-based ceramics, are demonstrated in Fig. 9.2. As shown, perovskite ceramics including lead and lead-free materials provide higher dielectric and piezoelectric properties than non-perovskite-based materials. However, it should be noted that lead-free-based piezoelectric ceramics generally have inferior piezoelectric activity to lead-based piezoelectric ceramics. In addition to the lower dielectric and piezoelectric properties, the presence of depolarization temperature (T_d) of BNT-based system and orthorhombic-tetragonal

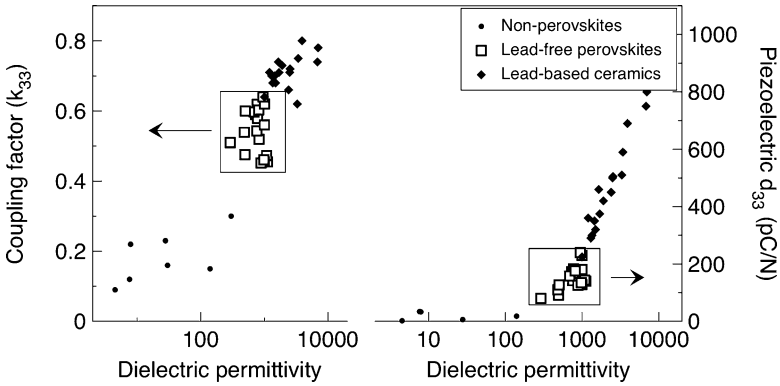

Fig. 9.2 Room temperature electromechanical coupling k_{33} (*left*) and piezoelectric coefficient d_{33} (*right*) as a function of dielectric permittivity for various piezoelectric ceramics. (Non-perovskites include piezoelectric polymer, lithium niobate, tungsten bronze, and bismuth layer structured ferroelectrics.) Data from refs. [8, 12, 17, 19, 21, 22, 24, 25, 28, 36, 37, 43, 46, 47, 54, 60, 62, 63, 67, 69, 76]

phase transition ($T_{O–T}$) of KNN-based system below T_C causes strong temperature dependence of piezoelectric properties, resulting in a serious limiting factor for their implementation. Considerable research and developments have been made on lead-free piezoelectric ceramics to overcome the issues, and some progresses have been made, which are presented in the following sections.

9.4 Barium Titanate

Barium titanate is one of the most widely studied ferroelectric materials. In particular, the effects of various additives on the PPTs of this material have been extensively studied. The notable example of the effects of additives on barium titanate is depicted in Fig. 9.3. As can be seen, the substitution of isovalent ions effectively shifts PPTs of barium titanate. For example, the addition of calcium (Ca^{2+}) and/or lead (Pb^{2+}) to barium titanate leads to a decrease in two low PPTs (i.e., rhombohedral-orthorhombic ($T_{R–O}$) and orthorhombic-tetragonal ($T_{O–T}$) transition temperatures), without lowering T_C, while B site (Ti^{4+}) substitution, such as Zr^{4+}, Hf^{4+}, and Sn^{4+}, raises $T_{R–O}$ and $T_{O–T}$, with lowering T_C, resulting in a single PPT when the concentration of the B site substitution is above critical value ($\geq$15 mol%).

Based on the relationship between PPT and additives, Liu and Ren [27] reported new barium titanate-based ferroelectric system, $(1 - x)Ba(Zr_{0.2}Ti_{0.8})O_3–x(Ba_{0.7}Ca_{0.3})TiO_3$ (abbreviated as $(1 - x)$BZT-xBCT), whose composition shows high dielectric ($\varepsilon_r = 3{,}060$) and piezoelectric properties ($d_{33} = 620$ pC/N) at $x = 0.50$, which are comparable to those of soft PZTs.

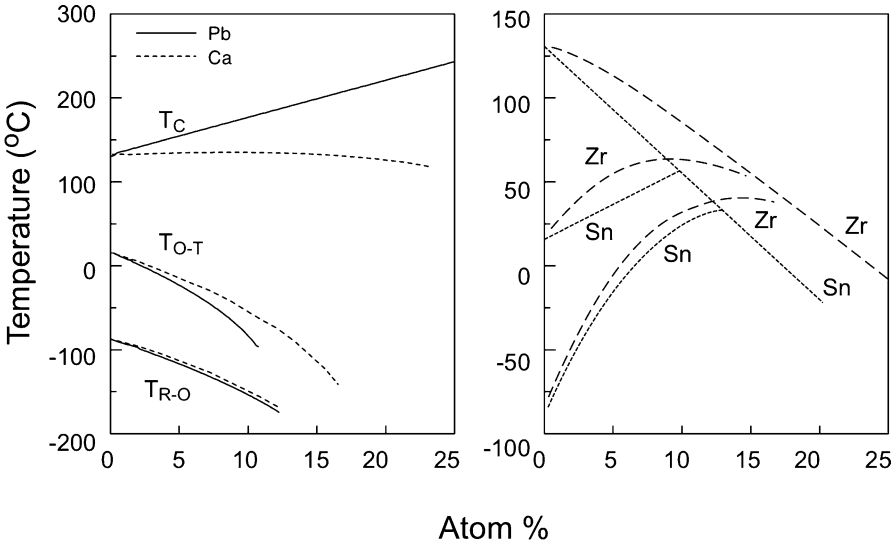

Fig. 9.3 Phase transition temperatures of the $BaTiO_3$ ceramic system as a function of the amount (x) of the substituted ions [19]

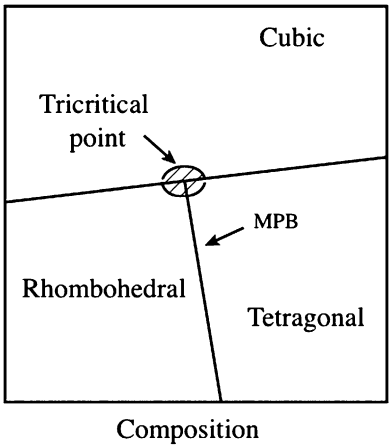

Fig. 9.4 Schematic of a triple-point-type MPB between tetragonal and rhombohedral phases [27]

According to Liu and Ren [27], a large piezoelectricity of this system is due to the existence of cubic-rhombohedral-tetragonal (C-R-T) triple point, as depicted in Fig. 9.4. In fact, lead-free-based MPB systems generally have polymorphic type MPB, which yields a large energy barrier between two polarization states, impeding polarization rotation mechanism. However, in the case of $(1 - x)$BZT-xBCT system, BZT is in the rhombohedral phase at room temperature as the three transition temperatures are pinched into one rhombohedral-cubic phase transition

with the addition of 20 mol% Zr. Likewise, the substitution of 30 mol% Ca at Ba sites shifts low transition temperatures, $T_{O–T}$ and $T_{R–O}$, downward, stabilizing tetragonal phase $(Ba_{0.7}Ca_{0.3})TiO_3$ (BCT) at room temperature (see Fig. 9.3). Therefore, the solid solution of these two end members yield MPB, starting from a triple point of cubic phase (C), rhombohedral (R), and tetragonal (T) phases, similar to lead-based MPB systems.

Another approach to achieve high piezoelectricity is through microstructural optimization. It is well known that the properties of barium titanate are strongly dependent on the grain size, reported that ε_r of coarse-grained ($\geq$10 μm) barium titanate is on the order of 1,500–2,000, while that of fine-grained (~1 μm) barium titanate is approximately 6,000, as a result of ferroelectric domain effects [1, 3]. The high level of piezoelectricity reported with reduced grain size. For example, Takahashi et al. [49, 50] synthesized barium titanate ceramic by microwave sintering method, and found that barium titanate with grain size ~3.4 μm showed high dielectric and piezoelectric properties ($\varepsilon_r \sim 4{,}000$ and $d_{33} = 350$ pC/N). Karaki et al. [20] reported more improved dielectric ($\varepsilon_r \sim 5{,}000$) and piezoelectric properties ($d_{33} = 460$ pC/N) with grain size of ~1.6 μm, approaching the properties observed in lead-based piezoelectric materials. The origin of these improved piezoelectric properties is believed to be due to the increased domain density with decreasing grain size [58]. However, even with comparable dielectric and piezoelectric properties to those of PZT, its low T_C is still a major hindrance for use in various piezoelectric applications.

9.5 BNT-Based System

BNT is a perovskite, ferroelectric material with rhombohedral symmetry at room temperature, discovered by Smolenskii et al. [48]. A large remnant polarization, $P_r = 38$ μC/cm^2 and a high coercive field, $E_C = 73$ kV/cm, together with high T_C of ~320°C make this system attractive alternative to lead-based piezoelectric materials.

An MPB separating rhombohedral and tetragonal phase exists in the BNT system with other perovskite materials with tetragonal symmetry, such as $BaTiO_3$(BT) and $Bi_{0.5}K_{0.5}TiO_3$ (BKT). The phase diagram of $(1 - x)$BNT-xBKT (BNKT) and $(1 - x)$BNT-xBT (BNBT) are schematically shown in Fig. 9.5, note that a phase boundary that separates rhombohedral and tetragonal phase can be found at $x \sim 6$–7 mol% for $(1 - x)$BNT-xBT and at $x \sim 16$–20 mol% for $(1 - x)$ BNT-xBKT [44, 54].

Figure 9.6 shows the dielectric properties of BNT-based solid solutions as a function of composition, with those of PZT for comparison. Analogous to PZT, a maximum in dielectric permittivity was reported near MPB, whose compositions also give a maximum in piezoelectric properties as a result of enhanced polarizability. Selected properties of MPB compositions of BNT-based solid solutions are summarized in Table 9.2.

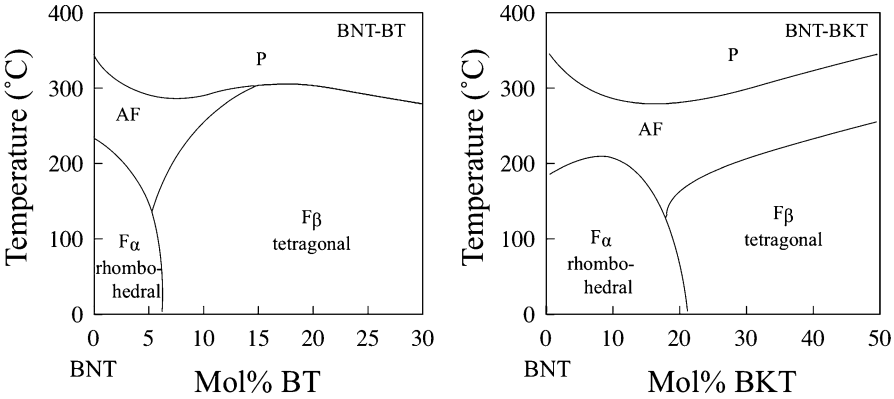

Fig. 9.5 Simplified phase diagram for $(Bi_{0.5}Na_{0.5})TiO_3$-$BaTiO_3$ (*left*) [54] and $(Bi_{0.5}Na_{0.5})TiO_3$-$Bi_{0.5}K_{0.5}TiO_3$ [55]. Copyright 2009 IEEE (*right*) (F_α ferroelectric rhombohedral phase; F_β ferroelectric tetragonal phase; *AF* antiferroelectric phase; *P* paraelectric phase)

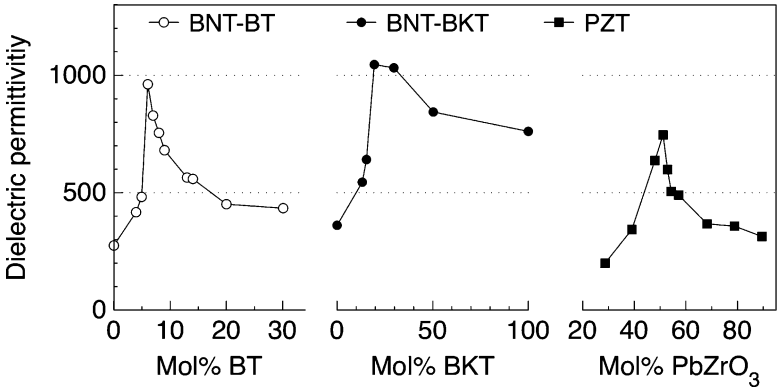

Fig. 9.6 Enhanced dielectric permittivity in PZT- and BNT-based system near MPB. Data from refs. [19, 44, 54]

Table 9.2 Various properties of $(Bi_{0.5}Na_{0.5})TiO_3$ (BNT)-based piezoceramics (BNKT(x) = $(1-x)$BNT-xBKT, BNBT(x) = $(1-x)$BNT-xBT)

System	T_C/T_d (°C)	ε_r	d_{33} (pC/N)	d_{31} (pC/N)	k_p	k_{31}	k_{33}
BNKT (0.20) [44]	280/160 [14]	650	~150 [14]	46.9	0.27	0.165	–
BNBT (0.06) [54]	288/130	580	125	40		0.19	0.55

In contrast to PZT system, however, some drawbacks have been noted for BNT-based systems. In general, the working temperature range of piezoelectric applications is limited by T_C of the piezoelectric material since above T_C, the perovskite structure is centro-symmetry (cubic phase); thus, there is no spontaneous polarization and hence no piezoelectric properties. As a general rule of thumb, piezoelectric materials can be safely used to approximately half of their T_C in order to avoid partial depoling. In the case of BNT-based systems, however, there is

Table 9.3 Dielectric and piezoelectric properties of binary BNBT (0.06) and BNBT (0.06) with additives

Dopant	T_d (°C)	ε_r	d_{33} (pC/N)	k_p	References
–	130	580	125	0.32	[54]
Nd (0.4 wt.%)	110	1,947	175	0.31	[8]
La (1.5 mol%)	100	1,520	133	0.29	[24]
Nb (1 wt.%)	100	1,614	118	0.2	[25]
Ag (6 mol%)	100	920	168	0.31	[21]
Ta (1 mol%)	89	1,861	171	0.33	[76]
$CeO_2 + La_2O_3$	60	831	162		[60]
CaO + MnO	95	1,137	179	0.37	[63]

ferroelectric to anti-ferroelectric phase transformation prior to the prototypic cubic phase transformation, with the strongly curved phase boundaries between rhombohedral and tetragonal phase (see Fig. 9.5). This causes thermal instability at elevated temperatures, and reduces the working temperature range.

Due to the limitations of low thermal stability with moderate piezoelectric properties of binary MPB compositions, several different approaches have been proposed, such as chemical modifications with dopants, compositional adjustment near MPB, and more complex systems through the use of ternary solid solutions. Various additives have been employed to improve the dielectric and piezoelectric properties. The application of these dopants only provides limit success due to the presence of depolarization temperature, T_d. Table 9.3 shows some of the properties of $(Bi_{0.5}Na_{0.5})_{0.94}Ba_{0.06}TiO_3$ (BNBT0.06) solid solutions with various additives. As can be seen, the addition of these dopants appears to improve dielectric and piezoelectric properties; however, the improvements of piezoelectric properties were accompanied with a significantly reduced T_d, limiting practical use of this system.

The properties of ternary solid solutions with MPB and off MPB, e.g., tetragonal and rhombohedral phases, have been explored. It was reported that ternary BNT-BKT-BT and BNT-BKT-$Bi_{0.5}Li_{0.5}TiO_3$ (BLT) solid solutions exhibit highest piezoelectric properties near MPB, but have low T_d. Off MPB ternary compositions, on the other hand, offer comparable piezoelectric properties to binary systems, with higher T_d. An example of this is demonstrated in Fig. 9.7. It can be observed that although room temperature d_{33}s of both binary- and ternary-based system decreases with increasing T_d, ternary systems have higher piezoelectric properties in relation to their respective T_d.

One of the characteristics of BNT system is high coercive field, ($E_C = 73$ kV/cm) and high mechanical quality factor ($Q_m = \sim 450$) [44, 48]. Even soft BNT-based systems (MPB composition) possess high $E_C > 30$ kV/cm, which is higher than that of the hard PZTs. ($E_C \sim 20$ kV/cm) [70]. However, the reported mechanical Q_ms of binary or ternary BNT-based system are only 100–200, limiting the use of modified BNT-based system in many high-power applications. In an effort to improve the mechanical Q_m, acceptor-modified BNT-based systems have been reported, and it was found that $Mn^{2+,3+}$ and/or Co^{3+} ions effectively improve mechanical Q_m of BNT-based systems, increasing Q_m from 100 to 600–800 [13, 16].

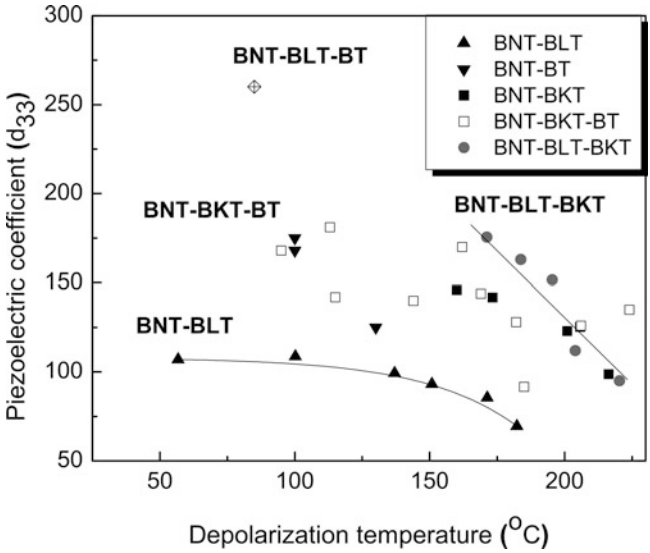

Fig. 9.7 Room temperature piezoelectric coefficients (d_{33}) of binary and ternary BNT-based lead-free piezoceramics as a function of depolarization temperature (T_d). Data from refs. [8, 12, 21, 24, 25, 36, 54, 60, 62, 63, 67, 76]

One of the interesting features of BNT-based system is its superior high-power characteristics to hard PZT system. In fact, although mechanical Q_m is a good indication of material performance for high-power applications, it does not provide high-power characteristics under high electrical drive (>1 V). This is because the electromechanical properties are usually determined under small signal condition (~1 V). For example, hard PZT ceramics possess high Q_m (500–1,000) under small signal drive, but it was shown that Q_m significantly decreased with increasing drive, limiting maximum vibration velocity [52, 53, 57]. Interestingly, Mn-modified BNT-based system exhibited relatively small decrease in Q_m with vibration velocity, resulting in higher maximum vibration velocity than hard PZT ceramics [13]. The results indicate that acceptor-modified BNT-based systems are promising candidates for high-power applications.

9.6 KNN and Modified KNN System

$KNbO_3$ is another class of lead-free piezoelectric material with perovskite structure, exhibiting phase transitions similar to barium titanate. The transitions from cubic to tetragonal, tetragonal to orthorhombic, and then orthorhombic to rhombohedral occur at 435, 225, and −10°C, respectively [35, 61].

$KNbO_3$ (KN) and $NaNbO_3$ (NN) can form a solid solution over the whole composition range and undergo similar structural phase transitions to KN upon

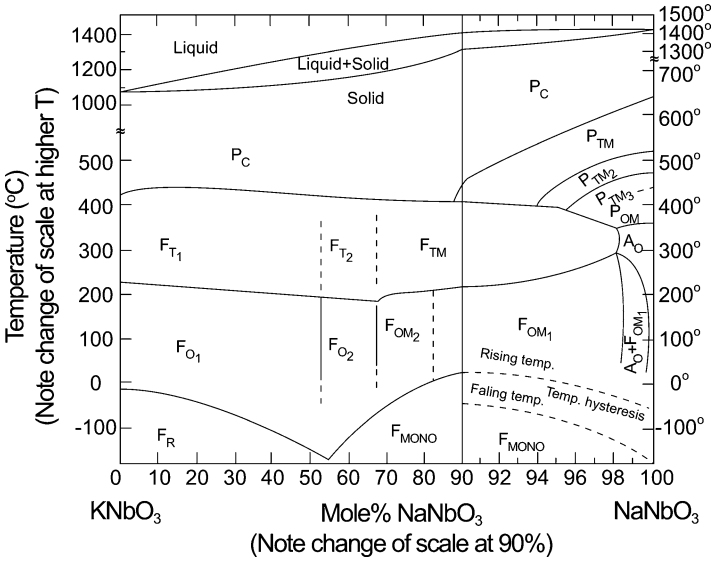

Fig. 9.8 Structural phase diagram for the $KNbO_3$ – $NaNbO_3$ (*note*: the orthorhombic-orthorhombic MPB is at 50 mol% $NaNbO_3$) [19]

Table 9.4 Various properties of KNN ceramics prepared by air sintering, hot pressing or spark-plasma sintering (SPS)

Properties	Air fired [7]	Hot pressing [18]	SPS [26, 65]
Density (g/cm^3)	4.25	4.46	4.47
ε_r	290	420	606
tan δ	0.04	0.02	0.04
k_p (%)	36	45	38.9
d_{33} (pC/N)	80	160	148
Q_m	130	240	

Theoretical density of KNN is 4.51 g cm^3

cooling (see Fig. 9.8). The dielectric and piezoelectric properties of KN-NN have been examined as a function of K/Na ratio, and highest planar coupling (k_p) was found when the ratio of K/Na is equal to 1, reaching $k_p \sim 0.36$ [19]. The enhanced coupling factor of $(K_{0.5}Na_{0.5})NbO_3$ has been attributed to the formation of MPB between two orthorhombic ferroelectric phases.

A major issue of KNN materials is difficulty in the processing of dense ceramics because of the instability of the phase at elevated temperatures and the evaporation of the alkali components during sintering. The importance of material density on the properties is evident from Table 9.4; the samples using pressure or electric field-assisted sintering yielded a high value of dielectric and piezoelectric properties as a result of improved material density. Note that recently processed KNN ceramics with optimized processing conditions, such as modifying starting particle sizes and/or

Table 9.5 The relative density, dielectric permittivity and loss, piezoelectric properties of doped KNN ceramics

Additives	Relative density (%)	ε_r	tan δ	k_p	d_{33} (pC/N)
Sn (1 mol%) [29, 30]	98	627	0.05	39	108
Ca (0.5 mol%) [29, 30]	94	495	0.12	–	95
Ba (0.5 mol%) [29, 30]	94.1	–	–	43.1	–
Sr (0.5 mol%) [29, 30]	96	500	0.04	–	95
Zn (1 mol%) [74]	97	652	0.03	44	117
Zn (1 mol%) [45]	97	500	–	40	121
Cu (0.4 mol%) [34]	97	400	<0.003	40	–

Theoretical density of KNN is 4.51 g cm^3

optimizing sintering conditions, also led to improved density and compositional uniformity, account for the enhanced dielectric ($\varepsilon_r \sim 600$) and piezoelectric properties ($d_{33} \sim 120$ pC/N) [2, 6, 74].

One of the cost-effective means to promote the densification of KNN ceramics is to use sintering aids. The improved density of KNN ceramics has been reported through A-site or B-site addition and/or substitution under conventional solid-state sintering method. For example, an improvement in density was achieved by introducing CuO and the excess of the B-site ions in the ABO_3 lattice, caused by the formation of a liquid phase [32, 33]. The authors also reported that the incorporation of CuO (and/or KCuTaO, KCuNbO) into KNN system led to hardening, increasing the coercive field and mechanical quality factor [31, 34, 66]. The addition of Zn^{2+}, Sc^{2+}, Sn^{4+}, Cd^{2+}, and Ca^{2+} also led to the improved density and piezoelectric properties. By contrast, some of dopant ions degrade densification of KNN ceramics, such as Mg^{2+} and Ba^{2+} [29, 30]. The incorporation of CeO_2, Y_2O_3, and WO_3 into KNN also severely degrades the densification of KNN ceramics [74]. The effects of sintering aids on the density and properties of KNN ceramics are summarized in Table 9.5.

In recent years, Saito and coworkers [42, 43] reported new MPB composition of KNN system, induced by the mixture of high T_C end members, perovskite KNN ($T_C = 420°C$), and pseudo-ilmenite-type $LiTaO_3$ ($T_C = 615°C$). The most interesting feature of this system is its comparable piezoelectric properties and T_C to those of PZT system, as can be seen in Fig. 9.9. The discovery of large piezoelectricity in Li, Ta, and Sb-modified KNN ceramics stimulated a number of systematic investigations on KNN materials.

Subsequent work has been followed to investigate the role of additives on KNN system, and revealed that the enhanced piezoelectric properties of Li, Ta, and Sb-modified KNN ceramics are, in fact, as a result of shifting the PPT to near room temperature (RT) [46, 70, 72]. For instance, it was found that the T_C shifts upward, and $T_{O–T}$ shifts downward compared to pure KNN by substituting lithium at A site of KNN. With 6 mol% $LiNbO_3$, the $T_{O–T}$ shifted to ~RT, and the samples showed peak values of piezoelectric and electromechanical properties, with $d_{33} \sim 200–235$ pC/N and $k_p \sim 0.38–0.44$ [9, 15, 59]. Similarly, with increasing $LiTaO_3$ content up to 5 mol%, the T_C shifted to a higher temperature (~430°C),

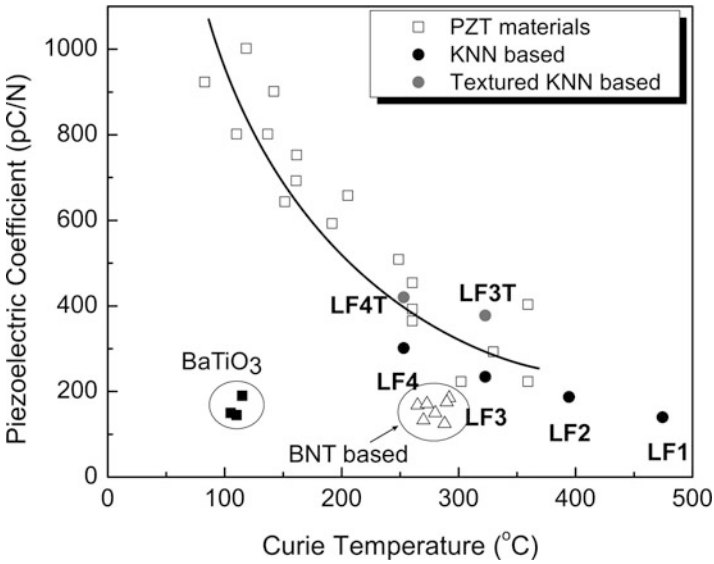

Fig. 9.9 Room temperature piezoelectric coefficient (d_{33}) as a function of Curie temperature (T_C) for lead-free (LF) and PZT ceramics. Data from refs. [8, 12, 19, 21, 24, 25, 36, 43, 46, 54, 60, 62, 63, 67, 76]

while T_{O-T} shifted to a lower temperature (~50°C) [10]. In $LiSbO_3$-modified KNN ceramics, both T_C and the T_{O-T} were found to decrease with increasing $LiSbO_3$ content [64].

New solid solution of KNN with other perovskite end members has been explored in the search for new MPBs. The effects of adding perovskite compounds, such as $BaTiO_3$ and $SrTiO_3$, into KNN system are quite similar to those of Li, Ta, and Sb-modified KNN system, exhibiting a decrease in polymorphic T_{O-T} and T_C, except for $AgNbO_3$ [23]. Interestingly, the formation of solid solution of xKNN-$(1 - x)AgNbO_3$ system demonstrates a relatively small shift of T_{O-T} with increasing x. With the addition of 18 mol% $AgNbO_3$ to KNN, the T_{O-T}, k_p and d_{33} were reported to be 170°C, 42.5%, and 186 pC/N, respectively. The reported properties of modified KNN compositions are summarized in Table 9.6.

Such a shift of T_{O-T} to near RT causes several problems, such as strong temperature-dependent properties and property degradation during thermal cycling. An example of this is demonstrated in Fig. 9.10. From the small insets in Fig. 9.10, a maximum value of the piezoelectric properties can be observed in proximity to RT, but the degraded properties can be observed as deviating from RT. Moreover, as shown in Fig. 9.10, the electromechanical coupling factors were found to decrease by 10% with thermal cycling as a result of cycling through regions with distinctly different domain configuration, significantly limiting their temperature range of operations [68].

Table 9.6 Dielectric and piezoelectric properties of $(1 - x)$ KNN-$x$$ABO_3$

ABO_3	x	T_C/T_{O-T} (°C)	ε_r	k_p	d_{33} (pC/N)	References
$LiNbO_3$	0.06	470/40	500	0.42	235	[9]
$LiTaO_3$	0.05	430/50	570	0.36	200	[10]
$LiSbO_3$	0.05	392/45	1,288	0.50	283	[64]
$CaTiO_3$	0.05	306/~RT	1,316	0.41	241	[40]
$BaTiO_3$	0.05	T_{O-T} ~ RT	1,058	0.36	225	[39]
$SrTiO_3$	0.05	T_{O-T} ~ RT	1,447	0.40	220	[5]
$BiScO_3$	0.02	340/~RT	–	0.45	210	[75]
$AgNbO_3$	0.18	355/~170	~500	0.425	186	[23]

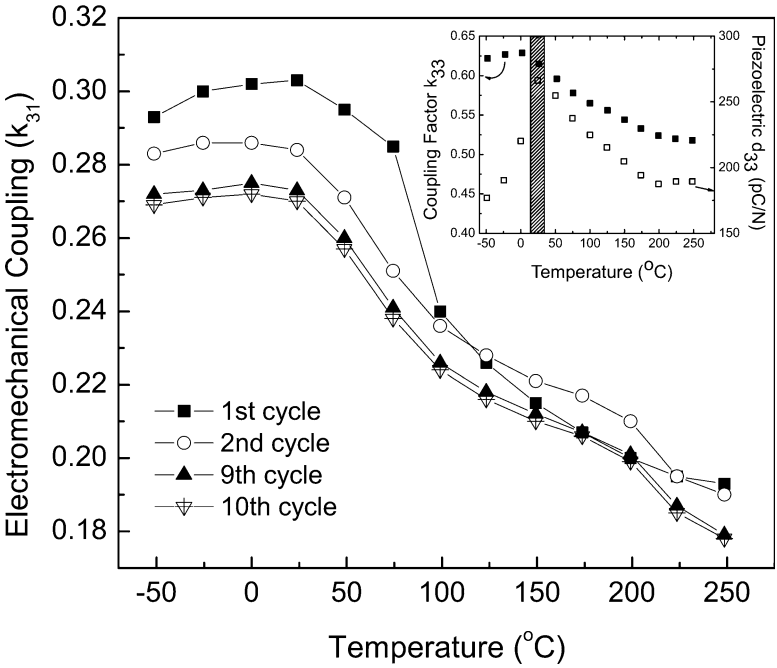

Fig. 9.10 Electromechanical coupling factor (k_{31}) as a function of thermal cycle for KNN-$LiSbO_3$ lead-free piezoelectric materials (*insets* show temperature dependence of electromechanical coupling (k_{33}) and piezoelectric (d_{33}) properties) (reprinted with permission from ref. [72]. Copyright 2006. American Institute of Physics)

In an attempt to improve thermal stability and mitigate property degradation, further modification has been made on KNN system with the addition of calcium to the KNN system because calcium is known as an effective dopant to shift lower PPTs of $BaTiO_3$ downward without decreasing T_C.

Figure 9.11 shows the temperature-dependent properties of modified KNN system. It can be seen that the change of the electromechanical coupling of unmodified KNN-$LiSbO_3$ ceramics is on the order of >16%, while the change of the $CaTiO_3$

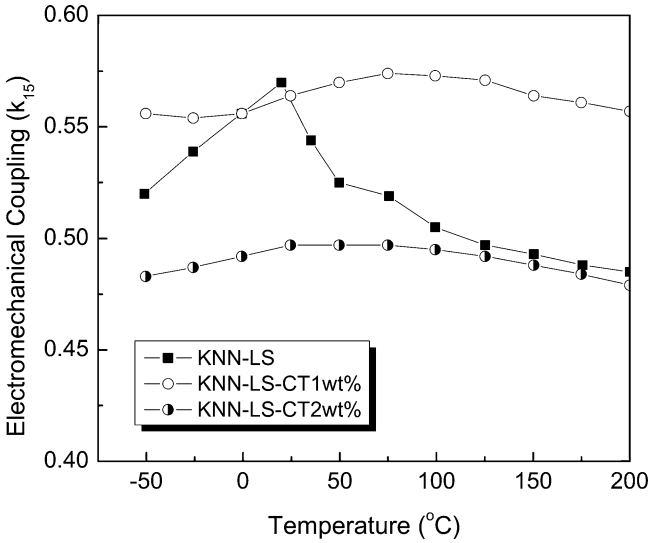

Fig. 9.11 Temperature dependence of shear mode electromechanical coupling factor (k_{15}) for unmodified and $CaTiO_3$ modified KNN-$LiSbO_3$ piezoelectric ceramics (reprinted with permission from ref. [71]. Copyright 2007. American Institute of Physics)

(CT) modified materials is less than 1% in the temperature range of −50 to 200°C. Although the dielectric and piezoelectric properties of KNN-$LiSbO_3$ system decreased with increasing CT ($\varepsilon_r = 1{,}020$ and $d_{33} \sim 180$ pC/N with the addition of 2 wt.% CT), the thermal stability of KNN-$LiSbO_3$ greatly improved over the range of −50 to 200°C [72, 73].

9.7 Summary

Environmental and safety concerns of utilization, recycling, and disposal of lead containing piezoelectric materials have induced a new surge in developing lead-free piezoelectric materials. The perovskite families of barium titanate, sodium potassium niobate and BNT described being promising candidates for lead-free piezoelectric materials to replace lead-based PZT family.

Although the dielectric and piezoelectric properties of these systems have been improved with the application of the concept of the MPB, the properties of presently available lead-free materials are still inferior to those of PZT ceramics. Additionally, a low Curie temperature of barium titanate and the presence of secondary phase transition, such as depolarization temperature of BNT- and the PPT of KNN-based materials, are serious limiting factors for the implementation of these materials into various piezoelectric applications. Moreover, in almost all

cases, chemical modification to lead-free piezoelectric ceramics degraded thermal stability, lowering Curie temperature and/or the polymorphic phase transitions.

For a replacement of PZT ceramics, it is necessary that the required piezoelectric properties are classified and developed for specific applications. Despite lower piezoelectric properties and thermal instability of lead-free piezoelectric ceramics, there are some advantages over lead-based piezoelectric materials. For instance, lead-free-based piezoelectric materials offer comparable thickness coupling factor, lower density, and lower dielectric permittivity, compared to PZT ceramics. This is clearly advantage for single element ultrasound transducers in medical imaging since the low density and low dielectric permittivity result in better impedance matching to tissue and electronics, respectively, allowing an efficient energy transfer from the transducer to tissue or vice versa. For high-power applications, the reported mechanical quality factor of acceptor-doped lead-free piezoelectric ceramics were comparable to those of hard PZT ceramics. In particular, acceptor-doped BNT-based ceramics offer much higher coercive field than hard PZT ceramics, promising for high-power applications. For the case of actuator applications that require broad temperature range with high d_{33}s, $CaTiO_3$-modified KNN-based ceramic seems to be an attractive candidate since it offers good thermal stability and fatigue-free characteristics in the temperature range of −50 to 200°C.

Acknowledgment The authors thank Prof. Thomas R. Shrout for the helpful discussions.

References

1. Arlt G, Hennings D, de With G (1985) Dielectric properties of fine-grained barium titanate ceramics. J Appl Phys 58(4):1619–1625
2. Birol H, Damjanovic D, Setter N (2006) Preparation and characterization of $(K_{0.5}Na_{0.5})NbO_3$ ceramics. J Eur Ceram Soc 26(6):861–866
3. Buessem W, Cross A, Goswami A (1992) Phenomenological theory of high permittivity in fine-grained barium titanate. J Am Ceram Soc 49(1):279
4. Carl K, Hardtl K (1978) Electrical after-effects in Pb(Ti, Zr)O_3 ceramics. Ferroelectrics 17:473–486
5. Cho K, Park H, Ahn C, Nahm S, Uchino K, Park S, Lee H (2007) Microstructure and piezoelectric properties of $0.95(Na_{0.5}K_{0.5})NbO_3$-$0.05SrTiO_3$ ceramics. J Am Ceram Soc 90(6):1946–1949
6. Du H, Li Z, Tang F, Qu S, Pei Z, Zhou W (2006) Preparation and piezoelectric properties of $(K_{0.5}Na_{0.5})NbO_3$ lead-free piezoelectric ceramics with pressure-less sintering. Mater Sci Eng B 131(1–3):83–87
7. Egerton L, Dillon DM (1959) Piezoelectric and dielectric properties of ceramics in potassium-sodium niobate system. J Am Ceram Soc 42:438–442
8. Fu P, Xu Z, Chu R, Li W, Zang G, Hao J (2010) Piezoelectric, ferroelectric and dielectric properties of Nd_2O_3-doped $(Bi_{0.5}Na_{0.5})_{0.94}Ba_{0.06}TiO_3$ lead-free ceramics. Mater Sci Eng B 167 (3):161–166
9. Guo Y, Kakimoto K, Ohsato H (2004) Phase transitional behavior and piezoelectric properties of $(Na_{0.5}K_{0.5})NbO_3$-$LiNbO_3$ ceramics. Appl Phys Lett 85:4121

10. Guo Y, Kakimoto K, Ohsato H (2005) $(K_{0.5}Na_{0.5})NbO_3$-$LiTaO_3$ lead-free piezoelectric ceramics. Mater Lett 59(2–3):241–244
11. Haerdtl K (1982) Electrical and mechanical losses in ferroelectric ceramics. Ceram Int 8 (4):121–127
12. Hiruma Y, Nagata H, Takenaka T (2007) Phase-transition temperatures and piezoelectric properties of $(Bi_{1/2}Na_{1/2})TiO_3$-$(Bi_{1/2}Li_{1/2})TiO_3$-$(Bi_{1/2}K_{1/2})TiO_3$ lead-free ferroelectric ceramics. IEEE Trans Ultrason Ferroelectr Freq Control 54(12):2493–2499
13. Hiruma Y, Watanabe T, Nagata H, Takenaka T (2008) Piezoelectric properties of $(Bi_{1/2}Na_{1/2})TiO_3$-based solid solution for lead-free high-power applications. Jpn J Appl Phys 47 (9):7659–7663
14. Hiruma Y, Yoshii K, Nagata H, Takenaka T (2008) Phase transition temperature and electrical properties of $(Bi_{1/2}Na_{1/2})TiO_3$-$(Bi_{1/2}A_{1/2})TiO_3$ (A = Li and K) lead-free ferroelectric ceramics. J Appl Phys 103(8):084121
15. Hollenstein E, Davis M, Damjanovic D, Setter N (2005) Piezoelectric properties of Li-and Tamodified $(K_{0.5}\ Na_{0.5})NbO_3$ ceramics. Appl Phys Lett 87:182905
16. Hu H, Zhu M, Xie F, Lei N, Chen J, Hou Y, Yan H (2009) Effect of Co_2O_3 additive on structure and electrical properties of $85(Bi_{1/2}Na_{1/2})TiO_3$-$12(Bi_{1/2}K_{1/2})TiO_3$-$3BaTiO_3$ lead-free piezoceramics. J Am Ceram Soc 92(9):2039–2045
17. Ikegami S, Ueda T, Nagata T (1971) Electromechanical properties of $PbTiO_3$ ceramics containing La and Mn. J Acoust Soc Am 50(4):1060–1066
18. Jaeger R, Egerton L (1962) Hot pressing of potassium-sodium niobates. J Am Ceram Soc 45 (5):209–213
19. Jaffe B, Cook W, Jaffe H (1971) Piezoelectric ceramics. Academic, New York
20. Karaki T, Kang Y, Miyamoto T, Adachi M (2007) Lead-free piezoelectric ceramics with large dielectric and piezoelectric constants manufactured from $BaTiO_3$ nano-powder. Jpn J Appl Phys 46(4):L97–L98
21. Lang W, Xiao D, Dunmin L, Jianguo Z, Ping Y, Xiang L (2007) Temperature dependence of electric properties of $[Bi_{0.5}(Na_{1-x}Ag_x)_{0.5}]_{1-y}Ba_yTiO_3$ ceramics. Jpn J Appl Phys 46 (11):7382–7387
22. Lee H, Kimura T (1998) Effects of microstructure on the dielectric and piezoelectric properties of lead metaniobate. J Am Ceram Soc 81(12):3228–3236
23. Lei C, Ye Z (2008) Lead-free piezoelectric ceramics derived from the $(K_{0.5}Na_{0.5})NbO_3$-$AgNbO_3$ solid solution system. Appl Phys Lett 93:042901
24. Li H, Feng C, Xiang P (2003) Electrical properties of La^{3+}-doped $(Na_{0.5}Bi_{0.5})_{0.94}Ba_{0.06}TiO_3$ ceramics. Jpn J Appl Phys 42:7387
25. Li H, Feng C, Yao W (2004) Some effects of different additives on dielectric and piezoelectric properties of $(Bi_{1/2}Na_{1/2})TiO_3$-$BaTiO_3$ morphotropic-phase-boundary composition. Mater Lett 58(7–8):1194–1198
26. Li JF, Wang K, Zhang BP, Zhang LM (2006) Ferroelectric and piezoelectric properties of fine-grained $(Na_{0.5}K_{0.5})NbO_3$ lead-free piezoelectric ceramics prepared by spark plasma sintering. J Am Ceram Soc 89(2):706–709
27. Liu W, Ren X (2009) Large piezoelectric effect in Pb-free ceramics. Phys Rev Lett 103 (25):257602
28. Lopatin S, Lupeiko T, Vasil'tsova T, Basenko N, Berlizev I (1988) Properties of bismuth titanate ceramic modified with group V and VI elements. Inorg Mater 24(9):1328–1330
29. Malic B, Bernard J, Holc J, Jenko D, Kosec M (2005) Alkaline-earth doping in $(K_{0.5}Na_{0.5})NbO_3$ based piezoceramics. J Eur Ceram Soc 25(12):2707–2711
30. Malic B, Bernard J, Holc J, Kosec M (2005) Strontium doped $(K_{0.5}Na_{0.5})NbO_3$ based piezoceramics. Ferroelectrics 314(1):149–156
31. Matsubara M, Kikuta K, Hirano S (2005) Piezoelectric properties of $(K_{0.5}Na_{0.5})(Nb_{1-x}Ta_x)O_3$-$K_{5.4}CuTa_{10}O_{29}$ ceramics. J Appl Phys 97(11):4105
32. Matsubara M, Yamaguchi T, Kikuta K, Hirano S (2004) Sinterability and piezoelectric properties of (K, Na)NbO_3 ceramics with novel sintering aid. Jpn J Appl Phys 43(10):7159–7163

33. Matsubara M, Yamaguchi T, Kikuta K, Hirano S (2005) Sintering and piezoelectric properties of potassium sodium niobate ceramics with newly developed sintering aid. Jpn J Appl Phys 44 (1A):258–263
34. Matsubara M, Yamaguchi T, Sakamoto W, Kikuta K, Yogo T, Hirano S (2005) Processing and piezoelectric properties of lead-free (K, Na)(Nb, Ta)O_3 ceramics. J Am Ceram Soc 88 (5):1190–1196
35. Matthias BT, Remeika JP (1951) Dielectric properties of sodium and potassium niobates. Phys Rev 82(5):727–729
36. Nagata Y (2007) Investigation of phase transition temperatures on $(Bi_{1/2}Na_{1/2})TiO_3(Bi_{1/2}K_{1/2})TiO_3$ and $(Bi_{1/2}Na_{1/2})TiO_3$-$BaTiO_3$ lead-free piezoelectric ceramics by electrical measurements. Ferroelectrics 346:114–119
37. Nanamatsu S, Kimura M, Kawamura T (1975) Crystallographic and dielectric properties of ferroelectric $A_2B_2O_7$ (A = Sr, B = Ta, Nb) crystals and their solid solutions. J Phys Soc Jpn 38 (3):817
38. Okazaki K, Maiwa H (1992) Space charge effects on ferroelectric ceramic particle surfaces. Jpn J Appl Phys 31:3113–3116
39. Park H, Ahn C, Song H, Lee J, Nahm S, Uchino K, Lee H (2006) Microstructure and piezoelectric properties of $0.95(Na_{0.5}K_{0.5})NbO_3$-$0.05BaTiO_3$ ceramics. Appl Phys Lett 89 (6):2906
40. Park H, Cho K, Paik D, Nahm S, Lee H, Kim D (2007) Microstructure and piezoelectric properties of lead-free $(1\text{-}x)(Na_{0.5}K_{0.5})NbO_3$-$xCaTiO_3$ ceramics. J Appl Phys 102(12):4101
41. Randall C, Kelnberger A, Yang G, Eitel R, Shrout T (2005) High strain piezoelectric multilayer actuators – a material science and engineering challenge. J Electroceramics 14 (3):177–191
42. Saito Y, Takao H (2006) High performance lead-free piezoelectric ceramics in the (K, Na) NbO_3LiTaO_3 solid solution system. Ferroelectrics 338(1):17–32
43. Saito Y, Takao H, Tani T, Nonoyama T, Takatori K, Homma T, Nagaya T, Nakamura M (2004) Lead-free piezoceramics. Nature 432(7013):84–87
44. Sasaki A, Chiba T, Mamiya Y, Otsuki E (1999) Dielectric and piezoelectric properties of $(Bi_{0.5}Na_{0.5})TiO_3$-$(Bi_{0.5}K_{0.5})TiO_3$ systems. Jpn J Appl Phys 38:5564–5567
45. Seungho P, Cheol-Woo A, Sahn N, Jae-Sung S (2004) Microstructure and piezoelectric properties of ZnO-added $(Na_{0.5}K_{0.5})NbO_3$ ceramics. Jpn J Appl Phys 43:L1072–L1074
46. Shrout T, Zhang S (2007) Lead-free piezoelectric ceramics: alternatives for PZT? J Electroceramics 19(1):113–126
47. Smith R, Welsh F (1971) Temperature dependence of the elastic, piezoelectric, and dielectric constants of lithium tantalate and lithium niobate. J Appl Phys 42(6):2219–2230
48. Smolenskii GA, Isupov VA, Agranovskaya AI, Krainik NN (1961) New ferroelectrics of complex composition. Sov Phys Solid State 2(11):2651–2654
49. Takahashi H, Numamoto Y, Tani J, Matsuta K, Qiu J, Tsurekawa S (2006) Lead-free barium titanate ceramics with large piezoelectric constant fabricated by microwave sintering. Jpn J Appl Phys 45(1):L30–L32
50. Takahashi H, Numamoto Y, Tani J, Tsurekawa S (2006) Piezoelectric properties of $BaTiO_3$ ceramics with high performance fabricated by microwave sintering. Jpn J Appl Phys 45 (9B):7405–7408
51. Takahashi S (1982) Effects of impurity doping in lead zirconate-titanate ceramics. Ferroelectrics 41(1):143–156
52. Takahashi S, Hirose S (1992) Vibration-level characteristics of lead-zirconate-titanate ceramics. Jpn J Appl Phys 31:3055–3057
53. Takahashi S, Hirose S (1993) Vibration-level characteristics for iron-doped lead-zirconate-titanate ceramic. Jpn J Appl Phys 32:2422–2425
54. Takenaka T, Maruyama K, Sakata K (1991) $(Bi_{1/2}Na_{1/2})TiO_3$-$BaTiO_3$ system for lead-free piezoelectric ceramics. Jpn J Appl Phys 30(9B):2236–2239

55. Takenaka T, Nagata H, Hiruma Y (2009) Phase transition temperatures and piezoelectric properties of $(Bi_{1/2}Na_{1/2})TiO_3$-and $(Bi_{1/2}K_{1/2})TiO_3$-based bismuth perovskite lead-free ferroelectric ceramics. IEEE Trans Ultrason Ferroelectr Freq Control 56(8):1595–1610
56. Uchino K, Zheng J, Joshi A, Chen Y, Yoshikawa S, Hirose S, Takahashi S, De Vries J (1998) High power characterization of piezoelectric materials. J Electroceramics 2(1):33–40
57. Uchino K, Zheng J, Joshi A, Chen Y, Yoshikawa S, Hirose S, Takahashi S, Vries JD (1998) High power characterization of piezoelectric materials. J Electroceramics 2(1):33–40
58. Wada S, Yako K, Kakemoto H, Tsurumi T, Kiguchi T (2005) Enhanced piezoelectric properties of barium titanate single crystals with different engineered-domain sizes. J Appl Phys 98:014109
59. Wang K, Li J, Liu N (2008) Piezoelectric properties of low-temperature sintered Li-modified (Na, K) NbO_3 lead-free ceramics. Appl Phys Lett 93:092904
60. Wang XX, Chan H, Choy CL (2005) $(Bi_{0.5}Na_{0.5})_{0.94}Ba_{0.06}TiO_3$ lead-free ceramics with simultaneous addition of CeO_2 and La_2O_3. Appl Phys A Mater Sci Process 80(2):333–336
61. Wood EA (1951) Polymorphism in potassium niobate, sodium niobate, and other ABO_3 compounds. Acta Crystallogr 4(4):353–362
62. Yoo J, Oh D, Jeong Y, Hong J, Jung M (2004) Dielectric and piezoelectric characteristics of lead-free $Bi_{0.5}(Na_{0.84}K_{0.16})_{0.5}TiO_3$ ceramics substituted with Sr. Mater Lett 58(29):3831–3835
63. Yoon MS, Lee YG, Ur SC (2009) Effects of co-doped CaO/MnO on the piezoelectric/dielectric properties and phase transition of lead-free $(Bi_{0.5}Na_{0.5})_{0.94}Ba_{0.06}TiO_3$ piezoelectric ceramics. J Electroceramics 23(2–4):564–571
64. Zang G, Wang J, Chen H, Su W, Wang C, Qi P, Ming B, Du J, Zheng L, Zhang S, Shrout T (2006) Perovskite $(Na_{0.5}K_{0.5})_{1-x}(LiSb)_xNb_{1-x}O_3$ lead-free piezoceramics. Appl Phys Lett 88:212908
65. Zhang B, Li J, Wang K, Zhang H (2006) Compositional dependence of piezoelectric properties in $(Na_xK_{1-x})NbO_3$ lead-free ceramics prepared by spark plasma sintering. J Am Ceram Soc 89(5):1605–1609
66. Zhang S, Lim JB, Lee HJ, Shrout TR (2009) Characterization of hard piezoelectric lead-free ceramics. IEEE Trans Ultrason Ferroelectr Freq Control 56:1523–1527
67. Zhang S, Shrout T, Nagata H, Hiruma Y, Takenaka T (2007) Piezoelectric properties in $(K_{0.5}Bi_{0.5})TiO_3$-$(Na_{0.5}Bi_{0.5})TiO_3$-$BaTiO_3$ lead-free ceramics. IEEE Trans Ultrason Ferroelectr Freq Control 54(5):910–917
68. Zhang S, Xia R, Hao H, Liu H, Shrout T (2008) Mitigation of thermal and fatigue behavior in $(K_{0.5}Na_{0.5})NbO_3$-based lead free piezoceramics. Appl Phys Lett 92:152–904
69. Zhang S, Xia R, Lebrun L, Anderson D, Shrout T (2005) Piezoelectric materials for high power, high temperature applications. Mater Lett 59(27):3471–3475
70. Zhang S, Xia R, Shrout T (2007) Lead-free piezoelectric ceramics vs PZT? J Electroceramics 19(4):251–257
71. Zhang S, Xia R, Shrout T (2007) Modified $(K_{0.5}Na_{0.5})NbO_3$ based lead-free piezoelectrics with broad temperature usage range. Appl Phys Lett 91:132913
72. Zhang S, Xia R, Shrout T, Zang G, Wang J (2006) Piezoelectric properties in perovskite 0.948 $(K_{0.5}Na_{0.5})NbO_3$-0.052$LiSbO_3$ lead-free ceramics. J Appl Phys 100:104108
73. Zhang S, Xia R, Shrout TR, Zang G, Wang J (2007) Characterization of lead free $(Na_{0.5}K_{0.5})NbO_3$-$LiSbO_3$ piezoceramic. Solid State Commun 141:675–679
74. Zuo R, Rodel J, Chen R, Li L (2006) Sintering and electrical properties of lead-free $Na_{0.5}K_{0.5}NbO_3$ piezoelectric ceramics. J Am Ceram Soc 89(6):2010–2015
75. Zuo R, Ye C, Fang X (2007) Dielectric and piezoelectric properties of lead free $(Na_{0.5}K_{0.5})NbO_3BiScO_3$ ceramics. Jpn J Appl Phys 46(10A):6733–6736
76. Zuo R, Ye C, Fang X, Li J (2008) Tantalum doped 0.94$(Bi_{0.5}Na_{0.5})TiO_3$-0.06$BaTiO_3$ piezoelectric ceramics. J Eur Ceram Soc 28(4):871–877

Chapter 10
Processing and Properties of Textured BNT-Based Piezoelectrics

Toshihiko Tani and Toshio Kimura

10.1 Introduction

There are two major strategies for the development of lead-free piezoelectric ceramics: compositional exploration and microstructural control. The compositional design by the formation of solid solution often improves the room temperature properties of lead-free piezoelectrics while it generally lowers Curie temperature (T_C) and limits the potential applications of the ceramics. Texture control of polycrystals, on the other hand, is an effective approach to improve the piezoelectric properties of lead-free materials without changing the composition and T_C of the ceramics [34, 35].

One of the most convenient processing methods of textured ceramics is the templated grain growth (TGG) technique [16]. This technique uses a small fraction of anisometric particles as seeds for the alignment of fine matrix particles through epitaxial growth during sintering. It is often difficult to synthesize single-crystalline anisometric particles for the seeds with a pseudocubic crystal structure such as a regular perovskite-type and/or a complex composition that would be desirable for material performance. The reactive-templated grain growth (RTGG) was proposed as a processing method originally for textured regular perovskite-type ceramics by using reactive template materials with an anisotropic crystal structure. This method was first demonstrated by the fabrication of $Bi_{0.5}Na_{0.5}TiO_3$ (BNT) and $Bi_{0.5}(Na,K)_{0.5}TiO_3$

T. Tani (✉)
Toyota Central R&D Labs., Inc., 41-1 Yokomichi, Nagakute, Aichi 480-1192, Japan

Toyota Technological Institute, 2-12-1 Hisakata, Tempaku-ku, Nagoya 468-8511, Japan

Toyota Research Institute of North America, Ann Arbor, MI 48105, USA
e-mail: e0628@mosk.tytlabs.co.jp

T. Kimura
Keio University, 3-14-1 Hiyoshi, Kohoku-ku, Yokohama 223-8522, Japan
e-mail: kimura@applc.keio.ac.jp

S. Priya and S. Nahm (eds.), *Lead-Free Piezoelectrics*,
DOI 10.1007/978-1-4419-9598-8_10, © Springer Science+Business Media, LLC 2012

(BNKT) ceramics with a uniaxial (pseudocubic) <100> orientation by using bismuth layer-structured $Bi_4Ti_3O_{12}$ (BiT) platelet with a developed basal plane as a reactive template as well as TiO_2 and Na_2CO_3 (+K_2CO_3) powders as complementary reactants [33]. In this process, aligned BNT-based "homo"-template is formed in situ with preserved orientation of aligned BiT through the topotactic reaction with the complementary reactants during heat-treatment. The in situ reaction is followed by the solid-state epitaxial growth similar to the TGG processing, leading to a dense and highly textured polycrystal.

BNT-based ceramics and single crystals have gained attention as lead-free piezoelectrics because of their large values of field-induced strain [2, 43]. The enhancement of ceramic properties through texture engineering has also been anticipated. The degree of crystallographic grain orientation of the RTGG-processed BNT-based ceramics is remarkably dependent on the composition and processing conditions as well as size and amount of BiT template. The design and fabrication of dense and highly textured ceramics require basic understanding of microstructure development process during heat-treatment and determination of the optimum processing conditions. There have been many studies devoted to sintering and grain growth, mainly regarding uniform material systems such as powders with narrow size distribution, a green compact with a homogeneous packing structure, and so on [5]. However, the RTGG process utilizes a system composed of a mixture of powders with quite different particle characteristics. The sintering behavior between different particles plays an important role for the texture development.

In this chapter, the key parameters to determine macroscopic texture of the BNT-based ceramics and leading mechanisms for grain orientation in the RTGG processing are discussed. Enhanced electrical properties by the developed texture are also presented.

10.2 Brief Description of Preparation Method

The preparation method is explained using BNT as an example of target composition. In this case the reactive template is BiT and complementary reactants are Na_2CO_3 and TiO_2. Platelike BiT particles prepared by molten salt synthesis [10] are mixed with Na_2CO_3 and TiO_2 and then a solvent, binder, and plasticizer are added to form slurry for tape casting. Tape casting of the slurry produces a green compact in which platelike BiT particles are dispersed in the Na_2CO_3 and TiO_2 particles and aligned with their plate faces parallel to the cast sheet. Calcination of the green compact at about 700°C promotes the reaction between BiT, Na_2CO_3, and TiO_2, and platelike BNT particles and small equiaxed BNT particles form. The platelike BNT particles with the pseudocubic <100> axis perpendicular to the plate face are dispersed in the matrix of equiaxed BNT particles. The terms "template grains" and "matrix grains" will be used to refer to platelike and equiaxed BNT particles, respectively. When the BNT-based materials are formed in a compact of their constituent oxides, the volume of the compact expands. The formation of template grains by the in situ reaction between BiT and complementary reactants in this case

is accompanied by a volume expansion, and the density of the compact is decreased by calcination. Therefore, the calcined compact is often subject to cold-isostatic pressing (CIP) to increase green density. Finally, the resulting compact is sintered under appropriate conditions, and dense, highly textured BNT ceramics are obtained.

10.3 Selection of Reactive Template and Batch Formulation

The first step of processing design for the RTGG is the selection of the compound for the reactive template [33, 41]. Because the template grains are formed by the in situ reaction of aligned reactive template particles with complementary reactants, the following conditions are required for the reactive template [34]:

1. It contains all or a part of elements composing the target compound and the in situ reaction from the reactive template and complementary reactants into the target is thermodynamically feasible.
2. Either its precursor or itself has a highly anisotropic crystal structure so it can be prepared as anisometric particles.
3. It has crystallographic similarity such as epitaxial or topotaxial relation with the target compound.
4. The overall reaction from the reactive template to the target compound does not have a major intermediate phase that could disturb the succession of the crystallographic similarity.

In the case of BNT-based piezoelectrics, platelike particles of bismuth layer-structured ferroelectrics (BLSFs), BiT, and related compounds such as $Na_{0.5}Bi_{4.5}Ti_4O_{15}$ and $MeBi_4Ti_4O_{15}$ (Me = Ca, Sr, Ba or Pb), are most used as the reactive template. The complementary reactants are Na_2CO_3, TiO_2, and so forth. A few formation reactions are shown below:

$$4Bi_4Ti_3O_{12} + 3Na_2CO_3 \rightarrow 12Bi_{0.5}Na_{0.5}TiO_3 + 5Bi_2O_3 + 3CO_2 \tag{10.1}$$

$$4Bi_4Ti_3O_{12} + 3(xNa_2CO_3 + (1-x)K_2CO_3) \rightarrow 12Bi_{0.5}(Na_xK_{1-x})_{0.5}TiO_3 + 5Bi_2O_3 + 3CO_2 \tag{10.2}$$

$$4BaBi_4Ti_4O_{15} + 3Na_2CO_3 \rightarrow 16(Bi_{0.5}Na_{0.5})_{0.75}Ba_{0.25}TiO_3 + 5Bi_2O_3 + 3CO_2 \tag{10.3}$$

These reactions are caused by the unidirectional diffusion of alkali ions into BLSF. Figure 10.1 shows the schematic model of the topotaxial reaction between BLSF and alkaline oxide which forms the BNT and BNT-based materials with their *a*-axis parallel to the *c*-axis of BLSF. However, the conversion of BLSF to BNT is not a simple process. Figure 10.2 shows transmission electron microscopy (TEM) images of a reactive template particle before and after heating at 700°C for the

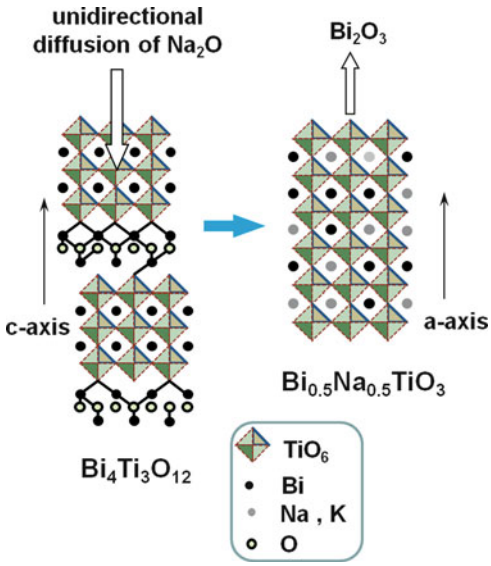

Fig. 10.1 Schematic model of the conversion of $Bi_4Ti_3O_{12}$ (BiT) into $Bi_{0.5}Na_{0.5}TiO_3$ (BNT) by unidirectional diffusion of Na_2O into BiT. The orientation of perovskite-blocks is preserved. Bi_2O_3 diffuses out as a by-product

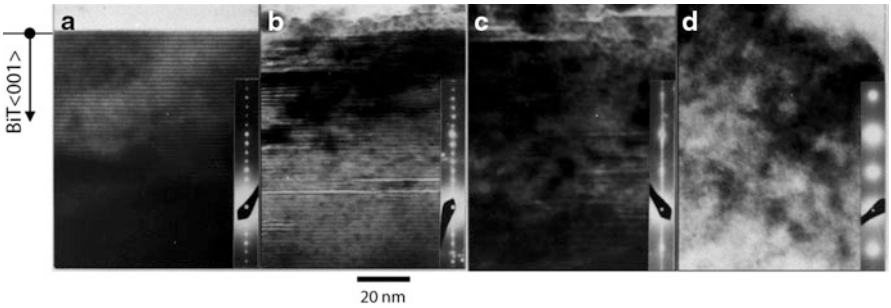

Fig. 10.2 Bright field images and electron diffraction patterns of a platelike reactive template in a $BiT/Bi_2O_3/TiO_2/Na_2CO_3/K_2CO_3$ powder compact for $Bi_{0.5}(Na_{0.87}K_{0.13})_{0.5}TiO_3$ in the vicinity of surface at the plane containing pseudotetragonal *c*-axis. Observation was made (**a**) before heat-treatment and after heating at 700°C for (**b**) 5 min, (**c**) 30 min, and (**d**) 120 min [25]

observation of microstructural change during the conversion reaction from a layered BiT single crystal into a regular perovskite BNKT in a $BiT/Bi_2O_3/TiO_2/Na_2CO_3/K_2CO_3$ powder compact [25]. It should be noted that the long-range periodic structure of BiT was partially disturbed and slightly bent at multiple sites after heat-treatment at 700°C for 5 min, suggesting the multinucleation of perovskite in a single crystal BiT. After heating for 2 h a vague electron diffraction pattern of a regular perovskite-type structure appeared, indicating the conversion

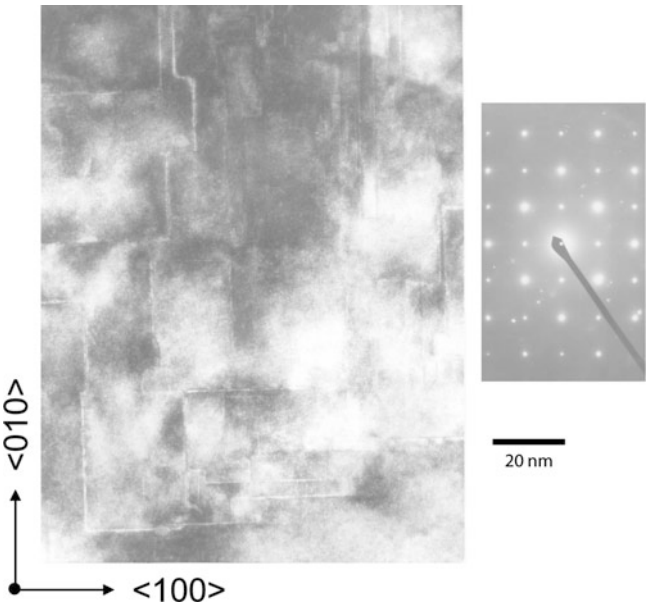

Fig. 10.3 Bright field image and electron diffraction pattern of a basal plane of a platelike reactive template in a BiT/Bi_2O_3/TiO_2/Na_2CO_3/K_2CO_3 powder compact for $Bi_{0.5}(Na_{0.87}K_{0.13})_{0.5}TiO_3$ after heating at 700°C for 30 min [25]

was proceeded topotaxially and the formed perovskite grain was not a "clean" single crystal but a defective single crystal or a biaxially oriented polycrystal. Figure 10.3 shows a plan view of the template grain after being heated at 700°C for 30 min. Rectangular "domains" were clearly seen with the straight "domain boundaries" parallel to pseudocubic <100> axes of a perovskite phase. This domain structure resulted from the multinucleation of perovskite in a BiT single crystal which has a periodic discontinuity in the –Ti–O–Ti–O– bond chain along c-direction unlike regular perovskite (see Fig. 10.1).

The direction of material transport between the reactive template and complementary reactants is important to obtain template grains. If the elements in the reactive template diffuse into the complementary reactants, the reactive template decreases its volume and finally disappears or forms inner voids as observed in RTGG-processed $SrTiO_3$ ceramic from $Sr_3Ti_2O_7$ and TiO_2 [29]. The direction of material transport is determined by the chemical composition of reactive template and complementary reactants. In the cases of BNT and BNKT, the Na_2O and K_2O diffuse into BiT and template grains form. In the case of BNKT-Pb(Zr,Ti)O_3 (PZT), the PZT composition determines the diffusion direction; Ti-rich PZT diffuses into BNKT, but BNKT diffuses into Zr-rich PZT [1]. In the case of BNKT-$BiFeO_3$, the direction of material transport is determined by the BNKT composition; when the template is BKT, $BiFeO_3$ diffuses into BKT, resulting in the formation of template

grains, but BNT diffuses into $BiFeO_3$ and the template grains disappear [8]. In the case of BNKT-$BaTiO_3$, the template grains form by the addition of presynthesized $BaTiO_3$, but do not form by the addition of $BaCO_3$ + TiO_2 [12].

The starting batch formulation is determined by two considerations; (a) to convert the by-products of the template formation reaction into the target compound and (b) to fix the volume ratio of template to matrix grains. Reactions (10.1)–(10.3) form Bi_2O_3 as by-product, which must be converted into BNT-based materials. In the case of BNT, the reaction is

$$Bi_2O_3 + Na_2CO_3 + 4TiO_2 \rightarrow 4Bi_{0.5}Na_{0.5}TiO_3 + CO_2 \tag{10.4}$$

BNT grains formed by reaction (10.4) are equiaxed and serve as the matrix grains. The total reaction is the combination of reactions (10.1) and (10.4).

$$Bi_4Ti_3O_{12} + 2Na_2CO_3 + 5TiO_2 \rightarrow 8Bi_{0.5}Na_{0.5}TiO_3 + 2CO_2 \tag{10.5}$$

Reaction (10.5) forms 8 moles of BNT, in which 3 moles are derived from BiT, i.e., 37.5 vol% of BNT grains are the template grains derived from reactive template particles. It is not possible to increase the relative amount of template BNT grains, but it is possible to decrease the amount by simply adding the starting materials of BNT (Bi_2O_3 + Na_2CO_3 + $4TiO_2$). For example, when the amount of template BNT grains is designed to be 20 vol%, the addition of BNT by 7 moles to reaction (10.5) is necessary because reaction (10.5) forms 3 moles of template grains and 5 moles of matrix grains. The addition of 7 moles BNT results in the formation of 12 moles of matrix grains. The starting batch is formulated by the calculation based on reaction (10.6).

$$\begin{aligned} &4Bi_4Ti_3O_{12} + 7Bi_2O_3 + 15Na_2CO_3 + 48TiO_2 \\ &\rightarrow 60Bi_{0.5}Na_{0.5}TiO_3 + 15CO_2 \end{aligned} \tag{10.6}$$

Presynthesized BNT particles can be added instead of the starting materials of BNT to reduce the volume expansion accompanying the in situ formation reaction of matrix BNT.

10.4 Preparation of Reactive Template Particles

The preparation of platelike BLSF particles is described in Chap. 15 dealing with the fabrication process of textured BLSFs by the TGG. Here, the preparation of platelike BiT particles by molten salt synthesis is briefly described. Bi_2O_3 and TiO_2 with the stoichiometric ratio are reacted to form BiT under the presence of molten salt such as KCl or a mixture of NaCl and KCl. In the practical procedure, a mixture of Bi_2O_3, TiO_2, and salt is heated at a temperature between 950 and 1150°C for

several hours. Prolonged heating at high temperatures causes particle growth by Ostwald ripening and particles with well-developed crystal habit are obtained. The particle size and aspect ratio are determined mainly by the heating temperature and the chemical species of the salt [11].

10.5 Tape Casting

The next step is the consolidation of the mixture of starting materials (reactive template and complementary reactants). A green compact must contain aligned reactive template particles such as platelike BiT. The most convenient method to align platelike particles is tape casting. Slurries for tape casting are prepared based on the standard formulation (p. 176–183 in [42]). The slurries contain particulate materials, solvent, binder, plasticizer, and surfactant (dispersant) (p. 15–56 in [18]). Because the binder can act as dispersant (p.57 in [18]), the use of a dispersant is sometimes omitted in laboratory experiments to simplify the slurry formulation.

The reactive template particles (platelike BLSF particles) must be uniformly dispersed and aligned parallel in the cast sheet. The slurry is subject to shear stresses during casting, and the gradient of shear stresses aligned the platelike particles [9, 40]. The factors determining the degree of orientation of the platelike particles are the dispersion of powders in the slurry, the viscosity of the slurry, and the sizes of platelike and equiaxed particles (see Chap. 15). In the case of BNT-based materials, these factors are related to each other. Some experimental results are shown as an example.

Example 1: The first example shows the effect of the size of platelike BiT particles on the degree of orientation of those particles in the cast sheet for the preparation of $Bi_{0.5}(Na_{0.85}K_{0.15})_{0.5}TiO_3$ (BNKT15) [12]. The platelike BiT particles were prepared at 950, 1050, and 1150°C using NaCl–KCl flux; the plate face diameters were 1–5, 15–20 and 20–30 μm, respectively. In this experiment, the amount of BNKT15 grains derived from the reactive template is designed to be 26.25 vol%. The degree of orientation of BiT particles in the cast sheets was determined as $I_{0014}/(I_{0014} + I_{117})$ from the intensities of (117) and (0014) XRD lines [40]. It was 0.67, 0.85, and 0.96 for the BiT particles prepared at 950, 1050, and 1150°C, respectively. These cast sheets gave pseudocubic {100}-oriented BNKT15 with the degree of orientation (Lotgering *F* factor) of 0.19, 0.52, and 0.97, respectively, by sintering at 1200°C for 2 h. This result shows the large platelike BiT particles give a high degree of orientation in terms of {001} BiT in the cast sheet and also in terms of {100} BNKT15 in the sintered compact.

Example 2: The second example shows the effect of dispersant on the degree of orientation of the platelike BiT particles in the cast sheet for the preparation of $Bi_{0.5}(Na_{0.5}K_{0.5})_{0.5}TiO_3$ (BNKT50) [4]. The platelike BiT particles were prepared at 950, 1050, and 1130°C using NaCl–KCl; the diameters of the plate face were 1–5, 5–15, and 20–30 μm, respectively. In this experiment, the amount of BNKT50 grains

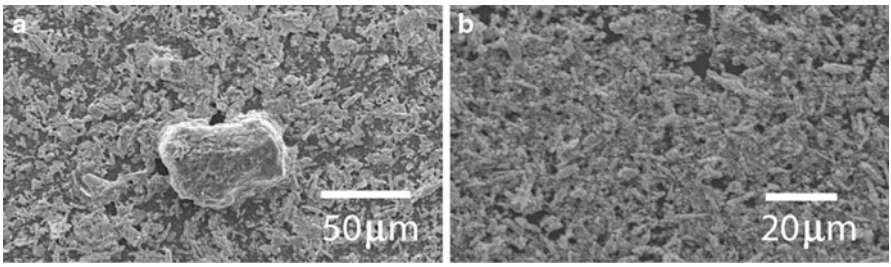

Fig. 10.4 Observation of dispersion of powder particles in the slurry containing (**b**) Bi_2O_3, TiO_2, and $CaCO_3$ and (**b**) Bi_2O_3 and TiO_2. The slurry was spin-coated on a specimen holder and examined with a scanning electron microscopy. Large agglomerates form in slurry (**a**) but not in slurry (**b**) [39]

derived from the reactive template is designed to be 20 vol%. A dispersant was used in the preparation of the slurries. The Lotgering *F* factor in the cast sheets was 0.79, 0.84, and 0.87 for BiT particles prepared at 950, 1050, and 1130°C, respectively. These cast sheets gave BNKT50 with the Lotgering *F* factor of 0.83, 0.85, and 0.74, respectively, by sintering at 1150°C for 2 h. This evidence shows the orientation of platelike BiT particles is not dependent on their size, on the contrary to Example 1.

The use of dispersant in Example 2 dramatically improved the texture of BNKT50 ceramics prepared with small-sized platelike BiT particles. This suggests the formation of agglomerates in the slurry is responsible for the hindrance to the alignment of particles in the cast sheet. Textured BLSF ceramics prepared by the TGG process using the same slurry system as the BNKT50 without a dispersant, the agglomeration is not a major problem and cast sheets with well-aligned platelike particles are obtained. In this BLSF case, the solid materials in the slurries have the same composition. In the BNKT50 case, on the other hand, particles with dissimilar composition can cause agglomeration (heterocoagulation) (p. 52–53 in [6]). The heterocoagulation has been examined in the slurries for RTGG-processed $CaBi_4Ti_4O_{15}$ and $SrBi_4Ti_4O_{15}$ [39]. Large agglomerates were found in slurries containing BiT, Bi_2O_3, TiO_2, $CaCO_3$ (or $SrCO_3$), solvent, binder, and plasticizer. To find out the origin of the agglomerate formation, two slurries were spin-coated on glass substrates; one contained Bi_2O_3, $CaCO_3$, and TiO_2 particles and the other contained Bi_2O_3 and TiO_2 particles. Large agglomerates formed in the slurry containing Bi_2O_3, $CaCO_3$, and TiO_2 particles (Fig. 10.4a) but did not form in the slurry containing Bi_2O_3 and TiO_2 particles (Fig. 10.4b). These findings indicate that heterocoagulation occurs extensively between Bi_2O_3 and $CaCO_3$ (or $SrCO_3$) particles.

In the present BNKT15 case shown in Example 1, heterocoagulation between Bi_2O_3 and Na_2CO_3 (or K_2CO_3) can occur, which leads to the formation of large agglomerates. It is found in the TGG process of $CaBi_4Ti_4O_{15}$ when the size of equiaxed particles exceeds 1 μm, the orientation of platelike particles is hindered (see Chap. 15). Therefore, large agglomerates hinder the orientation of platelike BiT particles. The degree of hindrance is dependent on the size of platelike

particles; smaller platelike particles are subject to a higher degree of hindrance. In Example 2, the dispersant reduced the size of agglomerates and did not hinder the orientation of small BiT particles.

10.6 Calcination

The most important phenomenon in the calcination step is the formation of template grains from reactive template particles. Figure 10.5 shows the microstructures of original platelike BiT particles and BNT grains just after the formation (heated at 750°C for 10 h) from platelike BiT, Na_2CO_3, and TiO_2 [19]. Each particle of platelike BiT is a single crystal, as judged from the flat and smooth plate face. The in situ formed BNT is a mixture of platelike grains and equiaxed grains. In this case, the amount of template grains is designed to be 37.5 vol%. Only the side faces are observed for most of the platelike BNT grains, indicating good alignment. A slightly misoriented grain is observed in the figure. The plate face of this grain is not flat as the original BiT particles are, but is rugged, indicating that the outer shape is platelike but the grain is polycrystalline. The polycrystalline, platelike grain is referred to as a skeleton grain. The pseudocubic *a*-axis of primary grains in the skeleton grain is perpendicular to the plate face of original platelike particle. The primary grains grow during sintering as shown in Fig. 10.6, for the same specimen shown in Fig. 10.5, after heating at 800 and 900°C for 2 h. These oriented grains are larger than the grains which are formed with random orientation in the matrix by the reaction between Na_2CO_3, TiO_2, and by-product Bi_2O_3, resulting in an increase in the degree of orientation above 1050°C because of Ostwald ripening. This indicates that the template grain (large, oriented BNT grain) can be formed from the reactive template grain (platelike BiT), but the size of the template grain is

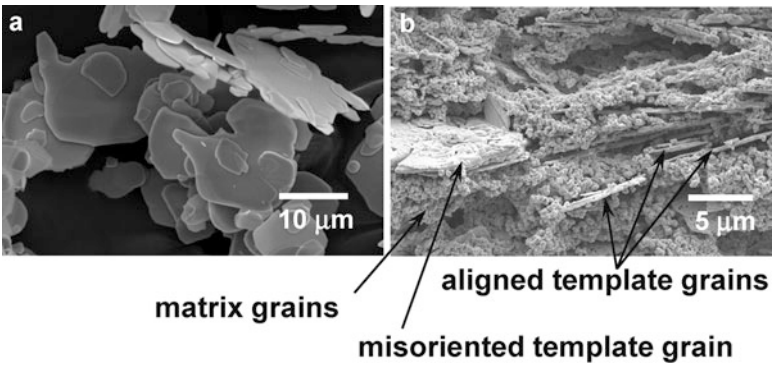

Fig. 10.5 Scanning electron micrographs of (**a**) platelike BiT particles used as reactive template and (**b**) BNT compact in situ formed from platelike BiT, Na_2CO_3, and TiO_2 by calcination at 750°C for 10 h. The surface of the original reactive template particles is flat and smooth. The calcined compact is composed of platelike template grains and small equiaxed matrix grains. The surfaces of template grains are rugged

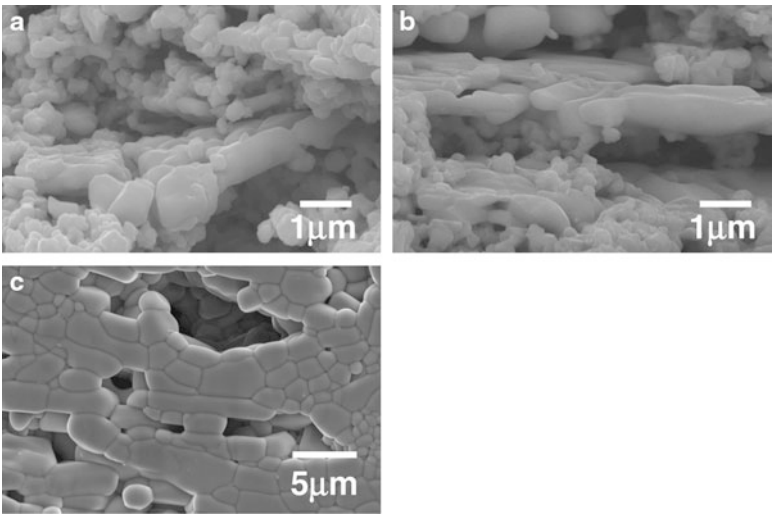

Fig. 10.6 Microstructure development of BNT compact formed from platelike BiT, Na_2CO_3, and TiO_2 by heating for 2 h. The heating temperatures are (**a**) 800, (**b**) 900, and (**c**) 1,100°C. The fractured surfaces are observed for (**a**, **b**) and the polished and thermally etched section for (**c**). The template grains in (**a**) are composed of many small primary grains, and the primary grains grow to form platelike grains in (**b**, **c**) but their size is smaller than that of original platelike BiT grains [19]

smaller than that of the original BiT particles; the size of plate face of BiT is about 20 μm (Fig. 10.5a) but that of platelike BNT grains in Fig. 10.6c) is less than 10 μm.

A BiT particle is converted into a BNT grain by unidirectional diffusion of Na_2O, as shown in Fig. 10.1. The product has a multidomain structure as a result of multinucleation shown in Fig. 10.3. Furthermore, although the orientation of perovskite blocks in BiT is preserved, the vertical direction, parallel to the *c*-axis of BiT, shrinks by 29% and the lateral direction expands by 1% [19]. Multinucleation, discontinuous bond chain along c-direction and a large volume change are the origin of the formation of skeleton grain during the formation of BNT.

In the stoichiometric BNT specimen shown in Fig. 10.6, the oriented template grains are obtained but their size is smaller than that of platelike BiT particles. The template grain with almost the same size and shape of the platelike BiT particle can be obtained by selecting chemical composition. Figure 10.7 shows the formation of template grain in BNT containing excess Na_2CO_3 [19]. The skeleton grain is formed just after the BNT formation (680°C). Each primary grain in the skeleton grain coalesces with each other (725°C) and finally a platelike grain forms with nearly the same size and shape of the platelike BiT particle (775°C). This grain acts as a template for texture formation at high temperatures. Figure 10.8 shows the development of texture in the stoichiometric and Na-excess specimens, indicating that large template grains in the Na-excess specimen have higher ability to develop texture. The addition of excess Bi_2O_3 and the substitution of K for Na also results in the formation of template grains with the same size and shape as platelike BiT particles [3, 14].

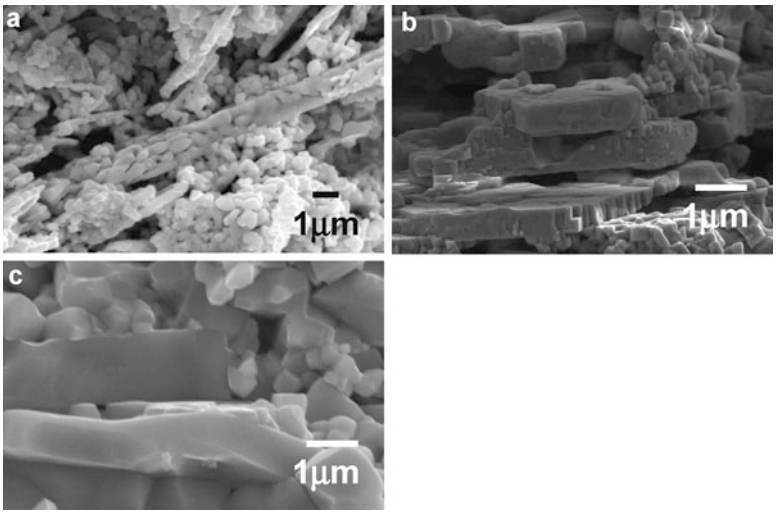

Fig. 10.7 Microstructure development of Na-excess BNT compact. Heating conditions are (**a**) at 680°C for 10 h, (**b**) at 725°C for 2 h, and (**c**) at 775°C for 2 h. The fractured surfaces are observed. The template grains in (**a**) are composed of many small primary grains, and they coalesce to form platelike grains in (**b**, **c**) with almost the same size as that of platelike BiT grains [19]

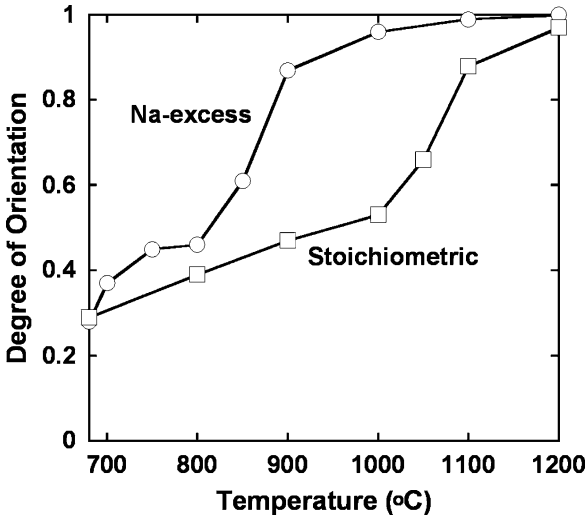

Fig. 10.8 Texture development in stoichiometric and Na-excess BNT heated for 2 h. The Na-excess specimen contains large template grains, and texture develops extensively at low temperatures [19]

The surface structure of primary grains determines the possibility of the formation of template grains with the same size and shape as platelike BiT particles [19]. Figure 10.9 shows the grain morphologies of stoichiometric BNT, BNT containing excess Na_2CO_3, and $Bi_{0.5}(Na_{0.5}K_{0.5})_{0.5}TiO_3$. The surface of BNT grains is curved,

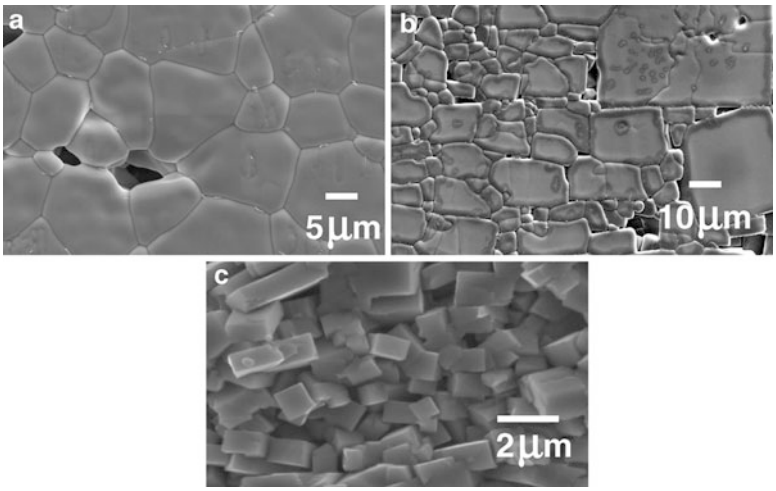

Fig. 10.9 Microstructures of sintered compacts of (**a**) stoichiometric BNT, (**b**) Na-excess BNT, and (**c**) $Bi_{0.5}(Na_{0.5}K_{0.5})TiO_3$. The sintering conditions are at (**a**) 1,200, (**b**) 1100, and (**c**) 1,150°C for 2 h. (**a**, **b**) Polished and thermally etched sections. (**c**) Fractured surface. The grain boundaries are rounded in stoichiometric BNT but they are facetted in Na-excess BNT and $Bi_{0.5}(Na_{0.5}K_{0.5})_{0.5}TiO_3$ [19]

whereas those of BNT containing excess Na_2CO_3, and $Bi_{0.5}(Na_{0.5}K_{0.5})_{0.5}TiO_3$ are facetted. The template grain just after the formation of BNT is the skeleton grain composed of many small primary grains. The surfaces of the primary grains of BNT containing excess Na_2CO_3, and $Bi_{0.5}(Na_{0.5}K_{0.5})_{0.5}TiO_3$ are facetted and, more importantly, mutually parallel. In these cases, the coalescence of primary grains eliminates void space and grain boundary between them, because they have the same crystallographic orientation. Thus, the skeleton grain transforms into a single crystalline grain with the same outer shape. In the case of stoichiometric BNT, on the other hand, the surface is curved and the coalescence of primary grains leaves a small void space between them. Therefore, the skeleton grain disintegrates into several grains. The primary grains have the same crystallographic orientation and grain growth in the disintegrated grain is fast, resulting in small platelike grains. These platelike grains act as template for texture development, but the efficiency in developing texture is smaller than that of platelike grains with the same size of BiT particles (Fig. 10.8).

When the amount of template grains derived from the reactive template particles (platelike BiT particles) is designed to be 20 vol%, texture does not develop in stoichiometric BNT, but it develops extensively in K-substituted BNT [3]. The origin of this difference is caused by low efficiency to develop texture because of a small size of template grains in stoichiometric BNT. The degree of orientation can be increased by increasing the amount of template grains to 37.5 vol% [13, 19]. In other words, low efficiency to develop texture can be compensated by increasing the amount of template grains.

10.7 Cold-Isostatic Pressing

The template grains are formed by an in situ reaction between platelike BiT particles and Na_2CO_3/K_2CO_3 as well as TiO_2. This solid-state reaction increases the volume of the compact due to the formation of Kirkendall voids, and the postcalcination CIP treatment can increase the density of a green compact to obtain a dense sintered compact with improved texture. The effect of the CIP treatment was examined for the RTGG processing for $Bi_{0.5}(Na_{0.85}K_{0.15})_{0.5}TiO_3$ (BNKT15) with the reaction design of the amount of template grains to be 20 vol% [37]. Two kinds of starting formulations are used in this experiment. The additional matrix BNKT15 gains are introduced as a mixture of reactants (Bi_2O_3, Na_2CO_3, K_2CO_3, and TiO_2) in one specimen, and as presynthesized and equiaxed BNKT15 in another specimen. These specimens are referred to as the nonfiller and 20% filler specimens, respectively. Tape-cast and laminated specimens were cut into square plates with approximately 15 mm in width and 1.5–2.0 mm in thickness before calcination.

Figure 10.10 gives the X-ray diffraction (XRD) patterns of the nonfiller specimens calcined at 600, 700, 800, and 900°C for 2 h. Perovskite-type BNKT15

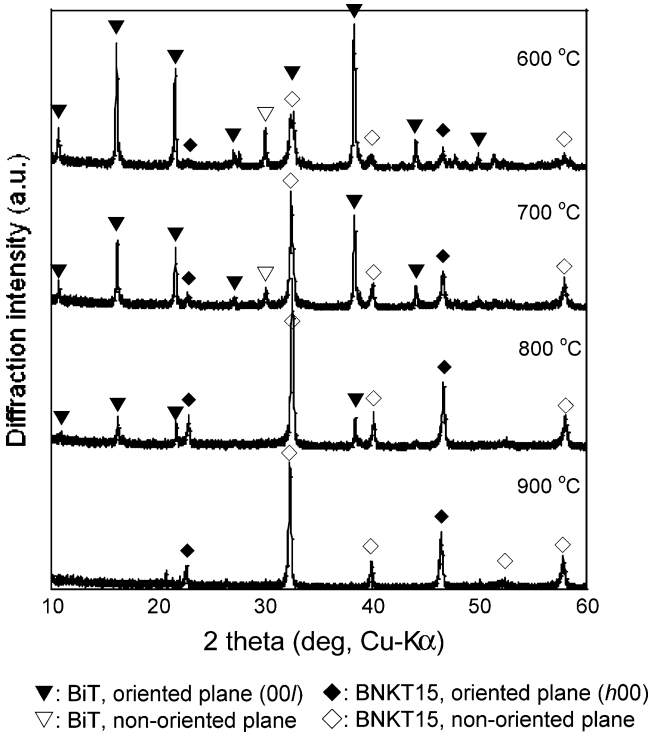

Fig. 10.10 XRD patterns for nonfiller BNKT15 specimens calcined at 600–900°C for 2 h [37]

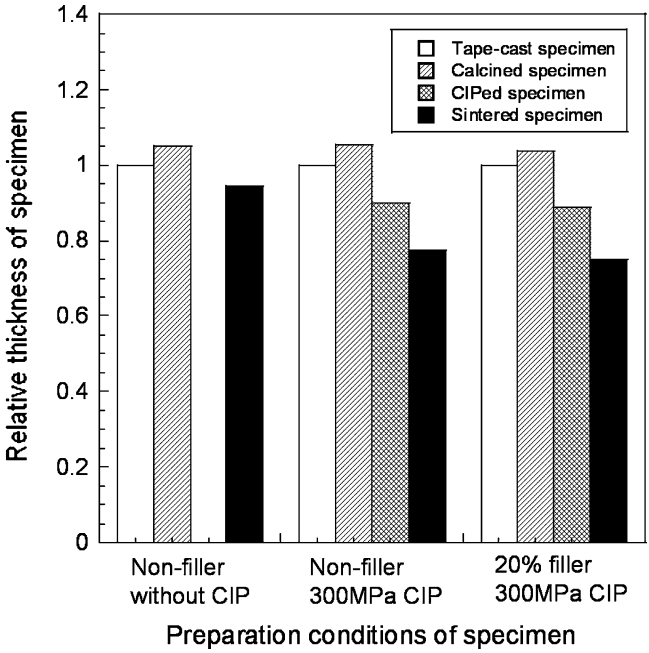

Fig. 10.11 Relative thickness changes of RTGG-processed BNKT15 ceramics with and without CIP treatment before sintering. Calcination and sintering were carried out at 600°C for 2 h and at 1,100°C for 10 h, respectively [37]

phase was already formed partly in the specimen heat-treated at 600°C although there were still strong diffraction lines for the {00 1} plane of oriented BiT template. The diffraction intensities of BiT decreased and those of BNKT15 increased as the calcination temperature increased. BiT was totally converted into BNKT15 and disappeared after the calcination at 900°C although grain orientation was barely observable. Figure 10.11 shows the relative thickness of the RTGG-processed BNKT15 specimens at each processing step. More than 5% of expansion was observed in thickness upon calcination at 600°C for 2 h for nonfiller specimens, due to the in situ formation reaction of the regular perovskite [21]. The specimen without CIP treatment resulted in a poor relative density (~80%) even after the shrinkage of 10% upon sintering at 1100°C. The CIP treatment at 300 MPa after the calcination reduced the thickness by nearly 15% and width by 5–6%, and thus increased the green density by 24% before sintering. The sintered specimen with CIP treatment exhibited 14% of additional reduction in thickness and showed the relative density of 90%. The CIP treatment after the calcination improved the packing density of partially reacted powder compacts and increased the final density after sintering. The use of presynthesized BNKT15 powder as "filler" reduced the volume expansion upon the calcination at 600°C down to 3.6% in thickness with no change in width. The use of filler powder improved the densities and degrees of <100> orientation of sintered specimens when compared with the nonfiller specimens prepared under the same conditions.

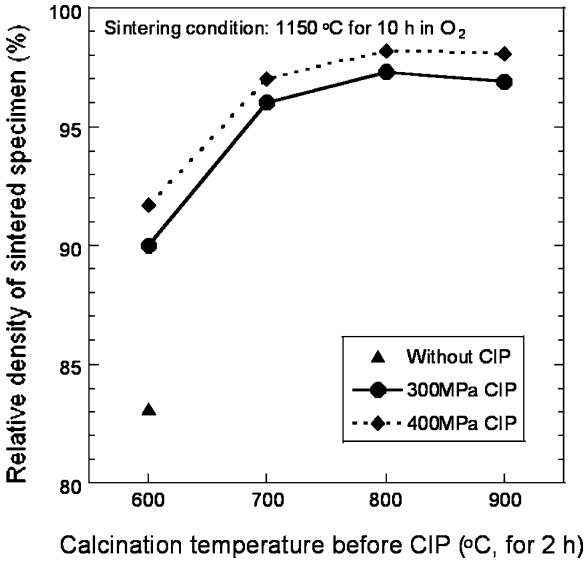

Fig. 10.12 Relative density of sintered specimens prepared with 20% BNKT15 filler powder and under various presintering conditions [37]

Figure 10.12 gives the relative density of the 20% filler BNKT15 specimens sintered at 1150°C for 10 h as a function of calcination temperature. The application of higher isostatic pressure produced denser specimens after sintering due to the achievement of higher green density before sintering. The sintered density increased as the calcination temperature increased up to 800°C. The sintered specimens that were subjected to the CIP treatment after the calcination at 700°C and higher temperatures reached relative densities higher than 96%. The improvement in the sintered density when processed through the calcination at higher temperatures than 600°C is attributed to the smaller amount of BiT phase in the calcined specimens, which would cause further volume expansion in the first stage of sintering. Figure 10.13 gives the Lotgering *F* factor of pseudocubic <100> orientation for the 20% filler BNKT15 specimens sintered at 1150°C for 10 h as a function of calcination temperature. The degree of orientation decreased as the calcination temperature increased. This is because aligned template grains are more susceptible to fracture and misorientation upon applied mechanical pressure when they contain a smaller amount of anisotropic BiT phase. The application of higher isostatic pressure resulted in a lower degree of orientation after sintering. This is because higher isostatic pressure could disturb the parallel alignment of the template grains during the course of increased packing density. The combination of the CIP treatment after the partial in situ formation of perovskite phase produced both dense and highly textured BNKT15 ceramics.

10.8 Sintering

The density and degree of orientation increase during sintering. Figure 10.14 shows typical behavior of densification and texture development. After calcination and CIP treatment, the relative density of a compact is between 50 and 60% and the

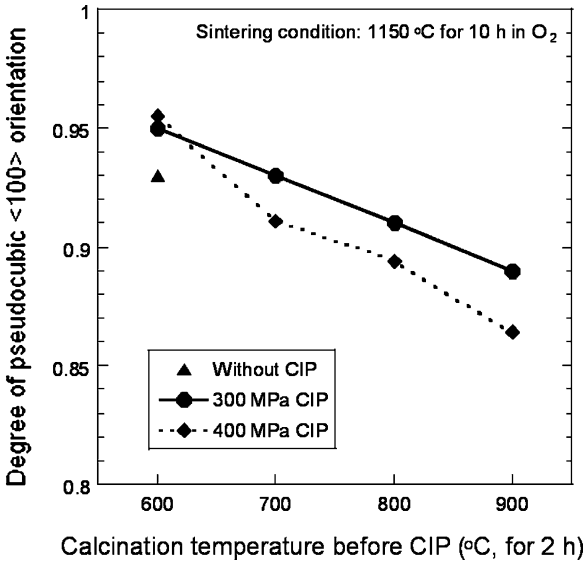

Fig. 10.13 Lotgering's degree of pseudocubic <100> orientation of sintered specimens prepared with 20% BNKT15 filler powder and under various presintering conditions [37]

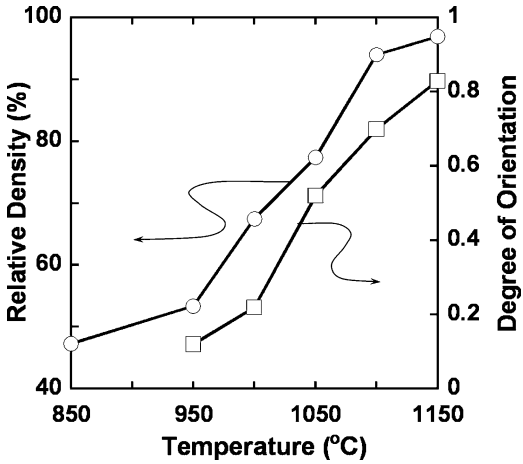

Fig. 10.14 Densification and texture development in $Bi_{0.5}(Na_{0.5}K_{0.5})_{0.5}TiO_3$ sintered at various temperatures for 2 h

degree of orientation is about 0.2. The density and degree of orientation are gradually increased by heating and finally the relative density reaches more than 90% and the degree of orientation is more than 0.8 by sintering at 1150–1200°C for BNT-based materials. The compacts after calcination are composed of oriented, platelike template grains and small, equiaxed matrix grains with random orientation, as shown in Figs. 10.6 and 10.7. The growth of template grains at the expense of matrix grains is responsible for an increase in the degree of orientation. The grain growth behavior of RTGG-processed BNT-based materials is different from the previous theory of sintering.

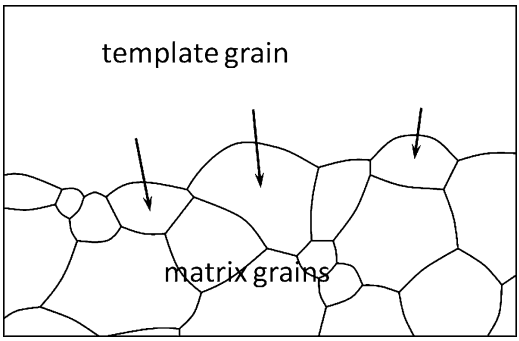

Fig. 10.15 Grain growth by the migration of grain boundaries toward the center of curvature as indicated by arrows. Normally, a large grain is surrounded by convex boundaries, and the boundary migration results in the growth of the grain

The following growth behavior is explained according to the theory of sintering [5]. When the compact is composed of large and small grains, like the TGG- and RTGG-processed compacts, a typical microstructure is shown in Fig. 10.15 for materials with curved grain boundaries as shown in Fig. 10.9a. The grain boundaries are curved and the center of curvature is located in a small grain. Grains grow by the migration of grain boundaries toward the center of curvature. In the case shown in Fig. 10.15, the migration of grain boundaries results in the growth of large template grains at the expense of small matrix grains. Thus, the degree of orientation increases. However, in the BNKT case, the grain boundary is faceted as shown in Fig. 10.9c, and the driving force for grain boundary migration does not develop.

Figure 10.16 shows the microstructure development at the initial stage of grain growth observed in $Bi_{0.5}(Na_{0.5}K_{0.5})_{0.5}TiO_3$ [4], and Figure 10.17 shows the schematic illustration of morphological change [15]. At first, matrix grains adhere to a template grain, forming grain boundary between (100) of the template grain and an arbitrary plane (*hkl*) of the matrix grain (Figs. 10.16a and 10.17a). The boundary structure is expressed by $(100)_{Tp}//(hkl)_M$, where Tp and M stand for template and matrix grains, respectively. In the next step, the third grain, which is referred to as terrace, develops between the template and matrix grains (Figs. 10.16b and 10.17b). The (100) face of terrace is parallel to the (100) face of the template grain. Therefore, the boundary structure between the terrace and the template grain is $(100)_{Tr}//(100)_{Tp}$, where Tr stands for terrace, and that between the terrace and the matrix grain is $(100)_{Tr}//(hkl)_M$. As shown later, the terrace and template grain have an epitaxial relationship, and the boundary between the terrace and template grain disappears, i.e., the terrace and template grain coalesce. The boundary between the terrace and matrix grain is curved as shown in Fig. 10.17b, migrates toward the center of curvature, and finally disappears as shown in Fig. 10.17c. Because the grain boundaries are facetted in $Bi_{0.5}(Na_{0.5}K_{0.5})_{0.5}TiO_3$, as shown in Fig. 10.9c, the curved surface of terrace becomes facetted (Figs. 10.16c and 10.17d).

The epitaxial relationship between the terrace and template grains is expected from the disappearance of the boundary between these grains (Fig. 10.16c). The epitaxial relation is confirmed by using a single crystal of $SrTiO_3$ as a substrate [27]. Figure 10.18 shows the microstructure of BNKT grains on the $SrTiO_3$ substrate.

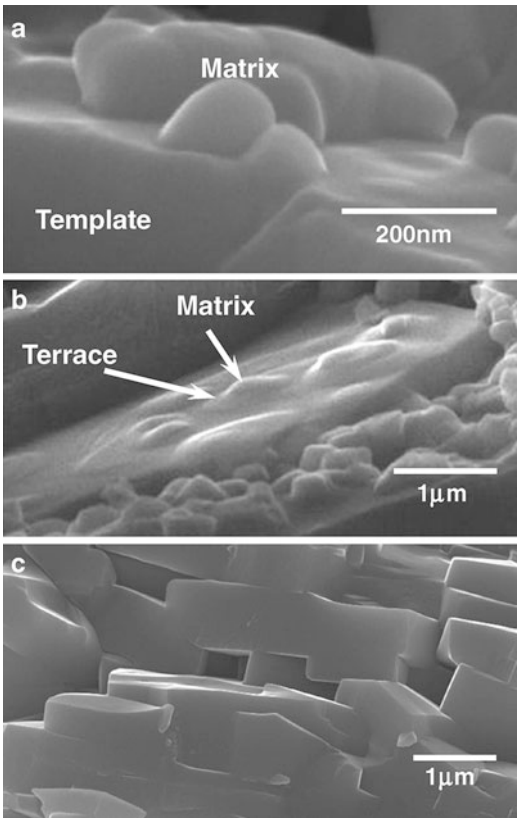

Fig. 10.16 Grain growth by solid-state epitaxial growth observed in $Bi_{0.5}(Na_{0.5}K_{0.5})_{0.5}TiO_3$. (**a**) Matrix grains adhere to a template grain. (**b**) A terrace forms between the matrix and template grains. The terrace has an epitaxial relation to the matrix grain. (**c**) The template grain grows as a result of coalescence of terraces into the matrix grain. (**a**, **b**) are SEM images for RTGG-processed specimens after heat-treatment at 1,000°C and (**c**) at 1,100°C for 2 h [4]

The grains with an irregular shape are BNKT grains and thin square sheets between the substrate and BNKT grains are terraces. The edges of square terraces are parallel to each other, indicating an epitaxial relationship between the terrace and the substrate (template). It is expected that the same epitaxial relationship develops between the BNKT terrace and BNKT template. Thus, the formation and coalescence of epitaxial terrace are the origin of grain growth, i.e., solid-state epitaxial growth, and texture formation.

One of the possible mechanisms of terrace formation is solid-state spreading [17]. Shi et al. have observed the material flow from a small, spherical TiO_2 particle to a flat surface of TiO_2; several lattice layers from the spherical particle spread over the flat surface [26]. Although Shi et al. have proposed it is surface diffusion, we consider this phenomenon is material flow that is spreading. A similar material transport is operative for the formation of terrace in BNKT.

The shape of template grains is platelike during growth, but the aspect ratio decreases; the grains thicken but the dimension of plate face is practically constant [3]. The crystal structure of BNKT is cubic at the sintering temperature, and an equilibrium

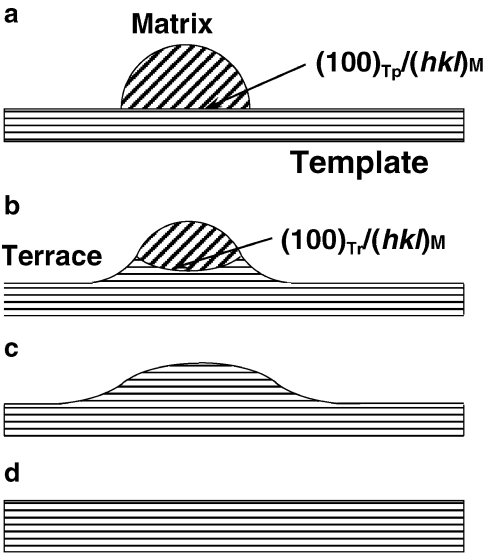

Fig. 10.17 Schematic diagram of grain growth by solid-state epitaxial growth. (**a**) A matrix grain adheres to a template grain, forming grain boundary with the structure $(100)_{Tp}/(hkl)_M$, where Tp and M stand for template and matrix respectively. (**b**) A terrace forms between the matrix and template grains. The terrace has an epitaxial relation to the template grain. The boundary between the terrace and matrix grain has the structure of $(100)_{Tr}/(hkl)_M$, where Tr stands for terrace, and migrates toward the center of curvature. (**c**) The matrix grain disappears, remaining the terrace with the same orientation as that of the template grain. (**d**) The surface of terrace becomes facetted. The coalescence of terraces into the matrix grain results in the growth of template grain

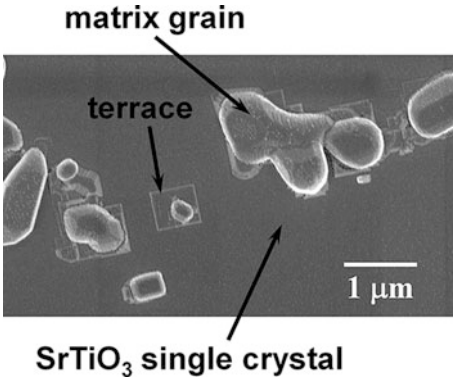

Fig. 10.18 The model experiment of terrace formation. $Bi_{0.5}(Na,K)_{0.5}TiO_3$ (BNKT) particles are dispersed on a (100) $SrTiO_3$ single crystal substrate and heated at 1,150°C. The square BNKT terraces form between the BNKT particles and substrate. The edges of terraces are mutually parallel, indicating an epitaxial relation between the terraces and substrate [27]

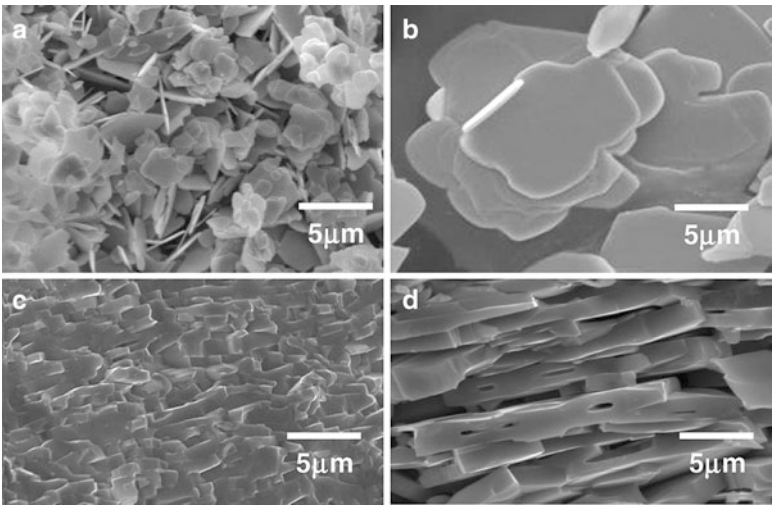

Fig. 10.19 (**c**, **d**) are microstructures of RTGG-processed $Bi_{0.5}(Na_{0.5}K_{0.5})_{0.5}TiO_3$ compacts (sintered at 1,150°C for 2 h) prepared using different-sized reactive templates (platelike BiT) shown in (**a**, **b**), respectively. The width of platelike grains is determined by the diameter of platelike BiT particles. The template grains grow along the thickness direction [4]

shape of grain is cubic (Fig. 10.9c). When the driving force for grain growth is small, as in the present case, the grain approaches to an equilibrium shape. The grain shape is platelike before sintering, and it approaches to an equilibrium shape by thickening, but departs from it by widening. Therefore, the width of the grains can be controlled by selecting the size of reactive template as shown in Fig. 10.19 [4].

One of the merits of RTGG process is the applicability to piezoelectric ceramics with complex compositions. In many cases, high properties can be expected for the composition near the morphotropic phase boundary (MPB). In the RTGG process, the template and matrix grains are formed by in situ reactions between BiT, Na_2CO_3, K_2CO_3, and TiO_2. Diffusivity of these reactants is different, resulting in wide compositional variation in the calcined compact. Homogenization of composition is necessary during sintering to obtain the sintered compact with a narrow compositional distribution. As we discussed in Section 10.3, the formation of any major intermediate phase that does not have crystallographic similarity to perovskite could disturb the succession of texture from the reactive template to the targeted ceramic [30].

10.9 Improvement of Piezoelectric Properties

The increase in the amount of reactive template increases the area of available interface for solid-state epitaxial growth in a unit volume and eventually enhances the degree of orientation. $Bi_{0.5}(Na_{0.85}K_{0.15})_{0.5}TiO_3$ (BNKT15) ceramics were fabricated through

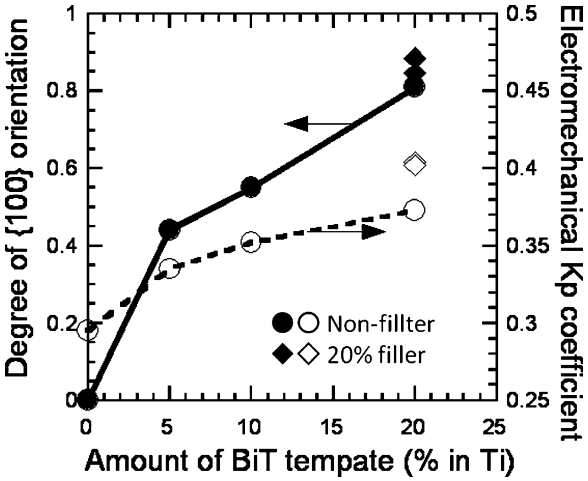

Fig. 10.20 Lotgering's degree of {100} orientation and electromechanical coupling factor K_p of BNKT15 ceramics as a function of amount of platelike BiT particles as the Ti source ratio in all raw materials

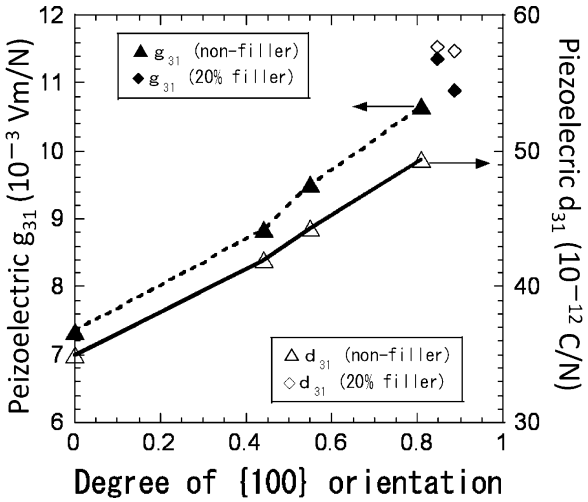

Fig. 10.21 Piezoelectric g_{31} and d_{31} coefficient as a function of Lotgering's degree of {100} orientation of BNKT15 ceramics prepared by RTGG and conventional methods

the RTGG method by using different amounts of platelike BiT particles; the designed amount of template grains was 5, 10, and 20 vol%. Tape-cast specimens were laminated, heat-treated, CIP-processed, and sintered at 1,150°C for 10 h in O_2. The sintered specimens were machined into disks with a diameter of 11 mm and a thickness of 0.5 mm for dielectric and piezoelectric property measurements. The gold electrodes were sputter-deposited on the both surfaces of the disks. The electroded disks were poled at 4 kV/mm for 30 min in an oil bath at 100°C. The piezoelectric properties were measured by the resonance–antiresonance method with an impedance/gain-phase analyzer (HP 4194A).

Figure 10.20 gives the Lotgering F factor of pseudocubic {100} orientation and the electromechanical coupling factor of the RTGG-processed ceramics in comparison with those of conventionally processed ceramic with the same composition. It should be noted that the partial use of presynthesized BNKT15 filler powder improved the texture and coupling coefficient (Tani et al. unpublished). Figure 10.21 gives the

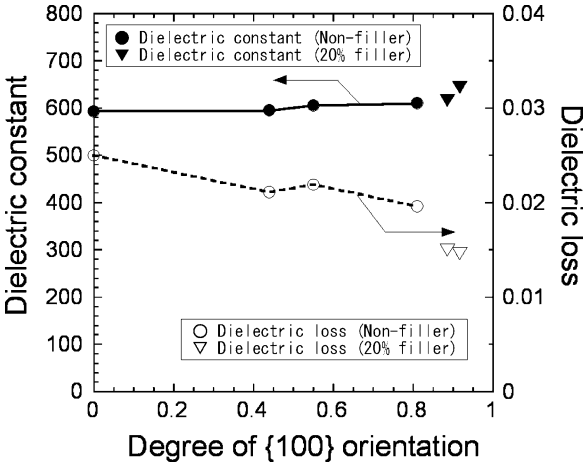

Fig. 10.22 Dielectric constant and dielectric loss as a function of Lotgering's degree of {100} orientation of BNKT15 ceramics prepared by RTGG and conventional methods

piezoelectric g_{31} and d_{31} coefficient as a function of degree of {100} orientation. Both coefficients are increased linearly as the degree of orientation is increased. Figure 10.22 shows dielectric constant and loss measured at 1 V and 1 kHz; the dielectric constant did not vary for specimens with different texture, while the dielectric loss was reduced as the texture was improved.

10.10 Conclusion

Texture control of BNT-based ceramics through the RTGG process has been described in terms of key processing parameters, texture development mechanism, and piezoelectric properties. A marked improvement in piezoelectric properties has been achieved by the application of the RTGG method to BNT-based materials. The most important stage in this method is the in situ formation of platelike perovskite-type template from the reactive template and complementary reactants in a powder compact. Therefore, the selection of materials for the reactive template and complementary reactants is the key issue. The sintering stage is also important to reduce the volume of matrix grains, and it is necessary to understand the mechanisms of microstructure development in the compacts containing at least two kinds of particles with different powder characteristics. In the BNT-based materials, solid-state epitaxial growth is the dominant process for the growth of template grains, and the processing parameters are designed based on this mechanism to obtain better textured ceramics with controlled microstructure.

The application of the RTGG method is not limited to BNT-based materials but widely extended to other materials. They are $BaTiO_3$, $K_{0.5}Na_{0.5}NbO_3$, and $Bi_{0.5}K_{0.5}TiO_3$-based ceramics with the regular-perovskite structure [20, 23, 24, 28]. Highly textured ceramics of BLSFs have also been prepared by the RTGG

processing [31, 32]. In addition, the RTGG method has been applied to the processing of textured electrical conductor ceramics: superconducting bismuth layered oxides and p-type and n-type thermoelectric oxide ceramics [7, 36, 38].

Another approach for textured BNT ceramics must be addressed: the TGG process using presynthesed platelike perovskite-type template. The platelike BNT particles were prepared by the topochemical microcrystal conversion (TMC) method from a mixture of platelike precursor particles of layer-structured $Na_{0.5}Bi_{4.5}Ti_4O_{15}$ and TiO_2 in a molten NaCl salt [22]. The TMC-/TGG-processed BNT ceramics also reached a high degree of orientation ($F = 0.87$) and enhanced piezoelectricity (nearly double in d_{31} of nontextured).

Texture engineering is an effective approach for the improvement of performance for lead-free piezoelectric materials which would otherwise have inferior properties to lead-containing compositions. Further understanding of texture development mechanisms is necessary for the fabrication of highly textured ceramics for a given composition. Additionally, theoretical prediction of electrical properties for a given microstructure is desired for designing optimum microstructure and texture of ceramics.

References

1. Abe Y, Kimura T (2002) Factors determining grain orientation in bismuth sodium potassium titanate – lead zirconate titanate solid solutions made by reactive templated grain growth method. J Am Ceram Soc 85(5):1114–1120
2. Chiang Y-M, Farrey GW, Soukhojak AN (1998) Lead-free high-strain single-crystal piezoelectrics in the alkaline–bismuth–titanate perovskite family. Appl Phys Lett 73:3683–3685
3. Fukuchi E, Kimura T, Tani T, Takeuchi T, Saito Y (2002) Effect of potassium concentration on the grain orientation in bismuth sodium potassium titanate. J Am Ceram Soc 85 (6):1461–1466
4. Fuse K, Kimura T (2006) Effect of particle size of starting materials on microstructure development in textured $Bi_{0.5}(Na_{0.5}K_{0.5})_{0.5}TiO_3$. J Am Ceram Soc 89(6):1957–1964
5. German RM (1996) Sintering Theory and Practice. John Wiley & Sons, New York
6. Hunter RJ (1993) Introduction to Modern Colloid Science. Oxford University Press, Oxford
7. Kashimura T, Isobe T, Senna M, Itoh M, Koizumi T (1996) Reactive sintering for oriented and connected Bi-2223 superconductive oxides from a mixture of delaminated Bi-2212 and fine powdered supplemental ingredients. Physica C 270(3–4):297–304
8. Kato K, Kimura T (2006) Preparation of textured $Bi_{0.5}(Na, K)_{0.5}TiO_3$-$BiFeO_3$ solid solutions by reactive-templated grain growth process. J Korean Ceram Soc 43(11):693–699
9. Kim HJ, Krane MJM, Trumble KP, Bowman KJ (2006) Analytical fluid flow models for tape casting. J Am Ceram Soc 89(9):2769–2775
10. Kimura T, Yamaguchi T (1983) Fused salt synthesis of $Bi_4Ti_3O_{12}$. Ceram Int 9(1):13–17
11. Kimura T, Yamaguchi T (1987) Morphology control of electronic ceramic powders by molten salt synthesis. Adv Ceram 21:169–177
12. Kimura T, Yoshida Y, Sakuma Y, Murata M (2004) "Microstructure development in textured $MBi_4Ti_4O_{15}$ (M=Sr, Ba) and $Bi_{0.5}(Na_{0.85}K_{0.15})_{0.5}TiO_3$, Proceedings of the 1st Workshop on Anisotropic Science and Technology of Materials and Devises, pp 53–60

13. Kimura T, Takahashi T, Tani T, Saito Y (2004) Crystallographic texture development in bismuth sodium titanate by reactive templated grain growth method. J Am Ceram Soc 87 (8):1424–1429
14. Kimrua T, Fukuchi E, Tani T (2005) Fabrication of textured bismuth sodium titanate using excess bismuth oxide. Jpn J Appl Phys 44(11):8055–8061
15. Kimura T, Miyazaki C, Tsuzuki K, Fuse K, Motohashi T (2007) Effect of surface energy anisotropy on microstructure development of piezoelectric ceramic made by templated grain growth process In: Heinrich JG, Aneziris C. Proc. 10th ECerS Conf., Göller Verlag, Baden-Baden, pp 626–631 .
16. Messing GL, Trolier-McKinstry S, Sabolsky EM, Duran C, Kwon S, Brahmaroutu B, Park P, Yilmaz H, Rehrig PW, Eitel KB, Suvaci E, Seabaugh M, Oh KS (2004) Templated grain growth of textured piezoelectric ceramics. Crit Rev in Solid State and Mater Sci 29(2):45–96
17. Missiaen JM, Voytovych R, Gilles G, Eustathopoulos N (2005) Solid state spreading in the Cu/Cu System. J Mater Sci 40(9–10):2377–2381
18. Mistler RE, Twiname ER (2000) Tape Casting. The American Ceramic Society, Westerville, OH
19. Motohashi T, Kimura K (2008) Formation of homo-template grains in $Bi_{0.5}Na_{0.5}TiO_3$ prepared by the reactive-templated grain growth process. J Am Ceram Soc 91(12):3889–3895
20. Nemoto M, Hiruma Y, Nagata H, Takenaka T (2008) Fabrication and piezoelectric properties of grain-oriented $(Bi_{1/2}K_{1/2})TiO_3$-$BaTiO_3$ ceramics. Jpn J Appl Phys 47(5):3829–3832
21. Okazaki K (1957) On the sintering phenomena of barium titanate ceramics, especially the expansion and shrinkage characteristics at high temperature. J Ceram Soc Jpn 65:67–73
22. Saito Y, Takao H (2007) Synthesis of plate-like $(Bi_{0.5}Na_{0.5})TiO_3$ particles by using a topochemical microcrystal conversion method and grain-oriented ceramics. J Korean Phys Soc 51(2):790–797
23. Saito Y, Takao H (2010) Synthesis of polycrystalline platelike $NaNbO_3$ particles by the topochemical micro-crystal conversion from $K_4Nb_6O_{17}$ and fabrication of grain-oriented $(K_{0.5}Na_{0.5})NbO_3$ ceramics. J Electroceram 24(1):39–45
24. Saito Y, Takao H, Tani T, Nonoyama T, Takatori K, Homma T, Nagaya T, Nakamura M (2004) Lead-free piezoceramics. Nature 432:84–87
25. Seno Y, Tani T (1999) TEM observation of a reactive template for textured $Bi_{0.5}(Na_{0.87}K_{0.13})_{0.5}TiO_3$ polycrystals. Ferroelectrics 224(1–4):793–800
26. Shi J-L, Deguchi Y, Sakabe Y (2005) Relation between grain growth, densification and surface diffusion in solid state sintering - a direct observation. J Mater Sci 40:5711
27. Shoji T, Fuse K, Kimura T (2009) Mechanism of texture development in $Bi_{0.5}(Na, K)_{0.5}TiO_3$ prepared by the templated grain growth process. J Am Ceram Soc 92(S1):S140–S145
28. Sugawara T, Nomura Y, Kimura T, Tani T (2001) Fabrication of (111) oriented $BaTiO_3$ bulk ceramic by reactive templated grain growth method. J Ceram Soc Jpn 109(10):897–900
29. Takeuchi T, Tani T (2002) Texture development of $SrTiO_3$ ceramics during reactive templated grain growth processing. J Ceram Soc Jpn 110(4):232–236
30. Takeuchi T, Tani T (2002) Texture engineering of lead-containing perovskite-type ceramics by RTGG method. Key Eng Mater 216:3–6
31. Takeuchi T, Tani T, Saito Y (1999) Piezoelectric properties of bismuth layer-structured ferroelectric ceramics with a preferred orientation processed by the reactive templated grain growth method. Jpn J Appl Phys 38(9B):5553–5556
32. Takeuchi T, Tani T, Saito Y (2000) Unidirectionally textured $CaBi_4Ti_4O_{15}$ ceramics by the reactive templated grain growth with an extrusion. Jpn J Appl Phys 39(9B):5577–5580
33. Tani T (1998) Crystalline-oriented piezoelectric bulk ceramics with a perovskite-type structure. J Korean Phys Soc 32:S1217–S1220
34. Tani T (2006) Texture engineering of electronic ceramics by the reactive-templated grain growth method. J Ceram Soc Jpn 114(5):363–370
35. Tani T, Kimura T (2006) Reactive-templated grain growth processing for lead free piezoelectric ceramics. Adv Appl Ceram 105(1):55–63

36. Tani T, Isobe S, Seo W-S, Koumoto K (2001) Thermoelectric properties of highly textured $(ZnO)_5In_2O_3$ ceramics. J Mater Chem 11(9):2324–2328
37. Tani T, Fukuchi E, Kimura T (2002) Relationship between pre-sintering conditions and sintering behavior of $Bi_{0.5}(Na, K)_{0.5}TiO_3$ ceramics textured by reactive templated grain growth method. J Jpn Soc Powder Powder Metall 49(3):198–202
38. Tani T, Itahara H, Xia C, Sugiyama J (2003) Topotactic synthesis of highly-textured thermoelectric cobaltites. J Mater Chem 13(8):1865–1867
39. Umezawa K, Kimura T (2008) Effect of heterocoagulation on the preparation of textured $CaBi_4Ti_4O_{15}$ and $SrBi_4Ti_4O_{15}$ made by reactive-templated grain growth process [in japanese]. J Jpn Soc Powder Powder Metall 55(4):270–275
40. Watanabe H, Kimura T, Yamaguchi T (1989) Particle orientation during tape casting in the fabrication of grain-oriented bismuth titanate. J Am Ceram Soc 72(2):289–293
41. West DL, Payne DA (2003) Microstructure development in reactive-templated grain growth of $Bi_{1/2}Na_{1/2}TiO_3$-based ceramics: Template and formulation effects. J Am Ceram Soc 86(5): 769–774
42. Williams JC (1976) Doctor-Blade Process. In: Wang FFY, Wang FFY (eds) Treatise on Materials Science and Technology, vol 9, Ceramic Fabrication Processes. Academic Press, New York
43. Zhang S-T, Kounga AB, Aulbach E, Ehrenberg H, Rödel J (2007) Giant strain in lead-free piezoceramics $Bi_{0.5}Na_{0.5}TiO_3$-$BaTiO_3$-$K_{0.5}Na_{0.5}NbO_3$ system. Appl Phys Lett 91:1,12,906

Chapter 11
Crystal Growth and Electric Properties of $Na_{0.5}Bi_{0.5}TiO_3$-$BaTiO_3$ Single Crystals

Qinhui Zhang, Xiangyong Zhao, and Haosu Luo

11.1 Introduction

Owing to relatively high piezoelectric performances, the A-site complex perovskite solid solution, $Na_{0.5}Bi_{0.5}TiO_3$-$BaTiO_3$ (NBBT), has been considered to be an excellent candidate material for lead-free piezomaterials, since it was discovered in 1991 by Takenaka et al. [1]. However, as is well known, there are still many problems that need urgent solutions in NBBT solid system solution. For example, the piezoelectric properties of NBBT solution system piezoceramics are much lower than lead-based ones. Moreover, some problems are controversial, such as the nature of phase transition at depolarization temperature (T_d). Many researchers proposed that the phase transition at T_d was from rhombohedral ferroelectric to tetragonal antiferroelectric phase [1], while other experimental results did not indicate the existence of antiferroelectric phase, such as X-ray diffraction (XRD) [2] and Roman and neutron scattering [3, 4]. NBBT single crystals can present a good research platform to study and understand these problems.

Many researchers have reported the methods to obtain NBBT single crystals, such as Bridgman method [5, 6], flux method [6–10], and metal strip heated zone melting (MSHZM) method [9]. Hosono et al. reported the NBBT single crystals grown by the flux method and Bridgman method, but only small crystals with low electric properties were obtained [6]. Babu et al. reported the MSHZM technique was employed for the growth of NBBT single crystal, and crystals with an approximate maximum size of $15 \times 12 \times 12$ mm^3 were obtained [9]. Noguchi et al. have acquired transparent high quality NBBT91/9 single crystal by the O_2-blowing flux method, while the maximum size of crystal grains were only $5 \times 5 \times 3$ mm^3 [10]. Besides, our group tried to obtain NBBT single crystals by top-seeded solution

Q. Zhang • X. Zhao • H. Luo (✉)
Shanghai Institute of Ceramics, Chinese Academy of Sciences, 215 Chengbei Road, Jiading, Shanghai 201800, China
e-mail: hsluo@mail.sic.ac.cn

S. Priya and S. Nahm (eds.), *Lead-Free Piezoelectrics*,
DOI 10.1007/978-1-4419-9598-8_11, © Springer Science+Business Media, LLC 2012

growth (TSSG) method. Ge et al. have successfully obtained NBBT96/4 single crystal with dimension of Φ30 mm × 10 mm, grown by the TSSG method using platinum (Pt) wire as the seed [11].

In this chapter, large-size and high quality (100−x) $Na_{0.5}Bi_{0.5}TiO_3$-$x$$BaTiO_3$ (NBBT (100−x)/x) single crystals were grown by controlled TSSG method, with the $<001>_C$-oriented seed. The dimension of the as-grown NBBT (100−x)/x single crystals can reach up to Φ35 mm × 10 mm. The composition dependence of crystal structure was studied by X-ray diffraction (XRD). The dielectric, piezoelectric, and ferroelectric properties of NBBT single crystals with different compositions were measured and summarized. Moreover, Mn-doped NBBT95/5 single crystal was grown and studied, which exhibited excellent piezoelectric and ferroelectric properties. At last, domain structure of NBBT single crystals was discussed.

11.2 Crystal Growth of NBBT Single Crystals

11.2.1 Polycrystalline Material Synthesis

Raw oxide powders with purity higher than 99.99% were used as starting reagents, comprising Na_2CO_3, Bi_2O_3, Ba_2CO_3, and TiO_2. The $Na_{0.5}Bi_{0.5}TiO_3$ and $BaTiO_3$ powders with stoichiometric ratio were mixed completely, and then put them together into muffle furnace for solid-state reactions. The summary solid-state reaction is as follows:

$$Na_2CO_3 + Bi_2O_3 + BaCO_3 + TiO_2 \rightarrow (Na_{0.5}Bi_{0.5})TiO_3 - BaTiO_3 + CO_2 \uparrow \tag{11.1}$$

In Ref [2], the TG-DTA curves for the mixture powders of NBT and BT were presented. According to thermogravimetric analyses, the decomposition temperatures of carbonate are about 628°–862°C and 814°–1,160°C for NBT and BT, respectively. Figure 11.1 shows the XRD patterns of NBBT96/4 and NBBT90/10 raw powders calcined at different temperatures for 10 h. As calcination temperatures increase to 1,000°C, all diffraction peaks for both NBBT powders with different compositions are corresponding to pure perovskite structure, while there were some nonperovskite diffraction peaks in XRD patterns of powders calcined at 800°C. So the calcination condition of NBBT polycrystalline powders is 1,000°C for 10 h. Then excess 20 wt% Bi_2O_3 and Na_2CO_3 as self-flux were mixed with NBBT polycrystalline powders. The mixture powders with self-flux were calcined again in muffle furnace at about 900°C, for the decomposition of Na_2CO_3.

Further, the melting-points of NBBT (100−x)/x polycrystalline powders were determined by TG-DTA curves, as shown in Fig. 11.2. The melting-points of NBBT polycrystalline powders with different compositions were all about 1,240°C. Moreover, the melting-point decreased with an increase of $BaTiO_3$, which have important significance to the growth process of NBBT single crystal.

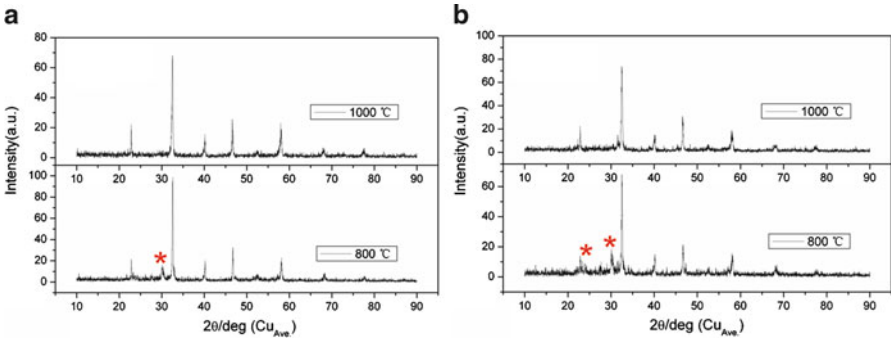

Fig. 11.1 X-ray diffraction (XRD) patterns of (**a**) NBBT94/6 and (**b**) NBBT90/10 raw powders calcined at different temperatures for 10 h (nonperovskite diffraction peaks were marked with *asterisk*)

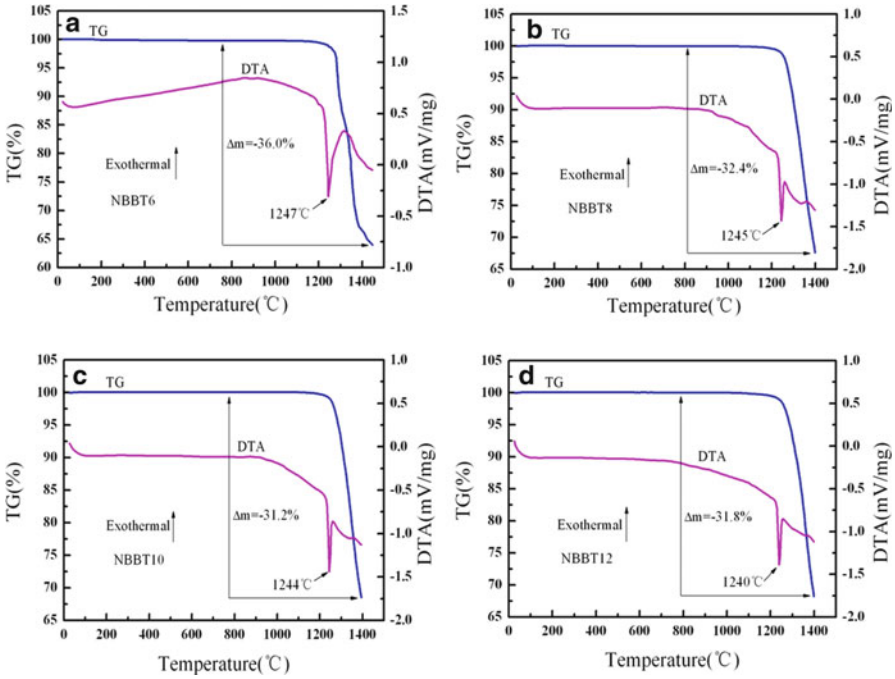

Fig. 11.2 TG-DTA curves for NBBT $(100-x)/x$ polycrystalline powders

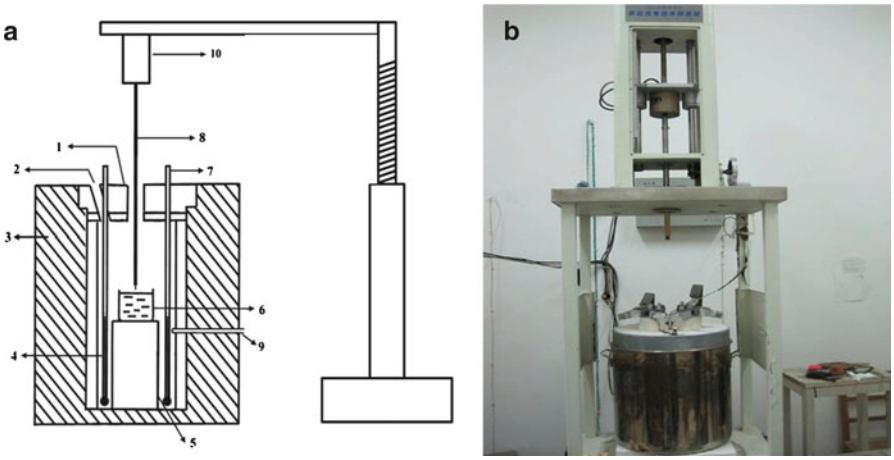

Fig. 11.3 The resistance furnace used for NBBT crystal growth: 1 alumina cap; 2 observation window; 3 adiabatic brick; 4 $MoSi_2$ heater; 5 substrate for crucible; 6 platinum crucible; 7 $MoSi_2$ heating elements; 8 seed crystal; 9 thermocouple; 10 lifting system

11.2.2 Crystal Growth of NBBT

All the NBBT single crystals were grown by TSSG method. Firstly, NBBT polycrystalline powders were put into platinum (Pt) crucible. Then, the Pt crucible was heated by using a resistance furnace (see Fig. 11.3) at air atmosphere. Small $<001>_C$-oriented NBBT crystals were used as the seeds for crystal growth. Before the process of crystal growth, the solution should be incubated for 10 h at about 20°C above the melting-point. Velocities of rotation and pulling of the seed were, respectively, in the ranges of 6–12 rpm and 1.2–2.5 mm per day. The higher the BT concentration in NBBT crystal, the lower the pulling velocity. It is worth emphasizing that the crystal growth speed must be controlled carefully because of the slow solute diffusion process. At the end of crystal growth, the crystal was separated from the flux-melt surface and cooled down to room temperature at a rate of 50–60°C/h. Figure 11.4 shows the photos of NBBT single crystals with different compositions.

The segregation of Ba^{2+} ions in NBBT single crystals deserves our attention, which affect the electric properties of crystals obviously. Table 11.1 shows the concentration difference of Ba^{2+} between NBBT crystals and raw powders, which were measured by Inductive Coupled Plasma Atomic Emission Spectrometry (ICP-AES). We can find that the concentration of Ba^{2+} ions in as-grown NBBT single crystals was lower compared with polycrystalline powders. This result indicated that the Ba^{2+} ions incorporated into crystals and occupied the A-sites difficultly, because of the larger ionic radius.

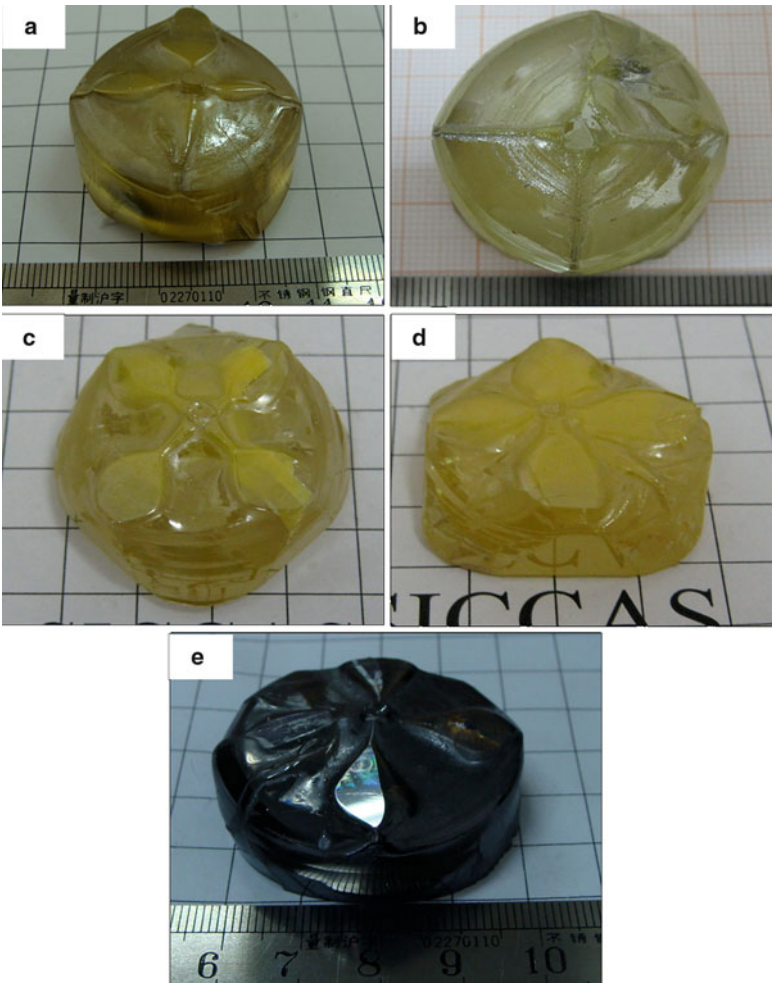

Fig. 11.4 As-grown NBBT single crystals: (**a**) NBBT96/4; (**b**) NBBT95/5; (**c**) NBBT94/6; (**d**) NBBT93/7, (**e**) Mn:NBBT95/5

Table 11.1 The concentration difference of Ba^{2+} between NBBT crystals and polycrystalline powders

Nominal composition in polycrystalline powders	NBBT90/10	NBBT89/11	NBBT88/12
Real composition in NBBT single crystals	NBBT96/4	NBBT95/5	NBBT94/6

11.3 Composition Dependence of NBBT Crystal Structure

Figure 11.5 shows the XRD patterns of NBBT $(100-x)/x$ ($x = 4, 5, 6, 7$) single crystals. All the crystals have a pure perovskite structure and no second phases are observed, implying BT and NBT have formed a solid solution. As is well known, NBT crystal possesses rhombohedral symmetry (R) at room temperature, while BT has a tetragonal structure (T), as shown in the phase diagram of NBBT ceramics, which was presented by Takenaka et al. in 1991 [1]. As the concentration of BT increased, the R and T phases would coexist in NBBT crystals, which was the MPB region. To further identify the MPB region, the evolutions of diffraction peaks with composition were measured.

Figure 11.6a, b show the evolutions of <111> and <200> diffraction peaks with composition, in the 2θ ranges of 38–42° and 44–48°, respectively.

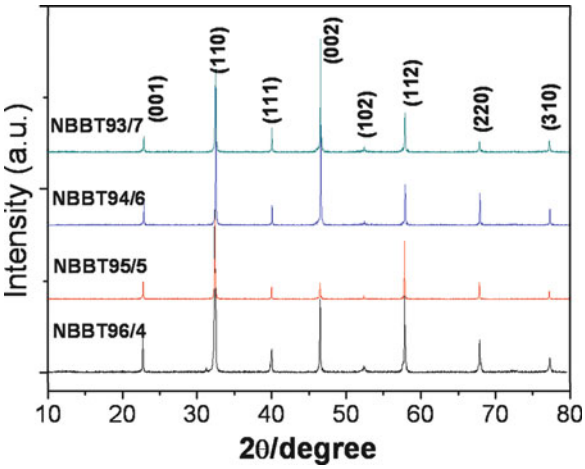

Fig. 11.5 X-ray powder diffraction patterns of NBBT single crystals

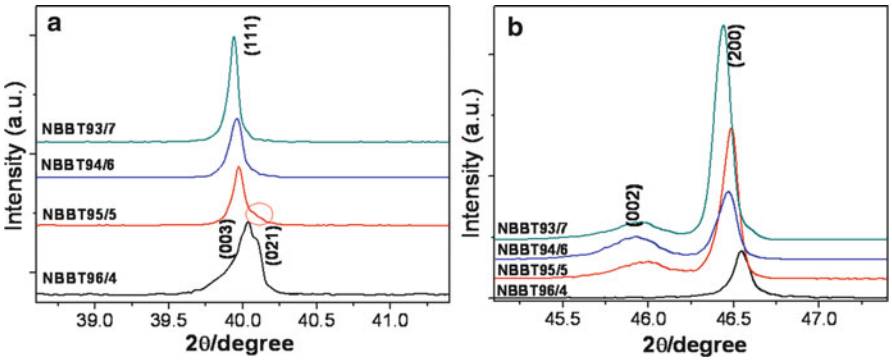

Fig. 11.6 Evolution of (111) and (200) diffraction peaks with composition

The rhombohedral symmetry is characterized by the peak splitting into <003> and <021> from the single <111> peak [12, 13]. Similarly, the splitting of <200> diffraction peak indicated the tetragonal phase [14–16]. We can find that a tetragonal phase appeared and increased slightly when $x > 5$, as the intensity of <002> diffraction peak increased. Moreover, the splitting of <111> can be observed at the same time. So we can conclude that the MPB region of NBBT crystals began at about $x > 5$, while the MPB in NBBT ceramics was reported to exist at $x = 0.06$–0.07 [1]. We considered that the difference of MPB was attributed mainly to the existence of grain boundaries in ceramics, where the Ba^{2+} could aggregate. In addition, D.Viehland et al. investigated the relative phase stability of Mn-doped NBBT95/5 crystals under dc electric bias [16]. They found that an induced phase transition from R to T phases was observed under an electric field along <001> orientation, and this T phase can remain stable after the removal of electric field. In other words, the free energies of R and T phases are close to each other in NBBT crystals with compositions near the MPB.

11.4 Electric Properties of NBBT Crystals

11.4.1 Dielectric Properties

Figure 11.7 shows the temperature and frequency dependences of dielectric permittivity ε_r and loss tanδ for <001>-oriented poled NBBT single crystals. Two abnormal dielectric peaks can be seen, as indicated by T_d and T_m. The T_d plays an important role with regard to practical applications of NBT-BT single crystals: as it was previously been reported as the temperature of a ferroelectric (FE) phase to antiferroelectric (AFE) phase transformation [1], whereas T_m that of an AFE to paraelectric (PE) one. The T_d can be derived from the temperature of the first peak of tanδ [17]. Recently, other perspectives of the nature of the phase transition at T_d were presented [18–20]. Tai et al. considered that the depolarization was induced by the weakening of macroscopic ferroelectric domains, which is associated with the reduction of octahedral tilting [20]. Besides, the lower temperature phase transition near T_d is diffusive obviously, but the shifts of temperature T_m with frequency characteristic of relaxors cannot be observed. Similar results were found in Pb-based piezoelectric ceramics [21]. Therefore, we considered that this phenomenon might be related with the macrodomain–microdomain transition. Below T_d, NBBT samples remained the ferroelectric macrodomain structure forming in poling processes. When the temperature exceeded T_d, the change from macrodomain to microdomain occurred because of the phase transition from rhombohedral ferroelectric to tetragonal antiferroelectric state, and the dispersive character was observed.

To further identify our above assertion, the temperature dependences of dielectric permittivity ε_r for <001>-oriented unpoled NBBT crystals were presented, as

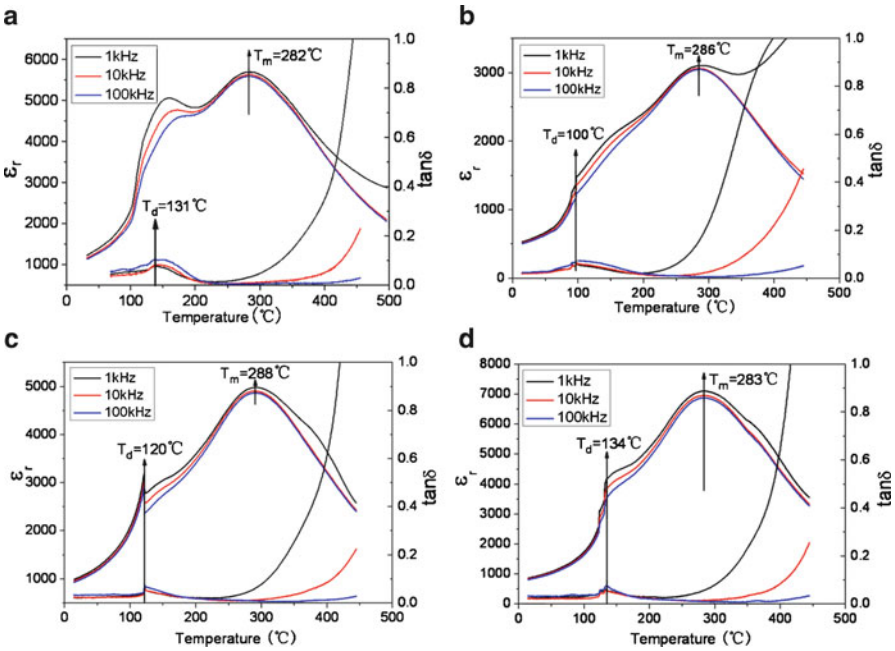

Fig. 11.7 Temperature dependences of dielectric permittivity ε_r and loss tanδ for <001>-oriented poled NBBT crystals at 1, 10, and 100 kHz: (**a**) NBBT96/4; (**b**) NBBT95/5; (**c**) NBBT 94/6; (**d**) NBBT93/7

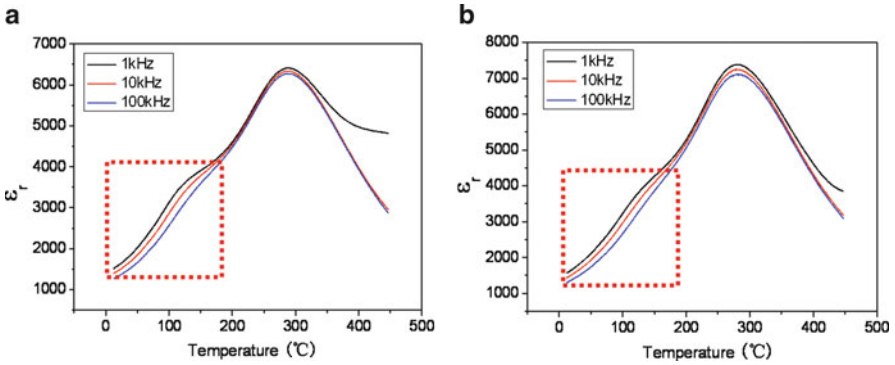

Fig. 11.8 Temperature dependences of dielectric permittivity ε_r for <001>-oriented unpoled NBBT crystals at 1, 10 and 100 kHz: (**a**) NBBT 94/6 and (**b**) NBBT93/7

shown in Fig. 11.8. For both unpoled NBBT crystals, the dispersive character was observed below T_d because of the microdomain structure in unpoled samples, while this phenomenon only existed near T_d in poled one. However, clearly explained further studies concerning the mechanism of depolarization are needed.

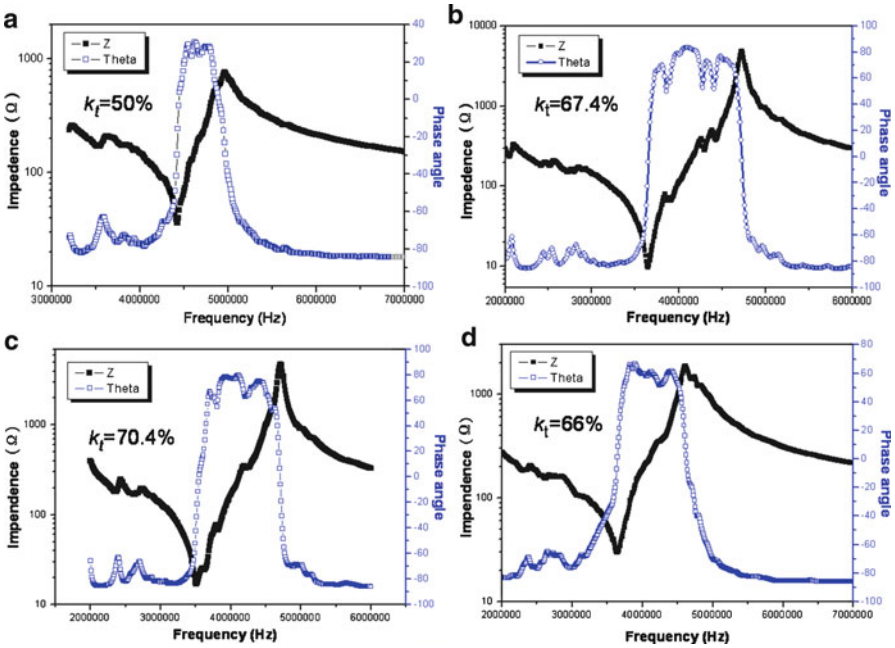

Fig. 11.9 Room temperature impedance spectra for <001>-oriented poled samples: (**a**) NBBT96/4; (**b**) NBBT95/5; (**c**) NBBT94/6; (**d**) NBBT93/7

Moreover, the orientation dependence of dielectric permittivity ε_r and loss tanδ for <001>, <110>, and <111> oriented poled NBBT96/4 single crystals samples was reported by Ge et al. [11]. According to this paper, the (T_m, ε_m) values for <001>, <110>, and <111> oriented samples are (306°C, 3718), (305°C, 3613), and (307°C, 3600) at 1 kHz, respectively. So it can be concluded that the dielectric properties are almost independent of crystal orientations at the same measuring conditions.

11.4.2 Piezoelectric and Ferroelectric Properties

The piezoelectric contants d_{33} were measured by a quasi-static Berlincourt-type meter, of ZJ-3A type made by Institute of Acoustics, Chinese Academy of Sciences. The electromechanical coupling factors k_t was determined by a resonance–antiresonance method with Agilent 4294A impedance analyzer. The polarization (*P-E*) and strain (*S-E*) hysteresis loops were measured by using a ferroelectric test system (aixACCT TFanalyzer 1000).

Figure 11.9 shows the impedance and phase angle as a function of frequency for $<001>_C$-oriented NBBT(100−*x*)/*x* (*x* = 4, 5, 6, 7) single crystals plates at room temperature. It should be noted that the thickness electromechanical coupling

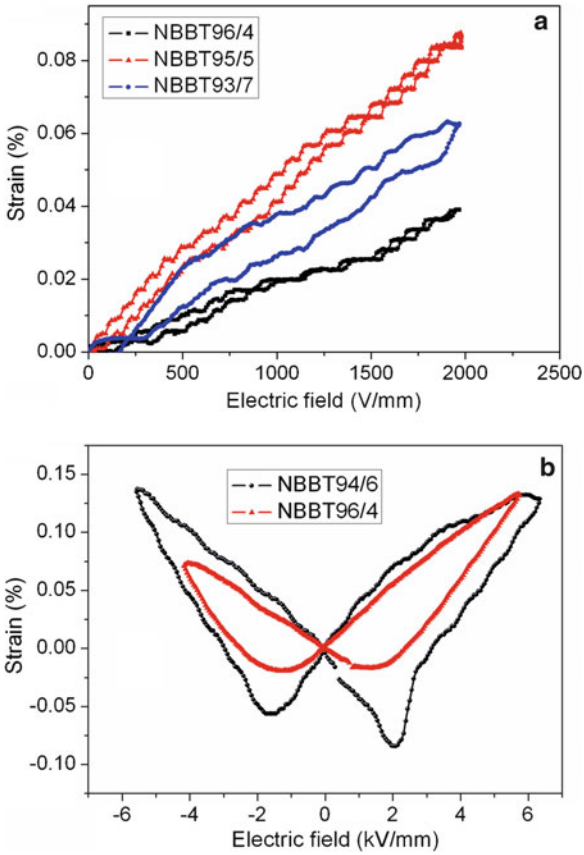

Fig. 11.10 Unipolar and dipolar *S-E* loops for poled NBBT single crystals measured at 1 Hz

factors k_t of NBBT(100−x)/x (x = 5, 6, 7) calculated according to IEEE standards are 67.4, 70.4, and 66%, respectively, which are even higher than Pb-based piezoelectric single crystals (PMNT and PZNT). Such NBBT crystals with high piezoelectric properties will be promising candidates for practical applications, such as medical ultrasonic transducers.

Figure 11.10a, b show the unipolar and dipolar *S-E* loops for poled NBBT single crystals measured at 1 Hz, respectively. The unipolar *S-E* curves of the NBBT96/4 and NBBT95/5 were almost linear and had a little hysteresis compared with NBBT93/7, as shown in Fig. 11.10a. Moreover, the average values of d_{33} calculated based on unipolar *S-E* curves were in accordance with the values measured by quasi-static Berlincourt-type meter.

Strain vs. bipolar electric field curves for NBBT96/4 and NBBT94/6 crystals at room temperatures are shown in Fig. 11.10b, in which asymmetric piezoelectric butterfly curves were observed in both NBBT crystals. The internal bias field formed by defects may be one reason for the phenomenon.

Table 11.2 Piezolectric and dielectric properties of NBBT single crystals

	ε_r (1 kHz)	tanδ (1 kHz)	d_{33}(pC/N)	k_t(%)	N (Hz m)
NBBT96/4	1,230	0.018	283	50	2,210
NBBT95/5	1,100	0.027	420	66–67	1,825
NBBT94/6	1,040	0.019	400	68–70	1,755
NBBT93/7	993	0.027	373	66	1,825

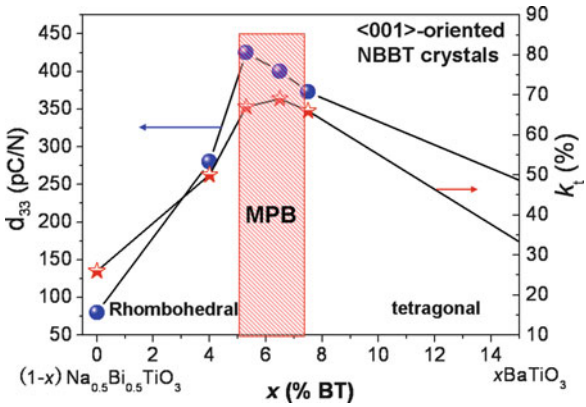

Fig. 11.11 The compositional dependences of piezoelectric properties in NBBT system

Table 11.2 summarizes the piezoelectric and dielectric properties of NBBT $(100-x)/x$ ($x = 4, 5, 6, 7$) and Mn-doped NBBT95/5 single crystals. It was found that NBBT95/5, NBBT94/6, and NBBT93/7 exhibit excellent piezoelectric properties, which near the rhombohedral-tetragonal morphotropic phase boundary. It can be attributed to an increase in the number of possible spontaneous polarization direction for the compositions near the MPB according to the domain engineering mechanism, which was first presented in Pb-based relaxor ferroelectrics [22]. Figure 11.11 shows the compositional dependences of the piezoelectric properties of NBBT single crystals near the MPB. After the addition of BT to NBT, the piezoelectric properties increase sharply with increasing x and then decrease, giving good performances at around $0.05 < x < 0.07$.

Figure 11.12 shows the P-E hysteresis loops of <001>-oriented NBBT96/4 and NBBT94/6 single crystals measured at 1 Hz at room temperature. We can find that the P-E loop of NBBT96/4 was saturated, while the one of NBBT94/6 was unsaturated because of the relatively large leakage current. Moreover, the sample breakdown of NBBT94/6 occurred when the higher voltage was applied. The remnant polarizations P_r were 32 and 23 μC/cm^2 for NBBT96/4 and NBBT94/6, respectively. However, the unsaturated P-E loop of NBBT94/6 did not show the actual ferroelectric properties. The similar results were found in NBBT95/5 and NBBT93/7 single crystals.

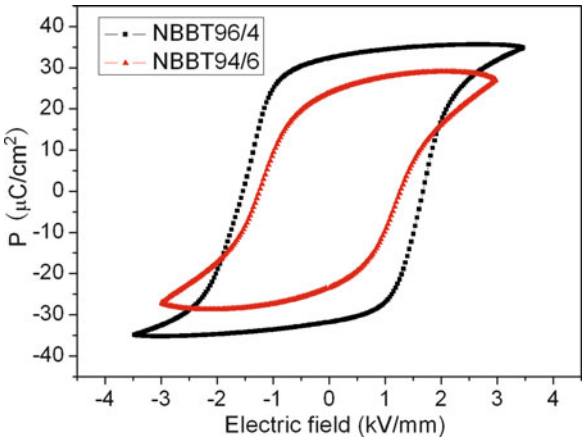

Fig. 11.12 *P-E* loops for <001>-oriented NBBT96/4 and NBBT94/6 measured at 1 Hz

11.5 Electric Properties of Mn-Doped NBBT95/5 Crystal

As discussed earlier in this chapter, relatively large leakage current was a major problem in NBBT single crystals, especially in NBBT95/5, 94/6, and 93/7. Therefore, this problem was exigent to be solved. Modest concentrations of Mn dopants have been reported to be an effective method to enhance the resistivity of NBT ferroelectric ceramics [23]. So, Mn-doped NBBT95/5 single crystal was grown in order to obtain more excellent electric properties, and the photo of Mn-doped NBBT95/5 single crystal is shown in Fig. 11.4e.

The dielectric and piezoelectric properties of Mn-doped NBBT95/5 are also shown in Table 11.3. The piezoelectric constant d_{33} reached up to 483pC/N, which was obviously higher than undoped ones. Meanwhile, a saturated *P-E* hysteresis loop was obtained, as shown in Fig. 11.13. The value of remnant polarizations P_r was 45.3 μC/cm^2. We attributed this mainly to the decrease of leakage current in NBBT single crystal by doping Mn [24].

Additionally, the defect structure of Mn-doped NBBT95/5 single crystal was studied by the low frequency (100–500 Hz) dielectric constant as a function of temperature, as shown in Fig. 11.14. These data reveal a dramatically enhanced dielectric constant for undoped NBBT in the temperature range of 300 ~ 600°C, yielding values in excess of 10^5, which were extremely frequency dispersive. These data evidence the presence of a space charge conduction mechanism at elevated temperatures as previously reported [18], which results in correspondingly high loss factors. It is important to note in this temperature range of 300 ~ 600°C, that Mn was extremely effective in suppressing such conduction effects as can be seen in the inset. In fact, for Mn-doped NBBT, no evidence of enhanced permittivity was observed in this elevated temperature range. Rather, the maximum dielectric constant was only 6,000 which was ~15× lower than that of undoped NBBT crystal. Space charge in NBBT crystals may result from bismuth $V_{Bi}^{'''}$ and oxygen $V_O^{\bullet\bullet}$ vacancies, due to the Bi_2O_3 volatility during crystal growth. When Mn is incorporated

Table 11.3 Piezolectric and dielectric properties of Mn-doped NBBT95/5 single crystals, compared with Pb-based materials

	ε_r (1 kHz)	tanδ (1 kHz)	d_{33}(pC/N)	k_t(%)	T_m
Mn:NBBT95/5	1,090	0.019	483	55	282
NBBT95/5	1,100	0.027	420	66–67	285
PZT-5H ceramics	3,800	0.02	650	55	225
PMNT71/29 crystal	5,000	0.006	2,000	60	135

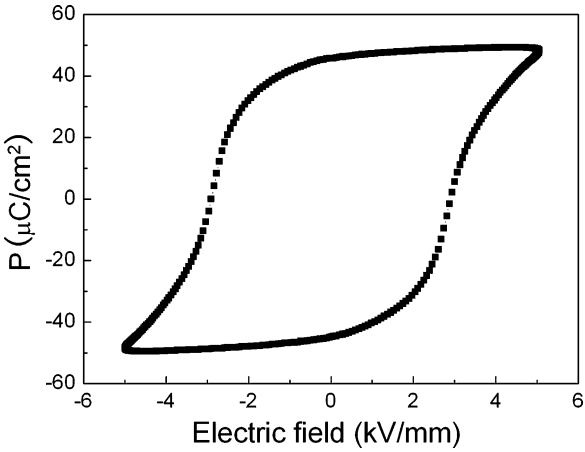

Fig. 11.13 *P-E* loop for <001>-oriented Mn-doped NBBT95/5 single crystal

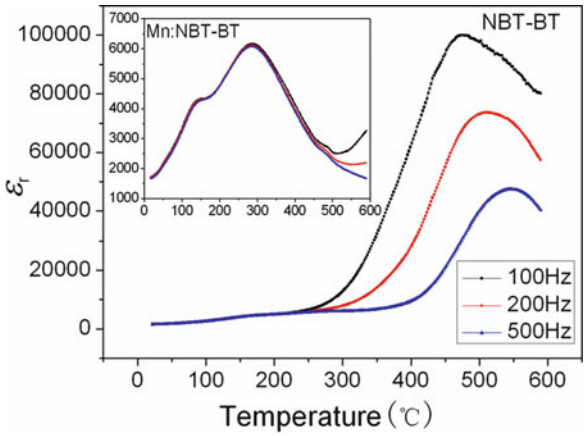

Fig. 11.14 Low frequency (100–500 Hz) dielectric constant of <001>-oriented poled Mn-doped NBBT and NBBT single crystals as a function of temperature

into the A-sites of NBBT, the concentration of $V_O^{\bullet\bullet}$ will be decreased as $2Mn^{3+} + 2Bi^{3+} + 3O^{2-} \leftrightarrow 2Mn_{Bi}^{\times} + Bi_2O_3$. Accordingly, space charge conduction might be suppressed by Mn substitution, enhancing the high temperature dc electrical resistivity and decreasing the leakage current density. However, more studies are needed in order to understand the doping mechanism of Mn in NBBT single crystal clearly.

11.6 Conclusions

A series of NBBT single crystals with different compositions were grown by the top-seed solution growth method. The crystal growth, crystalline structure, and electric properties were investigated. The results of XRD indicated that the tetragonal phase formed as the increase of BT. Diffusive phase transition at the T_d was observed obviously, which could be explained by the macro–microdomain model. The main piezoelectric properties of NBBT crystals were summarized, and excellent performances were observed when the compositions were near the MPB. It should be noted that large thickness coupling coefficients were obtained, which are promising candidates for practical applications, such as medical ultrasonic transducers. Moreover, doping Mn in NBBT crystals was certified as an effective method to enhance the piezoelectric and ferroelectric properties.

References

1. Takenaka T, Maruyama K, Sakata K (1991) $(Bi_{1/2}Na_{1/2})TiO_3$-$BaTiO_3$ system for lead-free piezoelectric ceramics. Jpn J Appl Phys 30:2236–2239
2. Park SE, Chung SJ, Kim IT, Hong KS (1994) Nonstoichiometry and the long-range cation odering in crystals of $(Bi_{1/2}Na_{1/2})TiO_3$. J Am Ceram Soc 77:2641–2647
3. Zhang MS, Scott JF, Zvirgzds JA (1986) Raman-spectroscopy of $(Bi_{0.5}Na_{0.5})TiO_3$. Ferroelectr Lett 6:147–152
4. Vakhrushev SB, Isupov VA, Kvyatkovsky BE, Okuneva NM, Pronin IP, Smolensky GA, Syrnikov PP (1985) Phase-transitions and soft modes in sodium bismuth titanate. Ferroelectrics 63:153–160
5. Xu G, Duan Z, Wang X, Yang D (2005) Growth and some electrical properties of lead-free piezoelectric crystals $(Bi_{1/2}Na_{1/2})TiO_3$ and $(Bi_{1/2}Na_{1/2})TiO_3$-$BaTiO_3$ prepared by a Bridgman method. J Cryst Growth 275:113–119
6. Hosono Y, Harada K, Yamashita Y (2001) Crystal growth and electric properties of lead-free piezoelectric material $(Bi_{1/2}Na_{1/2})TiO_3$-$BaTiO_3$. Jpn J Appl Phys 40:5722–5726
7. Chiang YM, Farrey GW, Soukhojak AN (1998) Lead-free high-strain single-crystal piezoelectrics in the alkaline-bismuth-titanate perovskite family. Appl Phys Lett 73:3683–3685
8. Babu JB, He M, Zhang D, Chen X (2007) Enhancement of ferroelectric properties of $Bi_{1/2}Na_{1/2}TiO_3$-$BaTiO_3$ single crystals by Ce dopings. Appl Phys Lett 90:102901–102903
9. Babu JB, Madeswaran G, He M, Zhang D, Chen X, Dhanasekaran R (2008) Inhomogeneity issues in the growth of $Bi_{1/2}Na_{1/2}TiO_3$-$BaTiO_3$ single crystals. J Cryst Growth 310:467–472
10. Noguchi Y, Tanabe I, Suzuki M, Miyayama M (2008) High-quality single crystal growth of Bi-based perovskite ferroelectrics based on defect chemistry. J Ceram Soc Japan 116:994–1001
11. Ge W, Liu H, Zhao X, Li X, Pan X, Lin D, Xu H, Jiang X, Luo H (2009) Orientation dependence of electrical properties of $0.96Bi_{0.5}Na_{0.5}TiO_3$-$0.04BaTiO_3$ lead-free piezoelectric single crystal. Appl Phys A 95:761–767
12. Xu Q, Chen S, Chen W, Wu S, Lee J, Zhou J, Sun H, Li Y (2004) Structure, piezoelectric properties and ferroelectric properties of $(Bi_{0.5}Na_{0.5})_{1-x}Ba_xTiO_3$ system. J Alloy Compd 381:221–225

13. Xu Q, Chen X, Chen W, Chen M, Xu S, Kim B, Lee JH (2006) Effect of MnO addition on structure and electrical properties of $(Bi_{0.5}Na_{0.5})_{0.94}Ba_{0.06}TiO_3$ ceramics prepared by citrate method. Mater Sci Eng B 130:94–100
14. Suchanicz J, Kusz J, Bohm H, Duda H, Mercurio JP, Konieczny K (2003) Structure and dielectric propertis of $(Bi_{0.5}Na_{0.5})_{0.70}Ba_{0.30}TiO_3$ ceramics. J Eur Ceram Soc 23:1559–1564
15. Xu C, Lin D, Kwok KW (2008) Structure, electrical properties and depolarization temperature of $(Bi_{0.5}Na_{0.5})TiO_3$-$BaTiO_3$ lead-free piezoelectric ceramics. Solid State Sci 10:934–940
16. Ge W, Cao H, Li J, Viehland D, Zhang Q, Luo H (2009) Influence of dc-bias on phase stability in Mn-doped $Na_{0.5}Bi_{0.5}TiO_3$-5.6 at% $BaTiO_3$ single crystals. Appl Phys Lett 95:162903–162905
17. Yoshii K, Hiruma Y, Nagata H, Takenaka T (2006) Electrical properties and depolarization temperature of $(Bi_{1/2}Na_{1/2})TiO_3$-$(Bi_{1/2}K_{1/2})TiO_3$ lead-free piezoelectric ceramics. Jpn J Appl Phys 45:4493–4496
18. Park SE, Chung SJ (1996) Ferroic phase transitions in $(Bi_{1/2}Na_{1/2})TiO_3$ crystals. J Am Ceram Soc 79:1290–1296
19. Jones GO, Thomas PA (2002) Investigation of the structure and phase transitions in the novel A-site substituted distorted perovskite compound $Na_{0.5}Bi_{0.5}TiO_3$. Acta Cryst B 58:168–178
20. Tai CW, Choy SH, Chan HLW (2008) Ferroelectric domain morphology evolution and octahedral tilting in lead-free $(Bi_{1/2}Na_{1/2})TiO_3$-$(Bi_{1/2}K_{1/2})TiO_3$-$(Bi_{1/2}Li_{1/2})TiO_3$-$BaTiO_3$ ceramics at different temperatures. J Am Ceram Soc 91:3335–3341
21. Yao X, Chen Z, Cross LE (1983) Polarization and depolarization behavior of hot pressed lead lanthanum zirconate titanate ceramics. J Appl Phys 54:3399–3403
22. Park SE, Shrout TR (1997) Ultrahigh strain and piezoelectric behavior in relaxor based ferroelectric single crystals. J Appl Phys 82:1804–1811
23. Nagata H, Takenaka T (2001) Additive effects on electrical properties of $(Bi_{1/2}Na_{1/2})TiO_3$ ferroelectric ceramics. J Eur Ceram Soc 21:1299–1302
24. Zhang Q, Zhang Y, Wang F, Wang Y, Lin D, Zhao X, Luo H, Ge W, Viehland D (2009) Enhanced piezoelectric and ferroelectric properties in Mn-doped $Na_{0.5}Bi_{0.5}TiO_3$-$BaTiO_3$ single crystals. Appl Phys Lett 95:102904–102906

Chapter 12
Nonstoichiometry in $(Bi_{0.5}Na_{0.5})TiO_3$ Ceramics

Yeon Soo Sung and Myong Ho Kim

12.1 Introduction

Among Bi alkali metal titanate piezoceramics [1–10], $(Bi_{0.5}Na_{0.5})TiO_3$ (BNT) is a typical system that has been known for many years. Its structure was identified as ABO_3 perovskite with rhombohedral symmetry. However, it was long ago concluded that, due to its properties, it was not viable to compete with $Pb(Zr,Ti)O_3$ (PZT)-based ceramics. Not surprisingly, it did not draw much attention until the toxicity of the PZT oxide became a critical environmental issue. In particular, Pb and Pb oxide processing and waste disposal are harmful to the environment. Restrictions have been imposed on the use of hazardous substances; however, PZT-based ceramics have been an exception because substitute materials have not been available. In light of this situation, Pb-free materials have been rigorously studied. Thus far, none of the currently available Pb-free materials has shown properties comparable to those of PZT.

BNT is such a Pb-free material frequently mentioned in the literature. However, there are still ambiguities in the characteristics of BNT itself because most of the research piling up on BNT has been based solid solutions with morphotropic phase boundary (MPB) compositions which are expected to have a similar success to PZT solid solutions [11–24]. As expected, high properties have been obtained but the values themselves have been below expectations as compared with PZT. In particular, key properties such as the piezoelectric coefficient (d_{33}) and the depolarization temperature (T_d) are not good enough to replace PZT. To be able to improve the BNT properties, it is necessary to understand the end members of solid solutions. Here, T_d is a unique property in BNT, not observed in PZT, but acting as a counterpart of the Curie temperature (T_c) of PZT, which has been observed to be

Y.S. Sung • M.H. Kim (✉)
School of Nano and Advanced Materials Engineering, Changwon National University, Changwon, Gyeongnam 641-773, South Korea
e-mail: mhkim@changwon.ac.kr

S. Priya and S. Nahm (eds.), *Lead-Free Piezoelectrics*,
DOI 10.1007/978-1-4419-9598-8_12, © Springer Science+Business Media, LLC 2012

inversely proportional to d_{33}. Relatively low T_d ~ 200°C and d_{33} ~ 200 pC/N is the biggest hurdle that should be overcome before BNT-based ceramics can find any practical applications.

In the literature, Bi and Na oxides in BNT ceramics are considered to be lost during processing. Thinking that their volatile tendency is similar to Pb occurred in PZT, the properties of BNT would be prone to be compositionally inhomogeneous. In addition, Na_2CO_3, a typical raw powder used in processing BNT, is hygroscopic, absorbing moisture from the surrounding air and gaining weight. It should be completely dried before weighted. Otherwise, the nominal starting composition would be off-stoichiometric. Moreover, ABO_3 perovskite is a structure allowing compositional variations. In that aspect, A-site nonstoichiometry that could occur during any stage of processing gives rise to intrinsic defects. In comparison, B-site nonstoichiometry accompanied by doping with aliovalent ions induces extrinsic defects. Both A- and B-site nonstoichiometry apparently have a profound influence on the properties of BNT [25–44] as in the case of PZT [13, 45–50].

The effects of nonstoichiometry on d_{33} and T_d of BNT need to be systematically studied. It is a vital step to take not only for understanding but also for improving the properties of BNT. Thus, controlling compositions that cause variations in its structure and properties followed by a comprehensive analysis of the coupling between them is the objective of this chapter dedicated to nonstoichiometry followed by A-site intrinsic and B-site extrinsic disorders in BNT.

12.2 Preparation and Characterization

Powders of Bi_2O_3 (99.9%), Na_2CO_3 (99.95%), TiO_2 (99.9 + %), Nb_2O_5 (99.9%), Mn_2O_3 (99.999%), and $BaCO_3$ (99.9%) with least 3 N purity were used to prepare $(Bi_{0.5+x}Na_{0.5+y})(Ti_{1-z}D_z)O_3$ (D = Nb, Mn) ceramics and solid solutions. In handling raw powders, hygroscopic Na_2CO_3 was thoroughly dried in a dry oven so that no change in weight occurred before weighing. Then it was weighed quickly in air; otherwise, it absorbed moisture from ambient air and gained weight, resulting in incorrect composition from the beginning.

The powders for each composition were ball-milled using yttria-stabilized zirconia balls and anhydrous ethanol to keep the powders from absorbing water. After milling, the powders were dried and calcined twice in air at a temperature of 780 and 800°C for 2 h. This repetition allowed all the components to be kept intact during calcination but also to have homogeneous powders after calcination. Subsequently, they were mixed with polyvinyl alcohol (PVA) up to 0.5 wt% and screened using a 150-μm sieve for pelletizing. Pellets of 10 or 18 mm in diameter and ~1 mm in thickness were produced by uniaxial pressing at a pressure of 150 MPa. Then, the samples were sintered in air at a temperature of 1,150°C for 2 h. The heating rate was controlled so as to burn out PVA at a temperature of approximately 500°C.

The Archimedes principle was applied to estimate the apparent densities of the sintered pellets and compare them with the theoretical densities. X-ray diffraction (XRD) patterns obtained from the polished surfaces of sintered pellets or softly crushed powders using a diffractometer with Cu Kα radiation ($\lambda = 1.541838$ Å) at 40 kV and 30 mA were analyzed to identify phases and determine lattice parameters. Scanning electron microscopy (SEM) together with energy dispersive spectroscopy was also used to detect any secondary phase formation other than the BNT phase as well as to examine how grain morphology evolved during sintering.

To measure the properties of the ceramics produced, samples were polished on both sides down to 0.5 mm in thickness using #400, 800, and 1,200 emery papers. The next step was to paint them with Ag paste and cure them in air at a temperature of 650°C for 0.5 h. The poling of samples was carried out in silicone oil at room temperature under a direct current (DC) field of 40 kV/cm for 0.5 h using a high voltage supply (Keithley 248). At the same time, the leakage current was monitored using an electrometer (Keithley 6514). A four-point probe method was applied to estimate the electrical conductivity at elevated temperature.

After aging for 24 h, the composition dependence of room temperature d_{33} was estimated using a quasi-static piezo d_{33} meter (ZJ-6B, IACAS) at 0.25 N and 110 Hz. The temperature dependence of dielectric constant (ε) and loss tangent ($\tan\delta$) at various frequencies was estimated during heating and cooling using an impedance analyzer (HP4192A). T_d was determined from the temperature where the peak $\tan\delta$ was observed by depoling of the pre-poled samples upon heating. Planar electromechanical coupling factors (k_p) and mechanical quality factors (Q_m) were calculated based on the resonance frequencies (f_r), antiresonance frequencies (f_a), resonant impedances (Z_r), and capacitances (C_p) measured at 1 kHz using an impedance gain phase analyzer (HP4194A). Electric field dependent polarization (P-E) hysteresis loops were estimated using a Sawyer-Tower circuit.

12.3 Nonstoichiometry by Means of A-Site Intrinsic Disorders in $(Bi_{0.5+x}Na_{0.5+y})TiO_3$

A-site Bi and Na nonstoichiometry in BNT results in intrinsic disorders. In light of this, Bi and Na vacancies and the corresponding O vacancies are of the ones to consider for charge compensation. Taking into account the volatility of Bi and Na oxides during processing, A-site nonstoichiometry is inevitable and is expected to affect both structure and properties of BNT, which need to be better understood.

Bi nonstoichiometry of the samples was controlled to be at $x = -1 \sim +2$ mol% while keeping $y = 0$ mol%. Na nonstoichiometry was, on the other hand, controlled to be at $y = -5 \sim +1$ mol% while keeping $x = 0$ mol%. The apparent densities of the pellets after sintering were all above ~95% as compared with the theoretical density. Polishing both sides of the sintered pellets from ~1 to 0.5 mm in thickness ensured consistency between measurements and minimized inconsistent or erroneous results due to evaporation of volatile Bi and/or Na oxides during processing.

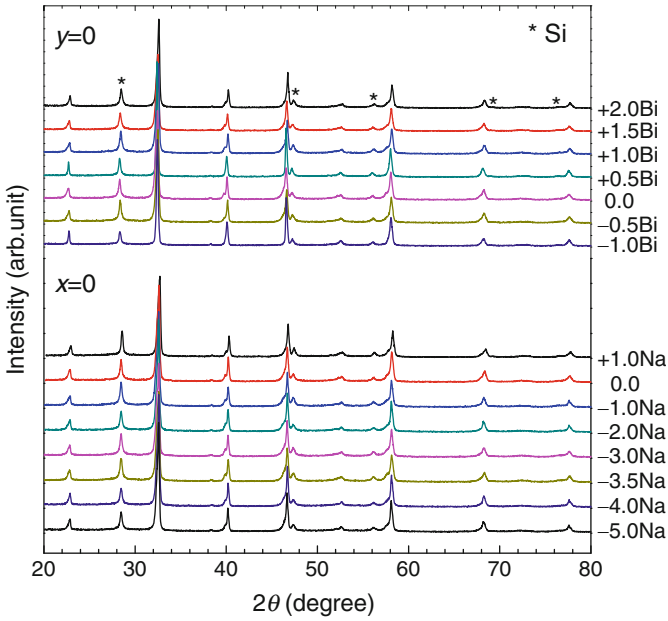

Fig. 12.1 X-ray diffraction (XRD) patterns of $(Bi_{0.5+x}Na_{0.5+y})TiO_3$ ceramics of varying x at $y = 0$ mol% and varying y at $x = 0$ mol% which had been sintered in air at a temperature of 1,150°C for 2 h. 5 N Si powder peaks were used as an internal standard

The XRD patterns of BNT samples with Bi and Na nonstoichiometry after sintering in air at a temperature of 1,150°C for 2 h are shown in Fig. 12.1. The peaks correspond to the rhombohedral BNT phase, but no secondary phase peak was observed within the samples tested for deficient to excessive compositions of Bi or Na. These XRD patterns were further analyzed to calculate variations in lattice parameters, and lattice distortion turned out to be a key factor, affecting both d_{33} and T_d [51–53].

Lattice distortion, rhombohedral $90-\alpha$ and tetragonal c_T/a_T, induced by nonstoichiometry affected considerably d_{33} and T_d. It should be noted that a relatively smaller lattice distortion was favorable for higher d_{33} achieved via better poling by field and lower T_d achieved via easier depoling by temperature, and vice versa. This structure-properties relation coupled with lattice distortion was observed not only in BNT but also in its solid solutions.

The phase purity of BNT was further confirmed by the SEM images shown in Fig. 12.2. No secondary phase was observed other than BNT grains confirming the flexibility of BNT perovskite in A-site nonstoichiometry. Besides the BNT phase formation, there was an obvious trend in grain size in all SEM images. In the case of the samples with Bi nonstoichiometry, grains became small as the Bi content was increased and in particular, when was in excess. In the case of the samples with Na nonstoichiometry, grains became small as the Na content was decreased and became deficient. In other words, Bi and Na nonstoichiometry had opposite effects on the microstructure of BNT, which could not be distinguished through XRD patterns.

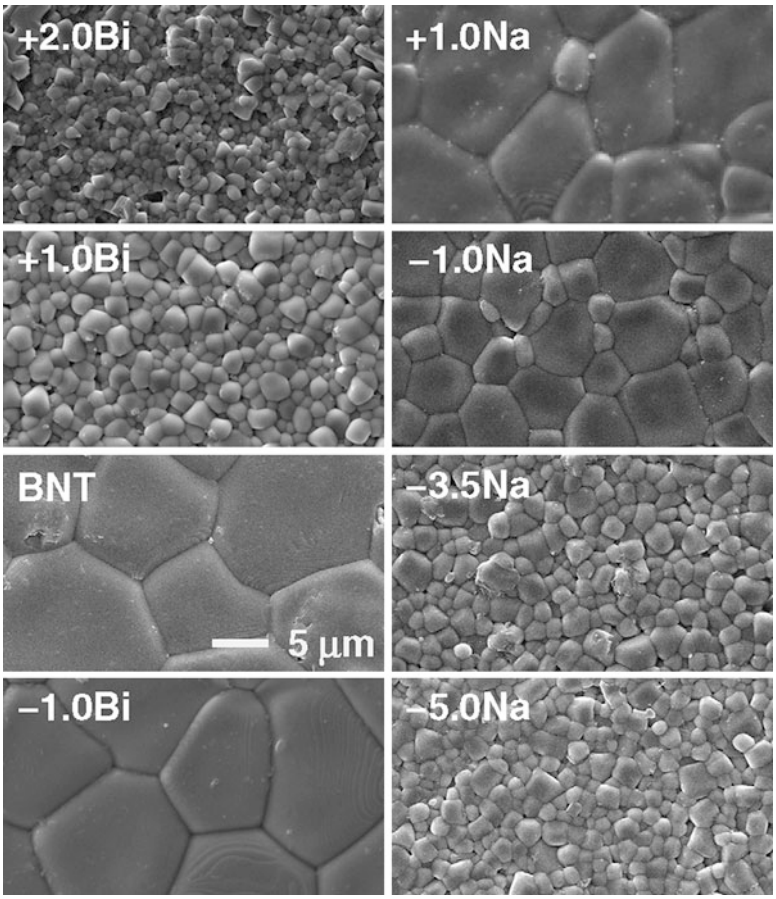

Fig. 12.2 Scanning electron microscopy (SEM) secondary electron images taken from the surfaces of $(Bi_{0.5+x}Na_{0.5+y})TiO_3$ ceramics with varying x at $y = 0$ mol% and varying y at $x = 0$ mol% sintered in air at a temperature of 1,150°C for 2 h. No secondary phase was observed other than $(Bi_{0.5}Na_{0.5})TiO_3$ (BNT) grains confirming the phase purity and clearly revealing the opposite trends in grain size which were caused by Bi and Na nonstoichiometry

Figure 12.3 shows the temperature-dependent dielectric properties of BNT with Bi and Na nonstoichiometry. BNT became lossy at lower frequency, abnormally high ε and tanδ due to space charges, [54] at either Bi-deficient compositions or compositions with excessive Na. ε was also smaller at either Bi or Na nonstoichiometry where the grain size was relatively small. T_d was determined from the temperature where the peak tanδ was observed in prepoled samples upon heating. It was relatively higher for both Bi-deficient compositions and compositions with excessive Na, which were frequency dependent. Overall, as in the case of grain size, Bi and Na nonstoichiometry affected the dielectric properties of BNT differently, indicating a correlation between its microstructure and the corresponding dielectric properties.

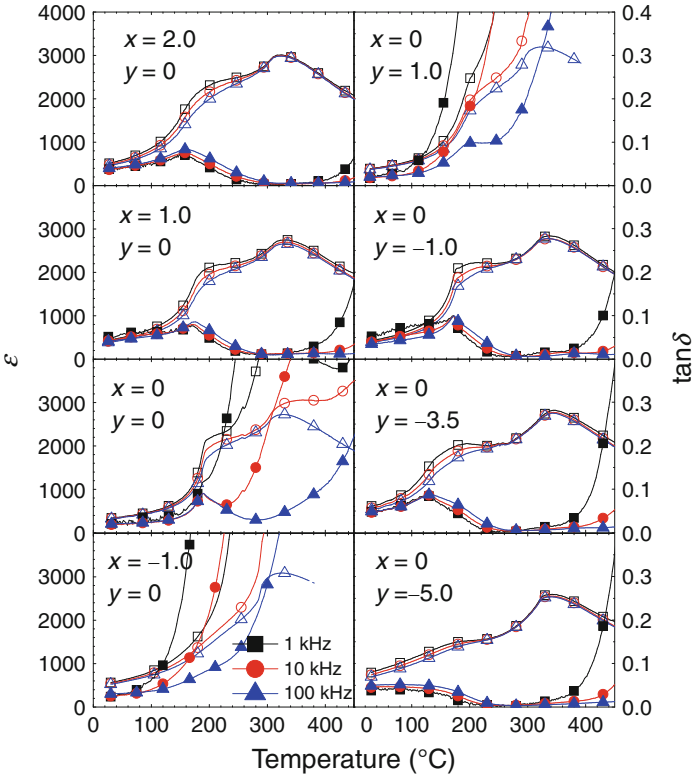

Fig. 12.3 Temperature dependence of dielectric constant (ε) and loss tangent (tanδ) in prepoled $(Bi_{0.5+x}Na_{0.5+y})TiO_3$ ceramics with varying x at $y = 0$ mol% and varying y at $x = 0$ mol% upon heating at 1, 10, and 100 kHz. Contrasting responses to Bi and Na nonstoichiometry can be clearly observed

Figure 12.4 illustrates the composition-dependent d_{33} together with T_d shown in Fig. 12.3. In the case of Bi nonstoichiometry, d_{33} increased to approximately 80 pC/N in compositions with excessive Bi but decreased in Bi-deficient compositions comparing to 74 pC/N for the nominally stoichiometric sample with $x = y = 0$ mol %. T_d, on the contrary, was higher in Bi-deficient compositions but lower in compositions with excessive Bi than 190°C for the nominally stoichiometric sample with $x = y = 0$ mol%. In the case of Na nonstoichiometry, d_{33} was increased up to 91 pC/N at $y = -3.5$ mol% but was decreased in compositions with excessive Na. T_d, on the contrary, was as low as 127°C at $y = -3.5$ mol% in Na-deficient compositions and higher in compositions with excessive Na. An inversely proportional relation between d_{33} and T_d induced by either Bi or Na nonstoichiometry became obvious and was attributed to lattice distortions in the case of Na nonstoichiometry [52]. From these results, it is clear that Bi and Na nonstoichiometry affected piezoelectric and dielectric properties in an opposite way. Lattice distortion is expected to play the same role in the case of Bi nonstoichiometry; this is currently under study.

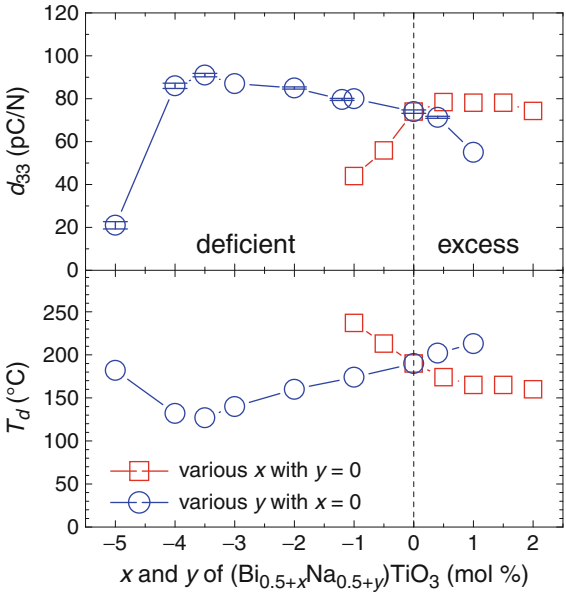

Fig. 12.4 Composition dependence of piezoelectric coefficient (d_{33}) in $(Bi_{0.5+x}Na_{0.5+y})TiO_3$ ceramics with varying x at $y = 0$ mol% and varying y at $x = 0$ mol% shown together with depolarization temperature (T_d) which was determined in Fig. 12.3. Their inverse relations are clearly observed

For the increase in d_{33}, donor doping in the B-site of ABO_3 perovskite structure yielding A-site vacancies can be considered, which leads to an increase in d_{33}, ε, and tanδ in PZT [13, 49, 50]. Specifically, Na deficiency that should have induced Na-site vacancy resulted in an increase in d_{33}, but Bi deficiency that should also have induced Bi-site vacancy did not. In other words, the increase observed in d_{33} should be attributed to the Na deficiency and not the Bi deficiency, clearly indicating that their roles are different in BNT even if both deficiencies result in A-site vacancies. Correspondingly, O-site vacancies should be induced for charge compensation. As a result, A-site vacancies cannot explain the decrease in d_{33} in the case of Bi-deficient compositions. There must be some difference in the interactions between Bi/Na vacancies and O vacancies.

A-site cation vacancies induced by cation deficiencies are intrinsic defects, causing O vacancies to keep the charge neutrality of the lattice. A similarity between B-site donor doping and A-site deficiencies is the formation of A-site cation vacancies while a difference between the two is in the presence of O vacancies. In other words, O vacancies are not formed in the former but only in the latter case.

O vacancies can be either mobile or immobile depending on their interaction with other defects. They themselves are mobile and thus, pin domain walls [45, 46], hindering domains from being aligned and leading to low d_{33}. However, O vacancies tied up with cation vacancies forming defect complexes that are relatively immobile. In that case, they become ineffective in pinning domain walls [47, 48] but effective in pinning grain boundaries and blocking grain growth. The large grains shown in

Fig. 12.2 and low d_{33} shown in Fig. 12.4 for the Bi nonstoichiometry imply that grain boundaries are mobile while domain walls are immobile.

Considering the ionic radii of Bi^{3+} and Na^{1+} which ranges between 1.3 and 1.4 Å [55–57], Frenkel disorders would hardly form. Instead, Schottky disorders described by (12.1) and (12.2) can be considered as intrinsic ionic disorders in the case of Bi and Na nonstoichiometry [58].

$$\text{nil} \rightarrow 2V_{\text{Bi}}''' + 3V_{\text{O}}^{\bullet\bullet} \tag{12.1}$$

$$\text{nil} \rightarrow 2V_{\text{Na}}' + V_{\text{O}}^{\bullet\bullet} \tag{12.2}$$

Using (12.1) and (12.2), defect complexes can be described by the following equations:

$$\text{nil} \rightarrow 2(V_{\text{Bi}}'''V_{\text{O}}^{\bullet\bullet})'V_{\text{O}}^{\bullet\bullet} \tag{12.3}$$

$$\text{nil} \rightarrow (V_{\text{Na}}'V_{\text{O}}^{\bullet\bullet}V_{\text{Na}}') \tag{12.4}$$

Five intrinsic defects are involved forming a neutral defect complex in (12.3), which is unfavorable. Therefore, O vacancies formed by Bi deficiency would be untied and free to pin domain walls. As a result, the domain walls would be segregated with O vacancies while grain boundaries would be relatively free, leading to relatively low d_{33} but large grains, as shown in Figs. 12.2 and 12.4. In the case of compositions with excessive Bi, there would be relatively less or no Bi and O vacancies, yielding opposite results to those of a Bi deficiency; namely, relatively high d_{33} but small grains, as shown in Figs. 12.2 and 12.4. Bi^{3+} ions in interstitial sites of compositions with excessive Bi are not plausible, thus any excess in Bi beyond a certain limit is lost instead of being added to the BNT lattice. In the case of ABO_3 perovskite structure, it is known that the formation of B-site vacancies as a result of an excessive A-site or doping would not occur without the formation of secondary phases. As no secondary phase was formed in the BNT within the range of the Bi and Na nonstoichiometry, the composition of BNT would be self-corrected by letting the components to be lost as in PZT [13].

For Na-deficient compositions, on the other hand, neutral defect complexes may form as described in (12.4). O vacancies formed by a Na deficiency are tied up with Na vacancies and thus become immobile. As a result, domain walls are not pinned but grain boundaries are pinned by those defect complexes yielding high d_{33} but small grain sizes, as shown in Figs. 12.2 and 12.4. Furthermore, as in the case of compositions with excessive Bi, there would be relatively less or no Na and O vacancies yielding opposite results to those of Na-deficient compositions; namely, low d_{33} and large grain size, as shown in Figs. 12.2 and 12.4.

12.4 Nonstoichiometry by Means of B-Site Extrinsic Doping in $(Bi_{0.5}Na_{0.5})(Ti_{1-z}D_z)O_3$

Contrary to A-site nonstoichiometry with intrinsic disorders, B-site nonstoichiometry is about extrinsic disorders by doping with aliovalent ions. Defects by ionic and/or electronic charge compensation are also considered. Specifically, Nb^{5+} and Mn^{3+} are chosen as donor and acceptor for Ti^{4+} because they are commonly used. The overall doping effects observed in BNT ceramics were compared with those in PZT ceramics that have been extensively studied in the past.

B-site nonstoichiometry was controlled with $z = 0 \sim 1$ mol% in the case of Nb donors and $z = 0 \sim 2$ mol% in the case of Mn acceptors; namely, as a typical donor or acceptor substituting B-site Ti in BNT. Figure 12.5 shows XRD patterns of undoped BNT and $(Bi_{0.5}Na_{0.5})(Ti_{1-x}D_x)O_3$ doped with D = Nb or Mn. When the ionic radii of Nb^{5+} and Mn^{3+} are compared with that of Ti^{4+} at B-site, they are 0.64, 0.645, and 0.605 Å, respectively [57]. Therefore, it was expected that substitutions would readily occur (see Fig. 12.5). No secondary phase peaks were observed for Nb donor doping up to 1 mol% and for Mn acceptor doping up to 2 mol%. All peaks identified were indexed as rhombohedral. Further compositional variation was not pursued to determine the solubility limit of Nb or Mn.

In the XRD patterns of Fig. 12.5, there was no apparent variation in peaks' position and shape. This was different when compared with A-site nonstoichiometry that exhibited shifts in the peaks' position. This difference was attributed to the similarities between B-site ions which do not cause any significant change for concentrations ranging between 1 and 2 mol%. In the case of A-site Bi and Na nonstoichiometry, on the other hand, the ionic radii, ranging between 1.3 and 1.4 Å, are large enough to cause detectable variations in the lattice parameters.

The phase purity of the sintered $(Bi_{0.5}Na_{0.5})(Ti_{1-x}D_x)O_3$ with D = Nb or Mn pellets was also confirmed using SEM images. No secondary phase other than the BNT was seen in Fig. 12.6. With respect to the grain morphology, the grains were in general well

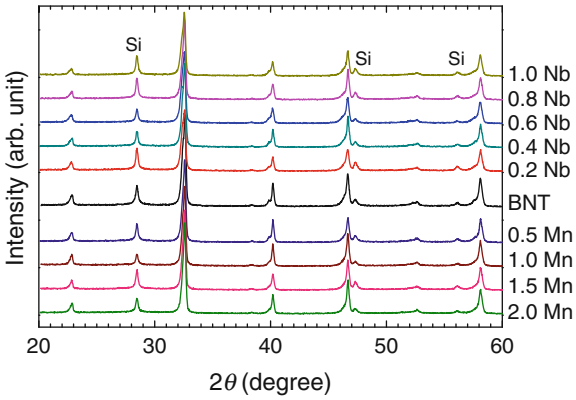

Fig. 12.5 XRD patterns of $(Bi_{0.5}Na_{0.5})(Ti_{1-x}D_x)O_3$ ceramics (D = Nb, Mn) sintered in air at a temperature of 1,150°C for 2 h. BNT was XRD pure for Nb concentrations up to 1 mol% and Mn concentrations up to 2 mol%. 5 N silicone powder peaks were used as an internal standard

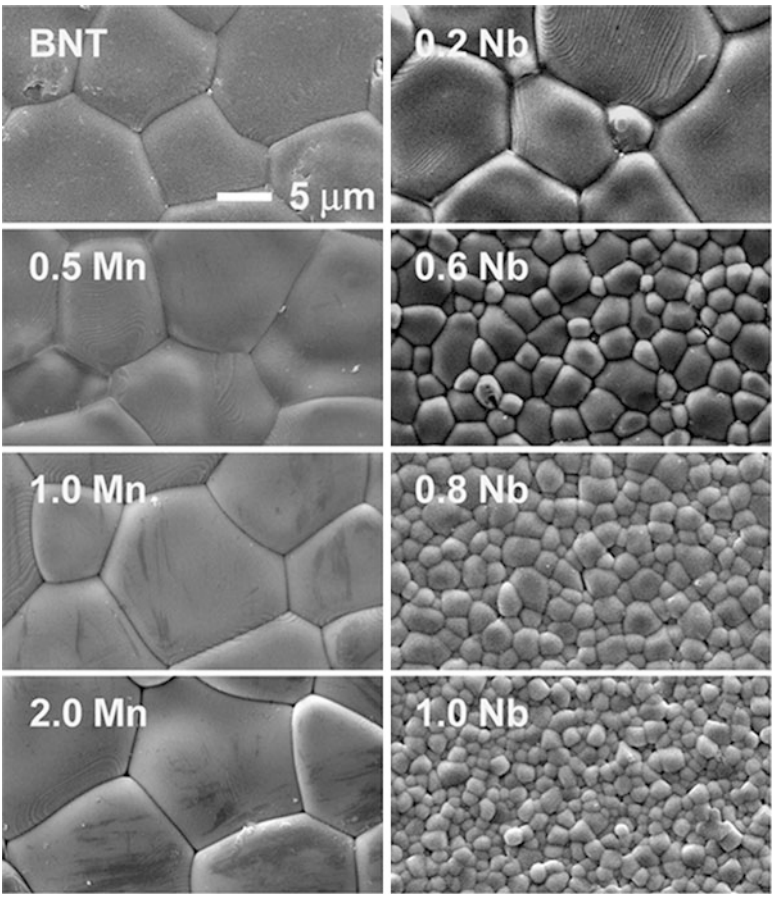

Fig. 12.6 SEM secondary electron images of $(Bi_{0.5}Na_{0.5})(Ti_{1-z}D_z)O_3$ pellets (D = Nb, Mn) sintered in air at a temperature of 1,150°C for 2 h. No secondary phase other than BNT was observed, while the grain size was decreased with Nb doping and increased with Mn doping

developed in the case of Nb as well as Mn doping, indicating that the sintering conditions were similar for the donor- and acceptor-doped pellets. Nonetheless, a difference can be clearly observed in the SEM images; the grain size decreased with Nb doping and increased with Mn doping, depending on the amount of Nb and Mn added.

The decrease in grain size in the case of Nb donor doping can be explained based on A-site cation vacancies created with the B-site donor doping in order to maintain charge neutrality in the lattice. These cation vacancies would be present along grain boundaries rather than inside grains because it is thermodynamically more stable. Grain boundaries would be pinned by these defects, inhibiting grain growth. As a consequence, the size of grains would be relatively small in the case of donor doping. Mn acceptor doping, on the other hand, induces O vacancies instead of A-site vacancies in order to maintain charge neutrality in the lattice. Apparently, grain

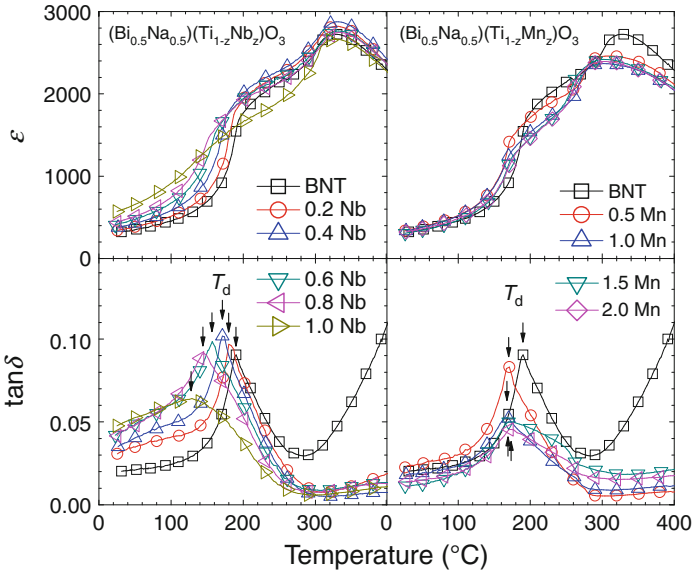

Fig. 12.7 Temperature dependence of dielectric constant (ε) and loss tangent ($\tan\delta$) of the prepoled $(Bi_{0.5}Na_{0.5})(Ti_{1-z}D_z)O_3$ ceramics (D = Nb, Mn) at 100 kHz upon heating

growth was not inhibited by Mn doping which induces the formation of O vacancies, as shown in Fig. 12.6. These different roles of donor and acceptor, which are observed in the microstructure of BNT ceramics, affect their properties in different ways.

To measure the dielectric properties after doping, the samples were prepoled to define T_d, as indicated by arrow marks in Fig. 12.7. In the case of Nb donor doping, both room temperature ε and $\tan\delta$ increased, while with Mn acceptor doping ε did not change significantly and $\tan\delta$ decreased, as shown in Fig. 12.7. These trends in BNT after B-site donor and acceptor doping are similar to those of PZT after doping. Nonetheless, they are dielectrically different with respect to shape and polymorphic phase transition.

Specifically, two different transitions appeared: the first at the temperature maximum (T_m) at ε maximum (ε_m) and the second at T_d. It should be noted that, unlike PZT, T_d is unique in BNT. With respect to their potential applications, T_d ~200°C is considered as a critical drawback of BNT-based ceramics, because its temperature stability is relatively smaller than that of PZT ceramics. In the case of Nb donor doping, T_m did not chnage significantly while T_d decreased gradually, as shown in Fig. 12.7. In the case of Mn acceptor doping, both T_m and T_d decreased when the concentration of Mn did not exceed 0.5 mol%; as the concentration of Mn increased no further change was observed, as shown in Fig. 12.7. In comparison with PZT, BNT behaves as a relaxor and exhibits frequency dependence. Furthermore, broad transitions are dielectrically different from PZT. In particular, polymorphic phase transition occurs as lattice symmetry changes from rhombohedral at room temperature to tetragonal, and then to cubic.

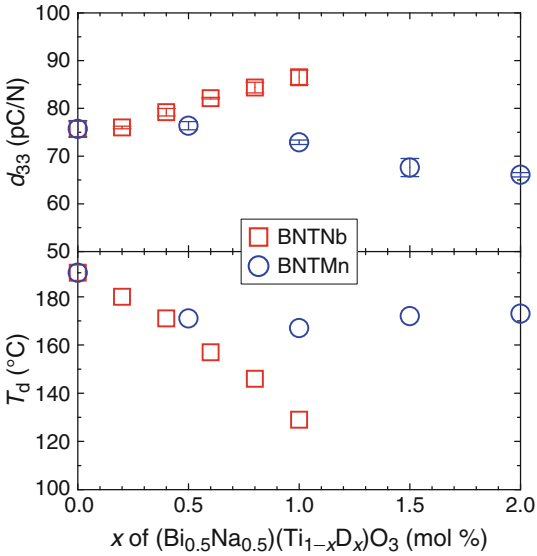

Fig. 12.8 The inversely proportional relation between piezoelectric coefficient (d_{33}) and depolarization temperature (T_d) of $(Bi_{0.5}Na_{0.5})(Ti_{1-z}D_z)O_3$ ceramics (D = Nb, Mn). T_d was taken from Fig. 12.7

The variations in T_d and d_{33} observed in BNT ceramics with donor and acceptor doping are shown in Fig. 12.8. Specifically, d_{33} gradually increased with Nb donor doping and decreased with Mn acceptor doping. An inverse relation between d_{33} and T_d was clearly observed in the case of Nb donor doping. The relation between d_{33} and T_d was less pronounced in the case of Mn acceptor doping.

As mentioned earlier, B-site donor doping induces A-site vacancies in order to maintain charge neutrality in the lattice. With respect to the piezoelectric properties, A-site vacancies are known to facilitate domain wall motion. Consequently, domain alignment during poling results in higher d_{33}. On the other hand, B-site acceptor doping reduces A-site vacancies or induces O vacancies for the charge neutrality in the lattice to be maintained. O vacancies are known to be relatively mobile, to pin domain walls and ultimately lowering d_{33} unless they are immobile. Then, they form defect complexes with other defects as mentioned earlier. The increase observed in d_{33} by donor doping and the decrease induced by acceptor doping in d_{33} of BNT ceramics are in general consistent with the variations in d_{33} observed in PZT ceramics. In respect to their microstructure, d_{33} appears to be inversely proportional to grain size.

Table 12.1 summarizes the doping effects of various aliovalent ions added to BNT ceramics on various properties. Ta [59] and W data [60] are also provided to demonstrate the consistent results among the vaious donors. It should be noted that the phase purity values do not represent the solubility limits but the phase purity, as it has been confirmed experimentally. With relatively smaller doping amount of W^{6+} relatively similar doping effects were observed. On the other hand, no significant difference was observed between Nb^{5+} and Ta^{5+} doping. It indicates a difference in the valence rather than the atomic weight is a factor in doping. The variations in parameters of BNT ceramics are thought to be mostly due to differences in processing.

Table 12.1 Effects of B-site doping with various aliovalent ions on the properties of $(Bi_{0.5}Na_{0.5})(Ti_{1-x}D_x)O_3$ ceramics

	BNT	Donor			Acceptor
	Ti^{4+}	Nb^{5+}	Ta^{5+}	W^{6+}	Mn^{3+}
Ionic radius (Å)	0.605	0.64	0.64	0.60	0.645
Phase purity (mol%)	Yes	1.0	0.8	0.4	2.0
Grain size (μm)	~20	~2	~5	~5	>20
d_{33} (pC/N)	74	87	84	84	66
k_p	0.17	0.17	–	0.16	0.13
Q_m	320	160	202	205	369
ε	324	↑	–	↑	~
$\tan\delta$	0.02	↑	–	↑	↓
T_d (°C)	190	129	–	–	167
E_c @ 60 Hz (kV/cm)	~41*	~24*	~18	~19	–
P_r @ 60 Hz (pC/cm^2)	~35*	–	–	~42	–

*The values of E_c and P_r were taken from [59] and [60]
The ionic radius of Ti^{4+} is given for BNT in comparison with donors and acceptors [57]

In addition to Mn, the use of a number of alternative acceptors with valence 3+ was examined, but their effects were not as consistent as those of donors. The inconsistency was thought to be due to positioning of 3+ accceptors in A-site as well as B-site.

Acceptor doping can be charge compensated by Ti interstitials, O vacancies, or holes, among which O vacancies appear to be the most probable to occur. In the case of donor doping, charge compensation can be achieved by O interstitials, Ti vacancies, electrons, or A-site vacancies. However, considering Bi and/or Na volatility, A-site vacancies seem to be the best choice for the compensating defects. In terms of defect chemistry, the extrinic disorders in B-site nonstoichiometry induced by the addition of aliovalent ions can be described as follows:

$$Mn_2O_3 \xrightarrow{(2TiO_2)} 2Mn_{Ti}^{'} + V_O^{\bullet\bullet} + 3O_O^x \tag{12.5}$$

$$Nb_2O_5 \xrightarrow{(2TiO_2)} 2Nb_{Ti}^{\bullet} + V_A^{''} + 5O_O^x \tag{12.6}$$

where (12.5) is for acceptor doping while (12.6) is for donor doping and A stands for A-site $(Bi_{0.5}Na_{0.5})$. Conductivity is expected to change [58].

12.5 Electrical Conduction

Ionic or electronic charge compensation occurs to maintain electroneutrality in the lattice. Cation vacancies or electrons are the ones that need to be taken into account in the case of donor doping and in the case of acceptor doping, anion vacancies or holes when examining the defect chemistry. Electrical conductivity measurements can provide crucial information regarding the conduction behavior of BNT ceramics.

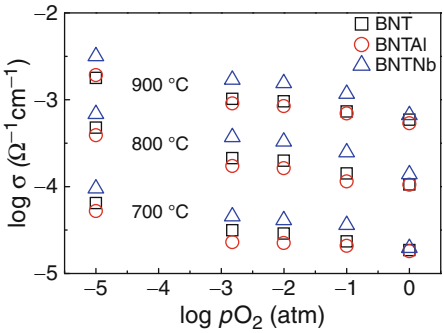

Fig. 12.9 Electrical conductivity (σ) of $(Bi_{0.5}Na_{0.5})(Ti_{1-z}D_z)O_3$ ceramics as a function of the partial oxygen pressure (pO_2) at 700, 800, and 900°C (D = Nb, Al)

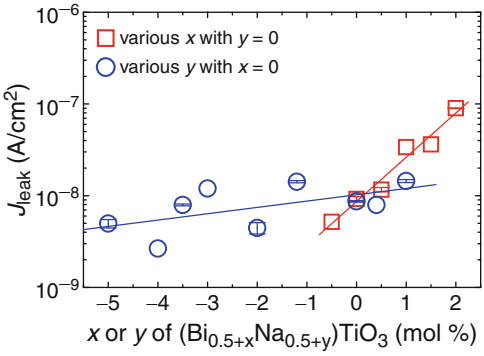

Fig. 12.10 Composition dependence of leakage current density (J_{leak}) of $(Bi_{0.5+x}Na_{0.5+y})TiO_3$ ceramics with varying x and y at room temperature under a DC poling field of 40 kV/cm. The solid lines were drawn by linear fitting of the data points

For the electrical conductivity of BNT with and without doping, the resistivity of each sample was measured as a function of temperature (T) and oxygen partial pressure (pO_2), and then converted into electrical conductivity (σ). The measurements were carried out with a standard four-point probe DC method using Pt wires ($\phi = 0.2$ mm). The oxygen pressure was established by O_2/Ar.

Figure 12.9 shows σ of BNT doped with aliovalent ions, Nb donor and Al acceptor, in comparison with undoped BNT at $T = 700 \sim 900°C$ and $pO_2 = 1 \sim 10^{-5}$ atm. According to the experimental results, the slopes ($\Delta\log\sigma/\Delta\log pO_2$) are clearly negative within the temperature range tested. A number of difficulties were encountered during the measurements, mainly due to the long stabilization time at low T and the interaction BNT evaporing with Pt wires at low pO_2. Nevertheless, there is an increasing trend in σ which can be clearly observed with Nb donor doping and a decreasing trend with Al acceptor doping when compared with undoped BNT. This result supports the assumption that the conduction behavior of BNT can be considered as n-type at elevated temperature. At low temperature below 600°C, BNT seemed to exhibit the ionic conduction behavior.

The leakage current was monitored during poling because it could provide additional clues regarding the conduction mechanism. The leakage current density (J_{leak}) of BNT with A-site nonstoichiometry is shown in Fig. 12.10. It was consistent with the results for σ, shown in Fig. 12.9. As A-site cation deficiency increased,

charge neutrality in the lattice was necessary to be maintained by either ionic or electronic compensation; in other words, O vacancies or holes. In any case, J_{leak} should decrease if BNT is an *n*-type conductor, as shown in Fig. 12.10.

The difference between the slopes of Bi and Na nonstoichiometry ($\Delta J_{leak}/\Delta x$, $\Delta J_{leak}/\Delta y$) is ~3 indicating a valence difference between Bi and Na. The decreasing trend in J_{leak} observed with either Bi or Na deficiency indicates *n*-type conduction rather than *p*-type conduction. In addition, the continuous increase in J_{leak} with the addition of further compositions of Bi and Na indicates an intrinsic deficiency was formed in both components due to volatility during processing.

PZT is a *p*-type conductor with intrinsic A-site vacancies attributed to PbO evaporation [13]. Because BNT includes volatile A-site components similar to PZT, this *n*-type behavior of BNT is a rather counterintuitive result. With respect to the aforementioned difficulties encountered at low temperatures, which became even more serious at low pO_2 due to the instability of BNT even reacting with Pt wires, it needs to be further examined with more elaborate measurements. The changes observed in conductivity as a result of doping (see Fig. 12.9) are smaller than expected, even though the trends observed in undoped and doped BNT are as expected very similar to each other. Complementary measurements using different techniques such as alternating current (AC) impedance measurements are needed to confirm these results.

12.6 Summary

The effects of nonstoichiometry on the properties of BNT ceramics were investigated in terms of A-site intrinsic disorders and B-site extrinsic doping. The A-site Bi and Na nonstoichiometry were controlled with $Bi_{0.5}$- or $Na_{0.5}$-deficient compositions and compositions with excessive $Bi_{0.5}$ or $Na_{0.5}$. On the other hand, B-site nonstoichiometry was controlled by doping with aliovalent donor or acceptor ions. In all cases, a rhombohedral ABO_3 perovskite structure was maintained without the formation of a secondary phase.

Specifically, A-site Bi and Na nonstoichiometry had the opposite effects on the structure and properties of BNT ceramics. Grain size decreased with the addition of excessive amounts of Bi- or Na-deficient compositions, while d_{33} increased with decreasing T_d, and vice versa. With B-site donor or acceptor doping, BNT ceramics showed the typical behavior of PZT ceramics. Namely, d_{33} increased with donor doping and decreased with acceptor doping, while T_d fluctuated inversely proportional to d_{33}. With respect to their microstructure, variations in grain size and other properties were attributed to the presence of defects. At elevated temperature ranging from 700 to 900°C and pO_2 ranging between 1 and 10^{-5} atm, nominally undoped BNT ceramics exhibited *n*-type conductivity, which increased with donor doping and decreased with acceptor doping.

Lastly, the results revealed a structure–property relation in BNT ceramics. Both A-site intrinsic disorders and B-site extrinsic doping had a significant influence on the lattice structure and the defect chemistry, which ultimately affect the properties of BNT ceramics.

Acknowledgments This work was supported by the National Research Foundation of Korea Grant funded by the Korean Government (2009–0088570) and the Basic Science Research Program through the National Research Foundation of Korea (NRF) funded by the Ministry of Education, Science and Technology (2010–0025055).

References

1. Isupov VA (2005) Ferroelectric $Na_{0.5}Bi_{0.5}TiO_3$ and $K_{0.5}Bi_{0.5}TiO_3$ perovskites and their solid solutions. Ferroelectrics 315:123
2. Zhou ZH, Xue JM, Li WZ, Wang J, Zhu H, Miao JM (2004) Ferroelectric and electrical behavior of $(Na_{0.5}Bi_{0.5})TiO_3$ thin films. Appl Phys Lett 85:804
3. Park SE, Chung SJ, Kim IT (1996) Ferroic phase transitions in $(Na_{1/2}Bi_{1/2})TiO_3$ crystals. J Am Ceram Soc 79:1290
4. Vakhrushev SB, Ivanitskii BG, Kvyatkovsii BE, Maistrenko AN, Malysheva RS, Okuneva NM, Parfenova NN (1983) Neutron scattering studies of the structure of sodium bismuth titanate. Sov Phys Solid State 25:1504
5. Zvirgzds JA, Kapostins PP, Zvirgzde JV (1982) X-ray study of phase transitions in ferroelectric $Na_{0.5}Bi_{0.5}TiO_3$. Ferroelectrics 40:75
6. Pronin IP, Syrnikov PP, Isupov VA, Egorov VM, Zaitseva NV (1980) Peculiarities of phase transitions in sodium-bismuth titanate. Ferroelectrics 25:395
7. Tu CS, Siny IG, Schmidt VH (1994) Sequence of dielectric anomalies and high-temperature relaxation behavior in $Na_{1/2}Bi_{1/2}TiO_3$. Phys Rev B 49:11550
8. Hiruma Y, Nagata H, Takenaka T (2007) Grain-size effects on electrical properties of $(Bi_{1/2}K_{1/2})TiO_3$ ceramics. Jpn J Appl Phys 46:1081
9. Hiruma Y, Aoyagi R, Nagata H, Takenaka T (2005) Ferroelectric and piezoelectric properties of $(Bi_{1/2}K_{1/2})TiO_3$ ceramics. Jpn J Appl Phys 44:5040
10. Li ZF, Wang CL, Zhong WL, Li JC, Zhao ML (2003) Dielectric relaxor properties of $K_{0.5}Bi_{0.5}TiO_3$ ferroelectrics prepared by sol-gel method. J Appl Phys 94:2548
11. Takenaka T, Nagata H, Hiruma Y (2008) Current developments and prospective of lead-free piezoelectric ceramics. Jpn J Appl Phys 47:3787
12. Zhang S, Xia R, Shrout TR (2007) Lead-free piezoelectric ceramics vs. PZT? J Electroceram 19:251
13. Jaffe B, Cook WR Jr, Jaffe H (1971) Piezoelectric ceramics. Academic Press, New York
14. Hiruma Y, Nagata H, Takenaka T (2009) Formation of morphotropic phase boundary and electrical properties of $(Bi_{1/2}Na_{1/2})TiO_3$-$Ba(Al_{1/2}Nb_{1/2})O_3$ solid solution ceramics. Jpn J Appl Phys 48:09KC08.
15. Hiruma Y, Yoshii K, Nagata H, Takenaka T (2008) Phase transition temperature and electrical properties of $(Bi_{1/2}Na_{1/2})TiO_3$-$(Bi_{1/2}A_{1/2})TiO_3$ (A=Li and K) lead-free ferroelectic ceramics. J Appl Phys 103:084121
16. Yu H, Ye ZG (2008) Dielectric, ferroelectric, and piezoelectric properties of the lead-free $(1-x)(Na_{0.5}Bi_{0.5})TiO_3$-$xBiAlO_3$ solid solution. Appl Phys Lett 93:112902
17. Hiruma Y, Nagata H, Takenaka T (2007) Phase-transition temperatures and piezoelectric properties of $(Bi_{1/2}Na_{1/2})TiO_3$-$(Bi_{1/2}Li_{1/2})TiO_3$-$(Bi_{1/2}K_{1/2})TiO_3$ lead-free ferroelectric ceramics. IEEE T Ultrason Ferr 54:2493

18. Lin D, Xiao D, Zhu J, Yu P (2006) Piezoelectric and ferroelectric properties of $[Bi_{0.5}(Na_{1-x-y}K_xLi_y)_{0.5}]TiO_3$ lead-free piezoelectric ceramics. Appl Phys Lett 88:062901
19. Grinberg I, Suchomel MR, Davies PK, Rappe AM (2005) Predicting morphotropic phase boundary locations and transition temperature in Pb- and Bi-based perovskite solid solutions from crystal chemical data and first-principle calculations. J Appl Phys 98:094111
20. Li Y, Chen W, Zhou J, Xu Q, Sun H, Liao M (2005) Dielectric and ferroelectric properties of lead-free $Na_{0.5}Bi_{0.5}TiO_3$-$K_{0.5}Bi_{0.5}TiO_3$ ferroelectric ceramics. Ceram Int 31:139
21. Wang XX, Tang XG, Chan LW (2004) Electromechanical and ferroelectric properties of $(Bi_{1/2}Na_{1/2})TiO_3$-$(Bi_{1/2}K_{1/2})TiO_3$-$BaTiO_3$ lead-free piezoelectric ceramics. Appl Phys Lett 85:91
22. Yilmaz H, Trolier-McKinstry S, Messing GL (2003) (Reactive) Templated grain growth of textured sodium bismuth titanate ($Na_{1/2}Bi_{1/2}TiO_3$-$BaTiO_3$) ceramics-II Dielectric and piezoelectric properties. J Electroceram 11:217
23. Kreisel J, Glazer AM, Jones G, Thomas P, Abello L, Lucazeau G (2000) An x-ray diffraction and Raman spectroscopy investigation of A-site substituted perovskite compounds: the $(Na_{1-x}K_x)_{0.5}Bi_{0.5}TiO_3$ ($0 \leq x \leq 1$) solid solution. J Phys Condens Mat 12:3267
24. Sasaki A, Chiba T, Mamiya Y, Otsuki E (1999) Dielectric and piezoelectric properties of $(Bi_{0.5}Na_{0.5})TiO_3$-$(Bi_{0.5}K_{0.5})TiO_3$ systems. Jpn J Appl Phys 38:5564
25. Takenaka T, Maruyama K, Sakata K (1991) $(Bi_{1/2}Na_{1/2})TiO_3$-$BaTiO_3$ system for lead-free piezoelectric ceramics. Jpn J Appl Phys 30:2236
26. Elkechai O, Manier M, Mercurio JP (1996) $Na_{0.5}Bi_{0.5}TiO_3$-$K_{0.5}Bi_{0.5}TiO_3$ (NBT-KBT) system: A structural and electrical study. Phys Status Solidi A 157:499
27. Aksel E, Erdem E, Jakes P, Jones JL, Eichel RA (2010) Defect structure and materials "hardening" in Fe_2O_3-doped $[Bi_{0.5}Na_{0.5}]TiO_3$ ferroelectrics. Appl Phys Lett 97:012903
28. Daniels JE, Jo W, Rodel J, Jones JL (2009) Electric-field-induced phase transformation at a lead-free morphotropic phase boundary: case study in a 93%$(Bi_{0.5}Na_{0.5})TiO_3$-7%$BaTiO_3$ piezoelectric ceramics. Appl Phys Lett 95:032904
29. Zuo R, Su S, Wu Y, Fu J, Wang M, Li L (2008) Influence of A-site nonstoichiometry on sintering, microstructure and electrical properties of $(Bi_{0.5}Na_{0.5})TiO_3$ ceramics. Mater Chem Phys 110:311
30. Hu GD, Fan SH, Yang CH, Wu WB (2008) Low leakage current and enhanced ferroelectric properties of Ti and Zn codoped $BiFeO_3$ thin film. Appl Phys Lett 92:192905
31. Watanabe Y, Hiruma Y, Nagata H, Takenaka T (2008) Phase transition temperatures and electrical properties of divalent ions (Ca^{2+}, Sr^{2+} and Ba^{2+}) substituted $(Bi_{1/2}Na_{1/2})TiO_3$ ceramics. Ceram Int 34:761
32. Spreitzer M, Valant M, Suvorov D (2007) Sodium deficiency in $Na_{0.5}Bi_{0.5}TiO_3$. J Mater Chem 17:185
33. Shan D, Qu Y, Song J (2007) Ionic doping effects on crystal structure and relaxation character in $Bi_{0.5}Na_{0.5}TiO_3$ ferroelectric ceramics. J Mater Res 22:730
34. Kimura T, Fukuchi E, Tani T (2005) Fabrication of textured bismuth sodium titanate using excess bismuth oxide. Jpn J Appl Phys 44:8055
35. Nagata H, Shinya T, Hiruma Y, Takenaka T, Sakaguchi I, Haneda H (2005) Piezoelectric properties of bismuth sodium titanate ceramics. Ceram Trans 167:213
36. Yan H, Xiao D, Yu P, Zhu J, Lin D, Li G (2005) The dependence of the piezoelectric properties on the differences of the A-site and B-site ions for $(Bi_{1-x}Na_x)TiO_3$-based ceramics. Mater Design 26:474
37. Qu Y, Shan D, Song J (2005) Effects of A-site substitution on crystal component and dielectric properties in $Bi_{0.5}Na_{0.5}TiO_3$ ceramics. Mat Sci Eng B 121:148
38. Kim JS, Kim IW (2005) Role of the doped Nb ion in ferroelectric bismuth titanate and bismuth lanthanum titanate ceramics: different dielectric behaviors. J Korean Phys Soc 46:143
39. Li H, Feng C, Yao W (2004) Some effects of different additives on dielectric and piezoelectric properties of $(Bi_{1/2}Na_{1/2})TiO_3$-$BaTiO_3$ morphotropic-phase-boundary composition. Mater Lett 58:1194

40. Yi JY, Lee JK, Hong KS (2002) Dependence of the microstructure and the electrical properties of lanthanum-substituted $(Na_{1/2}Bi_{1/2})TiO_3$ on cation vacancies. J Am Cram Soc 85:3004
41. Lee JK, Hong KS, Kim CK, Park SE (2002) Phase transitions and dielectric properties in A-site ion substituted $(Na_{1/2}Bi_{1/2})TiO_3$ ceramics (A=Pb and Sr). J Appl Phys 91:4538
42. Nagata H, Takenaka T (2001) Additive effects on electrical properties of $(Bi_{1/2}Na_{1/2})TiO_3$ ferroelectric ceramics. J Eur Ceram Soc 21:1299
43. Herabut A, Safari A (1997) Processing and electromechanical properties of $(Bi_{0.5}Na_{0.5})_{(1-1.5x)}La_xTiO_3$ ceramics. J Am Ceram Soc 80:2954
44. Park SE, Chung SJ, Kim IT, Hong KS (1994) Nonstoichiometry and the long-range cation ordering in crystals of $(Ba_{1/2}Bi_{1/2})TiO_3$. J Am Ceram Soc 77:2641
45. Zhang Q, Whatmore RW (2003) Improved ferroelectric and pyroelectric properties in Mn-doped lead zirconate titanate thin films. J Appl Phys 94:5228
46. Park CH, Chadi DJ (1998) Microscopic study of oxygen-vacancy defects in ferroelectric perovskites. Phys Rev B 57:R13961
47. Zhang Z, Wu P, Lu L, Shu C (2008) Defect and electronic structures of acceptor substituted lead titanate. Appl Phys Lett 92:112909
48. Erhart P, Eichel R, Traskelin P, Albe K (2007) Association of oxygen vacancies with impurity metal ions in lead titanate. Phys Rev B 76:174116
49. Randall CV, Kim N, Kucera J, Cao W, Shrout TR (1998) Intrinsic and extrinsic size effects in fine-grained morphotropic-phase-boundary lead zirconate titanate ceramics. J Am Ceram Soc 81:677
50. Gerson R (1960) Variation in ferroelectric characteristics of lead zirconate titanate ceramics due to minor chemical modifications. J Appl Phys 31:188
51. Sung YS, Kim JM, Cho JH, Song TK, Kim MH, Park TG (2010) Roles of lattice distortion in $(1-x)(Bi_{0.5}Na_{0.5})TiO_3$-$xBaTiO_3$ ceramics. Appl Phys Lett 96:202901
52. Sung YS, Kim JM, Cho JH, Song TK, Kim MH, Chong HH, Park TG, Do D, Kim SS (2010) Effects of Na nonstoichiometry in $(Bi_{0.5}Na_{0.5})TiO_3$ ceramics. Appl Phys Lett 96:022901
53. Sung YS, Lee HM, Du W, Yeo HG, Lee SC, Cho JH, Song TK, Kim MH (2009) Enhanced piezoelectric properties of $(Bi_{0.5}K_{0.5+x}Li_y)TiO_3$ ceramics by K nonstoichiometry and Li addition. Appl Phys Lett 94:062901
54. Hong KS, Park SE (1996) Phase relations in the system of $(Na_{1/2}Ni_{1/2})TiO_3$-$PbTiO_3$. II. Dielectric property. J Appl Phys 79:388
55. Suchomel MR, Davies PK (2004) Predicting the position of the morphotropic phase boundary in high temperature $PbTiO_3$-Bi(B'B")O_3 based dielectric ceramics. J Appl Phys 96:4405
56. Eitel RE, Randall CA, Shrout TR, Rehrig PW, Hackenberger W, Park SE (2001) New high temperature morphotropic phase boundary piezoelectrics based on Bi(Me)O_3-$PbTiO_3$ ceramics. Jpn J Appl Phys 40:5999
57. Shannon RD (1976) Revised effective ionic radii and systematic studies of interatomic distances in halides and chalcogenides. Acta Cryst A32:751
58. Smyth DM (2000) The defect chemistry of metal oxides. Oxford University Press, New York
59. Yeo HG, Sung YS, Song TK, Cho JH, Kim MH (2009) Donor doping effects on the ferroelectric and the piezoelectric properties of Pb-free $(Bi_{0.5}Na_{0.5})TiO_3$ ceramics. J Korean Phys Soc 54:896
60. Cho JH, Yeo HG, Sung YS, Song TK, Kim MH (2008) Dielectric and piezoelectric characteristics of W-doped lead-free $(Bi_{0.5}Na_{0.5})Ti_{1-x}W_x)O_3$ ceramics. New Phys Sae Mulli (Korean Phys Soc) 57:409

Part IV
Bismuth Layer Structured Ferroelectric

Chapter 13
Resonator Characteristics of Bismuth Layer Structured Ferroelectric Materials

Akira Ando and Masahiko Kimura

13.1 Introduction

Crystallographic studies of Bismuth (Bi) layer structured ferroelectric (BLSF) materials were first carried out by Aurivillius [1–3] and their ferroelectric or piezoelectric properties have been revealed by a large number of researchers [4–106, 108, 110–117]. The piezoelectric properties of $Na_{0.5}Bi_{4.5}Ti_4O_{15}$ (NBT) [17, 23, 25, 26], $BaBi_4Ti_4O_{15}$ [41], $SrBi_4Ti_4O_{15}$ (SBTi) [17, 40, 54], and $CaBi_4Ti_4O_{15}$ (CBT) [39, 53, 63] ceramic materials have been reported in terms of resonator application. Their applicability to practical application seemed to be quite high because the electromechanical coupling factors for thickness extensional mode vibrations were between 15 and 20%, and the typical values for the mechanical quality factor (Q_m) were higher than 2,000 [39], and these properties are favorable for the oscillator applications. However, their temperature coefficient of resonance frequency (TCF) is not sufficiently low for the oscillator applications which require a stable resonance frequency with fine tolerance against various condition changes such as temperature changes.

Ando and coresearchers have studied the resonance characteristics of the BLSF materials, and reported that $SrBi_2Nb_2O_9$ (SBN) ceramic material has small TCF values and can be used in the fine tolerance oscillator applications [38, 44, 72, 73, 84–86, 89]. Single mode resonant characteristics were also successfully obtained for the second harmonic of the thickness extensional (TE2) mode generated by a double-layered resonator structure with SBN material [38, 84]. Moreover, a highly stable resonator characteristic at high temperatures is expected for the SBN since its measured Curie temperature was around 400°C [38, 44, 72, 85], which is higher than that of typical lead containing materials such as PZT- or PbTiO3-based ceramics.

A. Ando (✉) • M. Kimura
Murata Mfg. Co. Ltd., Murata, Japan
e-mail: a_ando@murata.co.jp

S. Priya and S. Nahm (eds.), *Lead-Free Piezoelectrics*,
DOI 10.1007/978-1-4419-9598-8_13, © Springer Science+Business Media, LLC 2012

Kimura and coresearchers also reported superior resonance characteristics of TE2-mode vibration of CBT, and its very high Curie temperature above 800°C [39]. Piezoelectricity of a CBT-based material was observed even above 600°C, and it can be used for high temperature applications [96]. Ogawa and coresearchers showed that superior resonance characteristics and TCF are obtained for the thickness shear (TS1)-mode vibration by fabricating grain-oriented CBT ceramics [63]. The grain orientation technique was introduced to the SBN-based ceramics, and the oriented SBN ceramics exhibit better temperature characteristics of resonance frequencies than AT-cut quartz resonator in wide temperature range from −50°C through 200°C [91, 97]. TCF values less than 0.5 ppm/°C were reported there.

Another important characteristic of the BLSF ceramic materials is high-power characteristic. Conventional hard PZT materials show high Q_m values when the vibration velocity is low; however, their Q_m values show sudden drops when the vibration velocity becomes higher. When the Q_m drop occurs, the piezoelectricity of the material disappears because of the temperature rise by the heat generation with the vibration. A vibration velocity at which the Q_m value shows the sudden drop is defined as the maximum velocity (v_{max}). The v_{max} values for the hard PZT lie around 1 m/s [110]. On the other hand, the v_{max} values of BLSF ceramic materials are more than 2 m/s [111–114]. The BLSF materials have good advantages for the high-power applications such as ultrasonic transducers, ultrasonic motors, piezoelectric transformers, and so on.

The resonator characteristics of the BLSF ceramic materials for the oscillator applications will be reviewed in this article, followed by the review of their high-power characteristics.

13.2 Resonance Characteristics of BLSF for Oscillator Applications

13.2.1 Materials for Resonators of Signal Processor Applications

The crystalline structures of the BLSF were obtained by Aurivillius [1–3]. Pseudoperovskite unit cells are placed between Bi_2O_2 layers in *c*-axis direction. The number of the pseudoperovskite layers sandwiched by two Bi_2O_2 layers is denoted by "*m*." The ferroelectric phase of the BLSF material shows the orthorhombic symmetry. Noguchi et al. [75] showed the detailed structural analysis on SBT material as shown in Fig. 13.1. The Bi_2O_2 layers are perpendicular to the *c*-axis here. The spontaneous polarization is parallel to the *a*-axis. The screw axes exist in parallel to the *a*-axis, and the *a*-glide plane exists in parallel to the *b*-plane.

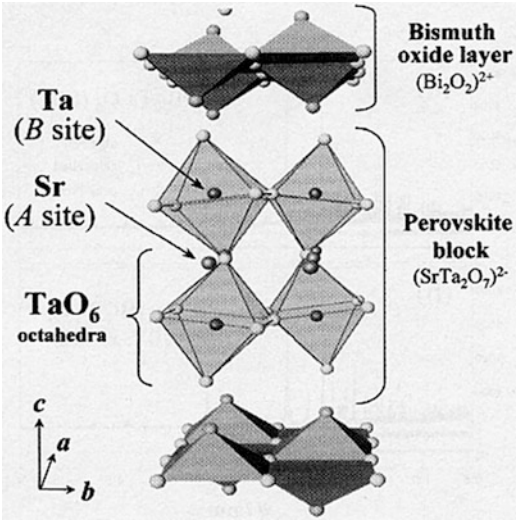

Fig. 13.1 The schematic view of the crystalline structure of $SrBi_2Ta_2O_9$ after Noguchi et al. [75]. Two pseudoperovskite layers are placed between Bi_2O_2 layers

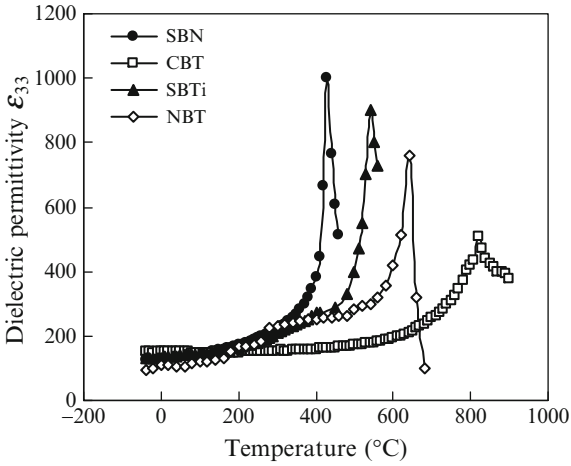

Fig. 13.2 Dielectric permittivity change against temperature for various BLSF materials (measured at 1 MHz)

13.2.1.1 Dielectric and Piezoelectric Properties of BLSF

Dielectric and piezoelectric properties of the typical BLSF materials are introduced in this section. SBN-, NBT-, SBTi-, and CBT-based ceramics were fabricated by conventional powder processing and their dielectric and piezoelectric properties were investigated. Each composition has 1 wt.% of MnO_2 as a sintering aid. Figure 13.2 shows the dielectric permittivity changes against temperature and Fig. 13.3 shows resonance frequency changes of thickness extensional mode against temperature.

The SBN-based material has the smallest TCF value among these materials although its Curie temperature is the lowest. Among these four materials, only the SBN has a temperature where the resonance frequency gives the minimum value

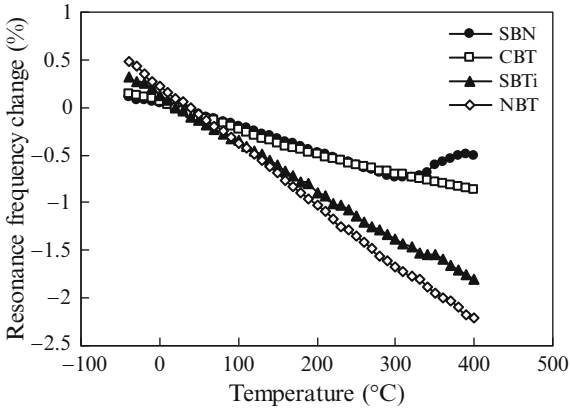

Fig. 13.3 Resonance frequency change against temperature for various BLSF materials. The resonance frequency was measured for the TE1-mode vibration of single ceramic plate resonators

Table 13.1 Piezoelectric properties of various BLSF materials for the TE1 vibration

	$\varepsilon_{33}^{T}/\varepsilon_0$	k_t (%)	TCF (ppm/°C) (−20 to 80°C)	T_c (°C)
SBN	130	15	−20	420
CBT	150	13	−30	810
SBTi	130	20	−50	520
NBT	120	25	−150	650

$\varepsilon_{33}^{T}/\varepsilon_0$ relative dielectric permittivity; k_t electromechanical coupling coefficient; T_c Curie temperature

below the Curie temperature. This behavior seems to have strong relation to the low TCF value of the SBN.

TCF was calculated by the following formula:

$$\mathrm{TCF} = (f_{\mathrm{rmax}} - f_{\mathrm{rmin}})/(f_{\mathrm{r25}}{}^{\circ}\mathrm{C} \times 100),$$

where f_{rmax} and f_{rmin} are the maximum and minimum values of resonance frequency within the measurement temperature range, respectively, and $f_{\mathrm{r25^{\circ}C}}$ is the resonance frequency at 25°C. TCF is defined as a positive number in the case where the resonance frequency increases with increasing temperature, and as a negative number in the case where the resonance frequency decreases with increasing temperature.

A comparison of dielectric and piezoelectric properties between the above BLSF materials is shown in Table 13.1. A low electromechanical coupling coefficient and a small TCF value can be obtained for the SBN-based material, and these properties are preferable for the oscillator applications.

13.2.2 Vibration-Mode Selection for Oscillator Application

The BLSF ceramic materials show anisotropic properties of their piezoelectricity. Their electromechanical coupling for the lateral effect k_{31} is much smaller than that

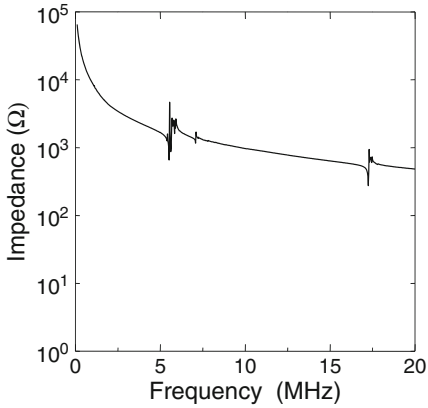

Fig. 13.4 Resonance characteristics for the TE1-mode vibration of SBN single plates

of the longitudinal effect k_{33}. The BLSF materials also show sufficient value of the electromechanical coupling coefficient for shear deformation k_{15}. Therefore, considering practically available applications of the BLSF materials, thickness vibration modes should be taken into account. The possible vibration modes for conventional single plate piezoelectric ceramics of the BLSF are the fundamental thickness extensional mode (TE1 mode), and the third harmonics mode of the thickness extensional mode (TE3 mode), the fundamental thickness shear mode (TS1 mode), and the third harmonic mode of the thickness shear mode (TE3 mode). Even number order harmonic modes are not able to generate for the single plate resonators. Moreover, fifth or higher order harmonic modes are difficult to utilize as vibration modes of the piezoelectric ceramic resonators, because of their low Q_m values.

The single mode resonance characteristics for the TE1-mode vibration can be obtained for materials having their Poisson ratio over 1/3. These materials are very limited besides PZT materials around the morphotropic phase boundary (MPB) compositions. This means that the single plate-type resonator using the TE1-mode vibration cannot be made of the BLSF piezoelectric ceramic materials. When the TE1-mode resonator is made of a BLSF ceramic material, it shows terribly insufficient resonance characteristics as shown in Fig. 13.4. Similar limitation exists for the TS3-mode vibration, where the single mode resonance characteristic is obtained for the material with their Poisson ratio more than 0.4 [79].

The TE3 mode on the piezoelectric single plate resonator was also used in the practical resonator application field, and their electromechanical couplings are small (less than 10%). However, because of the large electromechanical coupling for the TE1-mode vibration, the TE1-mode or the fifth harmonic resonance acts as inevitable spurious vibrations to TE3-mode resonance, and causes significant problems on the stable oscillation of the TE3-mode oscillator. A suitable circuit design is necessary to suppress these spurious oscillations. Furthermore, electric quality factor Q_e values for harmonic vibrations are generally much lower than those for the fundamental vibrations at around each resonance frequency. The TE3-mode application is also difficult for the BLSF ceramic materials.

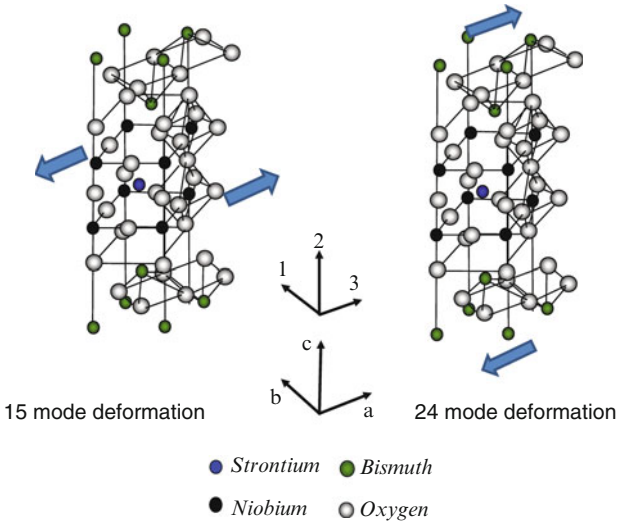

Fig. 13.5 Relationship between crystallographic structure and shear deformations of SBN

On the other hand, the TS1-mode vibration is one of the most useful modes for practical piezoelectric ceramic resonators. However, this mode is also difficult to use as a conventional single plate-type resonator for the BLSF ceramic materials. As seen above, the SBN-based ceramic materials show good TCF for thickness extensional modes. However, the TCF value is not sufficiently small for the TS1-mode vibrations.

Regarding the TS1 mode, electromechanical coupling coefficients for the shear mode deformations i.e., k_{15} and k_{24} are different in BLSF family single crystal [22, 63]. As shown in Fig. 13.5, the vibration mode corresponding to k_{24} is affected by the interface between Bi_2O_2 layers and pseudoperovskite blocks. The chemical bonding in this interface region is weak [77, 79], and much affected by temperature change. In other words, the vibration mode corresponding to k_{24} shows inferior TCF to that corresponding to k_{15}.

The ordinarily fired (randomly oriented) BLSF ceramic shear mode resonators show mixed characteristics of the above two vibration modes corresponding k_{15} and k_{24} as shown in Fig. 13.6. It is difficult to obtain a superior TCF for the TS1-mode resonator.

From the above arguments, it can be concluded that there are no precise vibration modes of conventional single plate-type resonators of the BLSF ceramic materials for the practical oscillator applications.

In order to solve this tough problem, two approaches were taken. Those are utilizations of

1. The second harmonic mode of the thickness extensional vibration (TE2 mode) generated by ceramic layering technique
2. The TS1 mode generated in oriented BLSF ceramics

These two approaches are introduced below.

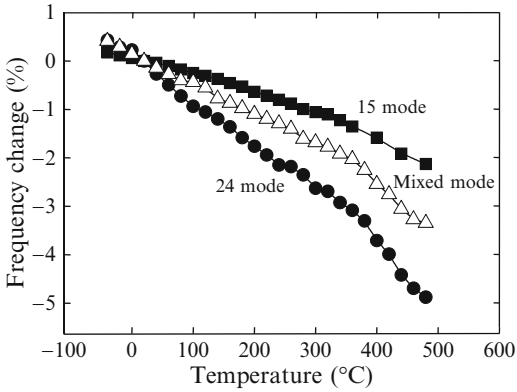

Fig. 13.6 Temperature characteristics of resonance frequency of shear mode vibrations of CBT

13.2.3 TE2-Mode Vibration Generated by Double Layer Structured Plate of BLSF Ceramics

Ando et al. reported that the second harmonic of the thickness extensional vibration by their developed double layer structured resonator of SBN-based ceramic exhibits a beautiful single mode resonance characteristic [38]. Their electromechanical coupling coefficients, mechanical quality factors, electrical quality factors, and temperature coefficients of resonance frequencies are described here. We will show that the TE2-mode vibration on the double-layered SBN plate has superior advantages for practical applications.

13.2.3.1 Sample Preparation for Layered Ceramic Resonator

The ceramic specimens were prepared by the conventional powder processing. $SrCO_3$, Bi_2O_3, Nb_2O_5, and $MnCO_3$ were chosen as the starting materials. These materials were weighed to compose the following compositions, and mixed with ball milling in water.

$$SrBi_2Nb_2O_9 + 1\ \text{wt.\%}\ MnCO_3$$

The mixed materials were calcined at 900°C for 2 h. The ceramic green sheet was made by the conventional doctor blade method with the calcined powder. The internal and external electrodes are screen-printed platinum. The green sheets were stacked and fired at 1,200°C for 2 h in air, and the double-layered piezoelectric ceramic plate with an internal electrode was obtained. Silver electrodes were formed on both surfaces of the samples by the evaporation method, and the sample was polarized at 5 kV/mm during 10 min at 200°C. The structure of the double-layered resonator is schematically shown in Fig. 13.7.

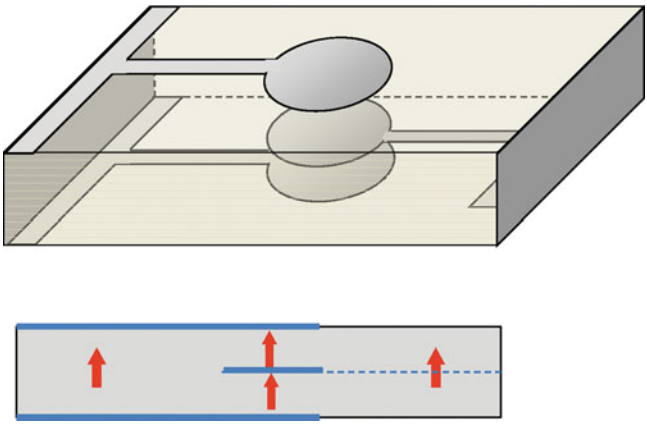

Fig. 13.7 Schematic view of the double-layered resonator

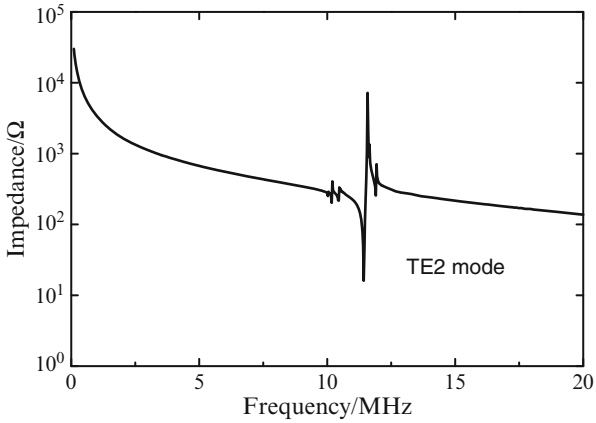

Fig. 13.8 Resonance characteristics of TE2-mode resonator with double-layer structure of SBN-based ceramic material

Figure 13.8 shows a beautiful single mode resonance characteristic of the double-layered resonator of the SBN. The reason why the single mode resonance characteristics are realized in the double-layered resonator is clearly explained by Ando with a mode coupling consideration and dispersion characteristics of the TE2-mode wave propagation [79, 84].

The dispersion characteristic of the TE2-mode wave is shown in Fig. 13.9.

13.2.3.2 Compositional Optimization for SBN-Based Ceramic Materials

As seen above, the double-layered resonator of the SBN showed good characteristics as conventional lead-based piezoelectric ceramic resonators. However, finer

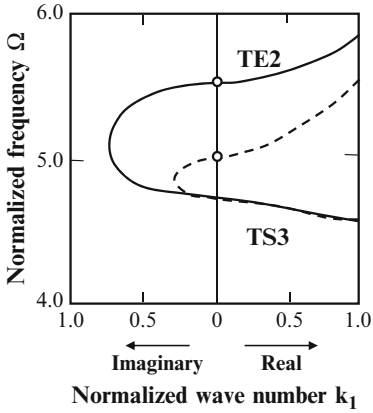

Fig. 13.9 Dispersion characteristics of TE2-mode vibration; Normalized frequency Ω is defined as $\omega \cdot h/\sqrt{c_{44}^{E}/\rho}$, h is a half the thickness of the plate. *Solid* and *broken lines* represent characteristics in the unelectroded regions and electroded region, respectively. *Small open circles* indicate intercepts of TE2 vibration mode branches for the electrode and unelectroded regions. Between these two intercepts, wave number of TE2 vibration is real and imaginary for the electrode and unelectroded regions, respectively

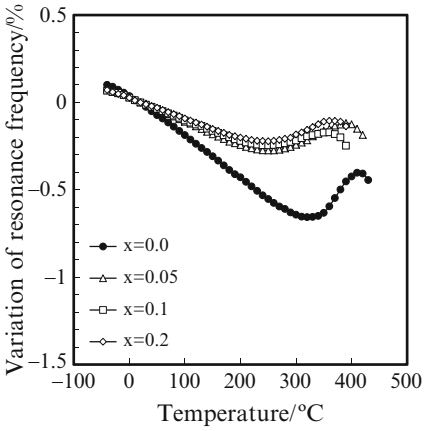

Fig. 13.10 Temperature characteristic of resonance frequency for modified SBN ceramics

frequency tolerance is required for oscillators in advanced electronics, and a smaller TCF value is necessary. Studies on compositional modifications for the TCF improvement of SBN-based materials have been still limited. The piezoelectric properties of the modified SBN materials with Sr site substitutions by Ba and Nd [73] were reported by Ando et al. These modified SBN materials show excellent TCF depending on smooth elastic anomalies which lie between 200 and 300°C as shown in Fig. 13.10.

Table 13.2 Resonance characteristics for TE2-mode vibration of the double-layered resonator of modified SBN ceramics

	SBN	Ba-SBN	Nd-SBN	Nd-SBN30
$\varepsilon_{33}^{T}/\varepsilon_0$	130	170	150	180
k_t (%)	17.0	15.0	16.0	11.0
Q_m	2,200	2,000	2,500	1,600
TCF (ppm/°C) (−20 to 80°C)	−20	−10	−14	−2
Q_{emax}	~12	~10	~20	8
T_c (°C)	420	380	380	280

$\varepsilon_{33}^{T}/\varepsilon_0$relative dielectric permittivity; k_t electromechanical coupling coefficient; Q_m mechanical quality factor; Q_{emax} maximum value of electric quality factor; T_c Curie temperature
SBN $SrBi_2Nb_2O_9$ + 1 wt.% $MnCO_3$; *Ba-SBN* $(Sr_{0.7}Ba_{0.3})Bi_2Nb_2O_9$ + 1 wt.% $MnCO_3$; *Nd-SBN* $(Sr_{0.9-\delta}Nd_{0.1})Bi_2Nb_2O_9$ + 0.5 wt.% $MnCO_3$; *SBN30* $(Sr_{0.7-\delta}Nd_{0.3})Bi_2Nb_2O_9$ + 0.5 wt.% $MnCO_3$

This smooth elastic anomaly might correspond to a relaxor ferroelectric characteristics of the Ba-substituted SBN [44, 72, 85]. The TE2 resonator characteristics of the modified SBN ceramics are summarized in Table 13.2.

Ba substitution to Sr site of SBN leads to the relaxor ferroelectric characteristics [44, 72, 85]. Kholkin et al. [67] reported that the large ionic radius of Ba enhances the compositional inhomogeneity in $SrBi_2Ta_2O_9$ (SBT) material, which has similar crystalline structure to SBN. They emphasize that one of the origins of the relaxor behaviors of SBT material is the large ionic radius of Ba ion. However this relation has not been proved sufficiently, and further studies are necessary.

13.2.4 TS1-Mode Vibration of Oriented BLSF Ceramics

BLSF ceramics have large crystal anisotropy [7], and the piezoelectricity of the polycrystalline ceramics is generally smaller than that of the widely used lead-based perovskite-type piezoelectric ceramics [17]. Therefore, the textured ceramics have been studied to improve their piezoelectric properties in the last few decades. Several methods were examined to obtain textured ceramics. Hot-forging, templated grain growth (TGG) method and reactive TGG method were proposed [32, 101, 102], and highly ⟨001⟩ textured ceramics were obtained for several BLSFs of $Bi_4Ti_3O_{12}$, NBT, and CBT [23, 103, 104]. It was reported that the electromechanical coupling coefficients and piezoelectric constants of highly textured BLSF ceramics were two or three times larger than those of randomly oriented ceramics.

On the other hand, temperature stability of the piezoelectric properties is also important for the practical usage. Especially, high accuracy of resonance frequency is necessary for piezoelectric filter or resonator applications. Crystalline symmetry of poled, ⟨001⟩ textured BLSF ceramics is lower than that of the poled, randomly oriented ceramics. The symmetry of the poled, textured ceramics is denoted as mm2 (C_{2v}), while that of the poled, randomly oriented ceramics is

denoted as ∞mm (C_∞). Therefore, as seen in Fig. 13.5, and 24-mode vibration separates from 15-mode vibration in the case of thickness shear vibration for the textured ceramics [105], and TCF of 15-mode vibration for the textured ceramics is smaller than those of 15-mode vibration for the randomly oriented ceramics and 24-mode vibration for the textured ceramics, and electromechanical coupling coefficient of 15-mode vibration for the textured ceramics is larger than those of 15-mode vibration for the randomly oriented ceramics and 24-mode vibration for the textured ceramics [63].

Meanwhile, piezoelectric characteristics of SBN were first reported by Subbarao [8]. SBN has a low electromechanical coupling coefficient around 15% and a high mechanical quality factor around 2,000. It has been also reported that SBN has a relatively small TCF of about −20 ppm/°C, compared to other BLSFs, and the TCF further decreases with Ba or Nd substitution on the Sr site [38, 72, 73, 84, 85] as seen in the previous section. From these points, SBN-type compounds have been considered as candidate materials for fine tolerance filter or resonator applications. In the authors' studies, textured ceramics of Nd-substituted SBN ceramics were fabricated by the TGG method, and piezoelectric properties of the thickness shear vibration were evaluated. Dependence of orientation degree upon the piezoelectric properties and the TCF were also studied. Moreover, specimens with the major faces formed at various angles to the oriented direction were fabricated from the textured ceramics, and their properties were determined. In this chapter, piezoelectric characteristics of these oriented ceramics will be described.

13.2.4.1 Sample Preparation and Measurements

The starting raw materials were high purity $SrCO_3$, Nd_2O_3, Bi_2O_3, Nb_2O_5, and $MnCO_3$ (99.9%). They were weighed with the composition represented by the following chemical formula:

$$Sr_{0.9}Nd_{0.1}Bi_2Nb_2O_9 + 0.5\ \text{wt.\%}\ MnCO_3\ (\text{Nd-SBN}).$$

Nd substitution to Sr site improves TCF characteristics of the materials, and it is also effective to obtain template particles with large shape anisotropy, which were required for fabricating highly textured ceramics by the TGG method [91]. $MnCO_3$ was added as a sintering aid. The weighed powder was ball-milled with deionized water and calcined at 800°C for 2 h. The template particles were prepared by a molten salt synthesis with KCl flux. The calcined powder was mixed with an equal weight of high purity KCl (99.5%) and heated in a high purity alumina crucible at the temperatures from 1,000 to 1,200°C for 10 h. After heating, those mixtures were washed with deionized water to remove KCl flux. Dimensions of the plate-like template particles varied from approximately 3.0–7.5 μm in diameter, and the aspect ratio ranged from about 4 to 7. The normally calcined powder was ball-milled again with deionized water, and average diameter of the milled powder was 0.8 μm. Then, the template particles and the calcined powders were mixed with

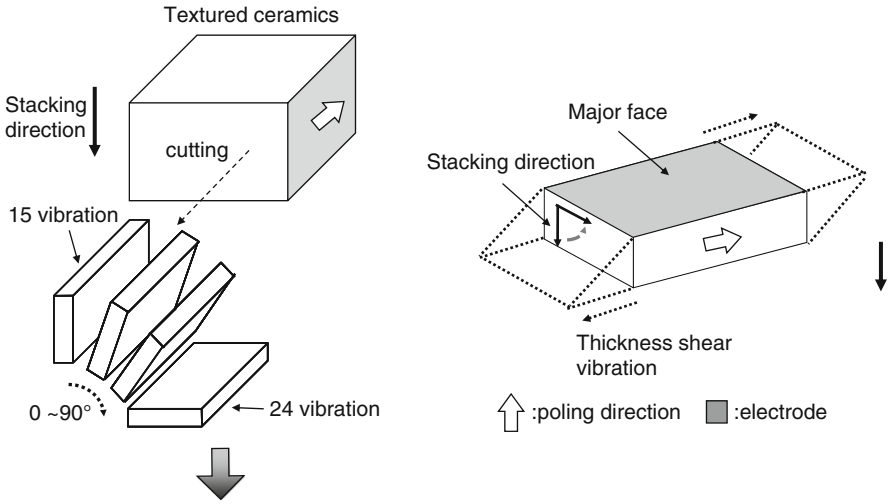

Fig. 13.11 Schematic figure of resonator specimens for texture SBN ceramics with various major face angles. The textured ceramics were cut into plates with the major faces formed at angles of 0° (15-mode vibration), 15, 30, 45, and 90° (24-mode vibration) to the stacking direction, and five types of resonator specimens for thickness shear vibration were obtained from these plates

weight ratio of 1:4, respectively, and tape-casting slurries were prepared by adding 10 wt.% polyvinyl acetate-based binder to these mixtures. Green tapes were prepared with a thickness of 60 μm by doctor-blade technique. They were stacked and pressed into green bodies with a thickness of 5 mm under a pressure of 10 MPa. After that, the green bodies were heated at 500°C for 2 h to remove the binder, and fired at 1,200°C for 5 h in an oxygen atmosphere. The textured ceramics with various texture fractions were fabricated using template particles with a wide range of the average diameter. Randomly oriented ceramics were also prepared using the same process without the template particles. The sintered ceramics were poled perpendicular to the tape stacking direction under the electric field of 10 kV/mm for 30 min in silicone oil at 200°C.

The 15- and 24-mode vibration resonator specimens were prepared by cutting the textured ceramics into plates parallel and perpendicular to the stacking direction, respectively. The 15-mode vibration should be excited in plates with the major faces parallel to both the tape stacking direction, which corresponded to the ⟨001⟩ oriented direction, and the poling direction. On the other hand, the 24-mode vibration should be excited in plates with major faces perpendicular to the stacking direction and parallel to the poling direction. Specimens with major faces formed at angles of 15, 30, and 45° to the stacking direction were also fabricated. Figure 13.11 shows relationship between the stacking direction of the textured ceramics and the major face of the specimens.

Density of the sintered ceramics was measured by the Archimedes method. Microstructure was observed by scanning electron microscopy (SEM), and

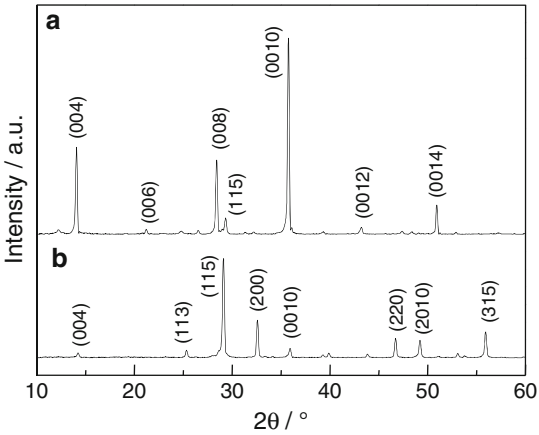

Fig. 13.12 X-ray diffraction (XRD) profiles for (**a**) surface perpendicular to the stacking direction of 96%-textured Nd-SBN ceramics and (**b**) ground powder of the randomly oriented ceramics

crystalline structure was evaluated by the X-ray diffraction (XRD) technique. The texture fraction F was determined from the XRD profiles using the Lotgering method [107]. Piezoelectric properties were measured with the standard resonance method (IEEE). Silver electrodes were made on the major faces of the specimens by sputtering method. All specimens had dimensions of 3.0 mm (length) × 0.5 mm (width) × 0.3 mm (thickness).

13.2.4.2 Highly Textured SBN Ceramics

The textured ceramics with a texture fraction of 96% were obtained using template particles with an average diameter of 7.5 μm. Relative density of these ceramics achieved 98%. Figure 13.12a, b show XRD profiles for polished face perpendicular to the stacking direction of the textured ceramics and ground powder of the randomly oriented ceramics, respectively. Intensity of each ⟨001⟩ peak for the textured ceramics is much stronger than that for the powder, on the contrary, intensity of other reflections was weak. Therefore, it is recognized that the ceramics are highly ⟨001⟩ oriented parallel to the stacking direction.

Figure 13.13a, b show SEM micrographs of surfaces perpendicular and parallel to the stacking direction for the textured ceramics, respectively. It indicates that most of the plate-like grains aligned perpendicular to the stacking direction.

Dielectric and piezoelectric properties for the textured 15- and the randomly oriented 15-mode specimens are summarized in Table 13.3. Curie temperature and relative dielectric permittivity $\varepsilon_{11}^{\mathrm{T}}/\varepsilon_0$ of the textured specimen are almost the same as those of the randomly oriented specimen. Electromechanical coupling coefficient k_{15} and piezoelectric constant d_{15} of the textured 15-mode vibration specimen are three times and twice larger than those of the randomly oriented 15-mode vibration specimen, respectively. Mechanical quality factor Q_{m} of the textured 15-mode vibration specimen is also larger than that of the randomly oriented specimen.

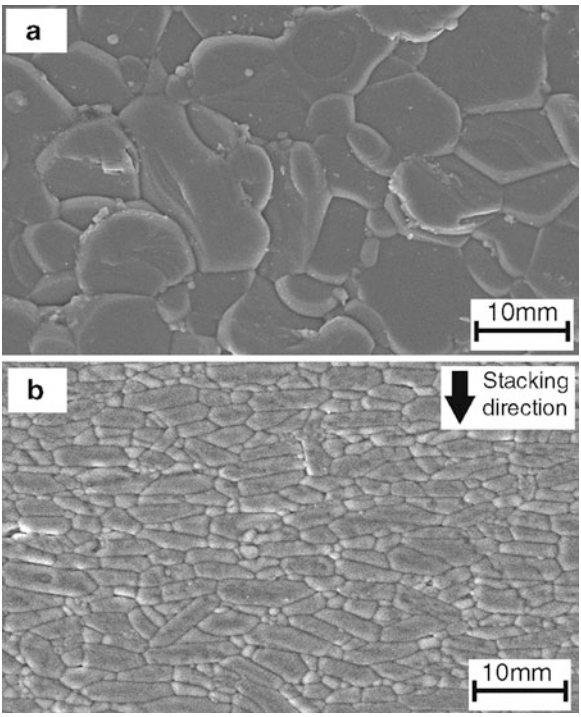

Fig. 13.13 SEM micrographs of 96%-textured Nd-SBN ceramics (**a**) and (**b**) show surfaces of perpendicular and parallel to the stacking direction, respectively

Table 13.3 Piezoelectric properties of textured Nd-SBN ceramics

	96% textured	Randomly oriented
Curie temperature (°C)	390	390
Dielectric permittivity $\varepsilon_{11}^{T}/\varepsilon_0$	160	165
Coupling coefficient k_{15} (%)	24.8	8.2
Piezoelectric constant d_{15} (pC/N)	32	14
Mechanical quality factor Q_m	2,950	2,400

TCF of the textured specimen is also different from that of the randomly oriented specimen. The TCF of the 96%-textured ceramics is +20.9 ppm/°C, while that of the randomly oriented ceramics was −30.6 ppm/°C. The temperature dependence of resonance frequency for the highly textured ceramics shows a completely different behavior compared with the randomly oriented ceramics, although the temperature dependences of resonance frequency for the highly textured and randomly oriented CBT ceramics indicated similar behavior [63]. The resonance frequency decreases with increasing temperature for the randomly oriented specimen; on the contrary, the resonance frequency increases with increasing temperature for the textured specimens in the case of Nd-SBN. This result suggests that the TCF of the textured Nd-SBN ceramics might be remarkably improved by precise grain orientation controls.

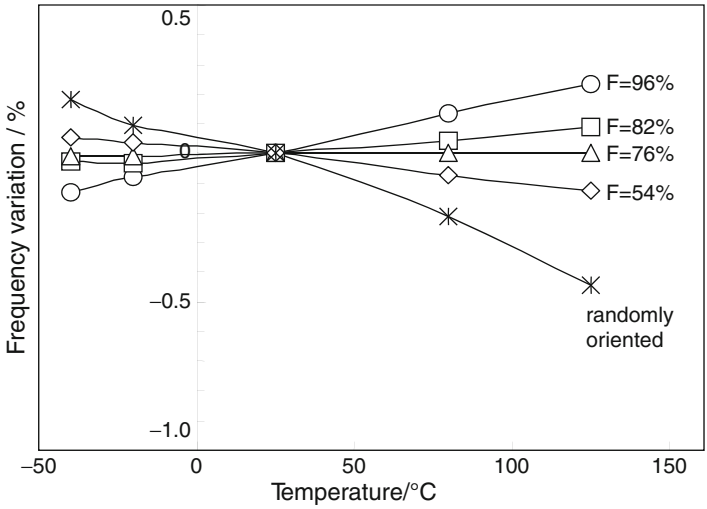

Fig. 13.14 Temperature dependence of resonance frequency for the textured 15 vibration specimens with texture fraction (F) from 54 to 96%, and the randomly oriented 15 vibration specimen

13.2.4.3 Textured Ceramics with Various Texture Fraction and Major Face Angle [106]

Textured ceramics with their orientation degrees from 54 to 82% were fabricated using template particles of dimension from 3.1 to 7.5 μm in diameter. Relative density of all specimens was over 97%. Figure 13.14 shows temperature dependence of resonance frequency of 15-mode vibration for the textured and the randomly oriented specimens. The resonance frequency varies linearly with increasing temperature for all specimens. However, their gradients are quite different. TCF value changes from negative to positive with increasing grain orientation, and the absolute value of the TCF became the smallest for the 76%-textured specimen.

Figure 13.15 shows the orientation degree dependence of the TCF and the electromechanical coupling coefficient k_{15}. The TCF increases linearly with the increase of the orientation degree, and the minimum value of TCF of −0.4 ppm/°C is obtained. The k_{15} also increases linearly with the increase of the orientation degree, and the k_{15} is 20.2% for the specimen with the smallest TCF.

Another approach to obtain a small TCF for the SBN ceramics is a cut angle control of the oriented ceramic specimens. Specimens with the major faces formed at angles of 0, 15, 30, 45, and 90° to the stacking direction were also fabricated for the 96%-textured ceramics as shown in Fig. 13.11, and dependence of the TCF and the electromechanical coupling coefficient on the angles between the major face and the ⟨001⟩ oriented direction was studied for the TS1 vibration. The specimen with angles of 0 and 90° corresponds to the 15- and the 24-mode vibration,

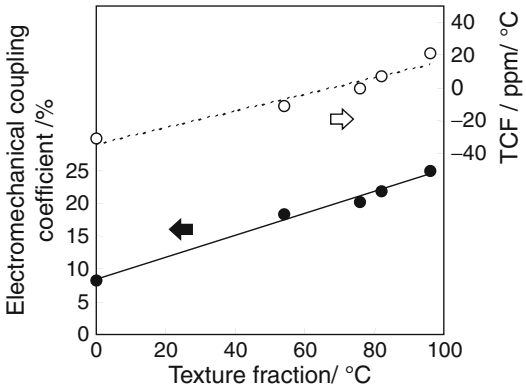

Fig. 13.15 Dependence of TCF and electromechanical coupling coefficient on the texture fraction. The texture fraction of randomly oriented specimen was assumed to be 0°

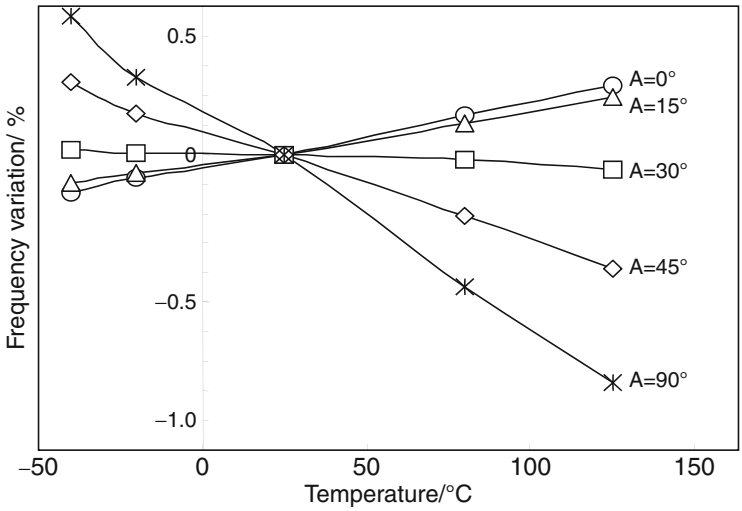

Fig. 13.16 Temperature dependence of resonance frequency for the 96%-textured specimens. The samples had their major faces formed at angles of (*A*) of 0, 15, 30, 45, and 90° to the stacking direction

respectively. Figure 13.16 shows temperature dependence of resonance frequency for the specimens with angles from 0 to 90°. The resonance frequency varies linearly with increasing temperature for all specimens, and their gradients change from negative to positive with the decrease of the angle.

Figure 13.17 shows dependence of the TCF and the electromechanical coupling coefficient on the angle between the major face and the ⟨001⟩ oriented direction, respectively. The TCF decreases linearly with increasing the angle, and the minimum value of TCF was −2.6 ppm/°C for the specimen with an angle of 30°.

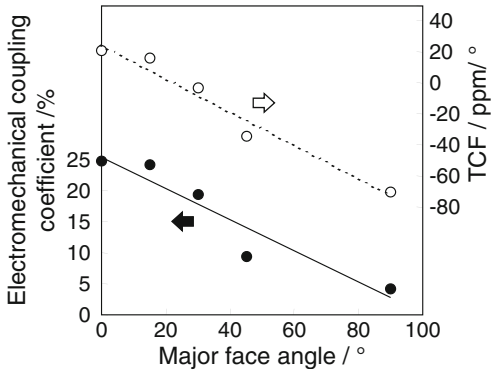

Fig. 13.17 Dependence of TCF and electromechanical coupling coefficient on the angle between the major face and the ⟨001⟩ oriented direction

The electromechanical coupling coefficient also decreases linearly with increasing the angle, and the electromechanical coupling coefficient is 19.5% at the specimen with the angle of 30°. It is probable that intermediate characteristics between the 15- and 24-mode vibration are observed for the specimens with the angle of 15, 30, and 45°.

The dependence of the angle is similar to that of the texture fraction, and the piezoelectric properties of the specimen with the angle of 45°, which is midway between 15- and 24-vibration modes, is approximately same as the randomly oriented samples. These results suggest that intermediate characteristics between the 15- and 24-mode vibrations could be obtained when the orientation degree changes.

Optimization of the texture fraction or the angle between the major face and ⟨001⟩ oriented direction is shown to be valuable to obtain excellent TCF for thickness shear vibration of SBN-based ceramics. Textured SBN-based ceramics should be strong candidates for the fine tolerance resonator applications.

13.2.4.4 Temperature Stability Within a Wide Temperature Range [108]

Quartz crystal is a well-known piezoelectric material with high frequency accuracy, and the temperature stability of resonance frequency is generally higher than that of a ceramic resonator around room temperature. Temperature variation of resonance frequency for the 76%-textured ceramics is still larger than that for a typical quartz oscillator around room temperature. However, the frequency variation is probably smaller than that of the quartz oscillator over a wide temperature range from −50 to 250°C, because the resonance frequency of the 76%-oriented Nd-SBN varies almost linearly over a wide temperature range. The temperature dependence of resonance frequency in thickness shear vibration mode for the 76%-oriented SBN from −50 to 250°C is shown in Fig. 13.18. The TCF of −0.85 ppm/°C is obtained there.

The temperature dependence of oscillation frequency of commonly used AT-cut quartz crystal oscillator (14.4 MHz) is also plotted in Fig. 13.18 for comparison. The oscillation frequency of the quartz oscillator is almost constant around room

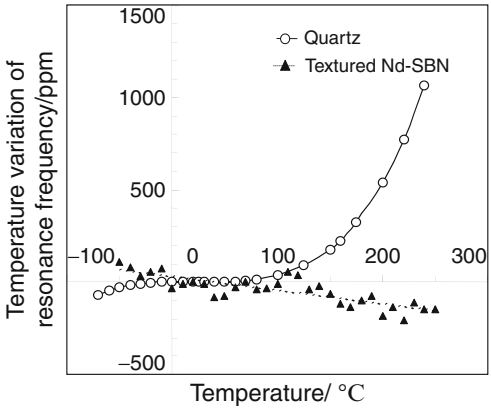

Fig. 13.18 Temperature dependences of resonance frequency in thickness shear vibration mode for 76%-textured Nd-SBN specimens and oscillation frequency for the quartz crystal oscillator within a temperature range from −50 to 250°C

temperature, and the frequency variation was smaller than that of the textured Nd-SBN ceramics. However, the variation of quartz oscillator rapidly became larger above 150°C, and the frequency variation of the textured Nd-SBN was smaller than that of the quartz oscillator in the wide temperature range form −50 to 250°C.

Textured SBN-type ceramics is major candidate material for resonators used in wide temperature ranges.

13.3 Resonance Characteristics of BLSF for High-Power Applications

Recently, many high-power piezoelectric ceramic devices, such as ultrasonic motors, piezoelectric transducers, and transformers, have been developed [109]. For these applications, hard-type $Pb(Zr,Ti)O_3$ (PZT) ceramics have usually been used. However, there are some problems with their high-power characteristics; the vibration velocity does not increase with applied electric field above about 1.0 m/s, and the resonance frequency decreases with increasing vibration velocity [110].

BLSF ceramics are major candidates among various lead-free materials for piezoelectric devices such as filters or oscillators due to their high Curie temperature and excellent heat resistance, and several ⟨001⟩ texturing methods have been adapted for BLSF ceramics to improve piezoelectric properties by a number of research groups, as mentioned in the previous section. On the other hand, it is known that piezoelectric single crystals, such as $LiNbO_3$, exhibit excellent high-power characteristics [110]. BLSF-textured ceramics are also expected to exhibit excellent high-power characteristics because of their high Q_m characteristics. In this section, high-power characteristics of the textured ceramics of BLSF fabricated by TGG method are described [111].

13.3.1 Sample Preparation and Measurements

Chemical formulae of $Sr_{0.9}Nd_{0.1}Bi_2Nb_2O_9 + 0.5$ wt.% $MnCO_3$(Nd - SBN), $Ca_{0.8}Bi_{4.2}Ti_4O_{15}$ +0.5 wt.% $MnCO_3$(CBT), $Bi_{3.25}La_{0.75}Ti_{2.97}Nb_{0.03}O_{12} + 0.3$ wt.%-$MnCO_3$(BIT), were selected as test materials, and the highly textured ceramics were fabricated by the TGG method on the similar procedure mentioned in the previous section. The Nd-SBN specimens with the texture fractions of 54–95% were also fabricated using template particles with various average diameters. Hard PZTs with a composition of $0.1Pb(Mn_{1/3}Nb_{2/3})O_3$-$0.9Pb(Zr_{0.49}Ti_{0.51})O_3$ were also prepared by the ordinary solid-state reaction for comparison. These textured ceramics were poled perpendicular to the tape stacking direction. Then, rod-shaped 33-mode specimens with a long side parallel to the poling direction were prepared by cutting of the sintered ceramics. The specimens had dimensions of $5 \times 2 \times 2$ mm. Silver electrodes were formed on both faces perpendicular to the long side by sputtering. Silver wires were bonded on both electrodes. Plate-type 15-mode specimens of Nd-SBN were also fabricated to estimate thickness shear mode vibration, and the specimens had dimensions of $10 \times 5 \times 3$ mm. Silver electrodes were formed on both main surfaces of 10×5 mm.

Small amplitude piezoelectric properties were measured by the resonance–antiresonance method. Vibration velocity was measured using a laser Doppler vibrometer. The resonance frequency was estimated from the frequency dependence of vibration velocity under a constant-voltage driving, because the maximum value of the vibration velocity is generally obtained at the resonance frequency under the constant-voltage driving.

13.3.2 High-Power Characteristics of Highly Textured SBN Ceramics [112]

Figure 13.19 shows the applied electric field dependences of vibration velocities of 95%-textured Nd-SBN and $Pb(Mn,Nb)O_3$-PZT specimens in 33-mode vibration. Vibration velocity of the textured Nd-SBN specimen is proportional to the applied electric field up to 2.6 m/s. On the other hand, vibration velocity of $Pb(Mn,Nb)O_3$-PZT specimen is saturated at around 1.0 m/s and the resonance vibration became unstable at a vibration velocity of about 1.0 m/s.

Figure 13.20 shows the vibration velocity dependences of the resonance frequency changes of the 95%-textured Nd-SBN and the $Pb(Mn,Nb)O_3$-PZT specimens. Resonance frequency of the textured Nd-SBN specimen is almost constant up to a vibration velocity of 2.6 m/s, while the resonance frequency of the $Pb(Mn,Nb)O_3$-PZT specimen decreases with increasing vibration velocity. Highly textured Nd-SBN specimen exhibits excellent high-power characteristics.

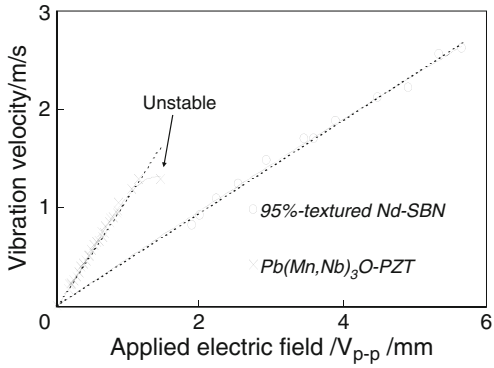

Fig. 13.19 Applied electric field dependences of vibration velocity for the 95%-textured Nd-SBN and $Pb(Mn,Nb)O_3$-PZT specimens in 33-mode vibration

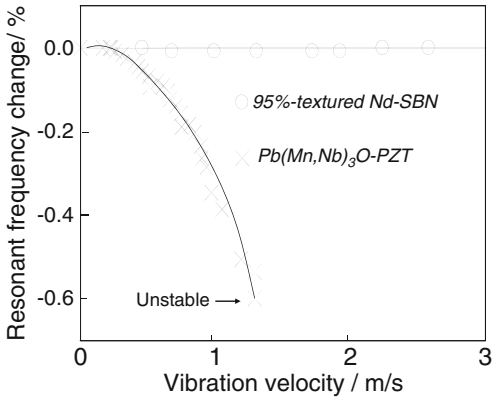

Fig. 13.20 Vibration velocity dependences of frequency change for 95%-textured SBN and $Pb(Mn,Nb)O_3$-PZT specimens in 33-mode vibration

Table 13.4 Piezoelectric properties of textured and randomly oriented Nd-SBN specimens

	Textured			Randomly oriented
	$F = 95\%$	$F = 75\%$	$F = 54\%$	
Dielectric permittivity $\varepsilon_{33}^{T}/\varepsilon_0$	125	117	128	100
Coupling coefficient k_{33} (%)	32.7	28.0	27.0	16.6
Piezoelectric constant d_{33} (pC/N)	27	24	23	14

13.3.3 Texture Fraction Dependence [113]

Textured SBN specimens with texture fractions of 54, 75, and 95% were prepared by the TGG method using template particles with various average diameters. Small-amplitude piezoelectric properties of the specimens are summarized in Table 13.4. The piezoelectric constant of 33-mode vibration (d_{33}) and the electromechanical coupling factor (k_{33}) increase with increasing orientation degree F.

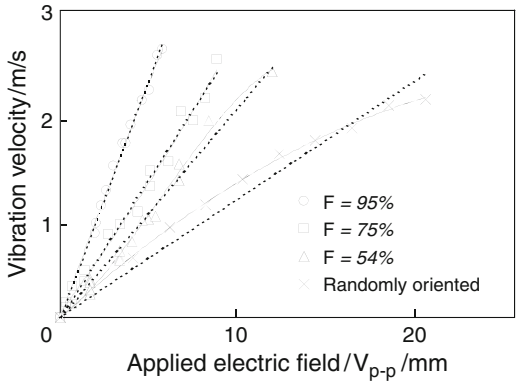

Fig. 13.21 Applied electric field dependences of vibration velocity for the textured ($F = 95$, 75, and 54%) and randomly oriented Nd-SBN specimens in 33-mode vibration

Figure 13.21 shows the applied electric field dependences of vibration velocities of the textured and randomly oriented Nd-SBN specimens in 33-mode vibration. Slope of vibration velocity increases with the increase of the orientation degree. It is reasonable because the vibration velocity is affected by d_{33} value, and d_{33} increases with the increase of the orientation degree. Vibration velocity of the 95%-textured and the 75%-textured Nd-SBN specimens changes linearly with the applied electric field, on the other hand, that of the randomly oriented and 54%-textured Nd-SBN specimens changes nonlinearly with applied electric field. This result suggests that the linearity of vibration velocity decreases with decreasing of the orientation degree.

Figure 13.4 shows the vibration velocity dependences of resonance frequency changes of the textured and randomly oriented Nd-SBN specimens in 33-mode vibration. Resonance frequency of the 95%-textured and the 75%-textured Nd-SBN specimens is almost constant, and the resonance frequency changes are below 0.01% for the vibration velocity up to 2.6 m/s. Meanwhile, resonance frequency of the randomly oriented and the 54%-textured SBN specimens decreases with increasing vibration velocity, and the absolute value of resonance frequency change of the randomly oriented Nd-SBN specimen is larger than that of the 54%-textured Nd-SBN specimen. From these results, it is seen that the stability of resonance frequency decreases with the decrease of the orientation degree. although no significant differences are seen between the results of 95%-textured and 75%-textured Nd-SBN specimens as shown in Fig. 13.22.

13.3.4 Crystal Structure Dependence [114]

BLSF crystal structure consists of pseudoperovskite layers and Bi_2O_2 layers. In the case of SBN, two pseudoperovskite layers exist between Bi_2O_2 layers [8]. The number of the pseudoperovskite layers between the Bi_2O_2 layers is denoted as "*m*" number. The m number of SBN is 2. On the other hand, the m numbers for BIT and CBT are 3 and 4, respectively. The component of spontaneous polarization along the *c*-axis did

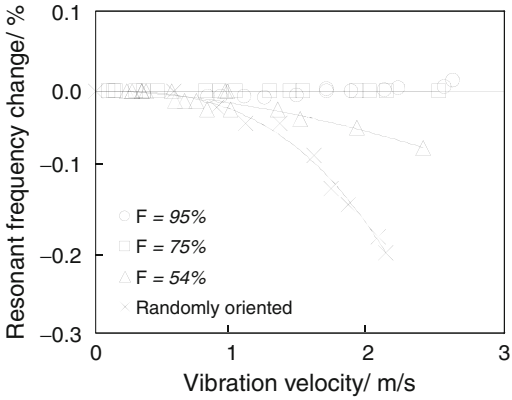

Fig. 13.22 Vibration velocity dependences of frequency change for the textured ($F = 95$, 75, and 54%) and randomly oriented Nd-SBN specimens in 33-mode vibration

Table 13.5 Piezoelectric properties of textured Nd-SBN, BIT, and CBT specimens

	SBN	BIT	CBT
Lotegering factor (%)	95	97	99
Dielectric permittivity $\varepsilon_{33}^{T}/\varepsilon_0$	125	185	128
Coupling coefficient k_{33} (%)	32.7	26.7	33.6
Piezoelectric constant d_{33} (pC/N)	27	27	28

not exist if the m number is even. On the contrary, it could exist if the m number is odd [15, 115]. Therefore, the c-axis component of spontaneous polarization exists in the BIT, and it does not exist in the SBN and CBT. This difference in the spontaneous polarization direction corresponding to the "m" number is clearly explained from a crystallographic viewpoint by Newnham [116]. Oxygen octahedrons of the pseudoperovskite layers as shown in Fig. 13.1 are easy to tilt rather than to deform when apices oxygen ions move to the direction perpendicular to c axis with the phase transition from the paraelectric phase to the ferroelectric phase. When the "m" number is odd, a mirror plane perpendicular to c axis cannot exist in order to avoid the deformation of the octahedrons. On the contrary, when the "m" number is even, the mirror plane is energetically stable. The existence of the mirror plane perpendicular to c axis means that the polarization component along c axis is zero.

The effect of c-axis component of spontaneous polarization upon the high-power characteristics was studied by comparing the BIT specimen with the Nd-SBN and CBT specimens [114].

Table 13.5 shows the small-amplitude piezoelectric properties of highly textured Nd-SBN, BIT, and CBT specimens. Electromechanical coupling coefficient of the BIT specimen was smaller than those of Nd-SBN and CBT. However, the piezoelectric constants (d_{33}) of these specimens were almost the same.

Figure 13.23 shows the applied electric field dependences of the vibration velocities of the Nd-SBN, BIT, and CBT specimens in 33-mode vibration. The slopes of vibration velocity for these specimens are almost the same, because the d_{33} of these specimens was almost the same. However, the vibration velocity of the BIT

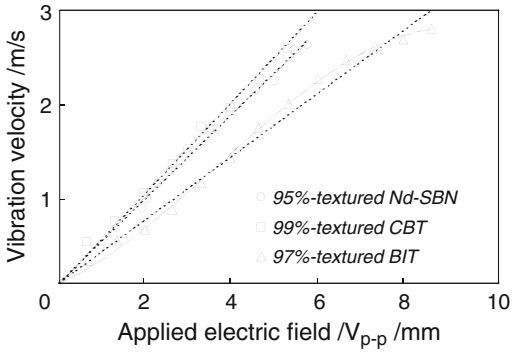

Fig. 13.23 Applied electric field dependences of vibration velocity for the highly textured Nd-SBN, BIT, and CBT specimens in 33-mode vibration

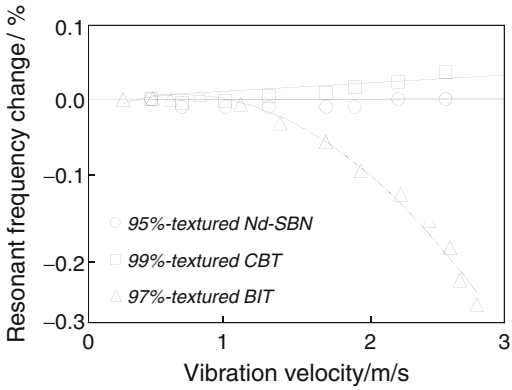

Fig. 13.24 Vibration velocity dependences of frequency change for the highly textured Nd-SBN, BIT, and CBT specimens in 33-mode vibration

specimen changes nonlinearly with applied electric field, on the other hand, that of the Nd-SBN and CBT specimens changes linearly with the applied electric field.

Figure 13.24 shows the vibration velocity dependences of the frequency changes of the highly textured Nd-SBN, BIT, and CBT specimens in 33-mode vibration. Resonance frequency of the Nd-SBN and CBT specimens was almost constant, and the resonance frequency changes were within 0.05% for the vibration velocity up to 2.6 m/s. Meanwhile, the resonance frequency of the BIT specimen decreases with increasing vibration velocity. From these results, it is considered that the *c*-axis component of spontaneous polarization causes the nonlinearity of vibration velocity and the instability of resonance frequency.

The linearity of the vibration velocity and the stability of resonance frequency decrease with the decrease of the orientation degree in the Nd-SBN specimens. On the other hand, among the highly textured BLSF specimens (Nd-SBN, BIT, and CBT specimens), only the textured BIT specimen exhibits the instability of resonance frequency and the nonlinearity of vibration velocity. The component of spontaneous polarization nonparallel to the vibration direction exists also in the highly textured BIT specimen unlike the highly textured Nd-SBN and CBT specimens. From these considerations, it can be concluded that the component of spontaneous polarization nonparallel to the vibration direction affects the nonlinearity or the resonance frequency instability.

Table 13.6 Piezoelectric properties of thickness shear vibration mode of textured and randomly oriented Nd-SBN

	Textured ($F = 95\%$)	Randomly oriented
Dielectric permittivity $\varepsilon_{11}^{T}/\varepsilon_0$	161	151
Coupling coefficient k_{15} (%)	17.4	7.5
Piezoelectric coefficient d_{15} (pC/N)	27	12
Mechanical quality factor Q_{m15}	2,300	2,070

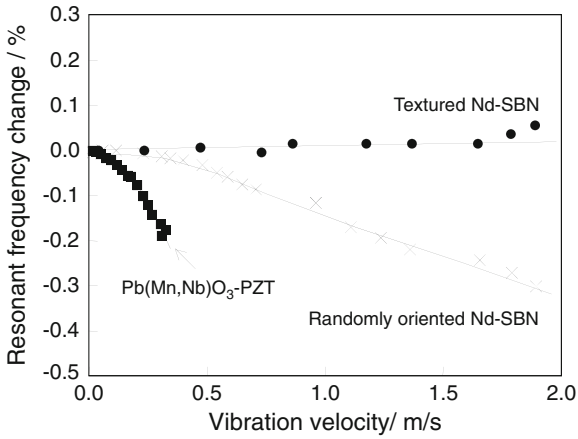

Fig. 13.25 Vibration velocity dependences of resonance frequency change for the textured Nd-SBN, randomly oriented SBN, and $Pb(Mn,Nb)O_3$-PZT ceramics in thickness shear 15-vibration mode

13.3.5 Thickness Shear Vibration Mode [117]

Application of the thickness shear deformation has recently attracted much attention in piezoelectric devices. The piezoelectric constant and the electromechanical coupling coefficient of the thickness shear vibration mode are relatively larger than those of the longitudinal vibration mode, especially for several kinds of lead-free piezoelectric materials [118]. Therefore, the thickness shear vibration mode probably becomes more important for the design of piezoelectric devices. In this section, high-power piezoelectric characteristics of thickness shear 15-mode vibration mode for the textured Nd-SBN ceramics were investigated and compared with those of the randomly oriented Nd-SBN and a typical lead-based $Pb(Mn_{1/3}Nb_{2/3})O_3$-$Pb(Zr,Ti)O_3$ ceramics.

Table 13.6 shows piezoelectric properties of 15-mode deformation in the textured- and randomly oriented-Nd-SBN and $Pb(Mn,Nb)O_3$-PZT ceramics. Electromechanical coupling coefficient k_{15} and piezoelectric constant d_{15} of the textured ceramics increases almost twofold compared with those of the randomly oriented Nd-SBN ceramics. The mechanical quality factor Q_{m15} of the textured Nd-SBN ceramics was almost the same as that of the randomly oriented Nd-SBN ceramics.

Figure 13.25 shows the vibration velocity dependences of resonance frequency in the textured and randomly oriented Nd-SBN and $Pb(Mn,Nb)O_3$-PZT ceramics.

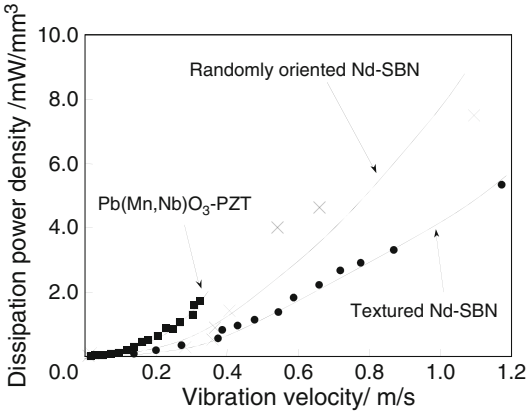

Fig. 13.26 Vibration velocity dependence of dissipation power density for the textured and randomly oriented Nd-SBN, and Pb(Mn,Nb)O_3-PZT ceramics in thickness shear 15-vibration mode

Thickness shear vibration mode is stable up to the vibration velocity of 2.0 m/s in the textured and randomly oriented Nd-SBN ceramics. However, vibration velocity of Pb(Mn,Nb)O_3-PZT ceramics is saturated at around 0.3 m/s. The resonance frequency is almost constant with increasing vibration velocity for the textured Nd-SBN ceramics, while it decreases with increasing vibration velocity in the randomly oriented Nd-SBN ceramics. In the case of Pb(Mn,Nb)O_3-PZT ceramics, the resonance frequency decreases with increasing vibration velocity at a lower vibration velocity than in the case of Nd-SBN ceramics. Similar results with the 33-mode vibration are also obtained in the thickness shear vibration mode.

Figure 13.26 shows the vibration velocity dependences of dissipation power densities of these specimens. The dissipation power density of textured Nd-SBN ceramics is lower than that of randomly oriented Nd-SBN ceramics, which is lower than that of Pb(Mn,Nb)O_3-PZT ceramics. It is considered that the internal heat generation rate of the textured Nd-SBN ceramics is the lowest among those of other ceramics, because the dissipation power density is proportional to the internal heat generation rate.

It seems that the difference in the high-power properties of the textured Nd-SBN ceramics is related to the relationship between the crystalline structure of the Nd-SBN ceramics and the shear distortion. The crystalline structure of SBN is highly anisotropic. Crystal symmetry of the poled textured Nd-SBN ceramics is lower than that of the poled randomly oriented Nd-SBN ceramics. The crystalline symmetry of the poled textured Nd-SBN ceramics is mm2 (C_{2v}), whereas that of the poled randomly oriented SBN ceramics is ∞mm(C_{∞}). The thickness shear vibration parallel to the oriented *c*-axis is separated from that perpendicular to the oriented *c*-axis in the textured Nd-SBN ceramics. The thickness shear vibration of the textured Nd-SBN ceramics is parallel to the oriented *c*-axis. On the other hand, that of the randomly oriented Nd-SBN ceramics is a mix of vibration parallel and perpendicular to the oriented *c*-axis. Therefore, it was considered that thickness shear vibration perpendicular to the oriented *c*-axis induces the internal loss in the high-power driving. However, this relation should be clarified in the future study.

13.4 Conclusions

Unique characteristics of the BLSF ceramic materials were reviewed here. The SBN-based materials are appropriate for the fine frequency tolerance oscillator applications in advanced electronics. They showed more stable characteristics in a wide temperature range than the quartz resonators. Especially at high temperatures more than 150°C, the SBN-based material shows the best resonator performance in piezoelectric materials discovered ever.

On the other hand, BLSF materials show superior high-power characteristics. They can vibrate with the velocity more than 2 m/s, which is 2 times higher than that of conventional hard PZT. From this viewpoint, BLSF ceramic materials are considered as one of the best piezoelectric materials for the high-power application such as ultrasonic vibrators, ultrasonic motors, piezoelectric motors, ultrasound emitters, and so on. These high-power applications are increasing their importance. The authors believe that the BLSF materials will give significant influences on the future electronics or mechatronics.

References

1. Aurivillius B (1949) Mixed bismuth oxides with layer lattices I. The structure type of $CaNb_2Bi_2O_9$. Ark Kemi 1:463–480
2. Aurivillius B (1949) Mixed bismuth oxides with layer lattices II. Structure of $Bi_4Ti_3O_{12}$. Ark Kemi 1:499–512
3. Aurivillius B (1950) Mixed oxides with layer lattices III. Structure of $BaBi_4Ti_4O_{15}$. Ark Kemi 2:519–527
4. Uitert LGV, Egerton L (1961) Bismuth titanate. A ferroelectric. J Appl Phys 32:959
5. Subbarao EC (1961) Ferroelectricity in $Bi_4Ti_3O_{12}$ and its solid solutions. Phys Rev 122:804–807
6. Subbarao EC (1961) Ferroelectricity in mixed bismuth oxides with layer-type structure. J Chem Phys 34:695–696
7. Subbarao EC (1962) Crystal chemistry of mixed bismuth oxides with layer-type structure. J Am Ceram Soc 45:166–169
8. Subbarao EC (1962) A family of ferroelectric bismuth compounds. J Phys Chem Solids 23:665–676
9. Aurivillius B, Fang PH (1962) Ferroelectricity in the compound $Ba_2Bi_4Ti_5O_{18}$. Phys Rev 126:893–896
10. Cummins SE, Cross LE (1968) Electrical and optical properties of ferroelectric $Bi_4Ti_3O_{12}$ single crystals. J Appl Phys 39:2268–2274
11. Cross LE, Pohanka RC (1968) A thermodynamic analysis of ferroelectricity in bismuth titanate. J Appl Phys 39:3992–3995
12. Wolfe RW, Newnham RE, Kay MI (1969) Crystal structure of Bi_2WO_6. Solid State Commun 7:1797–1801
13. Fouskova A, Cross LE (1970) Dielectric properties of bismuth titanate. J Appl Phys 41:2834–2838
14. Wolfe RW, Newnham RE, Smithf DK, Kay MI (1971) Crystal structure of Bi_3TiNbO_9. Ferroelectrics 3:1–7

15. Newnham RE, Wolfe RW, Dorrian JF (1971) Structural basis of ferroelectricity in the bismuth titanate family. Mater Res Bull 6:1029–1039
16. Newkirk HW, Quadflieg P, Liebertz J, Kockel A (1972) Growth, crystallography and dielectric properties of Bi_2WO_6. Ferroelectrics 4:51–55
17. Ikegami S, Ueda I (1974) Piezoelectricity in ceramics of ferroelectric bismuth compound with layer structure. Jpn J Appl Phys 13:1572–1577
18. Kikuchi T, Watanabe A, Uchida K (1977) A family of mixed-layer type bismuth compounds. Mater Res Bull 12:299–304
19. Ismailzade IH, Aliyev IM, Ismailov RM, Alekberov AI, Rzayev DA (1979) Ferroelectricity in Bi_2MoO_6. Ferroelectrics 22:853–854
20. Hellwege KH (ed) (1981) "Landolt-Bornstein", group III: crystal and solid state physics, vol 16. Springer, Berlin
21. Smolenskii GA, Bokov VA, Isupov VA, Krainik NN, Pasynkov RE, Sokolov AI (1984) Ferroelectrics and related materials. In: Smolenskii GA (ed) Ferroelectricity and related phenomena, vol 3. Gordon & Breach Science Publishers, Amsterdam
22. Takenaka T (1984) Grain orientation of bismuth layer structured ferroelectric ceramics and its application to piezoelectric and pyroelectric materials. Doctoral thesis, Kyoto University, Kyoto (in Japanese)
23. Takenaka T, Sakata K (1985) Piezoelectric properties of bismuth layer-structured ferroelectric $Na_{0.5}Bi_{4.5}Ti_4O_{15}$ ceramic. Jpn J Appl Phys 24(Suppl 24–2):730–732
24. Takenaka T, Sakata K (1985) Compositions and electrical properties of complex bismuth layer-structured ferroelectric ceramics. Jpn J Appl Phys 24(Suppl 24–3):117–119
25. Takenaka T, Sakata K (1988) Grain-oriented and Mn-doped $(NaBi)_{(1-x)/2}Ca_xBi_4Ti_4O_{15}$ ceramics for piezo- and pyrosensor materials. Sensors Mater 1:35–46
26. Takenaka T, Okuda T, Takegawara K (1997) Lead-free piezoelectric ceramics based on $(Bi_{1/2}Na_{1/2})TiO_3$-$NaNbO_3$. Ferroelectrics 196:175–178
27. Madelung O (ed) (1990) "Landolt-Bornstein", group III: crystal and solid state physics, vol 28. Springer, Berlin
28. Chu F, Damjanovic D, Steiner O, Setter N (1995) Piezoelectricity and phase transitions of the mixed-layer bismuth titanate niobate $Bi_7Ti_4NbO_{21}$. J Am Ceram Soc 78:3142–3144
29. Takenaka T, Otoh T, Mutoh S, Sasaki T (1996) Possibility of new bismuth layer-structured ferroelectrics $Na_{m-1.5}Bi_{2.5}Nb_mO_{3m+3}$ ($2<m<5$). Ferroelectrics 185:55–58
30. Jiménez B, Durán-Martín P, Castro A, Millán P (1996) Obtention and characterization of modified $Bi_2SrNb_2O_9$ Aurivillius-typeceramics. Ferroelectrics 186:93–96
31. Shulman HS, Testorf M, Damjanovic D, Setter N (1996) Microstructure, electrical conductivity, and piezoelectric properties of bismuth titanate. J Am Ceram Soc 79:3124–3128
32. Horn JA, Zhang SC, Selvaraj U, Messing GL, Trolier-McKinstry S, Yokoyama M (1996) Fabrication of textured $Bi_4Ti_3O_{12}$ by templated grain growth. Proceedings of the 10th IEEE international symposium on applications of ferroelectrics, pp 943–946
33. Takenaka T, Sasaki T (1997) New bismuth layer-structured ferroelectrics with niobium ions as B-site. Ferroelectrics 201:117–126
34. Komura K, Nagata H, Takenaka T (1998) Ferroelectric properties of bismuth layer-structured oxides. Ferroelectrics 218:233–240
35. Hayashi T, Sawayanagi S, Hara T, Takahashi H, Ueno S (1998) Influence of Bi excess and Sr deficient compositions on the microstructure and dielectric properties of $Sr_{1-x}Bi_{2+y}Ta_2O_9$ ferroelectric ceramics. J Korean Phys Soc 32:S1195–S1197
36. Thomazini D, Gelfuso MV, Eiras JA (1998) Synthesis, dielectric and ferroelectric characterization of bismuth titanate ceramics. J Korean Phys Soc 32:S1178–S1179
37. Durán-Martín P, Castro A, Millán P, Jiménez B (1998) Influence of Bi-site substitution on the ferroelectricity of the Aurivillius compound $Bi_2SrNb_2O_9$. J Mater Res 13:2565–2571
38. Ando A, Kimura M, Sakabe Y (1999) Energy trapping phenomenon of piezoelectric $SrBi_2Nb_2O_9$ ceramics. Proceedings of the 11th IEEE international symposium on applications of ferroelectrics, pp 303–306

39. Kimura M, Sawada T, Ando A, Sakabe Y (1999) Energy trapping characteristics of bismuth layer structured compound $CaBi_4Ti_4O_{15}$. Jpn J Appl Phys 38:5557–5560
40. Hirose M, Suzuki T, Oka H, Itakura K, Miyauchi Y, Tsukada T (1999) Piezoelectric properties of $SrBi_4Ti_4O_{15}$-based ceramics. Jpn J Appl Phys 38:5561–5563
41. Nakai Y, Fukuoka S (1999) Piezoelectric and mechanical properties of $BaBi_4Ti_4O_{15}$/$Ba_4Ti_{13}O_{30}$ ceramics. Jpn J Appl Phys 38:5568–5571
42. Voisard C, Damjanovic D, Setter N (1999) Electrical conductivity of strontium bismuth titanate under controlled oxygen partial pressure. J Eur Ceram Soc 19:1251–1254
43. Villegas M, Caballero AC, Moure C, Durán P, Fernández JF (1999) Factors affecting the electrical conductivity of donor-doped $Bi_4Ti_3O_{12}$ piezoelectric ceramics. J Am Ceram Soc 82:2411–2416
44. Ando A, Kimura M, Sakabe Y (1999) Crystalline structure and piezoelectric properties of Bi layer structured compound $SrBi_2Nb_2O_9$. In: Extended abstract of the 9th US-Japan seminar on dielectric and piezoelectric ceramics, pp 115–118
45. Jiménez B, Durán-Martín P, Jiménez-Rioboo R, Jiménez R (1999) Thermal behavior of the elastic (Young's) modulus in SBN-derived compounds ($Bi_2SrNb_2O_9$). J Eur Ceram Soc 19:1315–1319
46. Yan F, Wang Y, Liu J, Zhang Z, Chen X (1999) Mechanical relaxation in $SrBi_2Ta_2O_9$ ceramics. Appl Phys Lett 74:2794–2796
47. Jiménez B, Durán-Martín P, Jiménez-Rioboo R, Jiménez R (2000) On the existence of a second phase transition in ferroelectrics with Aurivillius-type structure through the study of the Young's modulus. J Phys Condens Matter 12:3883–3895
48. Jiménez B, Pardo L, Castro A, Millán P, Jiménez R, Elaatmani M, Oualla M (2000) Influence of the preparation on the microstructure and ferroelectricity of the $(SBN)_{1-x}(BTN)_x$ ceramics. Ferroelectrics 241:279–286
49. Nagata H, Takahashi T, Chikushi N, Takenaka T (2000) A series of bismuth layer-structured ferroelectrics. Ferroelectrics 241:309–316
50. Pardo L, Castro A, Millán P, Alemany C, Jiménez R, Jiménez B (2000) $(Bi_3TiNbO_9)_x$ $(SrBi_2Nb_2O_9)_{1-x}$ Aurivillius type structure piezoelectric ceramics obtained from mechanochemically activated oxides. Acta Mater 48:2421–2428
51. Shulman HS, Damjanovic D, Setter N (2000) Niobium doping and dielectric anomalies in bismuth titanate. J Am Ceram Soc 83:528–532
52. Sagalowicz L, Chu F, Durán-Martin P, Damjanovic D (2000) Microstructure, structural defects, and piezoelectric response of $Bi_4Ti_3O_{12}$ modified by Bi_3TiNbO_9. J Appl Phys 88:7258–7263
53. Yan H, Li C, Zhou J, Zhu W, He L, Song Y (2000) A-site (MCe) substitution effects on the structures and properties of $CaBi_4Ti_4O_{15}$ ceramics. Jpn J Appl Phys 39:6339–6342
54. Oka H, Hirose M, Tsukada T, Watanabe Y, Nomura T (2000) Thickness-shear vibration mode characteristics of $SrBi_4Ti_4O_{15}$-based ceramics. Jpn J Appl Phys 39:5613–5615
55. Ramulu NV, Prasad G, Suryanarayana SV, Sankaram TB (2000) Studies on electrical properties of $SrBi_4Ti_{4-3x}Fe_{4x}O_{15}$. Bull Mater Sci 23:431–437
56. Shimakawa Y, Imai H, Kimura H, Kimura S, Kubo Y, Nishibori E, Takata M, Sakata M, Kato K, Hiroi Z (2002) Orbital hybridization and covalency in paraelectric and ferroelectric $SrBi_2Nb_2O_9$. Phys Rev B66:144110
57. Nagata H, Takahashi T, Yano Y, Takenaka T (2001) Electrical properties of bismuth layer-structured ferroelectrics. Ferroelectrics 261:219–224
58. Makovec D, Pribošic I, Samardžija Z, Drofeniki M (2001) Incorporation of aliovalent dopants into the bismuth-layered Perovskite-like structure of $BaBi_4Ti_4O_{15}$. J Am Ceram Soc 84:2702–2704
59. Yan H, Li C, Zhou J, Zhu W, He L, Song Y, Yu Y (2001) Effects of A-site (NaCe) substitution with Na-deficiency on structures and properties of $CaBi_4Ti_4O_{15}$-based high-Curie-temperature ceramics. Jpn J Appl Phys 40:6501–6505
60. Noguchi Y, Miyayama M (2001) Large remanent polarization of vanadium-doped $Bi_4Ti_3O_{12}$. Appl Phys Lett 78:1903–1905

61. Moure A, Pardo L, Alemany C, Millán P, Castro A (2001) Piezoelectric ceramics based on Bi_3TiNbO_9 from mechanochemically activated precursors. J Eur Ceram Soc 21:1399–1402
62. Ricote J, Pardo L, Moure A, Castro A, Millán P, Chateigner D (2001) Microcharacterisation of grain-oriented ceramics based on Bi_3TiNbO_9 obtained from mechanochemically activated precursors. J Eur Ceram Soc 21:1403–1407
63. Ogawa H, Kimura M, Ando A, Sakabe Y (2001) Temperature dependence of piezoelectric properties of grain-oriented $CaBi_4Ti_4O_{15}$ ceramics. Jpn J Appl Phys 40:5715–5718
64. Nanao M, Hirose M, Tsukada T (2001) Piezoelectric properties of Bi_3TiNbO_9-$BaBi_2Nb_2O_9$ ceramics. Jpn J Appl Phys 40:5727–5730
65. Shibata K, Shoji K, Sakata K (2001) $Sr_{1-x}Ca_xBi_2Ta_2O_9$ piezoelectric ceramics with high mechanical quality factor. Jpn J Appl Phys 40:5719–5721
66. Noguchi Y, Shimizu H, Miyayama M, Oikawa K, Kamiyama T (2001) Ferroelectric properties and structure distortion in A-site-modified $SrBi_2Ta_2O_9$. Jpn J Appl Phys 40:5812–5815
67. Kholkin AL, Avdeev M, Costa MEV, Baptista JL (2001) Ba-based layered ferroelectric relaxors. Integr Ferroelectr 37:305–313
68. Kholkin AL, Avdeev M, Costa MEV, Baptista JL (2001) Dielectric relaxation in Ba-based layered perovskites. Appl Phys Lett 79:662–664
69. Miranda C, Costa MEV, Avdeev M, Kholkin AL, Baptista JL (2001) Relaxor properties of Ba-based layered perovskites. J Eur Ceram Soc 21:1303–1306
70. Noguchi Y, Miyayama M, Kudo T (2001) Direct evidence of A-site-deficient strontium bismuth tantalate and its enhanced ferroelectric properties. Phys Rev B 63:214102
71. Wu Y, Nguyen C, Seraji S, Forbess MJ, Limmer SJ, Chou T, Cao G (2001) Processing and properties of strontium bismuth vanadate niobate ferroelectric ceramics. J Am Ceram Soc 84:2882–2888
72. Ando A, Kimura M, Sawada T, Hayashi K, Sakabe Y (2002) Piezoelectric and ferroelectric properties of the modified $SrBi_2Nb_2O_9$ ceramics. Ferroelectrics 268:65–70
73. Ando A, Sawada T, Ogawa H, Kimura M, Sakabe Y (2002) Fine-tolerance resonator applications of bismuth-layer-structured ferroelectric ceramics. Jpn J Appl Phys 41:7057–7061
74. Noguchi Y, Miyayama M, Oikawa K, Kamiyama T, Osada M, Kakihana M (2002) Defect engineering for control of polarization properties in $SrBi_2Ta_2O_9$. Jpn J Appl Phys 41:7062–7075
75. Noguchi Y, Shimizu H, Miyayama M (2002) Lattice distortion and ferroelectric properties in Pb-substituted $SrBi_2Ta_2O_9$. J Ceram Soc Japan 110:999–1024
76. Komagata K, Takeda H, Shiosaki T (2002) Synthesis and ferroelectric properties of $M_{0.5}Bi_{2.5}Ta_2O_9$(M=Na, K) ceramics. J Ceram Soc Jpn 110:255–258
77. Shimakawa Y, Imai H, Kimura H, Kimura S, Kubo Y, Nishibori E, Takata M, Sakata M, Kato K, Hiroi Z (2002) Orbital hybridization and covalency in paraelectric and ferroelectric $SrBi_2Nb_2O_9$. Phys Rev B66:144110
78. Sugaya Y, Kishi Y, Koike Y, Shoji K, Sakata K (2002) $(Sr_{0.2}Ca_{0.8})Bi_2Ta_2O_9$-based piezoelectric ceramics substituted by neodymium with high mechanical quality factor. J Ceram Soc Jpn 110:1032–1034 (in Japanese)
79. Ando A (2003) Doctoral thesis, Tokyo Institute of Technology, Tokyo
80. Sanson A, Whatmore RW (2002) Properties of $Bi_4Ti_3O_{12}$-$(Na_{1/2}Bi_{1/2})TiO_3$ piezoelectric ceramics. Jpn J Appl Phys 41:7127–7130
81. Yokosuka M (2002) Dielectric and piezoelectric properties of Mn-modified $Bi_4CaTi_4O_{15}$ based ceramics. Jpn J Appl Phys 41:7123–7126
82. Zhao M, Wang C, Zhong W, Wang J, Chen H (2002) Ferroelectric, piezoelectric and pyroelectric properties of $Sr_{1+x}Bi_{4-x}Ti_{4-x}Ta_xO_{15}$ ceramics (x=0–1). Jpn J Appl Phys 41:1455–1458
83. Nagata H, Takenaka T (2002) Piezoelectric properties of bismuth layer-structured ferroelectric ceramics with Sr-Bi-Ti-Ta system. Ferroelectrics 273:359–364
84. Ando A, Kimura M, Sakabe Y (2003) Piezoelectric resonance characteristics of $SrBi_2Nb_2O_9$-based ceramics. Jpn J Appl Phys 42:150–156
85. Ando A, Kimura M, Sakabe Y (2003) Piezoelectric properties of Ba and Ca doped $SrBi_2Nb_2O_9$ based ceramic materials. Jpn J Appl Phys 42:520–525

86. Sawada T, Ando A, Sakabe Y, Damjanovic D, Setter N (2003) Properties of the elastic anomaly in $SrBi_2Nb_2O_9$-based ceramics. Jpn J Appl Phys 42:6094–6098
87. Nagata H, Itagaki M, Takenaka T (2003) Piezoelectric properties of bismuth layer-structured ferroelectric $SrBi_2Ta_2O_9$-Bi_3TiTaO_9 ceramics. Ferroelectrics 286:85–92
88. Suzuki M, Nagata H, Ohara J, Funakubo H, Takenaka T (2003) $Bi_{3-x}M_xTiTaO_9$ (M = La or Nd) ceramics with high mechanical quality factor Q_m. Jpn J Appl Phys 42:6090–6093
89. Ando A, Kimura M, Minamikawa T, Sakabe Y (2005) Layered piezoelectric ceramics for fine-tolerance resonator applications. Int J Appl Ceram Technol 2:33–44
90. Horiuchi S, Nagata H, Takenaka T (2005) Piezoelectric properties of $Sr_2Bi_4Ti_5O_{18}$-$Ca_2Bi_4Ti_5O_{18}$ solid solution ceramics. Ferroelectrics 324:3–9
91. Ogawa H, Sawada T, Kimura M, Shiratsuyu K, Wada N, Ando A, Tamura H, Sakabe Y (2005) Piezoelectric properties of $SrBi_2Nb_2O_9$ textured ceramics. Jpn J Appl Phys 44:7050–7054
92. Aoyagi R, Inai S, Hiruma Y, Takenaka T (2005) Piezoelectric properties of vanadium-substituted strontium bismuth niobate. Jpn J Appl Phys 44:7055–7058
93. Miyayama M, Noguchi Y (2005) Polarization properties and oxygen-vacancy distribution of $SrBi_2Ta_2O_9$ ceramics modified by Ce and Pr. J Eur Ceram Soc 25:2477–2482
94. Moure A, Pardo L (2005) Microstructure and texture dependence of the dielectric anomalies and D.C. conductivity of Bi_3TiNbO_9 ferroelectric ceramics. J Appl Phys 97:084103
95. Aoyagi R, Inai S, Hiruma Y, Takenaka T (2006) Piezoelectric properties of $SrBi_2M_{2-x}V_xO_9$ (M = Nb and Ta) ceramics. J Electroceram 17:1087–1090
96. Zhang S, Kim N, Shrout TR, Kimura M, Ando A (2006) High temperature properties of manganese modified $CaBi_4Ti_4O_{15}$ ferroelectric ceramics. Solid State Commun 140:154–158
97. Sawada T, Ogawa H, Kimura M, Shiratsuyu K, Ando A (2006) Piezoelectric properties in textured ceramics of $SrBi_2Nb_2O_9$. Key Eng Mater 320:15–18
98. Zheng L, Li G, Yin Q, Kwok KW (2006) Phase transition and failure at high temperature of bismuth-layered piezoelectric ceramics. J Am Ceram Soc 89:1317–1320
99. Inai S, Sato J, Aoyagi R, Hiruma Y, Suzuki M, Nagata H, Takenaka T (2007) Piezoelectric properties of V and Ba substituted $SrBi_2Nb_2O_9$ ceramics. Ferroelectrics 358:148–152
100. Suzuki M, Inai S, Tokutsu T, Nagata H, Takenaka T (2007) Ferroelectric property of Bi_3TiTaO_9 based ceramics with Nd substitution. Ferroelectrics 356:62–66
101. Takenaka T, Shoji K, Takai H, Sakata K (1976) Ferroelectric and dielectric properties of press forged $Bi_4Ti_3O_{12}$ ceramics. In: Proceedings of the19th Japan congress on materials research. The Society of Materials Science, Kyoto, pp 230–233
102. Tani T (1998) Crystalline-oriented piezoelectric bulk ceramics with a perovskite-type structure. J Korean Phys Soc 32:S1217–S1220
103. Watanabe H, Kimura T, Yamaguchi T (1989) Particle orientation during tape casting in the fabrication of grain-oriented bismuth titanate. J Am Ceram Soc 72:289–293
104. Takeuchi T, Tani T, Saito Y (1999) Piezoelectric properties of bismuth layer-structured ferroelectric ceramics with a preferred orientation processed by the reactive templated grain growth method. Jpn J Appl Phys 38:5553–5556
105. Takenaka T, Sakata K (1989) Preparations and properties of grain-oriented ceramics and their applications to electronic materials. Ceram Jpn 24:965–974 (in Japanese)
106. Kimura M, Ogawa H, Sawada T, Shiratsuyu K, Wada N, Ando A (2008) Piezoelectric properties in textured ceramics of bismuth layer-structured ferroelectrics. J Electroceram 21:55–60
107. Lotgering FK (1959) Topotactical reactions with ferrimagnetic oxides having hexagonal crystal structures—I. J Inorg Nucl Chem 9:113–123
108. Kimura M, Ogawa H, Kuroda D, Sawada T, Higuchi Y, Takagi H, Sakabe Y (2007) Temperature dependence of piezoelectric properties for textured SBN ceramics. IEEE Trans Ultrason Ferroelectr Freq Control 54:2482–2486
109. Wersing W (2002) Applications of piezoelectric materials: an introductory review. In: Setter N (ed) Piezoelectric materials in devices. EPFL, Lausanne, pp 29–82
110. Takahashi S, Hirose S (1992) Vibration-level characteristics of lead-zirconate-titanate ceramics. Jpn J Appl Phys 31:3055–3057

111. Kawada S, Ogawa H, Kimura M, Higuch Y, Takagi H (2007) High-power characteristics of textured bismuth layer structured ferroelectric ceramics. Extended abstract of the 13th US-Japan seminar on dielectric and piezoelectric ceramics, pp 204–207
112. Kawada S, Ogawa H, Kimura M, Shiratsuyu K, Niimi H (2006) High-power piezoelectric vibration characteristics of textured $SrBi_2Nb_2O_9$ ceramics. Jpn J Appl Phys 45:7455–7459
113. Kawada S, Ogawa H, Kimura M, Shiratsuyu K, Niimi H (2007) Texture fraction dependences of high-power characteristics for textured $SrBi_2Nb_2O_9$ ceramics. Ferroelectrics 356:175–179
114. Ogawa H, Kawada S, Kimura M, Shiratsuyu K, Sakabe Y (2007) High-power piezoelectric characteristics of textured bismuth layer structured ferroelectric ceramics. IEEE Trans Ultrason Ferroelectr Freq Control 54:2500–2504
115. Cummins SE, Cross LE (1967) Crystal symmetry, optical properties, and ferroelectric polarization of $Bi_4Ti_3O_{12}$ single crystals. Appl Phys Lett 10:14–15
116. Newnham RE (1975) Ferroelectrics and other ferroic materials: structure-property relations, chapter IV-4. Springer, New York, pp 86–89
117. Ogawa H, Kawada S, Kimura M, Higuchi Y, Takagi H (2009) High-power characteristics of thickness shear mode for textured $SrBi_2Nb_2O_9$ ceramics. Jpn J Appl Phys 48:09KD05
118. Li E, Kakemoto H, Hoshina T, Tsurumi T (2008) A shear-mode ultrasonic motor using potassium sodium niobate-based ceramics with high mechanical quality factor. Jpn J Appl Phys 47:7702–7706

Chapter 14
Defect Control and Properties in Bismuth Layer Structured Ferroelectric Single Crystals

Yuji Noguchi and Masaru Miyayama

14.1 Introduction

The static and dynamic behaviors of ferroelectric domains are the underlying basis of various functional properties of ferroelectric materials, such as dielectricity, piezoelectricity, ferroelectricity, and electro-optic and acoustic-optic effects. Since the performance of ferroelectric devices is governed by these behaviors, various techniques for enhancing device performance have been widely investigated with the aim of controlling ferroelectric domains [19, 20, 88, 109]. Such control, however, is often prevented not only by a large leakage current but also by undesirable behaviors such as domain clamping [16, 73, 95], fatigue [17, 98], aging [63, 68], imprinting [110], and depoling [98]. Ferroelectric devices thus suffer from degraded polarization and poor reliability due to insufficient control over ferroelectric domains. It is considered that the poor polarization properties, fatigue, and aging, etc. are governed by the interaction between defects and ferroelectric domains.

Bismuth layer-structured ferroelectrics (BLSFs) have attracted much attention because of their high Curie temperature (T_C) and larger spontaneous polarization (P_s). The relation between crystal structure and ferroelectric properties of BLSFs has been widely investigated because of their anisotropy of ferroelectric polarization [10, 22, 113]. In the crystal structure of BLSFs, perovskite layers ($A_{m-1}B_mO_{3m+1}$) are sandwiched between Bi_2O_2 layers, where m is the number of BO_6 octahedral layers with A-site cations in the perovskite layers, as shown in Fig. 14.1. In general, the A site is occupied by relatively large and lower-valent cations such as Na^+, K^+, Ca^{2+}, Sr^{2+}, Ba^{2+}, Pb^{2+}, Bi^{3+}, and RE^{3+} (RE = rare earth elements), while the B site is positioned by relatively small and higher-valent cations such as W^{6+}, Ta^{5+}, Nb^{5+}, Ti^{4+}, Fe^{3+},

Y. Noguchi (✉) • M. Miyayama
Research Center for Advanced Science and Technology, University of Tokyo, 4-6-1 Komaba, Meguro-ku, Tokyo 153-8904, Japan
e-mail: ynoguchi@crm.rcast.u-tokyo.ac.jp

S. Priya and S. Nahm (eds.), *Lead-Free Piezoelectrics*,
DOI 10.1007/978-1-4419-9598-8_14, © Springer Science+Business Media, LLC 2012

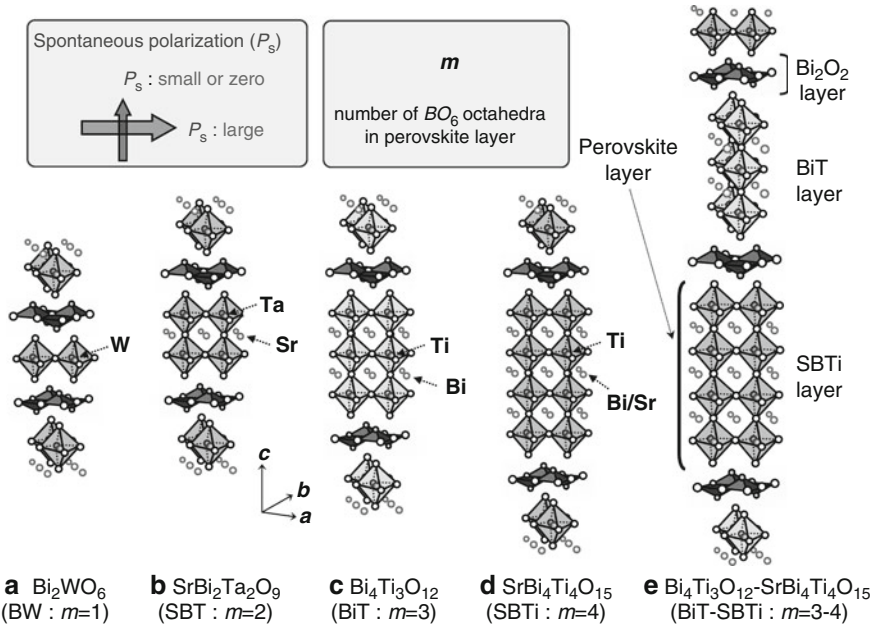

Fig. 14.1 Schematic crystal structures of bismuth layer-structured ferroelectrics. The crystals are composed of perovskite layers and Bi_2O_2 layers. The number of BO_6 octahedra in the perovskite layers along the c axis is denoted as m

etc. Representative BLSFs are as follows: Bi_2WO_6 ($m = 1$), (Ca, Sr, Ba, Pb)Bi_2(Ta, Nb)$_2O_9$ ($m = 2$), Bi_3(Ti,Nb)$_2O_9$ ($m = 2$), $Bi_4Ti_3O_{12}$ ($m = 3$), (Bi, RE)$_4Ti_3O_{12}$ ($m = 3$), (Ca, Sr, Ba, Pb)$Bi_4Ti_4O_{15}$ ($m = 4$), (Na, K)$_{0.5}Bi_{4.5}Ti_4O_{15}$ ($m = 4$), and (Ca, Sr, Ba, Pb)$_2Bi_4Ti_5O_{18}$ ($m = 5$), etc.

There are several kinds of modes of cooperative ionic displacements originating from ferroelectric polarization [113]. In particular, relative displacements of the whole of perovskite layers with respect to Bi_2O_2 layers, i.e., $F2mm$ mode, result in a large P_s along the a axis. Although large ionic displacements are also found along the b axis, the dipole moments of the constituent ions are canceled by each other due to the presence of glide plane normal to the b axis. As a result, major ferroelectric polarization appears along the a axis. P_s along the a axis is large, while P_s along the c axis is small or zero, which is determined by whether m is odd (small P_s) or even ($P_s = 0$). For example, in the case of $Bi_4Ti_3O_{12}$ ($m = 3$), the value of P_s along the a axis is 50 μC/cm^2, whereas that along the c axis is as small as 4 μC/cm^2 [10, 34].

Recently, intergrowth BLSFs, discovered by Kikuchi and coworkers [52, 53], have received a renewed interest as a candidate for ferroelectric materials with a relatively large remanent polarization (P_r) [79]. For intergrowth $Bi_4Ti_3O_{12}$-$SrBi_4Ti_4O_{15}$, two kinds of perovskite layers of $Bi_4Ti_3O_{12}$ ($m = 3$) and $SrBi_4Ti_4O_{15}$ ($m = 4$) are in turn sandwiched between Bi_2O_2 layers (see Fig. 14.1e). A lattice mismatch between the two

blocks and their different chemical character induce the large lattice distortion in Bi_2O_2 layers, leading to a quite distinct type of ionic displacement of Bi in Bi_2O_2 layers along the *a* axis [79]. This Bi displacement is suggested to contribute partly to a larger P_r observed for $Bi_4Ti_3O_{12}$-$SrBi_4Ti_4O_{15}$ ceramics compared with constituent ceramics of $Bi_4Ti_3O_{12}$ or $SrBi_4Ti_4O_{15}$ [79].

In this chapter, the effects of defect control on the polarization and leakage-current properties of BLSF single crystals, especially of Bi_2WO_6 ($m = 1$), $SrBi_2Ta_2O_9$ ($m = 2$), and $Bi_4Ti_3O_{12}$ ($m = 3$). Here, the material properties along the *a* axis (the major polarization component) are focused.

14.2 $m = 1$: Bi_2WO_6-Based Single Crystals

Bi_2WO_6 (BW) has been regarded as a potential candidate for ferroelectric and piezoelectric materials because of its high Curie temperature of 940°C and high electromechanical coupling coefficient [26, 38, 72, 118]. Especially, BW has the largest P_s estimated from the structural data based on ionic model among BLSFs [90, 113]. Thin films [26, 38] and crystals [108] of BW, however, suffer from a high leakage current, and polarization switching had not yet been achieved in the BW system.

Here, the leakage current mechanism of BW single crystals along the *a* axis (polarization direction) is discussed to establish the guiding principle of defect control for polarization switching in the BW system. It is shown that Mn substitution and subsequent annealing in air is effective for suppressing leakage current of BW crystals. Polarization switching with a remanent polarization (P_r) of 50 μC/cm^2 is achieved for Mn-doped crystals.

14.2.1 Crystal Growth and Measurements

Single crystals of BW were grown by a flux method in air. Details as described elsewhere [13, 82]. Single crystals of Mn-doped BW (Mn-BW) were also grown. Optical microscope observations confirmed that the crystals without twin boundaries such as 90° domain walls were obtained, because the soaking temperature was set below the Curie point (940°C) [13, 72, 108, 118]. Inductively coupled plasma (ICP) emission spectroscopy analysis showed the composition of Mn-BW crystals was $Bi_2W_{0.98}Mn_{0.02}O_x$ (2 mol%-Mn substitution at the W site). The crystals were annealed at 900°C for 10 h in air. Some of the crystals were annealed at 750°C for 10 h at a high oxygen pressure (Po_2) of 35 MPa to reduce the number of oxygen vacancies. Impedance spectroscopy was applied to estimate electrical conductivity (σ), as described in ref. [104].

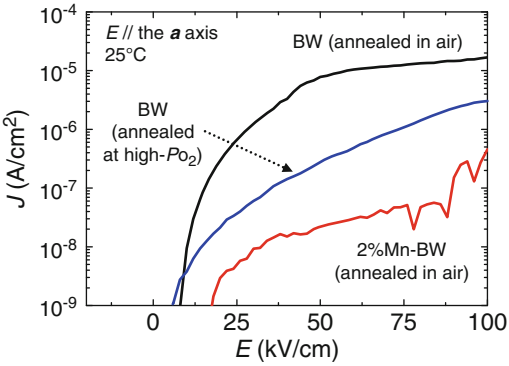

Fig. 14.2 Leakage current density (J) as a function of electric field (E) applied along the a axis at 25°C for Bi_2WO_6-based crystals

14.2.2 Defect Control and Properties

Figure 14.2 indicates the leakage current density (J) along the a axis at 25°C as a function of electric field. BW crystals annealed in air exhibited a high J of the order of 10^{-5} A/cm^2 over 50 kV/cm. High-Po_2 annealing reduced J by about one order of magnitude for BW crystals. The decrease in J by the oxygen annealing is attributed to the following oxidation reaction:

$$\frac{1}{2}O_2 + V_O^{\bullet\bullet} + 2e' \rightarrow O_O^{\times}, \tag{14.1}$$

where $V_O^{\bullet\bullet}$ denotes oxygen vacancy with two positive charges and $O_O^{\times}$ is oxide ion at the oxygen site. This experimental fact leads to the conclusion that the leakage current properties of BW along the a axis is governed by electron (e') conduction (n-type conduction), which is a marked contrast with the leakage current mechanism observed for $Bi_4Ti_3O_{12}$ crystals along the a axis [76, 83]. It is interesting to note that Mn-BW annealed in air had a lower J of the order of 10^{-8} A/cm^2. Mn substitution is found to be effective for suppressing J in the BW system.

Figure 14.3 shows the polarization hysteresis loops measured along the a axis. Polarization hysteresis could not be obtained for BW crystals annealed in air due to their high J, while BW crystals annealed under high-Po_2 atmosphere gave an apparent polarization hysteresis (Fig. 14.3a). Note that Mn-BW crystals annealed in air exhibited a well-saturated hysteresis loop with a remanent polarization (P_r) of 50 μC/cm^2 and a coercive field (E_c) of 65 kV/cm. The polarization switching was achieved only after J was reduced to a sufficiently low value of the order of 10^{-8} A/cm^2 by Mn substitution.

Figure 14.4 shows the σ along the a axis as a function of oxygen partial pressure (Po_2) at 500 and 600°C. The σ of BW and Mn-BW was independent of Po_2 from 400 to 800°C. These results reveal that in-plane electrical conduction at high temperatures in the BW system is governed by oxide-ion conduction through $V_O^{\bullet\bullet}$ [13, 104, 118], as observed also for paraelectric $Bi_4Ti_3O_{12}$ along the a axis [4, 39]. Mn-BW exhibited

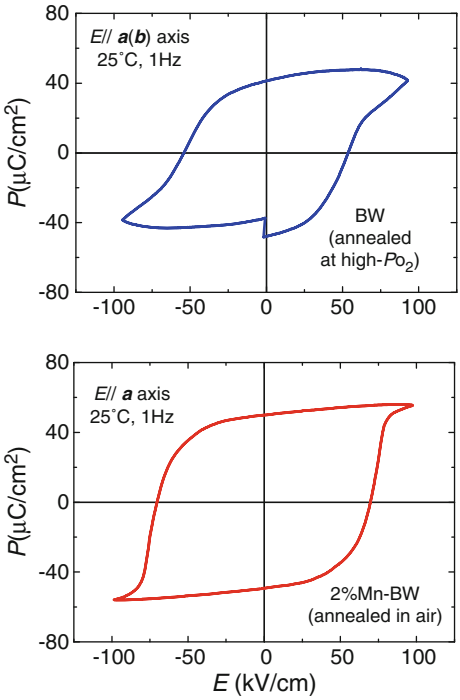

Fig. 14.3 Polarization hysteresis loops along the *a* axis measured at 25°C for Bi_2WO_6-based crystals

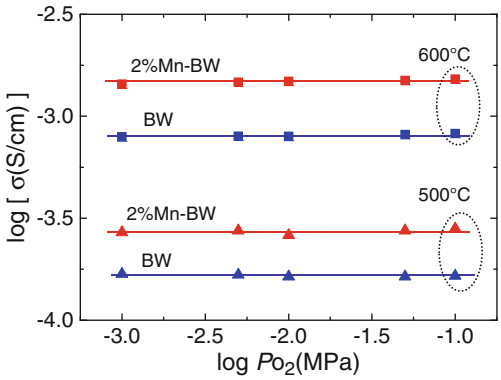

Fig. 14.4 Conductivity (σ) at 500 and 600°C estimated by ac impedance spectroscopy as a function of oxygen partial pressure (Po_2) for Bi_2WO_6-based crystals. The data measured at 400, 700, and 800°C are not shown. Po_2-independent σ shows that σ is attributed to oxide-ion conduction

a higher σ by about half orders of magnitude than BW. It has been reported that Mn occupies the *B* site in perovskite oxides [41, 119]. The higher oxide-ion conductivity for Mn-BW is direct evidence that Mn substitution at the W^{6+} site leads to an increase in $V_O^{\bullet\bullet}$, which is a result of the charge compensation as described below. The activation energy of oxide-ion conduction along the *a* axis was estimated to be 0.43 eV for BW, which is in good agreement with those for $Bi_2Co_{0.1}V_{0.9}O_x$ [61] and $Bi_4Ti_3O_{12}$ [104].

Here, the leakage current mechanism at room temperature in BW crystals is discussed. High-temperature impedance spectroscopy shows that a considerable

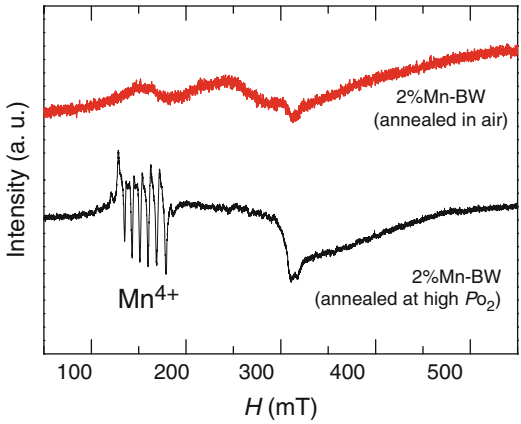

Fig. 14.5 Electron spin resonance spectra of the crushed powder of 2% Mn-Bi_2WO_6 crystals annealed in air (900°C) and at an high Po_2 of 35 MPa (750°C)

concentration of $V_O^{\bullet\bullet}$ is present in the crystals. It is assumed that the formation of Bi vacancies (V'''_{Bi}) during crystal growth is the trigger for generating $V_O^{\bullet\bullet}$, as has been reported for $Bi_4Ti_3O_{12}$ [76]. Taking these vacancies into account, the composition of BW can be rewritten as $Bi_{2-x}WO_{6-y}$. At high temperatures, the relation of $3x = 2y$ is maintained in the crystals, i.e., the charge neutrality is satisfied through the ionic defects of V'''_{Bi} and $V_O^{\bullet\bullet}$. As a result, oxide-ion conduction is dominant at high temperatures in the BW system. In contrast, the leakage current measurements at 25°C indicate that the charge carrier in BW crystals is electron. This *n*-type conduction is explained by the following defect condition: $3x < 2y$. Excess $V_O^{\bullet\bullet}$ ($2y$) compared with V'''_{Bi} ($3x$) acts as electron donor for leakage current, as expressed by $V_O^{\times} \rightarrow V_O^{\bullet\bullet} + 2e'$, where $V_O^{\times}$ denotes neutral oxygen vacancy. The decrease in J by high-Po_2 annealing is understood by the decrease in electron concentration n (see (14.1)).

The influences of Mn substitution on the defect structures and leakage-current properties at room temperature are considered. Electron spin resonance (ESR) investigations were performed for crushed powders of Mn-BW crystals to clarify the valence state of Mn. Figure 14.5 shows the X-band ESR spectra observed at −160°C. Mn-BW crystals annealed in air did not show any detectable signal, while the crystals annealed under high-Po_2 atmosphere indicated the hyperfine structure with prominent lines of isolated Mn^{4+} [27]. The hyperfine structure associated with Mn^{2+} was not observed for Mn-BW. Our ESR investigations reveal that Mn in BW crystals annealed in air is present mainly as Mn^{3+} (Mn^{3+} is silent in X-band ESR).

High-temperature impedance analysis shows that the substitution of Mn leads to an increase in $V_O^{\bullet\bullet}$. It is reasonable to consider that, at high temperatures, Mn is substituted at the W^{6+} site as Mn^{3+} (Mn'''_W) accompanied by the formation of $V_O^{\bullet\bullet}$ as expressed by

$$Mn_2O_3 \xrightarrow{(2WO_3)} 2Mn'''_W + 3O_O^{\times} + 3V_O^{\bullet\bullet}. \tag{14.2}$$

At high temperatures, the occupation of Mn^{3+} at the W^{6+} site (Mn'''_W) is electrically compensated by the formation of $V_O^{\bullet\bullet}$. During annealing, crystals absorb

oxygen into the lattice, and the oxide ion occupies $V_O^{\bullet\bullet}$ with a decrease in carrier (e') concentration n. The decrease in J by Mn substitution is explained by the following equation:

$$\frac{3}{2}O_2 + Mn_2O_3 + 6e' \xrightarrow{(2WO_3)} 2Mn'''_W + 6O_O^{\times}. \tag{14.3}$$

Mn^{3+} acts as an effective acceptor for trapping electron (carrier) and then for suppressing J. Thus, the influences of Mn are classified into two kinds of defect control; one is higher $[V_O^{\bullet\bullet}]$ (14.2) and the other is lower n (14.3). Mn-BW exhibited an E_c of 65 kV/cm, and this value was comparable to that of BW (50 kV/cm). Mn-BW is suggested to have a high $[V_O^{\bullet\bullet}]$ compared with BW also at room temperature, whereas the well-saturated hysteresis loop was obtained only for Mn-BW. This experimental fact indicates that $V_O^{\bullet\bullet}$ present in Mn-BW crystals does not deteriorate polarization-switching property. The first influence of defect change, i.e., the increase in $[V_O^{\bullet\bullet}]$, plays a minor role in polarization switching. It seems valid that the low J for Mn-BW results from a reduced n. A sufficiently low J enables us to obtain a larger P_r for Mn-BW. The second effect of defect control, i.e., the decrease in n, is dominant for the polarization properties in the BW system.

14.2.3 Summary

It is shown that electron originating from oxygen vacancies act as detrimental carrier of leakage current of BW crystals. The substitution of Mn is demonstrated to be effective for enhancing polarization switching as well as reducing leakage current in the BW system.

14.3 $m = 2$: $SrBi_2Ta_2O_9$-Based Single Crystals

Since thin films of BLSFs have been reported to have higher durability against repeated switching of its bistable polarization states [89], $SrBi_2Ta_2O_9$ (SBT) and lanthanum-substituted $Bi_4Ti_3O_{12}$ (BLT) [87] have emerged as proficient candidates for nonvolatile memory materials. Ferroelectric SBT has advantages of a lower switching field and a lower leakage current in the form of ultrathin films [24, 51, 67]. However, the integration of SBT films into high-density memories is confronted with some problems, one being that the capacitors constructed to data suffer from low remanent polarization (P_r). Thin films [49, 71, 89] and ceramics [80] of SBT with near-stoichiometric composition showed a P_r value of 6–8 μC/cm^2. Strenuous efforts have been made to improve the P_r value of SBT; these include $SrBi_2Nb_2O_9$ and its solid solutions with SBT (P_r of 7–10 μC/cm^2) [14, 111], composition-modified SBT (P_r of 10–12 μC/cm^2) [2, 75], Ca-substituted SBT (P_r of 12 μC/cm^2) [11], *a*-axis

oriented SBT (P_r of 15 μC/cm^2) [33], and epitaxially grown films (P_r of 12 μC/cm^2) [37]. Although extensive research on the development of SBT had been conducted mainly on these types of thin films, much reliable experimental data related to spontaneous polarization (P_s) have not still been reported because of the lack of single crystals. Therefore, the investigation using single crystals was critically important for the device applications as well as for the material design for property improvement. Here, an enhancement of P_s by defect-related modification through the investigation using SBT single crystals is shown. It is demonstrated that the heterovalent substitution of Bi^{3+} with Sr vacancies at the perovskite *A* site is effective for enhancing P_s without increasing coercive field (E_c).

14.3.1 Structural Analysis, Electronic Structure Calculations, Crystal Growth

Powders of $SrBi_2Ta_2O_9$ and $Sr_{0.80}Bi_{2.14}Ta_2O_9$ were prepared by using a solid-state reaction from the ground powders of $SrCO_3$, Bi_2O_3, and Ta_2O_5 of 99.99% purity. The mixed powder was calcined at 1,100°C for 4 h, several times with intermediate grinding. The crystal structures of the powders of $SrBi_2Ta_2O_9$ and $Sr_{0.80}Bi_{2.14}Ta_2O_9$ were analyzed by the Rietveld analysis of high-resolution synchrotron-radiation X-ray diffraction [80] as well as neutron diffraction [81]. The synchrotron-radiation powder data were recorded at BL-4B2 at KEK, and analyzed by the program RIETAN-2000 [43]. The powder data of time-of-flight neutron diffraction were collected using the Vega diffractometer at KENS [47], and structural parameters were refined using the program RIETAN-2001T [84]. These analyses confirmed the presence of Sr vacancies at the *A* site, and indicated that the charge neutrality is satisfied through the substitution of Bi^{3+} at the A^{2+} site with the formation of Sr vacancies [80, 81, 99]. Thus, the composition of non-stoichiometric SBT is expressed as $ABi_2Ta_2O_9$ ($A = Sr_{1-x}Bi_{2x/3}\square_{x/3}$), where □ denotes Sr vacancies.

An electron charge-density study was performed on the basis of the maximum entropy method (MEM) [107]. The synchrotron-radiation data were analyzed by the MEM-based pattern fitting by the RIETAN-2000. The details of the analysis are described elsewhere [42]. Furthermore, the electronic structure of SBT by electronic band-structure calculations was studied. The calculations were performed within density functional theory (DFT) via the generalized gradient approximation [64] using a plane wave basis set. The projector-augmented wave (PAW) method [5] was applied to construct all-electron valence wave functions from non-norm-conserving pseudo wave functions and atomic functions using the Vienna Ab initio Simulation Package (VASP) [60]. The cutoff energy of 400 eV and *k*-point sampling grid of $7 \times 7 \times 3$ were used. $SrBi_2Ta_2O_9$ is known to show a series of phase transitions: a high-temperature tetragonal phase (*I*4/*mmm*), an intermediate orthorhombic phase with paraelectric *Amam* symmetry, and a low-temperature orthorhombic one with a

ferroelectric $A2_1am$ structure. Onodera et al. [85] have clarified these successive phase transitions in SBT by performing single-crystal structure analysis.

Single crystals of SBT with near-stoichiometric composition (hereafter referred to as SBT crystals) were grown in air by a flux method similar to the one reported by Sih et al. [101]. Bi_2O_3 and B_2O_3 were used as flux for the crystal growth. The mixed powder with the composition (Bi_2O_3: B_2O_3: $SrBi_2Ta_2O_9$ = 65:5:30 wt.%) was put into a Pt crucible, and was heated at 1,100°C for 5 h. After soaking at 1,375°C for 10 h, the materials were slowly cooled to 1,300°C at a rate of 1°C/h. This crystal-growth procedure resulted in plate crystals with a maximum size of $10 \times 10 \times 0.2\ mm^3$, and the major surface was normal to the *c* axis. The remaining flux on the crystals was removed by washing them in hot nitric acid. Annealing of the crystals was performed in air to eliminate mechanical and thermal stress induced during the process of crystal growth. The composition of the crystals determined by ICP spectrometry was $Sr_{0.99(2)}Bi_{2.01(2)}Ta_2O_9$, where the value in the parenthesis denotes the standard deviation.

For the crystal growth of SBT with Sr vacancies, special attention to starting SBT powder and to soaking temperature was paid. The weight ratio of $Sr_{0.80}Bi_{2.14}Ta_2O_9$ powder and flux was fixed at the above ratio for the crystal growth. The crystals of near-stoichiometric SBT were obtained when the mixed powder was soaked at a temperature above 1,350°C. Thus, the mixed powder was soaked at 1,300°C for 50 h, and then slowly cooled to 1,250°C at a rate of 0.25°C/h. The ICP measurements showed that the composition of the crystals was $Sr_{0.81(2)}Bi_{2.13(2)}Ta_2O_9$, and approximately 6% vacancies were induced at the *A* site in this growth condition. Here, the crystals with Sr vacancies are defined as defect-engineered SBT.

14.3.2 Domain Structure and Properties

Figure 14.6a shows the domain structure of a SBT crystal observed by optical microscope. The piezoelectric-force microscopy (PFM) study was also conducted to elucidate the direction of P_s. The details of the PFM measurements are described in ref. [103]. As illustrated in the PFM image (Fig. 14.6b), a 90° rotation of P_s across domain walls was clearly identified in the *a–b* plane. A nearly similar domain structure was observed also for defect-engineered crystals, and there were almost no differences in domain width, etc.

Polarization (*P*)-electric field (*E*) hysteresis loops were measured at a frequency of 3 Hz using the virtual ground mode, as shown in Fig. 14.7. The rectangular and well-saturated hysteresis loops were observed. For the SBT crystals, the P_s and E_c values were 19 $\mu C/cm^2$ and 20 kV/cm, respectively. This P_s value is 300% of P_r reported for thin films [2, 89] and dense ceramics [81]. Note that the P_s value for defect-engineered crystals could be enhanced to 29 $\mu C/cm^2$. The value of E_c was 20 kV/cm, which was the same as that of the SBT crystals.

To better understand the notable enhancement of P_s by the Bi substitution with Sr vacancies, the displacements of constituent ions by neutron diffraction analysis

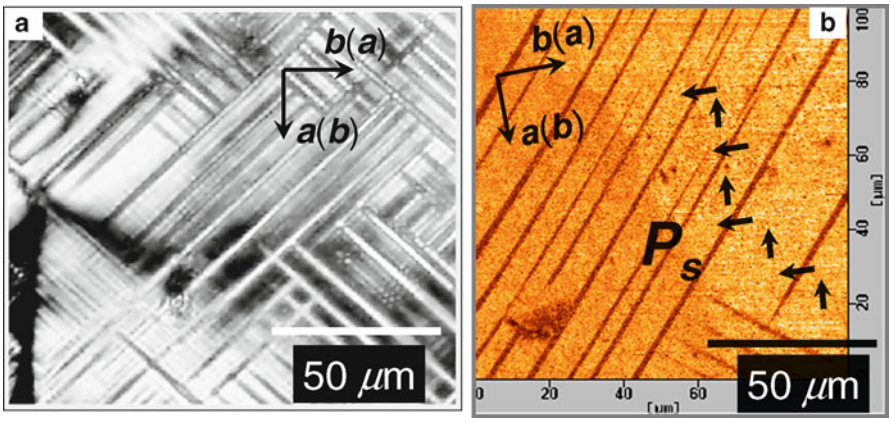

Fig. 14.6 Domain structure of $Sr_{0.99}Bi_{2.01}Ta_2O_9$ crystals at 25°C: (**a**) optical micrograph, and (**b**) piezoelectric-force micrograph. The *arrow* indicates the direction of spontaneous polarization (P_s), which was determined by the piezoelectric-force signal due to thickness-share piezoelectric vibration

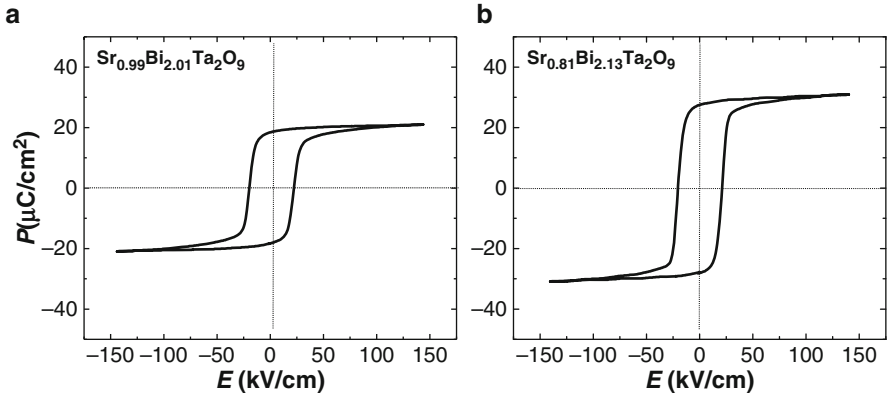

Fig. 14.7 Polarization (P)-electric field (E) hysteresis loops of single crystals measured at 25°C; (**a**) $Sr_{0.99}Bi_{2.01}Ta_2O_9$ and (**b**) $Sr_{0.81}Bi_{2.13}Ta_2O_9$. In these measurements, the electric field at a frequency of 3 Hz was applied along the *a* and/or *b* axis

were estimated. In the paraelectric state, Sr, Ta, shared oxygen (O1), and apex oxygen (O2) are all positioned on the same *b*–*c* plane, which means that the fractional coordinates of *x* (the position along the [100] direction) of these ions are exactly the same. In the ferroelectric SBT, the polar axis lies along the [100] direction. The dipole moments along the [010] direction cancel each other due to the glide plane normal to the *b* axis. As depicted in Fig. 14.8a, the entire shift of the TaO_6 octahedra along the [100] direction with respect to Bi_2O_2 layers induces a ferroelectric P_s. Figure 14.8b shows the ionic displacements (Δx) of the constituent ions along the [100] direction from the corresponding positions in the parent

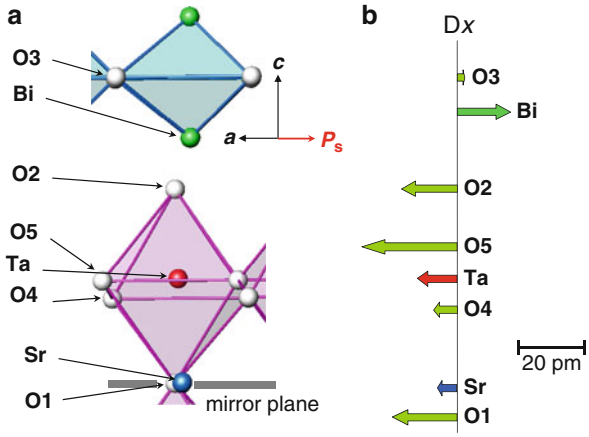

Fig. 14.8 Ionic Displacements along the [100] direction (polar direction) in $SrBi_2Ta_2O_9$ (25°C); (**a**) the crystal structure projected along the [010] direction, (**b**) the ionic displacements from the corresponding positions in the parent tetragonal (paraelectric) structure

Table 14.1 Structural data at 25°C determined by the Rietveld analysis of neutron powder diffraction

	$SrBi_2Ta_2O_9$ (A = Sr)	$Sr_{0.80}Bi_{2.14}Ta_2O_9$ ($A = Sr_{0.80}Bi_{2.14}$)
*P*ion (μC/cm^2)	16.7	18.9
Ionic displacement Δx (pm)		
O3	−2.18 (7)	−3.03 (6)
Bi	−15.54 (3)	−16.30 (3)
O2	16.21 (5)	18.33 (4)
O5	27.62 (6)	31.41 (5)
Ta	11.48 (3)	12.35 (3)
O4	6.86 (5)	6.67 (4)
Sr	5.58 (3)	2.96 (3)
O1	18.75 (4)	21.58 (4)
A-O1 bond length (pm)		
[100]	264.03 (7)	258.16 (5)
[$\bar{1}$00]	290.28 (7)	295.30 (5)
[010]	250.41 (7)	248.72 (5)
[0$\bar{1}$0]	302.66 (7)	248.72 (5)

The parenthesis denotes the standard deviation. For ionic displacements, the movement along the [100] direction is defined as plus

tetragonal (*I*4/*mmm*) structure, and the details of these displacements are listed in Table 14.1. The oxide ions in the perovskite layers are largely displaced, and these displacements are mainly responsible for the ferroelectric polarization. The P_s can be decomposed into its electronic and ionic terms: $P_s = P_{el} + P_{ion}$ [94]. Since Δx is estimated from the structure analysis, the P_{ion} can be calculated by using the

formula: $P_{ion} = \Sigma_i (m_i \times \Delta x_i \times Q_i e)/\Omega$, where m_i is the site multiplicity, $Q_i e$ is the ionic charge for the ith constituent ion, and Ω denotes unit-cell volume. Using the formal charge (+2 for Sr, +3 for Bi, +5 for Ta, and −2 for O), the P_{ion} of SBT was estimated to be 16.7 μC/cm^2. This result indicates that the contribution of P_{el} to P_s is small for the SBT crystals, and the P_{el} is estimated to be 2.3 μC/cm^2.

The substitution of Bi with Sr vacancies induced a larger shift of the TaO_6 octahedra along the [100] direction, and this led to a P_{ion} of 18.9 μC/cm^2 for $Sr_{0.80}Bi_{2.14}Ta_2O_9$. The larger P_{ion} is mainly attributed to Δx of O5. The Δx of O5 increased by 3.8 pm, and this raised the P_{ion} by 1.3 μC/cm^2. The P_s value observed for the defect-engineered crystals was 29 μC/cm^2, which was much larger than the P_{ion} value (18.9 μC/cm^2). This difference is ascribed to a larger P_{el} of about 10 μC/cm^2 for the defect-engineered crystals, and the substitution of Bi with Sr vacancies greatly enhances P_{el}.

Chemical bonding associated with electronic states plays a key role in P_{el}. While the ionic displacements of O5 is important for P_{ion}, the most prominent change in bond length was found between *A* and O1. The bond lengths of *A*-O1 are also listed in Table 14.1. For the ferroelectric SBT, O1 is displaced along both the [100] and [010] directions, resulting in two short bonds. The substitution of Bi with Sr vacancies induces a further displacement of O1 along the [100] direction. The bond length of *A*-O1 along the [100] direction decreased for $Sr_{0.80}Bi_{2.14}Ta_2O_9$ by 2.2%, and this decrease was three times as large as that along the [010] direction (0.7%). The marked change in the bonding characteristics is reflected from the electronic states around *A* and O1.

As a first step to get information about the electronic structure of SBT, the influence of the phase transition from the paraelectric *Amam* (400°C) phase to the ferroelectric $A2_1am$ one (25°C) was analyzed based on the total and partial density of sates (DOS). Figure 14.9 illustrates the DOS of (a) the paraelectric and (b) the ferroelectric SBT. In the paraelectric state, the valence band maximum is mainly composed of the O1 2*p* states, and the Ta 5*d* states form the conduction band minimum. The ferroelectric phase transition increases band gap from 2 eV (paraelectric) to 2.5 eV (ferroelectric), and leads to a marked change in DOS just below the Fermi energy (E_F). Band gap is usually underestimated by the calculations within DFT. The optical band gap of SBT has been reported to be 4.1 eV [96]. Although the O1 2*p* states constitute the valence band maximum in the paraelectric state, the 2*p* states of O2 and O3 have a larger DOS just below the E_F in the ferroelectric state. The orbital hybridization of Sr 4*d* and O1 2*p* is considered to decrease the total DOS just below the E_F, and the covalency between Sr and O1 stabilizes the ferroelectric distortion in the perovskite layers.

The electron-charge density determined by the MEM/Rietveld analysis enables us to obtain invaluable information of the effects of the Bi substitution with Sr vacancies on electronic states. Figure 14.10 depicts the isosurface of electron density at a level of 1.0×10^3/nm^3 in $Sr_{0.73}Bi_{2.18}Ta_2O_9$ at 25°C. The structural study has revealed that the *A* site composition in $Sr_{0.73}Bi_{2.18}Ta_2O_9$ is expressed as $A = Sr_{0.73}Bi_{0.18}\square_{0.09}$ [81]. The bonding electron distributions associated with orbital hybridization were observed not only for Ta-O2 but also for *A*-O1.

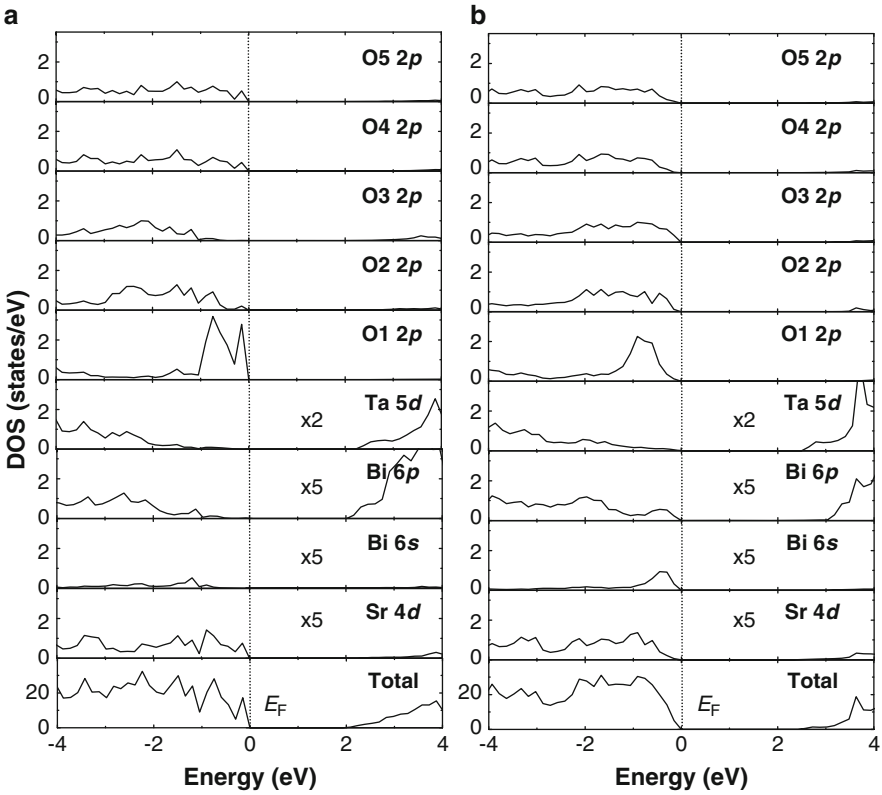

Fig. 14.9 Electronic density of state (DOS) of $SrBi_2Ta_2O_9$ calculated by band-structure calculations of (**a**) the paraelectric *Amam* phase (400°C) and (**b**) the ferroelectric $A2_1am$ phase (25°C). Total DOS and partial DOS are plotted, and E_F denoted the Fermi energy. The structure data determined by high-temperature neutron diffraction study were used for the calculations

Furthermore, the anisotropic nature of *A*-O1 bonding is clearly seen in the *a*–*b* plane. Figure 14.10b shows the charge-density counter map of *A* and O1 in the *a*–*b* plane. The electron densities of *A* and O1 is overlapped only along the [100] direction (the polar direction). The minimum electron density of the longer *A*-O1 bonding was $0.35 \times 10^3/nm^3$ along the [010] direction, which was as low as the background level. In contrast, the shorter *A*-O1 bonding had a minimum electron density of $1.15 \times 10^3/nm^3$ along the [100] direction, which was much larger than that in $SrBi_2Ta_2O_9$ ($0.7 \times 10^3/nm^3$). The covalency between Sr and O1 contributes to stabilize the ferroelectric distortion for $SrBi_2Ta_2O_9$, while the larger covalency caused by the additional valence states of Bi at the *A* site, especially Bi 6*s* states, plays a crucial role in the larger P_s observed for the defect-engineered crystals. For $PbTiO_3$, the overlapping electron distributions have been found for Pb-O bonding [62], and this originates from the hybridization between the Pb 6*s* and O 2*p* states [9].

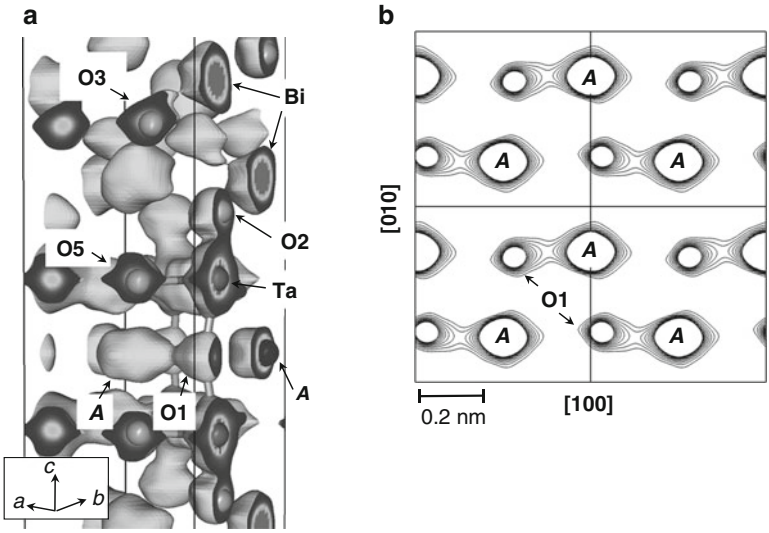

Fig. 14.10 Electron-density distributions determined by the MEM/Rietveld analysis of $Sr_{0.73}Bi_{2.18}Ta_2O_9$ at 25°C; (**a**) isosurface of electron density ($1.0 \times 10^3/nm^3$), and (**b**) counter map of electron-density distributions in the *A*-O1 plane (the counter lines are drown with the *solid lines* from $0.8 \times 10^3/nm^3$ to $3.0 \times 10^3/nm^3$ with $0.2 \times 10^3/nm^3$ steps). The resultant *R* factors were $R_w = 12.91\%$, $R_e = 12.43\%$, and $R_I = 4.14\%$. *A* denotes the *A*-site cations expressed as $A = Sr_{0.73}Bi_{0.18}\square_{0.09}$, where □ denotes Sr vacancies

The orbital hybridization between Bi 6*s* and 6*p* with stereoactive lone pair behavior at the *A* site and O1 2*p* causes the high electron density of *A*-O1 bonding along the [100] direction, and this induces a larger ferroelectric distortion. The stronger covalency due to the orbital hybridization of Bi 6*sp*-O1 2*p* in addition to Sr 4*d*-O1 2*p* is the origin of the large P_s (also P_{el}) observed for the defect-engineered SBT crystals.

14.3.3 Summary

Polarization measurement for SBT crystals provides experimental evidence of a major enhancement of P_s by the defect-engineering approach. Electronic band-structure calculations and MEM/Rietveld analysis indicate that the stronger covalent bonding between the perovskite *A* cations (Sr and Bi) and O along the [100] direction is responsible for the enhanced P_s. The orbital hybridization of perovskite *A* cations and O 2*p* induced by the defect engineering would be a key factor for designing novel layered ferroelectric oxide.

14.4 $m = 3$: $Bi_4Ti_3O_{12}$-Based Single Crystals

Ferroelectric bismuth titanate ($Bi_4Ti_3O_{12}$, BiT) has been regarded as a promising material because of its high Curie temperature (T_C), large spontaneous polarization (P_s), and large electro-optic coefficient [10, 44, 46]. However, leakage current often interferes with the polarization switching and poling process and makes BiT unsuitable for the ferroelectric devices [35, 112, 114].

It is recognized that defects are closely related to the leakage current and polarization properties of BiT [50, 77, 78, 87, 102]. Takahashi et al. [104–106] have revealed the conduction mechanism of BiT single crystals and polycrystalline ceramics at high temperatures. The electrical conductivity along the *a* axis is higher by several orders of magnitude than that along the *c* axis. Oxide-ion migration ascribed to a large number of oxygen vacancies in the perovskite layers controls the high electrical conduction along the *a* axis. With decreasing temperature, the contribution of oxide ions to the electrical conduction becomes less significant, and electron holes play a dominant role at low temperatures. Noguchi et al. [76] have clarified the origin of the leakage current of BiT crystals at room temperature. Electron holes arising from the incorporation of oxygen from ambient at oxygen vacancies, i.e., excess oxygen in the lattice, act as detrimental carriers of leakage current up to high electric fields. They have proposed that crystal growth under a high oxygen pressure is advantageous for suppressing the vacancy formation and for attaining a large remanent polarization (P_r) as well as a high insulating property in the BiT system.

La- and Nd-substituted BiT (BLT and BNT) have received a great deal of attention since these substitutions lead to better memory properties such as a large P_r, a high fatigue endurance, and a superior insulating property [87]. These rare-earth (RE) elements have been reported to preferentially occupy the perovskite *A* site [86]. The presence of RE at the *A* site reduces lattice distortion in the perovskite layers [25, 103] as well as provides an additional domain-nucleation site, an antiphase-domain boundary in the lattice [15]. Considerable effort has been made to realize a ferroelectric memory using BLT, and the device technology related to processing and integration is being developed.

14.4.1 Oxygen Stability and Leakage Current Mechanism in $Bi_4Ti_3O_{12}$-Based Single Crystals

Here, the defect structure in BiT and BLT through ab initio electronic band structure calculations is shown. A large number of the vacancies of Bi and oxygen in the perovskite layers are expected for BiT, while the presence of La at the perovskite *A* site stabilizes the adjacent oxide ions. The investigation on single crystals reveals that electron holes arising from the incorporation of oxygen at the oxygen vacancies in BLT crystals are much less than those in BiT crystals, which is responsible for the extremely low leakage current of BLT crystals along the *a* axis.

14.4.1.1 Experiments and Ab Initio Band Structure Calculations

Powder samples of $Bi_4Ti_3O_{12}$ and $Bi_{4-x}La_xTi_3O_{12}$ (BLT) were prepared by a solid-state reaction. The details are described in ref. [83]. Single crystals of BiT and BLT were grown in air by a self-flux method. The two kinds of Bi_2O_3 raw materials with different purities (99.99 and 99.9999%) were used for the crystal growth of BiT. For BLT, the raw material of Bi_2O_3 with 99.99% purity was used. The crystals were annealed at 700°C for 5 h in air. Some of the crystals were annealed at 700°C for 10 h at a high oxygen pressure of 35 MPa to reduce the number of oxygen vacancies.

Ab initio band structure calculations were performed to estimate the defect formation energies of Bi and O. The calculations were conducted within DFT via the generalized gradient approximation [64] using a plane wave basis set. The PAW method [5] was applied using the VASP [60]. The cutoff energy of 400 eV and a *k*-point sampling grid of $7 \times 7 \times 3$ were used. On the basis of the structural data of BiT at 700°C determined by the neutron diffraction study, the structural optimization was conducted within the *I*4/*mmm* symmetry until the force estimated from derivatives of the free energy with respect to the ionic positions was less than 0.1 eV/nm. The structure of $Bi_2La_2Ti_3O_{12}$ was optimized from the structural data of BiT, where the perovskite *A* site is occupied by La. The disordering of La and Bi [32] was not taken into account in the calculation of BLT.

The supercell method was adapted for estimating vacancy formation energy ($E_{vacancy}$) to reduce vacancy-vacancy interaction. The $2a \times 2a \times 1c$ supercell was created from the optimized unit cell, i.e., $Bi_{32}Ti_{24}O_{96}$ and $Bi_{16}La_{16}Ti_{24}O_{96}$, and then the symmetry was set to be *P*1. Total energy of the defective cell in which a vacancy is introduced is calculated. Here, $E_{vacancy}$ is discussed by comparing the difference in the total energies of the defective cell and the optimized unit cell. The lattice relaxation of the unit cell with a vacancy also gives the same results of relative $E_{vacancy}$ as the supercell calculation within 0.2 eV. The electronic band structures and density of states (DOS) were also calculated.

14.4.1.2 Defect Structure and Vacancy Formation in $Bi_4Ti_3O_{12}$

Figure 14.11 shows the fitting profile of the Rietveld analysis of the neutron powder diffraction data obtained in vacuum at 700°C. The resultant *R*-weighted pattern (R_{wp}) was 2.91% and the goodness of fit ($S = 1.01$) was close to 1.0. Recently, Noguchi et al. [83] have demonstrated, through the analysis of the thermal ellipsoids of this neutron powder diffraction data, that self-diffusion of oxide ions occurs through the O1 site at which a large number of oxygen vacancies ($V_O^{\bullet\bullet}$) are present.

Figure 14.12 indicates the relative $E_{vacancy}$ of Bi and O. Since Bi1 and O2 show the lowest $E_{vacancy}$ in Bi and O, these values are set to be the standard for comparison. The calculations for BiT show that the $E_{vacancy}$ of Bi1 is lower by about 2 eV

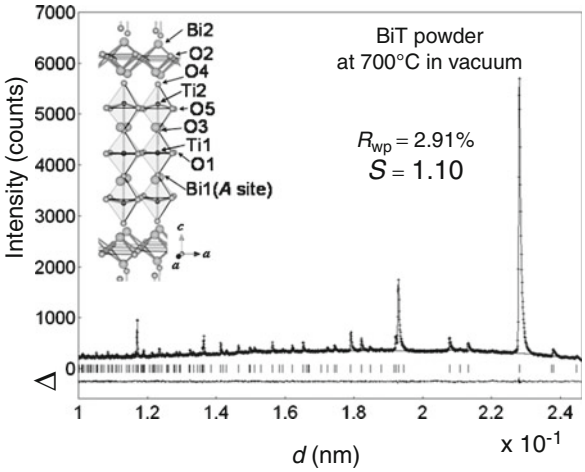

Fig. 14.11 Observed (+), calculated (*solid line*) and difference (Δ) neutron powder diffraction for $Bi_4Ti_3O_{12}$ at 700°C in vacuum. The *inset* shows the refined crystal structure with the details of constituent ions

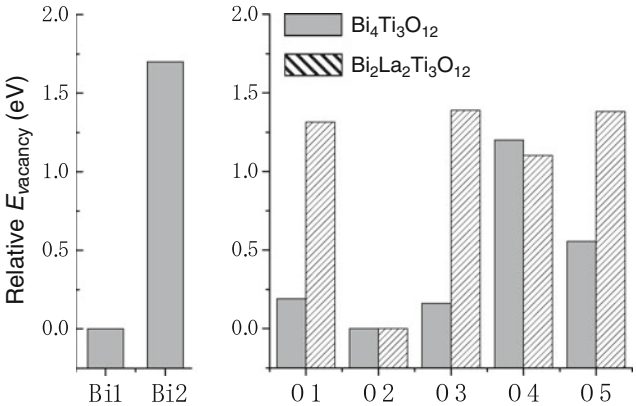

Fig. 14.12 Relative difference in vacancy formation energy ($E_{vacancy}$) in *I*4/*mmm* tetragonal symmetry calculated by ab initio band structure calculations. In the calculation for BLT, the perovskite *A* site is assumed to be occupied by La

than that of Bi2. The much lower $E_{vacancy}$ of Bi1 indicates that Bi vacancies are created preferentially at the Bi1 site in the perovskite layers rather than at the Bi2 site in the Bi_2O_2 layers. For oxygen vacancies, O1, O2, and O3 show similar $E_{vacancy}$ within 0.2 eV, which is lower by about 0.4–0.6 eV than those of O4 and O5.

Figure 14.13 shows the temperature dependence of electrical conductivity (σ). The σ along the *a* axis of BiT was by about two orders of magnitude higher than that along the *c* axis. Takahashi et al. have revealed that the high σ along the *a* axis is attributed to oxide ion conduction in the perovskite layers [104].

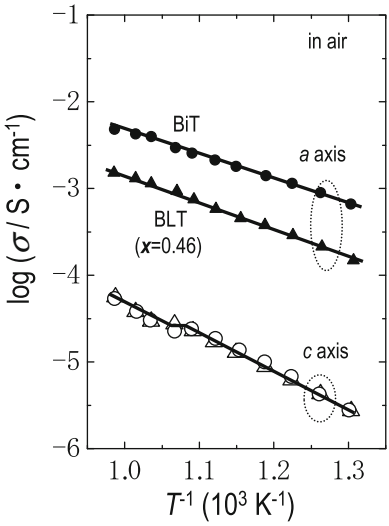

Fig. 14.13 Electric conductivity in air as a function of temperature observed for the crystals of BiT and BLT ($x = 0.46$). Both crystals were grown using the raw Bi_2O_3 powder with 99.99% purity

In contrast, the Bi_2O_2 layers act as a barrier to oxide ion migration along the *c* axis; hence this yields the low σ along the *c* axis ($h^{\bullet}$ conduction is dominant).

Here, a mechanism of vacancy formation for BiT at high temperatures is discussed. Our calculations have shown that the Bi vacancy at the Bi1 site (V'''_{Bi1}) is easily generated than V'''_{Bi2}, where $'$ denotes one negative charge. Furthermore, the nuclear-density analysis [83] has revealed that oxygen vacancies preferentially reside at the O1 site ($V_{O1}^{\bullet\bullet}$), where $^{\bullet}$ indicates one positive charge. Thus, the vacancy formation of V'''_{Bi1} is the trigger for generating $V_{O1}^{\bullet\bullet}$. At high temperatures, V'''_{Bi1} is formed accompanied with the nearest-neighbor $V_{O1}^{\bullet\bullet}$, which is the origin of the defect formation in the BiT system. The high oxide-ion conduction observed in the BiT crystals is ascribed to the large number of $V_{O1}^{\bullet\bullet}$ at the perovskite layers. The high oxide-ion conductivity also indicates that the electrical neutrality during the defect formation is satisfied through the generation of $2V'''_{Bi1}$ accompanied with $3V_{O1}^{\bullet\bullet}$ as follows:

$$2Bi_{Bi1} + 3O_{O1} \rightarrow 2V'''_{Bi1} + 3V_{O1}^{\bullet\bullet} + Bi_2O_3\ (g) \tag{14.4}$$

and $h^{\bullet}$ plays a minor role in the high-temperature defect formation.

As a result of the thermogravimetric analysis of BiT powder under different oxygen partial pressures (Po_2) [83], the weight loss due to vacancy formation was promoted in low-Po_2 (reducing) atmosphere. The weight loss due to vacancy formation was observed above 1,000°C in air [83]. Annealing in air at 1,000°C for 5 h led to a 0.25% decrease in weight, while annealing in O_2 ($Po_2 = 0.1$ MPa) at 1,000°C did not result in weight loss. The O_2 annealing at 1,050°C for 5 h resulted in a weight loss of 0.5%, which was much smaller than the annealing at 1,050°C for

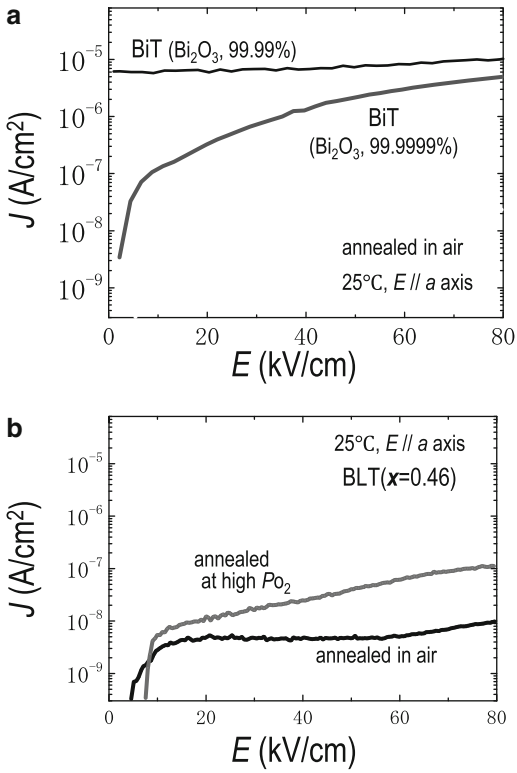

Fig. 14.14 Leakage current density (J) as a function of electric field (E) applied along the a axis at 25°C for (**a**) BiT crystals grown by using Bi_2O_3 powders with different purities and (**b**) BLT crystals. The annealing at 700°C under a high Po_2 of 35 MPa led to an increase in J. BLT crystals were grown using the raw Bi_2O_3 powder with 99.99% purity. BLT crystals annealed in high-pressure oxygen ($Po_2 = 35$ MPa) at 700°C showed a higher J than those annealed in air at 700°C

5 h in air (1.2% loss). The Po_2 dependence of weight loss shows that the limiting factor of the vacancy formation is the surface reaction on BiT powder, and this result gives valuable information that the vacancy formation can be suppressed by heat treatment in high-Po_2 atmosphere [83].

14.4.1.3 Electrical Conduction Mechanism in $Bi_4Ti_3O_{12}$ Crystals at Room Temperature

Figure 14.14 shows the leakage current density (J) as a function of electric field. In the measurements, electric field is applied along the a axis. The BiT crystals grown using Bi_2O_3 powder with 99.99% purity exhibited a much higher J than the crystals grown using high-purity powder (99.9999%). The low-purity Bi_2O_3 powder contained impurities of Ca at 10 ppm, Cu at 26 ppm and Fe at 8 ppm. The crystals are contaminated by these impurities during crystal growth, and the impurity atoms act mainly as lower-valent cations in the lattice, i.e., Ca^{2+} at the Bi^{3+} site, and Cu^{2+} and Fe^{3+} at the Ti^{4+} site. Ca^{2+} occupies the Bi1 site, because other foreign ions are hardly present at the Bi2 site [32]. The oxide-ion conduction [104] at relatively high temperatures indicates that the charge difference caused by the incorporation of

the lower-valent cations is compensated by the formation of $V_{O1}^{\bullet\bullet}$. The substitution of Cu^{2+} and Fe^{3+} at the Ti^{4+} site also yields $V_{O1}^{\bullet\bullet}$ for charge valance. Thus, the contamination by the lower-valent cations introduces a larger number of $V_{O1}^{\bullet\bullet}$s in the BiT crystals. During cooling, BiT absorbs ambient oxygen, and the oxygen are positioned at $V_{O1}^{\bullet\bullet}$ as $O_{O1}^{\times}$. This reaction gives rise to $h^{\bullet}$ generation as follows:

$$\frac{1}{2}O_2 + V_{O1}^{\bullet\bullet} \rightarrow O_{O1}^{\times} + 2h^{\bullet}. \tag{14.5}$$

A larger number of $h^{\bullet}$s are implanted for BiT with a higher concentration of $V_{O1}^{\bullet\bullet}$, which is the reason why the low-purity BiT crystals exhibited a poor insulating property at room temperature.

14.4.1.4 Effects of La Substitution on Defect Formation and Electrical Conduction at High Temperatures

It is interesting to note that the presence of La at the perovskite *A* site increases $E_{vacancy}$ of the adjacent oxygen atoms, O1, O3, and O5, by about 1 eV, as shown in Fig. 14.12. These results suggest that La substitution is effective for improving the chemical stability of oxygen in the perovskite layers. Since charge neutrality is satisfied in the lattice during the vacancy formation as expressed by (14.4), the higher stability of oxygen leads to fewer Bi1 vacancies in the BLT lattice. The total/partial density of states (DOS) analysis of BLT ($x = 2.0$) suggests that the La 5*d* is hybridized with the O 2*p* of the adjacent oxygen. The covalent bonding between La and O in the perovskite layers creates the DOS of the La 5*d* states in the valence band near the Fermi level (−5 to 0 eV), which is a possible origin of the high chemical stability of oxygen in BLT.

As shown in Fig. 14.13, the σ along the *c* axis of BLT ($x = 0.46$) crystals was the same as that of BiT, while the La substitution decreased the σ along the *a* axis. In BLT ($x = 0.46$) most La occupies the perovskite *A* site [86]. Since the Bi_2O_2 layers in BLT are likely to play the same role as those of BiT in the electrical conduction along the *c* axis, the BiT and BLT ($x = 0.46$) crystals indicate the same σ. The lower σ along the *a* axis of BLT strongly indicates that the La substitution is effective for decreasing $V_{O1}^{\bullet\bullet}$, which is essentially consistent with the results of the $E_{vacancy}$ calculations. The relatively high oxide-ion conductivity observed for BLT ($x = 0.46$) exhibits that a certain amount of $V_{O1}^{\bullet\bullet}$ is present even in the lattice.

14.4.1.5 Leakage Current and Polarization Properties of BLT Crystals at Room Temperature

Figure 14.14b shows the leakage current properties of BLT ($x = 0.46$) crystals along the *a* axis. Note that BLT ($x = 0.46$) crystals annealed in air at 700°C showed

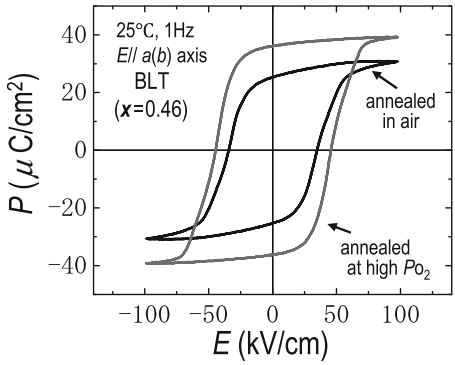

Fig. 14.15 Polarization hysteresis loops along the $a(b)$ axis measured at 25°C for BLT ($x = 0.46$) crystals

an extremely low J on the order of 10^{-9} A/cm^2. The high-pressure oxygen annealing ($Po_2 = 35$ MPa) at 700°C increased J. Even though the oxygen annealing indeed decreases $V_{O1}^{\bullet\bullet}$, the annealed crystals have a higher J. The oxygen annealing did not change the metal composition of the crystals. The fact of the high J caused by the oxygen annealing shows that the incorporation of oxygen in the lattice caused by the annealing generates $h^{\bullet}$. It is concluded that $h^{\bullet}$ due to the presence of the excess oxygen is the detrimental carrier in BLT crystals. The concentration of $h^{\bullet}$ is determined by the excess oxygen that is absorbed from the ambient during annealing or cooling. The La substitution reduces $V_O^{\bullet\bullet}$ in the perovskite layers and thus decreases the excess oxygen generating $h^{\bullet}$, which is the origin of the high insulating property observed for BLT crystals. Although BLT has a smaller number of oxygen vacancies, BLT is similar to BiT in terms of the mechanism of leakage current.

Figure 14.15 shows the polarization hysteresis loops of BLT ($x = 0.46$) crystals at 25°C. The high-Po_2 annealing improved the rectangularity of the hysteresis and increased P_r from 25 to 36 μC/cm^2. One of the reasons why the high-Po_2 annealing leads to the larger P_r is a weak pinning of domains for the annealed crystals due to the small numbers of $V_O^{\bullet\bullet}$s. The air-annealed crystals still have a certain amount of $V_O^{\bullet\bullet}$ in the perovskite layers, and $V_O^{\bullet\bullet}$ acts as a pinning center of the domain wall. The oxygen annealing increases the number of switchable domains by electric field. The high-Po_2 annealing has been demonstrated to be effective for improving polarization properties in the BLT system with a high insulating property.

14.4.1.6 Summary

The defect structure and the mechanism of leakage current at room temperature of BiT and BLT have been investigated by measuring the properties of single crystals and by ab initio band structure calculations. La substation at the perovskite A site improves the chemical stability of the adjacent oxide ions and reduces the concentration of oxygen vacancies. The results of the leakage current properties of the single crystals revealed that electron holes arising from the incorporation of

oxygen at oxygen vacancies act as detrimental carriers for leakage current at room temperature for both crystals. A high insulating property at room temperature was obtained for BLT crystals as a result of the small number of electron holes due to the small amount of oxygen vacancies. A high-pressure oxygen annealing was demonstrated to improve remanent polarization for the BLT system with a high insulating property.

14.4.2 Oxygen Stabilization in $Bi_{3.25}La_{0.75}Ti_3O_{12}$

It is widely recognized that the polarization fatigue and small P_r are attributed to domain clamping, i.e., a decrease in switchable domains by applying an electric field [87, 89, 98]. The domain clamping is caused by the strong interaction between domain walls and defects such as oxygen vacancies [76, 103]. Since the stability of oxygen ions strongly depends on the local crystallographic environment, it is essential to investigate the chemical bonding in BiT and BLT to elucidate the role of La and to develop materials design for high-performance BiT-based devices.

The aim of the present study is to clarify the role of La in BiT on the stability of oxygen ions in terms of chemical bonding obtained by electron charge density analysis. Analyzing X-ray diffraction data using the MEM/Rietveld method allows us to get information about the nature of chemical bonding directly in the electron density map for $PbTiO_3$ [62] and high-T_C superconductors [107].

14.4.2.1 Experimental Procedure

The experimental details are described in ref. [54]. It is known that the ferroelectric structure represents an extremely subtle monoclinic distortion with a monoclinic angle of 90.00° [91] from orthorhombic *B*2*cb* [29]. Here, the space group of BiT and BLT is regarded as *B*2*cb*, because the La substitution leads to a marked change in in-plane crystal structure in BiT (P_s along the *a* axis) [10, 103] compared with the monoclinic distortion (P_s along the *c* axis) [10, 100] and the structural change induced by the La substitution can be explained with orthorhombic *B*2*cb*.

14.4.2.2 Crystal Structure and Electron Density

Figure 14.16 shows the Rietveld profile fitting results of BiT and BLT. The substitution of La leads to a decrease in orthorhombicity defined by $2(a - b)/(a + b)$ from 7.11×10^3 for BiT to 1.95×10^3 for BLT. It is reasonable to consider that the smaller orthorhombic distortion caused by the La substitution is attributed to the smaller displacements of the constituent ions from the corresponding positions in the parent tetragonal *I*4/*mmm* structure, leading to a smaller P_s [100, 103] for BLT.

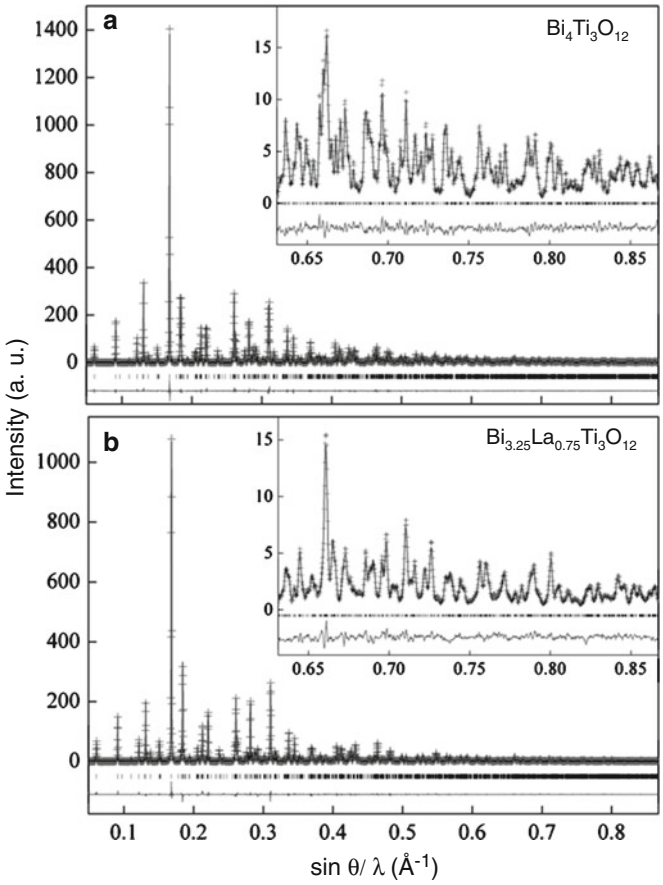

Fig. 14.16 Rietveld profile fitting of (**a**) BiT and (**b**) BLT at 300 K in the ferroelectric phase based on orthorhombic B2*cb* symmetry. Here, + and *solid line* stand for observed and calculated intensities, respectively. The reliability factors R_{wp}, R_I, and R_F, based on the weighted profile, Bragg intensity and the structure factor, respectively, were sufficiently small, i.e., $R_{wp} = 0.0293$, $R_I = 0.0219$, $R_F = 0.0258$ for BiT, and $R_{wp} = 0.0313$, $R_I = 0.0312$, $R_F = 0.0342$. The orthorhombic lattice parameters are determined to be $a = 5.44716(4)$ Å, $b = 5.40857(3)$ Å, and $c = 32.8219(2)$ Å for BiT, and $a = 5.42602(6)$ Å, $b = 5.41544(6)$ Å, and $c = 32.8785(3)$ Å for BLT, respectively

Figure 14.17a shows the crystal structure of ferroelectric BiT. There are two independent Bi sites, Bi1 in the perovskite layer and Bi2 in the Bi_2O_2 layer. It is found that most of La occupies the Bi1 site in BLT. The site occupancy of La was determined to be 0.310(1) at the Bi1 site and 0.059(1) at the Bi2 site, which is consistent with the results of Raman scattering [86] of BLT thin films.

From the electron density distributions $\rho(r)$ of BiT shown in Fig. 14.17b, information about ionic valence of each atom is obtained. The estimated valences based on the Mulliken's scheme are +2.3 for Bi1 and +0.6 for Bi2, so that the

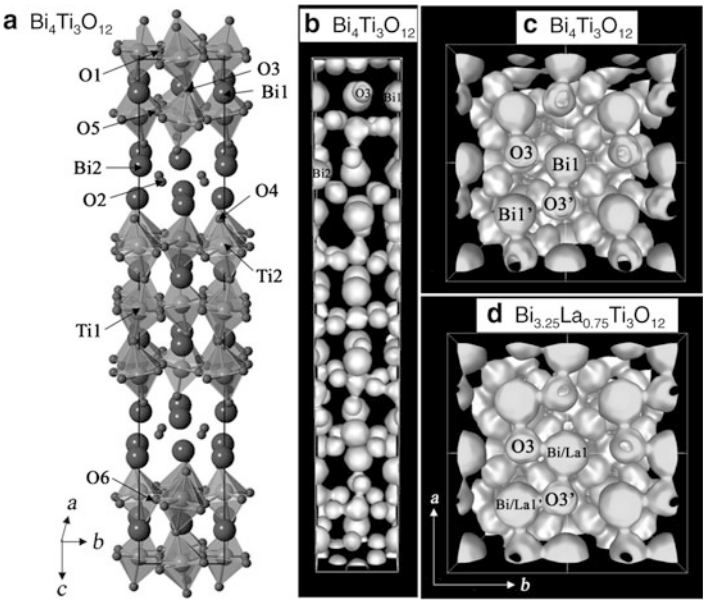

Fig. 14.17 Structures of BiT and BLT at 300 K in the ferroelectric phase. (**a**) Determined crystal structure of BiT. Perovskite $Bi_2Ti_3O_{10}$ and fluorite-like Bi_2O_2 layer stacks alternatively along the *c* axis. (**b**) Equidensity map of electron density distribution $\rho(r)$ of BiT derived by MEM/Rietveld analysis. The surface level is 1.0e $Å^{-1}$. (**c**) and (**d**) are the equidensity maps of BiT and BLT, respectively, in the perovskite layer indicated by "O3" and "Bi1" in (**b**). The depicted cell size is $2a \times 2b$. The surface level is 0.55e $Å^{-1}$. The interatomic distances and the minimum charge density values ρ_{min} between Bi1 or Bi/La1 and O3 are listed in Table 14.1

covalency of Bi1-O is less than that of Bi2-O. This result shows that Bi1 is more ionic than Bi2. It is known that La is almost completely ionized, i.e., the ionic valence of La is +3 in perovskite oxides as in $LaMnO_3$ [92]. It is demonstrated that the high ionic valence of Bi1 compared with Bi2 is the origin of the preferential substitution of La in the perovskite layer (the Bi1 site) rather than in the Bi_2O_2 layer (the Bi2 site).

14.4.2.3 Chemical Bonding

The substitution of La in the perovskite layer leads to a significant change in the chemical bonding of Bi1-O3. The Bi1 and O3 are located in nearly the same *ab* plane at the *c* axis coordinate $\approx 0.07c$, which are indicated by "O3" and "Bi1" in Fig. 14.2b. The interatomic distances *d* and the minimum charge density values ρ_{min} of Bi1(Bi/La1)-O3 are summarized in Table 14.2. Figure 14.17c and d exhibit the Bi1(La1)-O3 planes viewed along the *c* axis in BiT and BLT, respectively. The large ρ_{min} of Bi1–O3′ (the *a* axis direction) compared with Bi1–O3′ (the *b* axis direction) in BiT indicates that the chemical bonding of Bi1–O3′ along the *a*

Table 14.2 Interatomic distances d and minimum charge density values ρ_{min} between Bi1 and O3 in BiT (Fig. 14.2c) and Bi/La1 and O3 in BLT (Fig. 14.2d)

	BiT		BLT	
	Bi1−O3	Bi1−O3′	Bi/La1−O3	Bi/La1−O3′
d (Å)	2.41 (1)	2.28 (1)	2.34 (1)	2.47 (2)
ρ_{min} (e Å^{-3})	0.44	0.67	0.62	0.61

axis (polarization direction) is stronger than that of Bi1–O3 along the b axis. Thus, the d(Bi1−O3′) is much shorter than d(Bi1−O3).

The chemical bonding of Bi1–O3′ has been suggested to have a covalent character originating from the orbital hybridization between Bi1-6p and O-2p states [25]. It is implied that steric exclusion due to the stereoactive lone pair of electrons caused by Bi 6s-6p hybridization [18] induces the anisotropic bonding of Bi1-O3 in the perovskite layers.

Note that the chemical bonding around Bi/La1 in BLT is quite different from that around Bi1 in BiT. In BLT, the d(Bi/La1–O3) is almost the same as the d(Bi/La1–O3′). The La substitution provides an additional chemical bonding of Bi/La1–O3 along the b axis in addition to along the a axis. A strong chemical bonding of Bi/La1–O3 is proved by the much larger ρ_{min}(Bi/La1−O3) for BLT (0.61 e/A^3) compared with BiT (0.44 e/A^3). It is interesting to note that Bi/La1−O3′ still has a large ρ_{min} along the a axis in spite of having a longer d compared with BiT. The stabilization of O3 by the La substitution is suggested by ab initio electronic structure calculations [83]. The high endurance to polarization fatigue achieved for BLT films [87] can be ascribed to the stabilization of oxygen ions by the La substitution in the perovskite layer.

14.4.2.4 Summary

The chemical bonding of Bi1-O3 in the perovskite layer was observed only along the a axis for BiT, while the substitution of La in the perovskite layer resulted in an additional chemical bonding along the b axis as well as along the a axis. The high endurance to polarization fatigue observed for BLT films is suggested to originate from the stabilization of the oxygen ions in the perovskite layer due to the isotropic chemical bonding of Bi/La1–O3.

14.4.3 Domain Structure in $Bi_4Ti_3O_{12}$ Crystals Observed by Piezoresponse Force Microscopy

Polarization switching in ferroelectrics is established by nucleation of new domains followed by the movement of domain walls (DWs). The crystallography and thermodynamics of the domain structures have been extensively studied and well

understood not only in bulk systems [1, 6] but also in constrained films [31, 66]. Recently, in perovskite ferroelectrics such as $PbTiO_3$ and $BaTiO_3$, 90° DWs have been reported to strongly interact with charged defects such as oxygen vacancies [12, 28, 97]. The interaction between DWs and defects leads to a viscous movement of the DWs, and the domain structure inside ferroelectric crystals is expected to be different from that predicted by the existing theory without taking the influence of defects into account. Here, the three-dimensional domain structure in ferroelectric $Bi_4Ti_3O_{12}$ crystals investigated by piezoresponse force microscopy (PFM) is shown. Energetically favorable 90° DWs with faceted structure are established on the surface along the *a–b* plane, while the 90° DWs have complicated and curved surfaces along the *c* axis inside the crystals. The curved 90° domain structure can be explained by the strong interaction between local electric field near the 90° DWs and oxygen vacancies.

Despite having the large P_s, BiT has been reported to exhibit a polarization fatigue as well as a small remanent polarization (P_r). Numerous studies [23, 59, 77, 78, 87] have been conducted to overcome these drawbacks by element substitution and/or doping. It is widely recognized that the polarization fatigue and small P_r originate from domain clamping, i.e., a decrease in switchable domains by applying an electric field, which is caused by the interaction between DWs and defects such as oxygen vacancies [12, 97]. It is essential to understand the domain structures and the interaction between the DWs and oxygen vacancies for improving the polarization properties of BiT-based devices. Recent experimental observations have revealed that 90° DWs in $SrBi_2Nb_2O_9$ [121] are irregular and highly curved due to their extremely low ferroelastic distortion less than 0.01%. Phase-field simulations [65] have verified that the curved 90° DWs are a result of the dominant contribution of isotropic DW energy compared with the negligible elastic energy. For BiT with a relatively large ferroelastic distortion of about 0.8% [91], Cummins and Cross [10] have reported that 90° DWs observed by optical microscopy exhibit a crystallographically faceted structure. The domain structure with the faceted 90° DWs is commonly seen in $BaTiO_3$ [69] with a large ferroelastic distortion over 1%. Although domain-structure observations of BiT-based films have been conducted [3], the detailed domain structures of 180° DWs in addition to the 90° DWs have not been clarified yet. Soga et al. [103] have reported the 90° domain structures of BiT crystals in the *a–b* plane using PFM. The domain analysis by PFM enables us to obtain the information of P_s vector of each domain with a high spatial resolution.

14.4.3.1 Domain Structure Observations

Figure 14.18a shows the in-plane PFM image on the *a–b* surface of a BiT crystal. The schematic domain structure of the dashed square region in Fig. 14.18a is depicted in Fig. 14.18b. Striped 90° domains with faceted DWs were seen throughout the crystal. The 90° DWs appear to be a flat surface from this image. Charge-free 180° DWs ("1") were established to minimize their electrostatic energy,

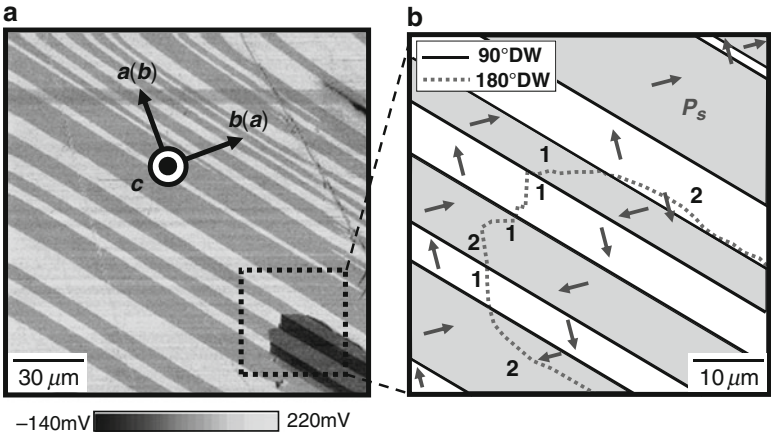

Fig. 14.18 (**a**) In-plane PFM image and (**b**) the schematic domain structure of the *dashed square* on the *a–b* surface of a BiT crystal. The directions of P_s are indicated by *arrows*. The *solid line* represents 90° DW, while the *dashed line* denotes 180° DW("1" for charge-free, and "2" for charged)

whereas charged 180° DWs ("2") with head-to-head and tail-to-tail configurations of P_s were also found in the 90° domain structure, as can be clearly seen in Fig. 14.18b.

Figure 14.19a shows the out-of-plane PFM image on the *a*(*b*)–*c* surface of the BiT crystal, and the schematic domain structure is depicted in Fig. 14.19b. The 90° DWs observed on the *a–b* surface (see Fig. 14.18) penetrated through the crystal along the *c* axis. Note that the 90° DWs were not a flat surface but a strongly curved one, which is quite different from the 90° DWs reported for perovskite ferroelectrics [69]. Curved 90° DWs have been reported for $SrBi_2Nb_2O_9$ [121], and the curved 90° DWs is associated with their small ferroelastic distortion less than 0.01% [65]. The inhomogeneous 90° domain structure observed in the BiT crystal cannot, however, be explained only by the contribution of elastic energy.

In addition to the 90° DWs, apparent 180° domains ("1" and "2" in Fig. 14.19b) were observed inside the crystal. Figure 14.20 shows the enlarged (a) out-of-plane and (b) in-plane PFM images obtained in the region indicated by the square in Fig. 14.19a with the schematic representation of the domain structure in Fig. 14.20c. It is clearly seen that the 90° DWs are highly curved and irregular inside the crystal. Unlike with the 90° DWs, the 180° DWs formed a flat surface without local charge.

Figure 14.21 shows the schematic representation of the three-dimensional domain structure expected from the PFM images on the *a–b* surface (Fig. 14.18) and the *a*(*b*)–*c* surface (Figs. 14.19 and 14.20) of the BiT crystal. The observations by PFM and optical microscope in the in-depth analysis of the crystal have demonstrated that the 90° DWs have a faceted structure on the same surface along the *a–b* plane (the same *a–b* surface). It is reasonable to consider that the 90°

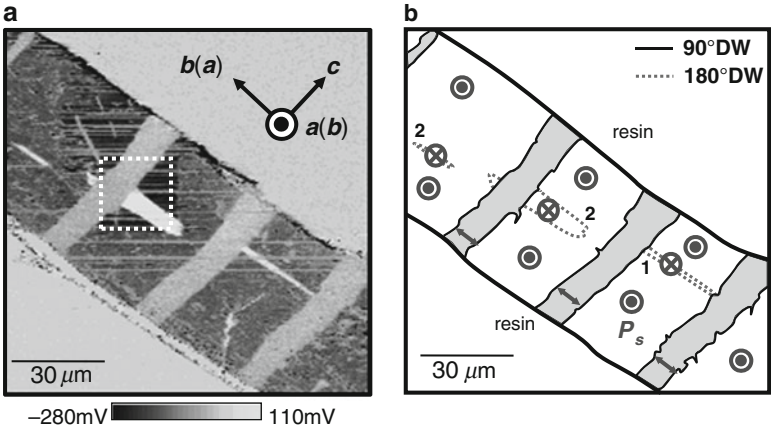

Fig. 14.19 (**a**) Out-of-plane PFM image and (**b**) the schematic domain structure in the *a*(*b*)–*c* plane of BiT crystal. "1" and "2" shows 180° domains inside the crystal

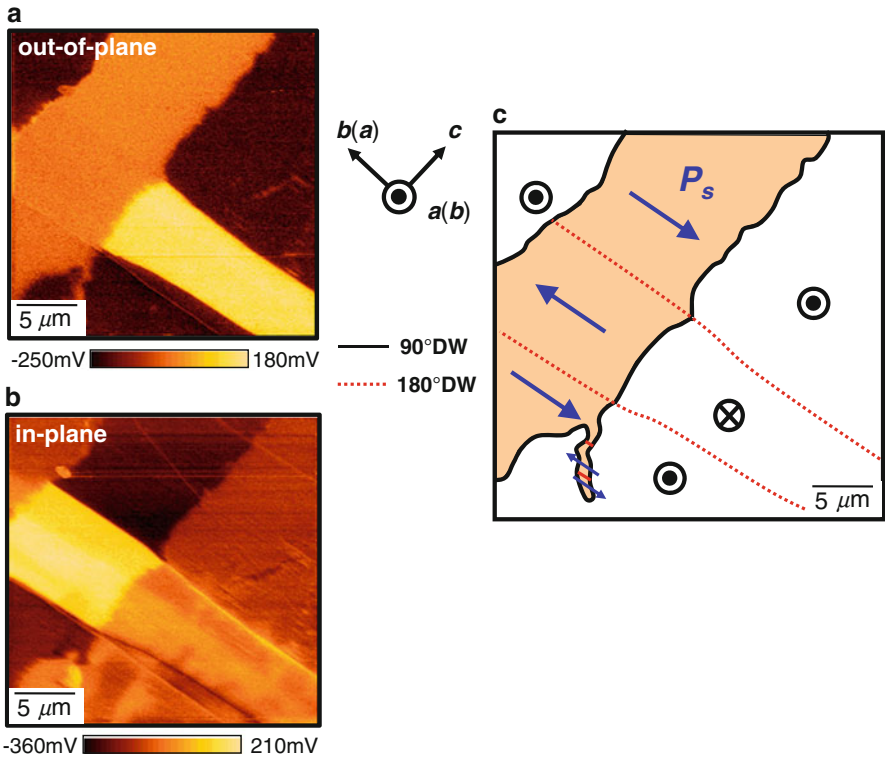

Fig. 14.20 (**a**) Out-of-plane and (**b**) in-plane PFM images obtained in the region indicated by the *square* in Fig. 14.19a. (**c**) is the schematic domain structures of the same area

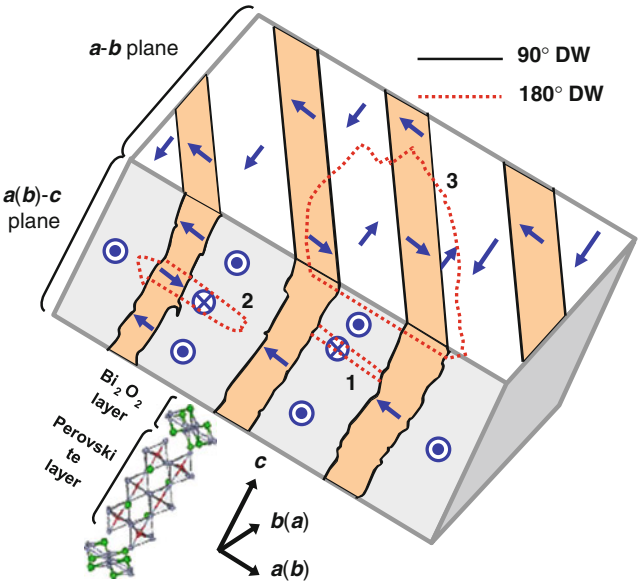

Fig. 14.21 Schematic image of the three-dimensional domain structure in BiT crystals. "1," "2," and "3" indicate 180° domains

DWs form the faceted structure on the same *a*–*b* surface throughout the crystal to satisfy the strain energy minimization due to the relatively large ferroelastic distortion. In contrast, the 90° DWs have the complicated and curved surface along the *c* axis. Point group analysis predicts that the 90° DWs with the minimum strain energy for monoclinic BiT (point group *m*) is the (11*a*) plane, where *a* is zero or very small [3, 10]. The energetically favorable configuration of the 90° DWs is attained on the same *a*–*b* surface, but the 90° DWs are curved along the *c* axis. These results indicate that ferroelectric and ferroelastic interactions across the Bi_2O_2 layers (along the *c* axis) are much smaller than those in the *a*–*b* plane, which leads to the curved 90° DWs only along the *c* axis.

14.4.3.2 Interaction Between Oxygen Vacancies and 90° Domain Walls

A possible origin of the complicated 90° DWs inside the crystals is the strong interaction between the 90° DWs and oxygen vacancies, which has been reported for perovskite-type ferroelectric oxides [12, 28, 97]. It has been demonstrated by ab initio studies [70, 120] that there is an electrostatic potential drop across the 90° DWs due to the spatial modulation of P_s, i.e., the discontinuity of the P_s component normal to the walls. This potential drop induces a charge double layer and the electric field near the 90° DWs exceeds 1 MV/cm for $BaTiO_3$ [120]. This electric field near the 90° DWs is expected to strongly interact with mobile charge such as oxygen vacancies, and the 90° DWs trap oxygen vacancies [12, 28, 97].

It has been demonstrated that oxygen vacancies are abundant in the perovskite layers in BiT [76]. In the temperature range from T_C to about 400°C, oxygen vacancies in the perovskite layers can move easily [106] and are stabilized near the 90° DWs due to the attractive interaction between them. Especially since the oxide-ion conductivity of BiT crystals are much higher along the *a*–*b* plane than along the *c* axis, the movement of the 90° DWs along the *a*(*b*) axis becomes viscous by the interaction with oxygen vacancies. When the crystals are cooled to room temperature, complicated structures of the 90° DWs are frozen before the flat 90° DWs with the (11*a*) plane which has already been established on the same *a*–*b* surface is not developed along the *c* axis. The strong interaction between the 90° DWs and oxygen vacancies in the BiT crystals is supported by the experimental fact that oxidation treatment (annealing at 950°C in air) led to a marked decrease in the number of the 90° DWs [48].

Here, 180° domains and their growth under the presence of the 90° DWs are discussed. PFM observations have shown that 180° domains have a plate-like structure originating from the anisotropic crystal structure of BiT. These thin 180° domains have also been identified during domain switching by applying an electric field along the *a* axis. The growth of the 180° domains is suggested to occur easily along the *a*–*b* plane compared with along the *c* axis. The *a*–*b* growth of some of the 180° domains (see "1" in Fig. 14.21) is terminated at the 90° DWs, which has been confirmed by the PFM observations on the *a*–*b* surface of another sample. The other 180° DWs ("2" and "3" in Fig. 14.21) go through the 90° DWs in the *a*–*b* plane, and this growth of the 180° domains is accompanied by the charged DWs at the edge of the thin 180° domains (also see Fig. 14.18b). These results imply that the 90° DWs act as a barrier against the growth of 180° domains along the *a*–*b* plane, because the 180° domain growth over the 90° DWs gives rise to the charged DWs with a high electrostatic energy density. It is suggested that the switching of the 180° domains is impeded by the presence of 90° DWs due to the charged DWs induced during the 180° domain growth along the *a*–*b* plane. In addition, the PFM observations of domain dynamics in the BiT crystals by applying an electric field along the *a*(*b*) axis have shown that the 90° DWs remained unchanged, whereas the electric-field application led to a marked change in the 180° domain structure. These experimental results indicate that the interaction between the 90° domain walls and oxygen vacancies plays a dominant role in the formation of the domain structures in the BiT crystals.

14.4.3.3 Summary

In $Bi_4Ti_3O_{12}$ crystals, energetically favorable 90° DWs were established on the same *a*–*b* surface, while 90° DWs showed a complicated and curved structure along the *c* axis inside the crystals. These curved DWs cannot be explained by the elastic energy minimization and are suggested to originate from the strong attractive interaction between the electric field near 90° DWs and oxygen vacancies. The knowledge of the ferroelectric domains obtained will be valuable for the further improvement of various macroscopic properties of Bi-layered ferroelectric materials.

14.4.4 90°-Domain Clamping in Ferroelectric $Bi_4Ti_3O_{12}$ Single Crystals

The phenomenon called "domain clamping," in which ferroelectric domains resist switching and become unswitchable under an applied electric field (E), is known to cause significant problems in ferroelectric memories and piezoelectric devices. Electrically charged defects such as oxygen vacancies, particularly, are thought to cause domain clamping [10, 12, 28, 95, 97], that is, to decrease switchable domains, which in turn leads to a low remanent polarization (P_r). Although several explanations have been offered for the mechanism of the interaction between such defects and various kinds of domain walls (DWs), it remains unclear how the behavior of ferroelectric domains is influenced by these defects owing to the difficulty involved in the direct observation of domain dynamics.

Bismuth titanate ($Bi_4Ti_3O_{12}$: BiT) has been regarded as a promising material for applications involving ferroelectric memories and piezoelectric devices operating at high temperatures. Although BiT possesses a large P_s, BiT-based ceramics and thin films often show poor polarization properties with a low P_r [45, 77, 78, 87]. During heat treatment, the vacancies of Bi and O are more or less formed in Bi-based ferroelectric oxides, including BiT. The vacancy formation of BiT at high temperatures [74, 83] is expressed by

$$2\mathrm{Bi}_{\mathrm{Bi}}^{\times} + 3\mathrm{O}_{\mathrm{O}}^{\times} \rightarrow 2\mathrm{V}'''_{\mathrm{Bi}} + 3\mathrm{V}_{\mathrm{O}}^{\bullet\bullet} + 2\mathrm{Bi}\ (\mathrm{gas}) + \frac{3}{2}\mathrm{O}_2\ (\mathrm{gas}), \tag{14.6}$$

where $\mathrm{V}'''_{\mathrm{Bi}}$ and $\mathrm{V}_{\mathrm{O}}^{\bullet\bullet}$ represent vacancies at the Bi site and the O site, respectively. This vacancy formation indicates that the concentration of $\mathrm{V}_{\mathrm{O}}^{\bullet\bullet}$, $[\mathrm{V}_{\mathrm{O}}^{\bullet\bullet}]$, is governed by that of $\mathrm{V}'''_{\mathrm{Bi}}$, $[\mathrm{V}'''_{\mathrm{Bi}}]$, as in the case of $BaTiO_3$ [7, 8, 93], in which $[\mathrm{V}_{\mathrm{O}}^{\bullet\bullet}]$ is mainly determined by the concentration of acceptor impurities. For BiT at high temperatures, the vacancy concentrations have been reported to vary according to oxygen partial pressure (Po_2) while the ratio of $[\mathrm{V}_{\mathrm{O}}^{\bullet\bullet}]/[\mathrm{V}'''_{\mathrm{Bi}}]$ is fixed at approximately 3/2 due to the charge neutrality restriction [83, 105]. These vacancies largely degrade the polarization properties even in bulk single crystals of BiT [76, 116]. Since the value of P_r is determined by the volume fraction of switchable domains obtained by applying E, a low P_r is caused by the clamping of the domains. The poor polarization properties observed for BiT single crystals suggests that domain clamping originates not from extrinsic factors such as grain boundaries in ceramics or strain effects of the substrates in thin films, but from the vacancies induced in the crystals.

Here, the structure and clamping of ferroelectric domains in BiT and $(Bi_{3.6}La_{0.4})Ti_3O_{12}$ (BLT) single crystals are shown. Piezoresponse force microscopy (PFM) observations provide direct evidence of the clamping of 90° domains during polarization switching. Experimental results and ab initio calculations show that an attractive interaction between 90° DWs and oxygen vacancies is the main origin of the clamping of 90° DWs in a BiT system.

14.4.4.1 Experiments

The experimental details are described in ref. [56]. Three grades of BiT crystals with different concentrations of the vacancies of Bi and O were prepared: "standard," "less-defective," and "more-defective" crystals. The details of their crystal growth and polarization properties are presented in Table 14.3. The crystals grown in air are denoted as "standard" BiT crystals. To obtain "less-defective" BiT crystals, as compared with the "standard" ones, Po_2 during crystal growth was controlled based on the defect chemistry at high temperatures. The vacancy formation reaction expressed by (14.6) is suppressed at a higher Po_2 and is accelerated at a lower Po_2 during heat treatment [116]. This allows us to change the concentrations of the vacancies in BiT crystals by controlling Po_2 during crystal growth. The standard BiT crystals were grown in air ($Po_2 = 0.02$ MPa), and the less-defective crystals were grown under an oxygen gas flow, i.e., $Po_2 = 0.1$ MPa. Since crystal growth at a higher Po_2 suppresses the vacancy formation reaction, less-defective crystals with lower $[V'''_{Bi}]$ and $[V_O^{\bullet\bullet}]$ could be realized, as compared to the standard BiT crystals. To remove the mechanical stress induced during crystal growth, the standard and less-defective crystals were annealed in air at 900°C for 10 h prior to electrical measurements and domain observation.

To obtain the more-defective crystals, heat treatment in a nitrogen gas flow at a Po_2 of 1×10^{-5} MPa at 1,000°C (nitrogen annealing) was performed on the standard crystals instead of the annealing treatment in air. Hereafter, this heat treatment in nitrogen gas is termed "defect-formation treatment." The results of thermogravimetric analysis [83, 105] have shown that vacancy formation (14.6) occurs above 1,000°C in a nitrogen gas flow. Defect-formation treatment at 1,000°C can introduce vacancies into the standard crystals, thereby producing the more-defective crystals that have a higher $[V'''_{Bi}]$ and $[V_O^{\bullet\bullet}]$ than the standard BiT crystals.

Single crystals of La-substituted BiT [$(Bi_{4-x}La_x)Ti_3O_{12}$: BLT] which were grown in air by using BLT powder and excess Bi_2O_3 powder were also prepared via a flux method [56], and then annealed in air at 900°C. The composition of the BLT crystals was determined to be $(Bi_{3.6}La_{0.4})Ti_3O_{12}$ ($x = 0.4$) by using inductively coupled plasma-atomic emission spectroscopy (ICP-AES). The preparation conditions of the BiT and BLT crystals in this study are listed in Table 14.3.

The domain structures of the crystals were observed by a commercial PFM unit (SII SPI3800N). Before the observation of domain structures, bipolar triangular waves with a maximum E of 80-100 kV/cm at a frequency of 1 Hz were applied to the crystals along the $a(b)$ axis at 25°C as a poling treatment. Since the condition of the poling treatment is the same as that for the measurement of polarization properties, the state of the domain structure observed is equivalent to that of the "$+P_r$" or "$-P_r$" state in the polarization hysteresis loops. Since the crystal structure of BiT has a monoclinic distortion ($B1a1$ space group) in the ferroelectric state, the P_s vector slightly tilts at an angle of 4–5° from the a axis to the c axis [91]. In this study, the major P_s component along the a axis to visualize three dimensional domain structure in the crystals, because the a-axis component of P_s (~50 μC/cm^2) is ten times as large as that along the c axis (4 μC/cm^2) [10].

Table 14.3 Preparation conditions and polarization properties of BiT and BLT crystals

Crystal	Crystal-growth condition	Defect-formation treatment	Annealing treatment	P_r (μC/cm^2)	E_c (kV/cm)
"Standard" BiT	Soaking: 1,200°C 10 h, slow cooling: ~1,000°C 40 h in air ($Po_2 = 0.02$ MPa)	–	900°C 10 h in air ($Po_2 = 0.02$ MPa)	43	32
"Less-defective" BiT	Soaking: 1,200°C 10 h, slow cooling: ~1,000°C 40 h in O_2 ($Po_2 = 0.1$ MPa)	–	900°C 10 h in air ($Po_2 = 0.02$ MPa)	45	30
"More-defective" BiT	Soaking: 1,200°C 10 h, slow cooling: ~1,000°C 40 h in air ($Po_2 = 0.02$ MPa)	1,000°C 10 h in N_2 ($Po_2 = 10^{-5}$ MPa)	–	30	45
BLT	Soaking: 1,200°C 10 h, slow cooling: ~1,000°C 40 h in air ($Po_2 = 0.02$ MPa)	–	900°C 10 h in air ($Po_2 = 0.02$ MPa)	36	42

14.4.4.2 Ab Initio Calculations

Ab initio calculations were performed to investigate the interaction between defects such as O vacancies and 90° DWs. Because modeling the 90° domain structure of BiT requires a huge supercell, tetragonal perovskite $PbTiO_3$ is chosen as a model material for the calculations. The calculations were conducted using DFT via the generalized gradient approximation [64] with a plane wave basis set. The details of the calculation method is described in the paper [56].

At first, an optimized supercell of the 90° DWs by carrying out the complete structural optimization of the starting supercell is obtained. Then, by using the optimized supercell, the 90° domain structures containing vacancies of Pb or O in order to investigate the interaction between the vacancies and the 90° DWs is prepared. In the supercell of $Pb_{12}Ti_{12}O_{36}$ with $Pmc2_1$ symmetry, all the constituent ions were positioned on the planes of $x = 0$ or 1/2 with a site multiplicity of two. That is, there were two equivalent ions in the supercell. Therefore, the $Pb_{12}Ti_{12}O_{36}$ supercell consisted of eighteen symmetrically different O ions and six symmetrically different Pb ions. For the modeling of the O-vacancy-containing supercell, two O ions at a symmetrically equivalent site were extracted from the optimized supercell. The O-vacancy-containing cells ($Pb_{12}Ti_{12}O_{34}$) were subjected to partial relaxation of the first- and second-nearest-neighbor ions around the vacancies within $Pmc2_1$ symmetry. Pb-vacancy-containing cells ($Pb_{10}Ti_{12}O_{36}$) were prepared and subjected to partial relaxation in the same manner.

Calculations of the total energy (E_{total}) of the vacancy-containing cell ($Pb_{12}Ti_{12}O_{34}$ and $Pb_{10}Ti_{12}O_{36}$) were conducted after the partial relaxation around the vacancies. By comparing the E_{total} with the vacancies in different positions, the stabilization energies of the 90° DWs induced by O vacancy and Pb vacancy were evaluated.

14.4.4.3 PFM Observations of Domain Switching Behavior in BiT Crystals

Figure 14.22 shows a PFM image observed on the *a*(*b*)–*c* surface (Fig. 14.22a) and the *a*–*b* surfaces (Fig. 14.22b) of the standard BiT crystals after poling treatment. The out-of-plane PFM image in the *a*(*b*)–*c* surfaces (Fig. 14.22a) reveals that a single-domain state was not established even after a much higher E (100 kV/cm) than the coercive field (E_c) of 32 kV/cm was applied in the poling treatment. A larger part of the crystals had a P_s parallel to the poling direction (the bright-colored domains in Fig. 14.22a), which indicates that the P_s in this part was switched by the poling treatment. Hereafter, the part with P_s parallel to the poling direction will be referred to as "switched domains." Along with the switched domains, unswitched 90° domains (the domains surrounded by dotted lines) with P_s normal to the poling direction were found in the poled crystals. In addition, 180° domains, i.e., the domains with P_s antiparallel to the poling direction (the dark-colored domains in Fig. 14.22a) were also observed in this PFM image.

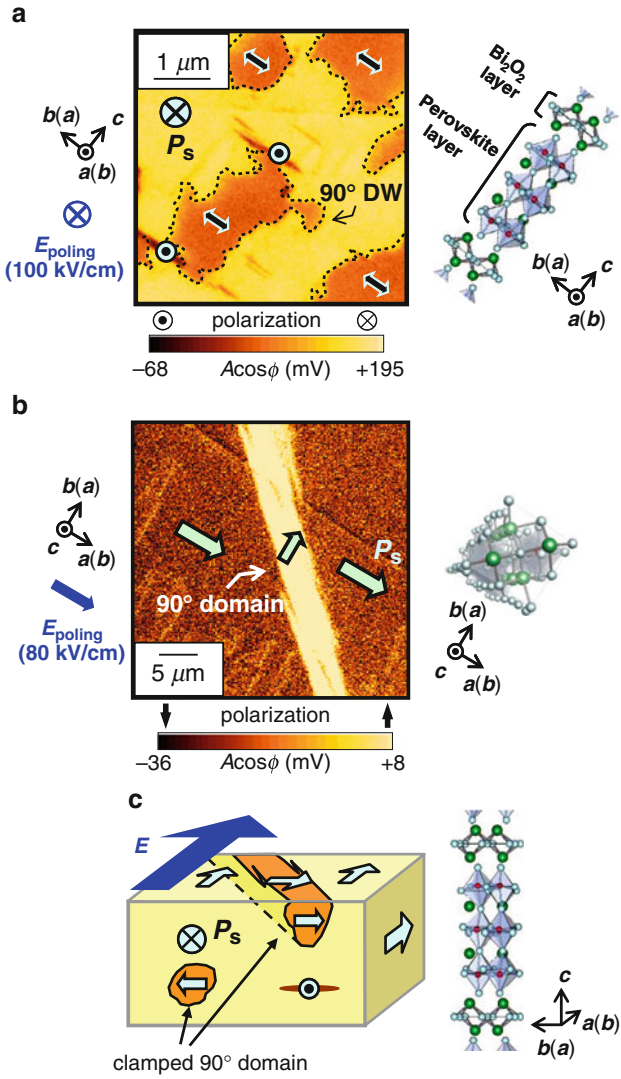

Fig. 14.22 (**a**) Out-of-plane PFM image on the *a*(*b*)–*c* surface, and (**b**) in-plane PFM image on the *a*–*b* surface of the standard BiT crystals (grown in air and annealed in air) after poling treatment. (**c**) Schematic three-dimensional domain structure of BiT after poling treatment. Poling treatment was conducted by applying a high electric field of 80–100 kV/cm along the *a*(*b*) axis at 25°C. The crystal structures shown in the figures in this article were drawn with the 3D visualization software VESTA

Figure 14.22b shows an in-plane PFM image on the *a*–*b* surface of the standard BiT crystals after poling treatment with an E of 80 kV/cm along the *a*(*b*) axis. As can be observed on the *a*(*b*)–*c* surfaces, an unswitched 90° domain was found on the *a*–*b* surfaces, manifesting as a bright-colored part in the middle of the image. Faceted (straight) 90° DWs were observed on the *a*–*b* surface of the BiT crystals before poling treatment (not shown) [55], while partially-curved 90° DWs were detected on the *a*–*b* surface of the poled crystals. Using these PFM observations a schematic three-dimensional domain structure in the poled BiT crystals can be obtained, as shown in Fig. 14.22c. Although the P_s vector in the larger part of the crystals was switched, the 90° DWs were strongly clamped, even after the application of an E that was much higher than E_c. The value of P_r is expressed by the following equation:

$$P_r = (1 - F_{90^\circ\ \mathrm{domain}} - 2F_{180^\circ\ \mathrm{domain}})P_s, \tag{14.7}$$

where $F_{90^\circ\ \mathrm{domain}}$ and $F_{180^\circ\ \mathrm{domain}}$ are the volume fractions of the clamped 90° domains and antiparallel 180° domains, respectively. Since $F_{90^\circ\ \mathrm{domain}}$ is much larger than $F_{180^\circ\ \mathrm{domain}}$ (see Fig. 14.22c), the clamping of 90° domains is proved to be responsible for the low P_r in BiT crystals.

Figure 14.23a shows an out-of-plane PFM image on the *a*(*b*)–*c* surfaces of the standard BiT crystals in which the poled domain structure (Fig. 14.22c) was partly switched by the following procedure: a high E of 100 kV/cm was applied to the crystals as the poling treatment, and then a moderate E of 31 kV/cm was applied in the direction antiparallel to the poling direction. Since the amplitude of the antiparallel E (31 kV/cm) is comparable to that of E_c (32 kV/cm), a partially-switched domain structure appears in Fig. 14.23a. While the 180° domains (dark-colored parts) grew markedly in Fig. 14.23a as compared to the poled domain structure in Fig. 14.22a, a significant difference in the form and size of the 90° domains was not observed either before (Fig. 14.22a) or after (Fig. 14.23a) the application of an antiparallel E.

Figure 14.23b schematizes the domain switching behavior in the standard BiT crystals. The comparison between the poled domain structure (Fig. 14.22a) and the partially-switched domain structure (Fig. 14.23a) indicates that polarization switching of BiT is achieved by the growth of 180° domains. It is interesting to note that the growth of the 180° domains proceeds markedly on the *a*–*b* plane compared to the growth along the *c* axis. This may be attributed to the Bi_2O_2 layers or stacking faults along the *c* axis, which act as a barrier to the growth of the 180° domains. In addition, no significant difference is found between unswitched 90° domains shown in Figs. 14.22a and 14.23a. This result strongly suggests that these 90° domains remained clamped during the polarization switching induced by the application of a much higher E (100 kV/cm) than E_c (32 kV/cm). Therefore, it is concluded that polarization switching is achieved by the growth of 180° domains with some 90° domains clamped in BiT crystals as shown in Fig. 14.23b.

Figure 14.24a-1–a-3 show the polarization properties of the standard, less-defective, and more-defective BiT crystals. While the standard crystals showed a

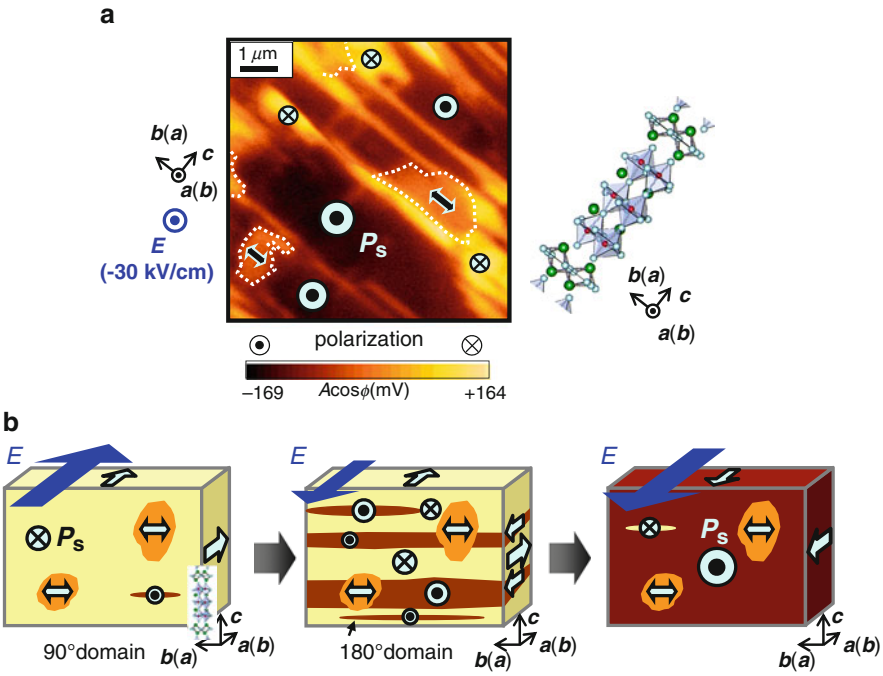

Fig. 14.23 (**a**) Out-of-plane PFM image on the $a(b)$–c surface of a poled BiT crystal (a standard one) after application of an electric field of 30 kV/cm antiparallel to the poling direction. (**b**) Schematic domain dynamics during polarization switching in BiT single crystals

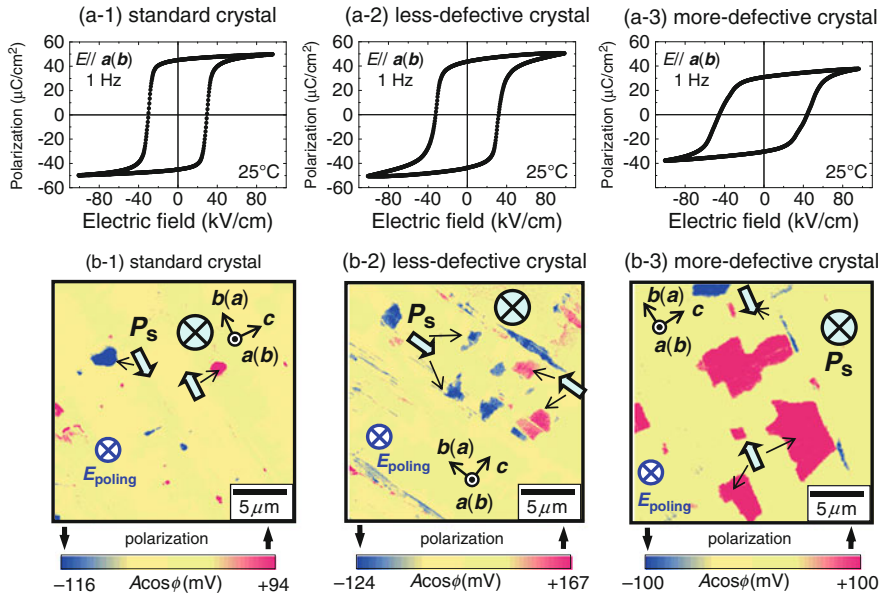

Fig. 14.24 Polarization hysteresis loops ((a-1)–(a-3)) and in-plane PFM images on the $a(b)$–c surfaces after poling treatment ((b-1)–(b-3)) of three grades of BiT crystals: standard crystals ((a-1) and (b-1)), less-defective crystals ((a-2) and (b-2)) and more-defective crystals ((a-3) and (b-3))

P_r of 43 μC/cm^2 (Fig. 14.24a-1), the less-defective crystals had a larger P_r of 45 μC/cm^2 (Fig. 14.24a-2). This result indicates that a higher Po_2 during crystal growth enhances polarization properties, which is consistent with the results previously reported [76, 116]. The more-defective crystals, in which the vacancy formation was promoted by the defect-formation treatment in nitrogen, exhibited a smaller P_r of 30 μC/cm^2 (Fig. 14.24a-3).

Figure 14.24b-1–b-3 show the in-plane PFM images on the *a*(*b*)–*c* surfaces of three grades of poled crystals: standard crystals (Fig. 14.24b-1), less-defective crystals (Fig. 14.24b-2), and more-defective crystals (Fig. 14.24b-3). Since only the 90° domains with P_s normal to the poling direction appear in the in-plane PFM signals for the poled crystals, the in-plane PFM observations can be used to visualize the clamped 90° domains remaining after the poling treatment. As the P_r value of the crystals was lower, the clamped 90° domains were enlarged, i.e., $F_{90^\circ\ \mathrm{domain}}$ increased. This result clearly indicates that the clamping of 90° domains is the origin of lowering P_r in BiT crystals.

Here, the formation of clamped 90° domains in the poled BiT crystals is discussed. As shown in Fig. 14.24, an increase in $F_{90^\circ\ \mathrm{domain}}$ and a resultant lower P_r were presented in the crystals to which a higher concentration of the Bi and O vacancies were induced during the preparation of the crystals. These results indicate that vacancies in the crystals are the origin of the 90°-domain clamping, providing a direct evidence of the interaction between the 90° DWs and the vacancies. As shown in Fig. 14.22c, the clamped 90° domains have a needle-like shape along the ⟨110⟩ direction and have irregularly-curved DWs. The configuration of these irregularly-curved 90° DWs has a large energy compared with that of a faceted 90° DW parallel to the (110) plane [21, 36, 40], as can be observed in certain perovskite-type ferroelectrics such as $BaTiO_3$ [69] and $PbTiO_3$ [58].

The substitution of La for BiT is well known to be an effective defect control measure to enhance polarization properties and fatigue endurance in the forms of thin films [87] and ceramics [77]. Since the vacancy formation in BLT is suppressed by the strong bonding between *A*-site cations (La ions) and oxygen ions [54], one can expect clamped 90° domains to be reduced in BLT crystals, as was observed in the less-defective BiT crystals. Figure 14.25a shows the polarization hysteresis loop of BLT crystals. Although the BLT crystals exhibited a well-saturated hysteresis loop, the value of P_r (36 μC/cm^2) was smaller than that of the standard BiT crystals (43 μC/cm^2). Figure 14.25b shows an in-plane PFM image of the *a*(*b*)–*c* surfaces of the BLT crystals after poling treatment, which visualizes the clamped 90° domains. Compared with the standard BiT crystals (Fig. 14.24b-1), the volume fraction of the clamped 90° domains was clearly reduced, and polarization switching was achieved in almost the entirety of each BLT crystal. These results also indicate that the smaller P_r observed in the BLT crystals can be attributed not to domain clamping but to the smaller P_s [54] of BLT. It is suggested that the larger P_r reported for ceramics and thin films of BLT can be attributed to a reduction of the clamped 90° domains beyond the disadvantage of the smaller P_s.

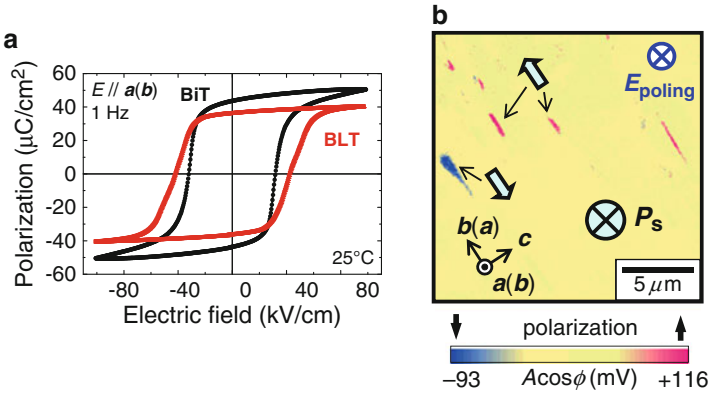

Fig. 14.25 (**a**) Polarization hysteresis loop of BiT and BLT single crystals grown in air and annealed in air. (**b**) In-plane PFM image of the *a*(*b*)–*c* surface of a poled BLT single crystal

14.4.4.4 Ab Initio Calculations of the Interaction Between the Vacancies and 90° DWs

Figure 14.26a exhibits the 90° domain structure of $PbTiO_3$ after structural optimization of the $Pb_{12}Ti_{12}O_{36}$ supercell, and Fig. 14.26b depicts the P_s vector of each perovskite $PbTiO_3$ unit. In this study, a $PbTiO_3$ unit is defined as a Ti-centered unit with six neighboring O shared by two units, and the eight neighboring Pb ions shared by eight units. The P_s value of the $PbTiO_3$ unit is evaluated by

$$P_s = \Sigma_j (w_j \times Q_j e \times u_j)/\Omega, \tag{14.8}$$

where the index j runs through all the constituent ions of the perovskite unit, w_j is the weight factor (1/8 for Pb, 1 for Ti, and 1/2 for O), Q_j is the valence number, e is the elementary charge, u_j is the displacement vector from the ideal cubic (nonpolar) position of each ion, and Ω is the volume of each perovskite unit. Here, the formal charge (+4 for Ti, +2 for Pb, and −2 for O) is adopted as Q_j. The structural optimization yields a reasonable 90° domain structure where the maximal angle of P_s with the z axis is 41.9°, which is in good agreement with the 40.4° reported in ref. [36]. In this study, the position of 90° DWs is defined as the z planes passing through the Ti ions (Pb-Ti-O planes) in which the angle that P_s forms with the z axis is almost zero (0.5°). The 90° DWs are shown as dashed lines in Figs. 14.5b and 14.26a.

Figure 14.27a presents the detailed crystal structure around the 90° DW in the optimized supercell. The tetragonal $PbTiO_3$ has two kinds of O: O_c and O_a. These oxygen atoms are determined by whether the bond between the O and the adjacent Ti is along the c axis (O_c) or the a axis (O_a) in the tetragonal unit cell. O_c has one short bond with the adjacent Ti, while O_a has two intermediate Ti–O bonds. The O_c and O_a are distinguished in the supercell of the 90° DW in the same manner. In addition, there are two kinds of O_a in the 90° domain structure: one is on the

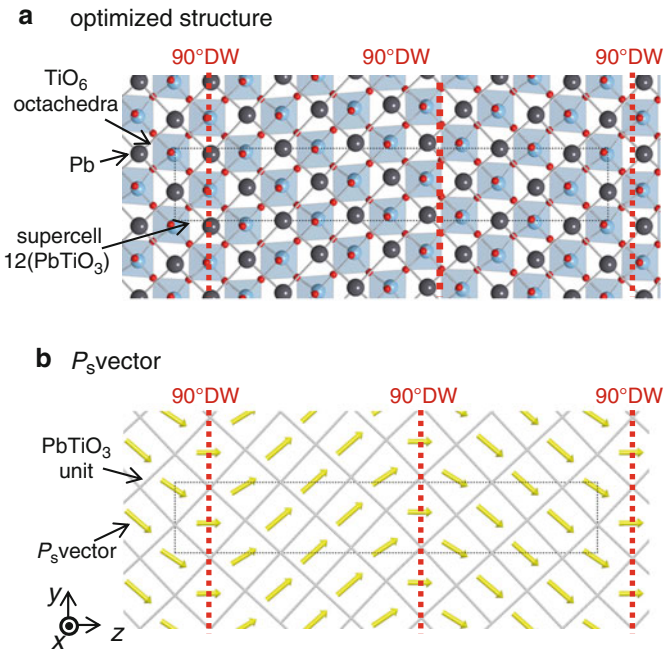

Fig. 14.26 (**a**) 90° domain structure after full atomic relaxation, and (**b**) P_s vector of each perovskite $PbTiO_3$ unit in the 90° domain structure

Pb-Ti-O plane (O_a^* unmarked in Fig. 14.27a) and the other is on the O–O plane parallel to the 90° DW (O_a marked in Fig. 14.27a). An extremely larger supercell along the x axis is required in order to properly calculate the E_{total} for the O_a^* vacancies. The E_{total} for the O_a^* vacancies is overestimated for the supercell adopted in this study, because Ti has to have two neighboring O_a^* vacancies in this supercell. Thus, the O_a^* vacancies are ruled out in the calculations.

Figure 14.27b shows the relative E_{total} with respect to the distance of the O vacancies from the 90° DW. The calculations show that the supercells with O vacancies near the 90° DW have a lower relative E_{total}. Note that the minimum of the relative E_{total} is found to lie at the adjacent O_c site at a distance of 0.1 nm from the 90° DW. The stabilization energy of the 90° DW induced by the O vacancy, corresponding to the depth of the minimum in the energy curve shown in Fig. 14.27a, is calculated to be 0.27 eV/cell (0.13 eV/vacancy). Meyer and Vanderbilt [70] have reported that the energy barrier for the motion of 90° DW in defect-free $PbTiO_3$ crystals evaluated in their DFT calculations is less than 1.6 mJ/m^2, which corresponds to 4.4×10^{-3} eV/cell. The stabilization energy of the 90° DW induced by the O vacancy (0.27 eV/cell) is much higher than 4.4×10^{-3} eV/cell for the energy barrier for the motion of 90° DWs without O vacancy. These calculation results indicate that a 90° DW is stabilized by the adjacent O vacancies at the O_c site.

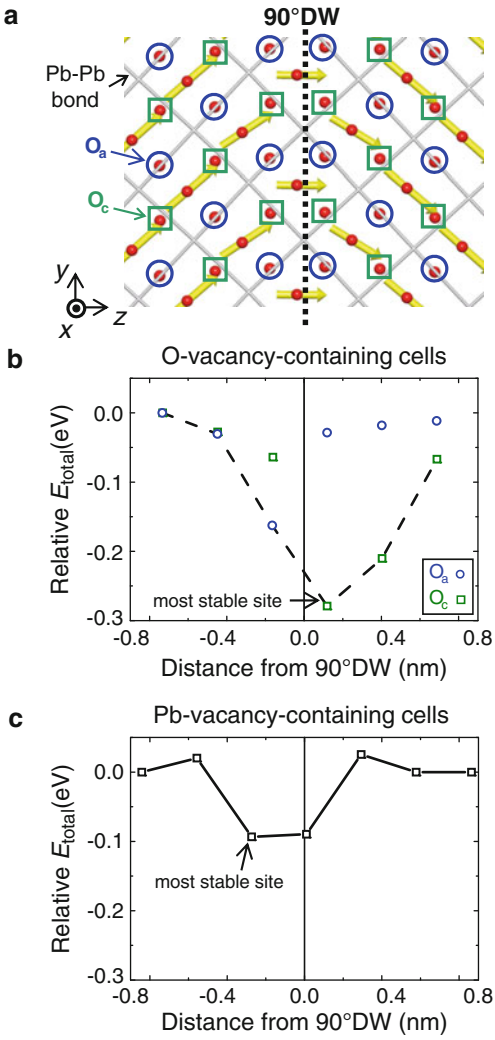

Fig. 14.27 (**a**) Detailed structure and polarization direction around the 90° DW with oxygen sites divided into three groups, and relative E_{total} of (**b**) O-vacancy-containing and (**c**) Pb-vacancy-containing cells as a function of the distance between the vacancy site and the 90° DW

Figure 14.27c shows the relative E_{total} for the Pb-vacancy-containing supercells. The results exhibit a slightly lower value for the relative E_{total} when the Pb vacancy neighbors are near to the 90° DW. The stable site of the Pb vacancy was found to be at or on the left side of the 90° DW, as indicated in Fig. 14.27c. The stabilization energy of the Pb vacancy is estimated to be 0.09 eV/cell (0.04 eV/vacancy), which is much smaller than that of the O vacancy.

It is interesting to note that the stable sites for the vacancies of O and Pb are positioned on the different sides of the 90° DW. The O vacancies are positively charged, while the Pb vacancies are negatively charged in the lattice. These results suggest that one of the major origins of the stabilization of the 90° DW by the adjacent vacancies is an electrostatic interaction between the charge of the vacancies and the

electrostatic potential modulated across the 90° DW. Theoretical calculations [70, 115] have shown that the component of P_s normal to 90° DWs is smaller at the 90° DWs than it is inside the bulk crystals. The decrease in the P_s component leads to a modulation of the electrostatic potential, according to Poisson's equation, so that an electric field produced by the partial differentiation of the electrostatic potential is built in across the 90° DW. This built-in electric field near the 90° DW has been reported to be as high as 1 MV/cm for $BaTiO_3$ [120]. The modulation of the electrostatic potential near the 90° DW yields an attractive interaction with the charged vacancies. Positively and negatively charged species energetically prefer to reside at the maximum and minimum sites of the electrostatic potential near the 90° DWs, respectively. This electrostatic interaction provides the stable sites of the vacancies of O and Pb adjacent to, but on different sides of the 90° DW. Our calculations of P_s (see Fig. 14.26b) show that the component of P_s along the z axis is suppressed at the 90° DWs by 1.2 μC/cm^2, which is comparable with the reported value [70]. This suppression of the P_s component results in a local modulation of the electrostatic potential near the 90° DW. The attractive interaction between the defect charge and the electrostatic potential modulation is considered one of the major origins of the stabilization of the 90° DW by O vacancies.

The O-vacancy-containing supercells in this study have a much high concentration of O vacancy (approximately 5.6%) than real ferroelectric oxide. For real $PbTiO_3$, the maximal concentration of O vacancy has been reported to be 3.3% [30], and the actual concentration of O vacancy is considered to be around 1%. However, oxygen vacancies can diffuse with random walk because they have sufficient mobility to migrate, even at room temperature. Furthermore, the migration of oxygen vacancies is accelerated by the application of an electric field during polarization switching. If an O vacancy gets within an effective range of the attractive interaction from 90° DW once, the O vacancy can readily find the most stable site adjacent to the 90° DW. The O vacancy is then trapped and cannot easily escape from the stable site. In addition, O vacancies can accumulate and form a defect plane at the 90° DW, because 90° DWs have a stable site of O vacancy in each $PbTiO_3$ unit cell. These 90° DWs, coupled with a defect plane composed of O vacancies, are expected to be strongly clamped and can no longer be moved through the application of an electric field.

14.4.4.5 Interaction Between the O Vacancies and 90° DWs in BiT System

Here, the origin of 90°-domain cramping observed in BiT crystals is discussed. From the calculated data for $PbTiO_3$, a similar interaction between 90° DWs and O vacancies is also suggested for BiT as well. The component of P_s normal to the 90° DW for $PbTiO_3$ (see Fig. 14.26b) is suppressed at the 90° DW, which is caused mainly by the strain caused by the vending of P_s across the 90° DW. The suppression of the P_s component leads to a modulation of the electrostatic potential. Because 90° DWs in BiT should have a similar modulation of electrostatic potential, the stable sites of O vacancies are present near the 90° DWs for BiT as well.

The formation energy of O vacancies differs in the Bi_2O_2 and the perovskite layers, because BiT crystals are composed of a regular stacking of the Bi_2O_2 layers and the perovskite layers of $Bi_2Ti_3O_{10}$. High-resolution synchrotron X-ray and neutron diffraction analyses show that O vacancies are abundant in the perovskite layers [76]. These results show that the stable sites of O vacancies are mainly in the perovskite layers, due to the weak bonding between Bi at the *A* site and O. A high concentration of O vacancies provides high oxide-ion conduction in BiT single crystals in the *a*–*b* plane, which indicates the presence of a fast diffusion path of O vacancies in the perovskite layers [105]. This fast diffusion path of O vacancies enhances the accumulation of O vacancies near 90° DWs, which then lead to the clamping of the 90° DWs in BiT crystals.

Another factor that may contribute to the strong clamping of 90° DWs is the high T_C of 675°C for BiT. In the temperature range from T_C to about 400°C, O vacancies in the perovskite layers can migrate much faster than they can at room temperature. Therefore, the probability that O vacancies get within an effective range of the attractive interaction from 90° DWs becomes high at high temperatures. As a result, a high concentration of O vacancies accumulates near 90° DW, and the 90° DWs are strongly clamped by O vacancies.

At high temperatures below T_C, not only O vacancies but also 90° DWs have high mobility in BiT crystals. The interaction between O vacancies and 90° DWs is considered to affect the domain structure and the clamping of 90° DWs. As described above, the oxide-ion conductivity of BiT crystals is much higher in the *a*–*b* plane than along the *c* axis, and the movement of the 90° DWs along the *a*(*b*) axis then becomes viscous due to the interaction with O vacancies. When the crystals are cooled to room temperature, the complicated structures of the 90° DWs are frozen before flat (faceted) 90° DWs with the (110) plane are developed throughout the crystals, as observed in as-grown BiT crystals. It is likely that some parts of the 90° DWs in the cooled crystals have already been clamped before the poling treatment, due to a local accumulation of O vacancies in the 90° DWs at high temperatures below T_C. The migration of O vacancies during cooling at high temperatures and in the subsequent domain switching induced by the application of an electric field at room temperature leads to a complicated structure of the clamped 90° domains observed in the poled crystals (see in Figs. 14.22–14.24).

One indirect way to verify the influence of O vacancies on the clamping of 90° DWs is the quenching of BiT at high temperatures above T_C. If the samples are quenched by high temperatures above T_C to room temperature, the clamping strength of 90° DWs by O vacancies can be expected to be reduced because of the low probability that the O vacancies will meet 90° DWs. Noguchi et al. [77] have reported that the value of P_r in BiT ceramics quenched at 800°C in an N_2 atmosphere was almost twice as large as that of BiT ceramics that were slowly cooled in air. In addition, BiT ceramics quenched at 800°C in an O_2 atmosphere exhibited almost the same P_r as those quenched at 800°C in an N_2 atmosphere. These results clearly show that the clamping of 90° DWs by O vacancies is governed not only by the total concentration of O vacancies, but also by the

diffusion process of O vacancies below T_C. The marked influence of the diffusion process of O vacancies suggests that the concentration of O vacancies near 90° DWs determines the clamping strength of the 90° DWs. It is concluded that the strong attractive interaction with O vacancies is the origin of the domain clamping of 90° DWs in a BiT system.

14.4.4.6 Summary

The structure and clamping of ferroelectric domains in single crystals of BiT and BLT were investigated through polarization measurements along the *a*(*b*) axis and PFM. It has been shown that polarization switching is achieved by the growth of 180° domains and that unswitched 90° domains with clamped DWs lead to a low remanent polarization. The formation of the vacancies of Bi and O in BiT crystals at high temperatures increased the volume fraction of the clamped 90° domains and thereby lowered the remanent polarization. BLT crystals exhibited a remarkable decrease in the volume fraction of the clamped 90° domains, which is responsible for the superior polarization properties observed in BLT ceramics and films. Ab initio calculations of $PbTiO_3$ showed that oxygen vacancy is stabilized adjacent to the 90° DW by 0.13 eV/vacancy mainly due to an attractive interaction between an electrostatic potential modulation near the 90° DW and O vacancies. A large stabilization energy of oxygen vacancies near 90° DWs, along with the high mobility of oxygen vacancies along the *a*–*b* plane, were suggested to be the origin of the strong clamping of 90° DWs in BiT crystals. It is concluded that the clamping of 90° DWs in BiT originates from a strong attractive interaction with the oxygen vacancies trapped at stable sites adjacent to the 90° DWs.

14.4.5 High-Oxygen-Pressure Crystal Growth of $Bi_4Ti_3O_{12}$ Single Crystals

Here, high-oxygen-pressure crystal growth is shown to be an effective process for obtaining high-quality BiT crystals with a large P_r and low coercive field (E_c) as well as low leakage current. Domain observations by piezoresponse force microscope (PFM) demonstrate that the clamping of 90° domains deteriorates P_r for the crystals grown at 0.02 MPa oxygen, which is suggested to originate from the strong attractive interaction [12, 28, 120] between 90° domain walls and oxygen vacancies. The vacancy formation of Bi and O during crystal growth at high temperatures is suppressed at a higher oxygen pressure, leading to a larger P_r of 47 μC/cm^2 and lower E_c of 26 kV/cm for the crystals grown at 1 MPa oxygen.

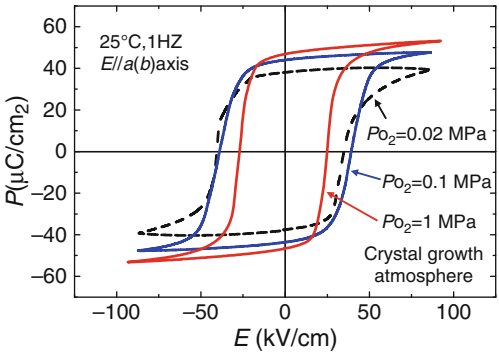

Fig. 14.28 Polarization hysteresis loops along the $a(b)$-axis for the BiT crystals grown at a Po_2 of 0.02, 0.1, and 1 MPa. These crystals were annealed at 900°C for 10 h in air. The measurements were conduced at 25°C using an E at a frequency of 1 Hz

14.4.5.1 Crystal Growth, Structural Analysis, and Property Measurements

The experimental details are described in the paper [116]. The crystals were grown in air ($Po_2 = 0.02$ MPa) and under O_2 gas flow of $Po_2 = 0.1$ MPa. High-oxygen-pressure crystal growth was performed using the pocketed-heat electronic furnace (HPF-1300, Crystal Systems Corp.) at a Po_2 of 1 MPa (Po_2 denotes oxygen pressure during crystal growth hereafter). The mixed raw materials were soaked at 1,200°C for 10 h in Pt crucible, slowly cooled to 1,000°C for 40 h, and then furnace cooled to room temperature. Before electrical measurements and domain observations by PFM, the crystals were annealed at 950°C for 10 h in air to reduce strain induced during crystal growth. The BiT crystals under different Po_2 atmosphere had almost the same lattice parameters: $a = 0.545\ 05(5)$ nm, $b = 0.541\ 08(4)$ nm, $c = 3.283\ 4(3)$ nm. Significant difference in lattice parameters was not detected, because the concentration of Bi vacancies and oxygen vacancies is expected to be less than 1% [76, 77].

For the domain observations by PFM, the crystals annealed in air were cut along the $a(b)$-axis, and the cut surface (the $a(b)$–c plane) was mechanically polished using alumina powder followed by colloidal silica. Domain structures were observed by a commercial PFM unit (SII SPI3800N). Since BiT belongs to the monoclinic system with $B1a1$ symmetry, the P_s vector slightly tilts at an angle of ~5° from the a-axis in the a–c plane [10, 91]. Here, the major P_s component along the a axis [$P_{s(a)}$] is focused to visualize domain structure, because $P_{s(a)}$ is ten times as large as P_s along the c axis [10, 55, 91].

14.4.5.2 Effect of Po_2 During Crystal Growth

Figure 14.28 shows the polarization hysteresis loops measured along the $a(b)$-axis (25°C, 1 Hz). The crystals ($Po_2 = 0.02$ MPa) exhibited a hysteresis with a P_r of 38 μC/cm^2 and an E_c of 38 kV/cm. The high-Po_2-grown crystals indicated a larger P_r of 44 μC/cm^2 ($Po_2 = 0.1$ MPa) and 47 μC/cm^2 ($Po_2 = 1$ MPa). Note that the crystals ($Po_2 = 1$ MPa) showed a well-saturated polarization hysteresis with an E_c of 26 kV/cm. This E_c value was much lower than those of the other crystals.

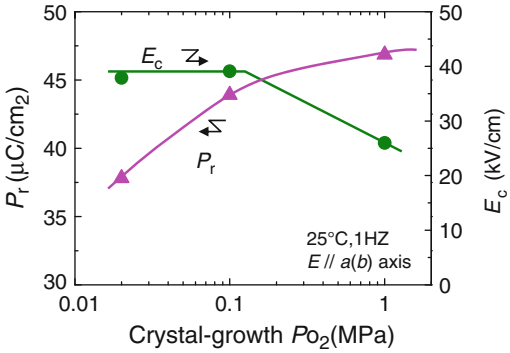

Fig. 14.29 Remanent polarization (P_r) and coercive field (E_c) as a function of Po_2 during crystal growth (25°C, 1 Hz). The values of P_r and E_c are average in positive and negative regions in the polarization hysteresis loops (Fig. 14.28)

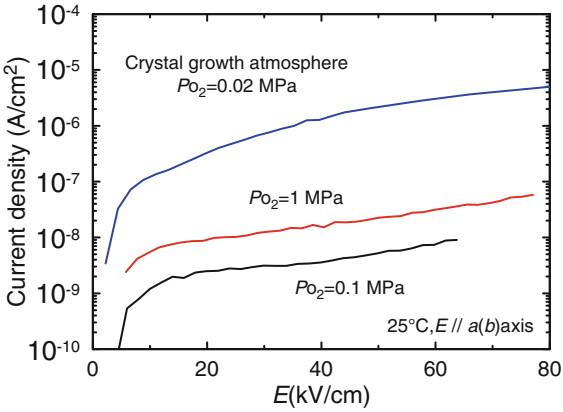

Fig. 14.30 Leakage current density (J) as a function of E along the a(b)-axis for the BiT crystals (25°C, 1 Hz)

Figure 14.29 shows the P_r and E_c as a function of Po_2 during crystal growth. With increasing Po_2, P_r monotonically increased, while the decrease in E_c was marked over $Po_2 = 0.1$ MPa.

Figure 14.30 shows the leakage current density (J) as a function of E along the a (b)-axis (25°C). The crystals ($Po_2 = 0.02$ MPa) indicated a high J of the order of 10^{-7} to 10^{-6} A/cm^2. The increase in Po_2 to 0.1 MPa led to a drastic decrease in J to the order of 10^{-9} A/cm^2. The crystals ($Po_2 = 1$ MPa) exhibited a relatively low J of the order of 10^{-8} A/cm^2.

Here, the defect formation of BiT at high temperatures is considered. Ab initio calculations [76, 83] within DFT have suggested that vacancy formation energy of Bi1 in the perovskite layers is lower by about 2 eV than that of Bi2 in the Bi_2O_2 layers. This result indicates that the vacancy formation of Bi proceeds preferentially at the Bi1 site rather than at the Bi2 site. The trigger of defect formation of BiT at high temperatures is suggested to be the formation of Bi1 vacancy (V'''_{Bi1}), which is accompanied by the formation of oxygen vacancy ($V_O^{\bullet\bullet}$) adjacent to Bi1 [83].

The vacancy formation of BiT at high temperatures is expressed by (14.6). This reaction of the vacancy formation has been reported to occur above 1,000°C in air [76].

It is interesting to note that the weight loss caused by the formation of V'''_{Bi1} and $V_O^{\bullet\bullet}$ at high temperatures are reduced under a higher Po_2 atmosphere [76]. The Po_2 dependence of weight loss indicates that the limiting factor of the vacancy formation is not diffusion of the vacancies inside the crystals but surface reaction on the crystal surface. The following model of the vacancy formation of BiT is proposed [83]. Two Bi_{Bi1}^{*} and three O_O^{*} in the perovskite layers migrate to the surface of BiT crystals, but do not react with each other because of the low possibility of Bi_{ad} to meet O_{ad} on the surface due to the low vacancy concentrations, where Bi_{ad} and O_{ad} are adsorbed Bi and O on the surface. At a relatively high Po_2, Bi_{ad} reacts with O_2 (gas) in the atmosphere promptly and evaporates as Bi_2O_3 (gas). In reducing atmosphere, Bi_{ad} detaches from the surface as Bi (gas). These reactions proceed quickly and do not limit the vacancy formation of (14.6). In contrast, O_{ad} has to meet another O_{ad} on the surface to form an O_2 molecule, and then diffuses to the atmosphere. The reaction related to O_{ad} that is suppressed at a higher Po_2 is the limiting factor of the vacancy formation. Consequently, a higher-Po_2 atmosphere during crystal growth is effective for synthesizing high-quality BiT crystals with less V'''_{Bi1} and $V_O^{\bullet\bullet}$.

During cooling or annealing below 1,000°C, in which the vacancy formation does not occur, BiT crystals absorb oxygen from the ambient and the following oxidation reaction produces electron hole ($h^{\bullet}$) as (14.5). The carrier of the leakage current at room temperature has been reported to be $h^{\bullet}$ generated by (14.5) [76]. As discussed above, the crystals grown under a lower Po_2 have a higher concentration of $V_O^{\bullet\bullet}$, $[V_O^{\bullet\bullet}]$, because the vacancy formation of (14.6) is accelerated under a lower Po_2. Thus the crystals ($Po_2 = 0.02$ MPa) with a higher $[V_O^{\bullet\bullet}]$, have a higher $[h^{\bullet}]$, leading to a higher J (see Fig. 14.30). Although the crystals ($Po_2 = 1$ MPa) with low $[V_O^{\bullet\bullet}]$ is expected to exhibit a low J, they showed a slightly higher J compared with the crystals ($Po_2 = 0.1$ MPa). The value of J is determined by two factors: $[V_O^{\bullet\bullet}]$ and the excess oxygen generated by the oxidation reaction (14.2). The slightly higher J observed for the crystals ($Po_2 = 1$ MPa) is probably due to a larger amount of the excess oxygen generated by the annealing at 950°C in air before measurements.

14.4.5.3 Domain Structure

The mechanism of the domain clamping during the polarization switching along the $a(b)$-axis is discussed. Figure 14.31 shows the PFM images observed on the $a(b)$–c surface of the crystals ($Po_2 = 0.02$ MPa). The in-plane PFM image of the as-annealed crystals (nonpoled crystals) (Fig. 14.31a) exhibits 180° DWs parallel to the a–b plane. After an E of 100 kV/cm was applied along the $a(b)$-axis at 25°C, the out-of-plane PFM image of the poled crystals was observed (Fig. 14.31b).

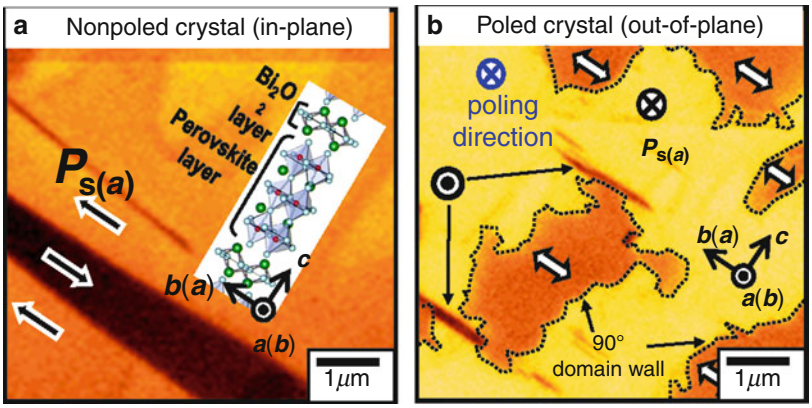

Fig. 14.31 PFM images of the $a(b)$–c surface of the BiT crystals grown in air ($Po_2 = 0.02$ MPa); (**a**) in-plane image of the nonpoled (as-annealed) crystal, and (**b**) out-of-plane image of the poled crystal. The poling was conducted by applying an E of 100 kV/cm along the $a(b)$-axis at 25°C

A single domain state was not established for the poled crystals even though the applied E (100 kV/cm) is much higher than the E_c value (38 kV/cm). The domains with $P_{s(a)}$ parallel to the poling direction were found. This experimental fact is direct evidence that 90° domain switching is achieved by applying an E of 100 kV/cm. Note that unswitched regions, i.e., 90° domains with $P_{s(a)}$ normal to the poling direction remained, and 90° DWs with irregular structure appeared. The irregular-shaped 90° DWs have been reported to originate from the attractive interaction [12, 28, 120] between $V_O^{\bullet\bullet}$ and the electric field established near the 90° DWs due to the discontinuity of the P_s component normal to the DWs. In the domains with $P_{s(a)}$ parallel to the poling direction, a small number of 180° domains with $P_{s(a)}$ antiparallel to the poling direction were observed. These 180° domains are a result of the domain backswitching due to depolarization field. Our PFM observations lead to the conclusion that the clamping of 90° DWs plays a detrimental role in the $P_{s(a)}$ polarization switching in the BiT crystals. The vacancy formation at high temperatures is suppressed under a higher-Po_2 atmosphere, and then $[V_O^{\bullet\bullet}]$ becomes lower for the crystals grown at a higher Po_2 [76, 83]. The larger P_r observed for the crystals ($Po_2 = 1$ MPa) is found to originate from suppressed 90° domain clamping because of a lower $[V_O^{\bullet\bullet}]$.

14.4.5.4 Summary

The effects of Po_2 during crystal growth of BiT on the domain switching behaviors have been shown through polarization measurements and domain observations by PFM. The crystals grown at a high Po_2 of 1 MPa showed a large P_r of 47 μC/cm^2 and low E_c of 26 kV/cm. PFM observations demonstrate that the clamping of 90° DWs plays a detrimental role in polarization switching, leading to a low P_r.

High-Po_2 sintering is proposed to be the effective process for suppressing the formation of the vacancies of Bi and O, leading to high-quality BiT-based devices with enhanced polarization-switching properties as well as low leakage current.

14.5 Conclusions and Future Trend

The crystal structure and ferroelectric polarization of BLSFs were briefly reviewed and the crystal growth, defect structure, domain structure, polarization, and leakage-current properties along the *a* axis were shown for the single crystals of Bi_2WO_6 ($m = 1$), $SrBi_2Ta_2O_9$ ($m = 2$), and $Bi_4Ti_3O_{12}$ ($m = 3$).

For Bi_2WO_6 crystals, the carrier of leakage current is found to be electron and the doping of Mn and subsequent annealing are effective for enhancing polarization switching properties. Oxygen vacancies are suggested to play a minor role in the polarization properties and suppressing leakage current is essential for the polarization switching in the BW system.

For $SrBi_2Ta_2O_9$ crystals, the defect-engineering approach was demonstrated to be effective for enhancing P_s. The defect engineering is based on the substitution of Bi^{3+} at the *A* site with Sr vacancies. The enhanced P_s observed for defect-engineered $SrBi_2Ta_2O_9$ crystals was suggested to originate from the orbital hybridization of perovskite *A* cations and O 2*p*.

For $Bi_4Ti_3O_{12}$ crystals, suppressing vacancy formation of Bi and O at high temperatures was shown to be crucial for obtaining high-quality and high-performance crystals. The results of the leakage current properties revealed that electron holes arising from oxidation reaction act as detrimental carriers for leakage current. A large stabilization energy of oxygen vacancies near 90° domain walls, along with the high mobility of oxygen vacancies along the *a*–*b* plane, were suggested to be the origin of the strong clamping of 90°domain walls in $Bi_4Ti_3O_{12}$ crystals. High-Po_2 sintering or crystal growth was proposed to be the effective process for suppressing the formation of the vacancies of Bi and O, leading to high-quality $Bi_4Ti_3O_{12}$-based devices with enhanced polarization-switching properties.

Recently, high-Po_2 crystal growth has been demonstrated to be effective also for Bi-based perovskite ferroelectrics of (Bi, Na)TiO_3 [117]. Furthermore, in the (K,Na)NbO_3 system, vacancy formation of K has been shown to deteriorate polarization and leakage current properties of their crystals [57]. It is expected that ferroelectric and piezoelectric properties are markedly enhanced by defect engineering, the control of vacancy concentrations, for ferroelectric oxides including volatile elements such as Bi, Pb, K, etc.

Acknowledgment A series of the study in this chapter was partly supported by Grant-in Aid for Scientific Research on Priority Areas "Novel States of Matter Induced by Frustration" (19052002), Grant-in-Aid for Scientific Research(A) (21246096) and the Fundamental R&D Program for Core Technology of Materials funded by the Ministry of Knowledge Economy, Republic of Korea.

References

1. Arlt G (1990) The influence of microstructure on the properties of ferroelectric ceramics. Ferroelectrics 104:217–227
2. Atsuki T, Soyama N, Yonezawa T, Ogi K (1995) Preparation of Bi-based ferroelectric thin-films by sol-gel method. Jpn J Appl Phys 34(9B):5096–5099
3. Barad Y, Lettieri J, Theis CD, Schlom DG, Gopalan V, Jiang JC, Pan XQ (2001) Probing domain microstructure in ferroelectric $Bi_4Ti_3O_{12}$ thin films by optical second harmonic generation. J Appl Phys 89(2):1387–1392
4. Baux N, Vannier RN, Mairesse G, Nowogrocki G (1996) Oxide ion conductivity in Bi2W1-xMExO6-x/2 (ME=Nb, Ta). Solid State Ionics 91(3–4):243–248
5. Blochl PE (1994) Projector augmented-wave method. Phys Rev B 50(24):17953–17979
6. Cao W, Cross LE (1991) Theory of tetragonal twin structures in ferroelectric perovskite with a first-order phase transition. Phys Rev B 44(1):5–12
7. Chan NH, Sharma RK, Smyth DM (1981) Non-stoichiometry in undoped Batio3. J Am Ceram Soc 64(9):556–562
8. Chen J, Harmer MP, Smyth DM (1994) Compositional control of ferroelectric fatigue in perovskite ferroelectric ceramics and thin-films. J Appl Phys 76(9):5394–5398
9. Cohen RE (1992) Origin of ferroelectricity in perovskite oxides. Nature 358:136–138
10. Cummins SE, Cross LE (1968) Electrical and optical properties of ferroelectric $Bi_4Ti_3O_{12}$ single crystals. J Appl Phys 39(5):2268–2274
11. Das RR, Bhattacharya P, Perez W, Katiyar RS, Desu SB (2002) Ferroelectric properties of laser-ablated $Sr_{1-x}A_xBi_2Ta_2O_9$ thin films (where A=Ba, Ca). Appl Phys Lett 80(4):637–639
12. Dawber M, Scott JF (2000) A model for fatigue in ferroelectric perovskite thin films. Appl Phys Lett 76(8):1060–1062
13. Deleprevier AG, Payne DA (1981) Flux growth of bismuth tungstate, Bi_2WO_6. J Crystal Growth 54(2):217–222
14. Desu SB, Vijay DP (1995) Novel fatigue-free layered structure ferroelectric thin-films. Mater Sci Eng B 32(1–2):75–81
15. Ding Y, Liu JS, Qin HX, Zhu JS, Wang YN (2001) Why lanthanum-substituted bismuth titanate becomes fatigue free in a ferroelectric capacitor with platinum electrodes. Appl Phys Lett 78(26):4175–4177
16. Drougard ME, Young DR (1954) Domain clamping effect in barium titanate single crystals. Phys Rev 94(6):1561–1564
17. Duiker HM, Beale PD, Scott JF, Paz de Araujo CA, Melnick BM, Cuchiaro JD, McMillan LD (1990) Fatigue and switching in ferroelectric memories: theory and experiment. J Appl Phys 68(11):5783–5791
18. Dunitz JD, Orgel LE (1960) Stereochemistry of ionic solids. Adv Inorg Chem 2:1–60
19. Eng LM (1999) Nanoscale domain engineering and characterization of ferroelectric domains. Nanotechnology 10(4):405–411
20. Feng D, Ming NB, Hong JF, Yang YS, Zhu JS, Yang Z, Wang YN (1980) Enhancement of 2nd-harmonic generation in $LiNbO_3$ crystals with periodic laminar ferroelectric domains. Appl Phys Lett 37(7):607–609
21. Fousek J, Janovec V (1969) Orientation of domain walls in twinned ferroelectric crystals. J Appl Phys 40(1):135–142
22. Frit B, Mercurio JP (1992) The crystal-chemistry and dielectric-properties of the aurivillius family of complex bismuth oxides with perovskite-like layered structures. J Alloys Compd 188(1–2):27–35
23. Garg A, Barber ZH, Dawber M, Scott JF, Snedden A, Lightfoot P (2003) Orientation dependence of ferroelectric properties of pulsed-laser-ablated $Bi_{4-x}Nd_xTi_3O_{12}$ films. Appl Phys Lett 83(12):2414–2416
24. Gonzalez A, Jimenez R, Mendiola J, Alemany C, Calzada ML (2002) Ultrathin ferroelectric strontium bismuth tantalate films. Appl Phys Lett 81(14):2599–2601

25. Goto T, Noguchi Y, Soga M, Miyayama M (2005) Effects of Nd substitution on the polarization properties and electronic structures of bismuth titanate single crystals. Mater Res Bull 40(6):1044–1051
26. Hamada M, Tabata H, Kawai T (1997) Microstructure and dielectric properties of epitaxial Bi_2WO_6 deposited by pulsed laser ablation. Thin Solid Films 306(1):6–9
27. Hayashi K, Ando A, Hamaji Y, Sakabe Y (1998) Study of the valence state of the manganese ions in $PbTiO_3$ ceramics by means of ESR. Jpn J Appl Phys 37(9B):5237–5240
28. He LX, Vanderbilt D (2003) First-principles study of oxygen-vacancy pinning of domain walls in $PbTiO_3$. Phys Rev B 68(13):134103
29. Hervoches CH, Lightfoot P (1999) A variable-temperature powder neutron diffraction study of ferroelectric $Bi_4Ti_3O_{12}$. Chem Mater 11(11):3359–3364
30. Holman RL, Fulrath RM (1973) Intrinsic nonstoichiometry in lead zirconate lead titanate system determined by Knudsen effusion. J Appl Phys 44(12):5227–5236
31. Hong S, Colla EL, Kim E, Taylor DV, Tagantsev AK, Muralt P, No K, Setter N (1999) High resolution study of domain nucleation and growth during polarization switching in Pb(Zr, Ti) O_3 ferroelectric thin film capacitors. J Appl Phys 86(1):607–613
32. Hyatt NC, Hriljac JA, Comyn TP (2003) Cation disorder in $Bi_2Ln_2Ti_3O_{12}$ aurivillius phases (Ln = La, Pr, Nd and Sm). Mater Res Bull 38(5):837–846
33. Iijima R (2001) Factors controlling the a-axis orientation of strontium bismuth tantalate thin films fabricated by chemical solution deposition. Appl Phys Lett 79(14):2240–2242
34. Irie H, Miyayama M, Kudo T (2001) Structure dependence of ferroelectric properties of bismuth layer-structured ferroelectric single crystals. J Appl Phys 90(8):4089–4094
35. Irie H, Saito H, Ohkoshi S, Hashimoto K (2005) Enhanced ferroelectric properties of nitrogen-doped $Bi_4Ti_3O_{12}$ thin films. Adv Mater 17(4):491–494
36. Ishibashi Y, Iwata M (2007) Domains and domain walls in ferroelectric $Bi_4Ti_3O_{12}$: a system with biquadratic order parameter coupling. Jpn J Appl Phys 46(1):272–275
37. Ishikawa K, Funakubo H (1999) Electrical properties of (001)- and (116)-oriented epitaxial $SrBi_2Ta_2O_9$ thin films prepared by metalorganic chemical vapor deposition. Appl Phys Lett 75(13):1970–1972
38. Ishikawa K, Watanabe T, Funakubo H (2001) Preparation of Bi_2WO_6 thin films by metalorganic chemical vapor deposition and their electrical properties. Thin Solid Films 392(1):128–133
39. Islam MS, Lazure S, Vannier RN, Nowogrocki G, Mairesse G (1998) Structural and computational studies of Bi_2WO_6 based oxygen ion conductors. J Mater Chem 8(3):655–660
40. Iwata M, Morishita T, Aoyagi R, Maeda M, Suzuki I, Ishibashi Y (2007) In situ observation of polarization reversal of $Bi_4Ti_3O_{12}$ with 90 degrees domain walls. Jpn J Appl Phys 46 (6A):3485–3490
41. Izaki T, Haneda H, Watanabe A, Uchida Y, Tanaka J, Shirasaki S (1992) Effects of Mn ions on the piezoelectric property of (Pb, La)(Zr, Ti)O_3. Jpn J Appl Phys 31(9B):3045–3047
42. Izumi F (2003) Development and applications of the pioneering technology of structure refinement from powder diffraction data. J Ceram Soc Jpn 111(9):617–623
43. Izumi F, Ikeda T (2000) Mater Sci Forum 321–324:198–203
44. Jo W, Yi GC, Noh TW, Ko DK, Cho YS, Kwun SI (1992) Structural and electrooptic properties of laser ablated $Bi_4Ti_3O_{12}$ thin-films on $SrTiO_3$(100) and $SrTiO_3$(110). Appl Phys Lett 61(13):1516–1518
45. Joshi PC, Krupanidhi SB (1993) Switching, fatigue, and retention in ferroelectric $Bi_4Ti_3O_{12}$ thin-films. Appl Phys Lett 62(16):1928–1930
46. Joshi PC, Mansingh A, Kamalasanan MN, Chandra S (1991) Structural and optical-properties of ferroelectric $Bi_4Ti_3O_{12}$ thin-films by sol-gel technique. Appl Phys Lett 59(19):2389–2390
47. Kamiyama T, Oikawa K, Tsuchiya N, Osawa M, Asano H, Watanabe N, Furusaka M, Satoh S, Fujikawa I, Ishigaki T, Izumi F (1995) A New TOF neutron powder diffractometer with arrays of one-dimensional PSDs. Physica B 213:875–877

48. Katayama S, Noguchi Y, Miyayama M (2006) Influence of annealing on domain structures of bismuth-titanate-based crystals. Key Eng Materials 320:27–30
49. Kato K, Zheng C, Finder JM, Dey SK, Torii Y (1998) Sol-gel route to ferroelectric layer-structured perovskite $SrBi_2Ta_2O_9$ and $SrBi_2Nb_2O_9$ thin films. J Am Ceram Soc 81 (7):1869–1875
50. Kawashima Y, Kijima T, Ishiwara H (2003) Ferroelectric characteristics control of (Bi, La) 4Ti3O12 and SrBi2Ta2O9 films by addition of silicates and germanates. Jpn J Appl Phys 42 (4B):2037–2040
51. Kijima T, Kawashima Y, Idemoto Y, Ishiwara H (2002) Effect of high-pressure oxygen annealing on Bi_2SiO_5-added ferroelectric thin films. Jpn J Appl Phys 41(10B):L1164–L1166
52. Kikuchi T (1977) Synthesis of a new, mix-layered bismuth titanate $SrBi_8Ti_7O_{27}$. J Less Common Metals 52(1):163–165
53. Kikuchi T, Watanabe A, Uchida K (1977) Family of mixed-layer type bismuth compounds. Mater Res Bull 12(3):299–304
54. Kim SJ, Moriyoshi C, Kimura S, Kuroiwa Y, Kato K, Takata M, Noguchi Y, Miyayama M (2007) Direct observation of oxygen stabilization in layered ferroelectric $Bi_{3.25}La_{0.75}Ti_3O_{12}$. Appl Phys Lett 91(6):062913
55. Kitanaka Y, Noguchi Y, Miyayama M (2007) Ferroelectric domain structure and *c*-axis polarization switching in monoclinic $Bi_4Ti_3O_{12}$ single crystals. Appl Phys Lett 90 (20):202904
56. Kitanaka Y, Noguchi Y, Miyayama M (2010) Oxygen-vacancy-induced 90 degrees-domain clamping in ferroelectric $Bi_4Ti_3O_{12}$ single crystals. Phys Rev B 81(9):094114
57. Kizaki Y, Noguchi Y, Miyayama M (2006) Defect control for low leakage current in $K_{0.5}Na_{0.5}NbO_3$ single crystals. Appl Phys Lett 89(14):142910
58. Kobayashi J (1958) Growing of ferroelectric $PbTiO_3$ crystals. J Appl Phys 29(5):866–867
59. Kojima T, Sakai T, Watanabe T, Funakubo H, Saito K, Osada M (2002) Large remanent polarization of (Bi, Nd)4Ti3O12 epitaxial thin films grown by metalorganic chemical vapor deposition. Appl Phys Lett 80(15):2746–2748
60. Kresse G, Hafner J (1994) Ab-Initio molecular-dynamics simulation of the liquid-metal amorphous-semiconductor transition in germanium. Phys Rev B 49(20):14251–14269
61. Krok F, Bogusz W, Jakubowski W, Dygas JR, Bangobango D (1994) Studies on preparation and electrical-conductivity of $BiCoVO_x$. Solid State Ionics 70:211–214
62. Kuroiwa Y, Aoyagi S, Sawada A (2001) Evidence for Pb-O covalency in tetragonal $PbTiO_3$. Phys Rev Lett 87(21):217601–217604
63. Lambeck PV, Jonker GH (1986) The nature of domain stabilization in ferroelectric perovskites. J Phys Chem Solids 47(5):453–461
64. Langreth DC, Perdew JP (1980) Theory of nonuniform electronic systems. 1. Analysis of the gradient approximation and a generalization that works. Phys Rev B 21(12):5469–5493
65. Li YL, Chen LQ, Asayama G, Schlom DG, Zurbuchen MA, Streiffer SK (2004) Ferroelectric domain structures in $SrBi_2Nb_2O_9$ epitaxial thin films: electron microscopy and phase-field simulations. J Appl Phys 95(11):6332–6340
66. Li YL, Hu SY, Liu ZK, Chen LQ (2002) Effect of electrical boundary conditions on ferroelectric domain structures in thin films. Appl Phys Lett 81(3):427–429
67. Lim M, Joshi V, Narayan S, Celinska J, Karasawa J (2002) Sub-100 nm $SrBi_2Ta_2O_9$ film with ultrathin $BiTaO_4$ capping layer for 3 V or lower-voltage ferroelectric memory operation. Appl Phys Lett 81(10):1863–1865
68. Lupascu DC, Genenko YA, Balke N (2006) Aging in ferroelectrics. J Am Ceram Soc 89 (1):224–229
69. Merz WJ (1954) Domain formation and domain wall motions in ferroelectric $BaTiO_3$ single crystals. Phys Rev 95(3):690–698
70. Meyer B, Vanderbilt D (2002) Ab initio study of ferroelectric domain walls in PbTiO3. Phys Rev B 65(10):104111

71. Mihara T, Yoshimori H, Watanabe H, Dearaujo CAP (1995) Characteristics of bismuth layered SrBi2Ta2O9 thin-film capacitors and comparison with Pb(Zr, Ti)O_3. Jpn J Appl Phys 34(9B):5233–5239
72. Muramatsu K, Watanabe A, Goto M (1978) Flux growth of Bi_2WO_6 single-crystal below transformation temperature. J Crystal Growth 44(1):50–52
73. Nagarajan V, Roytburd A, Stanishevsky A, Prasertchoung S, Zhao T, Chen L, Melngailis J, Auciello O, Ramesh R (2003) Dynamics of ferroelastic domains in ferroelectric thin films. Nat Mater 2(1):43–47
74. Nagata H (2008) Electrical properties and tracer diffusion of oxygen in some Bi-based lead-free piezoelectric ceramics. J Ceram Soc Jpn 116(1350):271–277
75. Noguchi T, Hase T, Miyasaka Y (1996) Analysis of the dependence of ferroelectric properties of strontium bismuth tantalate (SET) thin films on the composition and process temperature. Jpn J Appl Phys 35(9B):4900–4904
76. Noguchi Y, Matsumoto T, Miyayama M (2005) Impact of defect control on the polarization properties in $Bi_4Ti_3O_{12}$ ferroelectric single crystals. Jpn J Appl Phys 44(16–19):L570–L572
77. Noguchi YJ, Miwa I, Goshima Y, Miyayama M (2000) Defect control for large remanent polarization in bismuth titanate ferroelectrics doping effect of higher-valent cations. Jpn J Appl Phys 39(12B):L1259–L1262
78. Noguchi Y, Miyayama M (2001) Large remanent polarization of vanadium-doped $Bi_4Ti_3O_{12}$. Appl Phys Lett 78(13):1903–1905
79. Noguchi Y, Miyayama M, Kudo T (2000) Ferroelectric properties of intergrowth $Bi_4Ti_3O_{12}$-$SrBi_4Ti_4O_{15}$ ceramics. Appl Phys Lett 77(22):3639–3641
80. Noguchi Y, Miyayama M, Kudo T (2001) Direct evidence of A-site-deficient strontium bismuth tantalate and its enhanced ferroelectric properties. Phys Rev B 63(21):214102
81. Noguchi Y, Miyayama M, Oikawa K, Kamiyama T, Osada M, Kakihana M (2002) Defect engineering for control of polarization properties in $SrBi_2Ta_2O_9$. Jpn J Appl Phys 41 (11B):7062–7075
82. Noguchi Y, Murata K, Miyayama M (2007) Effects of defect control on the polarization properties in Bi_2WO_6-based single crystals. Ferroelectrics 355:55–60
83. Noguchi Y, Soga M, Takahashi M, Miyayama M (2005) Oxygen stability and leakage current mechanism in ferroelectric La-substituted $Bi_4Ti_3O_{12}$ single crystals. Jpn J Appl Phys 44 (9B):6998–7002
84. Ohta T, Izumi F, Oikawa K, Kamiyama T (1997) Rietveld analysis of intensity data taken on the TOF neutron powder diffractometer VEGA. Physica B 234:1093–1095
85. Onodera A, Yoshio K, Yamashita H (2003) Structural study of intermediate phase in layered perovskite $SrBi_2Ta_2O_9$ single crystal. Jpn J Appl Phys 42(9B):6218–6221
86. Osada M, Tada M, Kakihana M, Watanabe T, Funakubo M (2001) Cation distribution and structural instability in $Bi_{4-x}La_xTi_3O_{12}$. Jpn J Appl Phys 40(9B):5572–5575
87. Park BH, Kang BS, Bu SD, Noh TW, Lee J, Jo W (1999) Lanthanum-substituted bismuth titanate for use in non-volatile memories. Nature 401(6754):682–684
88. Park SE, Shrout TR (1997) Ultrahigh strain and piezoelectric behavior in relaxor based ferroelectric single crystals. J Appl Phys 82(4):1804–1811
89. Paz de Araujo CA, Cuchiaro JD, McMillan LD, Scott MC, Scott JF (1995) Fatigue-free ferroelectric capacitors with platinum electrodes. Nature 374:627–629
90. Rae AD, Thompson JG, Withers RL (1991) Structure refinement of commensurately modulated bismuth tungstate, Bi_2WO_6. Acta Crystallogr B 47:870–881
91. Rae AD, Thompson JG, Withers RL, Willis AC (1990) Structure refinement of commensurately modulated bismuth titanate, $Bi_4Ti_3O_{12}$. Acta Crystallogr B 46:474–487
92. Ravindran P, Kjekshus A, Fjellvag H, Delin A, Eriksson O (2002) Ground-state and excited-state properties of $LaMnO_3$ from full-potential calculations. Phys Rev B 65(6):064445
93. Raymond MV, Smyth DM (1996) Defects and charge transport in perovskite ferroelectrics. J Phys Chem Solids 57(10):1507–1511

94. Resta R, Posternak M, Baldereschi A (1993) Towards a quantum-theory of polarization in ferroelectrics – the case of $KNbO_3$. Phys Rev Lett 70(7):1010–1013
95. Robels U, Arlt G (1993) Domain-wall clamping in ferroelectrics by orientation of defects. J Appl Phys 73(7):3454–3460
96. Scott JF, Alexe M, Zakharov ND, Pignolet A, Curran C, Hesse D (1998) Nano-phase SBT-family ferroelectric memories. Integr Ferroelectrics 21(1–4):1–14
97. Scott JF, Dawber M (2000) Oxygen-vacancy ordering as a fatigue mechanism in perovskite ferroelectrics. Appl Phys Lett 76(25):3801–3803
98. Scott JF, Dearaujo CAP (1989) Ferroelectric memories. Science 246(4936):1400–1405
99. Shimakawa Y, Kubo Y, Nakagawa Y, Kamiyama T, Asano H, Izumi F (1999) Crystal structures and ferroelectric properties of $SrBi_2Ta_2O_9$ and $Sr_{0.8}Bi_{2.2}Ta_2O_9$. Appl Phys Lett 74(13):1904–1906
100. Shimakawa Y, Kubo Y, Tauchi Y, Asano H, Kamiyama T, Izumi F, Hiroi Z (2001) Crystal and electronic structures of $Bi_{4-x}La_xTi_3O_{12}$ ferroelectric materials. Appl Phys Lett 79 (17):2791–2793
101. Sih B, Tang J, Dong M, Ye ZG (2001) Ferroelectric $SrBi_2Ta_2O_9$ single-crystal growth and characterization. J Mater Res 16(6):1726–1733
102. Snedden A, Lightfoot P, Dinges T, Islam MS (2004) Defect and dopant properties of the Aurivillius phase $Bi_4Ti_3O_{12}$. J Solid State Chem 177(10):3660–3665
103. Soga M, Noguchi Y, Miyayama M, Okino H, Yamamoto T (2004) Domain structure and polarization properties of lanthanum-substituted bismuth titanate single crystals. Appl Phys Lett 84(1):100–102
104. Takahashi M, Nguchi Y, Miyayama M (2003) Effects of V-doping on mixed conduction properties of bismuth titanate single crystals. Jpn J Appl Phys 42(9B):6222–6225
105. Takahashi M, Noguchi Y, Miyayama M (2002) Electrical conduction mechanism in $Bi_4Ti_3O_{12}$ single crystal. Jpn J Appl Phys 41(11B):7053–7056
106. Takahashi M, Noguchi Y, Miyayama M (2004) Estimation of ionic and hole conductivity in bismuth titanate polycrystals at high temperatures. Solid State Ionics 172(1–4):325–329
107. Takata M, Nishibori E, Sakata M (2001) Charge density studies utilizing powder diffraction and MEM. Exploring of high Tc superconductors, C_{60} superconductors and manganites. Z Kristallogr 216(2):71–86
108. Takeda H, Nishida T, Okamura S, Shiosaki T (2005) Crystal growth of bismuth tungstate Bi_2WO_6 by slow cooling method using borate fluxes. J Eur Ceram Soc 25(12):2731–2734
109. Wada S, Suzuki S, Noma T, Suzuki T, Osada M, Kakihana M, Park SE, Cross LE, Shrout TR (1999) Enhanced piezoelectric property of barium titanate single crystals with engineered domain configurations. Jpn J Appl Phys 38(9B):5505–5511
110. Warren WL, Tuttle BA, Dimos D (1995) Ferroelectric fatigue in perovskite oxides. Appl Phys Lett 67(10):1426–1428
111. Watanabe H, Mihara T, Yoshimori H, Dearaujo CAP (1995) Preparation of ferroelectric thin-films of bismuth layer structured compounds. Jpn J Appl Phys 34(9B):5240–5244
112. Watanabe T, Saiki A, Saito K, Funakubo H (2001) Film thickness dependence of ferroelectric properties of *c*-axis-oriented epitaxial $Bi_4Ti_3O_{12}$ thin films prepared by metalorganic chemical vapor deposition. J Appl Phys 89(7):3934–3938
113. Withers RL, Thompson JG, Rae AD (1991) The crystal-chemistry underlying ferroelectricity in $Bi_4Ti_3O_{12}$, Bi_3TiNbO_9, and Bi_2WO_6. J Solid State Chem 94(2):404–417
114. Wu WB, Fumoto K, Oishi Y, Okuyama M, Hamakawa Y (1996) Bismuth titanate thin films on Si with buffer layers prepared by laser ablation and their electrical properties. Jpn J Appl Phys 35(2B):1560–1563
115. Xiao Y, Shenoy VB, Bhattacharya K (2005) Depletion layers and domain walls in semiconducting ferroelectric thin films. Phys Rev Lett 95(24):247603
116. Yamamoto K, Kitanaka Y, Suzuki M, Miyayama M, Noguchi Y, Moriyoshi C, Kuroiwa Y (2007) High-oxygen-pressure crystal growth of ferroelectric $Bi_4Ti_3O_{12}$ single crystals. Appl Phys Lett 91(16):162909

117. Yamamoto K, Suzuki M, Noguchi Y, Miyayama M (2008) High-performance $Bi_{0.5}Na_{0.5}TiO_3$ single crystals grown by high-oxygen-pressure flux method. Jpn J Appl Phys 47 (9):7623–7629
118. Yanovskii VK, Voronkova VI (1986) Polymorphism and properties of Bi_2WO_6 and Bi_2MoO_6. Phys Status Solid A Appl Res 93(1):57–66
119. Zhang LX, Chen W, Ren X (2004) Large recoverable electrostrain in Mn-doped (Ba, Sr)TiO_3 ceramics. Appl Phys Lett 85(23):5658–5660
120. Zhang QS, Goddard WA (2006) Charge and polarization distributions at the 90 degrees domain wall in barium titanate ferroelectric. Appl Phys Lett 89(18):182903
121. Zurbuchen MA, Asayama G, Schlom DG, Streiffer SK (2002) Ferroelectric domain structure of $SrBi_2Nb_2O_9$ epitaxial thin films. Phys Rev Lett 88(10):107601

Chapter 15
Processing and Properties of Textured Bismuth Layer-Structured Ferroelectrics

Toshio Kimura and Toshihiko Tani

15.1 Introduction

Bismuth layer-structured ferroelectrics (BLSFs) are one of the candidates for lead-free piezoelectrics for high temperature and high frequency applications. BLSFs have a layer structure with a general formula $(Bi_2O_2)(A_{m-1}B_mO_{3m+1})$, where A denotes mono-, di-, or trivalent ions with a large ionic radius, and B denotes tetra-, penta-, or hexavalent ions with a small ionic radius, and m is an integer between 1 and 5. The crystal structure is composed of pseudo-perovskite blocks $(A_{m-1}B_mO_{3m+1})^{2-}$ interleaved with $(Bi_2O_2)^{2+}$ layers along c-axis (pp. 226–229 in Jaffe et al. [8]).

Most BLSFs have tetragonal structure above and orthorhombic structure below the Curie temperature. The polar axis lies completely or almost perpendicular to the c-axis. Polycrystalline BLSFs prepared by ordinary ceramic powder processing are composed of grains with random orientation, and the number of grains with the polar axis parallel to the poling direction is limited, resulting in low piezoelectric properties. For example, the piezoelectric strain constant of $K_{0.5}Bi_{4.5}Ti_4O_{15}$ determined from the unipolar strain is 31 pC/N along the a-axis of a single crystal, whereas 10 pC/N for a polycrystal [19]. Therefore, enhanced properties are expected for textured ceramics, in which a specific crystal axis in each grain is aligned.

Various methods shown in Table 15.1 have been employed to prepare textured BLSFs. They are classified into two groups: (1) application of pressure during

T. Kimura (✉)
Keio University, 3-14-1 Hiyoshi, Kohoku-ku, Yokohama 223-8522, Japan
e-mail: kimura@applc.keio.ac.jp

T. Tani
Toyota Central R&D Labs., Inc., 41-1 Yokomichi, Nagakute, Aichi 480-1192, Japan

Toyota Technological Institute, 2-12-1 Hisakata, Tempaku-ku, Nagoya 468-8511, Japan

Toyota Research Institute of North America, Ann Arbor, MI 48105, USA
e-mail: e0628@mosk.tytlabs.co.jp

S. Priya and S. Nahm (eds.), *Lead-Free Piezoelectrics*,
DOI 10.1007/978-1-4419-9598-8_15, © Springer Science+Business Media, LLC 2012

Table 15.1 Preparation method of textured BLSF

Methods	References
Application of pressure during heating	
Hot pressing	[6]
Hot forging	[28]
Sintering of compact with oriented particles	
Tape casting	[27]
Extrusion	[30]
Slip casting under strong magnetic field	[1]
Electrophoretic deposition under strong magnetic field	[26]
Screen printing	[37]

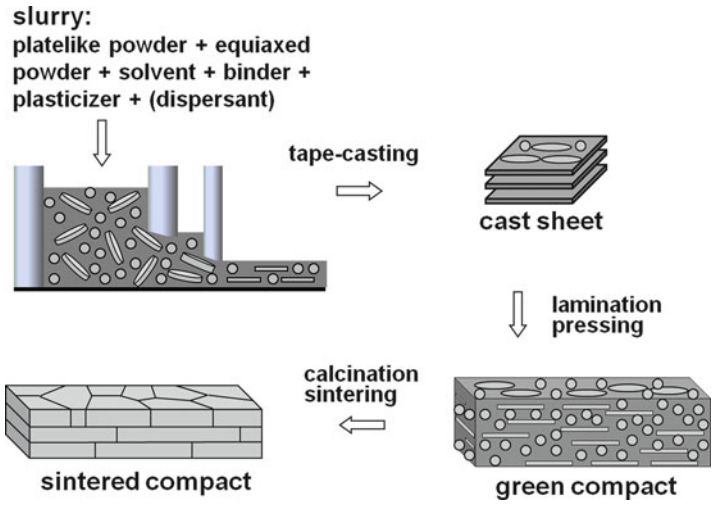

Fig. 15.1 Preparation procedure of textured ceramics by the templated grain growth (TGG) method

heating compacts composed of randomly oriented particles and (2) sintering of compacts containing particles with a specific orientation. The alignment of the particles in (2) is carried out by either (2-1) mechanical shear stress or (2-2) strong magnetic field. This chapter deals with the mechanical shear stress (2-1) method and covers the tape casting and extrusion as the forming process of green compacts. In this method, platelike particles are used to align the particles in the green compact. The aligned platelike particles act as template for texture development. Therefore, this method is called a templated grain growth (TGG) process. Sometimes, the platelike template particles are formed by an in situ reaction in the compact, and the method is called a reactive-templated grain growth (RTGG) process.

Figure 15.1 shows a schematic diagram of the procedure for preparation of a textured ceramic by using the TGG process. Starting materials are powders of platelike and equiaxed particles with the same composition. In most cases, the amount of platelike particles is between 5 and 20 vol.%. A mixture of two powders

is mixed with forming aids (solvent, binder, plasticizer, etc.) to form slurry which is tape-cast by a doctor-blade technique. The shear stresses acting on the slurry during casting align the platelike particles with their plate face parallel to the sheet surface [9, 35]. The cast sheet is cut and laminated to form a green compact. The green compact is calcined at about 500°C for binder burn-out, and then sintered at high temperatures.

In the RTGG method, on the other hand, platelike particles with simpler composition than that of a target material are used together with complementary reactants as starting powders in a slurry. For example, highly textured $Na_{0.5}Bi_{4.5}Ti_4O_{15}$, $CaBi_4Ti_4O_{15}$, and $SrBi_4Ti_4O_{15}$ ceramics were prepared by tape-casting and sintering for the powder mixtures including platelike $Bi_4Ti_3O_{12}$ as a reactive template for the following reaction schemes [33]:

$$\begin{aligned} &Bi_4Ti_3O_{12} + 0.25Na_2CO_3 + 0.25Bi_2O_3 + TiO_2 \\ &\quad \rightarrow Na_{0.5}Bi_{4.5}Ti_4O_{15} + 0.25CO_2 \end{aligned} \tag{15.1}$$

$$Bi_4Ti_3O_{12} + CaCO_3 + TiO_2 \rightarrow CaBi_{4.5}Ti_4O_{15} + CO_2 \tag{15.2}$$

$$Bi_4Ti_3O_{12} + SrCO_3 + TiO_2 \rightarrow SrBi_{4.5}Ti_4O_{15} + CO_2 \tag{15.3}$$

These reactions proceeded to the right since four-layered $MBi_4Ti_4O_{15}$ is thermodynamically more stable than a mixture of three-layered $Bi_4Ti_3O_{12}$ and simple perovskite $MTiO_3$ [7]. The conversion reactions from $Bi_4Ti_3O_{12}$ into four-layered perovskite titanates proceeded topochemically with preserved pseudo-tetragonal *c*-axis aligned perpendicular to the tape-casting surface. The relative amount of reactive template can be reduced to 5–20 vol.% similarly to that for the TGG method. The advantage of the RTGG method is that a common material such as $Bi_4Ti_3O_{12}$ can be used as a reactive template for a variety of BLSFs with different target compositions.

This chapter covers the preparation methods and piezoelectric properties of textured BLSFs made by the TGG and RTGG processes. The factors determining the degree of orientation and the density are described in detail. There are several methods to determine the degree of orientation [24], and the most convenient method is the Lotgering's method [17]. Figure 15.2 shows the X-ray diffraction (XRD) profiles of randomly oriented and textured $BaBi_4Ti_4O_{15}$ ceramics, which are shown as typical examples for BLSFs. The most intense peak of randomly oriented specimen is (119) at $2\theta = 30.1°$, but the textured specimens have intense (00*l*) diffraction lines. The degree of orientation (*F*) is evaluated from the following equations:

$$F = \frac{P - P_0}{1 - P_0}, \quad P = \frac{\sum I_{\{00l\}}}{\sum I_{\{hkl\}}}, \quad P_0 = \frac{\sum I_{0\{00l\}}}{\sum I_{0\{hkl\}}},$$

where I and I_0 are the peak heights of the textured and randomly oriented specimens, respectively, and $\{00l\}$ and $\{hkl\}$ are the Miller indexes. The F values of 1 and 0 indicate fully textured and completely random states, respectively.

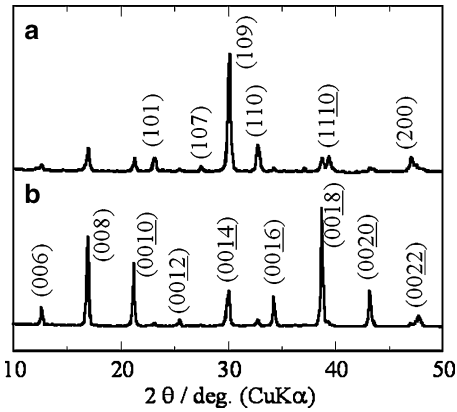

Fig. 15.2 X-ray diffraction (XRD) patterns of $BaBi_4Ti_4O_{15}$ which are typical for BLSF ceramics with (**a**) random and (**b**) *c*-axis orientation

15.2 Preparation of Powder Particles

15.2.1 Platelike Particles

The most effective methods for the preparation of anisometric particles are the hydrothermal and molten salt syntheses. The hydrothermal technique is mainly used to prepare nanotubes, nanowires, nanosheets, etc. However, the platelike particles for the TGG process must have diameter larger than several micrometers to align the particles in the cast sheet. Therefore, molten salt synthesis is most frequently employed in the TGG and RTGG processes.

Molten salt synthesis is one of the methods for preparing complex oxides, which are made by the reaction between constituent oxides (starting materials) in the presence of molten salt [13]. The mixture of starting materials for BLSFs (for example, Bi_2O_3, TiO_2, MCO_3 (M = Ca, Sr, Ba), etc.) is mixed with salt (NaCl, KCl, etc.) and then heated at temperatures above the melting point of the salt. Although the solubility of the oxides (carbonates) in the molten salt is small, a small amount of oxides (carbonates) dissolves in the salt and BLSF particles (for example, $MBi_4Ti_4O_{15}$) precipitate. Because the particles develop in a liquid phase, their shape reflects the crystal structure.

When the product has a crystal structure with large anisotropy such as BLSFs, the growth rate of each crystal face differs, leading to the formation of anisometric particles [13]. The growth rate is determined by the surface roughness at the atomic level, and the growth rate of a rough surface is larger than that of a flat surface (pp. 127–133 in Howe [5]). For the BLSF case, the {001} face has a quite smooth structure and the {*hk*0} faces, which are perpendicular to {001}, have a rough structure with various degrees of roughness depending on the chemical composition (Fig. 15.3). The growth rate of {001} face is small and that of {*hk*0} is large, leading to a platelike shape. The aspect ratio is determined by the difference in the growth rates of the {001} and {*hk*0} faces. The salt species also influence the aspect ratio [13]. For example, the aspect ratio of $Bi_4Ti_3O_{12}$ and Bi_2WO_6 particles

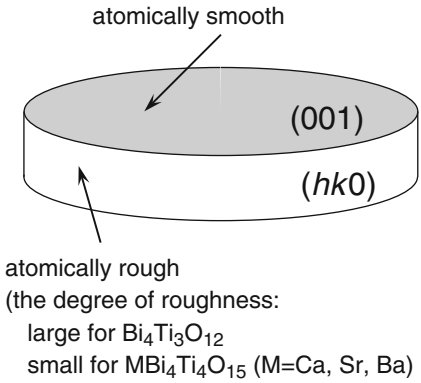

Fig. 15.3 Surface roughness at the atomic level of BLSF compounds. (001) Face has an atomically smooth structure; (*hk*0) faces which are perpendicular to the (001) face have a rough structure

obtained in NaCl-KCl is higher than that of $Bi_4Ti_3O_{12}$ and Bi_2WO_6 particles obtained in Na_2SO_4-Li_2SO_4 [11, 12].

Sometimes, aggregates form in the initial stage of molten salt synthesis [12]. The aggregates are a group of primary particles with random orientation, and reduce the degree of orientation of platelike particles in the green compact. Therefore, the formation of aggregates must be avoided. The formation of aggregate is caused by a large degree of supersaturation in the initial stage. In most cases, the constituent oxides do not fully dissolve in the molten salt and $MBi_4Ti_4O_{15}$ particles form in the presence of solid constituent oxides. The product $[MO][Bi_2O_3]^2[TiO_2]^4$, where [MO], $[Bi_2O_3]$, and $[TiO_2]$ are the solubility of MO, Bi_2O_3, and TiO_2, respectively, is much larger than the solubility product of $MBi_4Ti_4O_{15}$, leading to the formation of $MBi_4Ti_4O_{15}$ particles under a large degree of supersaturation. This situation results in a large nucleation rate, and aggregates form until the constituent oxides are consumed. Further heating after the consumption of the constituent oxides (the completion of the reaction) causes the growth of particles. At this stage, the constituent oxides are absent and the concentration of the oxides in molten salt is determined by the solubility of $MBi_4Ti_4O_{15}$ particles. The solubility of particles is dependent on the particle size, and small particles have larger solubility than large particles. Small particles dissolve into molten salt and precipitate on large particles. This process is called Ostwald ripening (pp. 425–430 in Kingery et al. [16]). The particle growth results in the disappearance of aggregates and the formation of single discrete particles. Therefore, heating at high temperatures for long durations is necessary to prepare platelike BLSF particles suitable for the TGG and RTGG processes.

The particle size (the diameter of plate face) is determined by heating conditions (temperature and duration) and the structure of {*hk*0} faces. The growth rate of BLSF particles in molten salt depends on the chemical species of BLSF. $Bi_4Ti_3O_{12}$ and $Na_{0.5}Bi_{4.5}Ti_4O_{15}$ have high growth rates whereas $MBi_4Ti_4O_{15}$ (M = Ca, Sr, and Ba) and $K_{0.5}Bi_{4.5}Ti_4O_{15}$ have low growth rates [14, 32]. In the former case, the particle size is determined by the heating conditions; heating at high temperatures for long durations gives a large size. In the latter case, the particle size is

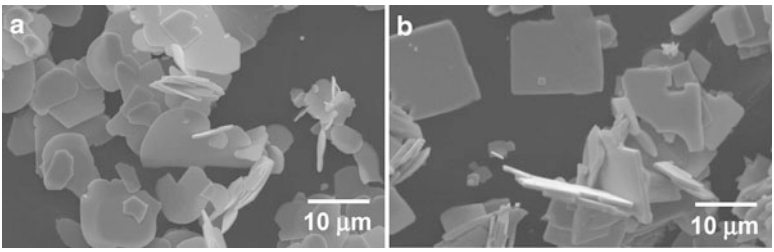

Fig. 15.4 Morphology of (**a**) $Bi_4Ti_3O_{12}$ and (**b**) $SrBi_4Ti_4O_{15}$ particles obtained by molten salt synthesis using KCl. Heating conditions are (**a**) 1,100 and 1,200°C for 1 h

not dependent on the heating conditions, and the particles can grow during the dissolution of aggregates but they practically cease growing after the disappearance of aggregates.

The growth rate of BLSF particles during Ostwald ripening is determined by the structure of {*hk*0} faces. Figure 15.4 shows the shape of $Bi_4Ti_3O_{12}$ and $SrBi_4Ti_4O_{15}$ particles. Both particles are platelike, but the shape of plate faces is different. The $Bi_4Ti_3O_{12}$ particles have a circular shape with rounded {*hk*0} faces, whereas the $SrBi_4Ti_4O_{15}$ particles have a rectangular shape with flat {100} faces. These shapes are indicative of the structure of {*hk*0} faces at the atomic level. The {*hk*0} faces are atomically rough, but the degree of roughness is dependent on the chemical composition (Fig. 15.3). A macroscopically rounded surface has a high degree of roughness and a macroscopically flat surface has a low degree of roughness. The surface with a high degree of roughness can grow under a low degree of supersaturation because additional atoms from molten salt can be incorporated into the crystal by bonding with several atoms on the surface. A high degree of supersaturation is necessary to grow the surface with a low degree of roughness because two-dimensional nucleation is necessary on the surface. $Bi_4Ti_3O_{12}$ particles having {*hk*0} faces with a high degree of roughness can grow under a low degree of supersaturation caused by the solubility difference between particles with different sizes. To grow $SrBi_4Ti_4O_{15}$ particles having {*hk*0} faces with a low degree of roughness, on the other hand, a larger driving force (a high degree of supersaturation) is necessary for two-dimensional nucleation but it is not supplied by the solubility difference between particles after the disappearance of aggregates.

The size control by selecting the heating conditions is difficult for $MBi_4Ti_4O_{15}$ (M = Ca, Sr, and Ba) particles. For these materials to obtain platelike particles with controlled particle size, two-step molten salt synthesis is used [14]. The $Bi_4Ti_3O_{12}$ particles with desired sizes can be obtained by selecting the heating temperature and duration, and then these particles are converted into $MBi_4Ti_4O_{15}$ particles, by heating the $Bi_4Ti_3O_{12}$ particles with MCO_3, TiO_2, and KCl. The $MBi_4Ti_4O_{15}$ particles with almost the same size as that of $Bi_4Ti_3O_{12}$ particles are obtained.

Molten salt synthesis is a convenient method to prepare platelike BLSF particles with the sizes in the μm range. Care must be paid to the reaction between BLSF and the salt. In the preparation of $Bi_4Ti_3O_{12}$ using NaCl-KCl as molten salt,

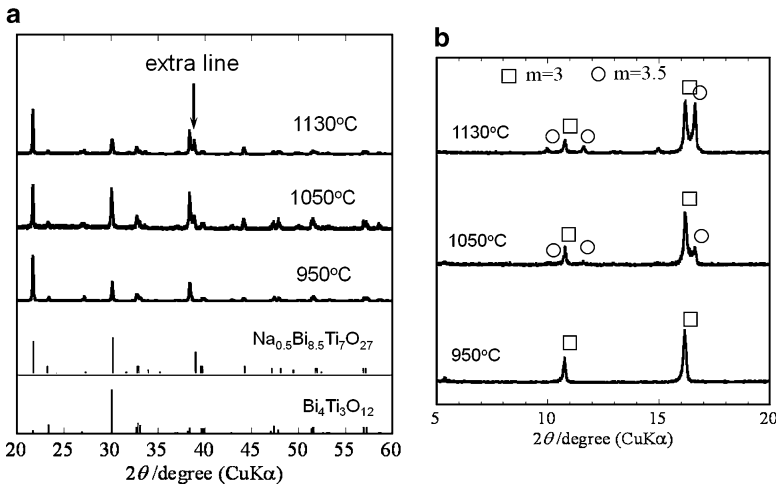

Fig. 15.5 XRD patterns in (**a**) higher and (**b**) lower diffraction angle range for $Bi_4Ti_3O_{12}$ platelike particles prepared at 950, 1,050, and 1,130°C for 2 h in NaCl-KCl mixed salt. The powder particles prepared at 950°C are phase pure $Bi_4Ti_3O_{12}$, but the second phase of $Na_{0.5}Bi_{8.5}Ti_7O_{27}$ is in the powders prepared at 1,050 and 1,130°C. m is an integer for general formula of BLSF, $(Bi_2O_2)(A_{m-1}B_mO_{3m+1})$ [3]

$Na_{0.5}Bi_{8.5}Ti_7O_{27}$ particles form at high temperatures [3]. Figure 15.5 shows the XRD patterns of the products of reaction between Bi_2O_3 and TiO_2 in NaCl-KCl at various temperatures. The product at 950°C gives the material with the diffraction lines belonging to only $Bi_4Ti_3O_{12}$. The diffraction patterns of the products at 1,050 and 1,130°C shown in Fig. 15.5a coincide with the pattern of $Bi_4Ti_3O_{12}$, except for the extra diffraction line at $2\theta = 38.9°$. The formation of BLSF with slightly different composition can be examined by the diffraction pattern between $2\theta = 5$ and 20° (Fig. 15.5b) [22]. BLSFs with $m = 3$ have the diffraction lines at $2\theta = 10.0$ and 16.2°, and that with $m = 3.5$ have the lines at $2\theta = 10.0$, 11.6, and 16.7°, where m is the integer in the chemical formula $(Bi_2O_2)(A_{m-1}B_mO_{3m+1})$. Figure 15.5b indicates the presence of BLSF with $m = 3.5$, which must be $Na_{0.5}Bi_{8.5}Ti_7O_{27}$. When only KCl is used as molten salt, phase-pure $Bi_4Ti_3O_{12}$ is obtained even at 1,130°C. These results indicate that $Bi_4Ti_3O_{12}$ reacts with NaCl and forms $Na_{0.5}Bi_{8.5}Ti_7O_{27}$ at high temperatures.

15.2.2 Equiaxed Particles

In most cases, the equiaxed particles are prepared by solid-state reaction; a mixture of starting materials is heated at an appropriate temperature. The requirement for the equiaxed particles is submicron sizes, and the product of solid-state reaction is crushed and ground with a ball mill. When the TGG process is first applied to BLSF, a sophisticated preparation method is used for the preparation of equiaxed,

small size particles [4], but results have shown that the particles made by solid-state reaction can be used to prepare highly textured BLSFs.

When the BLSF powder is prepared by solid-state reaction at high temperatures, aggregates of platelike particles form. The grinding of this powder changes the aggregates into discrete particles with various sizes and aspect ratios. Textured BLSF ceramics can be obtained by sintering the green sheets prepared by tape-casting of only this powder, because discrete platelike particles with a relatively large aspect ratio act as template for texture formation. However, the degree of orientation is rather small (the maximum is about 0.6). Highly textured BLSF ceramics (the degree of orientation is nearly 1.0) can be easily obtained by adding a small amount of platelike particles prepared by molten salt synthesis as template.

15.3 Tape-Casting and Extrusion

The TGG process requires green compacts in which platelike particles are oriented. To align platelike particles, tape-casting and extrusion are employed. To make slurry for tape-casting and extrusion, a mixture of platelike and equiaxed particles is mixed with forming aids such as solvent, binder, plasticizer, dispersant, and so forth. The slurry is subject to shear stresses during forming, and the gradient of shear stresses aligns the platelike particles [9, 35]. A high degree of particle alignment is essential to obtain highly textured BLSF ceramics, because the orientation of platelike particles in the green compact determines the orientation of grains in the sintered compact.

To obtain a green sheet with highly oriented particles, the characteristics of slurry are important. The powder particles must be uniformly dispersed in the slurry. In the case of BLSFs, the degree of agglomeration is not very high. A typical binder used for tape-casting is polyvinyl butyral which also acts as a dispersant (pp. 57–60 in Mistler and Twiname [18]). It is better to make the composition of slurry simple. Use of other dispersant is not necessary for equiaxed particles with sizes more than several tenth μm. The viscosity of the slurry is very important and high viscosity is preferable [35], because particle orientation is caused by the interaction between particles. Horn et al. have proposed that the interaction is determined by the average interparticle spacing (λ) in slurry, where λ is a function of the liquid volume fraction (ϕ_l) and the solid–liquid interface area per unit volume of slurry (S_V) as $\lambda = 4\phi_l/S_V$ [4]. The viscosity of slurry is determined by the viscosity of dispersing medium (solvent + binder + plasticizer) and solid loading. The latter is more important to obtain highly oriented particles; high solid loading increases viscosity and reduces the λ value.

In the BLSF case, the degree of particle alignment is not dependent on the size of template particles. Instead, the size of equiaxed particles is important. One example is $CaBi_4Ti_4O_{15}$ sheets with 20 vol.% platelike particles prepared by three samples of platelike and two samples of equiaxed particles [32]. The sizes of platelike particles are approximately 5, 10, and 18 μm, and those of equiaxed particles

were approximately 0.6 and 1.0 μm. When the equiaxed particles of 0.6 μm were used, the platelike particles of about 5, 10, and 18 μm gave almost the same F values of 0.57, 0.65, and 0.62 in the calcined compacts, respectively. When the platelike particles of about 5 μm were used, the equiaxed particles of 1.0 μm gave the F value of 0.25 in the calcined compact, whereas the equiaxed particles of 0.5 μm give $F = 0.57$. It is considered that larger equiaxed particles disturb the motion of platelike particles under the gradient of shear stresses and cause poorer alignment.

15.4 Sintering

The compacts after calcination (binder burn-out) are composed of platelike particles dispersed in a matrix of equiaxed particles. The platelike particles are aligned with their plate face parallel to the casting direction (sheet surface). The calcined compacts have density between 55 and 65% of the theoretical value. Figure 15.6 shows an example of the microstructure of the calcined compact. The compact is $Bi_4Ti_3O_{15}$ and contains platelike particles (20 vol.%) with diameters of about 5 μm and a thickness of about 0.3 μm and equiaxed particles (80 vol.%) with an average particle size of about 0.5 μm. The alignment of platelike particles is evident. The platelike and equiaxed particles are called "template" and "matrix" grains, respectively, hereafter.

The density and the degree of orientation increase by sintering. In this section, the densification behavior and texture development are explained by using an example of $BaBi_4Ti_4O_{15}$ [14], but similar densification behavior and texture development are observed in $Bi_4Ti_3O_{12}$ [15], $CaBi_4Ti_4O_{15}$ [32], and $SrBi_4Ti_4O_{15}$ [10]. Figure 15.7 shows the effect of heating conditions on the density and the degree of orientation (F value) of $BaBi_4Ti_4O_{15}$ containing template grains (20%) with a plate size about 10 μm, a thickness of about 0.5 μm, and matrix particles (80 vol.%) with an average particle size of about 0.7 μm [14]. The compact began to densify at about 1,050°C and reached about 95% of the theoretical value at 1,130°C with 2 h

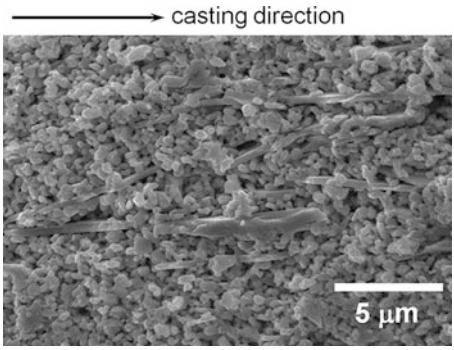

Fig. 15.6 Microstructure of calcined compact of $Bi_4Ti_3O_{12}$ prepared by tape-casting. Platelike particles are aligned with their plate faces parallel to the compact surface

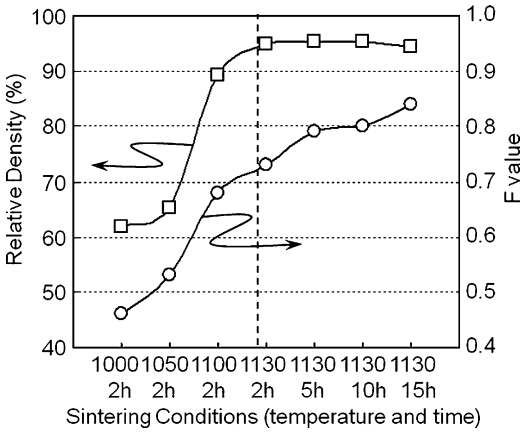

Fig. 15.7 Densification and texture development during sintering of $BaBi_4Ti_4O_{15}$ compacts containing 20 vol.% template grains [14]

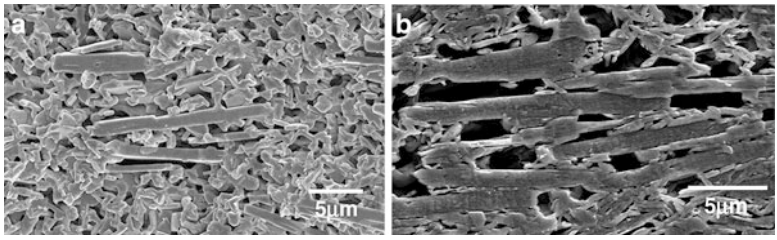

Fig. 15.8 Microstructures of $BaBi_4Ti_4O_{15}$ compacts heated at (**a**) 1,050 and (**b**) 1,100°C for 2 h. The matrix grains change their shape from nearly equiaxed to platelike at this temperature range [14]

heating. Prolonged heating at 1,130°C did not increase the density significantly. The F value increased on heating up to 1,130°C and reached 0.73 at 1,130°C with 2 h of heating. The F value slightly increased by prolonged heating at 1,130°C and reached 0.84 by heating for 15 h.

The texture development is caused by the morphological change of matrix grains but not by the growth of template grains [14]. Figure 15.8 shows the microstructures of the $BaBi_4Ti_4O_{15}$ compacts sintered at 1,050 and 1,100°C for 2 h. The density and the F value are shown in Fig. 15.7. The microstructure at 1,050°C was composed of large template and small matrix grains. Almost all the matrix grains changed their shape to become platelike at 1,100°C, while the template grains did not grow to a considerable extent. The plate face of the platelike matrix grains is parallel to that of the template grains. This morphological change is one of the origins of texture development ($F = 0.53$ at 1,050°C to $F = 0.68$ at 1,100°C). The mechanism of the morphological change is discussed later.

Prolonged heating at high temperatures causes another microstructural change. Figure 15.9 shows the microstructures of the $BaBi_4Ti_4O_{15}$ compacts sintered at

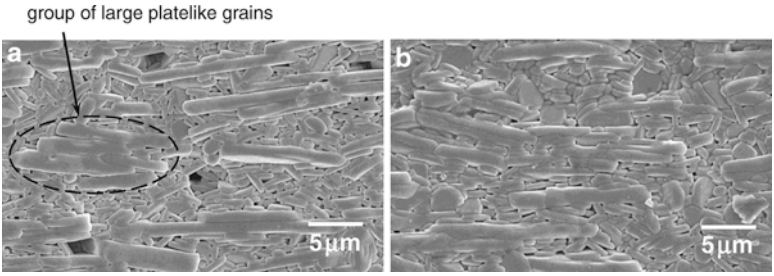

Fig. 15.9 Microstructures of $BaBi_4Ti_4O_{15}$ compacts heated at 1,130°C for (**a**) 2 h and (**b**) 10 h. Platelike matrix grains grow to form a group of large platelike grains with mutually parallel alignment. The number of grains in the group increases with soaking time [14]

1,130°C for 2 and 10 h [14]. The density and the F value are shown in Fig. 15.7. Heating at 1,130°C for 2 h reduced the volume of large pores, and the relative density reached about 95%. The remarkable change in microstructure is the formation of groups of the large platelike grains with mutually parallel alignment. Although the size and shape of large platelike grains did not change to any considerable extent, the number of grains in the group increased with soaking time. This formation of the grain groups is another origin of texture development: the growing grains engulfed small misoriented grains ($F = 0.73$ at 1,130°C for 2 h to $F = 0.84$ at 1,130°C for 15 h). The mechanism of the formation of the grain groups is discussed later.

Microstructure development shown in Figs. 15.8 and 15.9 indicates that the texture development in BLSF is not caused by the growth of template grains as in Al_2O_3 [23, 25] but is caused by the morphological change of matrix grains. The process of morphological change from an irregular shape to a platelike shape was observed in textured $Bi_4Ti_3O_{12}$ [15]. The morphological change of matrix grain and the development of texture are schematically illustrated in Fig. 15.10. At first, a matrix grain adheres to a template grain and forms grain boundary with the orientation $(001)_{temp}||(hkl)_{mat}$, implying that (001) of the template grain (temp) is parallel to (hkl) of the matrix grain (mat) along the grain boundary. The third grain (called as a terrace) forms between the template and matrix grains. The evidence of terrace formation is shown in Fig. 15.11, indicating that square grains develop between template and matrix grains. The terrace (terr) has $(001)_{terr}||(001)_{temp}$ and $(001)_{terr}||(hkl)_{mat}$ boundaries. Finally, the matrix grain on the terrace disappears, remaining platelike terrace grain with the c-axis parallel to that of the template grain. The formation of terraces is the origin of the morphological change and the texture development.

Several terraces form on a template grain at the stage shown in Fig. 15.8b. One of the terraces grows at the expense of other terraces and matrix grains. The plate face of the growing terrace cannot become larger than that of template grain, because the grain boundary between the growing terrace and template grain gives a driving force for grain growth. Therefore, the final size of the plate face is the same for growing terrace and template grain. Furthermore, the final thickness of the growing terrace is almost the same as the thickness of template grain (Fig. 15.9), because the

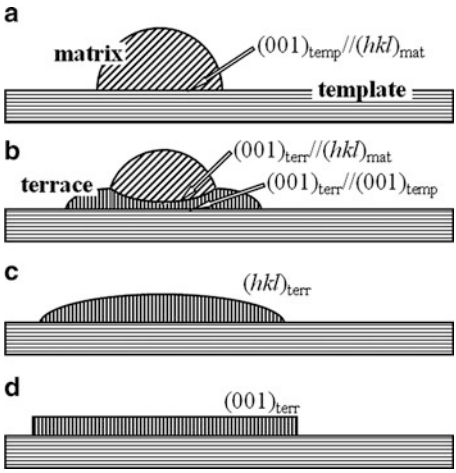

Fig. 15.10 Schematic diagram of morphological change of matrix grain from an irregular shape to a platelike shape. (**a**) A matrix grain adheres to a template grain and forms grain boundary. (**b**) A terrace grain forms between the template and matrix grains. (**c**) The matrix grain on the terrace disappears. (**d**) The platelike terrace grain remains with the *c*-axis parallel to that of the template grain. *Open arrows* indicate the boundary structures. The terms temp, mat, and terr stand for template, matrix, and terrace, respectively

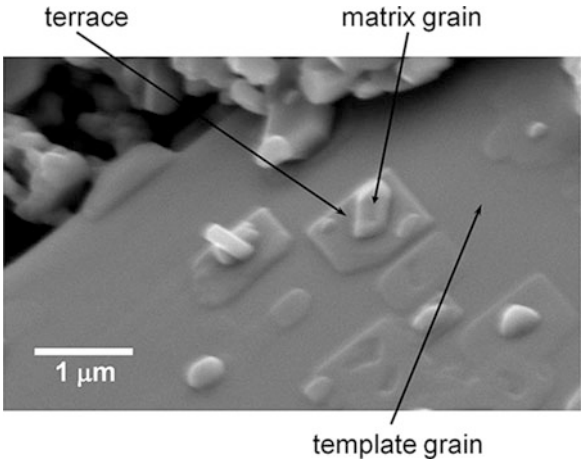

Fig. 15.11 Microstructure of specimen for a model experiment using platelike $Bi_4Ti_3O_{12}$ particles as template grains and $SrBi_4Ti_4O_{15}$ as matrix grains, heated at 950°C for 2 h. *Square plates* (terraces) form between the matrix and template grains

equilibrium condition with the lowest grain boundary energy determines the aspect ratio. The new terrace on the grown terrace starts to grow, and repeats the same process. Thus, a group of grains with almost the same shape forms.

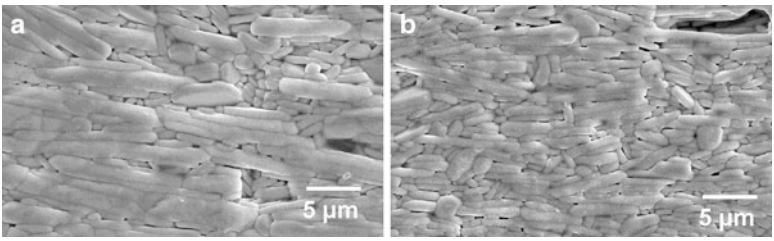

Fig. 15.12 Microstructure of textured $BaBi_4Ti_4O_{15}$ compacts heated at 1,130°C for 15 h. The grain size is determined by the size of platelike particles (*template grains*). The average sizes are (**a**) 10 and (**b**) 5 mm [14]

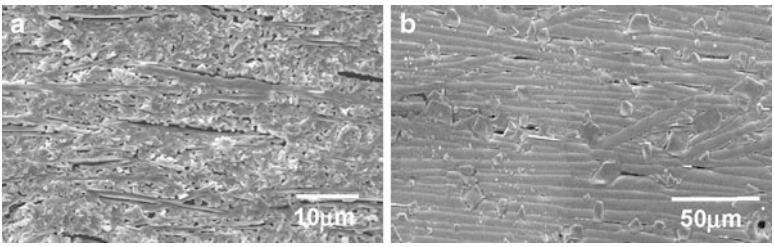

Fig. 15.13 Microstructure of textured $Bi_4Ti_3O_{12}$ compact heated at (**a**) 900 and (**b**) 1,150°C for 2 h, indicating the growth of template grains at high temperature [15]

In the cases of $MBi_4Ti_4O_{15}$ (M = Ca, Sr, and Ba), the growth of template grains hardly occur, because the side faces have a low degree of roughness (Fig. 15.3) and a low growth rate. Therefore, the final grain size is determined by the size of platelike particles, even heated at high temperatures. Figure 15.12 shows the final microstructure of $BaBi_4Ti_4O_{15}$ obtained large (about 10 μm) and small (about 5 μm) platelike particles [14]. The textured ceramics with controlled grain size were obtained. In the case of $Bi_4Ti_3O_{12}$, on the other hand, the side faces of platelike grain had a high degree of roughness, and the grains continue to grow. Figure 15.13 shows the microstructures of $Bi_4Ti_3O_{12}$ ceramics heated at 900 and 1,150°C for 2 h [15]. The average size of starting platelike particles is about 10 μm and that of platelike grains in the compact heated at 1,150°C is more than 100 μm. In the $Bi_4Ti_3O_{12}$ case, the grain size in the final sintered compact is controlled by sintering temperature and duration.

In most cases, the amount of template grains ranges from 5 to 20 vol.%. When the amount is less than 5 vol.%, the degree of orientation is small, except for a special case; 1 vol.% template grains gave a large degree of orientation in $Bi_4Ti_3O_{12}$ [34]. When the amount of template grains is more than 20%, highly textured BLSF ceramics can be obtained but the problem is low density.

15.5 Effects of Processing Parameters

The amount of template grains and the sizes of template and matrix grains have large effects on the relative density and the degree of orientation, and the suitable selection of these parameters is important to prepare dense, highly textured BLSF ceramics.

The effects of the amount of template grains on the densification and texture development are extensively examined for $SrBi_4Ti_4O_{15}$ [21] and $CaBi_4Ti_4O_{15}$ [31]. When the matrix grains are absent (the amount of template particles is 100%), dense ceramics are hardly obtained in many cases. Figure 15.14 shows the density and the *F* value of $SrBi_4Ti_4O_{15}$ obtained by heating the tape-cast compact of platelike particles with a diameter about 7 μm and a thickness about 0.3 μm. The *F* value is nearly 1.0 for specimens sintered at between 1,000 and 1,200°C, but the relative density is less than 80%. Figure 15.15 shows the microstructure of the

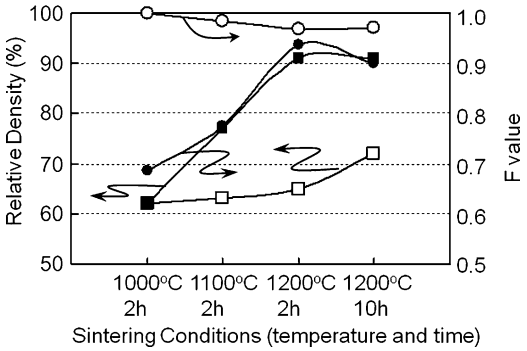

Fig. 15.14 Relative density and the degree of orientation (*F* value) of $SrBi_4Ti_4O_{15}$ compacts containing 100 vol.% (*open marks*) and 20 vol.% (*filled marks*) platelike particles. The compact containing 100 vol.% platelike particles gives a high degree of orientation but the density is low, whereas dense (about 95% of theoretical value) and highly textured material with the *F* value more than 0.9 is obtained by heating the compact containing 20 vol.% platelike particles at 1,200°C [21]

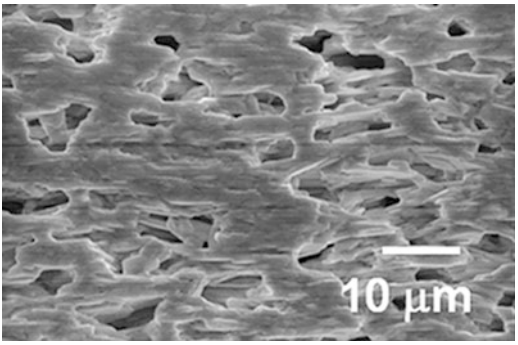

Fig. 15.15 Microstructure of $SrBi_4Ti_4O_{15}$ compact containing 100 vol.% platelike particles at 1,200°C for 2 h. The presence of large pores is the origin of low density [21]

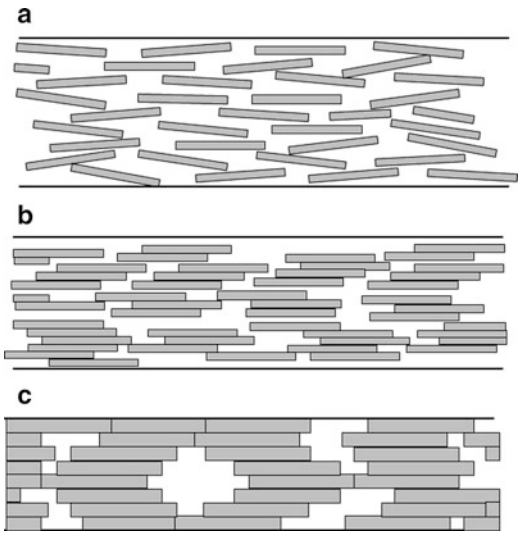

Fig. 15.16 Schematic diagram of large pore formation in the compact composed of 100 vol.% platelike particles. The stages are (**a**) platelike particles in the green compact, (**b**) formation of face-to-face contact between platelike particles at the onset of sintering, and (**c**) formation of large pores between particle groups at the final stage of sintering

compact sintered at 1,200°C for 2 h. Several groups of platelike grains with face-to-face contact form, resulting in a large *F* value. Pores are absent in the groups but observed between the groups. The formation of these large pores between the grain groups is responsible for a low density. Figure 15.16 schematically shows the mechanism of the formation of large pores. In the green compact, the platelike particles are well aligned with small misorientation. In an initial stage of sintering, neighboring particles make a face-to-face contact (particle rearrangement) and the spaces around the particles coalesce. By progress in particle rearrangement, the coalescence of space around particles results in the formation of large pores. These pores are practically stable, leading to a low density. The formation of large pores can be avoided by the use of platelike particles with a small degree of particle rearrangement, i.e., $Bi_4Ti_3O_{12}$ particles made in Li_2SO_4-Na_2SO_4 [2, 36], and by the addition of small equiaxed particles (TGG process) to prevent the face-to-face contact between platelike particles (Fig. 15.14).

When the amount of template grains is more than 20%, the sintered density slightly decreases due to the retardation of densification and the formation of large pores. The example is $CaBi_4Ti_4O_{15}$ prepared by using platelike particles with a diameter about 5 μm and a thickness about 0.2 μm, and equiaxed particles with an average particle size of 0.7 μm. The compacts containing platelike particles of 20, 30, and 40 vol.% had the same *F* value of 0.94, when heated at 1,150°C for 10 h. Figure 15.17 shows the densification curves of the compacts containing platelike particles of 0 and 20 vol.%. The densification is almost completed at about 1,000 and 1,100°C for the 0 and 20 vol.% compacts, respectively, indicating the

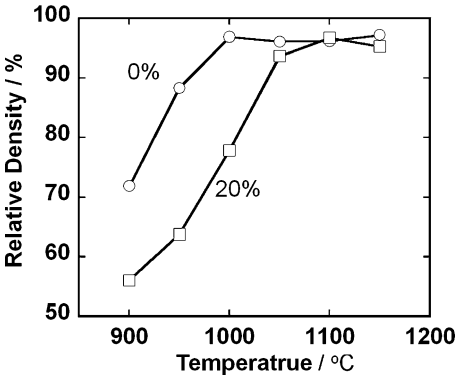

Fig. 15.17 Densification behavior of compacts containing platelike particles of 0 and 20 vol.%. The addition of platelike particles into equiaxed particles retards densification [31]

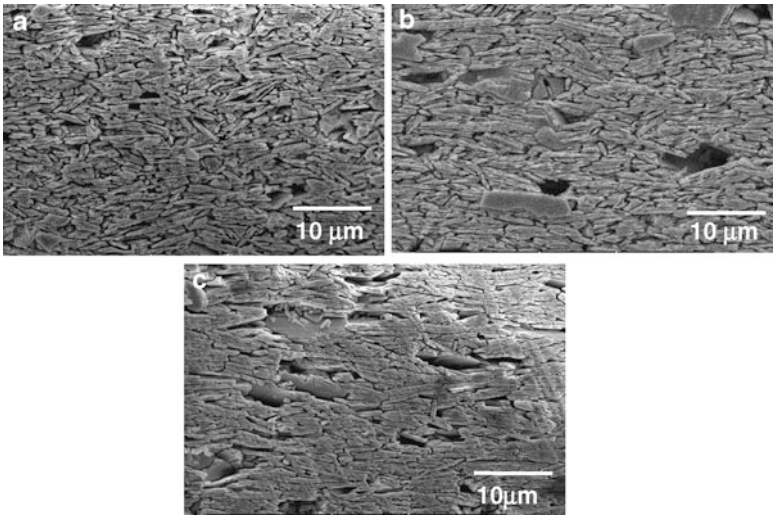

Fig. 15.18 Microstructures of $CaBi_4Ti_4O_{15}$ compacts containing (**a**) 20, (**b**) 30, and (**c**) 40 vol.% platelike particles, heated at 1,150°C for 10 h. The relative density does not dependent on the amount of platelike particles, but an increase in the amount of platelike particles increases the number of large, long and thin pores [31]

retardation of densification by the platelike particles. In general, large rigid inclusion particles hinder densification (pp. 702–723 in Rahaman [20]), and the platelike $CaBi_4Ti_4O_{15}$ particles act as such inclusions in the compact. The retardation of densification is not a big problem, because dense ceramics can be obtained by sintering at higher temperatures, but the characteristics of pores are important. The compacts containing platelike particles of 20, 30, and 40 vol.% had the relative density of 95, 96, and 93, respectively, when heated at 1,150°C for 10 h. Figure 15.18 shows the microstructures of these ceramics. The compacts contained long and thin

pores with the length about 5 μm, and the number of these pores increased with an increase in the amount of platelike particles. The pores with this shape are harmful for piezoelectric applications, because a large depolarization field develops during poling. Therefore, the use of fewer platelike particles is preferable.

The size of platelike particles (template grains) has a slight effect on the density and the degree of orientation. Dense, highly textured BLSF ceramics are obtained when the size of template particles is more than 5 μm. On the other hand, the size of grains in the final sintered compact is determined by the size of platelike particles, as shown in Fig. 15.12, in the case of $CaBi_4Ti_4O_{15}$, $SrBi_4Ti_4O_{15}$, and $BaBi_4Ti_4O_{15}$. Therefore, the grain size can be controlled by selecting the size of platelike particles.

The size of equiaxed particles influences the texture development in two aspects. Large equiaxed particles hinder the orientation of platelike particles in a cast sheet as described in Sect. 15.3 dealing with Tape-Casting and Extrusion. Furthermore, large equiaxed particles do not contribute to the texture development in the matrix phase. This aspect is reported for $SrBi_4Ti_4O_{15}$ using the platelike particles with a diameter of about 10 μm and a thickness of about 0.4 μm and the amount of platelike particles of 20 vol.% [10]. When matrix particles with the size less than 0.5 μm are used, textured ceramics with a relatively high degree of orientation ($F > 0.8$) are obtained, whereas the equiaxed particles with the size of 1.5 μm give the F value as low as 0.24. Figure 15.19b shows the microstructure of this compact. The compact is composed of large and small platelike grains, which are template and matrix grains, respectively. The matrix particles change their shape from equiaxed to platelike, but the groups of platelike grains with the same orientation (colonies) as shown in Fig. 15.12 do not form. The orientation of the platelike matrix grains is random. Small matrix particles change their shape from equiaxed to platelike under the influence of template grains (Fig. 15.19a), giving a high degree of orientation. Large matrix particles, on the other hand, change their shape without the influence of template grains, and do not contribute to texture development. Furthermore, pores remain in the compact with large matrix particles. Thus, small matrix particles are preferable.

15.6 Enhanced Piezoelectric Properties of BLSFs Textured by RTGG

Textured BLSF ceramics processed by TGG or RTGG are expected to possess more uniform and improved electrical properties than those by hot-forging or hot-pressing. Textured ceramics were prepared by the RTGG processing with tape-casting and extrusion as forming techniques and their electrical properties were compared with those of randomly oriented ceramics. The reaction schemes of RTGG for $CaBi_4Ti_4O_{15}$ and Ca-modified $Na_{0.5}Bi_{4.5}Ti_4O_{15}$ are designed in (15.4) and (15.5), respectively. The content of the reactive template, platelike $Bi_4Ti_3O_{12}$, was fixed in such a way that 20% of Ti in the target compositions was supplied from the reactive template [29].

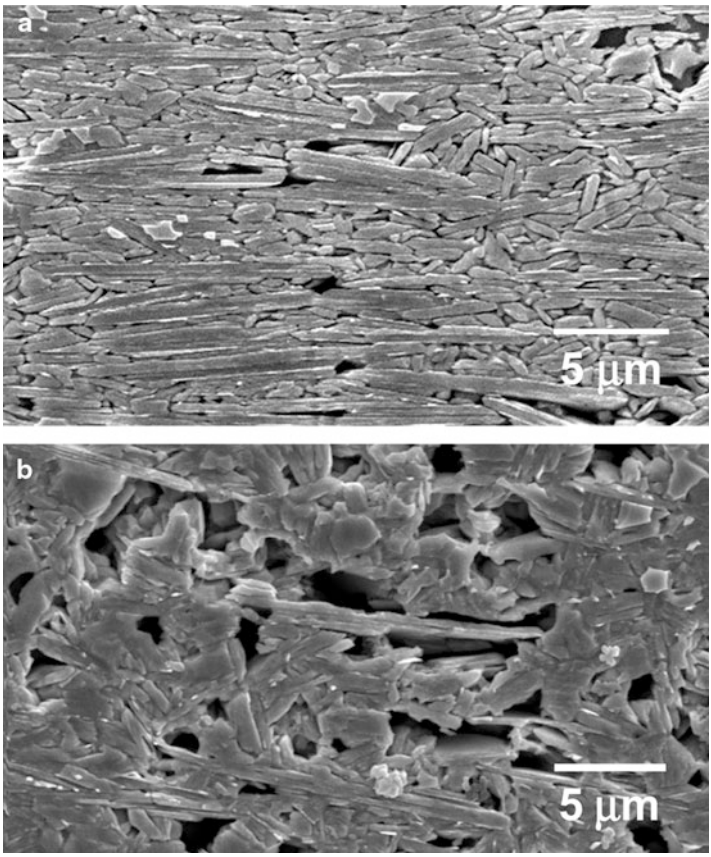

Fig. 15.19 Microstructures of $SrBi_4Ti_4O_{15}$ compacts containing equiaxed particles of about (**a**) 0.5 and (**b**) 1.5 μm, at 1,200°C for 10 h. Equiaxed particles more than 1 μm produce misoriented platelike grains [10]

$$4Bi_4Ti_3O_{12}\ (\text{platelet}) + 25.5625Bi_2O_3 + 3.5625Na_2CO_3 + 0.75CaCO_3 + 48TiO_2 \rightarrow 15Na_{0.475}Ca_{0.05}Bi_{4.475}Ti_4O_{15} + 4.3125CO_2 \tag{15.4}$$

$$4Bi_4Ti_3O_{12}\ (\text{platelet}) + 22Bi_2O_3 + 15CaCO_3 + 48TiO_2 \rightarrow 15CaBi_4Ti_4O_{15} + 15CO_2 \tag{15.5}$$

The slurries containing the designed powder mixtures were tape-cast and sintered at 1,150°C (for Ca-modified $Na_{0.5}Bi_{4.5}Ti_4O_{15}$) and 1,200°C (for $CaBi_4Ti_4O_{15}$) for 10 h. Both ceramic compositions reached nearly full density and the degree of {001} orientation $F > \sim 0.9$ [29]. Figure 15.20 gives SEM images of RTGG processed $CaBi_4Ti_4O_{15}$ ceramic on etched surfaces perpendicular and parallel to the original tape-casting plane. The microstructure of the perpendicular section is composed of two types of platelike grains with large and small aspect ratios; the former grains

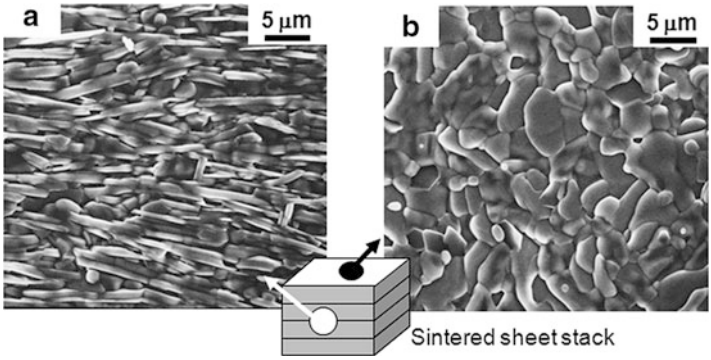

Fig. 15.20 SEM images of polished and etched surfaces of RTGG-processed $CaBi_4Ti_4O_{15}$ ceramic; (**a**) perpendicular and (**b**) parallel to original tape-casting plane [29]

were topochemically formed from the reactive template $Bi_4Ti_3O_{12}$ whereas the latter grains were formed in the matrix.

The piezoelectric and dielectric properties of the RTGG-processed specimens were compared in Table 15.2 with those of the conventionally processed and randomly oriented ceramics. The piezoelectric properties k_{33}, d_{33}, and g_{33} of the textured ceramics were greatly enhanced along the perpendicular direction to $\langle 001 \rangle$. The electromechanical coupling coefficient k_{33} of the RTGG-processed $CaBi_4Ti_4O_{15}$ ceramics exceeded 0.5, three times as large as that of conventionally processed ceramics [29].

Unidirectionally textured $CaBi_4Ti_4O_{15}$ ceramics were also prepared by RTGG processing with the same reaction scheme as in (15.5), but were formed by extrusion instead of tape-casting [30]. Since spontaneous polarization of BLSF lies on or nearly along the *ab*-plane, parallel alignment of the *ab*-plane by tape-casting is not necessarily required for high piezoelectric properties. Furthermore, extrusion has advantages for mass production because difficult multilamination process for bulk specimens is not necessary. The powders are mixed with binder and extruded through a die into a bar schematically shown in Fig. 15.21a. Disk specimens were machined out of a sintered bar and electroded for poling. The texture of a plane for electroding was evaluated by XRD as a degree of "antiorientation" factor, "$\overline{F}$," for the surface to be electroded for poling, defined by:

$$\overline{F} = \frac{P_0 - P}{P_0}, \quad P = \frac{\sum I_{\{00l\}}}{\sum I_{\{hkl\}}}, \quad P_0 = \frac{\sum I_{0\{00l\}}}{\sum I_{0\{hkl\}}}.$$

Figure 15.22 gives the electromechanical coupling coefficient k_{33} as well as piezoelectric d_{33} and g_{33} coefficients as a function of antiorientation factor $\overline{F}$ for $CaBi_4Ti_4O_{15}$ ceramics prepared by RTGG/extrusion with the properties for $CaBi_4Ti_4O_{15}$ ceramics processed by RTGG/tape-casting and conventional sintering.

Table 15.2 Piezoelectric and dielectric properties of RTGG- and conventionally-processed $CaBi_4Ti_4O_{15}$ and Ca-modified $Na_{0.5}Bi_{4.5}Ti_4O_{15}$ ceramics

	$CaBi_4Ti_4O_{15}$			Ca-modified $Na_{0.5}Bi_{4.5}Ti_4O_{15}$		
Specimen	RTGG/ tape casting	RTGG/ tape casting	Conventional	RTGG/ tape casting	RTGG/ tape casting	Conventional
Density (g/cm^3)	7.205	7.108	7.206	7.582	7.515	7.561
Lotgering's factor	1.00	0.83	–	0.93	0.86	–
Poling direction	‖Casting plane	⊥Casting plane	‖Press axis	‖Casting plane	⊥Casting plane	‖Press axis
$\varepsilon_{33}^{T}/\varepsilon_0 Z$	139	153	149	148	158	162
tan δ (%)	0.09	0.04	0.13	0.63	0.10	0.16
k_p (%)	4.8	1.4	4.7	1.8	1.7	2.3
k_{31} (%)	3.2	0.9	2.9	1.2	1.1	1.4
k_t (%)	53.4	16.2	16.2	49.0	8.5	13.3
k_{33} (%)	53.5	16.2	16.9	49.0	8.6	13.5
$-d_{31}$ ($\times 10^{-12}$ C/N)	2.8	0.9	2.8	0.9	1.1	1.4
d_{33} ($\times 10^{-12}$ C/N)	45	17	15	44	9	13
$-g_{31}$ ($\times 10^{-3}$ Vm/N)	2.3	0.6	2.1	0.7	0.8	1.0
g_{33} ($\times 10^{-3}$ Vm/N)	36.5	12.5	11.4	33.5	6.5	9.1

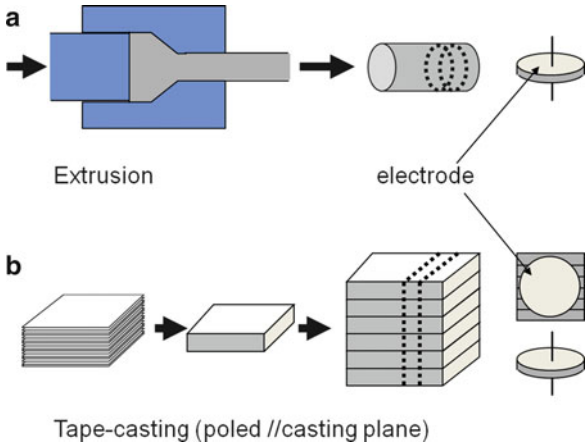

Fig. 15.21 Schematic diagrams of sample preparation for electrical measurements by (**a**) extrusion and (**b**) tape-casting in the RTGG method for textured BLSF ceramics

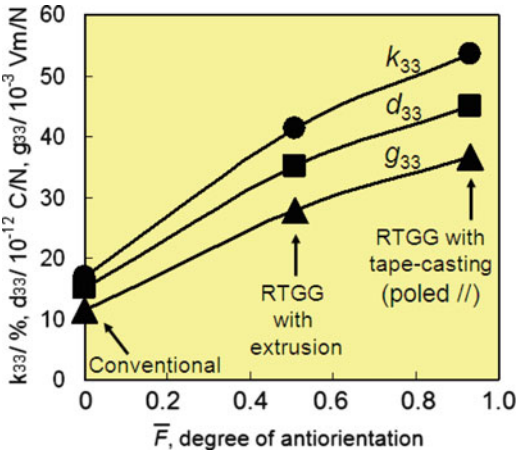

Fig. 15.22 Longitudinal-mode piezoelectric properties as a function of the degree of {001} antiorientation, $\overline{F}$. The $\overline{F}$ value of the electroded plane was evaluated as:

$\overline{F} = \{(1-p)-(1-p_0)\}/\{(1-(1-p_0)) = (p_0-p)/p_0$, where $p = \Sigma I(00l)/\Sigma I(hkl)$, and $p_0 = p$ for randomly oriented ceramic specimens

Although the ceramics by RTGG/extrusion gave lower piezoelectric properties than the ceramics by RTGG/tape-casting due to smaller $\overline{F}$ value, the properties were greatly improved when compared with conventionally processed, randomly oriented ceramics. Extrusion is widely used processing method for thermal-shock resistant cordierite honeycomb ceramics with preferred orientation. Although only limited numbers of reports have been known on textured BLSFs through extrusion, it must be useful when we need textured polycrystals for which a certain crystallographic axis is not favorable for applied direction. Both texture and properties can be improved by using techniques developed in manufacturing honeycomb ceramics.

15.7 Summary and Conclusions

The piezoelectric properties of BLSF textured by the TGG and RTGG processes are significantly dependent on the degree of orientation. Therefore, it is important to develop technology for the preparation of dense, highly textured BLSFs. This chapter mainly focuses on the factors determining the degree of orientation. The most important processes are the preparation of green compacts containing plate-like particles with the degree of orientation as high as possible and to increase the volume of grains with right orientation for which the understanding of mechanisms of texture development during sintering is necessary.

Main factors determining the degree of orientation of platelike particles (template grains) in green compacts are the size of equiaxed particles (matrix grains) and the slurry properties. The preferable particle size is less than 0.5 μm in order not to disturb alignment of platelike particles. Because the alignment of platelike particles

is caused by the interaction of particle motion in the slurry under shear stresses, high solid loading is desirable to reduce the average interparticle distance.

The morphological change of matrix grains in the presence of template grains is the origin of texture development. The formation of terraces on the template grains is an important process. The matrix grains with less than 0.5 μm are preferable to form terraces with a high degree of orientation and not to form misoriented grains. The amount of template grains has little effect on the degree of orientation in the compact sintered at high temperatures. However, too many template grains result in the formation of large pores, which reduce the piezoelectric properties. The suitable amount of template grains is between 5 and 20 vol.%.

Parallel alignment of *ab*-plane by tape-casting is not required for the enhancement of piezoelectric properties of BLSFs. Therefore, extrusion can be a useful alternative forming method for BLSFs with more practical texture; i.e., unidirectional orientation of axes within *ab*-plane. Improved productivity is also expected by the application of extrusion well developed in the manufacturing of honeycomb ceramics.

References

1. Bedoya C, Muller Ch, Jacob F, Gagou Y, Fremy M-A, Elkaim E (2002) Magnetic-field-induced orientation in Co-doped $SrBi_2Ta_2O_9$ ferroelectric oxide. J Phys Condens Matter 14 (45):11849–11857
2. Chazono H, Kimura T, Yamaguchi T (1986) Fabrication of grain-oriented $Bi_4Ti_3O_{12}$ ceramics by normal sintering (Part 2) sintering mechanisms. Yogyo Kyokai Shi 94(3):324–329
3. Fuse K (2006) Mechanisms of texture development in $Bi_{0.5}(Na_{1-x}K_x)TiO_3$ made by reactive-templated grain growth. Master thesis, Keio University, Japan, March 2006
4. Horn JA, Zhang SC, Selvaraj U, Messing GL, Trolier-McKinstry S (1999) Templated grain growth of textured bismuth titanate. J Am Ceram Soc 82(4):921–926
5. Howe JM (1997) Interfaces in materials. Wiley, New York
6. Igarashi H, Matsunaga K, Taniai T, Okazaki K (1978) Dielectric and piezoelectric properties of grain-oriented $PbBi_2Nb_2O_9$ ceramics. Am Ceram Soc Bull 57(9):815–817
7. Ikegami S, Ueda I (1974) Piezoelectricity in ceramics of ferroelectric bismuth compound with layer structure. Jpn J Appl Phys 13:1572–1577
8. Jaffe B, Cook WR Jr, Jaffe H (1971) Piezoelectric ceramics. Academic, London
9. Kim HJ, Krane MJM, Trumble KP, Bowman KJ (2006) Analytical fluid flow models for tape casting. J Am Ceram Soc 89(9):2769–2775
10. Kimura T, Miyazaki C (2007) Effect of matrix particle size on texture development in $SrBi_4Ti_4O_{15}$ made by templated grain growth. J Electroceramics 19(4):281–285
11. Kimura T, Yamaguchi T (1982) Morphology of Bi_2WO_6 powders obtained in the presence of fused salt. J Mater Sci 17(7):1863–1870
12. Kimura T, Yamaguchi T (1983) Fused salt synthesis of $Bi_4T_{i3}O_{12}$. Ceram Int 9(1):13–17
13. Kimura T, Yamaguchi T (1987) Morphology control of electronic ceramic powders by molten salt synthesis. Adv Ceram 21:169–177
14. Kimura T, Yoshida Y (2006) Origin of texture development in barium bismuth titanate prepared by the templated grain growth method. J Am Ceram Soc 89(3):869–874
15. Kimura T, Miyazaki C, Tsuzuki K, Fuse K, Motohashi T (2008) Effect of surface energy anisotropy on microstructure development of piezoelectric ceramics made by templated grain growth process. In: Proceedings of the 10th international conference of European ceramic society, Berlin, Germany, June 2007, pp 626–631

16. Kingery WD, Bowen HK, Uhlmann DR (1976) Introduction to ceramics, 2nd edn. Wiley, New York
17. Lotgering K (1959) Topotactical reactions with ferrimagnetic oxides having hexagonal crystal structures – I. J Inorg Nucl Chem 9(2):113–123
18. Mistler RE, Twiname ER (2000) Tape casting theory and practice. American Ceramic Society, Westerville
19. Noguchi Y, Suzuki N, Kitanaka Y, Teranishi S, Miyayama M (2008) Appl Phys Lett 93:032904
20. Rahaman MN (2003) Ceramic processing and sintering, 2nd edn. Marcel Dekker, New York
21. Sakuma Y, Kimura T (2005) Effects of processing methods on texture development and densification in $SrBi_4Ti_4O_{15}$ ceramics. J Mater Sci 40(18):4811–4817
22. Sanson A, Whatmore RW (2005) Phase diagram of the $Bi_4Ti_3O_{12}$-$BaTiO_3$-$(Na_{1/2}Bi_{1/2})TiO_3$ system. J Am Ceram Soc 88(11):3147–3153
23. Seabaugh MM, Kerscht IH, Messing GL (1997) Texture development by templated grain growth in liquid-phase-sintered α-alumina. J Am Ceram Soc 80(5):1181–1188
24. Seabaugh MM, Vaudin MD, Cline JP, Messing GL (2000) Comparison of texture analysis techniques for highly oriented α-Al_2O_3. J Am Ceram Soc 83(8):2049–2054
25. Suvaci E, Messing GL (2000) Critical factors in the templated grain growth of textured reaction-bonded alumina. J Am Ceram Soc 83(8):2041–2048
26. Suzuki M, Miyayama M, Noguchi Y, Uchikoshi T (2008) Enhanced piezoelectric properties of grain-oriented $Bi_4Ti_3O_{12}$-$BaBi_4Ti_4O_{15}$ ceramics obtained by magnetic-field-assisted electrophoretic deposition method. J Appl Phys 104:014102
27. Swartz S, Schulze WA, Biggers JV (1981) Fabrication and electrical properties of grain oriented $Bi_4Ti_3O_{12}$ ceramics. Ferroelectrics 38(1–4):765–768
28. Takenaka T, Sakata K (1980) Grain orientation and electrical properties of hot-forged $Bi_4Ti_3O_{12}$ ceramics. Jpn J Appl Phys 19(1):31–39
29. Takeuchi T, Tani T, Saito Y (1999) Piezoelectric properties of bismuth layer-structured ferroelectric ceramics with a preferred orientation processed by the reactive templated grain growth method. Jpn J Appl Phys 38(9B):5553–5556
30. Takeuchi T, Tani T, Saito Y (2000) Unidirectionally textured $CaBi_4Ti_4O_{15}$ ceramics by the reactive templated grain growth with an extrusion. Jpn J Appl Phys 39(Part I, No. 9B):5577–5580
31. Tamura K (2010) Preparation of textured $CaBi_4Ti_4O_{15}$ with high piezoelectric performances. Master thesis, Keio University, Japan, March 2010
32. Tamura K, Kimura T (2009) The effect of the grain size on piezoelectric properties of textured $CaBi_4Ti_4O_{15}$ ceramics. In: Presented at 11th international conference and exhibition of the European ceramic society, Krakow, 21–25 June 2009
33. Tani T, Kimura T (2006) Crystalline-oriented piezoelectric bulk ceramics with a perovskite-type structure. Adv Appl Ceram 105(1):55–63
34. Tsuzuki K (2009) Origin of texture development in $Bi_4Ti_3O_{12}$ made by templated grain growth. Master thesis, Keio University, Japan, March 2009
35. Watanabe H, Kimura T, Yamaguchi T (1989) Particle orientation during tape casting in the fabrication of grain-oriented bismuth titanate. J Am Ceram Soc 72(2):289–293
36. Watanabe H, Kimura T, Yamaguchi T (1991) Sintering of platelike bismuth titanate powder compacts with preferred orientation. J Am Ceram Soc 74(1):139–147
37. Zeng J, Li Y, Yang Q, Jing X, Yin Q (2005) Grain orientation $CaBi_4Ti_4O_{15}$ piezoceramics prepared by the screen-printing multilayer grain growth technique. J Eur Ceram Soc 25(12): 2727–2730

Part V
Applications

Chapter 16
Self-Biased Lead-Free Magnetoelectric Laminates

Su-Chul Yang and Shashank Priya

16.1 Definition of Magnetoelectric Material

Multiferroic materials possess two or more ferroic orders such as ferroelectric, ferromagnetic, or ferroelastic. Multiferroic magnetoelectric (ME) materials exhibit direct coupling between the ferroelectric and ferromagnetic order parameters. In composites, ME effect is a combination of two types of material property such as magnetostriction and piezoelectricity. On application of magnetic field, magnetostrictive phase produces strain which is transferred on to the piezoelectric phase that converts strain into electric charge. This conversion of applied magnetic field into electric field is termed as direct ME effect. On the other hand, under applied electric field piezoelectric phase produces strain which is transferred on to the magnetostrictive phase that converts it into magnetic field, termed as converse ME effect [1]. Figure 16.1 shows that ME materials exhibit cross-coupling between the applied magnetic field and electric polarization or vice versa.

In general, ME materials are categorized into four groups (i) single-phase materials, (ii) 3-0 type particulate composites, (iii) 2-2 type laminate composites, and (iv) 1-3 type cylinder-matrix composites. Single-phase materials exhibiting ME effects should show two coupled-transitions: one from ferroelectric to paraelectric state, and another from ferro/ferri/antiferro-magnetic to paramagnetic state: the ME effect then arises due to coupling between the magnetic and polar sublattices. Recent investigations of single-phase multiferroics have revealed that the origin of ME effect is often associated with a particular exchange mechanism for various families of compounds such as: orbital ordering, Jahn–Teller distortion, super/double exchange, and/or geometric magnetic frustration. Unfortunately, single-phase materials suffer from the drawback that the ME effect is extremely small at room temperature. For example, the highest ME coefficient has been reported for

S.-C. Yang • S. Priya (✉)
CEHMS, Virginia Tech, Blacksburg, VA 24061, USA
e-mail: spriya@vt.edu

S. Priya and S. Nahm (eds.), *Lead-Free Piezoelectrics*,
DOI 10.1007/978-1-4419-9598-8_16, © Springer Science+Business Media, LLC 2012

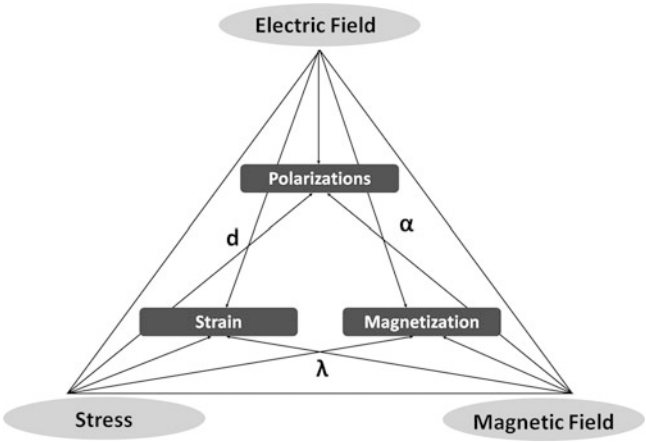

Fig. 16.1 Schematic representation of multiferroic magnetoelectrics showing the interrelation between electric field, magnetic field, and stress

antiferromagnetic Cr_2O_3 crystals, which is 2.67×10^{-12} s/m at a Neel temperature of 34°C. On the other hand, multi-phase ME composites were found to exhibit much higher magnitude of ME coefficient at room temperature [2]. The ME effect can be realized by using composites of piezomagnetic and piezoelectric phases or magnetostrictive and piezoelectric phases. Moreover, these composites are easy to fabricate compared to the single-phase materials, cost-effective, and have higher working temperature range. Composite geometry can be designed based on the connectivity. For two-phase system, there are ten types of connectivity. For three- and four-phase systems there are 20 and 35 types of connectivity. The connectivity in general can be given by the ratio $\frac{(n+3)!}{3!n!}$, where n is the number of phases. Figure 16.2 shows two types of connectivity for multi-phase ME composites. The 3-0 type particulate ME composites were constructed by embedding one-phase particles in a matrix of another phase and found to exhibit coupling coefficient of 10–100 mV/cm·Oe at room temperature. The ME coefficient in 3-0 type particulate composites can reach up to several V/cm·Oe at resonance frequency but this magnitude is still below the theoretical magnitude due to problems related to interdiffusion between piezoelectric and magnetostrictive phases during high-temperature sintering, thermal expansion mismatch between the two phases, and low resistivity. In order to improve the resistivity in ME composites, 2-2 type ME laminates have been synthesized by using piezoelectric and magnetostrictive layers and shown to exhibit giant ME coefficient of ~ several V/cm·Oe at room temperature due to reduction of the leakage problem. The 1-3 type ME composites were investigated for high ME coefficient by strong contribution of both piezoelectric coefficient d_{33} and piezomagnetic coefficient q_{11}. The PZT/Terfenol-D composites were reported to exhibit giant ME coefficient of 500 mV/cm·Oe at off-resonance condition and 18.2 V/cm·Oe at a resonance condition by Ma et al. [3].

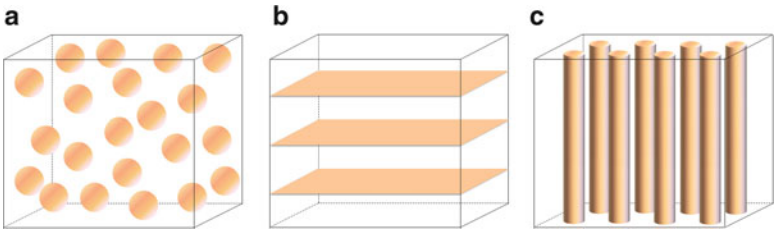

Fig. 16.2 Schematic diagram for connectivity of multi-phase ME composites: (**a**) 3-0 type particulate composite, (**b**) 2-2 type laminate composite, and (**c**) 1-3 type cylinder-matrix composite

16.1.1 Single-Phase ME Materials

The upper limit for ME susceptibility can be given as: [4]

$$\alpha_{ij}^2 < \left(\kappa_{ii}^e \chi_{jj}^m\right), \tag{16.1}$$

where $\kappa^e$and χ^m are the electric and magnetic susceptibilities, respectively. A similar relationship can be derived based on the thermodynamic considerations given as [5]:

$$\alpha_{ij} < (\varepsilon_{ii}\mu_{jj})^{1/2}, \tag{16.2}$$

where ε and μ are the electric permittivity and magnetic permeability, respectively. The magnetoelectric coupling coefficient has been defined as:

$$k_{\mathrm{ME}} = \frac{U_{\mathrm{mutual}}}{(U_{\mathrm{electric}} . U_{\mathrm{magnetic}})^{1/2}}, \tag{16.3}$$

where $U_{\mathrm{mutual}} = 1/2\alpha_{ij}E_iH_j$, where H_j is the magnetic field is the mutual energy, $U_{\mathrm{electric}} = 1/2\varepsilon_{ii}E_iE_i$ is the electric energy, and $U_{\mathrm{magnetic}} = 1/2\mu_{jj}H_jH_j$ is the magnetic energy. In order to evaluate the efficiency of energy conversion from magnetic to electric forms, or vice-versa, a working definition of the coupling coefficient can be written as:

$$k_{\mathrm{me}}^2 = k_{ij,\,\mathrm{piezo}}^2 k_{ij,\,\mathrm{magnetic}}^2 \tag{16.4}$$

where $k_{ij,\ \mathrm{piezo}}$ is the coupling coefficient of the piezoelectric phase, and $k_{ij,\ \mathrm{magnetic}}$ is the coupling coefficient of the magnetic phase. Many of the single-phase materials possess either low permittivity or low permeability or both, as a consequence of which the magnetoelectric coupling is small. For magnetoelectric composite materials, an indirect coupling between ferroelectric and ferromagnetic phase can be established via strain.

16.1.2 Sintered Particulate ME Composites

Magnetoelectric effect is product property of the composite. Other examples of product property are piezoresistance (piezoelectric and magnetoresistance), magnetoresistance (magnetostriction and piezoresistance), photostriction (photoconductivity and electrostriction), and piezoluminescence (piezoelectricity and electroluminescence). ME effect in 3-0 particulate ME composites can be illustrated by coupling between the piezoelectric matrix and magnetostrictive dispersant or vice versa through elastic strain given as [1]:

$$\mathrm{ME}_H = \frac{\text{magnetic}}{\text{mechanical}} \times \frac{\text{mechanical}}{\text{electric}} \tag{16.5}$$

$$\mathrm{ME}_E = \frac{\text{electric}}{\text{mechanical}} \times \frac{\text{mechanical}}{\text{magnetic}} \tag{16.6}$$

ME coefficient (α_{E}) for 3-0 type particulate composites has been proposed as a following equation by Zubkov [6].

$$\begin{aligned}\alpha_E &= \left(\frac{\mathrm{d}E}{\mathrm{d}H}\right)_{\text{comp}} = \left(\frac{\mathrm{d}S}{\mathrm{d}H}\right)_{\text{comp}} \left(\frac{\mathrm{d}E}{\mathrm{d}S}\right)_{\text{comp}} \\ &= m_v \cdot \left(\frac{\mathrm{d}S}{\mathrm{d}H}\right)_{\text{ferrite}} (1 - m_v) \cdot \left(\frac{\mathrm{d}E}{\mathrm{d}S}\right)_{\text{piezoelectric}},\end{aligned} \tag{16.7}$$

Where m_v is the volume fraction of ferrite, ($\mathrm{d}E/\mathrm{d}S$) is the inverse of change in strain per unit magnetic field. Since $\mathrm{d}E = g{\cdot}\mathrm{d}X$ and $\mathrm{d}S = \mathrm{d}X/C$, where X is the stress, S is the strain, g is the piezoelectric voltage constant, and C is the stiffness, the equation (7) can be demonstrated as:

$$\alpha_{E33} = \left(\frac{\mathrm{d}E}{\mathrm{d}H}\right)_{\text{comp}} = m_v \cdot \left(\frac{\mathrm{d}S}{\mathrm{d}H}\right)_{\text{ferrite}} (1 - m_v) \cdot (g_{33} \cdot C_{33})_{\text{piezoelectric}}. \tag{16.8}$$

Since $g_{33} = d_{33}/\varepsilon_{33}^T$, the ME coefficient for 3-0 type particulate composites directly depends on the charge coefficient d_{33} and the permittivity ε_{33}^T of piezoelectric phase.

The primary requirement for the synthesis of composites using the sintering route can be summarized as (i) individual phases should be in equilibrium, (ii) mismatch between grains should not be present, (iii) large magnetostriction and piezoelectric effects in the respective constituent phases, (iv) high dielectric insulation so that accumulated charge does not leak through the composite, and (v) the ability to pole the piezoelectric phase in the composite [1].

ME particulate composites have been optimized as a function of sintering temperature, magnetostrictive phase composition, geometry, piezoelectric grain

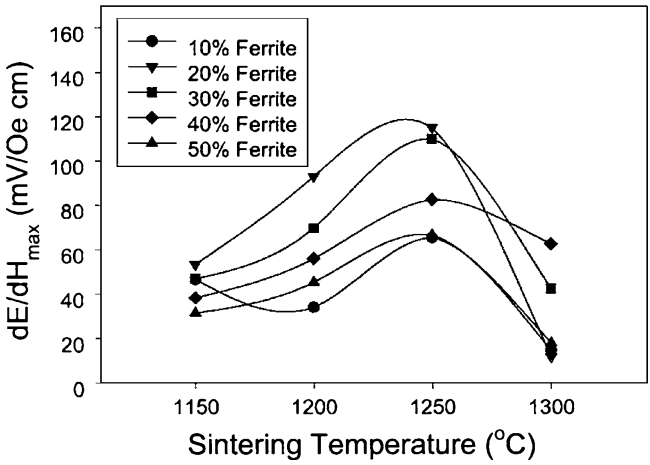

Fig. 16.3 Variation of ME voltage coefficient for PZT and Ni-ferrite particulate composite as a function of sintering temperature and Ni-ferrite mole fraction [7]

size, annealing and aging process, poling, and other composite variables. Figure 16.3 shows the maximum ME voltage coefficient of PZT and Ni-ferrite particulate composite as function of sintering temperature and Ni-ferrite fraction [7]. The composite consisting of 20 mol% Ni-ferrite exhibited maximum ME voltage coefficient of 115 mV/cmOe under magnetic bias of 1.2 kOe at 1 kHz. Figure 16.4 shows the partial laminate structure for ME composites which was shown to exhibit a high ME coefficient of 150 mV/cmOe [8]. The effect of grain size of piezoelectric materials on ME effect was reported by Islam et al. and it was shown that composites with grain size larger than 600 nm exhibited saturated ME coefficient [9]. Annealing and aging effects have been shown to provide enhancement in ME effect [10, 11]. However, the measured ME coefficient in 3-0 particulate composites has not reached the theoretical ME coefficient with high concentration of magnetic phase due to percolation [1]. Figure 16.5 shows that the dispersed ferrite particles in PZT matrix formed connected chains with increase in ferrite fraction and the ME coefficient was found to decrease due to high leakage resulting in poor poling. In order to improve the resistivity by suppressing percolation, we have proposed island–matrix microstructure that can reduce the diffusion and enhance the magnitude of percolation threshold. Figures 16.6a, b illustrates that the structure with isolated ferrite particles in a piezoelectric matrix can lead to reduction of the leakage by eliminating the connections between ferrite particles [12]. The island–matrix structure in Fig. 16.7 was reported by Ahn et al. [13] to achieve temperature independent piezoelectric properties and has been studied for high ME coefficient composites by optimizing the distribution of piezoelectric and magnetostrictive phase.

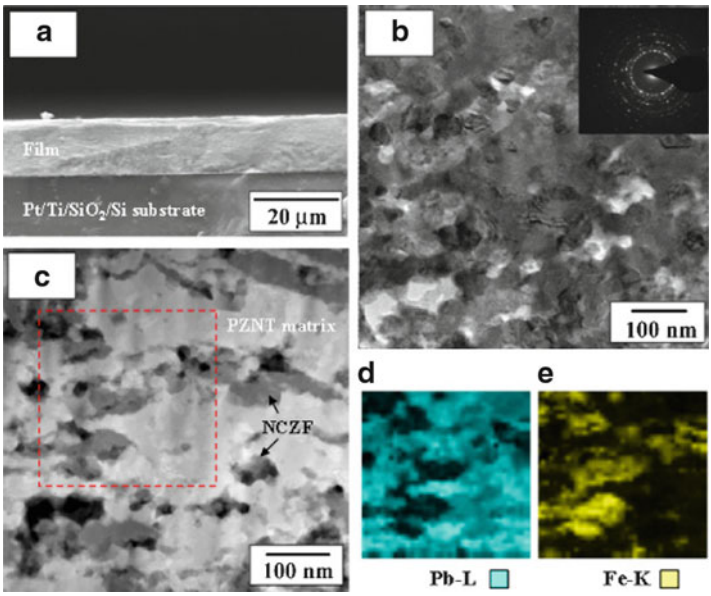

Fig. 16.4 Microstructure of 3-2 ME nanocomposite with formulation 0.8 [$0.8Pb(Zr_{0.52}Ti_{0.48})O_3$ – $0.2Pb(Zn_{1/3}Nb_{2/3})O_3$] – 0.2 [$(Ni_{0.6}Cu_{0.2}Zn_{0.2})Fe_2O_4$]: (**a**) cross-sectional SEM image, (**b**) TEM and SAED, (**c**) STEM, (**d**) and (**e**) EDX mapping. [8]

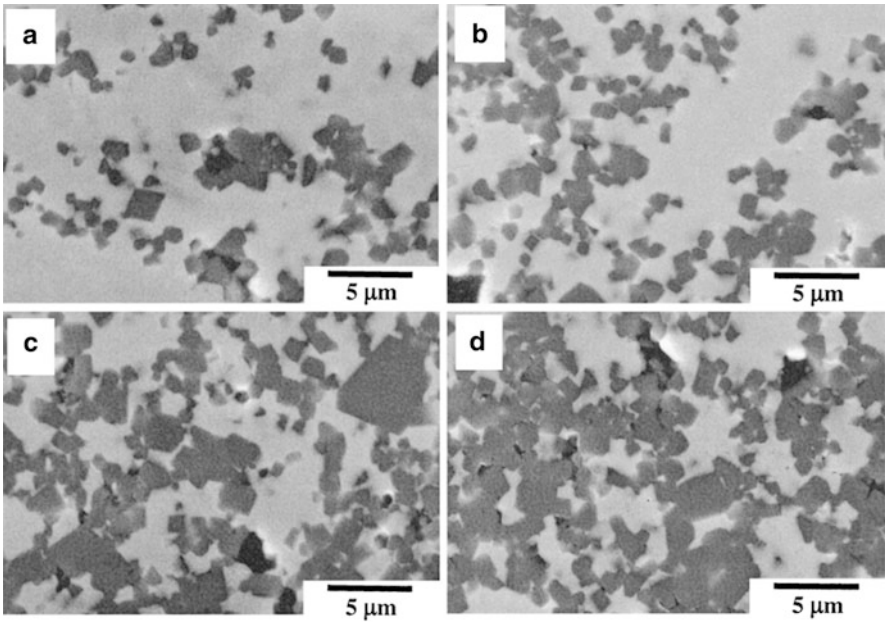

Fig. 16.5 SEM microstructures of PZT–Ni-ferrite composites: (**a**) 20 wt.%, (**b**) 30 wt.%, (**c**) 40 wt.%, and (**d**) 50 wt.% Ni-ferrite particles [7]

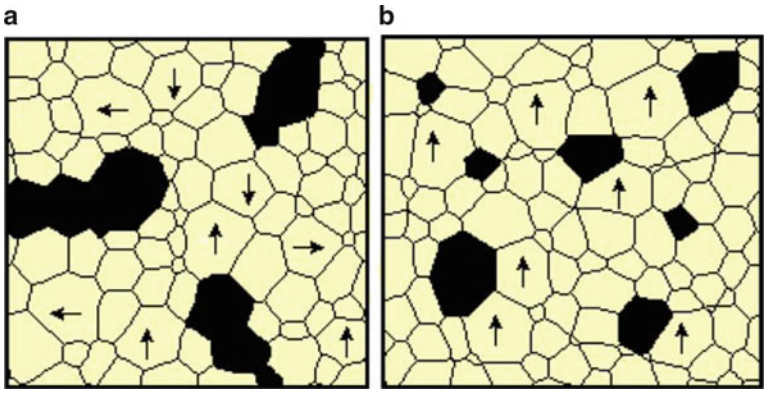

Fig. 16.6 Schematic diagram showing distribution of ferrite phase (in *black*) in piezoelectric matrix (in *yellow*) with two different connectivities. (**a**) composite materials prepared by mixing and sintering method, (**b**) composite materials produced by one-pot approach [12]

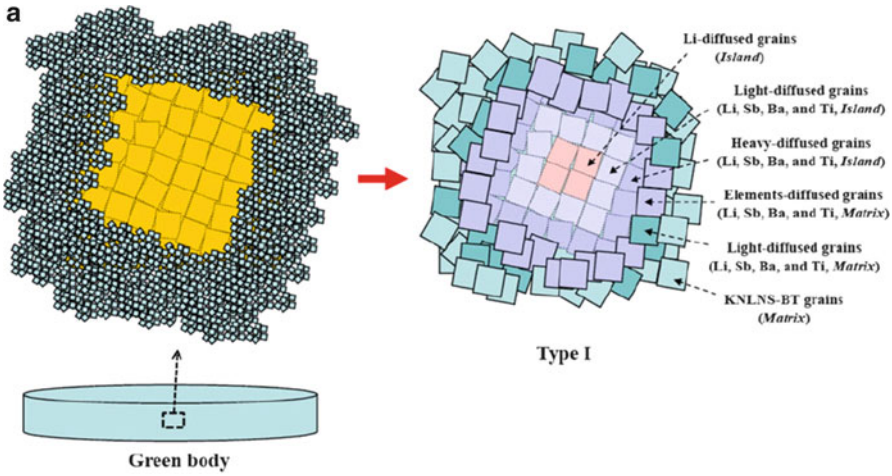

Fig. 16.7 Schematic diagram of island–matrix structure [13]

16.1.3 Laminate ME Composites

Laminate composites are generally fabricated by bonding magnetostrictive and piezoelectric layers using silver epoxy followed by annealing at lower temperature of ~100°C. The most common geometry for laminate composites is "sandwich" structure where the piezoelectric layer is arranged between two magnetostrictive ones. Under applied magnetic field, the strain in magnetostrictive layer is transferred to the piezoelectric layer through bonding layer resulting in the generation of electrical charge. In 2-2 ME laminate composites, there can be four possible modes

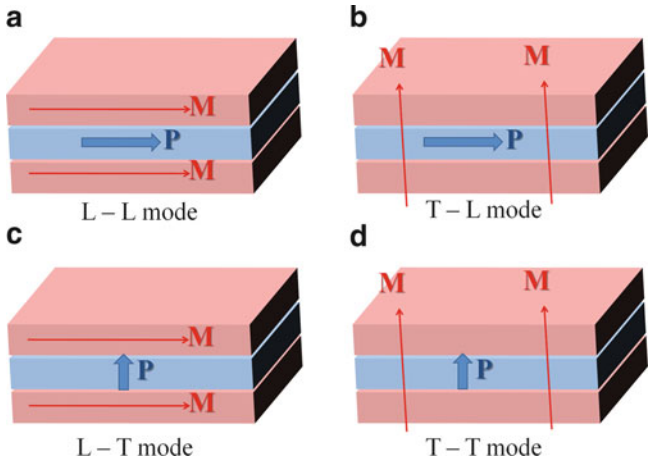

Fig. 16.8 Laminate ME composites operating in four types of vibration modes

as shown in Fig. 16.8. In L-L mode, both the applied H field and the measured E field are parallel to the principle vibration mode; in T-L mode the applied H field is perpendicular to the induced E field which is measured parallel to the principle mode; in L-T mode the applied H field is parallel and the induced E field is measured perpendicular to the principle mode; and in T-T mode the applied H field and induced E are perpendicular to the principle mode [14].

ME coefficient for 2-2 type laminate composites has been modeled by Srinivasan et al. [15]. The transverse ME coefficient for the laminate composites was given as:

$$\alpha_{E31} = \frac{\delta E_3}{\delta H_1} = \frac{-2d_{31}^p q_{11}^m v^m}{(s_{11}^m + s_{12}^m)\varepsilon_{33}^{T,P} v^p + (s_{11}^p + s_{12}^p)\varepsilon_{33}^{T,P} v^m - 2(d_{31}^p)^2 v_m} \tag{16.9}$$

The longitudinal ME coefficient for the laminate composites was given as [15]:

$$\alpha_{E33} = \frac{\delta E_3}{\delta H_3} = \frac{-2d_{31}^p q_{13}^m v^m}{(s_{11}^m + s_{12}^m)\varepsilon_{33}^{T,P} v^p + (s_{11}^p + s_{12}^p)\varepsilon_{33}^{T,P} v^m - 2(d_{31}^p)^2 v_m} \tag{16.10}$$

where d_{31}^p is piezoelectric coefficient, v^m and v^p are volumes of magnetostrictive and piezoelectric phases respectively, t^m and t^p are thicknesses of magnetostrictive and piezoelectric phases respectively, s_{11}^p, s_{12}^p are elastic compliances for piezoelectric phase, s_{11}^m, s_{12}^m are elastic compliances for magnetostrictive phase, $q_{11}$is piezomagnetic coefficient of the magnetostrictive phase, and $\varepsilon_{33}^{T,P}$is the permittivity of the piezoelectric phase.

In the laminate ME composites with 2-2 connectivity, detailed research has been conducted in the form of bilayers, trilayers, and multilayers of piezoelectric and magnetostrictive materials. The push–pull mode ME laminates consisting of PZT,

Terfenol D, and Metglas were found to exhibit a giant ME coefficient of ~20 V/cm·Oe with high magnetic sensitivity in resonance condition by Dong et al. [16]. Partial texturing of piezoelectric phase in 2-2 laminate composites shows 67% improvement of ME coefficient compared with random orientation [17]. Recently, self-biased ME effect in lead-free three-phase laminate composites was reported by Yang et al. [18]. The remnant ME effect at zero-magnetic bias has been studied for high-magnetic sensitivity and memory effect.

16.1.4 Cylinder-Matrix ME Composites

The 1-3 type cylinder-matrix structure for ME composites has been studied due to their considerable ME coupling compared to 2-2 laminate composites. In the 1-3 structure, the piezoelectric charge coefficient d_{33} and piezomagnetic coefficients q_{11} are determined by the stress components along the cylinders axis. The coefficients d_{33} and q_{11} are in general two times higher as compared to d_{31} and q_{12}, *thus there is possibility of higher response in 1-3 structure as compared to* 2-2 structure [3].

ME coefficient (α_E) for 1-3 type composites with piezoelectric cylinders aligned in magnetic matrix was given as [1]:

$$\alpha_{E33} = \frac{\delta E_3}{\delta H_3} = -\frac{f(1-f)q_{31}e_{31}}{\varepsilon_{33}{}^m k + \varepsilon_{33}{}^m m + \varepsilon_{33} f({}^p k - {}^m k)}, \tag{16.11}$$

where f is the volume fraction of the magnetic phase, q and e are the piezomagnetic and the piezoelectric coefficients, respectively. k and m are respectively the transverse in-plane bulk modulus and transverse shear modulus and superscripts m and p denote magnetic and piezoelectric phases, respectively. ε_{33} is the permittivity of piezoelectric phase.

ME coefficient for 1-3 type composites with magnetic cylinders aligned in piezoelectric matrix was given as [1]:

$$\alpha_{E33} = \frac{\delta E_3}{\delta H_3} = -\frac{f(1-f)q_{31}e_{31}}{\varepsilon_{33}{}^m k + \varepsilon_{33}{}^p m + \varepsilon_{33} f({}^p k - {}^m k)}. \tag{16.12}$$

In the cylinder-matrix ME composites with 1-3 connectivity, detailed analysis on PZT rods different size, shape and spacing has been conducted by Gebhardt et al. [19]. The 1-3 type composites with PZT rods embedded in a matrix of Terfenol-D/epoxy were reported to exhibit resonance shifts to lower frequency as increase in bias field by Lam et al. [20]. The 2-1-2 type ME composites with configuration of Metglas/$Ni_{0.6}Cu_{0.2}Zn_{0.2})Fe_2O_3$ (NCZF) pillar embedded $0.2Pb(Zn_{1/3}Nb_{2/3})O_3$ – $0.8Pb(Zr_{0.5}Ti_{0.5})O_3$ (PZNT) matrix/Metglas were found to exhibit effective coupling compared with the 2-2 laminate ME composites [21].

16.2 Background on Material Systems

Table 16.1 shows the list of piezoelectric materials commonly used for synthesizing ME composites. In this table, d_{33} is longitudinal piezoelectric strain constant, d_{31} is transverse piezoelectric strain constant, ε_r is relative dielectric constant, k_{33} is longitudinal coupling factor, and T_c is Curie temperature [14]. Table 16.2 shows the list of magnetostrictive materials used for fabricating ME composites. In this table, λ_s is saturation magnetization [14]. It is well known that the piezoelectric materials exhibiting high magnitude of piezoelectric voltage constant ($g = d/\varepsilon$) and low dielectric and piezoelectric losses are suitable as the piezoelectric phase. Thus, considerable effort has been devoted toward developing piezoelectric compositions based on relaxor ferroelectrics and grain texturing with improved g constant and low losses.

The ME coefficient of particulate composites has been reported to be of the order of ~100 mV/cmOe as shown in Table 16.3, which is significantly higher than that of single-phase ME materials. However, particulate ME composites exhibit much

Table 16.1 List of piezoelectric materials used for fabricating ME composites [14]

Material	d_{33} (pC/N)	d_{31} (pC/N)	εr (@ 1 kHz)	k_{33}	T_c (°C)
$BaTiO_3$	190	−78	1,700	0.49	120
APC 850 (soft PZT)	400	−175	1,750	0.72	360
APC 855 (soft PZT)	630	−276	3,300	0.76	250
APC 840 (hard PZT)	290	−125	1,250	0.72	325
PZT–$Pb(Ni_{1/3}Nb_{2/3})O_3$	600	−250	3,900	0.69	205
<001>0.92 $Pb(Zn_{1/3}Nb_{2/3})O_3$ – 0.08 $PbTiO_3$	2,230	−1,080	8,260 (ε_{33}^T)	0.94	170
PVDF (melting temperature)		−28	6	0.2 (k_t)	170
$SrBi_4Ti_4O_{15}$	20	−3	150	0.2	550
$(Na_{0.5}K_{0.5})NbO_3$	120	−40	400	0.4	350

Table 16.2 List of magnetostrictive materials for ME composites [14]

Material	$\lambda_s(\times 10^{-6})$
$MnFe_2O_4$	−5
Fe_3O_4	40
$CoFe_2O_4$	−110
$MgFe_2O_4$	−6
$Li_{0.5}Fe_{2.5}O_4$	−8
$NiFe_2O_4$	−26
$CuFe_2O_4$	−9
YFe_5O_{12}	−2
$SmFe_5O_{12}$	3.3
$DyFe_5O_{12}$	1.46
$EuFe_5O_{12}$	9.48

Table 16.3 List of 3-0 type particulate ME composites

Year	Compositions	DC Bias/ Frequency	dE/dH (mV/cm·Oe)	Ref.
1978	0.6 $BaTiO_3$ – 0.4 $Ni_{0.97}Co_{0.03}Mn_{0.1}Fe_{1.90}O_4$	500 Oe/1 kHz	80	[25]
2001	0.8 $Pb(Zr_{0.5}Ti_{0.5})O_3$ – 0.2 $NiCo_{0.02}Cu_{0.02}Mn_{0.1}Fe_{1.8}O_4$	1,250 Oe/1 kHz	115	[7]
2004	0.41 $Pb(Zr_{0.5}Ti_{0.5})O_3$ – 0.59 $Ni_{1-x}ZnxFe_2O_4$	250 Oe/100 Hz	45	[34]
2004	0.7 $Pb(Zr_{0.53}Ti_{0.47})O_3$ – 0.3 $CuFe_2O_4$	460 Oe/100 kHz	421	[35]
2004	0.68 $Pb(Zr_{0.57}Ti_{0.43})O_3$ – 0.32 $NiFe_2O_4$	1,000 Oe/1 kHz	80	[36]
2006	0.7 $Sr_{0.5}Ba_{0.5}Nb_2O_6$ – 0.3 $Ni_{0.8}Zn_{0.2}Fe_2O_4$	1,000 Oe/100 kHz	26	[37]
2007	0.9 $Pb(Zr_{0.52}Ti_{0.48})O_3$ – 0.1 $NiFe_{1.9}Mn_{0.1}O_4$	600 Oe/1 kHz	90	[38]
2008	0.8 $Pb(Zr_{0.52}Ti_{0.48})O_3$ – 0.2 $NiFe_2O_4$	454 Oe/1 kHz	195	[39]
2008	0.8 $Pb(Zr_{0.52}Ti_{0.48})O_3$ – 0.2 $Ni_{0.8}Zn_{0.2}Fe_2O_4$	1,200 Oe/1 kHz	155	[9]
2009	0.82 [0.69 $Pb(Mg_{1/3}Nb_{2/3})O_3$ – 0.31 $PbTiO_3$] – 0.18 $NiMn_{0.1}Fe_{1.9}O_4$	175 Oe/1 kHz	150	[40]
2010	0.6 $Pb(Zr_{0.5}Ti_{0.5})O_3$ – 0.4 $CoFe_2O_4$	3,000 Oe/1 kHz	70	[41]

Table 16.4 List of magnetostrictive materials used for fabricating laminate ME composites [2]

	$NiFe_2O_4$	Terfenol-D	Fe-Ga	Metglas 2,605
λ(ppm)	27	1,400	200	40
μ	20	6–10	20	>40,000
k_{33}		0.44		0.37
Q_m				1,000
ρ(g/cm^3)	5.37	7.8	7.7	7.18
R(Ω-m)	1×10^6	5.8×10^{-7}	6×10^{-7}	1.3×10^{-6}
T_c(°C)	535			395

lower ME coefficient than that theoretically predicted because of the problems related to low piezoelectric and magnetostrictive constants, interfacial defects, and low resistivity [22].

In order to overcome the limit of particulate ME composites, 2-2 type laminate ME composites were fabricated by bonding piezoelectric layer with magnetostrictive layer. Table 16.4 shows the list of magnetostrictive materials commonly used for fabricating laminate ME composites [2]. Terfenol-D has the largest magnetostriction but it has small permeability. Metglas on the other hand has extremely high relative permeability of >40,000 and thus is quite attractive magnetostrictive material in ME laminates. Table 16.5 shows that ME laminates can exhibit high ME coefficients even in the off-resonance condition. Park et al. have reported the

Table 16.5 List of 2-2 type laminate ME composites

Year	Compositions	DC Bias/ Frequency	dE/dH (mV/cm·Oe)	Ref.
2001	$Pb(Zr,Ti)O_3/TbDyFe_2$	4,200 Oe/1 kHz	4,680	[42]
2002	$Pb(Zr_{0.5}Ti_{0.5})O_3/Tb_{1-x}Dy_xFe_2$	4,000 Oe/1 kHz	5,900	[43]
2004	$Pb(Mg_{1/3}Nb_{2/3})O_3$-$PbTiO_3/Tb_{1-x}Dy_xFe_2$	400 Oe/1 kHz	4,300	[44]
2004	$BaTiO_3/Tb_{1-x}Dy_xFe_2$	350 Oe/1 kHz	2,100	[45]
2005	$Ni/Pb(Zr_{0.5}Ti_{0.5})O_3/Ni$	80 Oe/1 kHz	450	[46]
2006	$BaTiO_3/Ni_{0.8}Zn_{0.2}Fe_2O_4$	1,000 Oe/1 kHz	152	[47]
2006	Terfenol-D/$Pb(Zr,TiO)_3$/μ-metal	240 Oe/1 kHz	>1,400	[48]
2007	Fe-doped $BaTiO_3/Tb_{1-x}Dy_xFe_{2-y}$	350 Oe/100 Hz	2,100	[49]
2008	0.9 $Pb(Zr_{0.52}Ti_{0.48})O_3$ - 0.1 $Pb(Zn_{1/3}Nb_{2/3})O_3/Ni_{0.6}Cu_{0.2}Zn_{0.2}Fe_2O_4$	400 Oe/1 kHz	468	[50]
2009	$BaTi_{0.99}Cr_{0.01}O_3/Tb_{1-x}Dy_xFe_{2-y}$	355 Oe/100 Hz	2,753	[51]
2010	$Pb(Zr,Ti)O_3$-$Pb(Mg_{1/3}Nb_{2/3})O_3$ single crystal/Terfenol-D/Metglas	1,011 Oe/1 kHz	5,150	[23]
2010	Mn-doped $Na_{0.5}Bi_{0.5}TiO_3$–$BaTiO_3$ single crystal/Terfenol-D	400 Oe/1 kHz	1,320	[52]

Table 16.6 List of 1-3 type ME composites.

Year	Compositions	DC Bias/ Frequency	dE/dH (mV/cm·Oe)	Ref.
2006	$Pb(Zr_{0.5}Ti_{0.5})O_3$ pillars/Terfenol-D matrix	2,000 Oe/<40 kHz	300	[53]
2007	$Pb(Zr_{0.5}Ti_{0.5})O_3$ pillars/Terfenol-D matrix	1,500 Oe/100 Hz	500	[3]
2010	Metglas/$Ni_{0.6}Cu_{0.2}Zn_{0.2})Fe_2O_3$ (NCZF) pillar embedded 0.2Pb $(Zn_{1/3}Nb_{2/3})O_3$-0.8$Pb(Zr_{0.5}Ti_{0.5})O_3$ (PZNT) matrix/Metglas	90 Oe/1 kHz	352	[21]
2010	$Pb(Zr_{0.5}Ti_{0.5})O_3$ pillars/Terfenol-D/ epoxy matrix	1,500 Oe/1 kHz	130	[20]

maximum ME coefficient of 5,150 mV/cmOe in off-resonance condition by combining PZT-PMN, Metglas, and Terfenol-D [23].

The 1-3 type cylinder-matrix ME composites have been investigated for high ME coefficient owing to strong contribution from d_{33} and q_{11}. As shown in Table 16.6, the composites with configuration of PZT rods embedded in Terfenol-D matrix were found to exhibit maximum ME coefficient $\alpha_{E,\ max}$ under $H_{bias} = 1{,}000$–$2{,}000$ Oe. The 2-1-2 structure ME composites with Metglas show the ME coefficient of 352 mV/cm·Oe which is 15% higher magnitude than that for 2-2 laminate composites. This higher response is associated with the existence of NCNF pillars in the PZNT matrix causing strong coupling of elastic strain [21]. The 1-3 type ME composites were found to exhibit maximum ME coefficient of

Table 16.7 List of lead-free piezoelectric materials based on KNN, NBT, and BT

Year	Compositions	d_{33} (pC/N)	k_p	T_c (°C)	T_{O-T}/T_d (°C)	Ref.
1959	$(K_{0.5}Na_{0.5})NbO_3$	80	0.35	420	195	[54]
2005	$(K_{0.465}Na_{0.465}Li_{0.07})NbO_3$	240	0.45	460	~20	[55]
2006	$(K_{0.44}Na_{0.52}Li_{0.04})(Nb_{0.84}Ta_{0.1}Sb_{0.06})O_3$	410	0.61	253	25	[56]
2006	0.95 $(K_{0.5}Na_{0.5})NbO_3$ – 0.05 $SrTiO_3$	200	0.37	277	27	[57]
2005	0.95 $(K_{0.5}Na_{0.5})NbO_3$ – 0.05 $LiTaO_3$	200	0.36	430	55	[58]
2004	0.94 $(K_{0.5}Na_{0.5})NbO_3$ – 0.06 $LiNbO_3$	235	0.42	460	70	[59]
2006	0.95 $(K_{0.5}Na_{0.5})NbO_3$ – 0.05 $LiSbO_3$	283	0.5	392	45	[60]
2006	0.7 $Bi_{0.5}Na_{0.5}TiO_3$ – 0.2 $Bi_{0.5}K_{0.5}TiO_3$ – 0.1 $Bi_{0.5}Li_{0.5}TiO_3$	216	0.401	350	160	[61]
2007	x $(Na_{0.5}Bi_{0.5})TiO_3$ – y $(K_{0.5}Bi_{0.5})TiO_3$ – z $BaTiO_3$, [$x+y+z = 1$; $y:z = 2:1$]	145	0.162	302	224	[62]
2006	0.5 $Na_{0.5}Bi_{0.5}TiO_3$ – 0.5 $K_{0.5}Bi_{0.5}TiO_3$	150	0.22	320	210	[63]
1958	$BaTiO_3$	190	0.36	115	0	[64]
1957	0.95 $BaTiO_3$ – 0.05 $CaTiO_3$ – Co	150	0.31	105	−45	[65]

500 mV/cm·Oe under off-resonance frequencies of <40 kHz and giant ME coefficient of 18.2 V/cm·Oe under a resonance frequency of 84 kHz [3].

16.3 Why Is Lead-Free Magnetoelectric Composite Promising System?

Recently, investigations have focused on developing lead-free materials [24]. Lead-free piezoelectric materials considered for ME laminates can be classified into three material groups (i) $K_{0.5}Na_{0.5}NbO_3$ (KNN), (ii) $Na_{0.5}Bi_{0.5}TiO_3$ (NBT), and (iii) $BaTiO_3$ (BT). Table 16.7 shows piezoelectric and electromechanical properties for compositions based on KNN, NBT, and BT.

$BaTiO_3$-$CoFeO_4$ lead-free composites were the first ones investigated by Boomgaard et al. in 1978 and found to exhibit ME coefficient of 130 mV/cmOe [25]. Since that time, few studies have been conducted on lead-free ME composites as shown in Table 16.8, mainly because of the poor piezoelectric performance of lead-free materials. This problem still remains but the emphasis on developing lead-free ME composites has increased due to environmental concern.

Table 16.8 List of lead-free ME composites

Year	Compositions	Type	DC Bias/ Frequency	dE/dH (mV/cm·Oe)	Ref.
2005	$BaTiO_3 - CoFe_2O_4$	Particulate	270 Oe/ 160 kHz	2,540	[12]
2006	0.7 $Sr_{0.5}Ba_{0.5}Nb_2O_6$ – 0.3 $Ni_{0.8}Zn_{0.2}Fe_2O_4$	Particulate	1–3 kOe/ 100 kHz	26.6	[37]
2009	$BaTiO_3 - CoFe_2O_4$	Particulate	2,000 Oe/ 20 kHz	17.04	[66]
2009	$(K_{0.5}Na_{0.5})NbO_3$-$LiSbO_3 - CoFe_2O_4$	Particulate	2,200 Oe/ 1 kHz	15	[67]
2010	0.75 $BaZr_{0.08}Ti_{0.92}O_3$ – 0.25 $Co_{1.2-y}Mn_yFe_{1.8}O_4$, (y = 0–0.4)	Particulate	1,500 Oe/ 1 kHz	2.5	[68]
2006	$BaTiO_3/(Ni_{0.8}Zn_{0.2})Fe_2O_4$	Laminate	1,000 Oe/ 1 kHz	152	[47]
2010	0.885 $Bi_{0.5}Na_{0.5}TiO_3$ – 0.05 $Bi_{0.5}$ $K_{0.5}TiO_3$ – 0.015 $Bi_{0.5}Li_{0.5}TiO_3$ – 0.05 $BaTiO_3$/ Terfenol-D	Laminate	600 Oe/ 131 kHz	2,500	[69]
2010	Mn-doped $Na_{0.5}Bi_{0.5}TiO_3$–$BaTiO_3$ single crystal/Terfenol-D	Laminate	400 Oe/ 1 kHz	1,320	[52]

16.4 Problem of H_{DC} Bias for Various Magnetostrictive Materials

One of the problems related to the design of magnetic field sensors is the need for DC bias magnets. Additional magnets make the device bulky and require insulation. Thus, there is critical need for design of self-biased ME laminates. In this section, we first describe the magnitude of DC bias required for the 2-2 type laminates. 2-2 type laminate ME composites can be categorized by the type of magnetostrictive material used in the design (i) ferrite, (ii) Terfenol-D, and (iii) Metglas. Each of these ME laminate has different ME behavior due to difference in coercive field (H_c), permeability (μ), and magnetization (M). Especially, the optimum magnitude of DC magnetic bias field (H_{DC}) depends on material composition and volume fraction of magnetostrictive phase.

16.4.1 Ferrite-Based Laminates

Various ferrite-based materials have been used as magnetostrictive phase in the design of laminates including $Co_{0.6}Zn_{0.4}Fe_2O_4$, $Ni_{0.93}Co_{0.02}Mn_{0.05}Fe_{1.95}O_4$, $Ni_{0.6}Cu_{0.2}Zn_{0.2}Fe_2O_4$, $Li_{0.35}Zn_{0.3}Fe_{2.35}O_4$, $NiFe_{1.9}Mn_{0.1}O_4$, $NiFe_2O_4$, and $Ni_{0.8}Zn_{0.2}Fe_2O_4$. Table 16.9 shows the composition of ME laminates along with

Table 16.9 List of ME laminates based on ferrite

Year	Compositions	DC Bias (Oe)	Ref.
2001	$Pb(Zr, Ti)O_3/NiFe_2O_4$ – bilayer	100	[15]
2001	$Pb(Zr, Ti)O_3/NiFe_2O_4$ – multilayer	400	[15]
2002	$Pb(Zr, Ti)O_3/Ni_{0.8}Zn_{0.2}Fe_2O_4$	100	[70]
2003	$Pb(Zr, Ti)O_3/Co_{0.6}Zn_{0.4}Fe_2O_4$	450	[71]
2003	$Pb(Zr, Ti)O_3/Ni_{0.8}Zn_{0.2}Fe_2O_4$	150	[71]
2003	$Pb(Zr, Ti)O_3/Li_{0.35}Zn_{0.3}Fe_{2.35}O_4$	150	[72]
2003	$Pb(Zr, Ti)O_3/Ni_{0.93}Co_{0.02}Mn_{0.05}Fe_{1.95}O_4$	700	[73]
2006	$BaTiO_3/Ni_{0.8}Zn_{0.2}Fe_2O_4$	1,000	[47]
2006	$Pb(Zr, Ti)O_3/Ni_{0.8}Zn_{0.2}Fe_2O_4$	250	[74]
2008	$Ni_{0.6}Cu_{0.2}Zn_{0.2}Fe_2O_4/0.9Pb(Zr_{0.52}Ti_{0.48})O_3$–$0.1Pb(Zn_{1/3}Nb_{2/3})O_3/Ni_{0.6}Cu_{0.2}Zn_{0.2}Fe_2O_4$	400	[75]

Table 16.10 List of ME laminates based on Terfenol-D

Year	Compositions	DC Bias (Oe)	Ref.
2001	$Pb(Zr,Ti)O_3$/Terfenol-D	4,200	[42]
2002	$Pb(Zr_{0.5}Ti_{0.5})O_3$/Terfenol-D	4,000	[43]
2003	$Pb(Zr,Ti)O_3$/Terfenol-D	200	[76]
2003	$Pb(Zr_{0.52}Ti_{0.48})O_3$/Terfenol-D	700	[77]
2004	$Pb(Mg_{1/3}Nb_{2/3})O_3$-$PbTiO_3$/Terfenol-D	400	[44]
2004	$BaTiO_3$/Terfenol-D	350	[45]
2005	$Pb(Zr_{0.52}Ti_{0.48})O_3$/Terfenol-D	700	[78]
2005	$Pb(Mg_{1/3}Nb_{2/3})O_3$-$PbTiO_3$/Terfenol-D	450	[16]
2007	Fe-doped $BaTiO_3$/Terfenol-D	350	[49]
2008	$Pb(Mg_{1/3}Nb_{2/3})O_3$-$PbTiO_3$/Terfenol-D	400	[79]
2009	$Pb(Mg_{1/3}Nb_{2/3})O_3$-$PbTiO_3/Tb_{0.3}Dy_{0.7}Fe_{1.92}$	400	[80]
2009	$BaTi_{0.99}Cr_{0.01}O_3/Tb_{1-x}Dy_xFe_{2-y}$	355	[51]
2009	$Pb(Mg_{1/3}Nb_{2/3})O_3$-$PbTiO_3$/Terfenol-D	400	[81]
2010	$Pb(Zr,Ti)O_3$/Terfenol-D	300	[82]
2010	Mn-doped $Na_{0.5}Bi_{0.5}TiO_3$–$BaTiO_3$ single crystal/Terfenol-D	400	[52]

optimum magnitude of H_{DC}. The magnitude of optimum H_{DC} for ferrite-based composites lies in the wide range of 100–1,000 Oe.

16.4.2 Terfenol-D-Based Laminates

Since 2001, ME laminates based on Terfenol-D have been studied for realizing giant ME effect. Table 16.10 shows that these composites exhibit H_{DC} bias of several hundred oersted due to low relative permeability of 3–10.

Table 16.11 List of ME laminates based on Metglas

Year	Compositions	DC Bias (Oe)	Ref.
2006	PVDF/Metglas	8	[26]
2009	$Pb(Zr,Ti)O_3$ fiber/Metglas	<10	[83]
2009	PVDF/Metglas	52	[84]
2009	PVDF/Metglas	<10	[85]
2009	$Pb(Zn_{1/3}Nb_{2/3})_x(Zr_{0.5}Ti_{0.5})_{1-x}O_3$/Metglas	100–325	[27]

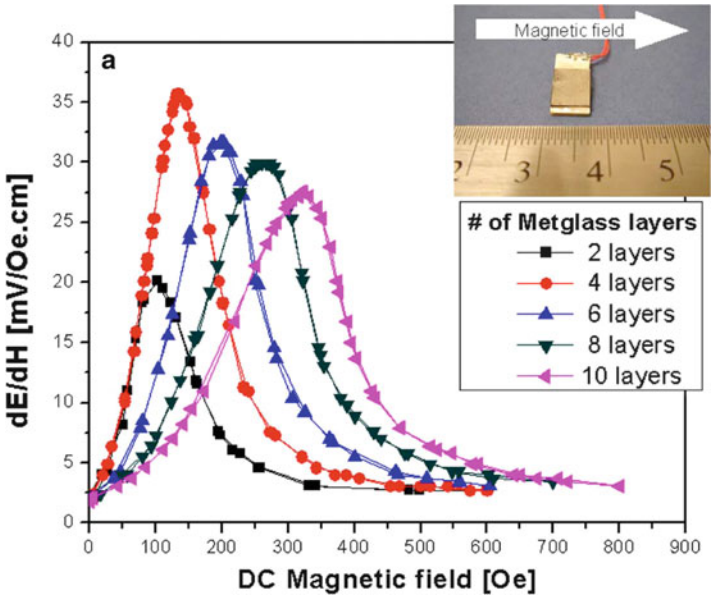

Fig. 16.9 H_{DC} bias as a function of number of Metglas layers in ME laminates [27]

16.4.3 Metglas-Based Laminates

Metglas-based laminates are attractive due to their low DC bias magnetic field of <20 Oe, which is highly desirable for magnetic field sensors. Table 16.11 shows that ME laminates based on Metglas have been found to exhibit extremely small H_{DC} of few Oe by Zhai et al. [26]. Recently, Park et al. have reported the effect of number of Metglas layers on the magnitude of H_{DC} as shown in Fig. 16.9 [27].

16.5 Can we Achieve Zero-Magnetic DC Bias?

As discussed in the previous section, ME composites consisting of magnetostrictive material exhibit maximum ME coefficient (α_E) at optimum magnetic DC bias (H_{dc}). The magnitude of H_{dc} corresponds with the maxima observed in piezomagnetic

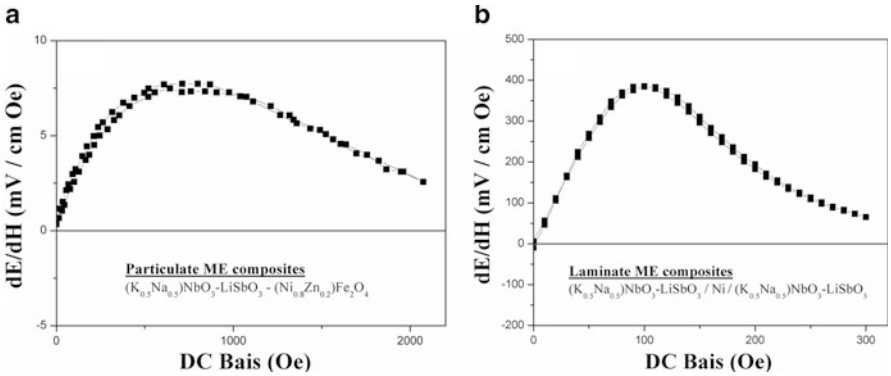

Fig. 16.10 α_E of ME composites for 3-0 type particulate and 2-2 type laminate composites

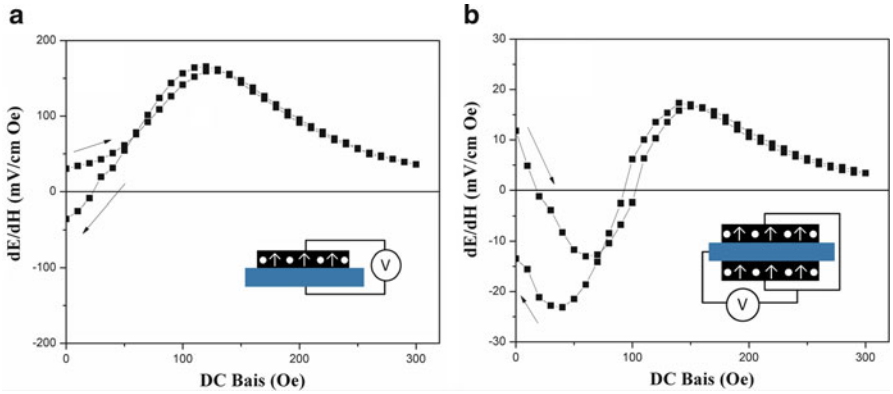

Fig. 16.11 α_E of ME laminates for (**a**) KNNLS-NZF/Ni bilayer and (**b**) KNNLS-NZF/Ni/KNNLS-NZF trilayer [18]

coefficient as a function of applied magnetic field. The magnitude of α_E is 0 mV/cm·Oe at zero H_{dc}. Figure 16.10 shows the general ME behavior for particulate and laminate composites operating in L-T mode, demonstrating zero α_E at zero H_{dc} and position of peak α_E for (a) 3-0 type particulate composite with composition 0.8 [$0.948K_{0.5}Na_{0.5}NbO_3 - 0.052LiSbO_3$] (KNNLS) – 0.2 $Ni_{0.8}Zn_{0.2}Fe_2O_4$ (NZF) and (b) 2-2 type laminate consisting of KNNLS and Ni.

Self-biased ME effect defined as "remnant ME coefficient (α_{ER}) at zero H_{dc}" was observed in lead-free laminate ME composites consisting of single-phase ferroelectric layer and multi-phase ferromagnetic materials. Figure 16.10 shows the ME laminates consisting of Ni plate and 3-0 type particulate ME composite with composition KNNLS-NZF. These laminates exhibit α_{ER} at zero H_{dc} and zero-crossing points at non-zero H_{dc} [18]. The ME bilayer in Fig. 16.11 (a) has α_{ER} of 30 mV/cm·Oe at $H_{dc} = 0$ Oe, zero-crossing point at $H_{dc} = 23$ Oe, and maximum α_E of 166 mV/cm·Oe at $H_{dc} = 120$ Oe. The ME trilayer laminate in

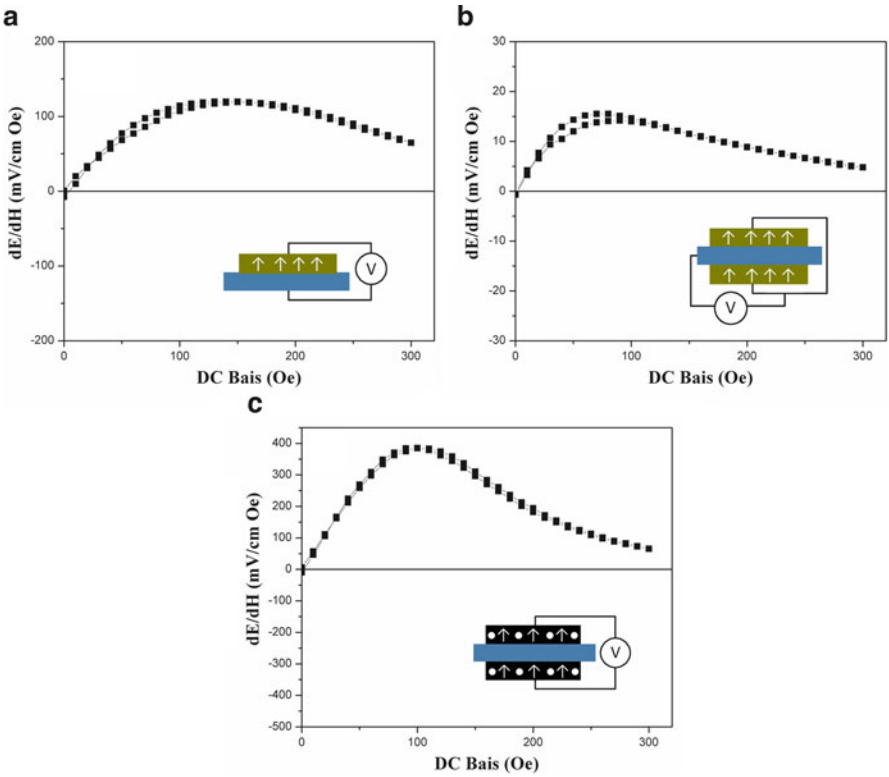

Fig. 16.12 α_E of ME laminates for (**a**) KNNLS/Ni bilayer, (**b**) KNNLS/Ni/KNNLS trilayer, and (**c**) KNNLS-NZF/Ni/KNNLS-NZF trilayer with radial circuit mode. [18]

Fig. 16.11b has α_{ER} of 11.78 mV/cm·Oe at $H_{dc} = 0$ Oe, minimum α_E of 23.1 mV/cm·Oe at $H_{dc} = 34$ Oe, maximum α_E of 16.6 mV/cm·Oe at $H_{dc} = 145$ Oe, and two zero-crossing points at $H_{dc} = 17.7$ and 92.8 Oe [18]. Thus, ME composites consisting of two magnetostrictive materials exhibit hysteresis and result in self-biased ME effect.

16.5.1 Important Variables and Their Effect on Self-Bias

ME laminates consisting of two magnetostrictive materials have gradient of magnetization (M) that yields an internal potential according to the equation given by Srinivasan et al. [28]:

$$-\nabla^2\varphi(r) = -\nabla \cdot M(r) = \nabla \cdot H_{\text{int}}(r), \tag{16.13}$$

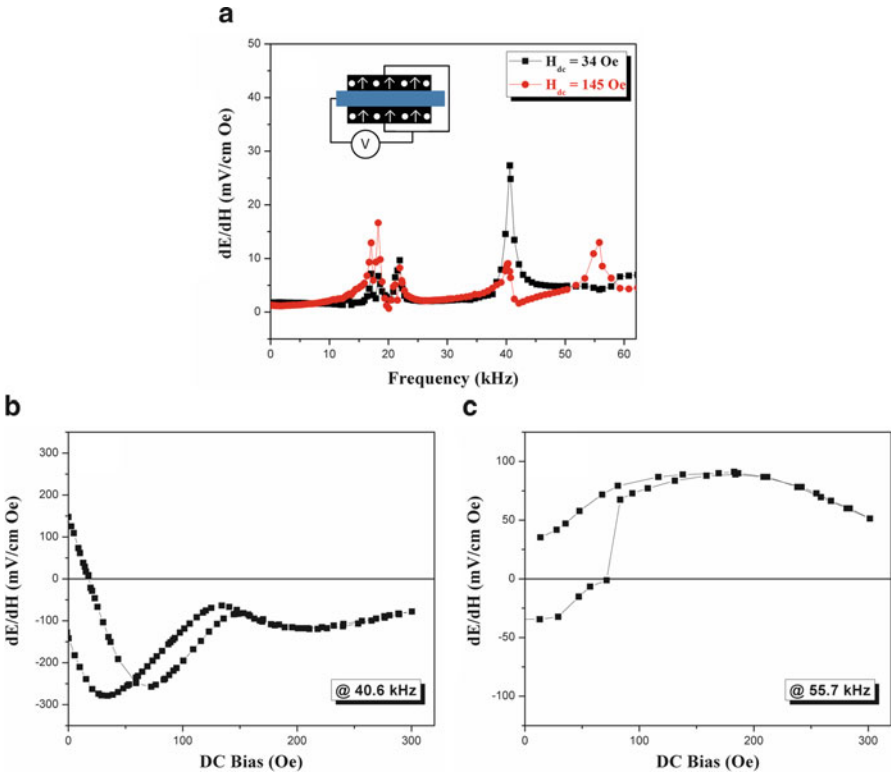

Figure 16.13 α_E of KNNLS-NZF/Ni/KNNLS-NZF laminate operating in bending mode: (**a**) variation as a function of frequency, (**b**) at resonance frequency of 40.6 kHz, and (**c**) at resonance frequency of 55.7 kHz [18]

where φ is magnetic scalar potential, and H_{int} is internal or built-in magnetic field. The variation of M depends on difference of permeability and spontaneous magnetization between magnetic materials. This explains the results shown in Fig. 16.11 for self-biased ME effect consisting of NZF and Ni. Figure 16.12a, b shows the results for bilayer and trilayer ME laminates with only Ni as magnetostrictive phase clearly demonstrating that composites with only one ferromagnetic layer do not have any α_{ER}. The ME laminate shown in Fig. 16.12c operating in radial vibration mode was also found not to exhibit any α_{ER}. The laminate shown in Fig. 16.11b operates in bending vibration mode and has finite α_{ER}. Thus for self-biased ME response it is important to have a combination of built-in bias field and bending strain [18].

Figure 16.13a shows the variation of α_E as a function of frequency for the laminates of KNNLS-NZF/Ni/KNNLS-NZF operating in bending mode. At two-resonance frequencies and DC bias fields of 34 and 145 Oe, the ME laminate shows quite different ME hysteresis due to the changes in coupling between H_{bias} and bending strain [18]. At the resonance frequency of 40.6 kHz and $H_{dc} = 34$ Oe, there

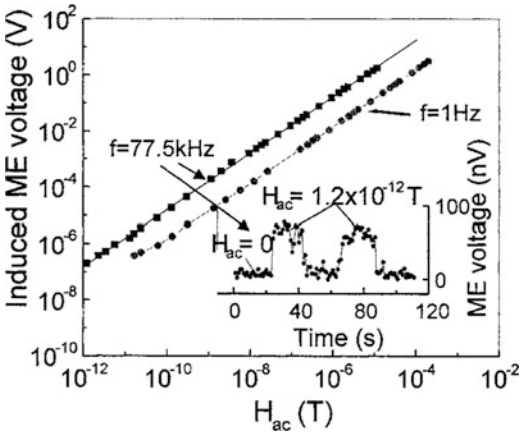

Fig. 16.14 Magnetic field sensitivity measurements taken under dc magnetic bias of 450 Oe. The inset shows the change in ME voltage as a function of time in response to minute magnetic field variation [16]

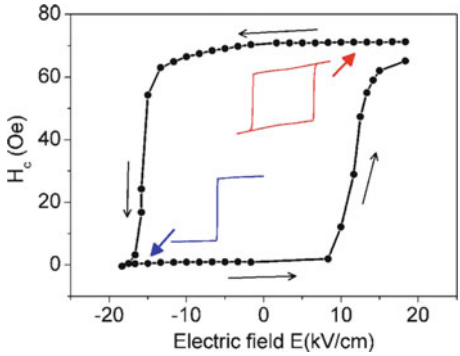

Fig. 16.15 Electric-field modulation of magnetic coercive field (H_c) in $Fe_{0.93}Ge_{0.07}$ film grown on fully poled BSPT ferroelectric oxide layer. The inset loops linked with the arrows to +E and −E show two typical Kerr hysteresis loops with the two different H_c states [33]

is high α_{ER} of 300 mV/cm·Oe with sharp slope. This behavior is mainly driven by H_{bias} and is extremely attractive for low-field high sensitivity magnetic sensors. At the resonance frequency of 55.7 kHz and $H_{dc} = 145$ Oe, the laminate has constant α_E for wide range of applied magnetic field 0–50 Oe which can provide the possibility for designing electrically tuned memory states.

Recently, ME effect has been used in magnetic field sensors and memory devices [14, 29–32]. Dong et al. have characterized the performance of push–pull ME Terfenol-D/PMN-PT/Terfenol-D three-layer laminates for AC/DC magnetic field sensitivity [16]. Figure 16.14 shows that these laminates exhibit a high AC magnetic field sensitivity of ~10^{-12} T at room temperature under resonance conditions [16]. Li et al. have reported a ME memory cell with two different coercivity state where writing was controlled by electric fields [33]. Figure 16.15 shows the possibility for ME memory with electric-write/magnetic-read controlled by two different magnetic coercive field (H_c) states [33]. A high magnitude of electric field is required to accomplish the write operation. Using the results shown for self-bias magnetoelectric effect, one can reduce the magnitude of field required for writing operation.

References

1. Nan CW, Bichurin MI, Dong SX, Viehland D, Srinivasan G (2008) Multiferroic magnetoelectric composites: Historical perspective, status, and future directions. J Appl Phys 103:031101
2. Zhai J, Xing Z, Dong S, Li J, Viehland D (2008) Magnetoelectric laminate composites: an overview. J Am Ceram Soc 91:351–358
3. Ma J, Shi Z, Nan CW (2007) Magnetoelectric properties of composites of single Pb(Zr, Ti)O3 rods and terfenol-d/epoxy with a single-period of 1–3-type structure. Adv Mater 19:2571–2573
4. Brown WF, Hornreich RM, Shtrikman S (1968) Upper bound on the magnetoelectric susceptibility. Phys Rev 168:574
5. O'Dell TH (1963) The Field Invariants in a Magnetoelectric Medium. Phila Mag 8:411
6. Zubkov AS (1978) On the magnetoelectric effect in segnetomagnetic composites based on piezoelectric and magnetostrictive materials. Elektrichestvo 10:77
7. Ryu J, Carazo AV, Uchino K, Kim HE (2001) Piezoelectric and magnetoelectric properties of lead zirconate titanate/Ni-Ferrite particulate composites. J Electroceram 7:17–24
8. Park CS, Ryu J, Choi JJ, Park DS, Ahn CW, Priya S (2009) Giant magnetoelectric coefficient in 3–2 nanocomposite thick films. Jpn J Appl Phys 48:080204
9. Islam RA, Priya S (2008) Effect of piezoelectric grain size on magnetoelectric coefficient of $Pb(Zr_{0.52}Ti_{0.48})O_3$-$Ni_{0.8}Zn_{0.2}Fe_2O_4$ particulate composites. J Mater Sci 43:3560–3568
10. Islam RA, Priya S (2006) Annealing and aging effect in 0.95 Pb(Zr0.52Ti0.48)O3–0.05 NiFe1.9Mn0.1O4 particulate magnetoelectric composites. Jpn J Appl Phys 45:L128–L131
11. Islam RA, Priya S (2006) Synthesis of high magnetoelectric coefficient composites using annealing and aging route. Int J Appl Ceram Technol 3:353–363
12. Ren SQ, Weng LQ, Song SH, Li F, Wan JG, Zeng M (2005) BaTiO3/CoFe2O4 particulate composites with large high frequency magnetoelectric response. J Mater Sci 40:4375–4378
13. Ahn CW, Park CS, Dittmer R, Hong SH, Priya S (2010) Effect of elemental diffusion on temperature coefficient of piezoelectric properties in KNN-based lead-free composites. J Mater Sci 45:3961–3965
14. Priya S, Islam R, Dong SX, Viehland D (2007) Recent advancements in magnetoelectric particulate and laminate composites. J Electroceram 19:147–164
15. Srinivasan G, Rasmussen ET, Gallegos J, Srinivasan R, Bokhan YI, Laletin VM (2001) Magnetoelectric bilayer and multilayer structures of magnetostrictive and piezoelectric oxides. Phys Rev B 64:214408
16. Dong S, Zhai J, Bai F, Li JF, Viehland D (2005) Push-pull mode magnetostrictive/piezoelectric laminate composite with an enhanced magnetoelectric voltage coefficient. Appl Phys Lett 87:062502
17. Islam RA, Priya S (2009) ME response of cofired trilayer magnetoelectric composites with partial texturing. J Mater Sci 44:5935–5938
18. Yang SC, Park CS, Cho KH, Priya S (2010) Self-biased magnetoelectric response in three-phase laminates. J Appl Phys 108:093706
19. Gebhardt S, Schonecker A, Steinhausen R, Seifert W, Beige H (2003) Quasistatic and dynamic properties of 1–3 composites made by soft molding. J Eur Ceram Soc 23:153–159
20. Lam KH, Lo CY, Chan HLW (2010) Frequency response of magnetoelectric 1-3-type composites. J Appl Phys 107:093901
21. Park CS, Ahn C, Priya S (2010) Enhanced magnetoelectric properties in three-phase composites with 2-1-2 connectivity. Philos Mag 90:4443–4452
22. Karmarkar M, Dong SX, Li JF, Viehland D, Priya S (2008) Magnetoelectric laminate based DC magnetic field sensor. Phys Status Solidi-Rapid Res Lett 2:108–110
23. Park CS, Cho KH, Arat MA, Evey J, Priya S (2010) High magnetic field sensitivity in Pb(Zr, Ti)O3-Pb(Mg1/3Nb2/3)O3 single crystal/Terfenol-D/Metglas magnetoelectric laminate composites. J Appl Phys 107:094109
24. Saito Y, Takao H, Tani T, Nonoyama T, Takatori K, Homma T, Nagaya T, Nakamura M (2004) Lead-free piezoceramics. Nature 432:84–87

25. Boomgaard J, Born RAJ (1978) A sintered magnetoelectric composite material $BaTiO_3$-Ni (Co, Mn)Fe_2O_4. J Mater Sci 13:1538–1548
26. Zhai JY, Dong SX, Xing ZP, Li JF, Viehland D (2006) Giant magnetoelectric effect in Metglas/polyvinylidene-fluoride laminates. Appl Phys Lett 89:083507
27. Park CS, Ahn CW, Ryu J, Yoon WH, Park DS, Kim HE, Priya S (2009) Design and characterization of broadband magnetoelectric sensor. J Appl Phys 105:094111
28. Mantese JV, Micheli AL, Schubring NW, Hayes RW, Srinivasan G, Alpay SP (2005) Magnetization-graded ferromagnets: The magnetic analogs of semiconductor junction elements. Appl Phys Lett 87:082503
29. Nan CW, Li M, Huang JH (2001) Calculations of giant magnetoelectric effects in ferroic composites of rare-earth-iron alloys and ferroelectric polymers. Phys Rev B 63:144415
30. Fetisov YK, Bush AA, Kamentsev KE, Ostashchenko AY, Srinivasan G (2006) Ferrite-piezoelectric multilayers for magnetic field sensors. IEEE Sens J 6:935–938
31. Bea H, Gajek M, Bibes M, Barthelemy A (2008) Spintronics with multiferroics. J Phys-Condes Matter 20:434221
32. Bibes M, Barthelemy A (2008) Multiferroics: Towards a magnetoelectric memory. Nat Mater 7:425–426
33. Li Z, Wang J, Lin YH, Nan CW (2010) A magnetoelectric memory cell with coercivity state as writing data bit. Appl Phys Lett 96:162505
34. Srinivasan G, DeVreugd CP, Flattery CS, Laletsin VM, Paddubnaya N (2004) Magnetoelectric interactions in hot-pressed nickel zinc ferrite and lead zirconante titanate composites. Appl Phys Lett 85:2550–2552
35. Dai YR, Bao P, Zhu JS, Wan JG, Shen HM, Liu JM (2004) Internal friction study on $CuFe_2O_4$/$PbZr_{0.53}Ti_{0.47}O_3$ composites. J Appl Phys 96:5687–5690
36. Zhai JY, Cai N, Shi Z, Lin YH, Nan CW (2004) Magnetic-dielectric properties of NiFe2O4/PZT particulate composites. J Phys D-Appl Phys 37:823–827
37. Li YJ, Chen XM, Lin YQ, Tang YH (2006) Magnetoelectric effect of $Ni_{0.8}Zn_{0.2}Fe_2O_4$/$Sr_{0.5}Ba_{0.5}Nb_2O_6$ composites. J Eur Ceram Soc 26:2839–2844
38. Islam RA, Jiang JC, Bai F, Viehland D, Priya S (2007) Correlation between structural deformation and magnetoelectric response in (1-x) $Pb(Zr_{0.52}Ti_{0.48})O_3$-$xNiFe_{1.9}Mn_{0.1}O_4$ particulate composites. Appl Phys Lett 91:162905
39. Islam RA, Bedekar V, Poudyal N, Liu JP, Priya S (2008) Magnetoelectric properties of core-shell particulate nanocomposites. J Appl Phys 104:104111
40. Agrawal S, Cheng JP, Guo RY, Bhalla AS, Islam RA, Priya S (2009) Magnetoelectric properties of microwave sintered particulate composites. Mater Lett 63:2198–2200
41. Miclea C, Tanasoiu C, Amarande L, Miclea CF, Plavitu C, Cioangher M, Trupina L, Miclea CT, Tanasoiu T, Susu M, Voicu I, Malczanek V, Ivanov A, David C (2010) Magnetoelectric properties of multiferroic cobalt ferrite and soft piezoelectric PZT particulate composites. J Optoelectron Adv Mater 12:272–276
42. Ryu J, Carazo AV, Uchino K, Kim HE (2001) Magnetoelectric properties in piezoelectric and magnetostrictive laminate composites. Jpn J Appl Phys 40:4948–4951
43. Ryu J, Priya S, Uchino K, Kim HE (2002) Magnetoelectric effect in composites of magnetostrictive and piezoelectric materials. J Electroceram 8:107–119
44. Dong SX, Li JF, Viehland D (2004) A longitudinal-longitudinal mode TERFENOL-D/Pb $(Mg_{1/3}Nb_{2/3})O_3$-$PbTiO_3$ laminate composite. Appl Phys Lett 85:5305–5306
45. Liu G, Nan CW, Cai N, Lin YH (2004) Dependence of giant magnetoelectric effect on interfacial bonding for multiferroic laminated composites of rare-earth-iron alloys and lead-zirconate-titanate. J Appl Phys 95:2660–2664
46. Laletin VM, Paddubnaya N, Srinivasan G, De Vreugd CP, Bichurin MI, Petrov VM, Filippov DA (2005) Frequency and field dependence of magnetoelectric interactions in layered ferromagnetic transition metal-piezoelectric lead zirconate titanate. Appl Phys Lett 87:222507
47. Islam RA, Priya S (2006) Magnetoelectric properties of the lead-free cofired $BaTiO_3$-$(Ni_{0.8}Zn_{0.2})Fe_2O_4$ bilayer composite. Appl Phys Lett 89:152911

48. Dong SX, Zhai JY, Li JF, Viehland D (2006) Magnetoelectric effect in Terfenol-D/Pb(Zr, TiO) 3/mu-metal laminate composites. Appl Phys Lett 89:122903
49. Zhang N, Fan JF, Rong XF, Cao HX, Wei JJ (2007) Magnetoelectric effect in laminate composites of $Tb_{1-x}Dy_xFe_{2-y}$ and Fe-doped $BaTiO_3$. J Appl Phys 101:063907
50. Islam RA, Priya S (2008) Effect of piezoelectric grain size on magnetoelectric coefficient of Pb $(Zr_{0.52}Ti_{0.48})O_3$-$Ni_{0.8}Zn_{0.2}Fe_2O_4$ particulate composites. J Mater Sci 43:2072–2076
51. Ke WL, Zhang N, Guo YS (2009) Magnetoelectric effect in laminate composites of $Tb_{1-x}Dy_xFe_{2-y}$ and Cr doped $BaTiO_3$. Mater Res Innov 13:15–17
52. Wang YJ, Zhao XY, Jiao J, Zhang QH, Di WN, Luo HS, Leung CM, Or SW (2010) Lead-free magnetoelectric laminated composite of Mn-doped $Na_{0.5}Bi_{0.5}TiO_3$-$BaTiO_3$ single crystal and $Tb_{0.3}Dy_{0.7}Fe_{1.92}$ alloy J Alloy Compd 496:L4–L6
53. Shi Z, Nan CW, Zhang J, Ma J, Li JF (2006) Magnetoelectric properties of multiferroic composites with pseudo-1-3-type structure. J Appl Phys 99:124108
54. Egerton L, Dillon DM (1959) Piezoelectric and dielectric properties of ceramics in the system potassium-sodium niobate. J Am Ceram Soc 42:438–442
55. Hollenstein E, Davis M, Damjanovic D, Setter N (2005) Piezoelectric properties of Li- and Ta-modified $(K_{0.5}Na_{0.5})NbO_3$ ceramics. Appl Phys Lett 87:182905
56. Lang SB, Zhu WY, Cross L (2006) Piezoelectric and pyroelectric properties of $(K_{0.5}Na_{0.5})$ (1-x)$(Nb_{1-y}Ta_y)O_3$ ceramics. Ferroelectrics 336:15–21
57. Wang RP, Xie RJ, Hanada K, Matsusaki K, Bando H, Sekiya T, Itoh M (2006) Phase diagram of the $(Na_{0.5}K_{0.5})NbO_3$-$ATiO_3$ solid solution. Ferroelectrics 336:39–46
58. Guo Y, K-i K, Ohsato H (2005) $(Na_{0.5}K_{0.5})NbO_3$-$LiTaO_3$ lead-free piezoelectric ceramics. Mater Lett 59:241–244
59. Guo YP, Kakimoto K, Ohsato H (2004) Phase transitional behavior and piezoelectric properties of $(Na_{0.5}K_{0.5})NbO_3$-$LiNbO_3$ ceramics. Appl Phys Lett 85:4121–4123
60. Zang GZ, Wang JF, Chen HC, Su WB, Wang CM, Qi P, Du J, Zheng LM (2006) Perovskite $(Na_{0.5}K_{0.5})$(1-x)(LiSb)(x)$Nb_{1-x}O_3$ lead-free piezoceramics. Appl Phys Lett 88:212908
61. Yuan Y, Zhang SR, Zhou XH, Liu JS (2006) Phase transition and temperature dependences of electrical properties of $[Bi_{0.5}(Na_{1-x-y}K_xLi_y)_{0.5}]TiO_3$ ceramics. Jpn J Appl Phys 45:831–834
62. Zhang SJ, Shrout TR, Nagata H, Hiruma Y, Takenaka T (2007) Piezoelectric properties in $(K_{0.5}Bi_{0.5})TiO_3$-$(Na_{0.5}Bi_{0.5})TiO_3$-$BaTiO_3$ lead-free ceramics. IEEE Trans Ultrason Ferroelectr Freq Control 54:910–917
63. Zhao S, Li G, Ding A, Wang T, Yin Q (2006) Ferroelectric and piezoelectric properties of (Na, $K)_{0.5}Bi_{0.5}TiO_3$ lead free ceramics. J Phys D-Appl Phys 39:2277
64. Jaffe H (1958) Piezoelectric ceramics. J Am Ceram Soc 41:494
65. Schofield D, Brown RF (1957) Barium titanate compositions for transducer applications. Can J Phys 35:594
66. Nie JW, Xu GY, Yang Y, Cheng CW (2009) Strong magnetoelectric coupling in $CoFe_2O_4$-$BaTiO_3$ composites prepared by molten-salt synthesis method. Mater Chem Phys 115:400–403
67. Zhou Y, Zhang JC, Li L, Su YL, Cheng JR, Cao SX (2009) Multiferroic composites in nano-microscale with non-solid solution by Co-ferrite and $(K_{0.5}Na_{0.5})NbO_3$-based ferroelectric matrix. J Alloy Compd 484:535–539
68. Kambale RC, Shaikh PA, Bhosale CH, Rajpure KY, Kolekar YD (2010) Studies on magnetic, dielectric and magnetoelectric behavior of (x) $NiFe_{1.9}Mn_{0.1}O_4$ and (1-x) $BaZr_{0.08}Ti_{0.92}O_3$ magnetoelectric composites. J Alloy Compd 489:310–315
69. Lo CY, Choy SH, Or SW, Chan HLW (2010) Magnetoelectric effect in lead-free BNKLBT ceramic/terfenol-D continue fiber composite laminates. J Appl Phys 107:093907
70. Srinivasan G, Laletsin VM, Hayes R, Puddubnaya N, Rasmussen ET, Fekel DJ (2002) Giant magnetoelectric effects in layered composites of nickel zinc ferrite and lead zirconate titanate. Solid State Commun 124:373–378
71. Srinivasan G, Rasmussen ET, Hayes R (2003) Magnetoelectric effects in ferrite-lead zirconate titanate layered composites: The influence of zinc substitution in ferrites. Phys Rev B 67:014418

72. Srinivasan G, Hayes R, Bichurin MI (2003) Low frequency and microwave magnetoelectric effects in thick film heterostructures of lithium zinc ferrite and lead zirconate titanate. Solid State Commun 128:261–266
73. Babu SN, Srinivas K, Suryanarayana SV, Bhimasankaram T (2008) Magnetoelectric properties in NCMF/PZT particulate and bulk laminate composites. J Phys D-Appl Phys 41:165407
74. Zhang N, Ke W, Schneider T, Srinivasan G (2006) Dependence of the magnetoelectric coupling in NZFO-PZT laminate composites on ferrite compactness. J Phys-Condes Matter 18:11013–11019
75. Islam RA, Ni Y, Khachaturyan AG, Priya S (2008) Giant magnetoelectric effect in sintered multilayered composite structures. J Appl Phys 104:044103
76. Dong SX, Cheng JR, Li JF, Viehland D (2003) Enhanced magnetoelectric effects in laminate composites of Terfenol-D/Pb(Zr, Ti)O3 under resonant drive. Appl Phys Lett 83:4812–4814
77. Wan JG, Liu JM, Chand HLW, Choy CL, Wang GH, Nan CW (2003) Giant magnetoelectric effect of a hybrid of magnetostrictive and piezoelectric composites. J Appl Phys 93:9916–9919
78. Wan JG, Li ZY, Wang Y, Zeng M, Wang GH, Liu JM (2005) Strong flexural resonant magnetoelectric effect in Terfenol-D/epoxy-Pb(Zr, Ti)O3 bilayer. Appl Phys Lett 86:202504
79. Wang YJ, Or SW, Chan HLW, Zhao XY, Luo HS (2008) Enhanced magnetoelectric effect in longitudinal-transverse mode Terfenol-D/Pb($Mg_{1/3}Nb_{2/3}$)O_3-$PbTiO_3$ laminate composites with optimal crystal cut. J Appl Phys 103:124511
80. Wang YJ, Leung CM, Wang FF, Or SW, Zhao XY, Luo HS (2009) Dual-mode magnetoelectric effect in laminate composite of Terfenol-D alloy and PMN-PT transformer with double output ports. J Phys D-Appl Phys 42:135414
81. Wang YJ, Leung CM, Or SW, Zhao XY, Luo HS (2009) Resonance converse magnetoelectric effect in a dual-mode bilayered composite of Pb($Mg_{1/3}Nb_{2/3}$)O_3-$PbTiO_3$ and $Tb_{0.3}Dy_{0.7}Fe_{1.92}$. J Alloy Compd 487:450–452
82. Guo YY, Zhou JP, Liu P (2010) Magnetoelectric characteristics around resonance frequency under magnetic field in Pb(Zr, Ti)O_3/Terfenol-D laminate composite. Curr Appl Phys 10:1092–1095
83. Wu T, Chung TK, Chang CM, Keller S, Carman G (2009) Influence of electric voltage bias on converse magnetoelectric coefficient in piezofiber/Metglas bilayer laminate composites. J Appl Phys 106:054114
84. Dong XW, Wang B, Wang KF, Wan JG, Liu JM (2009) Ultra-sensitive detection of magnetic field and its direction using bilayer PVDF/Metglas laminate. Sens Actuator A-Phys 153:64–68
85. Fang Z, Lu SG, Li F, Datta S, Zhang QM, El Tahchi M (2009) Enhancing the magnetoelectric response of Metglas/polyvinylidene fluoride laminates by exploiting the flux concentration effect. Appl Phys Lett 95:112903

Chapter 17
Applications of Lead-Free Piezoelectrics

Kenji Uchino

17.1 Introduction

17.1.1 Background of Sustainable Society

Let us start from the product planning strategy taken historically by the Japanese industries. In 1960s, the slogan was *heavier*, *thicker*, *longer*, *and larger* (重, 厚, 長, 大); that is, manufacturing heavier ships, thicker steel plates, constructing longer buildings, and larger power plants (dams) were the key strategies for recovering from the ruins of World War II. This societal mood made the author choose Electrical Engineering in the university to become a water-dam engineer (then-trendy job!). Though Japanese people became wealthy, subsidiary effects started to surface: i.e., *industrial pollution*. The southern part of the sea of Japan was contaminated by the heavy metal (mercury) disposal by Nippon Chisso Company (chemical fertilizer manufacturer), which created thousands of "Angel Babies (missing/dislocated arm disorder)" in that wide area. Steel industries produced air pollution (yellow sky!) and "asthma" even for small kids. Traffic congestion generated severe acoustic noise even in suburban areas. One of the most technological industries, nuclear power plants, leaked hazardous radioactive wastes multiple times.

A completely opposite slogan started in the 1980s; that is, *lighter*, *thinner*, *shorter*, *and smaller* (軽, 薄, 短, 小). Printers and cameras became lighter in weight, thinner computers and TVs (flat panel) gained popularity, printing time and information transfer period became shorter, and air-conditioners and tape recorders

K. Uchino (✉)
International Center for Actuators and Transducers, The Pennsylvania State University, University Park, PA 16802, USA

Office of Naval Research – Global, Roppongi, Minato-ku, Tokyo 106-0032, Japan
e-mail: kenjiuchino@psu.edu

S. Priya and S. Nahm (eds.), *Lead-Free Piezoelectrics*,
DOI 10.1007/978-1-4419-9598-8_17, © Springer Science+Business Media, LLC 2012

Table 17.1 Technology development paradigm in Japan

1960s	Heavier	Ship manufacturing
	Thicker	Steel industry
	Longer	Building construction
	Larger	Power plant (dam)
1980s	Lighter	Printer, camera
	Thinner	TV, computer
	Shorter	Printing time communication period
	Smaller	"Walkman" air conditioner
2000s	Beautiful	Well-known brand apparel
	Amusing	T.V. game
	Tasteful	Cellular phone (private commun.)
	Creative	"Culture" center made-to-order shoes

("Walk-man" by SONY) were smaller. Because of this societal mood, the author, as a young university professor then, started working on compact "piezoelectric actuators & motors." Refer to Table 17.1. Though the serious industrial pollution diminished gradually during this period, different subsidiary effects started: (1) "greenhouse effect" and "global warming" due to CO_2 gas generated by overproduced automobiles, (2) energy crisis due to overconsumption of energy and lack of fossil energy sources (oil), in addition to the political mismanagement, and (3) population growth due to advanced medical technologies. Longer life time is welcomed by individuals (now the average age for Japanese female is approaching to 87, male, 82 already; the world-eldest). However, over-population of humans will create an imbalance against other animals/natures, and senior population, in particular, causes societal and economic problems (pension, health insurance, work force, etc.).

Now, what, where, or how will be our twenty first century? We will inevitably face the concept of a *sustainable society*, including the population density. The sustainable society requires (a) usage of *nontoxic* materials, (b) *disposal technology* for existing hazardous materials, (c) new *energy source* creation, and (d) *energy-efficient* device development. Electric components such as motors and transformers are mostly based on electromagnetic transduction at present. With reducing their size (power level less than 30 W), the efficiency of these electromagnetic components reduces drastically due to the Joule heat in their thin coil wire (i.e., the resistivity in the coil becomes significant). Thus, piezoelectric actuators and transducers with much less losses are highly sought after in the twenty first century. In the past 30 years (i.e., after the 1980s), most researchers put efforts on improving the piezoelectric performance from the "real-part" property's viewpoint: that is, improved displacement, force, responsivity, etc. An example from this approach created single crystals based on $Pb(Zn_{1/3}Nb_{2/3})O_3$–$PbTiO_3$, which were discovered by our group [1], and now have become widely researched for medical and underwater applications. However, from the viewpoint of efficiency and reliability such as heat generation or performance degradation under high voltage/power drive, the key is the *imaginary-part*; that is, *loss and hysteresis mechanisms*. Thus, in the 2000s the author, as a senior professor, has been studying loss

mechanisms in piezoelectrics, including high-power characterization system (HiPoCS), and practical high-power piezoceramics, in addition to highly energy efficient compact piezoelectric actuators and transducers.

Piezoelectric devices seem to be all-around contributors and a key component to the above-mentioned four R&D areas in the sustainable society. Some of our research efforts include:

(a) Since the most widely used piezoelectric lead zirconate titante (PZT) ceramics will be regulated in less than 10 years politically in European and Japanese communities due to their toxicity (Pb^{2+} ion), lead-free piezoelectric ceramics based on $(K,Na)(Ta,Nb)O_3$, and $(Bi,Na,Ba)TiO_3$ have been developed with transducer performance equivalent to the conventional PZTs.
(b) Since hazardous organic substances such as "dioxin" can easily be dissolved by the irradiation of ultrasonic energy in water, a new technology for safe disposal of dioxin using high-power piezoelectric transducers has been developed.
(c) We demonstrated an energy recovery system on a hybrid car from its engine's mechanical vibration to the rechargeable battery (or fuel cell) for electric charging. A self-powered remote light switching system has also been developed using piezoelectric bimorphs.
(d) Microultrasonic motors based on piezoelectrics demonstrated 1/20 reduction in the volume and weight and a 20 time increase in efficiency of the conventional electromagnetic motors with equivalent output power (~100 mW). We also demonstrated compact and highly efficient high-voltage supplies with piezoelectric transformers, which have been widely commercialized for laptop backlight inverter applications.

Taking into account these societal mood, the author would like to propose a new four-Chinese-character slogan for the first 20 years of twenty first century; that is, "美, 遊, 潤, 創 (*beautiful*, *amusing*, *tasteful*, *and creative*)," which was originally suggested by Y. Hirashima in his book [2]. The best-selling products in the early 2000s include well-known brand apparel and accessories for females such as Louis Vuitton bags (beautiful!), amusing TV/computer games (Nintendo, SONY), cellular phone for private communication typically by small kids to escape from their parents' watching (tasteful life), and "culture centers" for continuous education, and made-to-order shoes for satisfying an individual's creative mind. Refer to Table 17.1.

17.1.2 External Environmental Factors on the Products

There are various constraints for commercializing piezoelectric actuators. *STEP* (*Social/cultural*, *Technological*, *Economic*, *and Political*) four forces are considered as external environmental factors in this section. The details can be learned in the author's new book, *Entrepreneurship for Engineers* [3].

Though piezoelectric transformers (PT) were used on trial in the color TVs in 1970s, serious problems were found in the mechanical strength (collapse happened

in the device) and in heat generation in color TVs, leading to the termination of production for 2 decades. However, recent laptop computers with a liquid crystal display requiring a very thin, and electromagnetic-noise free transformer to start the glow of a fluorescent back-lamp have accelerated the development after 1990s. This is a good example how the social demand creates the technology development (*needs-pull*).

The four-Chinese-character slogans discussed in Table 17.1 are typical social motivations for new product developments. Remember that "美, 遊, 潤, 創 (beautiful, amusing, tasteful, and creative)" is the key in the first 20 years of twenty first century, and the societal sustainability, including Pb-free piezoceramic development, is really in this direction.

Discovery of a new principle or material, and invention of a new device sometimes change the world drastically. Polyvinylidene difluoride, PVDF, a piezoelectric polymer discovered accidentally in early 1970s by Dr. Kawai., and a high-temperature superconducting ceramic discovered by Drs. Bednortz and Muller in 1980s are good examples of *serendipity*. The author's photostrictive materials were discovered along a systematic consideration of a composite effect; functionality matrixes of photovoltatic and piezoelectric effects. A new idea arising from "research" will create a *seed-push* market, while development is initiated by a *need-pull* force.

The multilayer piezoelectric actuators have been widely adopted in diesel injection valve mechanisms. However, their expensive manufacturing cost limits the spread-out speed in the world. Some researchers are working to reduce the drive voltage by reducing the layer thickness of piezoelectric multilayer actuators, in particular for mobile phone applications. However, it is not recommended for the large ML actuators for diesel injection valve control applications in diesel automobiles. Figure 17.1 graphs the piezo-stack price and its electronic driver cost as a function of drive voltage [4]. The ML actuator price increases with reducing its drive voltage (i.e., reducing its each layer thickness), while the driver cost increases with increasing the voltage. The minimum total cost is obtained around 160 V, leading the layer thickness of 80 μm. This "a-sort-of standard" thickness can be derived from the cost minimization principle, but not from the performance. Note that 20 μm layer thickness is not difficult technologically in ML actuators nowadays.

It is generally true that "cheaper" is more "competitive" in the product commercialization. However, note that the following "Political/Legal" constraint is much stronger force in the commercialization.

Twenty first century is called "The Century of Environmental Management." In 2006, European Community started RoHS (Restrictions of Hazardous Substances), which explicitly limits the usage of lead (Pb) in electronic equipments. Basically, we may need to regulate the usage of PZT, most famous piezoelectric ceramics, in the future. Japanese and European communities may experience governmental regulation on the PZT usage in these 10 years. Pb (lead)-free piezoceramics have started to be developed after 1999. Figure 17.2 shows statistics of various lead-free piezoelectric ceramics. The share of the papers and patents for

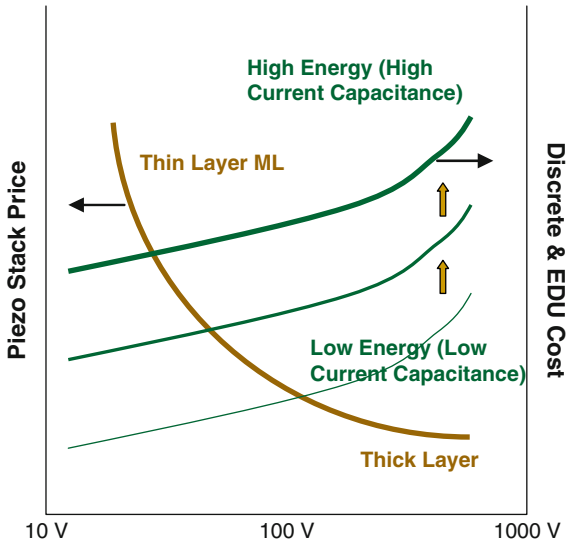

Fig. 17.1 Drive voltage dependence of piezo-stack price and the electronic driver cost [4]

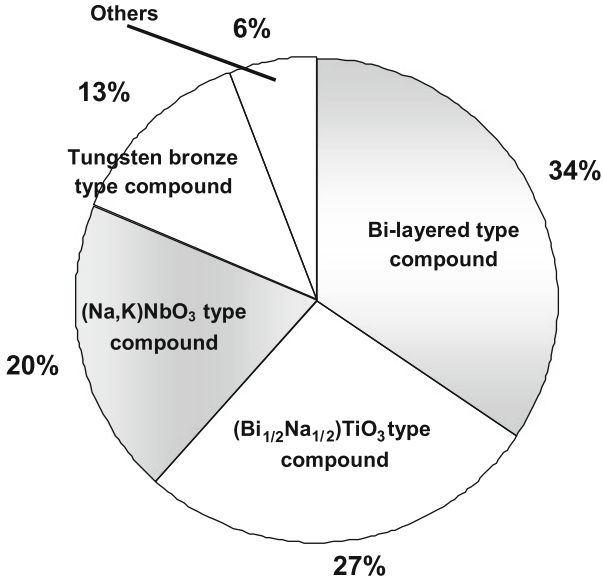

Fig. 17.2 Patent disclosure statistics for lead-free piezoelectric ceramics (total number of patents and papers is 102)

bismuth compounds (bismuth layered type and (Bi,Na)TiO_3 type) exceeds 61%. (K,Na,Li)(Nb,Ta,Sb)O_3 ceramics exhibit the best performance at present, and seem to be the most promising candidates [5]. RoHS seems to be a significant threat to piezoelectric companies, who have only PZT piezoceramics. However, this is an opportunity for the company which is preparing alternative piezoceramics to exchange the piezoelectric device share.

On the other hand, diesel engines are more recommended than normal gasoline cars, because the purification energy (extra electrical energy) of oil can be saved, which was contributing to global warming problem. However, the conventional diesel engine generates toxic exhaust gases such as SO_x and NO_x. In order to solve this problem, new diesel injection valves were developed by Siemens with piezoelectric PZT ML actuators. Of course, as the reader can imagine, the final goal of the technology will be the diesel injection valves with using Pb-free piezoelectric ML actuators.

This paper was authored to introduce promising applications of Pb-free piezoelectrics developed recently: (1) piezoelectric transducers for ultrasonic cleaners by Honda Electronics, (2) piezoelectric transformers by the author's group at The Penn State University, and (3) ultrasonic motors with multilayer piezoactuators by Taiyo Yuden. Note that the initial motivation for this movement came from the *Political Regulation* (i.e., RoHS), in conjunction with *Social/Cultural Pressure* (i.e., sustainable society). Though this movement is not recommended from *Economical Viewpoint* (i.e., too expensive for the products at this moment), we need to overcome the problem from the new *Technological Development* in the nearest future. The political force is the strongest factor for the practically successful commercialization.

17.2 Lead-Free Piezoelectric Materials

Patent statistics of lead-free piezoelectric ceramics in Fig. 17.2 shows that the share of the patents for bismuth compounds (*bismuth- layered* type and $(Bi,Na)TiO_3$ (*BNT*) type) exceeds 61%. This is because bismuth compounds are easily fabricated in comparison with other compounds. Note that the toxicity of Bi^{3+} is not very low compared with Pb^{2+}, but that a regulation may not be proposed because this atomic element is not familiar with "politicians" fortunately. $(Sr,Ba,Ca)\ Bi_2Nb_2O_9$, $Bi_4Ti_3O_{12}$ (Bi-Layer) was developed by TDK for high Q_m communication application. On the other hand, $(Bi_{1/2}Na_{1/2})TiO_3$–$BaTiO_3$ (BNT) have been developed by AIST, Japan, and Honda Electronics for transducer applications.

$(Na,K)NbO_3$ (*NKN*) systems exhibit the highest performance because of the morphotropic phase boundary usage. Figure 17.3 shows the current best data reported by Toyota Central Research Lab, where strain curves for oriented and unoriented $(K,Na,Li)\ (Nb,Ta,Sb)O_3$ ceramics are shown [5] [Recited from Chap. 12 of this book]. Note that the maximum strain reaches up to $1{,}500 \times 10^{-6}$, which is equivalent to the PZT strain. Drawbacks include their sintering difficulty and the necessity of the sophisticated preparation technique (topochemical method for preparing flaky raw powder). Tungsten-bronze (*TB*) types are another alternative choice for resonance applications, because of high Curie temperature and low loss. Taiyo Yuden demonstrated $(Sr,Ca)_2NaNb_5O_{15}$ for ultrasonic motor applications. Other materials include $(Sr,Ba,Ca)Bi_2Nb_2O_9$, $Bi_4Ti_3O_{12}$ (Bi-Layer), which TDK

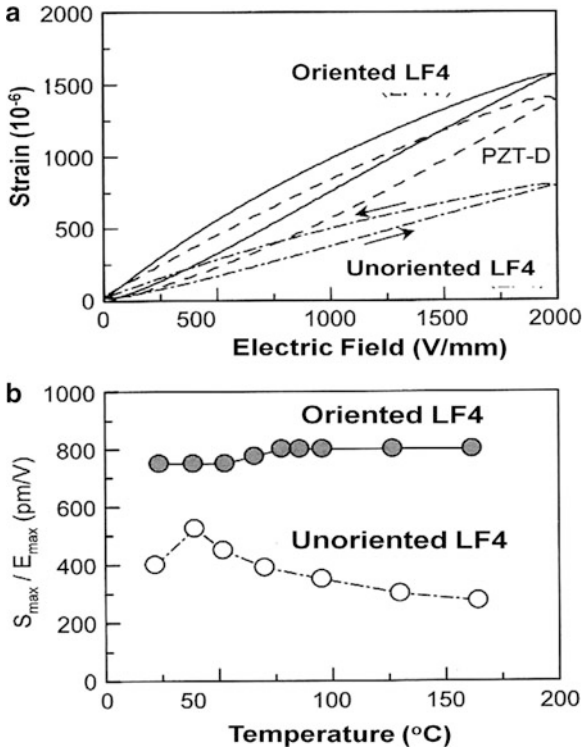

Fig. 17.3 Strain curves for oriented and unoriented (K, Na,Li)(Nb,Ta,Sb)O_3 ceramics [5]

applied for high Q_m and high T_C communication devices. Refer to various chapters in this book for the detailed performance of each material.

Since the piezoelectric performance of Pb-free materials is not superior to the PZTs in general in a similar randomly oriented ceramic configuration, commercialization efforts should include either (1) epitaxially oriented ceramic preparation method, or (2) sophisticated composite designing, in order to overcome the inferiority.

17.3 Langevin Transducers with BNT

Langevin transducers used popularly for underwater fish finders and hydrophones are also utilized for ultrasonic cleaning and hazardous material dissolving systems. For these ecological applications, it is reasonable to make the systems also environment-friendly. Honda Electronics, Japan developed Langevin transducers using the BNT-based ceramics for ultrasonic cleaner applications [6]. The composition $0.82(Bi_{1/2}Na_{1/2})TiO_3$–$0.15BaTiO_3$–$0.03(Bi_{1/2}Na_{1/2})(Mn_{1/3}Nb_{2/3})$

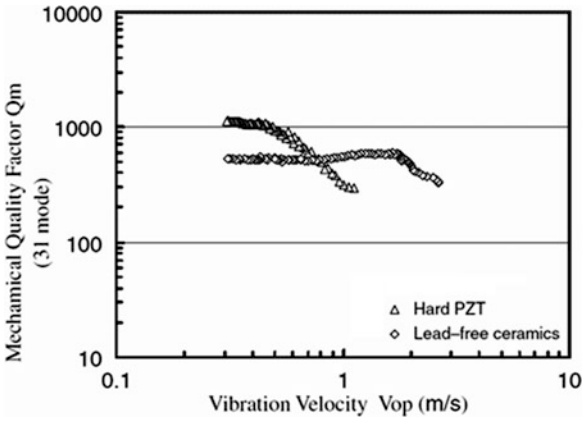

Fig. 17.4 High-power performance of the Honda Electronics' Pb-free piezoelectric, in comparison with a regular hard PZT [6]

O_3 exhibits $d_{33} = 110 \times 10^{-12}$ C/N, which is only 1/3 of that of a hard PZT. However, the electromechanical coupling factor $k_t = 0.41$ is larger because of much smaller permittivity ($\varepsilon = 500$) than that of the PZT. More importantly, since the figure of merit of the resonant vibration level (i.e., vibration velocity) is provided by the product of the piezoelectric d constant and mechanical quality factor Q_m, higher Q_m is desired under a practically high excitation state. The maximum vibration velocity of a rectangular plate (k_{31} mode) of Honda Electronics' BNT is close to 1 m/s (rms value), which is higher than that of typical hard PZTs. Figure 17.4 demonstrates high-power piezoelectric performance of the Honda Electronics' Pb-free piezoelectric, in comparison with a regular hard PZT. The mechanical quality factor Q_m was measured for a k_{31} type rectangular plate ($43 \times 7 \times 1$ mm^3) as a function of excited vibration velocity (0–p value in m/s in this figure). Notice that their measurement has been made under a burst mode for escaping from the temperature rise of the sample. This condition is different from the continuous drive measurement in the next section, which provides roughly a half of the value measured under a burst mode. A constant Q_m around 500 of the BNT-based ceramic is sustained up to 1.4 m/s (0–p) of the vibration velocity, while a regular hard PZT exhibits dramatic decay in Q_m under 0.5 m/s (0–p), though the initial Q_m under small excitation is reasonably high (~1,100).

Table 17.2 summarizes properties of the bolt-clamped Langevin-type transducer (28 kHz) with Pb-free and PZT-based piezoelectric ceramics [6]. The transducer design is shown in Fig. 17.5a. Note that the device performances are almost the same even though the material's properties are rather different, except for capacitance and impedance.

The Langevin transducer shown in Fig. 17.5a (28 kHz) was tested in an erosion chamber. The ultrasonic power of lead-free piezoelectric transducer was equivalent to that of a hard PZT type, and the cleansing effect of both types was verified to be practically the same by comparing the erosion areas on aluminum foils (see Fig. 17.5b).

Table 17.2 Properties of the bolt clamped Langevin-type transducer (28 kHz) with Pb-free and PZT-based piezoelectric ceramics [6]

Item	Symbol	Lead-free (Bi,Na) TiO_3–$BaTiO_3$–(Bi, Na)(Mn,Nb)O_3	Hard Pb(Zr,Ti) O_3 (HC–50GS)	Remarks
Resonance frequency	F_0	28.0 kHz	28.0 kHz	Measurement voltage: 1.0 V_{rms}
Impedance	Z	75 Ω	35 Ω	Measurement voltage: 1.0 V_{rms}
Capacitance	C_x	1,300 pF	3,300 pF	Measurement frequency: 1 kHz
Insulation resistance	IR	$\geqq 1 \times 10^4$ MΩ	$\geqq 1 \times 10^4$ MΩ	Measurement voltage and time: DC1000 V × 1 min
Maximum permissible velocity	V	0.5 m/s(0–p)	0.5 m/s(0–p)	Vibration velocity of radiation surface
Maximum permissible temperature	T_{max}	120°C	120°C	Surface temperature of ceramics
Storage temperature range	T_{st}	−5°C to +40°C	−5°C to +40°C	
Storage humidity range	H_{st}	60 ± 20%	60 ± 20%	

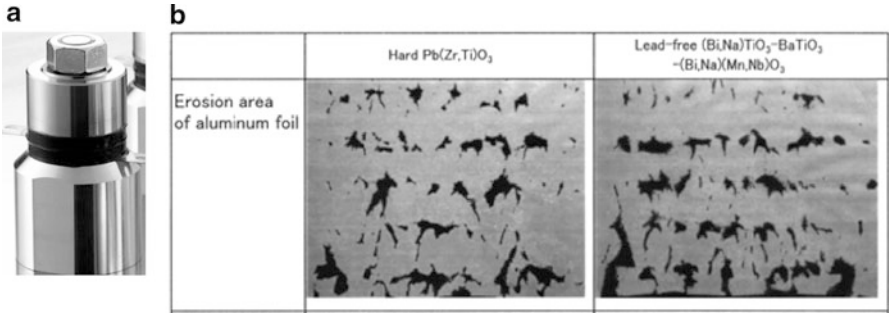

Fig. 17.5 (**a**) Langevin transducer (28 kHz) for cleaner applications, and (**b**) cleansing effect comparison among Pb-free and PZT types on aluminum foils [6]

17.4 Piezoelectric Transformer with NKN

In the trend of miniaturization of electronic devices, components used are also getting smaller. Traditional electromagnetic transformers cannot catch up with this trend. On the other hand, those made from piezoelectric ceramics have ease to follow this trend. Piezoelectric components show much higher power density in smaller scales.

The first piezoelectric transformer was introduced by C. A. Rosen et al. in 1957 as the Rosen-Type transformer [7]. Piezoelectric transformers can be divided into two types. One of them is the voltage transformer, exemplified by a Rosen-Type transformer as mentioned before, yields high voltage and low currents. The other group is the current transformer, which produces high current and relatively low voltage (or typically stepping-down voltage). The Penn State group designed the latter purpose transformers called "ring-dot" types. The common piezoelectric ceramics used so far are lead-based piezoelectric ceramics commonly known as PZT (Lead-Zirconate-Titanate). By doping, PZT's piezoelectric properties have been enhanced in terms of loss and heat generation, and by design optimization piezoelectric transformers' power capability has also been increased. Power density is typically around 10 ~ 20 W/cm^3, and the top data as high as 40 W/cm^3 has been reported by Laoratanakul et al. [8].

Though PZTs possess excellent piezoelectric properties and have been used for many applications, their continuous usage may be regulated by the RoHS (Restriction of Hazardous Substances). This raises the issue of safe disposability and recyclability of piezoelectric substances. The effect of RoHS and the promising results by Saito et al. of lead-free systems [5] made an impact on the number of the researches.

17.4.1 Hard NKN and Its High-Power Performance

In collaboration with Korea University, The Penn State University is concentrating on Sodium-Potassium-Niobate (NKN) due to its promising properties reported recently by H. –Y. Park et al. in 2008, based on $(Na_{0.5}\,K_{0.5})\,(Nb_{0.97}Sb_{0.03})O_3$ with 2 mol% CuO addition [9]: $k_p = 0.41$, $Q_m = 1{,}333$, $d_{33} = 111$ pC/N, and $\varepsilon_3\,x/\varepsilon_0 = 324$.

17.4.1.1 Low-Power Piezoelectric Characterization

After 24 h from poling the low-power characterization was handled. The d_{33} value was measured with the d_{33} meter at 100 Hz. Capacitance and dielectric loss (*tan δ*) values were measured with the HP-4272A LCR meter at 1 kHz and 1 V. Impedance spectrum was obtained with Agilent 4294A impedance analyzer (Fig. 17.6) for obtaining the mechanical quality factor Q_m (or the elastic loss factor). The electromechanical parameters obtained in the newly prepared specimens (Table 17.3) seem to be a little lower than the numbers reported in Ref. [9], indicating the preparation reproducibility problem.

17.4.1.2 High-Power Characterization

The high-power property of the disk sample and the transformer characteristic were measured by a High-Power Characterization System (HiPoCS™) developed by our group [10]. An amplitude controlled sinusoidal signal was produced by a function

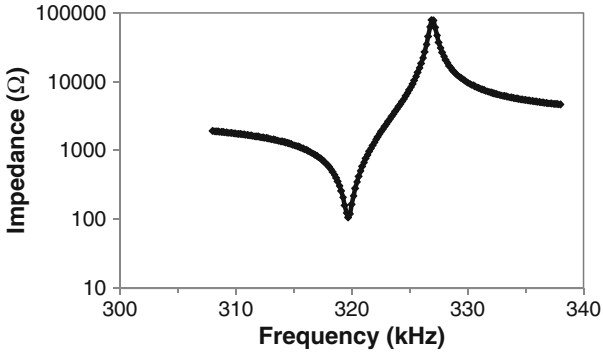

Fig. 17.6 Impedance analysis of the NKN disk (10.6 diameter × 1.5 mm thickness) measured under 0.5 V_{rms}

Table 17.3 Electromechanical properties of the NKN ceramic

d_{33} (pC/N)	tanδ (%)	$Q_{m\ (3dB\ method)}$
80	1.1	639

generator (HP 33120A) and amplified by NF 4010. The sample current was detected by a clamp-on AC current sensor (Tektronix TCP 305). The voltage, current, and displacement waveforms of the piezoelectric disks and transformers were monitored by two digitizing oscilloscopes (Tektronix TDS 3014B) and logged by a personal computer. The temperature on the surface of the sample nodal point was measured by an infrared spot thermometer (HIOKI 3445) and thermal images of the whole sample were taken with a thermal camera (ThermaCAM S40 Flir Systems outfitted with 200 μm lens). Vibration amplitudes on the edge of the piezoelectric disks/transformers were measured with laser interferometers (Polytec OFV 511). The HiPoCS™ characterized the behavior of the mechanical quality factor at various fixed vibration velocity frequency sweeps. The high-power characterization was performed on 10.6 mm diameter × 1.5 mm thick disks, driven under constant vibration velocity.

The impedance curves for the disks under various vibration velocities between 0.1 and 0.4 m/s were recorded in Fig. 17.7. The "rms" value was adopted for the vibration velocity. The resonance frequency appears to shift from higher to lower frequencies as the vibration velocity increased. This trend is a usual fashion in high-power characteristics even in the PZT-based piezoelectric materials. As the vibration velocity increases, the material tends to be softened and yields the resonance frequency to drop. On the other hand, there is an unusual behavior in the resonance impedance change. Even though the vibration velocity increases, the resonance impedance remained constant (Figs. 17.7 and 17.8a), which is significantly different from the PZT's case [11]. This novel characteristic of the sample is a result of its mechanical quality factor (Q_m). As shown in Fig. 17.8b, NKN's Q_m does not drop with increased vibration velocity. For high-power applications the Q_m vs. vibration velocity figure is

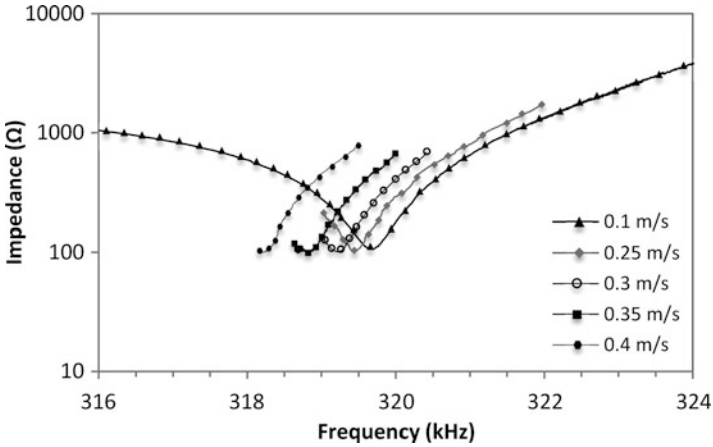

Fig. 17.7 Impedance curves for the NKN disk (10.6 diameter × 1.5 mm thickness) at certain constant vibration velocities

very important; as it represents the degradation of piezoelectric properties as power demand is increased. Note that even at a temperature change of about 20°C, the NKN does not show a significant Q_m drop (Refer to Fig. 17.8b).

The maximum vibration velocity (rms value defined at 20°C temperature rise) of 0.4 m/s for a disk shape corresponds to 1.4 m/s for a rectangular plate [11]. Since the maximum vibration velocity for a PZT rectangular plate is 0.3 m/s typically and 0.6 m/s for the best, we can conclude that the NKN ceramic seems to be better than the PZT ceramics in terms of the maximum vibration velocity. The unusual and promising result of an almost steady high mechanical quality factor (Q_m ~ 900) at extreme vibration velocities, exceeding current PZT's high-power performances, makes the evaluated composition a perfect candidate for high-power applications.

17.4.2 Lead-Free Piezoelectric Transformers

The above high-power study encouraged to examine the sample in a piezoelectric current-transformers (i.e., step-down type). Ring-dot high-power transformers with 10.6 mm diameter × 0.5 mm thickness were designed, manufactured, and characterized in terms of power density, equivalent impedance, and gain [12]. The picture and the design of the KNN ceramic ring-dot type transformer are shown in Fig. 17.9a. FEM simulation showing the vibration mode and the induced voltage is also illustrated in Fig. 17.9b.

Using low-power impedance spectra obtained at 0.5 V with an impedance analyzer, the matching impedance was calculated by (17.1):

$$Z_m = \frac{1}{2\pi f_r C_b(\text{output})}, \tag{17.1}$$

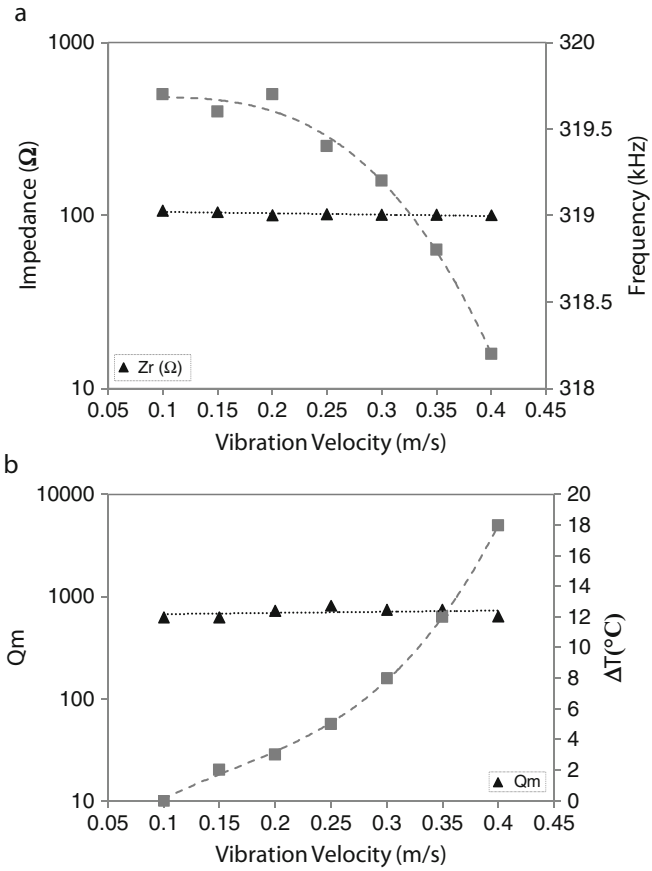

Fig. 17.8 (**a**) Impedance and resonance frequency change with vibration velocity (rms value). (**b**) Q_m and ΔT as a function of vibration velocity. The data were collected for the NKN disk (10.6 diameter × 1.5 mm thickness)

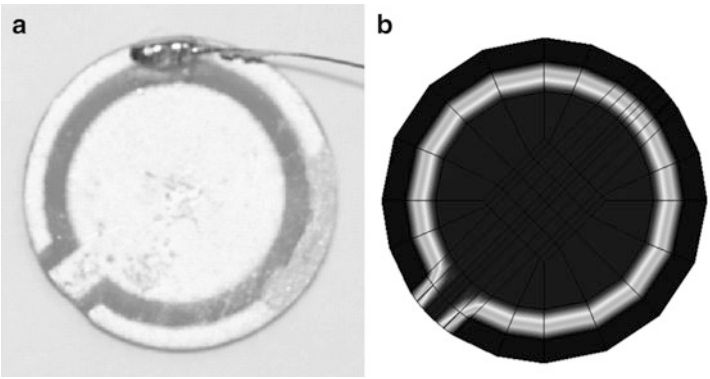

Fig. 17.9 High-power NKN-based lead-free piezoelectric transformer: (**a**) picture of a ring-dot sample. (**b**) FEM simulation showing the vibration mode and the induced voltage

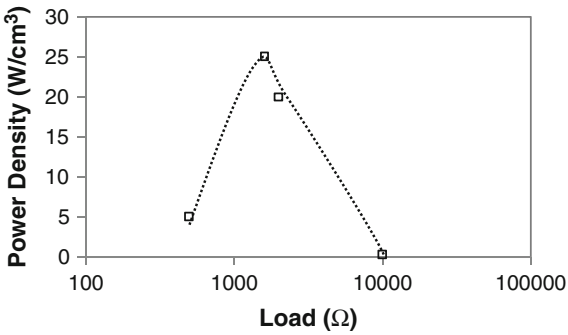

Fig. 17.10 Power density for the NKN-based ring-dot piezoelectric transformer under various external loads. Note that the maximum is obtained around the impedance matching load

where f_r is the resonance frequency and C_b is the damped capacitance of the piezoelectric transformer. The matching impedance for the NKN piezoelectric transformer was about 1.6 kΩ. As a rule of thumb, high-power characterization was performed under various impedance load (0.5, 1.6, 2, and 10 kΩ) until sample temperature reached 20°C above the ambient temperature (i.e., under the maximum vibration velocity drive). The output power was calculated from the output voltage and the output current drawn from the transformer. Thereafter, the output power was used to calculate the power density of the transformer. The power density showed dependence on the external loads, and is shown in Fig. 17.10. The maximum power density was obtained as 25 W/cm^3 under the matching impedance, i.e., 1.6 kΩ. By changing the external load the power level dropped to 0.25 W/cm^3, 20 W/cm^3, 5 W/cm^3 for 10, 2, and 0.5 kΩ respectively. Since the PZT-based ring-dot transformer exhibits typically 20 W/cm^3, our NKN ceramic again exceeds the PZT performance in a piezo-transformer device.

In conclusion, $(Na_{0.5}\,K_{0.5})(Nb_{0.97}Sb_{0.03})O_3$, prepared with 1.5% mol CuO addition, exhibited even better high-power characteristics than PZT. In this material, instead of dropping mechanical quality factor (Q_m) with increasing vibration velocity, Q_m remained constant up to 0.4 m/s in disk-shaped samples, which corresponds to 1.4 m/s in rectangular plates. This indicates that the candidate lead-free system has better characteristics under high-power levels. To explore the practical applicability, ring-dot piezo-transformers were designed and manufactured. Very high-power densities (as high as 25 W/cm^3) were obtained, which is comparable to that of PZT piezo-transformers.

17.5 Ultrasonic Motors with TB

Taking into account general consumer attitude on disposability of portable equipment (printers, cellular phones), Taiyo Yuden, Japan developed microultrasonic motors using non-Pb multilayer piezoactuators [13]. Their composition is based on tungsten bronze (TB) ($(Sr,Ca)_2NaNb_5O_{15}$) without heavy metal or even K (potassium seems to be a little more toxic in comparison with Na).

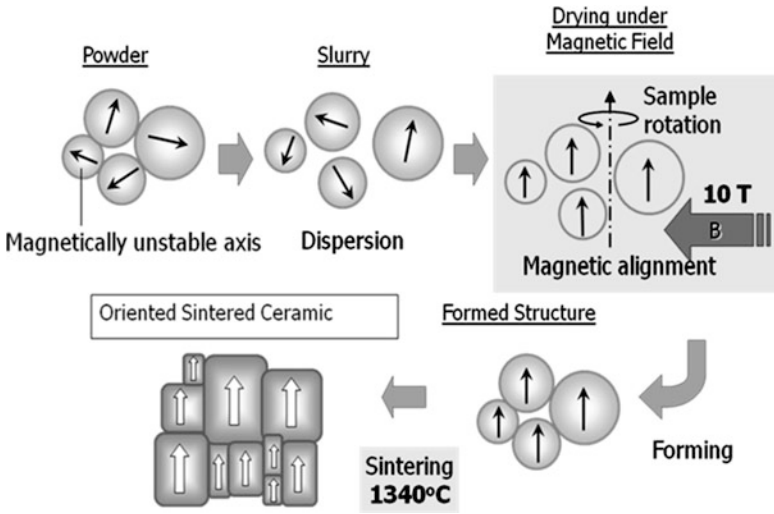

Fig. 17.11 Principle of ceramic powder orientation under magnetic field [13]

17.5.1 Preparation of Oriented Ceramic

The basic piezoelectric parameters in TB ($d_{33} = 55 \sim 80$ pC/N, $T_C = 300°C$) are not very attractive. However, once the c-axis oriented ceramics are prepared, the d_{33} is dramatically enhanced up to 240 pC/N. Further since the Young's modulus $Y_{33}{}^{E} = 140$ GPa is more than twice of that of PZT, the higher generative stress is expected, which is suitable to ultrasonic motor applications.

Taiyo Yuden developed a sophisticated preparation technology for fabricating oriented ceramics with a multilayer configuration: that is, preparation under strong magnetic field, much simpler than the flaky powder preparation introduced in Fig. 17.3. Figure 17.11 illustrates the principle of ceramic powder orientation under magnetic field. Since most of piezoceramics are diamagnetic, the ceramic powder suspended in slurry will be aligned along its magnetically stable axis under a strong magnetic field (such as 10 T) [13]. Because the polarization axis in their particular TB composition corresponds to the magnetically unstable axis, they used the magnetic field parallel to the green sheet. A cut-green-sheet was rotated practically under steady magnetic field during drying period. These oriented green sheets were electroded, laminated, and sintered. They reported beautiful crystal orientation degree of the sintered product with Lotgering factor 0.9, as shown in Fig. 17.12 [13].

17.5.2 Compact Ultrasonic Motor with Oriented Ceramic

Figure 17.13(a) shows their compact rotary ultrasonic motor with a piezoelectric multilayer actuator (MLA) [13]. A canti-lever rod is wobbled by a 2 × 2 arrayed

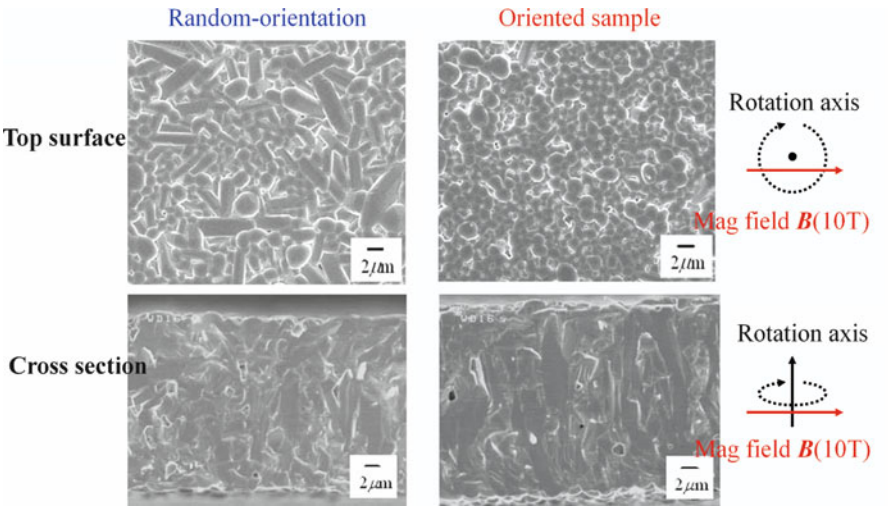

Fig. 17.12 Columnar grains grown along c-axis are normal to the tape plane (*right*-hand-side pictures), shown in comparison with the randomly oriented ceramic (*left*-hand-side pictures)

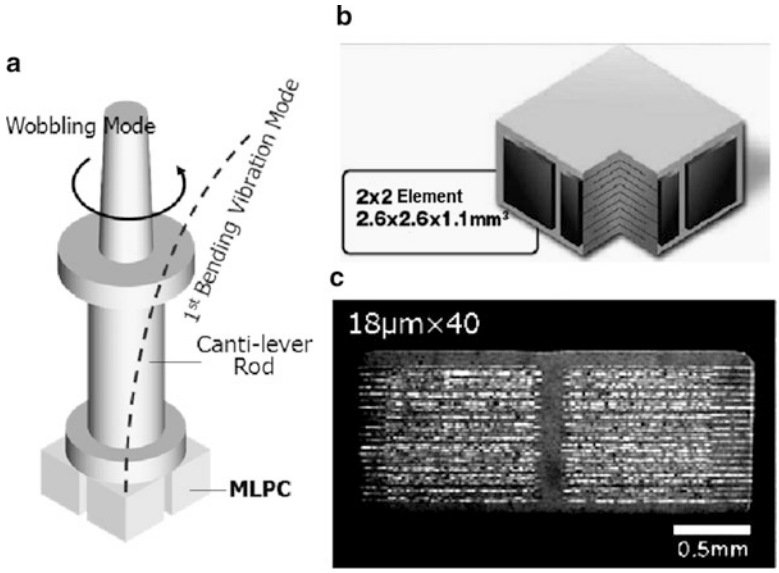

Fig. 17.13 (**a**) Compact rotary ultrasonic motor with a piezoelectric multilayer actuator, (**b**) 2 × 2 arrayed element, and (**c**) cross-section view of the 18 μm-layer ML element [13]

MLA element, driven by a 4-phase voltage (sine, cosine, –sine and –cosine). They fabricated monolithic 2 × 2 arrayed elements with the size 2.6 × 2.6 × 1.1 mm^3 including buffers with layer thickness as thin as 18 μm (Refer to Fig. 17.13b, c). Because of this layer thinness and dramatic enhancement in the piezoelectric

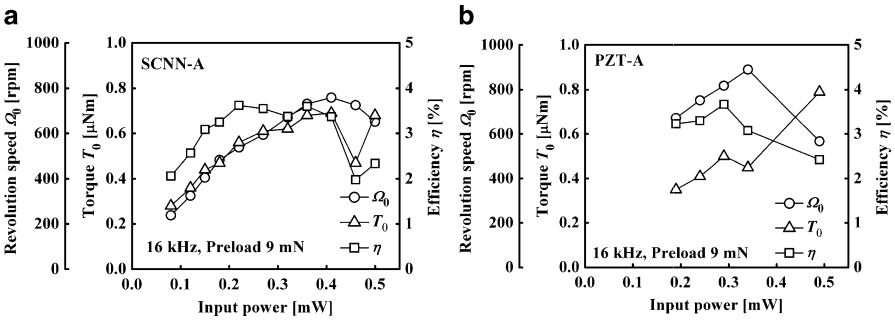

Fig. 17.14 Ultrasonic motor characteristics (revolution speed, torque, efficiency vs. input power) for SCNN ($(Sr,Ca)_2NaNb_5O_{15}$) (**a**) and PZT-A (**b**) multilayer motors

performance owing to the magnetic field alignment, the ultrasonic motor was successfully driven under only 3 V_{p-p} which is low enough to be adopted in mobile phones without coupling a step-up drive circuit. Figure 17.14a, b show ultrasonic motor characteristics (revolution speed, torque, efficiency vs. input power) for the Pb-free SCNN ($(Sr,Ca)_2NaNb_5O_{15}$), (a) and PZT-A (b) multilayer motors. Though the actual drive voltage for the SCNN motor is 3 V_{p-p}, 3 times higher than for the PZT motor (1 V_{p-p}), the equivalent motor characteristics can be obtained for both motors under normal battery operation.

17.6 Concluding Remarks

Note that the initial motivation for the Pb-free piezoelectrics came from the *Political Regulation* (i.e., RoHS), in conjunction with *Social/Cultural Pressure* (i.e., sustainable society). Though this movement is not recommended at present from *Economical Viewpoint* (i.e., too expensive for the products at this moment), we need to overcome the problem from the new *Technological Development* in the nearest future. The political force is the strongest factor for the practically successful commercialization.

Though the piezoelectric d constant and electromechanical coupling factor k (real parameters) of the present Pb-free materials are not superior to the values of PZTs, in general, in a similar randomly oriented ceramic configuration, commercialization efforts are overcoming this inferiority by using either (1) epitaxially oriented ceramic preparation method, or (2) sophisticated composite designing. It is also intriguing to note that the maximum vibration velocity for the Pb-free piezoelectrics seem to be larger than that of the hard PZTs; that is, the vibration velocity is given by the product of piezoelectric d and mechanical quality factor Q_m, and constant Q_m of the Pb-free ceramic is sustained up to 1.4 m/s (rms) of the vibration velocity (in a rectangular plate specimen), while a regular hard PZT

exhibits dramatic decay in Q_m under 0.3 m/s (rms), even though the initial Q_m under small excitation is reasonably high.

In conclusion, basic performances of the Pb-free piezoelectrics are almost satisfactory from the application viewpoints (transducers, transformers, and ultrasonic motors), though the off-resonance performance based on merely the piezoelectric constant d is not very excellent. The remaining issues include (1) reproducibility of the product's quality, and (2) inexpensive mass production process.

References

1. Kuwata J, Uchino K, Nomura S (1982) Jpn J Appl Phys 21:1298
2. Hirashima Y (1981) Product planning in the feeling consumer era (in Japanese). Jitsumu-Kyoiku Publisher, Tokyo
3. Uchino K (2009) Entrepreneurship for engineers. CRC Press, New York
4. Fujii A (2005) Proc Smart Actuators/Sensors Study Committee. JTTAS, Dec. 2, Tokyo
5. Saito Y (1996) Jpn J Appl Phys 35:5168–5173
6. Tou T, Hamaguchi Y, Maida Y, Yamamori H, Takahashi K, Terashima Y (2009) Jpn J Appl Phys 48:07GM03
7. Rosen CA (1957) Proc Electronic Compon Symp, p 205
8. Laoratanakul P, Carazo AV, Bouchilloux P, Uchino K (2002) Jpn J Appl Phys 41:1446–1450
9. Park H-Y, Seo I-T, Choi M-K, Nahm S, Lee H-G, Kang H-W, Choi B-H (2008) J Appl Phys 104(3):034103
10. Ural SO, Tuncdemir S, Zhuang Y, Uchino K (2009) Jpn J Appl Phys 48:056509
11. Ural SO, Zhuang Y, Tuncdemir S, Uchino K (2009) Jpn J Appl Phys 49:021502
12. Gurdal, EA, Ural SO, Park HY, Nahm S, Uchino K (2011) High power $(Na_{0.5}K_{0.5})NbO_3$-based lead-free piezoelectric transformer. Jpn J Appl Phys 50:027101
13. Doshida Y (2009) Proc 81st Smart Actuators/Sensors Study Committee. JTTAS, Dec. 11, Tokyo